PSIT-1178/
TR-1407

FUNDAMENTAL STUDY OF ASH FORMATION AND DEPOSITION: EFFECT OF REDUCING STOICHIOMETRY

Final Report for Contract No. DE-AC22-93PC92190
Period: 4/1/93-6/30/95

Prepared by:

Lawrence E. Bool III and Joseph J. Helble
PSI Technologies

Naresh Shah, Anup Shah, Gerald P. Huffman, F.E. Huggins, K.R.P.M. Rao
University of Kentucky

Adel F. Sarofim and Taofang Zeng
Massachusetts Institute of Technology

Ralf Reschke, Dennis Gallien, and Thomas W. Peterson
Department of Chemical and Environmental Engineering
University of Arizona, Tucson, Arizona

Prepared for:

Department of Energy
Pittsburgh Energy Technology Center
P.O. Box 10940
Pittsburgh, PA 15236-0940

RECEIVED
OSTI
96 FEB 16 AM 11:10

MASTER

September 1995

PSI
PHYSICAL SCIENCES INC.
20 New England Business Center ▮ Andover, MA 01810-1077 ▮ U.S.A.

CLEARED BY
PATENT COUNSEL

DISTRIBUTION OF THIS DOCUMENT IS UNLIMITED

PSIT-1178/
TR-1407

FUNDAMENTAL STUDY OF ASH FORMATION AND DEPOSITION: EFFECT OF REDUCING STOICHIOMETRY

Final Report for Contract No. DE-AC22-93PC92190
Period: 4/1/93-6/30/95

Prepared by:

Lawrence E. Bool III and Joseph J. Helble
PSI Technologies

Naresh Shah, Anup Shah, Gerald P. Huffman, F.E. Huggins, K.R.P.M. Rao
University of Kentucky

Adel F. Sarofim and Taofang Zeng
Massachusetts Institute of Technology

Ralf Reschke, Dennis Gallien, and Thomas W. Peterson
Department of Chemical and Environmental Engineering
University of Arizona, Tucson, Arizona

Prepared for:

Department of Energy
Pittsburgh Energy Technology Center
P.O. Box 10940
Pittsburgh, PA 15236-0940

September 1995

DISCLAIMER

This report was prepared as an account of work sponsored by an agency of the United States Government. Neither the United States Government nor any agency thereof, nor any of their employees, makes any warranty, express or implied, or assumes any legal liability or responsibility for the accuracy, completeness, or usefulness of any information, apparatus, product, or process disclosed, or represents that its use would not infringe privately owned rights. Reference herein to any specific commercial product, process, or service by trade name, trademark, manufacturer, or otherwise does not necessarily constitute or imply its endorsement, recommendation, or favoring by the United States Government or any agency thereof. The views and opinions of authors expressed herein do not necessarily state or reflect those of the United States Government or any agency thereof.

TABLE OF CONTENTS

TABLE OF CONTENTS (cont.)

TABLE OF CONTENTS (cont.)

TABLE OF CONTENTS (cont.)

LIST OF ILLUSTRATIONS

LIST OF ILLUSTRATIONS (cont.)

LIST OF ILLUSTRATIONS (cont.)

LIST OF ILLUSTRATIONS (cont.)

LIST OF ILLUSTRATIONS (cont.)

LIST OF TABLES

LIST OF TABLES (cont.)

LIST OF TABLES (cont.)

LIST OF TABLES (cont.)

SECTION 1

EXECUTIVE SUMMARY

1. EXECUTIVE SUMMARY

The technical objectives of this project are:

a: To identify the partitioning of inorganic coal constituents among vapor, submicron fume, and fly ash products generated during the combustion of pulverized coal under a variety of combustion conditions. Fuel lean and fuel rich combustion conditions are considered.

b: To identify and quantify the fundamental processes by which the transformations of minerals and organically-associated inorganic species occur. Emphasis is placed on identifying any changes that occur as a result of combustion under sub-stoichiometric combustion conditions.

c: To incorporate the effects of combustion stoichiometry into an Engineering Model for Ash Formation based upon the understanding developed in (a) and (b). This model predicts the particle size and chemical composition distributions of ash formed during the combustion of pulverized coal under a broad range of conditions.

A description of the work followed to accomplish these objectives is presented in Section 2 of this report.

The work discussed in this report represents the highlights of this two year program. Major accomplishments during this program are summarized below.

(1) ***Coal Selection and Characterization***

Four U.S. coals were selected and acquired for this program. These coals were selected because (1) they were deemed representative of coals currently being burned at power plants in the U.S., and (2) contained the major minerals that have been identified, under certain conditions, with ash deposition. These coals were a run-of-mine Pittsburgh #8 coal, containing 27.7% ash by weight (dry basis), a washed Pittsburgh #8 coal, containing 7.6% ash by weight (dry basis), a beneficiated Pittsburgh #8 coal, containing 5.3% ash by weight (dry basis), and a Wyodak Anderson (Black Thunder) sub-bituminous coal, containing 5.9% ash by weight (dry basis). Silica dominated the chemical composition of the ash derived from all four coals. Calcium oxide was also present in high concentrations in the ash derived from the sub-bituminous coal. For the three Pittsburgh coals, the iron oxide content as a percentage of the ash increased with decreasing coal ash content.

In addition, Silverdale bituminous coal, a British coal, was obtained from the utility National Power. This coal contained 16.7% ash by weight (dry basis). It was characterized in detail, and tested extensively at bench scale through power plant scale combustion facilities, as part of a slagging program led by the utility PowerGen. Silverdale was studied by selected groups during the research program described herein.

(2) ***Coal Mineralogical Characterization***

Computer-controlled scanning electron microscopy (CCSEM), Mössbauer spectroscopy, and x-ray absorption fine structure (XAFS) spectroscopy were used to characterize the mineral matter in the coal. Mineral size and chemical composition distributions were thus generated for each of the five coals. Kaolinite and quartz were the dominant minerals detected in the Black Thunder coal. A calcium aluminum phosphate (crandallite) mineral phase was also detected (approx. 6 wt% of the mineral matter); this had not been observed in any coal previously examined by this research team. Illite, quartz, kaolinite, and miscellaneous silicates not corresponding to a distinct mineral phase

dominated the mineralogy of the three Pittsburgh seam coals. Pyrite content ranged from 12% for the run-of-mine coal to 27% for the washed coal and 21% for the beneficiated coal. Mössbauer analysis indicated the presence of significant amounts of non-pyritic iron forms in the beneficiated coal. These findings are discussed in detail in sections 3 and 4 of this report.

Combustion-derived ash was also analyzed by CCSEM, Mössbauer, and XAFS techniques. Results are described in Sections 4 to 7.

(3) ***In-situ XAFS determination of the forms of iron in ash***

In a separate program, researchers from PSI, the University of Kentucky, and the Division of Applied Sciences at Brookhaven National Laboratory designed and built a combustion test facility for the high temperature, atmospheric pressure, in-situ collection of XAFS data. The facility permitted in-situ XAFS measurements to be made of flowing ash particles and of ash deposits immediately downstream of a drop-tube furnace reactor exit.

In this program, experiments using pyrite and iron-rich coal fractions were conducted in the facility in an attempt to isolate the transformations of iron as a function of time and combustion conditions. Under sub-stoichiometric combustion conditions, the development of a sticky iron oxide-sulfide was observed and resulted in ash deposition within the drop tube furnace. These and other experiments, including a comparison of samples generated in the in-situ furnace with ash samples generated "off-line" in the PSI drop tube furnace, are described in detail in Section 4 of this report.

(4) ***Fate of iron during combustion under a range of stoichiometric conditions***

Understanding the effect of combustion conditions on iron aluminosilicate ash particle formation is important to imported predictions of ash deposit formation. Iron aluminosilicate particles have lower viscosities than either iron oxide or aluminosilicate ash particles, and therefore stick to boiler tube surfaces under a broader temperature range. Experiments using the Pittsburgh coals were conducted at PSI and MIT under a range of oxygen partial pressures (stoichiometric ratios). In general, iron aluminosilicate particles formed under all combustion conditions, with the amount of crystalline iron oxide decreasing with increasing partial pressure of oxygen. Both Fe(II) and Fe(II) containing aluminosilicate particles were formed, with the ratio {Fe in glass as Fe(III) / Fe in glass as Fe(II)} increasing with increasing oxygen partial pressure. Because iron in the (+2) oxidation state creates a lower viscosity ash particle, deposition attributed to iron aluminosilicate particles may be more severe under low oxygen combustion conditions. These results are described in detail in Sections 5 and 7 of this report.

Experiments using iron in prepared glass samples were subsequently conducted to explore the effect of iron oxidation state on particle deposition. Glass particles of mass median diameter 20 μm, containing 20% by weight iron oxide (all of which was in the {+2} oxidation state) were impacted on ceramic tubes under a range of temperatures and oxygen partial pressures. Particle collection efficiency, a measure of deposition, decreased by a factor of 2-4 when the iron in the ash particles was oxidized to Fe(III). A melt diffusion controlled model of iron oxidation fit the data within the uncertainty of the experiments, suggesting that diffusion of oxygen through the glass controlled the rate of glassy iron oxidation. This study confirmed the importance of viscosity in determining particle deposition potential, and illustrated the role iron oxidation state plays in determining viscosity. These results are described in detail in Section 7.

(5) ***Effect of coal weathering on formation of an iron-containing fume***

In the scientific literature, a range of values have been reported for the amount of iron that is present in the submicron fume resulting from coal combustion. Values of less than 1% have been reported and attributed to the relative non-volatility of iron compounds during coal combustion, whereas values as high as 40 to 60% of iron being present in the submicron fume have also been reported. These higher values have been attributed to the reactive decomposition of pyrite. The wide range in reported iron values had been attributed to coal weathering; i.e. the suggestion that iron release is suppressed when the pyrite in coal has been slightly oxidized. To assess this hypothesis, samples of unweathered Illinois #6 coal were obtained from the Penn State University Coal Bank. Mössbauer analysis of the coal for forms of iron found that all of the iron was present in pyrite of clay minerals. No evidence for oxidized iron was found. Combustion experiments were conducted with this coal, and the resulting submicron fume examined for iron content. Less than 1% of the iron was found to be present in the submicron size range. These results are discussed in Section 7 of this report.

(6) ***Model of iron partitioning during coal combustion***

A model of iron partitioning during coal combustion developed under prior DOE funding was modified under this program. Specifically, the original model contains an adjustable parameter for the ratio of iron to silicate in combustion-derived aluminosilicate ash particles. The effect of system parameters (temperature, time, mineral particle size) on this parameter was examined, and used to derive a modified parameter in the model. Using the modified model, calculations were run and compared to results generated using the original model. Compared to experimental data, the new model produced slightly better agreement. This is discussed in Section 6 of this report.

(7) ***Effect of stoichiometric ratio on ash formation***

In general, the formation of non iron-containing ash phases was not greatly affected by changes in combustion conditions. For the Pittsburgh coals, the extent of calcium aluminosilicate formation decreased with decreasing stoichiometric ratio, a result of reduced interaction between calcite and clay minerals under sub-stoichiometric conditions (which resulted in incomplete char burnout). The Wyodak Anderson (Black Thunder) sub-bituminous coal showed little difference in the extent of calcium aluminosilicate formation with changing combustion conditions; the small change in burnout associated with changing stoichiometric ratio is believed responsible. These results are described in Sections 5 and 7 of this report.

(8) ***Effect of carbon on ash stickiness and deposition***

In this program, experiments conducted under sub-stoichiometric combustion conditions resulted in incomplete carbon burnout for all of the Pittsburgh coals. Experiments were conducted to examine the effect of the residual carbon in the ash on ash particle deposition. Results indicated that a critical carbon content existed; for carbon contents below the critical carbon content, carbon has little or no effect on ash stockiness. For higher carbon contents, however, ash stickiness decreased with increasing carbon content, with the decrease proportional to the carbon content of the ash. These results are discussed in Section 7 of this report.

(9) ***Engineering Model for Ash Formation (EMAF)***

The Engineering Model for Ash Formation (EMAF), which predicts coal-dependent ash particle size and chemical composition distributions, was modified during this program to describe the effects of char fragmentation and fuel-rich combustion. Predictions made with the modified version of EMAF were then compared with experimental data generated during this and other research programs. Improved fit to experimental data was observed with the incorporation of

these modifications. A parametric study of the effect of various model parameters on char structure and subsequently on ash particle size and composition distributions was also conducted. These results are described in detail in Section 8 of this report.

These results are described in the remainder of this report, with sections divided according to sub-topic and further by the group performing the work. Specifically, the report is broken down as follows:

In Section 3 the four program coals, and the PowerGen coal are discussed in detail. These coals include a sub-bituminous Black Thunder coal and three Pittsburgh No. 8 coals (a run-of-mine, a washed coal, and a beneficiated coal). The coal provided by PowerGen was a Silverdale bituminous coal. Standard coal analysis including ultimate, proximate, and ASTM ash are presented in Section 3. Data from more sophisticated analysis, including CCSEM and Mössbauer, are also presented.

In Section 4, the CCSEM and Mössbauer analysis of the individual coals is reported in detail by the University of Kentucky (UKy). Ash from short residence time and reducing condition combustion experiments at PSIT was also analyzed and the data presented. Data from ash samples from combustion experiments at DoE/PETC, Massachusetts Institute of Technology (MIT), and the University of Arizona (UA) are also presented in detail. In general, the data from these combustion experiments suggest that the degree of mineral interaction decreased with decreasing stoichiometric ratio. Further, the amount of lower oxidation state iron (eg; magnetite and Fe(II) in glassy particles) increases with decreasing stoichiometric ratio. Deposit samples obtained by PowerGen during field testing, and from PSIT deposition experiments are also presented. Finally, Section 4 discusses in detail the development and use of the in-situ XAFS reactor at Brookhaven National Laboratory.

In Section 5, results obtained during combustion studies at MIT of size-segregated samples of the washed Pittsburgh No. 8 coal are presented. Experiments were conducted at a gas temperature of 1650 K and under oxygen concentrations of 0 to 100% in nitrogen. As expected, the extent of inorganic species vaporization increased with increasing partial pressure of oxygen. A model to predict iron vaporization was developed based on these results.

The development of the UA iron evolution model is described in Section 6. Specifically, a model was developed to predict iron partitioning into iron oxide or iron containing glass (or residual pyrite products). A sub-model was also developed to describe the crystallization of iron from an oxidized melt at temperatures less than 1600 K. Work initiated to better define the empirical fit parameters in the model is also described. Both the original model and the modified model were found to be in good agreement with experimental data from the self-sustained combustor at UA. Experiments in the drop tube facility at UA are also discussed. This discussion includes a description of the facilities and experimental procedures and presentation of the iron partitioning data for experiments with the washed Pittsburgh No. 8. Data from these experiments suggested that significant unburned carbon and unreacted pyrite remains at low stoichiometric ratios (reducing conditions).

In Section 7, experimental results obtained during combustion experiments with the program coals, including the Silverdale coal, are described by PSI Technologies (PSIT). These results demonstrate the effect of carbon, present at short residence times or under reducing conditions, on ash deposition. In general, carbon contents above a critical value were found to decrease ash stickiness. The behavior of iron under these conditions is also presented. Experiments with synthetic ashes were performed to determine the effect of iron oxidation state on ash stickiness and to determine the controlling mechanism for iron oxidation in glassy melts. These experiments indicated that increasing the Fe(II)/Fe(III) ratio in the glassy ash particles dramatically increases ash stickiness. In addition, the data suggested that oxidation of the iron

in the glass was melt diffusion controlled. The data, and a model based on the data, are presented in Section 7. Also in Section 7, a discussion of the formation of an iron containing fume during combustion of a pristine Illinois No. 6, is provided. These experiments contradicted the proposed non-vaporization mechanism for iron fume formation presented in the literature by other researchers in the literature.

Section 8 consists of a discussion of the Engineering Model for Ash Formation (EMAF). This model was modified during the program to incorporate the effects of char fragmentation (from cenospheric chars) on ash formation. The model was then validated with data from drop tube experiments and field tests. Also included in Section 8 is a discussion of the model for submicron fume formation that was developed under separate funding; the discussion is included because the model is important to this work. Finally, modifications to incorporate the dominant effects of combustion under reducing conditions, low combustion temperatures and incomplete burnout, are described. Predictions from the modified model are then compared with the data discussed in Section 7. In general, the model accurately predicted the trend of decreased mineral interaction with decreasing stoichiometric ratio.

SECTION 2

OVERVIEW OF PROGRAM TASKS
(PSI Technologies)

2. OVERVIEW OF PROGRAM TASKS

This project is designed to examine the effects of combustion stoichiometry on the fundamental aspects of ash formation and ash deposit initiation. Emphasis will be placed on reducing stoichiometries associated with low-NOx combustion, although a range of oxidant/fuel ratios will be considered. Previous work has demonstrated that ash formation depends strongly upon coal mineralogy, including mineral type, size, amount, and the presence of organically associated inorganic species. Combustion temperature and the oxidation state of iron will also play a significant role. As these latter items will vary with changes in stoichiometry, research to determine the net effect on deposition is required.

To achieve these goals, a research program with the following technical objectives will be pursued:

(1) identify the partitioning of inorganic coal constituents among vapor, submicron fume, and fly ash products generated from the combustion of pulverized coal under a variety of combustion stoichiometries. Fuel-lean and fuel-rich combustion conditions will be considered.

(2) identify and quantify the fundamental processes by which the transformation of minerals and organically-associated inorganic species occur. Identify any differences from standard pulverized coal combustion conditions.

(3) modify, to incorporate the effects of combustion stoichiometry and based on the understanding developed in (1) and (2) above, an Engineering Model for Ash Formation. The previously developed model is capable of predicting the size and chemical composition distributions of the final ash products under standard pulverized coal combustion conditions of 20% excess air. These modifications will extend the model to include phenomena that may be dominant under a broad range of stoichiometries.

Experiments, sample analyses, and modeling will be conducted at several facilities as part of this program. Detailed coal and ash sample analysis using Mössbauer spectroscopy, x-ray absorption fine structure spectroscopy (XAFS), and computer controlled scanning electron microscopy will be carried out at the University of Kentucky (UKy). Small-scale drop tube combustion tests using size and density classified coal samples and possibly synthetic char samples will be carried out at the MIT to determine the extent of mineral coalescence and inorganic vaporization as a function of combustion stoichiometry. Combustion experiments utilizing utility grind coals will be conducted at PSI to examine the effects of stoichiometry on mineral interactions. Deposition experiments using ash generated from combustion experiments and using pure minerals will also be conducted to investigate deposit initiation as a function of combustion conditions. The engineering model for ash formation (EMAF) will be modified to include effects of combustion stoichiometry as part of this effort. Self-sustained pilot scale combustion experiments will be conducted in the University of Arizona (UA) 100,000 Btu/h facility to address issues of scaling in combustion processes. The interaction of iron with aluminosilicates as a function of changing combustion conditions will be the focus of this effort. Modeling of the iron-aluminosilicate interaction process will be conducted as part of the UA study. Finally, interaction with an integrated program led by the utility PowerGen will be used to address issues of deposit formation at full scale for comparison with the bench and laboratory scale results of this program. A work breakdown structure containing a brief

description of each task follows. The relationship among the participants is illustrated schematically in Figure 2-1.

Task 1 - Program Planning, Management, Reporting, and Peer Review

This task, to be performed by PSI Technologies, consists of: (1) preparing and annually updating a program plan; (2) coordinating, managing, and integrating the subcontracts and project results; (3) preparing project monthly reports; (4) integrating and preparing project quarterly reports; (5) integrating and preparing the program final report; (6) conducting annual peer review and project coordination meetings with the project principal investigators, either as a separate meeting or in conjunction with a technical conference, and including when appropriate the principal investigators of other DoE-supported ash formation research programs identified by the DoE project manager; and (8) acquiring and distributing coals to all of the project principal investigators.

Task 2 - Fundamental Study of Ash Formation and Deposit Initiation Under Reducing Conditions (PSI Technologies)

PSI will study the effect of combustion stoichiometry on mineral matter and inorganic species transformations with an emphasis on sub-stoichiometric combustion. This will occur through a series of experiments to be conducted in a well-characterized laboratory flow reactor on a minimum of two coals. Coal blends may also be examined if of benefit to the program and of mutual interest to PSI and DoE/PETC. One or more of the coals studied in this task may be coals previously studied at PSI under DoE contract number DE-AC22-86PC90751 to permit a direct comparison with results obtained under oxidizing conditions. Model mineral compounds will also be examined as necessary to identify the importance of the oxidation state of iron in determining mineral coalescence and ash deposition. Selection of any coal samples will be coordinated with the DoE/PETC program manager.

PSI will also conduct limited experiments to determine the effect of pyrite weathering on the evolution of an iron oxide fume. These experiments will be coordinated with a similar study at Sandia National Laboratories.

PSI will also conduct in-situ combustion experiments in conjunction with the University of Kentucky and Brookhaven National Laboratories using an in-situ combustion reactor at beamline X19-A of the National Synchrotron Light Source.

Activities under this task will include collection and examination of ash samples at varying combustion temperatures and/or oxidant concentrations. Ash samples will be collected using extractive sampling. In-situ deposit collection techniques will be used to measure ash particle collection efficiencies as a function of temperature and stoichiometric ratio. Extracted ash and deposit samples will be characterized as necessary to determine particle size and chemical composition distributions as well as the chemical state of key components such as iron and calcium.

Task 3 - PowerGen Collaboration (PSI)

In order to understand the effects of combustion scale on ash formation and deposition under reducing conditions, PSI will interact with a government and industrial program currently underway in Great Britain. Led by the utility PowerGen, this program includes experiments at scales ranging from fundamental bench reactors to operating power plants. As part of a collaborative effort, PSI hopes to conduct laboratory experiments either at PSI, at BNL on the in-situ XAFS combustor, or in both reactors

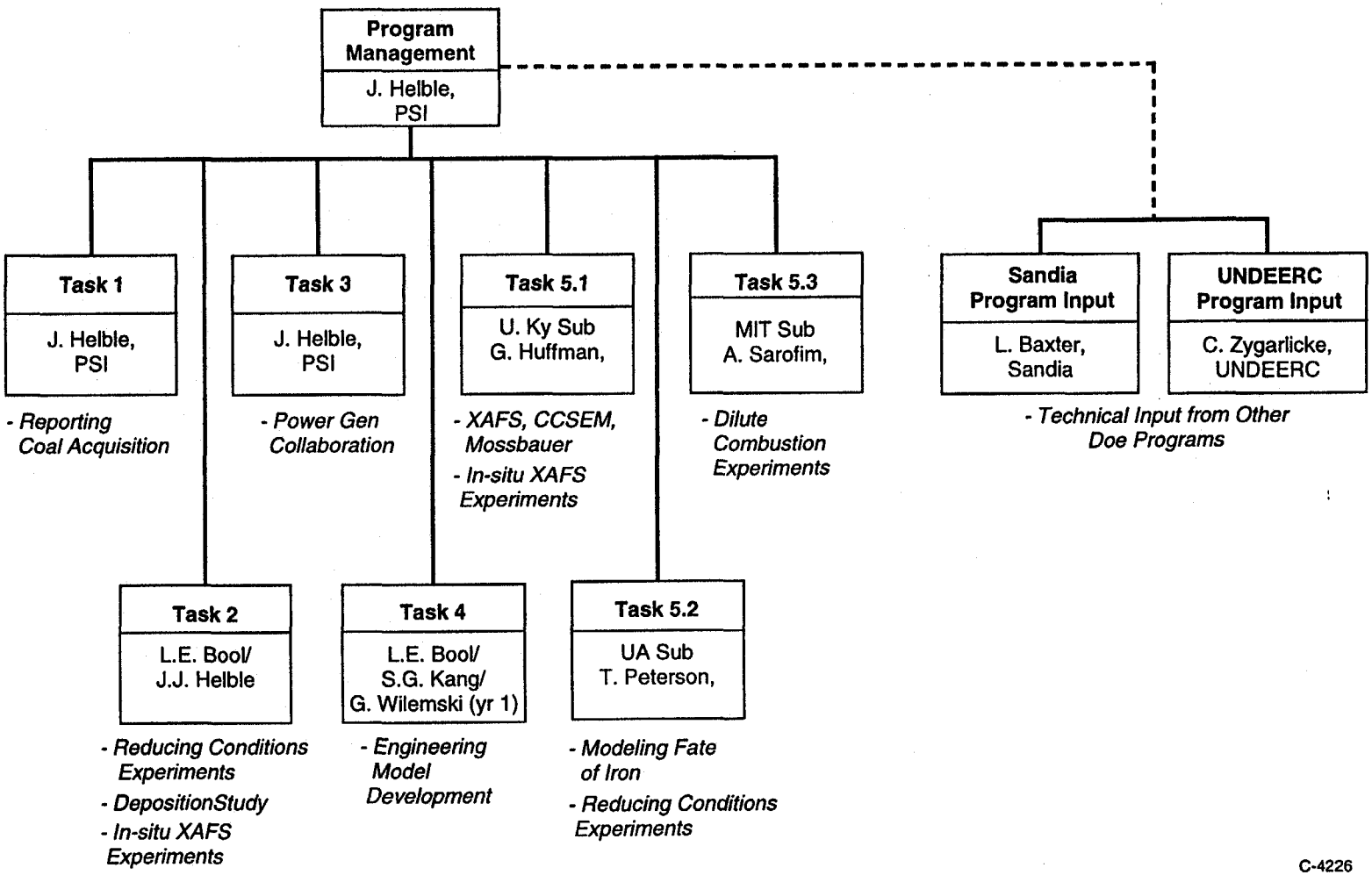

Figure 2-1. Program structure.

under a range of combustion conditions using a coal provided by PowerGen. If deemed appropriate by PSI, UA, and the DoE/PETC Program Manager, UA may also conduct combustion experiments with one of these coals. These experiments will permit direct comparison of results obtained in this project with those obtained at full scale in the PowerGen program. This interchange will also add to the database used in the modifications of the engineering model for ash formation described under Task 4.

Task 4 - Engineering Model for Ash Formation (PSI)

The results obtained by the organizations participating in this project will be applied by PSI to revise, test, and validate the EMAF developed previously. The work on this subtask includes analyzing the experimental results and identifying data and technical information related to extending EMAF. Specific areas of interest include the formation of ash under reducing stoichiometries, the formation (particularly the chemical composition) of the submicron ash fume, and the influence of char fragmentation on ash formation. As part of this task, PSI will also coordinate modeling activities to be conducted by the MIT and UA subcontractors.

Task 5.1 - Advanced Techniques for Coal and Ash Characterization Including In-situ XAFS Measurements (UKy)

The University of Kentucky will apply advanced analytical techniques such as computer-controlled scanning electron microscopy (CCSEM), Mössbauer spectroscopy, and x-ray absorption fine structure spectroscopy (XAFS) to characterize coal and ash samples from this program as needed by the individual principal investigators. If agreed upon by PSI, UKy, and the DoE program manager, UKy will also analyze selected coal and/or ash samples obtained from the PowerGen program in Great Britain.

As part of this task, UKy will conduct dynamic in-situ XAFS experiments at the Brookhaven National Laboratories (BNL) National Synchrotron Light Source (NSLS) with PSI and BNL using an in-situ drop tube furnace previously constructed by PSI. Static in-situ measurements at elevated temperatures will also be conducted using a cell previously built by UKy. The in-situ measurements will be used to investigate phenomena such as the transformation of pyrite under various conditions, the formation of iron aluminosilicate compositions as a function of combustion conditions, the formation of calcium aluminosilicate ash compositions as a function of combustion conditions, and the composition and oxidation state of key components in sticky, depositing ash particles as a function of combustion conditions.

Task 5.2 - Pulverized Coal Combustion Studies Under Reducing Conditions in a Continuous, Self-sustained Laboratory Scale Reactor (UA)

UA will conduct experiments to assess the interaction of iron and aluminosilicate minerals under reducing combustion conditions. UA will also examine the amount and chemical composition of the submicron fume generated under reducing conditions. This study will be conducted in the UA self-sustained 100,000 Btu/h combustion facility. UA will conduct this study using at least one of the coals studied by PSI and MIT under this program and including at least one coal studied previously under oxidizing conditions. As part of the experimental effort, UA will conduct Auger analyses for samples provided by other principal investigators on an as-needed basis. UA will also conduct Mössbauer analysis on selected ash samples generated at UA.

Based upon the results generated in this program, UA will modify the previously developed model for iron aluminosilicate formation to incorporate additional coals and/or combustion conditions.

Task 5.3 - Fundamental Study of Mineral Interactions and Ash Vaporization Under Reducing Conditions (MIT)

MIT will conduct drop tube experiments to study the fundamental aspects of ash formation under sub-stoichiometric conditions using narrowly sized and density classified coal samples and/or synthetic char samples. Size segregated chemical composition measurements will be conducted to assess the release of inorganic species to the vapor phase under sub-stoichiometric conditions. MIT will also conduct fundamental coalescence experiments under reducing conditions to elucidate the mechanism and rate of interaction of key mineral pairs. MIT will assist in the EMAF model testing and validation as described under Task 4.

SECTION 3

TASK 1: COAL SELECTION, ACQUISITION, AND CHARACTERIZATION
(PSI Technologies)

3. COAL SELECTION, ACQUISITION, AND CHARACTERIZATION

Five coals were studied under this program. These coals were 1) Black Thunder Powder River Basin sub-bituminous coal obtained from the University of North Dakota Energy and Environmental Research Center (EERC), 2) a run-of-mine Pittsburgh No. 8 Appalachian Basin bituminous coal, obtained from the mine, 3) a washed Pittsburgh No. 8 bituminous coal, obtained from the Pittsburgh Energy Technology Center of the US Department of Energy (DOE/PETC), 4) a beneficiated product produced from Pittsburgh No. 8 coal, being studied under another DOE/PETC supported program at ABB/Combustion Engineering and obtained from them, and 5) a Silverdale bituminous from England, being studied as part of an ash formation program led by the utility PowerGen; this coal was obtained from National Power.

Not all coals were studied by all participants in this program. A matrix identifying the coals examined by each group is provided in Table 3-1.

Table 3-1. Utilization of Program Coals

Group	Black Thunder	R.O.M. Pitt. 8	Washed Pitt. 8	Beneficiated	Silverdale
PSIT	X	X	X	X	X
U. Kentucky	X	X	X	X	X
MIT				X	
U. Arizona		X	X		

3.1 Black Thunder sub-bituminous

The Black Thunder coal was obtained from the EERC at the University of North Dakota. Ultimate and proximate analyses for this coal are reported in Table 3-2. A chemical analysis of the coal ash is reported in Table 3-3. The results of chemical fractionation of the coal for identification of the associations of the major inorganic elements are provided in Table 3-4. All analyses were provided by EERC.

The fractionation analysis shown in Table 3-4 indicated that the majority of the calcium, magnesium, and sodium within Black Thunder were extractable, indicative of organic association. Silicon, aluminum, and potassium were relatively insoluble, indicative of mineral forms of occurrence. Iron demonstrated a high acid-soluble fraction, suggesting that a portion of this element may have been present as iron carbonate or sulfate rather than as pyrite or as iron oxide.

The mineralogy of this coal was determined by computer controlled scanning electron microscopy (CCSEM) at the University of Kentucky as part of Task 5.1 of this program. Detailed results are provided in Section 4 of this report. CCSEM of this, and other program coals, were also provided by other laboratories. An inter-laboratory comparison can be seen in Appendix A.

Table 3-2. Ultimate and Proximate Analysis of Black Thunder Sub-bituminous Coal

	As-received	Dry
Proximate (wt %)		
Moisture	24.30	-
Volatile Matter	35.89	47.42
Fixed Carbon	35.32	46.64
Ash	4.49	5.94
Ultimate (wt %)		
C	52.84	69.83
H	7.04	5.73
N	0.70	0.92
O (ind)	34.54	17.07
S	0.39	0.51
Ash	4.49	5.94
Calculated HHV, Btu/lb	9,620	

Table 3-3. Ash Chemical Analysis - Black Thunder Sub-bituminous Coal (wt% of ash)

SiO_2	32.57
Al_2O_3	16.81
Fe_2O_3	5.69
CaO	22.09
MgO	4.79
Na_2O	0.93
K_2O	0.15
TiO_2	1.11
P_2O_5	1.17
SO_3	14.69

Table 3-4. Chemical Fractionation of Black Thunder Sub-bituminous Coal (wt%, normalized to zero Si loss)

Element	Initial Conc. in coal (ppm)	Removed by H_2O	Removed by NH_4OAc	Removed by HCl	Remaining (insoluble)
Si	7750	0	0	0	100
Al	4530	0	0	20	80
Fe	2020	8	0	70	22
Ti	340	0	0	19	81
P	261	3	0	87	10
Ca	8030	1	58	39	2
Mg	1470	0	72	22	5
Na	350	22	64	10	4
K	62	15	0	0	85

From the EERC CCSEM and chemical fractionation analyses, an approximate measure of the distribution between mineral-bound inorganic species and organically associated inorganic species can be derived. As shown in Table 3-5, CCSEM analysis indicates that mineral matter comprises 2.5 wt % of Black Thunder. The ultimate and proximate analyses of this coal indicated an ash content of 4.5 wt %, providing by subtraction an organically associated inorganic content of 2 wt %.[1] Chemical fractionation results compare favorably. If the elemental concentrations reported in Table 3-4 are converted to oxides, a total ash content of 4.3 wt % (sulfur-free basis) is obtained. In comparison, a sulfur-free ash content of 3.85% is obtained from ultimate/proximate and ash chemical composition analyses. The fraction of mineral matter in the coal, based on insoluble residues reported in the chemical fractionation analysis, was found to be 2.5%, or 2.7% if the HCl-extractable iron is included in the mineral total. From these analyses, it is concluded that approximately 60% of the Black Thunder coal inorganic species were mineral bound and 40% were inorganically associated.

A mineral size distribution for the EERC Black Thunder coal is given in Table 3-6. Greater than 60% of the minerals were less than 10 μm in diameter on an area percentage basis. Quartz, kaolinite, and other aluminosilicates were concentrated in the smaller particle sizes. Although little pyrite was detected, that found was generally greater than 22 μm in diameter. Included/excluded analysis of the EERC Black Thunder sample is provided in Table 3-7. Approximately 43% of the mineral matter was determined to be excluded from coal particles.

---

[1]Subtracting the weight percentage of mineral matter from the weight percentage of ash to obtain the weight percentage of inorganically associated inorganic species is not strictly accurate. Consideration must be given to the oxidation of minerals and organically associated inorganic species in the coal. The 2% figure quoted here therefore represents the weight percentage of organically associated inorganic species reported as oxides. For a high pyrite or calcite content coal, this approximation would be inaccurate because of the need to incorporate oxygen in converting CCSEM mineral weights to bulk ash chemistry weights (the latter always reported as oxides). Because of the low pyrite and calcite content of Black Thunder, the approximation - treating the mineral weights as oxidized weights - can be made.

Table 3-5. Distribution of Inorganic Species Between Mineral and Organically Associated Phases - Black Thunder coal

Analysis	Wt% Ash	Wt% Ash (S-free)	Wt% Minerals	Wt% Organ. Assoc.
ult/prox/ash	4.5	3.85	-	-
CCSEM*	-	-	2.6	1.9
chem. fract.+	-	4.3	2.5-2.7	1.6-1.8
* percent organically associated by difference (from total percent ash)				
+ on a sulfur-free basis (sulfur not measured during chemical fractionation)				

Table 3-6. Mineral Size Distribution Analysis for Black Thunder Coal by CCSEM (basis: % of mineral area)

Mineral	1 - 2.2 μm	2.2 - 4.6 μm	4.6 - 10 μm	10 - 22 μm	22 - 46 μm	46 - 100 μm
Quartz	18	15	28	14.5	21	3.5
Iron Oxide/Carb.	9.5	13	29.5	20	28	0
Kaolinite	13	29	22	17	13	6
Aluminosilicate	5	20	10	53	2	10
Montmorillonite	6	28	9	30	16	11
Pyrite	11	0	2	47	12	29
Ca Al Phosphate	16	31	40.5	9.5	2	0
Unknown	43	14	17	7	12	7
Total	16.0	23.2	22.9	17.5	13.5	7.0

CCSEM data for the PSIT sample of Black Thunder, as determined by UK, are provided in Section 4 of this report. Complete summaries of all Black Thunder CCSEM data are provided in Appendix A of this report.

Table 3-7. Excluded Mineral Analysis of Black Thunder Coal by CCSEM

Mineral	% of individual mineral area in each size bin that is excluded						Total % of mineral excluded
	1 - 2.2	2.2 - 4.6	4.6 - 10	10 - 22	22 - 46	46 - 100	
Quartz	28	37	41	37	56	100	43
Iron Ox./Car.	31	30	87	0	80	0	55
Kaolinite	50	66	31	23	36	30	43
Aluminosil.	30	88	63	30	100	100	53
Montmorill.	0	27	38	92	86	100	63
Pyrite	78	0	0	69	70	100	78
Ca Al P	18	39	11	0	0	0	19
Unknown	22	22	28	0	44	100	29
Total	31	46	34	37	52	74	43

3.2 Run-of-mine Pittsburgh No. 8 bituminous

A run-of-mine Pittsburgh No. 8 coal, representative of the parent of washed and beneficiated Pittsburgh No. 8 coals also under study here, was evaluated in this program. Ultimate and proximate analyses of this coal are reported in Table 3-8. Bulk ash chemical analysis is provided in Table 3-9. A coal particle size distribution, measured with a Malvern Instruments diffraction-based particle sizer, is reported in Table 3-10.

Table 3-8. Ultimate and Proximate Analysis of Run-of-Mine Pittsburgh No. 8 Bituminous Coal

Proximate (wt %)	As-received	Dry
Moisture	2.00	-
Volatile Matter	30.76	31.40
Fixed Carbon	40.09	40.88
Ash	27.15	27.72
Ultimate (wt %)		
C	57.16	58.35
H	4.00	3.86
N	0.98	1.00
O (ind)	8.43	6.76
S	2.28	2.32
Ash	27.15	27.72
Calculated HHV, Btu/lb	10,040	

Table 3-9. Ash Chemical Analysis of Run-of-Mine Pittsburgh No. 8 Bituminous Coal (wt% of ash)

SiO_2	54.82
Al_2O_3	23.06
Fe_2O_3	10.52
CaO	3.48
MgO	2.26
Na_2O	0.50
K_2O	1.74
TiO_2	0.87
P_2O_5	0.13
SO_3	2.63

Table 3-10. Coal Particle Size Distribution - Run-of-Mine Pittsburgh #8

Size Microns	% Under	% in band	Size Microns	% Under	% in band	
118.4	100.0	0.0	11.1	57.1	4.5	
102.1	100.0	0.1	9.6	52.6	4.8	
88.1	99.9	0.3	8.3	47.8	5.6	
76.0	99.6	0.6	7.2	42.2	6.1	
65.6	99.0	1.0	6.2	36.1	6.2	
56.6	98.0	1.5	5.3	29.9	5.8	
48.8	96.6	2.0	4.6	24.1	5.4	
42.1	94.6	2.7	4.0	18.8	5.3	
36.3	91.9	3.4	3.4	13.4	5.0	D(v,0.5)=8.9 µm
31.3	88.5	3.9	3.0	8.5	4.0	D(v,0.9)=33.3 µm
27.0	84.7	4.0	2.6	4.5	2.6	D(v,0.1)=3.1 µm
23.3	80.7	3.9	2.2	1.9	1.0	D(4,3)=13.4 µm
20.1	76.8	4.2	1.9	0.9	0.4	D(3,2) = 7.0 µm
17.4	72.6	5.1	1.6	0.5	0.1	
15.0	67.5	5.4	1.4	0.4	0.2	
12.9	62.2	5.0	1.2	0.2		

Coal mineral analysis was provided by UK using a small sample of coal provided by PSIT. Results of this analysis are provided in Section 4 of this report. UK data were used in subsequent comparisons of coal mineralogy with combustion-derived ash; MTI data (discussed in Appendix A) were used to provide an indication of the included and excluded mineral content.

Included/excluded mineral data for the run-of-mine Pittsburgh No. 8 are provided in Table 3-11. For this coal, over 80% of the mineral matter was identified as being excluded from the coal organic matrix.

Table 3-11. Excluded Mineral Analysis for Run-of-Mine Pittsburgh No. 8 Coal by CCSEM (data in this table are ZAF corrected).

Mineral	% of individual mineral area in each size bin that is excluded						Total % of mineral excluded
	1 - 2.2 μm	2.2 - 4.6 μm	4.6 - 10 μm	10 - 22 μm	22 - 46 μm	46 - 100 μm	
Quartz	77	90	87	78	94	100	87
Kaolinite	59	68	67	65	90	100	69
Montmorill.	86	88	62	100	96	100	84
K-Al Silicate	79	85	71	84	86	100	84
Pyrite	74	63	47	91	87	100	77
Misc. Sil.	81	85	84	86	94	100	86
Unknown	79	93	69	88	90	100	85
Total	79	84	78	85	89	100	83

3.3 Washed Pittsburgh No. 8 bituminous

A washed Pittsburgh No. 8 coal, having a lower ash content than the run-of-mine Pittsburgh No. 8 described in Section 3.2, was also studied in this program. This coal is considered representative of a commercial Pittsburgh #8. Ultimate, proximate, and ash chemical analyses for this coal are provided in Tables 3-12 and 3-13. A coal particle size distribution, measured with a Malvern Instruments diffraction-based particle sizer, is provided in Table 3-14. The measured coal particle size distribution was similar to that measured for the run-of-mine Pittsburgh No. 8 coal (Table 3-10). CCSEM analysis for this coal was provided by UK and is discussed in detail in Section 4 of this report.

Table 3-12. Ultimate and Proximate Analysis of DOE Pittsburgh No. 8 Bituminous Coal

Proximate (wt %)	As-received	Dry
Moisture	1.40	-
Volatile Matter	36.85	37.36
Fixed Carbon	54.27	55.06
Ash	7.48	7.58
Ultimate (wt %)		
C	77.05	78.11
H	4.79	4.70
N	1.39	1.41
O (ind)	7.40	6.27
S	1.89	1.92
Ash	7.48	7.58
Calculated HHV, Btu/lb	13,560	

Table 3-13. Ash Chemical Analysis of DOE Pittsburgh No. 8 Bituminous Coal (wt% of ash)

SiO_2	46.81
Al_2O_3	25.03
Fe_2O_3	14.76
CaO	4.80
MgO	1.71
Na_2O	0.94
K_2O	1.02
TiO_2	0.72
P_2O_5	0.19
SO_3	4.02

Table 3-14. Coal Particle Size Distribution - Washed DOE Pittsburgh #8

Size Microns	Under	% in band	Size Microns	Under	% in band	
118.4	100.0	0.2	11.1	47.7	5.1	
102.1	99.8	0.5	9.6	42.6	5.5	
88.1	99.4	0.7	8.3	37.1	6.3	
76.0	98.6	1.0	7.2	30.8	6.1	
65.6	97.6	1.1	6.2	24.8	5.0	
56.6	96.5	1.3	5.3	19.8	3.9	
48.8	95.2	1.6	4.6	15.9	3.3	
42.1	93.6	2.3	4.0	12.7	3.3	
36.3	91.3	3.2	3.4	9.4	3.3	D(v,0.5)=11.1 μm
31.3	88.1	4.1	3.0	6.1	2.8	D(v,0.9)=34.0 μm
27.0	84.0	4.8	2.6	3.3	1.2	D(v,0.1)=3.5 μm
23.3	79.3	5.4	2.2	2.0	0.9	D(4,3)=15.3 μm
20.1	73.8	6.2	1.9	1.1	0.4	D(3,2) = 8.5 μm
17.4	61.7	7.2	1.6	0.7	0.2	
15.0	60.4	6.9	1.4	0.5	0.2	
12.9	53.5	5.8	1.2	0.3		

3.4 Beneficiated Pittsburgh No. 8 bituminous

A beneficiated Pittsburgh No. 8 coal was also examined in this program. The fuel is a product being studied under the DOE/PETC supported ABB/Combustion Engineering (ABB/CE) program "Combustion Characterization of Beneficiated Coal-based fuels." Ultimate and proximate analyses for the specific sample being studied by PSIT and MIT under this program are compared with the ABB/CE bulk sample and with a smaller sample examined previously at PSIT. The analyses were similar (Table 3-15), with the high moisture level in the bulk ABB/CE sample being the major difference. Analysis of the moisture content of the PSIT sample by PSIT using the temperatures, sample mass, atmospheric composition, and time specified in ASTM standard procedure number D-3173 yielded a moisture content of 2.0%. Chemical analysis of the coal ash was provided by ABB/CE and is given in Table 3-16. CCSEM analysis was provided by UK and is discussed in Section 4 of this report.

3.5 Silverdale bituminous

In addition to the four US coals, a British bituminous coal was also studied. This coal, Silverdale, was one of three coals studied in depth in a slagging program currently concluding in the UK. Participants in the UK program included the utilities PowerGen and National Power, Imperial College, Bristol University, British Coal, and Babcock Energy; tests ranging from bench scale to field trials were conducted. The utility National Power provided a sample of Silverdale to PSIT as part of a collaborative effort with our program. Ultimate and proximate analyses of the Silverdale coal are provided in Table 3-17. Ash chemical analysis is provided in Table 3-18. All data were provided by Imperial College.

Table 3-15. Ultimate and Proximate Analysis of Beneficiated Pittsburgh No. 8 Bituminous Coal

	This sample.		ABB/CE analysis	
Proximate (wt %)	As-received	Dry	Dry (1992 PSI sample)	Dry (ABB/CE sample)
Moisture	2.00	-	-	-
Volatile Matter	36.37	37.13	39.4	35.7
Fixed Carbon	56.42	57.55	55.7	59.1
Ash	5.21	5.32	4.9	5.2
Ultimate (wt %)				
C	77.22	78.83	79.9	80.6
H	5.51	5.39	5.3	5.0
N	1.37	1.40	1.5	1.4
O (ind)*	8.98*	7.33*	6.7	6.1
S	1.71	1.74	1.7	1.8
Ash	5.21	5.32	4.9	5.1
Calculated HHV, Btu/lb	13,900	14,200	14,400	14,450

Table 3-16. Ash Chemical Analysis of Beneficiated Pittsburgh No. 8 Bituminous Coal (wt% of ash)

Compound	1992 PSI sample	ABB/CE sample
SiO_2	49.2	42.7
Al_2O_3	24.8	25.2
Fe_2O_3	19.0	20.8
CaO	2.4	2.8
MgO	1.2	1.0
Na_2O	0.6	0.1
K_2O	1.2	1.3
TiO_2	1.1	1.4
P_2O_5	0.5	0.4
SO_3	2.4	2.6

Table 3-17. Ultimate and Proximate Analysis of Silverdale Bituminous Coal

Proximate (wt%) (as determined)	
Moisture	1.9
Volatile matter	32.6
Fixed carbon	49.1
Ash	16.4
Ultimate (wt%) (dry basis)	
C	67.8
H	4.7
N	1.6
O (difference)	5.8
S	3.4
Ash	16.7
HHV, Btu/lb (daf)	14,740

Table 3-18. Ash Chemical Analysis -- Silverdale Bituminous Coal (wt% of ash)*

SiO_2	44.5
Al_2O_3	24.5
Fe_2O_3	22.0
CaO	2.4
MgO	1.0
Na_2O	0.6
K_2O	2.0
TiO_2	1.0
P_2O_5	0.2
So_3	1.7
Other	0.2

*Data provided by Imperial College.

The PSIT sample of Silverdale coal was analyzed by CCSEM at UK, and results are provided in Section 4 of this report. Another sample of Silverdale coal, taken from the same plant sample as the PSIT sample, was analyzed by CCSEM at Imperial College. These data are provided in Appendix B.

3.6 Additional data

3.6.1 Ash and Moisture Contents

As a quality assurance measure, the moisture and ash contents of the five program coals received by PSIT were determined in the PSIT laboratory. In all cases, duplicate measurements were performed. Moisture content was determined by placing a small quantity (1 to 2g) of coal in a ceramic boat, placing the boat in a drying oven, heating the sample to 120°C, holding it at temperature for 2 hrs, allowing it to

cool, and measuring the resulting weight loss. Ash content was subsequently determined by placing the dried samples in a tube furnace, heating under flowing air to a temperature of 500°C and holding it at this temperature for 30 min to allow the sample to devolatilize completely, and then heating to 900°C. The sample was held at 900°C for 20 min to complete combustion before being cooled to room temperature. The weight loss was then determined and used to calculate ash content. Results of the PSIT measurements are shown in Table 3-19. In all cases, good agreement with data provided by either the coal supplier or outside analytical laboratory was obtained.

Table 3-19. PSIT Measurements of Coal H_2O and Ash Content

	PSIT H_2O	Reported H_2O	PSIT Ash	Reported Ash
Pittsburgh No. 8 Run of Mine	1.2	1.02	27.5	27.44
Pittsburgh No. 8 Washed	0.8	1.4	7.5	7.48
Pittsburgh No. 8 Cleaned	2.0	2.0	5.1	5.21
Black Thunder	23.6	24.3	5.0	4.49
Silverdale	2.1	1.9	16.3	16.5

3.6.2 Forms of Iron: Comparison of CCSEM and Mössbauer Data

The amount of iron present in each of the major mineral phases identified by CCSEM (see discussion in Section 4) was calculated from the weight fraction of each mineral in the coal mineral matter and from the average weight fraction of iron within each mineral category. Raw CCSEM weight fraction iron data were modified to include carbon and oxygen as needed prior to calculation of the total iron content of the coal. Results for the three Pittsburgh bituminous coals are given in Tables 3-20, 3-21, and 3-22. The amount of iron present in pyrite as determined by CCSEM analysis was in good agreement with the amount of iron detected in pyrite by Mössbauer for all three coals. Agreement for other major iron-bearing phases was reasonable with the exception of carbonate phases, detected in much higher concentrations for two of the coals by CCSEM.

Table 3-20. Distribution of Iron in Coal Minerals - Pittsburgh No. 8 run-of-mine (wt % of total iron in each phase)

	Pyrite	Illite + Silicates	Jarosite + Sulfates	Siderite + Carbonates
Mössbauer	75	11	14	0
CCSEM	80	6	14	0

Table 3-21. Distribution of Iron in Coal Minerals - Pittsburgh No. 8 washed (wt % of total iron in each phase)

	Pyrite	Illite + Silicates	Jarosite + Sulfates	Siderite + Carbonates
Mössbauer	90	7	0	3
CCSEM	72	7	2	19

Table 3-22. Distribution of Iron in Coal Minerals - Pittsburgh No. 8 beneficiated (wt % of total iron in each phase)

	Pyrite	Illite + Silicates	Jarosite + Sulfates	Siderite + Carbonates
Mössbauer - as received	34	7	59	0
Mössbauer - washed	59	0	41	0
CCSEM	58	5	31	5

3.6.3 Comparison of Pittsburgh Coal Bulk Ash Compositional Analysis with CCSEM

CCSEM analysis of the Pittsburgh No. 8 coals indicated that as the ash content was reduced, there was a substantial reduction in the quartz content relative to other minerals (Table 3-23). To verify this finding, the ash composition on a sulfur free basis was calculated from CCSEM data and compared with ash composition measurements (the data presented in Tables 3-9, 3-13, and 3-16). The results of this comparison are provided in Table 3-24. Absolute values of silica were comparable. For other elements, the level of agreement between measured ash composition and CCSEM-derived ash composition varied greatly. This suggests that CCSEM compositional analysis may not be sufficiently sensitive to provide a measure of the true ash composition, particularly for lighter elements such as Al, Mg, and Na. For all coals, alumina contents measured by CCSEM at UK were low relative to the bulk ash value, suggesting attenuation of the aluminum signal.

Table 3-23. CCSEM Mineral Composition of Pittsburgh No. 8 Coals (weight percent of mineral matter)

	Run-of-mine	Washed (DOE)	Beneficiated (SCS)
Quartz	22	9	6
Illite	22	9	10
Kaolinite	6	4	7
Pyrite	12	27	21
Calcite	2	3	0
Mixed carbonates	4	6	< 1
Misc. Silicates	23	19	18
Other	9	23	38

Table 3-24. Comparison of Bulk Ash Composition with CCSEM-determined Ash Composition (weight percent oxides, sulfur-free basis)

Oxide	Run-of-Mine		Washed (DOE)		Beneficiated (SCS)	
	Bulk Ash	CCSEM Ash	Bulk Ash	CCSEM Ash	Bulk Ash	CCSEM Ash
Si	57	65	49	47	44	46
Al	24	12	26	11	26	15
Fe	11	12	16	26	22	30
Ca	3	6	5	10	3	5
Mg	2	0	2	0	1	0
Na	1	0	1	0	0	0
K	2	5	1	3	1	3
Ti	1	1	1	3	1	2

3.6.4 Overview of CCSEM Mineral Distributions for US Coals

CCSEM mineral distributions for the four US coals were plotted on ternary diagrams to provide an indication of the spread in mineral composition for each coal. Each ternary diagram shows three elements: Al, Si, and either K or Ca. Compositions identified by CCSEM are indicated by a point within each ternary diagram. The relative volume of particles with an indicated composition is indicated by the height of the associated peak. Only those particles containing at least 80 mole percent of the three indicated elements on an oxygen and carbon free basis are shown. UK CCSEM data were used in all cases.

In Figure 3-1, K-Al-Si ternary diagrams for the four US coals are shown. Comparison of Figure 3-1(a), the run-of-mine Pittsburgh #8, Figure 3-1(b), the washed Pittsburgh No. 8, and Figure 3-1(c), the beneficiated Pittsburgh No. 8 suggests that the K-Al-Si mineral composition range becomes narrower as the coal is more deeply cleaned. The fraction of minerals that are non potassium containing aluminosilicates also increases with increasing degree of coal cleaning. Caution must be exercised in interpreting these trends, however, because the coals are related but were not derived directly from one another. For example, the beneficiated Pittsburgh No. 8 was not derived from the washed Pittsburgh No. 8 studied in this program. Differences may therefore reflect slight differences in the parent coals.

Ternary Ca-Al-Si diagrams for the four US coals are presented in Figures 3-2(a) - (d). Figure 3-2(d), the Black Thunder sub-bituminous coal, is noticeably different than the three bituminous coals, a consequence of the relatively high calcium content of the Black Thunder coal.

A detailed description of CCSEM data is contained in Section 4. Summaries of CCSEM coal mineral analyses obtained from UNDEERC/MTI and Imperial College are contained in Appendicies B and C.

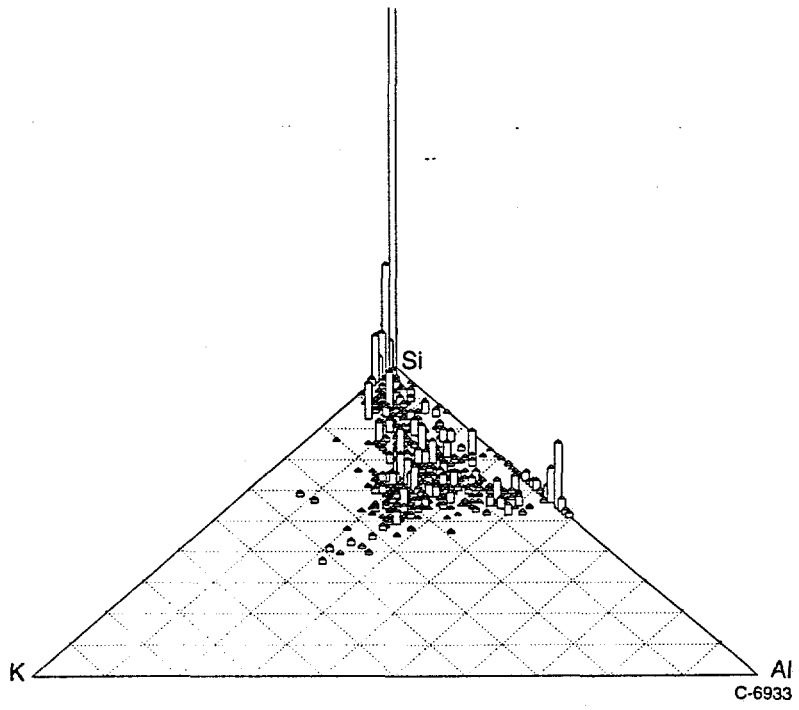

(a)

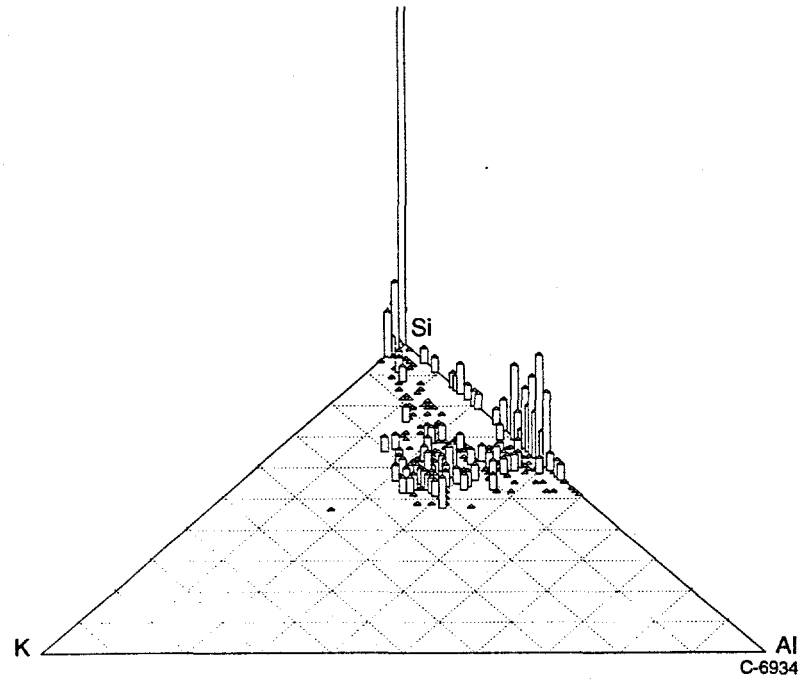

(b)

Figure 3-1. K-Al-Si mineral ternary diagrams for the four US coals. (a) run of mine Pittsburgh No. 8, (b) washed Pittsburgh No. 8.

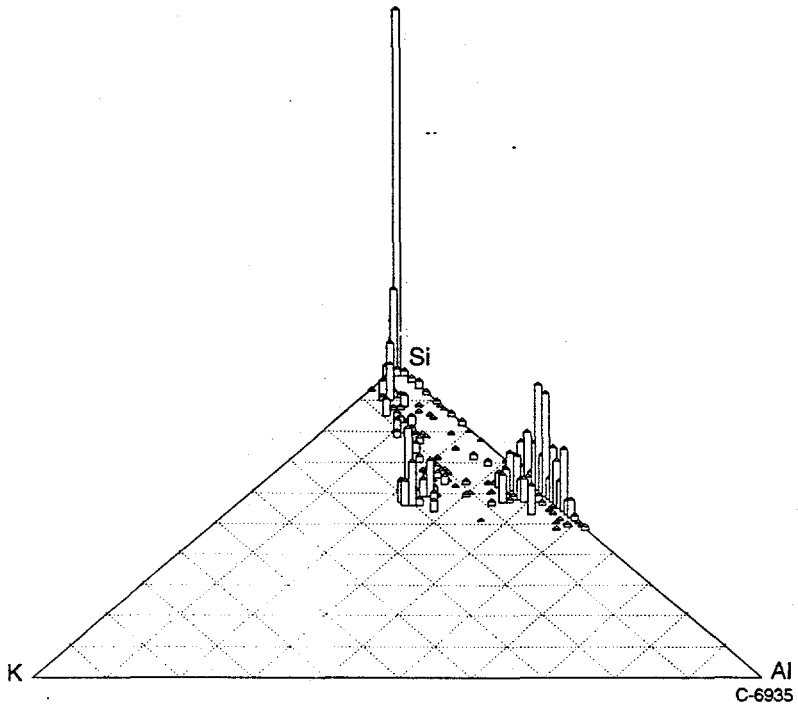

(c)

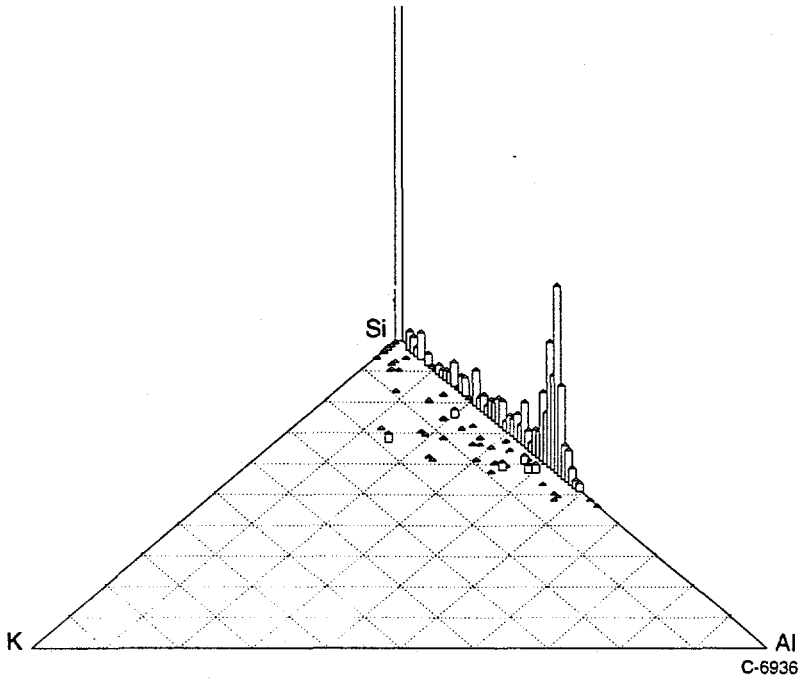

(d)

Figure 3-1. K-Al-Si mineral ternary diagrams for the four US coals. (c) beneficiated Pittsburgh No. 8, (d) Black Thunder (continued).

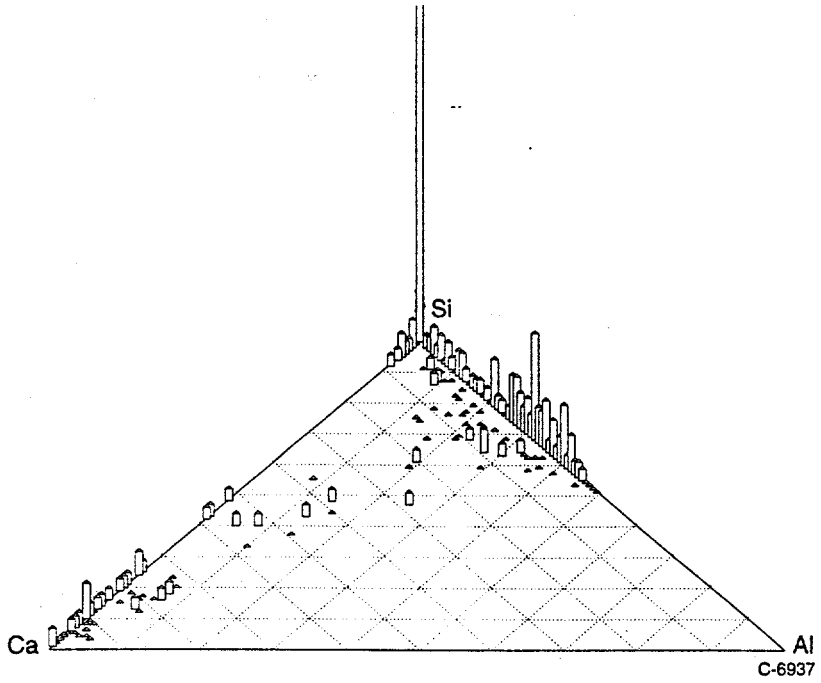

(a)

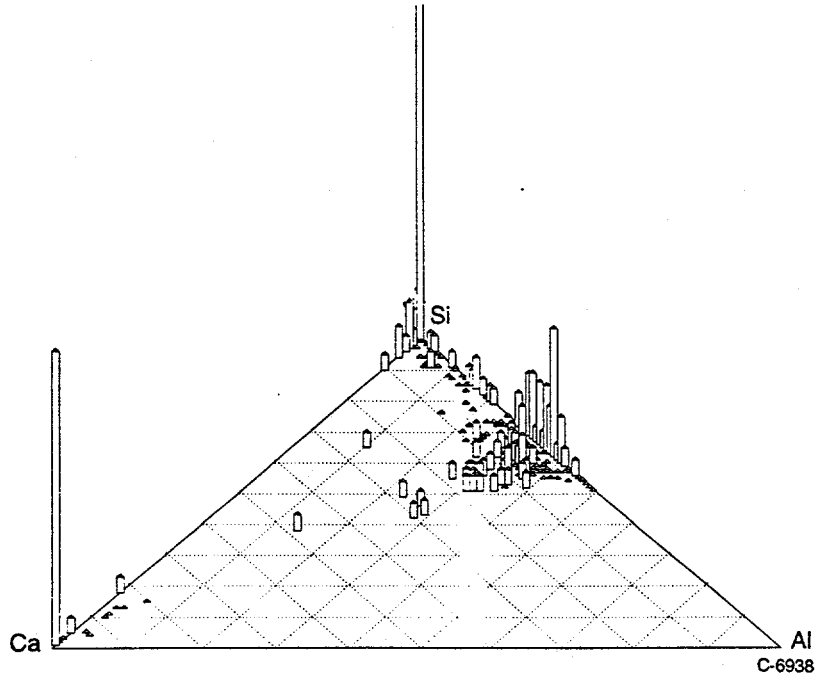

(b)

Figure 3-2. Ca-Al-Si mineral ternary diagrams for the four US coals. (a) run of mine Pittsburgh No. 8, (b) washed Pittsburgh No. 8.

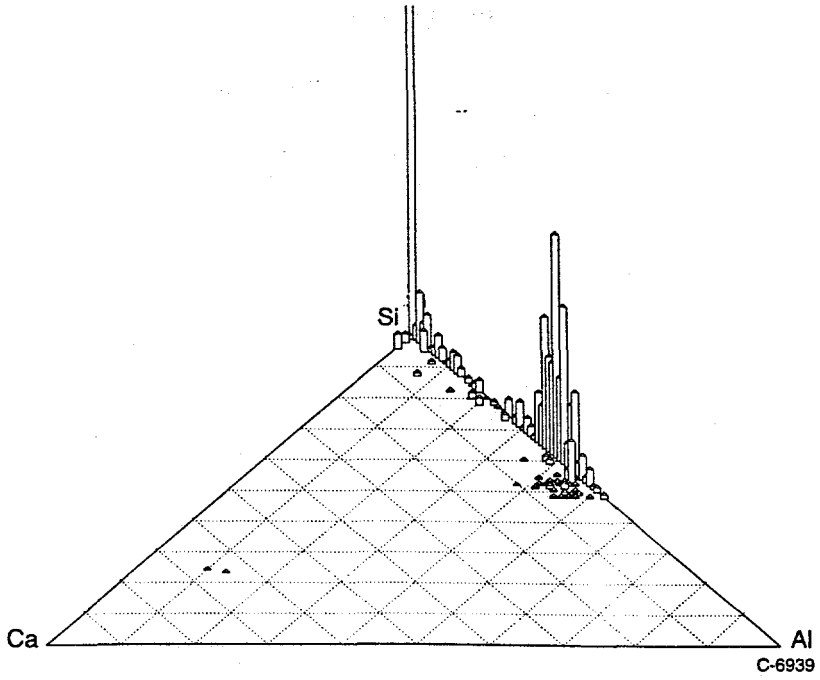

(c)

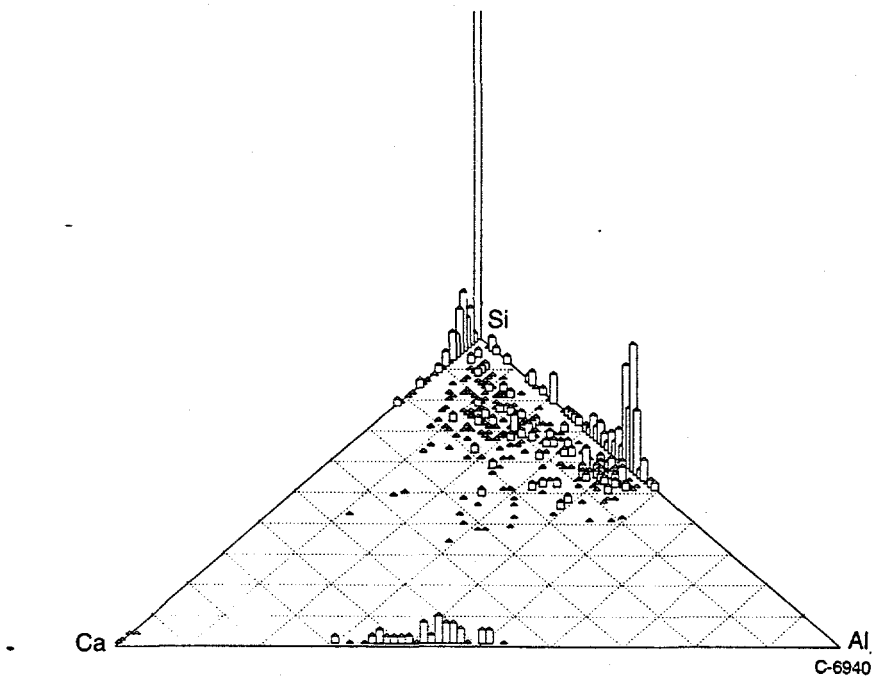

(d)

Figure 3-2. Ca-Al-Si mineral ternary diagrams for the four US coals. (c) beneficiated Pittsburgh No. 8, (d) Black Thunder (continued).

SECTION 4

TASK 5.1: ADVANCED TECHNIQUES FOR COAL AND ASH CHARACTERIZATION INCLUDING IN-SITU XAFS MEASUREMENT

(University of Kentucky)

4. ADVANCED TECHNIQUES FOR COAL, MINERAL AND ASH CHARACTERIZATION

The objective of this task was to apply modern, state-of-the-art, materials characterization techniques to thoroughly characterize the mineral matter and the organically associated minerals in a carefully chosen suite of coals, and to apply the same methods to determine the transformations and reactions these species undergo during coal combustion. The long range goal was to obtain a better understanding of the basic mechanisms of ash formation and slagging and fouling reactions.

The various techniques used to analyze the coals and ashes are outlined in Section 1. This section has been divided in several parts to distinguish results from different sets of samples. Section 2 deals with Mössbauer and CCSEM results from the following four US coals: 1) Black Thunder subbituminous coal, 2) run of mine Pittsburgh No. 8 coal, 3) washed Pittsburgh No. 8 coal, and 4) beneficiated Pittsburgh No. 8 coal. Section 3 discusses Mössbauer and CCSEM results for ashes from these program coals. The ashes/chars were produced by combusting the coals under varying residence times and stoichiometric conditions in the PSI drop tube furnace. Section 4 deals with samples obtained from the MIT drop tube furnace by combusting washed Pittsburgh No. 8 coal at varying oxygen partial pressure. Section 5 deals with the ash samples obtained from University of Arizona drop tube furnace tests. Section 6 deals with the Silverdale coal and ash from this coal (from laboratory scale drop tube furnace tests carried out at PSI) and ash samples collected during field sampling at the PowerGen Ratcliffe station in October 1992. Section 7 discusses design of the *in situ* XAFS furnace and the results for samples obtained during combustion experiments carried out using this furnace. Since the primary objective of this project was to study the effect of reducing stoichiometry on ash formation, the samples have been obtained under varying (sub and super) stoichiometric conditions and the results have been grouped accordingly within respective sections.

4.1 Analytical Tools

The analytical techniques applied in this task and the information they provided are summarized below. Complete details of the sample preparation and experimental procedures for these techniques have been reported elsewhere (Helble et al., 1992).

4.1.1 Computer-controlled Scanning Electron Microscopy (CCSEM)

For coal minerals, this method provides a determination of the approximate weight percentages of the minerals present, as well as a size distribution of each significant mineral phase identified (Huggins et al., 1980). For ash samples, the particles are categorized in terms of up to three major elements identified in their energy dispersive x-ray (EDX) (Huffman et al., 1993). Size distributions are determined for the major ash species, and software has been developed for graphical presentation of ash chemistry in binary, ternary, and volume percentage diagrams (Shah et al., 1992).

4.1.2 Mössbauer Spectroscopy

Fe Mössbauer spectroscopy determines the iron-bearing phases that are present in coals and ashes, and the percentages of the total iron in each phase (Huffman et al., 1978, 1990).

4.1.3 X-ray Absorption Fine Structure (XAFS) Spectroscopy

XAFS spectroscopy can, in principle, be applied to determine the structure or forms of occurrence of any element in coal or ash. Synchrotron generated x-ray beam is used to scan over the characteristic K-edge energy range of the element of interest (Koningsberger et al., 1988). X-ray Absorption Near Edge

Structure (XANES) is often used as a fingerprint to identify the formal oxidation state of the atom being excited. Fourier transforms of the Extended X-ray Absorption Fine Structure (EXAFS) part of the XAFS spectra yield Radial Structure Function (RSF), which is used to describe a few neighboring atomic shells of the element of interest. In the current investigation, however, it has been used primarily to develop a high temperature in situ XAFS furnace to investigate the transformations of iron and calcium bearing phases during coal combustion.

4.2 Coal Characterization

To study the effect of reducing stoichiometry on coal combustion characteristics, four coal samples were studied in this program:

(1) Pittsburgh No. 8 bituminous coal.
(2) Pittsburgh No. 8 bitumionus coal, washed to reduce ash.
(3) Beneficiated Pittsburgh No. 8 bituminous coal.
(4) Black Thunder (Wyodak-Anderson Seam) subbitumious coal.

4.2.1 CCSEM Analysis

Standard CCSEM samples were made by mixing coal with C-4 epoxy and pressing the mixture as a pellet. These pellets were polished and carbon coated to carry out CCSEM analysis. In the case of Black Thunder coal, moisture in the coal caused excessive bubbles and cracks in the pellet. Therefore, this coal was heated at 70°C for 12 hours and then it was mixed with epoxy to make a sample pellet. All coals were analyzed at three different magnifications for 1200 mineral particles. Tables 4-1 through 4-4 show the results from these analyses.

4.2.2 Mössbauer Analysis

Standard Mössbauer analysis was carried out on these coals to determine the distribution of the forms of iron (Figures 4-1 through 4-4). Table 4-5 shows the results from Mössbauer analysis. Black Thunder had only a weak pyrite quadrupole doublet in the Mössbauer spectrum. The run-of-mine and washed Pittsburgh No. 8 showed illite, siderite and jarosite peaks. Although there is significant difference in the ash content of these coals (washed sample has 72% less ash than run-of-mine sample), the pyrite content is reduced by only 15%. Thus the washing treatment to reduce ash seems to remove the clay partings of the seam while the pyrite in the coal matrix is unaffected.

We were not able to assign a specific phase to the major quadrupole doublet in the Mössbauer spectrum of the beneficiated Pittsburgh No. 8 coal. We suspected that the doublet is due to pyrite, but the Mössbauer parameters of the doublet do not match that of pyrite. Since the coal has been treated, we suspected some oxidation of the pyrite and the quadrupole doublet could be due to FeOOH. However, a low temperature (14K) Mössbauer spectrum did not show any splitting of this quadrupole doublet into a six-line magnetic spectrum. A new Mössbauer spectrum acquired after washing the coal with cold water showed a substantial decrease in this quadrupole doublet. From these observations, we can conclude that this doublet could be due to a water soluble ferric sulfate phase. As shown in Figure 4-4, after washing, we can easily differentiate the contribution to the Mössbauer spectrum from both the insoluble jarosite and pyrite. Using these parameters, we refit the original spectrum (before cold water wash) with pyrite, jarosite and sulfate peaks. Weight percent pyrite in both samples (calculated using the area under the curve) also agree well.

Table 4-1. CCSEM Analysis Results for Black Thunder Coal

CCSEM File:1113R6.cma
RUN 6 DATE 25-FEB-94 SUMMARY 132 TOTAL 1199

AVERAGE SPECIES COMPOSITION

No.	MINERAL SPECIES	Na	Mg	Al	Si	P	S	Cl	K	Ca	Ti	Fe	Weight %
331	Quartz	0.	0.	0.	99.	0.	0.	0.	0.	1.	0.	0.	26.6
260	Kaolinite	0.	0.	47.	52.	0.	0.	0.	0.	0.	0.	0.	14.4
10	Illite	0.	0.	31.	60.	0.	1.	0.	6.	1.	0.	1.	2.4
48	Montmorillonite	0.	0.	22.	65.	0.	2.	0.	0.	8.	1.	0.	3.9
256	Misc. Silicates	0.	0.	21.	68.	0.	3.	0.	1.	4.	2.	0.	23.8
27	Pyrite	0.	0.	0.	0.	0.	67.	0.	0.	0.	0.	33.	1.9
3	Misc. sulf.	0.	0.	0.	3.	0.	55.	0.	2.	6.	9.	23.	0.1
48	Misc. Phosphate ***	0.	0.	34.	0.	29.	0.	0.	0.	35.	1.	1.	6.2
13	Fe-rich	0.	0.	0.	0.	0.	0.	0.	0.	0.	0.	99.	3.0
9	Calcite	0.	0.	0.	1.	0.	0.	0.	0.	99.	0.	0.	0.2
1	Mixed Carbonate	0.	13.	0.	0.	0.	0.	0.	0.	87.	0.	0.	0.0
9	Ti oxide	0.	0.	0.	0.	0.	1.	0.	0.	0.	99.	0.	1.4
6	Quartz-Sulfate	0.	0.	1.	58.	0.	26.	0.	0.	15.	0.	0.	1.0
1	Sil-sulf	0.	0.	13.	32.	0.	38.	0.	0.	17.	0.	0.	0.0
2	Silicate-Pyrite	0.	0.	22.	33.	0.	24.	0.	0.	0.	0.	21.	0.0
135	Misc. Mixed	0.	0.	14.	54.	2.	11.	0.	2.	14.	1.	1.	15.2
1159	GRAND TOTALS	0.	0.	18.	63.	2.	4.	0.	1.	6.	2.	4.	100.0

***** Crandallite**

WEIGHT DISTRIBUTION

Size Ranges (Microns)

MINERAL SPECIES	WT. %	0.0 2.5	2.5 5.0	5.0 10.0	10. 20.	20. 40.	40. 80.	80. 500.
Quartz	26.6	9.	13.	23.	39.	12.	4.	0.
Kaolinite	14.4	23.	17.	24.	21.	12.	2.	0.
Misc. Silicates	23.8	9.	11.	24.	48.	4.	5.	0.
Misc. Mixed	15.2	2.	6.	42.	47.	4.	0.	0.
MINOR MINERALS	20.1	11.	24.	24.	20.	6.	7.	9.
GRAND TOTALS	100.0	10.	14.	26.	36.	8.	4.	2.

Table 4-2. CCSEM Analysis Results for Run-of-Mine Pittsburgh No. 8 Coal

CCSEM File:1120r2.cma (repolished)
RUN 2 DATE 28-FEB-94 SUMMARY 108 TOTAL 1199

AVERAGE SPECIES COMPOSITION

No.	MINERAL SPECIES	Na	Mg	Al	Si	P	S	Cl	K	Ca	Ti	Fe	Weight %
209	Quartz	0.	0.	0.	98.	0.	0.	0.	1.	0.	0.	0.	21.7
59	Kaolinite	0.	0.	47.	50.	0.	1.	0.	1.	0.	0.	0.	6.4
262	Illite	0.	0.	27.	54.	0.	2.	0.	14.	0.	1.	3.	22.0
14	K-Feldspar	0.	0.	18.	53.	0.	2.	0.	19.	0.	0.	8.	0.7
1	Chlorite	0.	0.	21.	33.	0.	0.	0.	2.	0.	2.	42.	0.1
1	Montmorillonite	9.	0.	15.	76.	0.	0.	0.	0.	0.	0.	0.	0.2
290	Misc. Silicates	0.	0.	17.	63.	0.	3.	0.	8.	1.	1.	6.	22.7
101	Pyrite	0.	0.	0.	0.	0.	65.	0.	0.	0.	0.	35.	11.9
6	Ferrous Sulfate	0.	0.	0.	3.	0.	48.	0.	1.	0.	0.	47.	1.1
10	Gypsum	0.	0.	0.	1.	0.	47.	0.	0.	52.	0.	0.	0.1
28	Misc. sulf.	0.	0.	1.	6.	0.	51.	0.	0.	7.	0.	34.	2.3
2	Apatite	0.	0.	2.	0.	29.	0.	0.	0.	70.	0.	0.	0.1
1	Fe-rich	0.	0.	0.	0.	0.	3.	0.	0.	0.	0.	97.	0.0
41	Calcite	0.	2.	0.	1.	0.	0.	0.	0.	97.	0.	0.	2.2
45	Mixed Carbonate	0.	6.	1.	8.	0.	0.	0.	1.	82.	0.	1.	3.6
2	Ti-rich	0.	0.	7.	16.	0.	0.	0.	5.	0.	70.	2.	0.3
17	Quartz-Sulfate	0.	0.	3.	53.	0.	35.	1.	0.	3.	0.	0.	0.3
4	Quartz-Pyrite	0.	0.	6.	33.	0.	36.	0.	1.	0.	0.	24.	0.4
20	Sil-sulf	0.	0.	23.	42.	0.	30.	0.	3.	0.	0.	1.	0.8
8	Silicate-Pyrite	0.	0.	16.	37.	0.	26.	0.	4.	0.	0.	17.	0.3
51	Misc. Mixed	1.	1.	13.	42.	1.	6.	0.	7.	24.	0.	3.	2.8
1173	GRAND TOTALS	0.	0.	14.	54.	0.	11.	0.	5.	6.	1.	8.	100.0

WEIGHT DISTRIBUTION

Size Ranges (Microns)

MINERAL SPECIES	WT. %	0.0 2.5	2.5 5.0	5.0 10.0	10. 20.	20. 40.	40. 80.	80. 500.
Quartz	21.7	9.	26.	27.	31.	2.	4.	1.
Illite	22.0	23.	36.	23.	11.	5.	3.	0.
Misc. Silicates	22.7	19.	29.	30.	10.	6.	4.	2.
Pyrite	11.9	0.	0.	26.	43.	15.	15.	0.
MINOR MINERALS	21.7	17.	23.	23.	24.	8.	3.	2.
GRAND TOTALS	100.0	15.	25.	26.	22.	6.	5.	1.

Table 4-3. CCSEM Analysis Results for Washed Pittsburgh No. 8 Coal

CCSEM File:1114r3.cma (repolished)
RUN 3 DATE 26-FEB-94 SUMMARY 136 TOTAL 1199

AVERAGE SPECIES COMPOSITION

No.	MINERAL SPECIES	Na	Mg	Al	Si	P	S	Cl	K	Ca	Ti	Fe	Weight %
106	Quartz	0.	0.	0.	98.	0.	0.	0.	0.	0.	0.	0.	9.1
57	Kaolinite	0.	0.	45.	52.	0.	1.	0.	1.	1.	0.	0.	4.0
106	Illite	0.	0.	29.	53.	0.	2.	0.	12.	1.	0.	2.	9.0
1	K-Feldspar	0.	0.	17.	63.	0.	0.	0.	20.	0.	0.	0.	0.0
9	Chlorite	0.	0.	20.	31.	0.	1.	0.	0.	1.	0.	47.	1.9
5	Montmorillonite	6.	0.	19.	61.	0.	6.	0.	2.	4.	0.	1.	0.6
207	Misc. Silicates	0.	0.	25.	64.	0.	3.	0.	3.	2.	0.	2.	19.2
9	Elem. Sulfur	0.	0.	0.	3.	1.	84.	0.	0.	3.	0.	5.	1.0
273	Pyrite	0.	0.	0.	0.	0.	64.	0.	0.	0.	0.	36.	27.2
44	Misc. sulf.	0.	0.	1.	8.	0.	71.	1.	1.	1.	2.	11.	3.7
1	Apatite	0.	0.	0.	0.	26.	3.	3.	0.	68.	0.	0.	0.0
25	Fe-rich	0.	0.	0.	0.	0.	1.	0.	0.	0.	0.	99.	4.7
30	Calcite	0.	3.	0.	0.	0.	0.	0.	0.	96.	0.	0.	2.8
39	Mixed Carbonate	0.	9.	0.	0.	1.	3.	0.	0.	78.	0.	9.	6.2
6	Ti oxide	0.	0.	0.	2.	0.	0.	0.	0.	0.	98.	0.	1.7
39	Quartz-Sulfate	0.	0.	2.	36.	0.	59.	0.	1.	0.	1.	0.	1.1
2	Quartz-Pyrite	0.	0.	5.	25.	0.	45.	0.	2.	0.	0.	23.	0.2
37	Sil-sulf	0.	0.	18.	35.	0.	38.	0.	6.	0.	0.	0.	2.5
8	Silicate-Pyrite	0.	0.	23.	31.	0.	31.	0.	1.	1.	0.	13.	0.9
66	Misc. Mixed	0.	0.	18.	35.	1.	19.	1.	3.	15.	2.	4.	4.1
1070	GRAND TOTALS	0.	1.	11.	33.	0.	25.	0.	2.	9.	2.	17.	100.0

WEIGHT DISTRIBUTION

Size Ranges (Microns)

MINERAL SPECIES	WT. %	0.0 2.5	2.5 5.0	5.0 10.0	10. 20.	20. 40.	40. 80.	80. 500.
Quartz	9.1	15.	7.	35.	34.	10.	0.	0.
Illite	9.0	24.	0.	43.	21.	1.	1.	10.
Misc. Silicates	19.2	24.	12.	15.	33.	3.	5.	8.
Pyrite	27.2	10.	19.	20.	9.	27.	15.	0.
MINOR MINERALS	35.5	12.	12.	21.	35.	5.	9.	5.
GRAND TOTALS	100.0	15.	12.	23.	26.	11.	8.	4.

Table 4-4. CCSEM Analysis Results for Beneficiated Pittsburgh No. 8 Coal

CCSEM File:1121r3.cma (repolished)
RUN 3 DATE 27-FEB-94 SUMMARY 104 TOTAL 1199

AVERAGE SPECIES COMPOSITION

No.	MINERAL SPECIES	Na	Mg	Al	Si	P	S	Cl	K	Ca	Ti	Fe	Weight %
64	Quartz	0.	0.	0.	98.	0.	1.	0.	0.	0.	0.	0.	6.0
153	Kaolinite	0.	0.	46.	52.	0.	1.	0.	1.	0.	0.	0.	7.1
57	Illite	0.	0.	26.	52.	0.	2.	0.	16.	0.	0.	3.	10.2
225	Misc. Silicates	0.	0.	30.	56.	0.	7.	0.	2.	0.	0.	4.	18.1
2	Elem. Sulfur	0.	0.	0.	9.	0.	82.	0.	0.	0.	0.	9.	0.1
167	Pyrite	0.	0.	0.	0.	0.	66.	0.	0.	0.	0.	34.	21.4
4	Ferrous Sulfate	0.	0.	0.	4.	0.	48.	0.	0.	0.	0.	47.	0.3
1	Jarosite	0.	0.	0.	6.	0.	42.	0.	10.	0.	0.	42.	0.1
89	Gypsum	0.	0.	0.	0.	0.	46.	0.	0.	54.	0.	0.	3.8
1	Chalcopyrite	0.	0.	0.	0.	0.	30.	0.	0.	0.	0.	62.	0.1
2	Sphalerite	0.	0.	0.	5.	0.	61.	0.	0.	0.	0.	13.	0.5
81	Misc. sulf.	0.	0.	2.	6.	0.	50.	0.	2.	12.	0.	26.	9.6
4	Fe-rich	0.	0.	0.	0.	0.	2.	0.	0.	0.	0.	97.	1.3
5	Mixed Carbonate	0.	0.	0.	5.	0.	12.	0.	0.	0.	0.	84.	0.3
13	Quartz-Sulfate	0.	0.	7.	42.	0.	40.	0.	6.	0.	0.	4.	2.8
11	Quartz-Pyrite	0.	0.	0.	24.	0.	28.	0.	1.	0.	0.	43.	1.8
50	Sil-sulf	0.	0.	17.	34.	0.	38.	0.	1.	0.	1.	2.	3.7
44	Silicate-Pyrite	0.	0.	19.	32.	0.	29.	0.	0.	0.	0.	18.	5.2
70	Misc. Mixed	0.	0.	9.	18.	0.	33.	2.	2.	1.	1.	30.	7.6
1045	GRAND TOTALS	0.	0.	14.	32.	0.	30.	0.	3.	3.	0.	17.	100.0

WEIGHT DISTRIBUTION

Size Ranges (Microns)

MINERAL SPECIES	WT. %	0.0 2.5	2.5 5.0	5.0 10.0	10. 20.	20. 40.	40. 80.	80. 500.
Kaolinite	7.1	1.	7.	60.	24.	8.	0.	0.
Illite	10.2	3.	91.	5.	0.	1.	0.	0.
Misc. Silicates	18.1	32.	34.	26.	7.	2.	0.	0.
Pyrite	21.4	4.	23.	23.	27.	3.	20.	0.
Misc. sulf.	9.6	4.	24.	34.	34.	1.	4.	0.
Misc. Mixed	7.6	19.	52.	12.	16.	0.	0.	0.
MINOR MINERALS	26.0	8.	35.	28.	21.	2.	6.	0.
GRAND TOTALS	100.0	11.	36.	26.	19.	2.	6.	0.

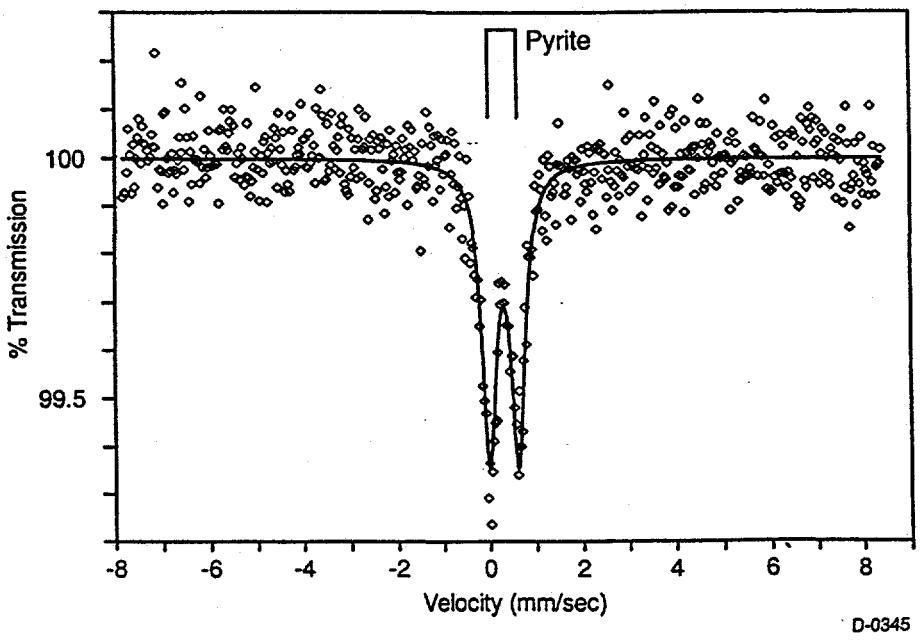

Figure 4-1. Mössbauer spectrum of Black Thunder coal (MK No. 1699)

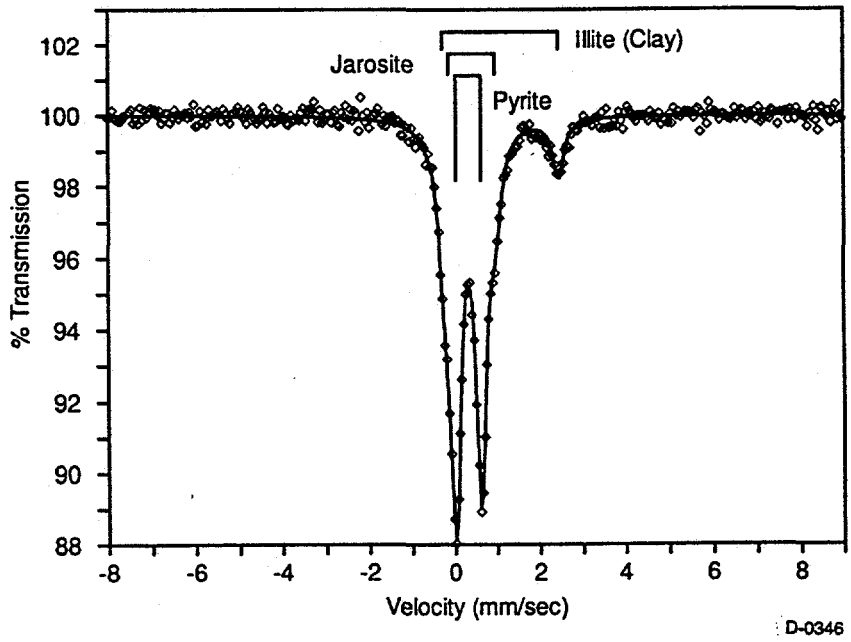

Figure 4-2. Mössbauer spectrum of run-of-mine Pittsburgh No. 8 (MK No. 1695)

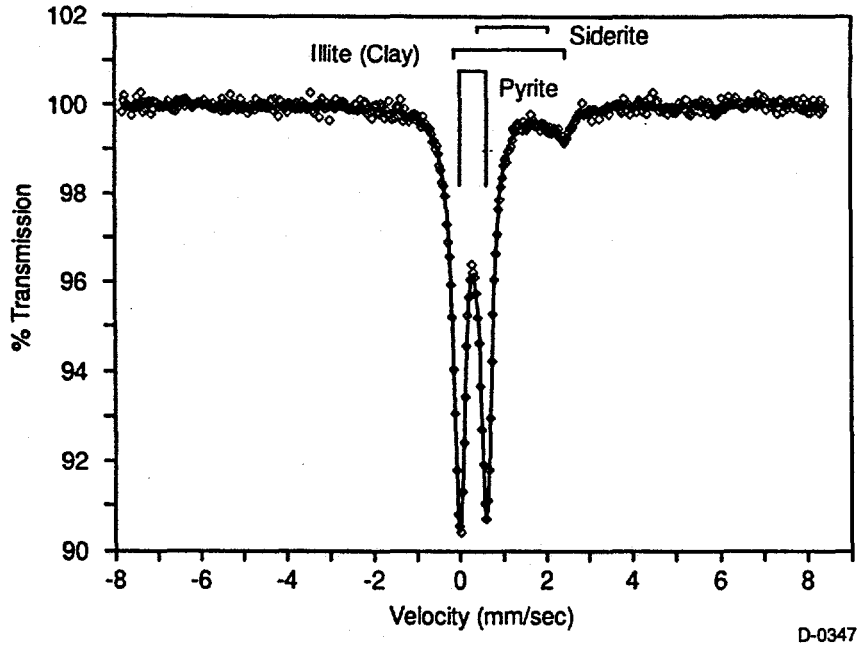

Figure 4-3. Mössbauer spectrum of washed Pittsburgh No. 8 coal (MK No. 1698)

4.3 Analysis of Drop Tube Furnace Produced Ashes of Program Coals

Ash samples of program coals were generated by PSI and PETC using drop tube furnaces under varying residence times and oxygen partial pressures.

4.3.1 Mössbauer Spectroscopy Results

4.3.1.1 Effect of Changes in Residence Times

Tables 4-6 and 4-7 show Mössbauer data for ashes produced at varying residence times. Both sets of experiments were carried out at 15% oxygen. In general under high temperature combustion conditions ferrous glass rapidly oxidized to ferric glass. Increasing residence times further increased the amount of crystalline (magnetite and hematite) forms.

4.3.1.2 Effect of Changes in Stoichiometric Ratios

Since the program objective was to study the effect of reducing stoichiometric conditions, further drop tube tests were carried out by combusting four program coals at a fixed furnace set point temperature, (1500°C see Section 7) and fixed residence time (2.6 s). To maintain the fixed residence time the gas flow rate (1 SCFM) and coal feed rate (3.5g/min) were kept constant while the oxygen partial pressure was varied to change the stoichiometric ratio. Although substantial amounts of residual carbon were observed in all ash samples (see discussion on CCSEM results), Mössbauer results indicated oxidation of pyrite to pyrrhotite and magnetite phases occurred. Hematite phase, usually observed under higher oxidation conditions, was missing in all samples. The wustite (FeO) phase was also observed under some conditions. Tables 4-8 through 4-11 show results from Mössbauer analysis carried out on ashes from the washed Pittsburgh No. 8, the run-of-mine Pittsburgh No. 8, the beneficiated Pittsburgh No. 8, and the Black Thunder.

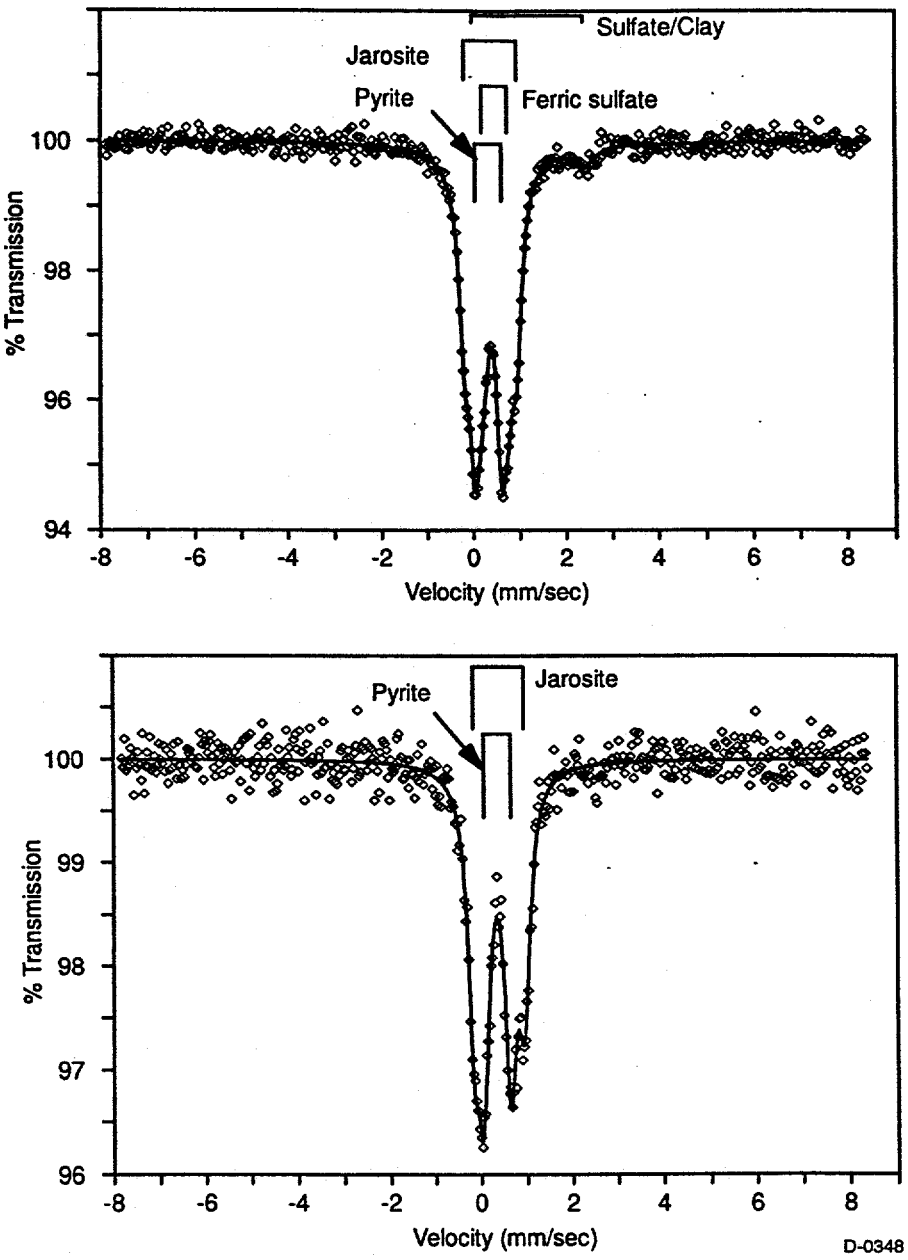

Figure 4-4. Mössbauer spectrum of beneficiated Pittsburgh No. 8 coal before (top, MK No. 1697) and after (bottom, MK1736) cold water wash

Table 4-5. Mössbauer Analysis of Coals

Möss File No.	Sample	Phase	I.S.	Q.S.	% Fe	Wt. % Pyrite
1695	Run-of-mine Pittsburgh No. 8	Pyrite Illite (Clay) Jarosite	0.33 1.08 0.41	0.60 2.72 1.11	75 11 14	0.86
1698	Washed Pittsburgh No. 8	Pyrite Illite (Clay) Siderite	0.31 1.15 1.23	0.61 2.57 1.62	90 7 3	0.73
1697	Beneficiated Pittsburgh No. 8	Pyrite Illite (Clay) Jarosite Ferric Sulfate (?)	0.31 1.19 0.37 0.47	0.58 2.40 1.14 0.56	34 7 22 37	0.23
1736	Beneficiated Pittsburgh No. 8 H_2O washed	Pyrite Jarosite	0.35 0.39	0.60 1.12	59 41	0.27
1699	Black Thunder	Pyrite[#]	0.31	0.62	100	0.071

[#] Very weak signal (see figure 12); chemical fractionation indicated approximately 50% iron as carbonate.

Table 4-6. Mössbauer results for washed Pittsburgh No. 8 coal ash, 1500°C Furnace set point, 15% O_2, 4 SCFM gas flow rate, Stoichiometric ratio=15.6

MK#	CFFLS	Res. Time	Phases Present	I.S	Q.S	H0	%Fe
1740	1155	0.248	Fe^{+++}/Glass Fe^{++}/Glass Magnetite Magnetite Magnetite $Fe_{1-x}S$	0.33 1.00 0.32 0.66 0.67 0.79	1.15 1.90 0.02 0.00 0.00 0.00	 495 458 416 305	14 12 38 21 7 8
1734	1156	0.4	Fe^{+++}/Glass Hematite Magnetite Magnetite	0.42 0.38 0.31 0.68	0.88 -0.08 0.00 0.00	 512 491 455	12 47 23 18
1737	1157	0.552	Fe^{+++}/Glass Hematite Magnetite Magnetite	0.36 0.38 0.31 0.65	0.88 -0.08 0.00 0.00	 515 490 456	11 40 27 23
1739	1158	0.718	Fe^{+++}/Glass Hematite Magnetite Magnetite	0.42 0.40 0.37 0.61	0.96 -0.08 0.00 0.00	 517 492 449	9 65 9 12

Table 4-7. Mössbauer results for washed Pittsburgh No. 8 coal ash, 1400°C Furnace set point, 15% O_2, 1 SCFM gas flow rate, stoichiometric ratio=3.9

MK#	CFFLS	Res. Time	Phases Present	I.S.	Q.S.	H0	%Fe
1727	1159	0.994	Fe^{+++}/Glass	0.36	1.12		17
			Fe^{++}/Glass	1.00	2.01		11
			Hema.+ Mag.	0.39	0.05	501	39
			Magnetite	0.67	0.00	462	20
			Magnetite	0.57	0.00	415	12
1728	1160	1.601	Fe^{+++}/Glass	0.27	1.28		16
			Fe^{++}/Glass	0.98	1.82		7
			Magnetite	0.33	0.00	493	49
			Magnetite	0.65	0.00	455	28
1729	1161	2.208	Fe^{+++}/Glass	0.29	1.18		20
			Fe^{++}/Glass	0.99	1.93		9
			Hema.+Mag.	0.36	-0.03	498	51
			Magnetite	0.62	0.00	456	14
			Magnetite	0.65	0.00	425	6
1730	1162	2.87	Fe^{+++}/Glass	0.37	1.07		18
			Hematite	0.43	-0.05	522	59
			Hematite	0.43	-0.04	501	13
			Magnetite	0.52	0.00	460	

Pittsburgh No. 8 Coal Ashes

Ashes from the three Pittsburgh No. 8 coals contained pyrrhotite at the stoichiometric ratio of 0.6. The amount of pyrrhotite decreased and the amount of magnetite increased with the increasing stoichiometric ratios. Similarly, the amount of the Fe^{++} phase incorporated in the glassy matrix decreased and the Fe^{+++}/glass content increased with increasing stoichiometric ratios in all samples. The washed Pittsburgh No. 8 coal ashes showed presence of a wüstite (FeO) phase. Usually this phase is not observed in coal ashes, therefore its unusual presence was verified by observing the magnetic transition effects on the Mössbauer spectra at cryogenic temperatures. The amount of this wüstite phase (25%) did not vary with the stoichiometric ratio.

Black Thunder Coal Ashes

The Black Thunder coal ashes also contained wüstite (FeO). However, the isomer shift values were slightly higher for the Black Thunder coal ashes, indicating that the Fe-O distances may have been a little higher. This suggests that Fe is present in the CaO matrix as a substitutional impurity, forming a calciowüstite phase and giving rise to this higher Fe-O distance. Unlike the washed Pittsburgh No. 8 coal ashes, the amount of this wüstite phase decreased slightly with increasing stoichiometric ratio. Black Thunder coal ashes did not show any pyrrhotite. Like the Pittsburgh No. 8 coal ashes, in the Black Thunder coal ashes the Fe^{++}/Fe^{+++} ratio decreased with the increasing stoichiometric ratio.

Table 4-8. Mössbauer Results for washed Pittsburgh No. 8 Coal Ashes, 1500°C Furnace Set Point, 2.6 s Res. Time

MK#	CFFLS	Stoichiometric ratio	Phases Present	I.S.	Q.S.	H0	%Fe
1751	1163	1.2	Fe^{++}/Wüstite	0.88	0.95		24
			Fe^{++}/Glass	1.03	2.12		25
			Fe^{+++}/Glass	0.29	0.75		9
			Magnetite	0.33	0.00	491	21
			Magnetite	0.67	0.00	454	15
			$Fe_{1-x}S$	0.73	0.00	306	6
1817	1164	0.9	Fe^{++}/ Wüstite	0.93	0.79		25
			Fe^{++}/Glass	1.02	1.98		36
			Magnetite	0.28	-0.01	492	12
			Magnetite	0.68	0.00	458	17
			$Fe_{1-x}S$	0.76	-0.08	307	10
1819	1165	0.6	Fe^{++}/ Wüstite	0.89	0.72		25
			Fe^{++}/Glass	0.87	1.83		21
			Fe^{++}/Glass	1.29	2.11		11
			Magnetite	0.26	0.00	490	6
			Magnetite	0.83	0.00	450	7
			$Fe_{1-x}S$	0.75	-0.08	307	30

Table 4-9. Run-of-mine Pittsburgh No. 8 Coal, 1500°C Furnace Set Point, 2.6 s Res. Time

MK#	CFFLS	Stoichiometric Ratio	Phases Present	I.S.	Q.S.	H0	%Fe
1754	1166	1.2	Fe^{++}/Glass	1.07	1.94		58
			Fe^{+++}/Glass	0.42	1.34		20
			Magnetite	0.34	0.00	488	8
			Magnetite	0.68	0.00	451	14
1755	1167	0.9	Fe^{++}/Glass	1.10	2.21		28
			Fe^{++}/Glass	1.06	1.58		23
			Fe^{+++}/Glass	0.59	1.25		19
			Magnetite	0.51	0.00	459	23
			$Fe_{1-x}S$	0.71	0.00	305	8
1818	1168	0.6	Fe^{++}/Glass	1.01	2.10		62
			Fe^{++}/Glass	1.01	1.17		19
			$Fe_{1-x}S$	0.74	-0.08	306	19

Table 4-10. Mössbauer Results for Beneficiated Pittsburgh No. 8 Coal Ashes, 1500°C Furnace Set Point, 2.6 s Res. Time

MK#	CFFLS	Stoichiometric Ratio	Phases Present	I.S.	Q.S.	H0	%Fe
1759	1169	1.2	Fe^{++}/Glass	1.03	1.96		41
			Fe^{+++}/Glass	0.37	1.01		44
			Magnetite	0.28	0.00	486	9
			Magnetite	0.75	0.00	454	6
1764	1170	0.9	Fe^{++}/Glass	1.07	2.10		48
			Fe^{++}/Glass	0.94	1.29		16
			Fe^{+++}/Glass	0.36	0.98		21
			Magnetite	0.30	0.00	488	3
			Magnetite	0.77	0.00	442	8
			$Fe_{1-x}S$	0.80	-0.08	306	4
1765	1171	0.6	Fe^{++}/Glass	1.07	2.22		36
			Fe^{++}/Glass	1.02	1.47		46
			$Fe_{1-x}S$	0.77	-0.08	305	13
			$Fe_{1-x}S$	0.73	0.14	257	5

Table 4-11 Mössbauer Results for Black Thunder Coal Ashes, 1500°C Furnace set point, 2.6 s Res. Time

MK#	CFFLS	Stoichiometric Ratio	Phases Present	I.S.	Q.S.	H0	%Fe
1792	1172	1.2	Fe^{++}/Glass	0.69	2.61		7
			Fe^{+++}/Glass	0.27	1.22		80
			Fe^{++}/Wüstite	1.00	0.61		13
1793	1173	0.9	Fe^{++}/Glass	0.69	2.48		11
			Fe^{+++}/Glass	0.35	1.11		68
			Fe^{++}/ Wüstite	1.01	0.71		17
			$Fe_{1-x}S$	0.22	0.13	287	4
1766	1174	0.6	Fe^{++}/Glass	0.73	2.32		24
			Fe^{+++}/Glass	0.48	0.96		54
			Fe^{++}/Wüstite	1.01	0.81		22

4.3.1.3 PETC Pilot Scale Combustor Generated Fly Ash Samples of Washed Pittsburgh No. 8 Coal

Table 4-12 shows the Mössbauer results for the washed Pittsburgh No. 8 coal and fly ash samples from its combustion in the PETC pilot scale combustor using low NO_x burner conditions. It appears that the transformation of the iron phases is complete at 1.7 s residence time, as there are no further changes in the forms of Fe after that. This coal was also combusted at PSI under varying residence time and stoichiometric conditions.

Table 4-12. Mössbauer Spectroscopy Results for Washed Pittsburgh No. 8 Coal and Fly Ash Samples from its Combustion in the PETC Pilot Scale Combustor Using Low No_x Burner Conditions

CFFLS/ MK#	Sample	Phases	I.S.	Q.S.	Hfs	%Fe
95-043	Washed	Pyrite	0.30	0.61		88
2009	Pitt No. 8 coal	Illite (Clay)	1.23	2.74		6
		Jarosite	0.38	1.04		6
95-044	No. 25, ash	Fe^{++}/Glass	0.83	1.94		20
2008	0.9 sec	Fe^{+++}/Glass	0.56	0.71		11
		Magnetite	0.28	0	490	25
		Magnetite	0.67	0	458	37
		Magnetite	0.37	-0.09	515	7
95-045	No. 26, ash	Fe^{++}/Glass	0.77	2.36		5
2005	1.7 sec	Fe^{+++}/Glass	0.37	0.96		22
		α-Fe_2O_3	0.37	-0.09	515	27
		Magnetite	0.64	0	456	20
		Magnetite	0.29	0	491	26
95-046	No. 27, ash	Fe^{++}/Glass	0.90	1.71		2
2006	2.6 sec	Fe^{+++}/Glass	0.28	1.16		19
		α-Fe_2O_3	0.36	-0.08	514	31
		Magnetite	0.27	0	489	22
		Magnetite	0.62	0	457	26

4.3.2 CCSEM Results

CCSEM Sample Preparation

As described in several of the references, Helble et al., (1992), Huggins et al., (1989), Huffman et al., (1993), Shah et al., (1992), CCSEM ash samples are usually prepared by dispersing a small amount of ash in acetone and depositing it onto a nucleopore filter paper such that particles do not overlap or touch each other. When we analyzed ash samples prepared in this manner with CCSEM, we encountered several problems: (1) CCSEM was rejecting particles due to low x-ray count rate, (2) most of the ash particles showed a similar composition which was similar to the bulk composition as misc.silicates and (3) particle sizes were quite large. From these results, we suspected that instead of examining each ash particle separately, we were looking at char aggregates comprising of residual carbon and partially transformed minerals. SEM micrographs (Figure 4-5) of a polished cross section of the char matrix confirms incomplete burn out. To avoid analyzing a single char particle with multiple ash particles within, we decided to try an alternate sample preparation technique. Chars were diluted with graphite so that total carbon content was 80 to 90 wt%. The chars were mixed with C-4 epoxy (approximately equal weights) and pressed into pellets. These pellets were cross sectioned, polished and carbon coated before CCSEM analysis. The data reduction program was also modified to account for cross sectional size parameters rather than overall sizes.

Dilution of the sample with graphite separated out char particles from each other, but we noticed ash/mineral particles within a single char particles clustered together and CCSEM methodology encountered

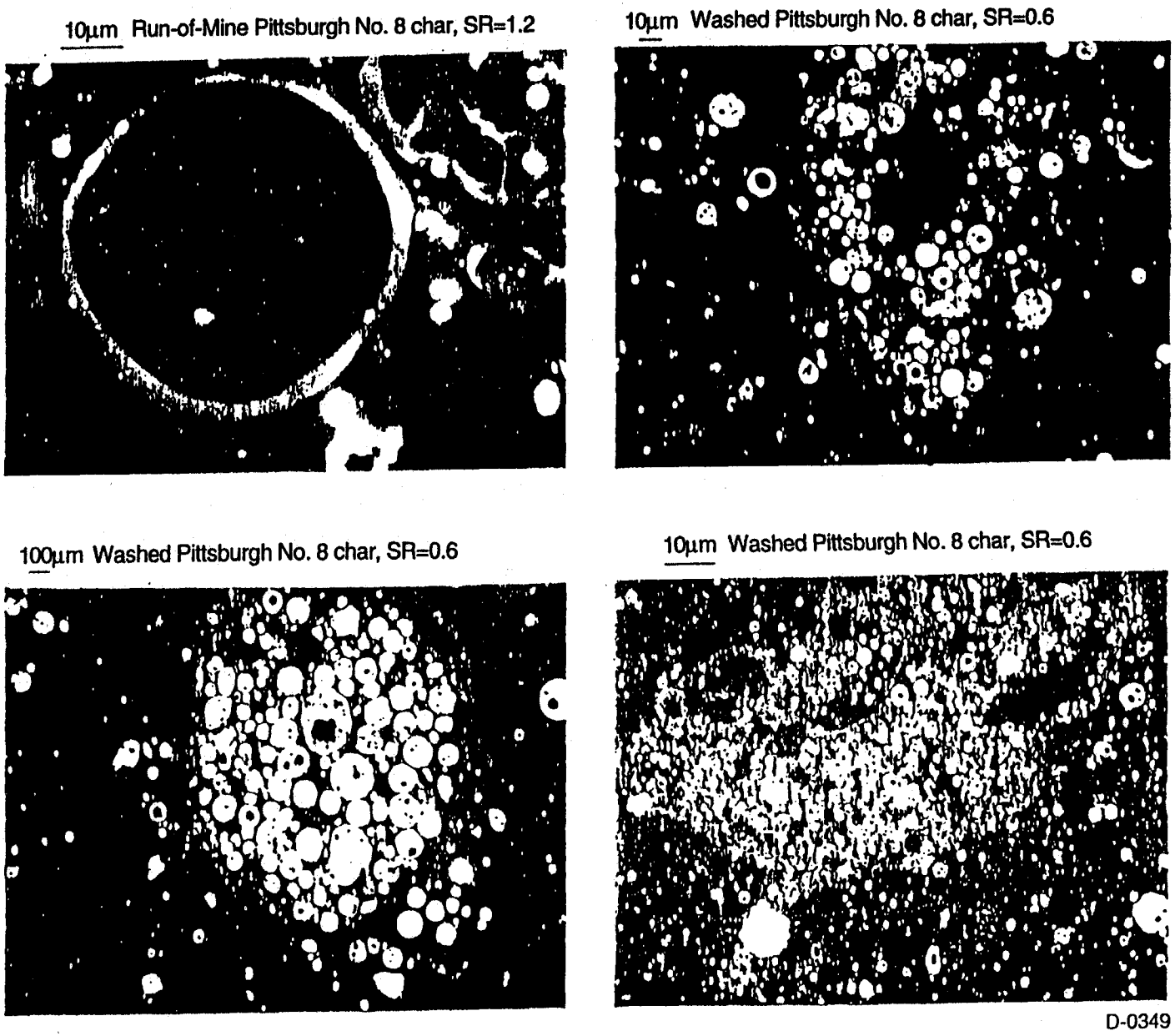

Figure 4-5. SEM micrographs of drop tube furnace produced ash samples indicating presence of large amounts of residual carbon in the form of unburnt char matrix.

problems analyzing such clusters. As a coal particle burns, the char matrix between minerals is eroded away and as the molten mesophase shrinks or forms cenospheres it drags the mineral particles with it. At the completion of the combustion process, these minerals will either react with each other, forming a large ash particle, or the char matrix between them will fragment giving rise to several small ash particles. Because of the incomplete combustion in the present samples, the mineral particles do not undergo complete transformation and generate rather inhomogenous fused minerals/ash still held together by char matrix. During CCSEM analysis, especially at higher magnifications, a single large char particle can fill the entire field of view. If this particle has many small mineral/ash particles it can bias the analysis. Just like frambroidal pyrite in coal mineral analysis, such char particles have to be avoided during CCSEM analysis to get statistically reliable information.

Because of the above mentioned difficulties, all the results presented here should be considered qualitative in nature. To get more accurate quantitative information, it would be necessary to burnout the char particles or crush the char to liberate individual minerals. Tables 4-13 through 4-24 show the CCSEM analysis of the run-of-mine Pittsburgh No. 8, washed Pittsburgh No. 8, beneficiated Pittsburgh No. 8 and the Black Thunder coal chars. The combustion conditions were: 1500°C furnace set point, 2.6 s residence time and stoichiometric ratios of 0.6, 0.9 and 1.2.

Pittsburgh No. 8 Chars

In all samples, the amount of Si (quartz) did not vary with stoichiometric ratios implying that quartz is quite inert under these conditions. The beneficiated Pittsburgh No. 8 coal ashes showed large iron-clay mineral-mineral interaction during combustion to form an Fe-Si-Al phase. The ASTM ash analysis of these coals showed that the beneficiated Pittsburgh No. 8 coal had higher Fe_2O_3 (20.8%) than either the run-of-mine (10.52%) or washed (14.76%) Pittsburgh No. 8 coals. Moreover, Mössbauer spectroscopy of these coals showed considerable pre-oxidation of the Fe phase (in form of jarosite and ferric sulfate formation) in the beneficiated Pittsburgh No. 8 coal which may have lead to this observed reactivity of iron phase. Though run-of-mine Pittsburgh No. 8 coal had a considerably higher ash content, primarily in the forms of quartz and clays, there were no significant differences in the reaction products (compared to other the Pittsburgh No. 8 coals) after combustion.

Figure 4-6 shows K-Si-Al volume frequency ternary diagrams of the ashes generated (SR=1.2) from the three Pittsburgh No. 8 coals (top: washed; middle: run-of-mine; bottom: beneficiated). It clearly shows that the illite phase in all three coals is same and it does not undergo any transformation. Our previous XAFS investigations (Huffman et al., 1990), had also shown that during combustion, illite tends to remain inert.

Figure 4-7, shows Fe-Si-Al volume frequency ternary diagrams for the same ashes as in Figure 4-6. The effect of cleaning on the chemical composition of ashes is quite evident. The CCSEM results are in agreement with the Mössbauer results. The run-of-mine coal has majority of the Fe-Si-Al phase locked up in illite phase which does not undergo any further changes. A peak at Fe apex is due to hematite formation from pyrite oxidation. The washed coal had lower amounts of aluminosilicates. Thus the washing primarily removed the illite phase. The remaining finer pyrite and pyrite oxidation products are more reactive and we see more interarction between Fe and aluminosilicates. The beneficiated coal showed absence of major peaks at any of the apexes or at Al:Si=1:1 point. As the Mössbauer spectrum of the coal had shown, a lot of pyrite in the original coal had undergone oxidation forming jarosite and FeOOH phases. These fine particles are quite reactive and form aluminosilicate ash particles with varying Fe content.

Table 4-13. CCSEM Analysis of Washed Pittsburgh No. 8 Coal Ash, 1500 °C Furnace Set Point, 2.6 s Res. Time, Stoichiometric Ratio=1.2

SAMPLE 1163 PSI ASH IN EPOXY, Pitt. No. 8 (DOE), 1500C; 2.6 RST, SR=1.2

AVERAGE SPECIES COMPOSITION

No.	SPECIES	C	O	Na	Mg	Al	Si	P	S	Cl	K	Ca	Ti	V	Cr	Mn	Fe	Ni	Cu	Zn	X	Vol %
57	Fe - -	0.	0.	0.	0.	0.	2.	0.	1.	0.	0.	1.	0.	0.	0.	0.	96.	0.	0.	0.	0.	1.7
57	Ca - -	0.	0.	0.	1.	0.	1.	0.	1.	0.	0.	97.	0.	0.	0.	0.	0.	0.	0.	0.	0.	2.0
151	Si - -	0.	0.	0.	0.	1.	93.	0.	0.	0.	2.	1.	0.	0.	0.	0.	2.	0.	0.	0.	0.	12.2
107	Si Al -	0.	0.	0.	0.	36.	56.	0.	1.	0.	4.	1.	1.	0.	0.	0.	2.	0.	0.	0.	0.	12.2
19	Al Si -	0.	0.	0.	0.	50.	46.	0.	0.	0.	3.	0.	0.	0.	0.	0.	0.	0.	0.	0.	0.	1.3
15	Si Al Ti	0.	0.	0.	0.	27.	50.	0.	2.	0.	5.	3.	9.	0.	0.	0.	4.	0.	0.	0.	0.	1.3
38	Si Fe Al	0.	0.	0.	0.	16.	43.	0.	1.	0.	5.	6.	2.	0.	0.	0.	28.	0.	0.	0.	0.	2.6
167	Si Al Fe	0.	0.	0.	0.	28.	49.	0.	1.	0.	6.	4.	1.	0.	0.	0.	11.	0.	0.	0.	0.	16.6
21	Fe Si Al	0.	0.	0.	0.	12.	28.	0.	0.	0.	1.	4.	3.	0.	0.	0.	51.	0.	0.	0.	0.	1.9
30	Si Ca Al	0.	0.	0.	0.	17.	44.	0.	1.	0.	3.	24.	2.	0.	0.	0.	9.	0.	0.	0.	0.	1.9
25	Ca Si Al	0.	0.	0.	0.	17.	29.	1.	1.	0.	2.	46.	0.	0.	0.	0.	4.	0.	0.	0.	0.	1.9
110	Si Al Ca	0.	0.	0.	0.	28.	46.	0.	1.	0.	4.	13.	2.	0.	0.	0.	6.	0.	0.	0.	0.	12.8
7	Si Ca Fe	0.	0.	0.	0.	7.	62.	0.	0.	0.	5.	15.	0.	0.	0.	0.	11.	0.	0.	0.	0.	0.5
6	Si Al Na	0.	0.	8.	0.	27.	58.	0.	0.	0.	5.	0.	0.	0.	0.	0.	1.	0.	0.	0.	0.	0.6
195	Si Al K	0.	0.	0.	0.	29.	57.	0.	1.	0.	8.	1.	0.	0.	0.	0.	4.	0.	0.	0.	0.	22.3
30	Si Al S	0.	0.	0.	0.	29.	47.	0.	13.	0.	5.	2.	2.	0.	0.	0.	2.	0.	0.	0.	0.	1.1
12	S Si Al	0.	0.	0.	0.	16.	27.	0.	46.	1.	3.	5.	2.	0.	0.	0.	0.	1.	0.	0.	0.	0.6
10	Si S Al	0.	0.	0.	0.	15.	49.	0.	20.	0.	8.	1.	0.	0.	1.	0.	5.	0.	0.	0.	0.	1.0
4	Fe Si S	0.	0.	0.	0.	2.	18.	0.	9.	0.	0.	4.	1.	0.	0.	0.	66.	0.	0.	0.	0.	0.6
1	S Si Zn	0.	0.	0.	0.	11.	29.	0.	35.	0.	0.	0.	12.	0.	0.	0.	0.	0.	0.	12.	0.	0.6
119	ALL CATEGORIES WITH VOLUME % LESS THAN 1.0 COMBINED IN ONE																					4.2
1181	TOTALS -	0.	0.	0.	0.	23.	52.	0.	2.	0.	5.	7.	1.	0.	0.	0.	9.	0.	0.	0.	0.	100.0

Volume DISTRIBUTION

SPECIES	Volume %	0.2-2.5	2.5-5.0	5.0-10.	10.- 20.	20.- 40.	40.- 80.	80.-500.
Si - -	12.2	10.	60.	14.	12.	3.	1.	0.
Si Al -	12.2	17.	62.	11.	8.	1.	0.	0.
Si Al Fe	16.6	27.	59.	5.	8.	2.	0.	0.
Si Al K	22.3	17.	65.	12.	5.	1.	0.	0.
Si Al Ca	12.8	12.	69.	9.	9.	1.	0.	0.
OTHERS -	23.9	13.	38.	19.	19.	6.	3.	2.
TOTALS -	100.0	16.	57.	12.	10.	3.	1.	0.

Table 4-14. CCSEM Analysis of Washed Pittsburgh No. 8 Coal Ash, 1500 °C Furnace Set Point, 2.6 s Res. time, stoichiometric ratio=0.9

AVERAGE SPECIES COMPOSITION

No.	SPECIES	C	O	Na	Mg	Al	Si	P	S	Cl	K	Ca	Ti	V	Cr	Mn	Fe	Ni	Cu	Zn	X	Vol %
147	Si - -	0.	0.	0.	0.	0.	1.	97.	0.	1.	0.	1.	0.	0.	0.	0.	0.	0.	0.	0.	0.	11.9
76	Fe - -	0.	0.	0.	0.	0.	1.	0.	3.	0.	0.	0.	0.	0.	0.	0.	96.	0.	0.	0.	0.	4.3
40	Ca - -	0.	0.	0.	0.	0.	1.	0.	1.	0.	0.	97.	0.	0.	0.	0.	1.	0.	0.	0.	0.	2.6
79	Fe S -	0.	0.	0.	0.	0.	0.	0.	28.	0.	0.	0.	0.	0.	0.	0.	71.	0.	0.	0.	0.	4.4
121	Si Al -	0.	0.	0.	0.	35.	58.	0.	1.	0.	3.	1.	1.	0.	0.	0.	1.	0.	0.	0.	0.	14.2
28	Al Si -	0.	0.	0.	0.	53.	46.	0.	0.	0.	1.	0.	0.	0.	0.	0.	0.	0.	0.	0.	0.	1.2
5	Ca Mg -	0.	0.	0.	21.	0.	0.	0.	2.	0.	0.	75.	0.	0.	0.	0.	2.	0.	0.	0.	0.	1.0
3	Si Ca -	0.	0.	0.	0.	0.	86.	0.	0.	0.	2.	11.	0.	0.	0.	0.	0.	0.	0.	0.	0.	0.5
14	Si Al Ti	0.	0.	0.	0.	23.	56.	0.	0.	0.	5.	3.	9.	0.	0.	0.	4.	0.	0.	0.	0.	1.1
28	Fe Si Al	0.	0.	0.	0.	15.	30.	0.	1.	0.	1.	5.	0.	0.	0.	0.	47.	0.	0.	0.	0.	2.1
17	Si Fe Al	0.	0.	0.	0.	16.	48.	0.	0.	0.	6.	4.	1.	0.	0.	0.	26.	0.	0.	0.	0.	0.8
85	Si Al Fe	0.	0.	0.	0.	28.	49.	0.	1.	0.	5.	3.	2.	0.	0.	0.	11.	0.	0.	0.	0.	7.8
31	Si Ca Al	0.	0.	0.	0.	19.	45.	0.	1.	0.	3.	24.	1.	0.	0.	0.	6.	0.	0.	0.	0.	2.8
18	Ca Si Al	0.	0.	0.	0.	14.	30.	0.	1.	0.	0.	50.	1.	0.	0.	0.	5.	0.	0.	0.	0.	1.9
57	Si Al Ca	0.	0.	0.	0.	30.	47.	0.	1.	0.	4.	13.	1.	0.	0.	0.	4.	0.	0.	0.	0.	9.1
2	Ca Al Si	0.	0.	0.	0.	12.	10.	0.	0.	0.	0.	74.	0.	0.	0.	0.	3.	0.	0.	0.	0.	0.5
191	Si Al K	0.	0.	0.	0.	32.	53.	0.	1.	0.	9.	2.	1.	0.	0.	0.	3.	0.	0.	0.	0.	20.7
4	Ca Si Fe	0.	0.	0.	0.	6.	23.	4.	3.	0.	2.	48.	1.	0.	0.	0.	13.	0.	0.	0.	0.	0.7
4	Si Al Na	0.	0.	8.	0.	40.	45.	0.	0.	0.	1.	0.	0.	0.	0.	0.	6.	0.	0.	0.	0.	0.5
3	Fe Si S	0.	0.	0.	0.	5.	17.	1.	9.	0.	0.	3.	3.	0.	2.	1.	59.	0.	0.	0.	0.	0.5
70	Si Al S	0.	0.	0.	0.	30.	52.	0.	10.	0.	3.	2.	1.	0.	0.	0.	2.	0.	0.	0.	0.	3.9
19	Si S Al	0.	0.	0.	0.	17.	44.	0.	26.	0.	7.	1.	3.	0.	0.	0.	2.	0.	0.	1.	0.	1.1
6	Ca S Si	0.	0.	0.	0.	2.	7.	0.	17.	0.	1.	71.	0.	0.	0.	0.	2.	0.	0.	0.	0.	0.9
134	ALL CATEGORIES WITH VOLUME % LESS THAN 1.0 COMBINED IN ONE																					5.4
1182	TOTALS -	0.	0.	0.	0.	21.	48.	0.	4.	0.	4.	10.	1.	0.	0.	0.	12.	0.	0.	0.	0.	100.0

Volume DISTRIBUTION

SPECIES	Volume %	0.2-2.5	2.5-5.0	5.0-10.	10.- 20.	20.- 40.	40.- 80.	80.-500.
Si - -	11.9	12.	21.	28.	33.	6.	0.	0.
Fe - -	4.3	4.	16.	15.	48.	16.	1.	0.
Fe S -	4.4	7.	29.	13.	35.	16.	0.	0.
Si Al -	14.2	14.	33.	33.	18.	1.	0.	0.
Si Al K	20.7	16.	39.	28.	16.	2.	0.	0.
Si Al Ca	9.1	11.	67.	16.	6.	0.	0.	0.
Si Al Fe	7.8	26.	39.	22.	11.	3.	0.	0.
OTHERS -	27.6	27.	23.	23.	21.	6.	0.	0.
TOTALS -	100.0	18.	33.	25.	20.	4.	0.	0.

Table 4-15. CCSEM Analysis of Washed Pittsburgh No. 8 Coal Ash, 1500°C Furnace Set Point, 2.6 s Res. Time, Stoichiometric Ratio=0.6

SAMPLE 1165 PSI ASH IN EPOXY, Pitt. No. 8 (DOE), 1500C, 2.6 RST, SR=0.6

AVERAGE SPECIES COMPOSITION

No.	SPECIES	C	O	Na	Mg	Al	Si	P	S	Cl	K	Ca	Ti	V	Cr	Mn	Fe	Ni	Cu	Zn	X	Vol %
202	Si - -	0.	0.	0.	0.	2.	90.	0.	0.	0.	4.	1.	0.	0.	0.	0.	2.	0.	0.	0.	0.	18.4
16	Ca - -	0.	0.	0.	1.	1.	3.	0.	1.	0.	0.	93.	0.	0.	0.	0.	0.	0.	0.	0.	0.	1.2
20	Fe - -	0.	0.	0.	0.	0.	2.	0.	1.	0.	0.	0.	0.	0.	0.	0.	97.	0.	0.	0.	0.	2.1
18	Si Al -	0.	0.	0.	0.	32.	63.	0.	0.	0.	4.	0.	0.	0.	0.	0.	1.	0.	0.	0.	0.	0.8
9	Fe Si -	0.	0.	0.	0.	0.	16.	0.	0.	0.	1.	1.	0.	0.	0.	0.	82.	0.	0.	0.	0.	0.8
9	Fe S -	0.	0.	0.	0.	0.	0.	0.	30.	0.	0.	0.	0.	0.	0.	0.	70.	0.	0.	0.	0.	0.8
401	Si Al K	0.	0.	0.	0.	24.	55.	0.	0.	0.	11.	3.	1.	0.	0.	0.	6.	0.	0.	0.	0.	35.5
31	Si K Al	0.	0.	0.	0.	11.	65.	0.	0.	0.	14.	2.	1.	0.	0.	0.	7.	0.	0.	0.	0.	3.0
9	Si Fe K	0.	0.	0.	0.	8.	60.	0.	0.	0.	12.	5.	1.	0.	0.	0.	13.	0.	0.	0.	0.	0.7
211	Si Al Fe	0.	0.	0.	0.	21.	50.	0.	0.	0.	9.	5.	2.	0.	0.	0.	12.	0.	0.	0.	0.	16.3
48	Si Fe Al	0.	0.	0.	0.	16.	48.	0.	0.	0.	8.	6.	1.	0.	0.	0.	22.	0.	0.	0.	0.	3.2
24	Fe Si Al	0.	0.	0.	0.	12.	29.	0.	0.	0.	5.	4.	1.	0.	0.	0.	49.	0.	0.	0.	0.	1.7
31	Si Ca Al	0.	0.	0.	0.	15.	46.	0.	0.	0.	6.	24.	0.	0.	0.	0.	9.	0.	0.	0.	0.	2.4
59	Si Al Ca	0.	0.	0.	0.	22.	49.	0.	0.	0.	7.	13.	0.	0.	0.	0.	8.	0.	0.	0.	0.	4.6
15	Ca Si Al	0.	0.	0.	0.	10.	26.	0.	0.	0.	0.	59.	1.	0.	0.	0.	4.	0.	0.	0.	0.	1.5
9	Si Fe Ca	0.	0.	0.	0.	8.	43.	0.	0.	0.	9.	11.	2.	0.	0.	0.	26.	0.	0.	0.	0.	0.8
7	Ca Si Fe	0.	0.	0.	4.	5.	32.	0.	0.	0.	1.	47.	1.	0.	0.	0.	11.	0.	0.	0.	0.	0.7
5	Si Ca Fe	0.	0.	0.	0.	11.	43.	0.	0.	0.	5.	25.	1.	0.	0.	0.	14.	0.	0.	0.	0.	0.8
3	Ca Si Mg	0.	0.	0.	7.	0.	27.	0.	0.	0.	0.	61.	0.	0.	0.	0.	5.	0.	0.	0.	0.	0.5
6	Si Al Ti	0.	0.	0.	0.	17.	50.	0.	0.	0.	9.	7.	12.	0.	0.	0.	5.	0.	0.	0.	0.	0.7
59	ALL CATEGORIES WITH VOLUME % LESS THAN 1.0 COMBINED IN ONE																					3.4
1193	TOTALS -	0.	0.	0.	0.	16.	56.	0.	0.	0.	8.	7.	2.	0.	0.	0.	11.	0.	0.	0.	0.	100.0

Volume DISTRIBUTION

SPECIES	Volume %	0.2-2.5	2.5-5.0	5.0-10.	10.- 20.	20.- 40.	40.- 80.	80.-500.
Si - -	18.4	2.	11.	27.	37.	12.	8.	3.
Si Al K	35.5	5.	20.	25.	38.	10.	1.	0.
Si Al Fe	16.3	6.	17.	16.	36.	17.	6.	3.
Si Al Ca	4.6	3.	17.	19.	36.	19.	6.	0.
OTHERS -	25.2	3.	8.	18.	35.	24.	13.	0.
TOTALS -	100.0	4.	15.	22.	37.	15.	6.	1.

Table 4-16. CCSEM Analysis of Run-of-Mine Pittsburgh No. 8 Coal Ash, 1500°C Furnace Set Point, 2.6 s Res. Time, stoichiometric ratio=1.2

SAMPLE 1166 PSI ASH IN EPOX Pitt. No. 8 (Kaiser Parent) 1500C 2.6 RST SR=1.2

AVERAGE SPECIES COMPOSITION

No.	SPECIES	C	O	Na	Mg	Al	Si	P	S	Cl	K	Ca	Ti	V	Cr	Mn	Fe	Ni	Cu	Zn	X	Vol %
61	Fe - -	0.	0.	0.	0.	0.	1.	0.	1.	0.	0.	0.	0.	0.	2.	0.	95.	1.	0.	0.	0.	2.6
23	Ca - -	0.	0.	0.	0.	0.	1.	0.	2.	0.	0.	95.	0.	0.	0.	0.	1.	0.	0.	0.	0.	1.0
183	Si - -	0.	0.	0.	0.	1.	97.	0.	1.	0.	1.	0.	0.	0.	0.	0.	0.	0.	0.	0.	0.	21.1
161	Si Al -	0.	0.	0.	0.	38.	55.	0.	1.	0.	4.	1.	0.	0.	0.	0.	1.	0.	0.	0.	0.	14.1
149	Fe S -	0.	0.	0.	0.	0.	0.	0.	29.	0.	0.	0.	0.	0.	0.	0.	70.	0.	0.	0.	0.	8.6
21	Ca P -	0.	0.	0.	0.	0.	0.	25.	0.	0.	0.	75.	0.	0.	0.	0.	0.	0.	0.	0.	0.	0.5
19	Ca S -	0.	0.	0.	0.	0.	0.	0.	30.	0.	0.	68.	0.	0.	0.	0.	1.	0.	0.	0.	0.	2.4
4	Si Ca -	0.	0.	0.	0.	0.	89.	0.	0.	0.	0.	11.	0.	0.	0.	0.	0.	0.	0.	0.	0.	0.5
2	Ca Si -	0.	0.	0.	0.	0.	23.	0.	0.	0.	0.	76.	0.	0.	0.	0.	2.	0.	0.	0.	0.	1.2
7	Ca Si Fe	0.	0.	0.	0.	12.	28.	0.	0.	0.	2.	45.	0.	0.	0.	0.	13.	0.	0.	0.	0.	1.5
43	Si Al Ca	0.	0.	0.	0.	30.	46.	0.	1.	0.	3.	12.	2.	0.	0.	0.	5.	0.	0.	0.	0.	1.7
19	Ca Si Al	0.	0.	0.	0.	11.	29.	0.	1.	0.	1.	51.	0.	0.	0.	0.	7.	0.	0.	0.	0.	1.6
224	Si Al K	0.	0.	0.	0.	29.	60.	0.	1.	0.	8.	0.	1.	0.	0.	0.	1.	0.	0.	0.	0.	22.7
11	Si K Al	0.	0.	0.	0.	17.	60.	0.	0.	0.	17.	1.	0.	0.	0.	0.	5.	0.	0.	0.	0.	0.8
47	Si Al Fe	0.	0.	0.	0.	29.	50.	0.	1.	0.	5.	4.	1.	0.	0.	0.	9.	0.	0.	0.	0.	6.9
8	Si Fe Al	0.	0.	0.	0.	12.	63.	0.	0.	0.	6.	0.	3.	0.	0.	0.	16.	0.	0.	0.	0.	0.8
6	Fe Si Al	0.	0.	0.	0.	21.	33.	0.	1.	0.	1.	2.	0.	0.	0.	0.	42.	0.	0.	0.	0.	0.5
8	Ca S Fe	0.	0.	0.	3.	0.	0.	0.	22.	0.	0.	60.	0.	0.	0.	0.	14.	0.	0.	0.	0.	1.1
8	Fe S Si	0.	0.	0.	0.	6.	15.	0.	28.	0.	0.	1.	1.	0.	1.	0.	48.	0.	0.	0.	0.	1.1
74	Si Al S	0.	0.	0.	0.	30.	49.	0.	14.	0.	3.	1.	1.	0.	0.	0.	1.	0.	0.	0.	0.	3.6
17	Si S Al	0.	0.	0.	0.	20.	40.	0.	27.	1.	2.	2.	3.	0.	0.	1.	3.	0.	1.	1.	0.	0.7
3	Ca P Si	0.	0.	0.	0.	3.	6.	17.	0.	0.	0.	73.	0.	0.	0.	0.	0.	0.	0.	0.	0.	0.6
74	ALL CATEGORIES WITH VOLUME % LESS THAN 1.0 COMBINED IN ONE																					3.9
1172	TOTALS -	0.	0.	0.	0.	17.	52.	0.	6.	0.	3.	8.	1.	0.	0.	0.	12.	0.	0.	0.	0.	100.0

Volume DISTRIBUTION

SPECIES	Volume %	0.2-2.5	2.5-5.0	5.0-10.	10.- 20.	20.- 40.	40.- 80.	80.-500.
Si - -	21.1	14.	27.	31.	24.	3.	0.	0.
Fe S -	8.6	2.	4.	19.	26.	25.	24.	0.
Si Al -	14.1	21.	34.	34.	9.	2.	0.	0.
Si Al K	22.7	16.	56.	19.	1.	5.	3.	0.
Si Al Fe	6.9	10.	68.	13.	7.	2.	0.	0.
OTHERS -	26.6	16.	15.	28.	14.	10.	10.	9.
TOTALS -	100.0	15.	32.	26.	13.	7.	5.	2.

Table 4-17. CCSEM Analysis of Run-of-Mine Pittsburgh No. 8 Coal Ash, 1500 °C Furnace Set Point, 2.6 s Res. Time, Stoichiometric Ratio=0.9

SAMPLE 1167 PSI ASH IN EPOXY, Pitt. No. 8 (Kaiser, parent), 1500C, 2.6 RST, SR=0.9

AVERAGE SPECIES COMPOSITION

No.	SPECIES	C	O	Na	Mg	Al	Si	P	S	Cl	K	Ca	Ti	V	Cr	Mn	Fe	Ni	Cu	Zn	X	Vol %
177	Si - -	0.	0.	0.	0.	2.	92.	0.	0.	0.	4.	1.	0.	0.	0.	0.	1.	0.	0.	0.	0.	17.0
14	Ca - -	0.	0.	0.	0.	1.	4.	2.	1.	0.	0.	92.	0.	0.	0.	0.	0.	0.	0.	0.	0.	1.9
10	Ca Si -	0.	0.	0.	0.	3.	24.	0.	0.	0.	0.	71.	0.	0.	0.	0.	2.	0.	0.	0.	0.	0.6
4	Si Ca -	0.	0.	0.	0.	2.	75.	0.	0.	0.	2.	17.	0.	0.	0.	0.	3.	0.	0.	0.	0.	0.6
31	Si Al -	0.	0.	0.	0.	39.	57.	0.	1.	0.	2.	0.	0.	0.	0.	0.	0.	0.	0.	0.	0.	2.8
4	Al Si -	0.	0.	0.	0.	52.	46.	0.	0.	0.	2.	0.	0.	0.	0.	0.	0.	0.	0.	0.	0.	1.1
65	Si Fe Al	0.	0.	0.	0.	17.	44.	0.	0.	0.	8.	6.	1.	0.	0.	0.	24.	0.	0.	0.	0.	3.9
211	Si Al Fe	0.	0.	0.	0.	23.	49.	0.	1.	0.	8.	5.	1.	0.	0.	0.	12.	0.	0.	0.	0.	14.3
20	Fe Si Al	0.	0.	0.	0.	10.	29.	0.	0.	0.	2.	4.	1.	0.	0.	0.	53.	0.	0.	0.	0.	1.1
406	Si Al K	0.	0.	0.	0.	24.	55.	0.	0.	0.	11.	2.	1.	0.	0.	0.	6.	0.	0.	0.	0.	39.0
26	Si K Al	0.	0.	0.	0.	10.	68.	0.	0.	0.	14.	2.	0.	0.	0.	0.	6.	0.	0.	0.	0.	1.1
3	Ca Si Mg	0.	0.	0.	9.	1.	13.	0.	0.	0.	0.	72.	0.	0.	0.	0.	5.	0.	0.	0.	0.	0.5
4	Si Fe K	0.	0.	0.	0.	10.	43.	0.	0.	0.	12.	0.	0.	0.	0.	0.	35.	0.	0.	0.	0.	0.7
55	Si Al Ca	0.	0.	0.	0.	22.	48.	0.	1.	0.	7.	14.	0.	0.	0.	0.	8.	0.	0.	0.	0.	5.0
49	Si Ca Al	0.	0.	0.	0.	15.	47.	0.	0.	0.	2.	27.	1.	0.	0.	0.	7.	0.	0.	0.	0.	3.5
8	Ca Si Al	0.	0.	0.	0.	8.	27.	0.	0.	0.	0.	61.	0.	0.	0.	0.	3.	0.	0.	0.	0.	0.9
13	Si Ca Fe	0.	0.	0.	2.	6.	37.	0.	2.	0.	5.	30.	2.	0.	0.	0.	17.	0.	0.	0.	0.	1.0
6	Si Al Ti	0.	0.	0.	0.	15.	50.	0.	1.	0.	9.	6.	13.	0.	0.	0.	7.	0.	0.	0.	0.	0.9
14	Si Al S	0.	0.	0.	0.	25.	49.	0.	12.	1.	5.	2.	0.	0.	0.	0.	6.	0.	0.	1.	0.	0.8
2	Si Al Na	0.	0.	9.	0.	21.	60.	0.	0.	0.	5.	0.	0.	0.	0.	0.	4.	0.	0.	0.	0.	0.7
67	ALL CATEGORIES WITH VOLUME % LESS THAN 1.0 COMBINED IN ONE																					2.7
1189	TOTALS -	0.	0.	0.	0.	18.	57.	0.	1.	0.	8.	8.	1.	0.	0.	0.	8.	0.	0.	0.	0.	100.0

Volume DISTRIBUTION

SPECIES	Volume %	0.2-2.5	2.5-5.0	5.0-10.	10.- 20.	20.- 40.	40.- 80.	80.-500.
Si - -	17.0	1.	7.	26.	54.	10.	2.	0.
Si Al Fe	14.3	7.	16.	27.	42.	7.	0.	0.
Si Al K	39.0	3.	10.	28.	52.	6.	0.	0.
Si Al Ca	5.0	3.	9.	31.	51.	5.	1.	0.
OTHERS -	24.7	2.	8.	24.	40.	16.	3.	6.
TOTALS -	100.0	3.	10.	27.	48.	10.	1.	1.

Table 4-18. CCSEM Analysis of Run-of-Mine Pittsburgh No. 8 Coal Ash, 1500 °C Furnace Set Point, 2.6 s Res. Time, Stoichiometric Ratio=0.6

SAMPLE 1168 PSI ASH IN EPOXY, Pitt. No. * (Kaiser, parent), 1500C, 2.6 RST, SR=0.6

AVERAGE SPECIES COMPOSITION

No.	SPECIES	C	O	Na	Mg	Al	Si	P	S	Cl	K	Ca	Ti	V	Cr	Mn	Fe	Ni	Cu	Zn	X	Vol %
205	Si - -	0.	0.	0.	0.	1.	94.	0.	0.	0.	3.	1.	0.	0.	0.	0.	1.	0.	0.	0.	0.	16.9
16	Ca - -	0.	0.	0.	0.	0.	1.	0.	1.	0.	0.	98.	0.	0.	0.	0.	0.	0.	0.	0.	0.	1.4
6	Ca Si -	0.	0.	0.	0.	1.	24.	0.	0.	0.	0.	75.	0.	0.	0.	0.	0.	0.	0.	0.	0.	1.0
24	Fe S -	0.	0.	0.	0.	0.	0.	0.	31.	0.	0.	0.	0.	0.	0.	0.	69.	0.	0.	0.	0.	2.5
19	Si Al -	0.	0.	0.	0.	31.	60.	0.	2.	0.	4.	1.	0.	0.	0.	0.	2.	0.	0.	0.	0.	1.6
4	Fe Si -	0.	0.	0.	0.	0.	29.	0.	1.	0.	2.	3.	0.	0.	0.	0.	65.	0.	0.	0.	0.	0.6
390	Si Al K	0.	0.	0.	0.	26.	56.	0.	0.	0.	11.	1.	1.	0.	0.	0.	5.	0.	0.	0.	0.	35.9
26	Si K Al	0.	0.	0.	0.	11.	65.	0.	1.	0.	14.	1.	1.	0.	0.	0.	7.	0.	0.	0.	0.	1.9
166	Si Al Fe	0.	0.	0.	0.	23.	50.	0.	1.	0.	9.	4.	1.	0.	0.	0.	12.	0.	0.	0.	0.	12.0
48	Si Fe Al	0.	0.	0.	0.	17.	44.	0.	0.	0.	7.	4.	1.	0.	0.	0.	25.	0.	0.	0.	0.	3.1
16	Fe Si Al	0.	0.	0.	0.	14.	28.	0.	1.	0.	3.	4.	1.	0.	0.	0.	49.	0.	0.	0.	0.	1.7
38	Si Ca Al	0.	0.	0.	0.	16.	48.	0.	0.	0.	4.	24.	0.	0.	0.	0.	7.	0.	0.	0.	0.	2.9
53	Si Al Ca	0.	0.	0.	0.	22.	49.	0.	1.	0.	6.	14.	1.	0.	0.	0.	7.	0.	0.	0.	0.	3.5
20	Ca Si Al	0.	0.	0.	1.	14.	33.	1.	0.	0.	2.	43.	1.	0.	0.	0.	5.	0.	0.	0.	0.	1.9
5	Fe S Si	0.	0.	0.	0.	1.	8.	0.	32.	0.	0.	2.	0.	0.	0.	0.	56.	0.	0.	0.	0.	0.6
15	Si S Al	0.	0.	0.	0.	13.	51.	0.	22.	1.	5.	2.	3.	0.	0.	0.	3.	0.	0.	0.	0.	1.5
7	Si Fe K	0.	0.	0.	0.	9.	61.	0.	0.	0.	12.	2.	1.	0.	0.	0.	14.	0.	0.	0.	0.	0.6
10	Si Ca Fe	0.	0.	0.	0.	7.	51.	0.	0.	0.	2.	29.	0.	0.	0.	0.	10.	0.	0.	0.	0.	0.6
7	Si Fe Ca	0.	0.	0.	0.	7.	48.	0.	0.	0.	6.	12.	1.	0.	0.	0.	27.	0.	0.	0.	0.	1.1
7	Ca Si Fe	0.	0.	0.	4.	2.	26.	0.	0.	0.	2.	56.	1.	0.	0.	0.	9.	0.	0.	0.	0.	1.5
5	Fe Si Ca	0.	0.	0.	0.	12.	27.	0.	1.	0.	1.	16.	0.	0.	0.	0.	44.	0.	0.	0.	0.	0.8
7	Si Al Ti	0.	0.	0.	0.	24.	45.	0.	2.	0.	9.	1.	12.	0.	0.	0.	7.	0.	0.	0.	0.	0.9
3	Si S K	0.	0.	0.	0.	1.	51.	0.	27.	0.	15.	0.	0.	0.	0.	0.	6.	0.	0.	0.	0.	0.5
92	ALL CATEGORIES WITH VOLUME % LESS THAN 1.0 COMBINED IN ONE																					4.5
1190	TOTALS -	0.	0.	0.	0.	17.	55.	0.	2.	0.	7.	7.	1.	0.	0.	0.	10.	0.	0.	0.	0.	100.0

Volume DISTRIBUTION

SPECIES	Volume %	0.2-2.5	2.5-5.0	5.0-10.	10.- 20.	20.- 40.	40.- 80.	80.-500.
Si - -	16.9	4.	16.	29.	27.	16.	5.	3.
Si Al K	35.9	9.	32.	21.	27.	9.	2.	0.
Si Al Fe	12.0	19.	36.	15.	14.	10.	6.	0.
OTHERS -	35.1	9.	20.	13.	25.	15.	12.	7.
TOTALS -	100.0	9.	26.	19.	25.	13.	6.	3.

Table 4-19. CCSEM Analysis of Beneficiated Pittsburgh No. 8 Coal Ash, 1500 °C Furnace Set Point, 2.6 s Res. Time, Stoichiometric ratio=1.2

SAMPLE 1169 PSI ASH IN EPOXY, Pitt. No. 8 (Kaiser, SCS-cleaned), 1500C, 2.6 RST, SR

AVERAGE SPECIES COMPOSITION

No.	SPECIES	C	O	Na	Mg	Al	Si	P	S	Cl	K	Ca	Ti	V	Cr	Mn	Fe	Ni	Cu	Zn	X	Vol %
17	Ca - -	0.	0.	0.	0.	1.	1.	0.	1.	0.	0.	94.	0.	0.	0.	0.	3.	0.	0.	0.	0.	0.7
55	Si - -	0.	0.	0.	0.	2.	93.	0.	0.	0.	1.	0.	0.	0.	0.	0.	3.	0.	0.	0.	0.	5.3
16	Fe - -	0.	0.	0.	0.	3.	5.	0.	1.	0.	0.	1.	1.	0.	0.	0.	89.	0.	0.	0.	0.	0.7
2	Al - -	0.	0.	0.	0.	99.	0.	0.	0.	0.	0.	0.	1.	0.	0.	0.	0.	0.	0.	0.	0.	0.7
29	Al Si -	0.	0.	0.	0.	51.	47.	0.	0.	0.	1.	0.	0.	0.	0.	0.	1.	0.	0.	0.	0.	3.1
87	Si Al -	0.	0.	0.	0.	39.	56.	0.	0.	0.	2.	0.	0.	0.	0.	0.	2.	0.	0.	0.	0.	9.4
14	Si Fe -	0.	0.	0.	0.	0.	79.	0.	1.	0.	2.	0.	1.	0.	0.	0.	17.	0.	0.	0.	0.	1.3
339	Fe Si Al	0.	0.	0.	0.	17.	28.	0.	1.	0.	1.	4.	2.	0.	0.	0.	47.	0.	0.	0.	0.	25.8
217	Si Al Fe	0.	0.	0.	0.	29.	47.	0.	0.	0.	5.	2.	1.	0.	0.	0.	15.	0.	0.	0.	0.	21.9
8	Al Si Fe	0.	0.	0.	0.	46.	41.	0.	0.	0.	2.	0.	0.	0.	0.	0.	10.	0.	0.	0.	0.	0.7
157	Si Fe Al	0.	0.	0.	0.	18.	43.	0.	1.	0.	3.	3.	1.	0.	0.	0.	30.	0.	0.	0.	0.	11.9
13	Fe Al Si	0.	0.	0.	0.	25.	20.	0.	2.	0.	1.	2.	0.	0.	0.	0.	50.	0.	0.	0.	0.	0.6
20	Fe Si Ca	0.	0.	0.	0.	11.	21.	0.	1.	1.	0.	15.	4.	0.	0.	0.	47.	0.	0.	1.	0.	1.5
6	Fe Ca Si	0.	0.	0.	0.	14.	21.	0.	0.	0.	0.	25.	4.	0.	0.	0.	35.	0.	0.	0.	0.	0.5
8	Si Fe K	0.	0.	0.	0.	3.	67.	0.	0.	0.	8.	0.	1.	0.	0.	0.	20.	0.	0.	0.	0.	0.6
13	Fe Si S	0.	0.	0.	0.	8.	28.	0.	14.	1.	1.	5.	2.	0.	0.	0.	40.	0.	0.	0.	0.	0.6
8	Fe S Si	0.	0.	0.	0.	8.	19.	0.	24.	2.	0.	5.	0.	0.	0.	0.	39.	0.	2.	0.	0.	0.6
70	Si Al K	0.	0.	0.	0.	31.	57.	0.	0.	0.	9.	0.	0.	0.	0.	0.	3.	0.	0.	0.	0.	6.9
4	Al Si K	0.	0.	0.	0.	48.	43.	0.	0.	0.	7.	0.	0.	0.	0.	0.	2.	0.	0.	0.	0.	0.7
106	ALL CATEGORIES WITH VOLUME % LESS THAN 1.0 COMBINED IN ONE																					6.8
1189	TOTALS -	0.	0.	0.	0.	23.	43.	0.	2.	0.	3.	4.	1.	0.	0.	0.	24.	0.	0.	0.	0.	100.0

Volume DISTRIBUTION

SPECIES	Volume %	0.2-2.5	2.5-5.0	5.0-10.	10.- 20.	20.- 40.	40.- 80.	80.-500.
Si - -	5.3	4.	29.	18.	37.	11.	0.	0.
Si Al -	9.4	1.	19.	40.	33.	8.	0.	0.
Fe Si Al	25.8	23.	34.	21.	15.	6.	2.	0.
Si Al Fe	21.9	6.	19.	33.	34.	7.	0.	0.
Si Fe Al	11.9	11.	41.	22.	15.	11.	0.	0.
Si Al K	6.9	1.	0.	37.	51.	10.	1.	0.
OTHERS -	18.8	15.	17.	28.	22.	10.	6.	3.
TOTALS -	100.0	12.	24.	28.	26.	8.	2.	1.

Table 4-20. CCSEM Analysis of Beneficiated Pittsburgh No. 8 Coal Ash, 1500 °C Furnace Set Point, 2.6 s Res. Time, Stoichiometric Ratio=0.9

SAMPLE 1170 PSI ASH IN EPOXY rerun

AVERAGE SPECIES COMPOSITION

No.	SPECIES	C	O	Na	Mg	Al	Si	P	S	Cl	K	Ca	Ti	V	Cr	Mn	Fe	Ni	Cu	Zn	X	Vol %
91	Si - -	0.	0.	0.	0.	1.	96.	0.	0.	0.	1.	0.	0.	0.	0.	0.	1.	0.	0.	0.	0.	9.1
29	Fe - -	0.	0.	0.	0.	2.	2.	0.	1.	0.	0.	0.	0.	0.	0.	0.	95.	0.	0.	0.	0.	1.2
19	Ca - -	0.	0.	0.	0.	0.	1.	0.	1.	0.	0.	95.	0.	0.	0.	0.	3.	0.	0.	0.	0.	0.5
46	Al Si -	0.	0.	0.	0.	52.	47.	0.	0.	0.	0.	0.	0.	0.	0.	0.	0.	0.	0.	0.	0.	1.7
79	Si Al -	0.	0.	0.	0.	41.	54.	0.	1.	0.	2.	0.	0.	0.	0.	0.	1.	0.	0.	0.	0.	3.8
17	Fe S -	0.	0.	0.	0.	0.	1.	0.	29.	0.	1.	0.	1.	0.	0.	0.	68.	0.	0.	0.	0.	0.7
15	Si Fe -	0.	0.	0.	0.	0.	79.	0.	1.	0.	3.	1.	0.	0.	0.	0.	16.	0.	0.	0.	0.	2.2
127	Si Fe Al	0.	0.	0.	0.	17.	44.	0.	2.	0.	4.	3.	2.	0.	0.	0.	28.	0.	0.	0.	0.	11.2
232	Fe Si Al	0.	0.	0.	0.	16.	27.	0.	2.	0.	1.	4.	2.	0.	0.	0.	48.	0.	0.	0.	0.	22.5
199	Si Al Fe	0.	0.	0.	0.	30.	46.	0.	2.	0.	5.	1.	1.	0.	0.	0.	15.	0.	0.	0.	0.	18.5
66	Si Al K	0.	0.	0.	0.	34.	53.	0.	1.	0.	9.	0.	0.	0.	0.	0.	3.	0.	0.	0.	0.	6.6
19	Fe Si Ca	0.	0.	0.	0.	10.	25.	0.	2.	0.	1.	14.	2.	0.	0.	0.	47.	0.	0.	0.	0.	1.9
8	Fe Ca Si	0.	0.	0.	0.	11.	16.	0.	2.	0.	0.	22.	4.	0.	0.	0.	45.	0.	0.	0.	0.	1.4
6	Fe Si Ti	0.	0.	0.	0.	8.	21.	0.	2.	0.	0.	4.	13.	0.	0.	0.	51.	0.	1.	0.	0.	0.6
5	Si Fe Ti	0.	0.	0.	0.	1.	67.	0.	0.	0.	4.	0.	9.	0.	0.	0.	19.	0.	0.	0.	0.	0.5
9	Si Al Ca	0.	0.	0.	0.	28.	44.	0.	0.	0.	2.	15.	0.	0.	0.	0.	10.	0.	0.	0.	0.	0.5
6	Ca Si Al	0.	0.	0.	0.	17.	22.	0.	0.	0.	0.	50.	0.	0.	0.	0.	11.	0.	0.	0.	0.	0.6
18	Fe S Si	0.	0.	0.	0.	2.	21.	0.	26.	3.	3.	3.	1.	0.	1.	0.	36.	2.	0.	2.	0.	1.7
13	S Si Fe	0.	0.	0.	0.	11.	24.	0.	39.	1.	0.	4.	4.	0.	0.	0.	17.	0.	0.	0.	0.	1.0
14	Si S Fe	0.	0.	0.	0.	9.	36.	0.	27.	1.	5.	1.	1.	0.	0.	0.	17.	1.	0.	2.	0.	1.9
14	Si Fe S	0.	0.	0.	0.	5.	38.	0.	16.	3.	5.	2.	0.	0.	0.	0.	27.	0.	0.	4.	0.	2.0
27	Fe Si S	0.	0.	0.	0.	11.	24.	0.	18.	1.	1.	3.	2.	0.	1.	0.	40.	0.	0.	1.	0.	2.6
7	S Fe Si	0.	0.	0.	0.	13.	19.	0.	29.	2.	6.	1.	1.	0.	1.	0.	23.	0.	0.	6.	0.	1.0
8	Si S Al	0.	0.	0.	0.	18.	48.	0.	27.	1.	0.	0.	0.	0.	0.	0.	3.	0.	0.	0.	0.	1.0
9	Si Al S	0.	0.	0.	0.	24.	45.	0.	17.	0.	2.	2.	0.	0.	0.	0.	10.	0.	0.	0.	0.	0.9
85	ALL CATEGORIES WITH VOLUME % LESS THAN 1.0 COMBINED IN ONE																					4.3
1168	TOTALS -	0.	0.	0.	0.	18.	43.	0.	5.	0.	3.	4.	1.	0.	0.	0.	25.	0.	0.	0.	0.	100.0

Volume DISTRIBUTION

SPECIES	Volume %	0.2-2.5	2.5-5.0	5.0-10.	10.- 20.	20.- 40.	40.- 80.	80.-500.
Si - -	9.1	4.	42.	33.	15.	4.	2.	0.
Si Fe Al	11.2	21.	32.	28.	14.	4.	1.	0.
Fe Si Al	22.5	29.	41.	14.	10.	4.	2.	0.
Si Al Fe	18.5	20.	32.	23.	22.	4.	0.	0.
Si Al K	6.6	18.	36.	22.	19.	4.	1.	0.
OTHERS -	32.0	16.	30.	26.	17.	7.	3.	0.
TOTALS -	100.0	19.	35.	23.	16.	5.	2.	0.

Table 4-21. CCSEM Analysis of Beneficiated Pittsburgh No. 8 Coal Ash, 1500 °C Furnace Set Point, 2.6 s Res. Time, Stoichiometric Ratio=0.6

SAMPLE 1171 PSI ASH IN EPOXY, Pitt No. 8 (Kaiser, SCS cleaned), 1500C, 2.6 RST, SR=0.6

AVERAGE SPECIES COMPOSITION

No.	SPECIES	C	O	Na	Mg	Al	Si	P	S	Cl	K	Ca	Ti	V	Cr	Mn	Fe	Ni	Cu	Zn	X	Vol %
69	Si - -	0.	0.	0.	0.	2.	94.	0.	1.	0.	1.	0.	0.	0.	0.	0.	2.	0.	0.	0.	0.	7.3
15	Fe - -	0.	0.	0.	0.	0.	1.	0.	2.	0.	0.	0.	0.	0.	0.	0.	97.	0.	0.	0.	0.	0.6
94	Al Si -	0.	0.	0.	0.	53.	45.	0.	0.	0.	1.	0.	0.	0.	0.	0.	0.	0.	0.	0.	0.	1.8
96	Si Al -	0.	0.	0.	0.	37.	57.	0.	1.	0.	3.	0.	0.	0.	0.	0.	2.	0.	0.	0.	0.	5.0
50	Fe S -	0.	0.	0.	0.	0.	2.	0.	32.	0.	0.	0.	0.	0.	0.	0.	66.	0.	0.	0.	0.	3.8
2	Si Ti -	0.	0.	0.	0.	0.	79.	0.	0.	0.	0.	0.	21.	0.	0.	0.	0.	0.	0.	0.	0.	0.7
4	Si Fe -	0.	0.	0.	0.	0.	75.	0.	1.	0.	2.	1.	0.	0.	0.	0.	21.	0.	0.	0.	0.	0.5
95	Fe Si Al	0.	0.	0.	0.	15.	26.	0.	5.	0.	1.	3.	1.	0.	0.	0.	49.	0.	0.	0.	0.	9.1
127	Si Al Fe	0.	0.	0.	0.	31.	46.	0.	3.	0.	4.	1.	0.	0.	0.	0.	15.	0.	0.	0.	0.	16.2
75	Si Fe Al	0.	0.	0.	0.	19.	42.	0.	5.	0.	4.	1.	0.	0.	0.	0.	28.	0.	0.	0.	0.	4.9
56	Si Al K	0.	0.	0.	0.	35.	52.	0.	2.	0.	7.	0.	0.	0.	0.	0.	4.	0.	0.	0.	0.	4.3
35	Si S Al	0.	0.	0.	0.	18.	40.	0.	27.	1.	2.	2.	1.	0.	0.	0.	9.	0.	0.	0.	0.	4.4
25	S Si Al	0.	0.	0.	0.	15.	28.	0.	45.	1.	1.	0.	1.	0.	0.	0.	9.	0.	0.	0.	0.	2.9
32	Si Al S	0.	0.	0.	0.	28.	47.	0.	13.	0.	4.	1.	1.	0.	0.	0.	6.	0.	0.	0.	0.	1.8
5	S Al Si	0.	0.	0.	0.	20.	17.	0.	44.	0.	0.	7.	0.	0.	0.	0.	11.	0.	0.	0.	0.	0.8
33	Si S Fe	0.	0.	0.	0.	9.	41.	0.	28.	0.	2.	1.	0.	0.	1.	0.	18.	0.	0.	0.	0.	3.0
67	S Si Fe	0.	0.	0.	0.	7.	26.	0.	45.	0.	1.	3.	1.	0.	0.	0.	16.	0.	0.	0.	0.	8.0
28	Fe Si S	0.	0.	0.	0.	10.	26.	0.	14.	0.	0.	1.	1.	0.	0.	0.	46.	0.	0.	0.	0.	2.4
18	Si Fe S	0.	0.	0.	0.	4.	48.	0.	15.	0.	3.	1.	2.	0.	0.	0.	23.	0.	0.	2.	0.	3.8
40	Fe S Si	0.	0.	0.	0.	7.	18.	0.	30.	0.	1.	1.	0.	0.	1.	0.	42.	0.	0.	0.	0.	3.5
49	S Fe Si	0.	0.	0.	0.	10.	17.	0.	45.	0.	2.	1.	0.	0.	0.	0.	25.	0.	0.	0.	0.	7.8
6	S Si Ca	0.	0.	0.	0.	6.	25.	0.	46.	0.	1.	14.	0.	0.	0.	0.	9.	0.	0.	0.	0.	0.7
7	S Si Ti	0.	0.	0.	0.	8.	30.	0.	43.	0.	0.	0.	13.	0.	0.	0.	5.	0.	0.	0.	0.	0.8
123	ALL CATEGORIES WITH VOLUME % LESS THAN 1.0 COMBINED IN ONE																					5.6
1151	TOTALS -	0.	0.	0.	0.	16.	39.	0.	18.	0.	2.	2.	1.	0.	0.	0.	21.	0.	0.	0.	0.	100.0

Volume DISTRIBUTION

SPECIES	Volume %	0.2-2.5	2.5-5.0	5.0-10.	10.- 20.	20.- 40.	40.- 80.	80.-500.
Si - -	7.3	13.	47.	28.	10.	2.	0.	0.
Si Al -	5.0	16.	18.	34.	20.	10.	1.	0.
Fe Si Al	9.1	49.	29.	11.	8.	2.	1.	0.
Si Al Fe	16.2	26.	53.	14.	6.	1.	0.	0.
Si Fe Al	4.9	56.	14.	28.	0.	1.	1.	0.
Si Al K	4.3	20.	24.	40.	12.	4.	0.	0.
Si S Al	4.4	7.	44.	27.	22.	0.	0.	0.
S Si Fe	8.0	15.	48.	27.	10.	1.	0.	0.
S Fe Si	7.8	12.	72.	16.	0.	0.	0.	0.
OTHERS -	33.1	33.	26.	21.	12.	5.	2.	1.
TOTALS -	100.0	28.	37.	21.	10.	3.	1.	0.

Table 4-22. CCSEM Analysis of Black Thunder Coal Ash, 1500 °C Furnace Set Point, 2.6 s Res. Time, Stoichiometric Ratio=1.2

SAMPLE 1172 PSI ASH IN EPOXY, Black Thunder, 1500C, 2.6 RST, SR=1.2

AVERAGE SPECIES COMPOSITION

No.	SPECIES	C	O	Na	Mg	Al	Si	P	S	Cl	K	Ca	Ti	V	Cr	Mn	Fe	Ni	Cu	Zn	X	Vol %
260	Ca - -	0.	0.	0.	2.	5.	2.	0.	0.	0.	0.	83.	1.	0.	0.	0.	6.	0.	0.	0.	0.	24.9
130	Si - -	0.	0.	0.	0.	0.	98.	0.	0.	0.	0.	2.	0.	0.	0.	0.	0.	0.	0.	0.	0.	11.4
16	Fe - -	0.	0.	0.	0.	0.	0.	0.	1.	0.	0.	1.	0.	0.	0.	0.	98.	0.	0.	0.	0.	1.1
36	Al Si -	0.	0.	0.	0.	54.	45.	0.	0.	0.	1.	0.	0.	0.	0.	0.	0.	0.	0.	0.	0.	3.5
34	Si Al -	0.	0.	0.	0.	39.	55.	0.	0.	0.	3.	2.	0.	0.	0.	0.	0.	0.	0.	0.	0.	2.6
42	Ca Si -	0.	0.	0.	2.	1.	26.	0.	0.	0.	0.	66.	1.	0.	0.	0.	3.	0.	0.	0.	0.	3.3
46	Si Ca -	0.	0.	0.	0.	0.	73.	0.	0.	0.	0.	24.	1.	0.	0.	0.	1.	0.	0.	0.	0.	4.5
32	Ca Al -	0.	0.	0.	1.	17.	1.	2.	0.	0.	0.	74.	1.	0.	0.	0.	4.	0.	0.	0.	0.	2.7
5	Ca Mg -	0.	0.	0.	18.	2.	1.	0.	0.	0.	0.	74.	1.	0.	0.	0.	4.	0.	0.	0.	0.	0.5
84	Ca Si Al	0.	0.	0.	0.	14.	23.	0.	0.	0.	0.	56.	1.	0.	0.	0.	4.	0.	0.	0.	0.	5.5
61	Si Al Ca	0.	0.	1.	0.	32.	47.	0.	0.	0.	2.	15.	1.	0.	0.	0.	2.	0.	0.	0.	0.	5.4
10	Al Si Ca	0.	0.	0.	0.	40.	36.	0.	0.	0.	1.	19.	2.	0.	0.	0.	2.	0.	0.	0.	0.	1.0
40	Ca Al Si	0.	0.	0.	0.	21.	14.	1.	0.	0.	0.	58.	2.	0.	0.	0.	4.	0.	0.	0.	0.	2.7
33	Si Ca Al	0.	0.	1.	0.	17.	46.	0.	0.	0.	2.	28.	2.	0.	0.	0.	3.	0.	0.	0.	0.	2.3
12	Si S Ca	0.	0.	0.	1.	1.	55.	0.	25.	3.	2.	13.	0.	0.	0.	0.	0.	0.	0.	0.	0.	1.2
5	Si Ca S	0.	0.	0.	0.	6.	53.	0.	14.	0.	0.	25.	2.	0.	0.	0.	0.	0.	0.	0.	0.	0.7
5	S Si Ca	0.	0.	0.	0.	0.	26.	0.	41.	10.	0.	22.	0.	0.	0.	0.	0.	0.	0.	1.	0.	0.7
31	Ca Si Fe	0.	0.	0.	1.	1.	25.	0.	0.	0.	0.	65.	1.	0.	0.	0.	6.	0.	0.	0.	0.	3.4
10	Si Ca Ti	0.	0.	0.	0.	0.	60.	0.	0.	0.	4.	24.	10.	0.	0.	0.	1.	0.	0.	0.	0.	0.7
10	Ca Si Ti	0.	0.	0.	0.	1.	25.	0.	0.	0.	0.	64.	7.	0.	0.	0.	3.	0.	0.	0.	0.	1.1
4	Si Ti Ca	0.	0.	0.	0.	7.	65.	0.	0.	0.	0.	10.	18.	0.	0.	0.	0.	0.	0.	0.	0.	1.2
46	Ca Al P	0.	0.	0.	0.	23.	0.	13.	0.	0.	0.	58.	3.	0.	0.	0.	3.	0.	0.	0.	0.	4.0
10	Ca P Al	0.	0.	0.	0.	13.	0.	20.	0.	0.	0.	61.	3.	0.	0.	0.	2.	0.	0.	0.	0.	0.8
65	Ca Al Fe	0.	0.	0.	1.	13.	1.	0.	0.	0.	0.	76.	1.	0.	0.	0.	8.	0.	0.	0.	0.	5.0
16	Ca Fe Al	0.	0.	0.	1.	10.	3.	0.	0.	0.	0.	70.	0.	0.	0.	0.	15.	0.	0.	0.	0.	0.6
7	Ca Mg Fe	0.	0.	0.	14.	3.	1.	0.	1.	0.	0.	74.	0.	0.	0.	0.	7.	0.	0.	0.	0.	0.8
4	Ca Mg Si	0.	0.	0.	12.	2.	9.	0.	0.	0.	0.	72.	0.	0.	0.	0.	5.	0.	0.	0.	0.	0.5
13	Si Al K	0.	0.	1.	0.	32.	54.	0.	0.	0.	9.	2.	0.	0.	0.	0.	2.	0.	0.	0.	0.	0.9
11	Ca Al Mg	0.	0.	0.	8.	13.	1.	2.	1.	0.	0.	71.	0.	0.	0.	0.	5.	0.	0.	0.	0.	0.5
15	Si Al Na	0.	0.	13.	0.	29.	46.	0.	1.	0.	6.	4.	1.	0.	0.	0.	1.	0.	0.	0.	0.	1.1
92	ALL CATEGORIES WITH VOLUME % LESS THAN 1.0 COMBINED IN ONE																					5.6
1186	TOTALS -	0.	0.	0.	1.	12.	31.	1.	1.	0.	1.	47.	2.	0.	0.	0.	5.	0.	0.	0.	0.	

Volume DISTRIBUTION

SPECIES	Volume %	0.2-2.5	2.5-5.0	5.0-10.	10.- 20.	20.- 40.	40.- 80.	80.-500.
Ca - -	24.9	5.	18.	22.	39.	14.	2.	0.
Si - -	11.4	7.	21.	19.	23.	21.	9.	0.
Si Ca -	4.5	1.	11.	17.	51.	20.	0.	0.
Ca Si Al	5.5	15.	9.	12.	23.	33.	8.	0.
Si Al Ca	5.4	16.	21.	17.	38.	7.	0.	0.
Ca Al P	4.0	14.	27.	19.	28.	12.	0.	0.
Ca Al Fe	5.0	13.	35.	22.	20.	11.	0.	0.
OTHERS -	39.4	10.	17.	20.	29.	20.	5.	0.
TOTALS -	100.0	9.	19.	20.	31.	18.	4.	0.

Table 4-23. CCSEM Analysis of Black Thunder Coal Ash, 1500 °C Furnace Set Point, 2.6 s Res. Time, Stoichiometric Ratio=0.9

SAMPLE 1173 PSI ASH IN EPOXY, Black Thunder, 1500C, 2.6 RST, SR=0.9

AVERAGE SPECIES COMPOSITION

No.	SPECIES	C	O	Na	Mg	Al	Si	P	S	Cl	K	Ca	Ti	V	Cr	Mn	Fe	Ni	Cu	Zn	X	Vol %
188	Si - -	0.	0.	0.	0.	0.	99.	0.	0.	0.	0.	1.	0.	0.	0.	0.	0.	0.	0.	0.	0.	16.8
254	Ca - -	0.	0.	0.	2.	5.	3.	0.	0.	0.	0.	83.	1.	0.	0.	0.	6.	0.	0.	0.	0.	22.4
35	Al Si -	0.	0.	0.	0.	53.	46.	0.	0.	0.	0.	1.	0.	0.	0.	0.	0.	0.	0.	0.	0.	3.9
21	Si Al -	0.	0.	0.	0.	38.	57.	0.	0.	0.	2.	2.	0.	0.	0.	0.	0.	0.	0.	0.	0.	1.6
60	Ca Si -	0.	0.	0.	1.	2.	20.	0.	0.	0.	0.	73.	1.	0.	0.	0.	3.	0.	0.	0.	0.	6.1
45	Si Ca -	0.	0.	0.	1.	0.	69.	0.	0.	0.	0.	27.	1.	0.	0.	0.	2.	0.	0.	0.	0.	3.9
45	Ca Al -	0.	0.	0.	0.	15.	1.	1.	0.	0.	0.	77.	1.	0.	0.	0.	5.	0.	0.	0.	0.	4.4
1	Si P -	0.	0.	0.	0.	0.	52.	44.	0.	0.	0.	4.	0.	0.	0.	0.	0.	0.	0.	0.	0.	0.5
97	Ca Al Fe	0.	0.	0.	0.	13.	1.	0.	0.	0.	0.	77.	0.	0.	0.	0.	8.	0.	0.	0.	0.	7.3
20	Ca Fe Al	0.	0.	0.	0.	8.	1.	0.	1.	0.	0.	78.	0.	0.	0.	0.	11.	0.	0.	0.	0.	1.6
11	Si Ca Ti	0.	0.	0.	0.	3.	55.	0.	0.	0.	0.	33.	8.	0.	0.	0.	2.	0.	0.	0.	0.	1.0
12	Ca Si Ti	0.	0.	0.	1.	3.	26.	0.	0.	0.	0.	56.	10.	0.	0.	0.	4.	0.	0.	0.	0.	1.2
29	Ca Si Fe	0.	0.	0.	0.	2.	21.	0.	0.	0.	0.	68.	1.	0.	0.	0.	8.	0.	0.	0.	0.	1.7
40	Si Ca Al	0.	0.	0.	0.	16.	51.	0.	0.	0.	1.	28.	1.	0.	0.	0.	3.	0.	0.	0.	0.	2.8
53	Si Al Ca	0.	0.	2.	0.	30.	48.	0.	0.	0.	3.	13.	1.	0.	0.	0.	2.	0.	0.	0.	0.	3.3
78	Ca Si Al	0.	0.	0.	0.	13.	23.	0.	0.	0.	0.	58.	1.	0.	0.	0.	4.	0.	0.	0.	0.	6.1
44	Ca Al Si	0.	0.	0.	0.	21.	13.	1.	0.	0.	0.	60.	1.	0.	0.	0.	4.	0.	0.	0.	0.	3.2
14	Al Si Ca	0.	0.	0.	0.	40.	38.	0.	0.	0.	2.	18.	0.	0.	0.	0.	2.	0.	0.	0.	0.	1.1
41	Ca Al P	0.	0.	0.	0.	25.	1.	12.	0.	0.	0.	56.	2.	0.	0.	0.	3.	0.	0.	0.	0.	2.6
18	Si Al K	0.	0.	1.	0.	33.	55.	0.	0.	0.	7.	3.	0.	0.	0.	0.	1.	0.	0.	0.	0.	1.9
1	P Ca Si	0.	0.	0.	0.	0.	31.	33.	0.	0.	0.	31.	0.	0.	0.	0.	4.	0.	0.	0.	0.	0.5
11	Si Al Na	0.	0.	10.	0.	37.	43.	0.	0.	0.	6.	3.	0.	0.	0.	0.	1.	0.	0.	0.	0.	0.9
78	ALL CATEGORIES WITH VOLUME % LESS THAN 1.0 COMBINED IN ONE																					5.3
1196	TOTALS -	0.	0.	0.	1.	11.	33.	1.	0.	0.	0.	48.	1.	0.	0.	0.	4.	0.	0.	0.	0.	100.0

Volume DISTRIBUTION

SPECIES	Volume %	0.2-2.5	2.5-5.0	5.0-10.	10.- 20.	20.- 40.	40.- 80.	80.-500.
Si - -	16.8	5.	13.	12.	35.	25.	10.	0.
Ca - -	22.4	3.	9.	17.	43.	27.	1.	0.
Ca Si -	6.1	1.	1.	15.	53.	30.	0.	0.
Ca Al -	4.4	2.	30.	18.	37.	9.	4.	0.
Ca Al Fe	7.3	9.	25.	16.	36.	14.	0.	0.
Ca Si Al	6.1	11.	15.	22.	34.	18.	0.	0.
OTHERS -	36.9	7.	24.	17.	23.	22.	8.	0.
TOTALS -	100.0	5.	17.	16.	34.	23.	5.	0.

Table 4-24. CCSEM Analysis of Black Thunder Coal Ash, 1500°C Furnace Set Point, 2.6 s Res. Time, Stoichiometric Ratio=0.6

SAMPLE 1174 PSI ASH IN EPOXY, Black Thunder, 1500C, 2.6 RST, SR=0.6

AVERAGE SPECIES COMPOSITION

No.	SPECIES	C	O	Na	Mg	Al	Si	P	S	Cl	K	Ca	Ti	V	Cr	Mn	Fe	Ni	Cu	Zn	X	Vol %
247	Ca - -	0.	0.	0.	2.	5.	2.	0.	2.	0.	0.	82.	1.	0.	0.	0.	5.	0.	0.	0.	0.	20.4
193	Si - -	0.	0.	0.	0.	0.	98.	0.	0.	0.	0.	1.	0.	0.	0.	0.	0.	0.	0.	0.	0.	17.8
44	Al Si -	0.	0.	0.	0.	53.	46.	0.	0.	0.	0.	1.	0.	0.	0.	0.	0.	0.	0.	0.	0.	3.9
44	Si Al -	0.	0.	0.	0.	40.	55.	0.	0.	0.	2.	2.	0.	0.	0.	0.	0.	0.	0.	0.	0.	5.0
34	Si Ca -	0.	0.	0.	0.	0.	70.	0.	0.	0.	0.	26.	1.	0.	0.	0.	2.	0.	0.	0.	0.	3.1
62	Ca Si -	0.	0.	0.	1.	1.	22.	0.	0.	0.	0.	72.	1.	0.	0.	0.	4.	0.	0.	0.	0.	4.1
38	Ca Al -	0.	0.	0.	0.	14.	1.	0.	1.	0.	0.	78.	1.	0.	0.	0.	4.	0.	0.	0.	0.	3.5
24	Ca Al P	0.	0.	0.	0.	29.	1.	13.	0.	0.	0.	52.	2.	0.	0.	0.	2.	0.	0.	0.	0.	1.6
6	Al Ca P	0.	0.	0.	0.	48.	0.	12.	1.	0.	0.	35.	3.	0.	0.	0.	0.	0.	0.	0.	0.	0.9
89	Ca Al Fe	0.	0.	0.	0.	14.	1.	0.	1.	0.	0.	75.	1.	0.	0.	0.	8.	0.	0.	0.	0.	8.4
9	Ca Fe Al	0.	0.	0.	1.	9.	2.	0.	1.	0.	0.	77.	0.	0.	0.	0.	11.	0.	0.	0.	0.	1.0
46	Si Al Ca	0.	0.	0.	0.	30.	49.	0.	1.	0.	2.	15.	0.	0.	0.	0.	2.	0.	0.	0.	0.	3.8
75	Ca Si Al	0.	0.	0.	0.	16.	24.	0.	1.	0.	0.	52.	1.	0.	0.	0.	4.	0.	0.	0.	0.	4.7
26	Si Ca Al	0.	0.	0.	0.	18.	49.	0.	1.	0.	2.	26.	1.	0.	0.	0.	4.	0.	0.	0.	0.	1.5
39	Ca Al Si	0.	0.	0.	1.	21.	14.	1.	1.	0.	0.	58.	1.	0.	0.	0.	4.	0.	0.	0.	0.	2.7
6	Ca Mg Al	0.	0.	0.	13.	9.	5.	0.	4.	0.	0.	61.	2.	0.	0.	0.	5.	0.	0.	0.	0.	0.5
18	Ca Si Fe	0.	0.	0.	0.	4.	20.	0.	0.	0.	0.	66.	2.	0.	0.	0.	8.	0.	0.	0.	0.	1.7
4	Si Ca Fe	0.	0.	0.	2.	3.	50.	0.	2.	0.	2.	31.	2.	0.	0.	0.	8.	0.	0.	0.	0.	0.6
7	Ca Fe Si	0.	0.	0.	0.	8.	16.	0.	1.	0.	0.	48.	1.	0.	0.	0.	25.	0.	0.	0.	0.	1.0
5	Si Ti Ca	0.	0.	0.	0.	5.	58.	0.	1.	0.	1.	12.	20.	0.	0.	0.	2.	0.	0.	0.	0.	0.5
10	Ca Si Ti	0.	0.	0.	1.	1.	34.	0.	0.	0.	0.	51.	10.	0.	0.	0.	4.	0.	0.	0.	0.	0.9
18	Si Al K	0.	0.	1.	0.	36.	51.	0.	0.	0.	8.	2.	0.	0.	0.	0.	2.	0.	0.	0.	0.	2.1
10	Ca Si S	0.	0.	0.	0.	8.	27.	0.	21.	0.	0.	40.	0.	0.	0.	0.	3.	0.	0.	0.	0.	1.1
8	Ca S Si	0.	0.	0.	0.	7.	13.	0.	21.	0.	0.	54.	4.	0.	0.	0.	1.	0.	0.	0.	0.	0.7
3	S Ca Si	0.	0.	0.	0.	9.	18.	0.	38.	0.	0.	25.	4.	0.	0.	0.	0.	2.	0.	3.	0.	0.6
5	Si Al Na	0.	0.	9.	0.	32.	49.	0.	1.	0.	4.	4.	0.	0.	0.	0.	0.	0.	0.	0.	0.	0.7
121	ALL CATEGORIES WITH VOLUME % LESS THAN 1.0 COMBINED IN ONE																					6.9
1191	TOTALS -	0.	0.	0.	1.	13.	34.	0.	2.	0.	1.	43.	1.	0.	0.	0.	5.	0.	0.	0.	0.	100.0

Volume DISTRIBUTION

SPECIES	Volume %	0.2-2.5	2.5-5.0	5.0-10.	10.- 20.	20.- 40.	40.- 80.	80.-500.
Ca - -	20.4	9.	28.	26.	25.	11.	2.	0.
Si - -	17.8	3.	7.	16.	45.	18.	10.	0.
Ca Si -	4.1	8.	22.	17.	20.	33.	0.	0.
Si Al -	5.0	5.	49.	20.	21.	6.	0.	0.
Ca Al Fe	8.4	12.	41.	25.	17.	6.	0.	0.
Ca Si Al	4.7	23.	26.	22.	10.	19.	0.	0.
OTHERS -	39.6	18.	29.	19.	23.	9.	2.	0.
TOTALS -	100.0	12.	26.	20.	26.	12.	3.	0.

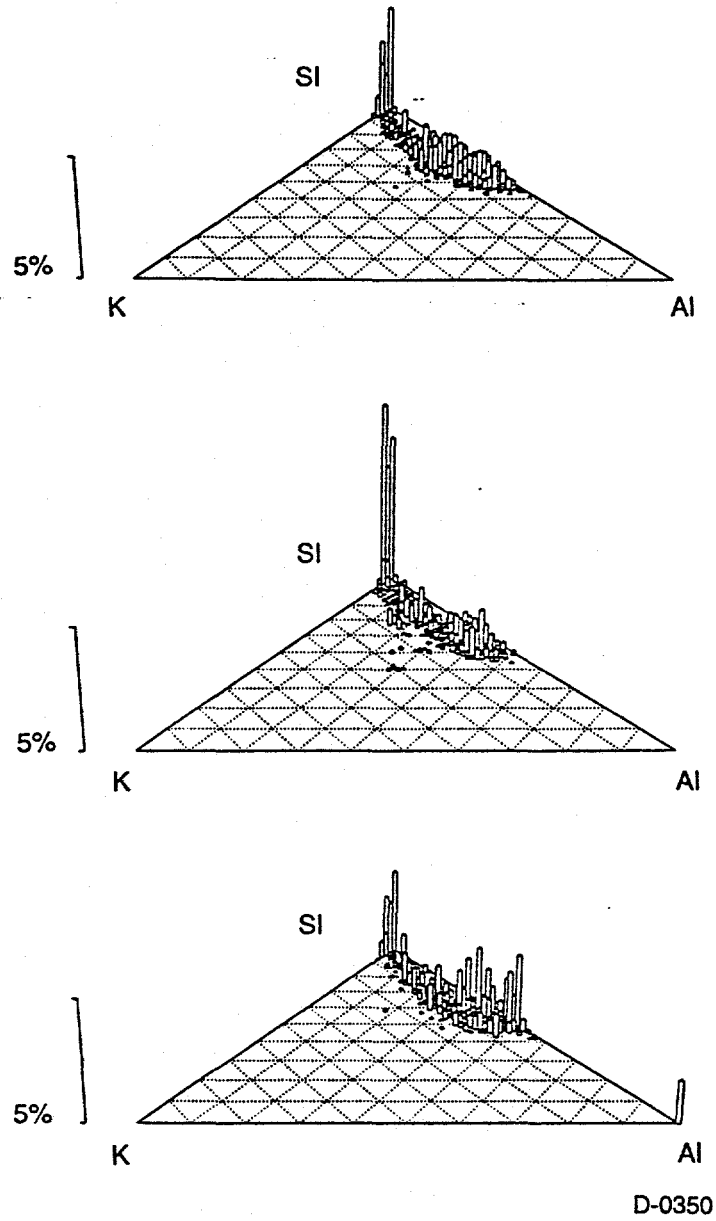

Figure 4-6. K-Si-Al volume frequency ternary diagrams for drop tube furnace generated ashes for three different Pittsburgh No. 8 coals. Top: washed, middle: run-of-mine and bottom: beneficiated. All ashes were generated at 1500°C furnace temperature, 2.6 s res. time, SR=1.2.

Figure 4-8 shows Fe-Si-Al volume frequency ternary diagrams for drop tube furnace generated ashes from the beneficiated Pittsburgh No. 8 coal (obtained at three different stoichiometric conditons). Ashes generated under all three conditions, exhibit extensive interactions between aluminosilicates and Fe.

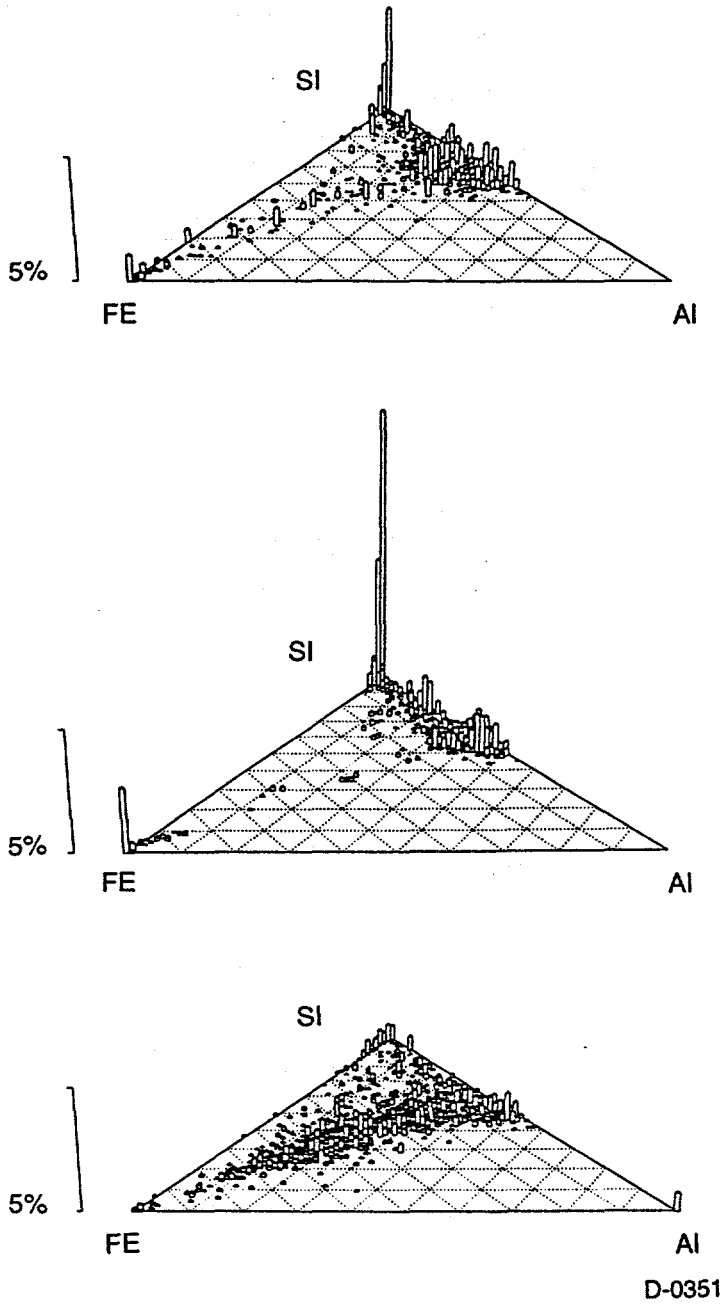

Figure 4-7. Fe-Si-Al volume frequency ternary diagrams for drop tube furnace generated ashes for three different Pittsburgh No. 8 coals. Top: washed, middle: run-of-mine and bottom: beneficiated. All ashes were generated at 1500°C furnace temperature, 2.6 s res. time, SR=1.2.

Black Thunder Chars

Ash analysis of Black Thunder coal shows a large amount of CaO present but CCSEM analysis did not show high amounts of calcite mineral. This calcium is present in a molecularly dispersed, carboxyl bound form. After combustion, this calcium shows up primarily as CaO and also as reaction products with quartz (as Ca-Si phase) and clays (as Ca-Si-Al) phase. Although the CCSEM analysis indicated a much larger CaO phase than SiO_2 phase, Ca-Si-Al volume frequency diagrams (Figure 4-9) show a very small

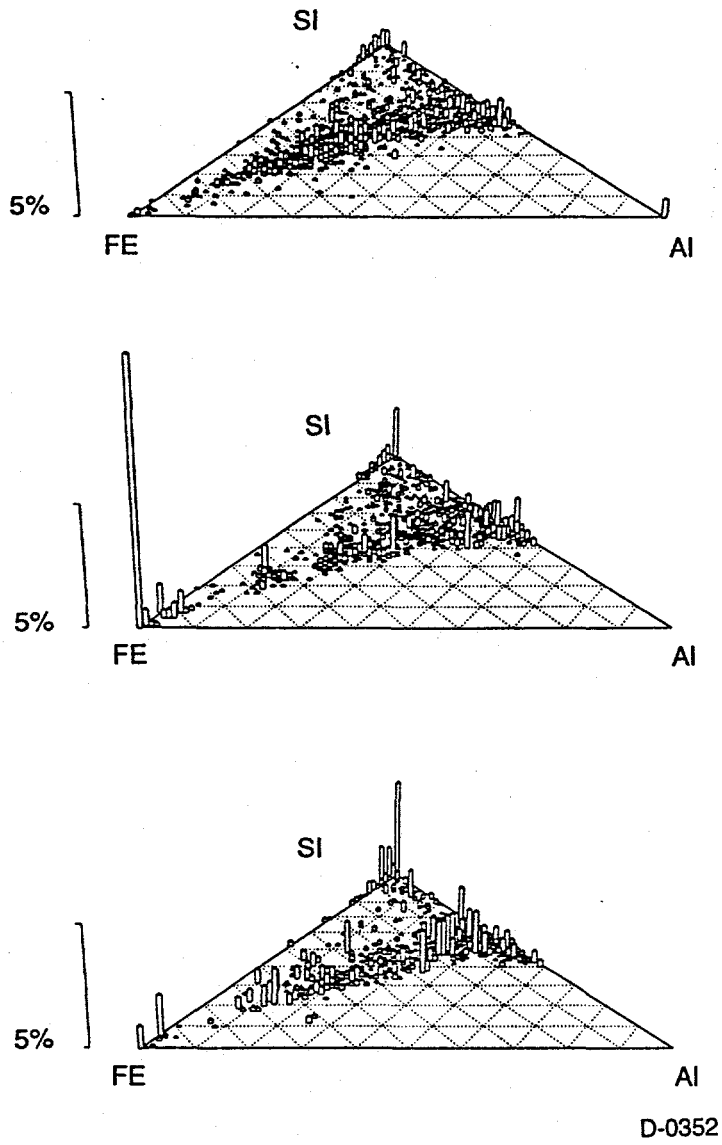

Figure 4-8. Fe-Si-Al volume frequency ternary diagrams for drop tube furnace generated ashes for beneficiated Pittsburgh No. 8 coal. Top: SR=2, middle: SR=0.9 and bottom: SR=0.6. All ashes were generated at 1500°C furnace temperature, 2.6 s res. time, SR=1.2.

peak at the Ca apex. Molecularly dispersed Ca becomes highly reactive during combustion. As a result, there are very few ash particles with only CaO phase present. Most of the Ca-rich particles have some amounts of Al, Si or other elements present. Therefore the large volume percentage at the Ca apex is distributed over a broader compositional range. Quartz, on the other hand, is not as reactive and after combustion it is in the form of essentially pure SiO_2 phase. Thus, even with relatively lower volume concentration it appears as a large peak at the Si apex in Ca-Si-Al volume frequency diagrams.

We also noticed significant amounts of products from reactions between crandallite and organically-bound Ca. Figure 4-10 shows Ca-Al-P volume frequency diagrams for the Black Thunder coal and its ashes at three different stoichiometric ratios.

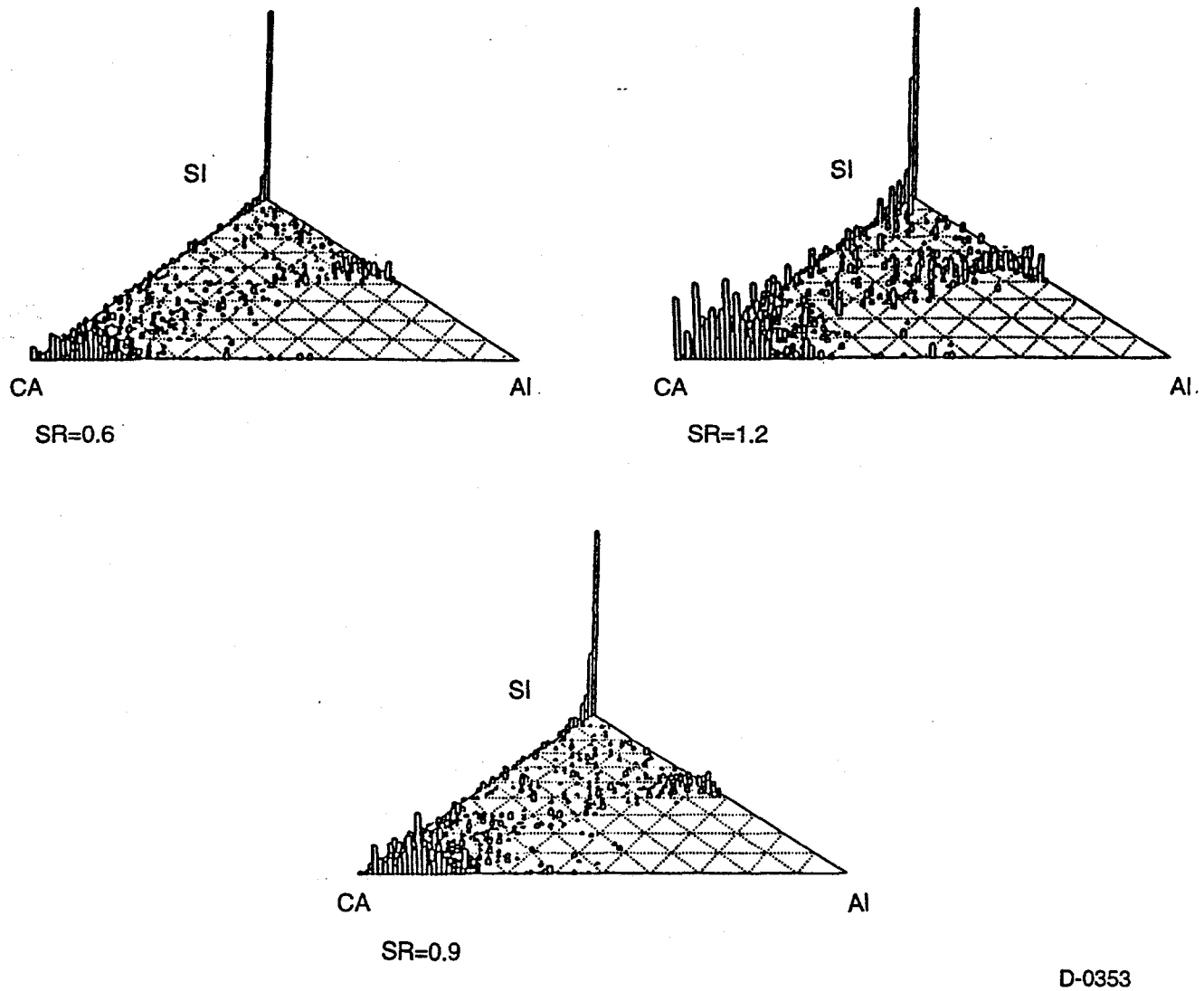

Figure 4-9. Ca-Al-Si volume frequency ternary diagrams of Black Thunder ash showing relatively small amounts of pure CaO phase indicating high degree of interaction between molecularly dispersed Ca with aluminosilicates. Also present is a large peak of quartz indicating its inertness during combustion.

Effect of Residence Time

CCSEM analysis of the washed Pittsburgh No. 8 coal ashes generated in the PSI residence time experiments also contained significant unburned carbon. Products of reactions between aluminosilicates and organically bound (sulfur and calcium) components, as well as between pyrrhotite and quartz, were observed. Tables 4-25 through 4-32 show the CCSEM results of two sets of ashes.

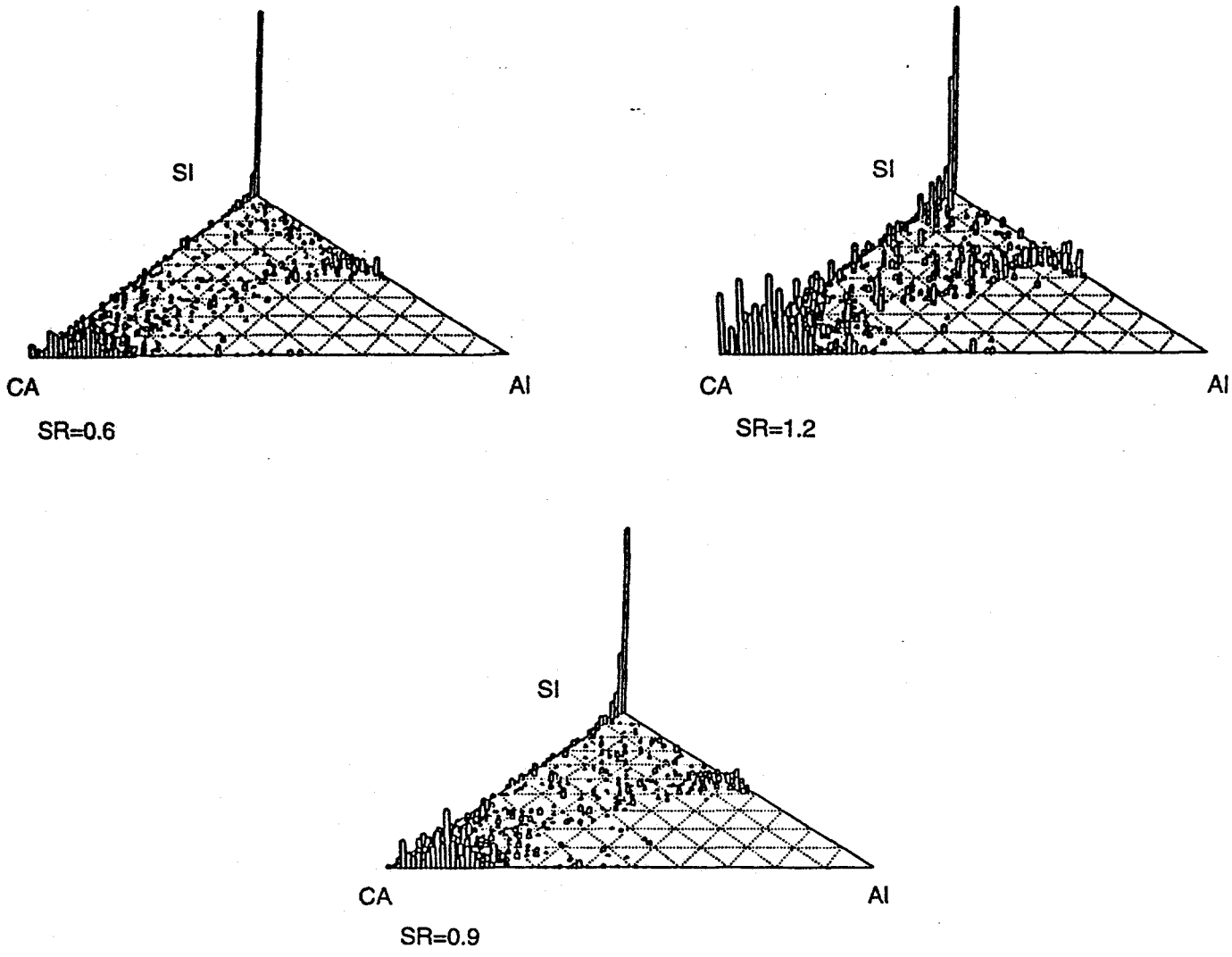

Figure 4-10. Ca-Al-P volume frequency ternary diagrams of Black Thunder ash showing significant amounts of reaction products from interactions between crandallite and organically bound Ca.

Table 4-25. CCSEM Results of Washed Pittsburgh No. 8 ash, 1500C, 15%O2, SR=15.6, RST=0.248 s

AVERAGE SPECIES COMPOSITION

No.	SPECIES	C	O	Na	Mg	Al	Si	P	S	Cl	K	Ca	Ti	V	Cr	Mn	Fe	Ni	Cu	Zn	X	Vol %
69	Ca - -	0.	0.	0.	0.	0.	2.	0.	2.	0.	0.	94.	0.	0.	0.	0.	1.	0.	0.	0.	0.	4.2
91	Fe - -	0.	0.	0.	0.	0.	0.	0.	0.	0.	0.	0.	0.	0.	0.	0.	99.	0.	0.	0.	0.	3.9
129	Si - -	0.	0.	0.	0.	1.	96.	0.	1.	0.	1.	1.	0.	0.	0.	0.	1.	0.	0.	0.	0.	12.1
3	Ca Si -	0.	0.	0.	0.	1.	16.	0.	4.	0.	0.	77.	0.	0.	0.	0.	2.	0.	0.	0.	0.	0.5
167	Si Al -	0.	0.	1.	0.	36.	57.	0.	1.	0.	3.	1.	1.	0.	0.	0.	1.	0.	0.	0.	0.	17.0
9	Al Si -	0.	0.	0.	0.	53.	45.	0.	0.	0.	0.	0.	0.	0.	0.	0.	2.	0.	0.	0.	0.	1.3
10	Fe S -	0.	0.	0.	0.	0.	0.	0.	35.	0.	0.	0.	0.	0.	0.	0.	65.	0.	0.	0.	0.	1.2
135	Si Al K	0.	0.	0.	0.	30.	56.	0.	1.	0.	9.	1.	1.	0.	0.	0.	2.	0.	0.	0.	0.	9.9
23	Si Al Ti	0.	0.	0.	0.	27.	52.	0.	1.	0.	4.	3.	10.	0.	0.	0.	3.	0.	0.	0.	0.	2.1
5	S Fe Si	0.	0.	0.	0.	2.	14.	0.	51.	0.	2.	3.	3.	0.	3.	0.	21.	0.	0.	0.	0.	0.6
8	S Si Fe	0.	0.	0.	0.	7.	27.	0.	39.	0.	2.	6.	2.	0.	1.	0.	17.	0.	0.	0.	0.	0.7
21	Si Fe Al	0.	0.	0.	0.	16.	45.	0.	0.	0.	5.	7.	2.	0.	0.	0.	25.	0.	0.	0.	0.	1.3
56	Si Al Fe	0.	0.	0.	0.	30.	48.	0.	1.	0.	4.	4.	1.	0.	0.	0.	12.	0.	0.	0.	0.	4.9
18	Fe Si Al	0.	0.	0.	0.	13.	28.	0.	1.	0.	1.	5.	1.	0.	0.	0.	52.	0.	0.	0.	0.	1.3
65	Si Al Ca	0.	0.	0.	0.	27.	50.	0.	1.	0.	3.	12.	2.	0.	0.	0.	4.	0.	0.	0.	0.	6.1
16	Si Ca Al	0.	0.	0.	0.	17.	45.	0.	2.	0.	3.	28.	2.	0.	0.	0.	3.	0.	0.	0.	0.	1.1
21	Ca Si Al	0.	0.	0.	0.	15.	25.	0.	1.	0.	0.	52.	2.	0.	0.	0.	4.	0.	0.	0.	0.	2.0
1	Al Si Ca	0.	0.	0.	0.	47.	43.	0.	2.	0.	2.	6.	0.	0.	0.	0.	0.	0.	0.	0.	0.	0.6
4	Ca P Si	0.	0.	0.	0.	6.	12.	19.	0.	0.	0.	62.	0.	0.	0.	0.	0.	0.	0.	0.	0.	0.9
8	Si Al Na	0.	0.	10.	0.	29.	59.	0.	0.	0.	0.	0.	0.	0.	0.	0.	1.	0.	0.	0.	0.	0.5
15	S Si Ca	0.	0.	0.	0.	4.	22.	0.	45.	0.	3.	16.	1.	1.	1.	0.	6.	0.	1.	1.	0.	1.0
13	Si S Ca	0.	0.	0.	0.	12.	38.	0.	25.	0.	3.	15.	0.	1.	0.	0.	5.	0.	1.	0.	0.	0.9
6	Ca S Si	0.	0.	0.	1.	3.	12.	0.	17.	3.	0.	57.	2.	0.	2.	0.	2.	0.	0.	0.	0.	0.8
40	Si S Al	0.	0.	0.	0.	19.	43.	0.	27.	1.	3.	2.	2.	0.	0.	0.	2.	0.	0.	0.	0.	3.6
94	Si Al S	0.	0.	0.	0.	30.	48.	0.	13.	0.	4.	2.	1.	0.	0.	0.	2.	0.	0.	0.	0.	7.3
48	S Si Al	0.	0.	0.	0.	15.	27.	0.	44.	1.	1.	5.	1.	0.	1.	0.	3.	1.	0.	0.	0.	5.4
4	S Si Ti	0.	0.	0.	0.	7.	19.	0.	49.	5.	5.	6.	10.	0.	0.	0.	0.	0.	0.	0.	0.	0.6
117	ALL CATEGORIES WITH VOLUME % LESS THAN 1.0 COMBINED IN ONE																					7.8
1196	TOTALS -	0.	0.	0.	0.	20.	46.	0.	9.	0.	3.	11.	1.	0.	0.	0.	9.	0.	0.	0.	0.	100.0

Volume DISTRIBUTION

SPECIES	Volume %	0.2-2.5	2.5-5.0	5.0-10.	10.- 20.	20.- 40.	40.- 80.	80.-500.
Ca - -	4.2	2.	9.	31.	28.	22.	7.	0.
Si - -	12.1	4.	18.	21.	42.	10.	5.	0.
Si Al -	17.0	9.	21.	32.	32.	2.	2.	1.
Si Al K	9.9	12.	40.	22.	15.	9.	3.	0.
Si Al Fe	4.9	12.	36.	34.	13.	2.	2.	0.
Si Al Ca	6.1	14.	25.	34.	23.	2.	1.	0.
Si Al S	7.3	17.	21.	25.	36.	1.	0.	0.
S Si Al	5.4	5.	16.	37.	41.	0.	0.	0.
OTHERS -	33.1	7.	16.	33.	26.	9.	6.	3.
TOTALS -	100.0	9.	21.	30.	29.	7.	4.	1.

Table 4-26. CCSEM results of Washed Pittsburgh No. 8 ash, 1500C, 15%O2, SR=15.6, RST=0.400 s

AVERAGE SPECIES COMPOSITION

No.	SPECIES	C	O	Na	Mg	Al	Si	P	S	Cl	K	Ca	Ti	V	Cr	Mn	Fe	Ni	Cu	Zn	X	Vol %
119	Si - -	0.	0.	0.	0.	1.	97.	0.	1.	0.	1.	0.	0.	0.	0.	0.	0.	0.	0.	0.	0.	12.0
98	Fe - -	0.	0.	0.	0.	0.	2.	0.	1.	0.	0.	0.	0.	0.	0.	0.	97.	0.	0.	0.	0.	8.0
63	Ca - -	0.	0.	0.	0.	0.	1.	0.	1.	0.	0.	96.	0.	0.	0.	0.	1.	0.	0.	0.	0.	4.1
133	Si Al -	0.	0.	0.	0.	35.	60.	0.	2.	0.	2.	1.	0.	0.	0.	0.	1.	0.	0.	0.	0.	13.9
19	Al Si -	0.	0.	0.	0.	52.	48.	0.	0.	0.	0.	0.	0.	0.	0.	0.	0.	0.	0.	0.	0.	0.9
10	Ca S -	0.	0.	0.	0.	0.	2.	0.	21.	0.	0.	77.	0.	0.	0.	0.	0.	0.	0.	0.	0.	1.2
8	Fe Si -	0.	0.	0.	0.	3.	14.	0.	3.	0.	0.	2.	0.	0.	0.	0.	78.	0.	0.	0.	0.	0.9
7	Ca Mg -	0.	0.	0.	14.	0.	1.	0.	0.	0.	0.	86.	0.	0.	0.	0.	0.	0.	0.	0.	0.	1.4
2	S Fe -	0.	0.	0.	0.	0.	4.	0.	51.	0.	0.	0.	0.	0.	0.	0.	45.	0.	0.	0.	0.	1.1
162	Si Al K	0.	0.	0.	0.	27.	56.	0.	2.	0.	11.	1.	1.	0.	0.	0.	2.	0.	0.	0.	0.	13.4
6	Ca Si S	0.	0.	0.	0.	2.	12.	0.	10.	0.	0.	75.	0.	0.	0.	0.	0.	0.	0.	0.	0.	0.7
26	S Si Ca	0.	0.	0.	0.	5.	25.	0.	49.	1.	1.	15.	0.	0.	2.	0.	2.	0.	0.	0.	0.	1.6
8	S Ca Si	0.	0.	0.	0.	0.	14.	0.	58.	3.	0.	19.	0.	0.	3.	0.	1.	2.	0.	0.	0.	0.8
74	Si S Al	0.	0.	0.	0.	17.	41.	0.	28.	1.	3.	3.	2.	0.	0.	0.	3.	0.	0.	0.	0.	6.7
99	Si Al S	0.	0.	0.	0.	31.	49.	0.	11.	1.	3.	2.	1.	0.	0.	0.	2.	0.	0.	0.	0.	7.7
6	S Al Si	0.	0.	0.	0.	20.	17.	0.	54.	1.	0.	1.	3.	4.	0.	0.	0.	0.	0.	0.	0.	0.5
58	S Si Al	0.	0.	0.	0.	15.	26.	0.	48.	1.	2.	3.	3.	0.	0.	0.	1.	0.	0.	1.	0.	5.7
3	Fe S Si	0.	0.	0.	0.	2.	12.	0.	18.	0.	3.	3.	3.	0.	0.	0.	58.	2.	0.	0.	0.	0.5
8	Si Al Ti	0.	0.	0.	0.	25.	49.	0.	3.	0.	6.	3.	12.	0.	0.	0.	2.	0.	0.	0.	0.	0.5
15	Si Ca Al	0.	0.	0.	0.	16.	46.	0.	3.	0.	2.	24.	2.	0.	0.	0.	5.	0.	0.	0.	0.	1.1
26	Si Al Ca	0.	0.	0.	0.	25.	50.	0.	4.	0.	5.	12.	1.	0.	0.	0.	3.	0.	0.	0.	0.	3.4
9	Ca Si Al	0.	0.	0.	0.	12.	30.	2.	4.	1.	2.	47.	1.	0.	0.	0.	2.	0.	0.	0.	0.	0.9
22	Si Al Na	0.	0.	10.	0.	34.	53.	0.	2.	0.	1.	0.	0.	0.	0.	0.	1.	0.	0.	0.	0.	1.6
6	S Si Ti	0.	0.	0.	0.	4.	26.	0.	48.	1.	1.	8.	12.	0.	0.	0.	0.	0.	0.	0.	0.	0.8
22	Si Al Fe	0.	0.	0.	0.	32.	47.	0.	2.	0.	3.	2.	1.	0.	0.	0.	14.	0.	0.	0.	0.	1.2
10	Si Fe Al	0.	0.	0.	0.	15.	49.	0.	2.	0.	6.	4.	0.	0.	0.	0.	24.	0.	0.	0.	0.	0.8
10	Fe Si Al	0.	0.	0.	0.	12.	25.	0.	3.	0.	1.	2.	0.	0.	0.	0.	58.	0.	0.	0.	0.	0.8
3	S Si Zn	0.	0.	0.	0.	0.	24.	0.	65.	1.	0.	0.	0.	0.	0.	0.	0.	0.	0.	10.	0.	0.7
110	ALL CATEGORIES WITH VOLUME % LESS THAN 1.0 COMBINED IN ONE																					7.2
1142	TOTALS -	0.	0.	0.	0.	16.	44.	0.	11.	0.	3.	10.	1.	0.	0.	0.	12.	0.	0.	0.	0.	100.0

Volume DISTRIBUTION

SPECIES	Volume %	0.2-2.5	2.5-5.0	5.0-10.	10.- 20.	20.- 40.	40.- 80.	80.-500.
Si - -	12.0	7.	40.	29.	11.	7.	5.	0.
Fe - -	8.0	1.	23.	17.	40.	16.	4.	0.
Ca - -	4.1	0.	0.	18.	22.	24.	7.	29.
Si Al -	13.9	10.	46.	29.	9.	5.	2.	0.
Si Al K	13.4	16.	25.	28.	18.	8.	4.	0.
Si S Al	6.7	13.	26.	26.	30.	5.	0.	0.
Si Al S	7.7	36.	37.	18.	7.	3.	0.	0.
S Si Al	5.7	14.	27.	36.	22.	1.	0.	0.
OTHERS -	28.5	16.	30.	24.	20.	8.	3.	0.
TOTALS -	100.0	13.	31.	25.	19.	8.	3.	1.

Table 4-27. CCSEM Results of Washed Pittsburgh No. 8 ash, 1500C, 15%O2, SR=15.6, RST=0.552 s

AVERAGE SPECIES COMPOSITION

No.	SPECIES	C	O	Na	Mg	Al	Si	P	S	Cl	K	Ca	Ti	V	Cr	Mn	Fe	Ni	Cu	Zn	X	Vol %
150	Si - -	0.	0.	0.	0.	1.	96.	0.	0.	0.	1.	1.	0.	0.	0.	0.	0.	0.	0.	0.	0.	13.3
54	Ca - -	0.	0.	0.	1.	0.	1.	0.	1.	1.	0.	97.	0.	0.	0.	0.	1.	0.	0.	0.	0.	4.4
104	Fe - -	0.	0.	0.	0.	0.	1.	0.	0.	0.	0.	0.	0.	0.	0.	0.	98.	0.	0.	0.	0.	10.1
178	Si Al -	0.	0.	0.	0.	38.	57.	0.	1.	0.	2.	0.	0.	0.	0.	0.	1.	0.	0.	0.	0.	17.3
13	Al Si -	0.	0.	0.	0.	52.	48.	0.	0.	0.	0.	0.	0.	0.	0.	0.	0.	0.	0.	0.	0.	1.0
5	Si Ca -	0.	0.	0.	0.	0.	83.	0.	0.	0.	0.	17.	0.	0.	0.	0.	0.	0.	0.	0.	0.	0.9
3	Ca S -	0.	0.	0.	0.	0.	0.	0.	38.	0.	0.	62.	0.	0.	0.	0.	0.	0.	0.	0.	0.	0.7
216	Si Al K	0.	0.	0.	0.	29.	56.	0.	1.	0.	10.	1.	1.	0.	0.	0.	2.	0.	0.	0.	0.	18.0
6	Si K Al	0.	0.	0.	0.	17.	53.	0.	0.	0.	24.	0.	1.	0.	0.	0.	4.	0.	0.	0.	0.	0.8
18	Fe Si Al	0.	0.	0.	3.	12.	25.	0.	1.	0.	1.	2.	0.	0.	0.	0.	56.	0.	0.	0.	0.	2.0
29	Si Al Fe	0.	0.	0.	0.	32.	46.	0.	1.	0.	3.	2.	1.	0.	0.	0.	15.	0.	0.	0.	0.	2.4
12	Si Fe Al	0.	0.	0.	0.	24.	41.	0.	1.	0.	1.	1.	0.	0.	0.	0.	32.	0.	0.	0.	0.	1.0
6	Ca Si Al	0.	0.	0.	0.	15.	33.	0.	0.	0.	0.	44.	3.	0.	0.	0.	3.	0.	0.	0.	0.	0.6
43	Si Al Ca	0.	0.	0.	0.	28.	48.	0.	2.	0.	5.	13.	1.	0.	0.	0.	3.	0.	0.	0.	0.	3.9
18	Si Ca Al	0.	0.	0.	0.	19.	41.	0.	1.	0.	4.	27.	2.	0.	0.	0.	6.	0.	0.	0.	0.	1.6
26	Si Al Na	0.	0.	10.	0.	30.	59.	0.	0.	0.	0.	0.	0.	0.	0.	0.	0.	0.	0.	0.	0.	3.1
13	Si Al Ti	0.	0.	0.	0.	19.	64.	0.	1.	0.	5.	1.	8.	0.	0.	0.	1.	0.	0.	0.	0.	0.8
92	Si Al S	0.	0.	0.	0.	31.	50.	0.	11.	1.	3.	1.	1.	0.	0.	0.	1.	0.	0.	0.	0.	5.4
22	Si S Al	0.	0.	0.	0.	18.	46.	0.	27.	1.	2.	2.	1.	0.	1.	0.	2.	0.	0.	1.	0.	1.6
19	S Si Al	0.	0.	0.	0.	16.	28.	0.	43.	2.	3.	1.	3.	0.	1.	0.	1.	0.	1.	1.	0.	1.3
11	S Si Ca	0.	0.	0.	0.	4.	23.	0.	48.	1.	1.	14.	2.	0.	1.	0.	2.	0.	1.	1.	0.	0.9
5	S Si Cl	0.	0.	0.	0.	1.	25.	0.	59.	12.	1.	1.	0.	0.	0.	0.	0.	0.	0.	1.	0.	0.6
125	ALL CATEGORIES WITH VOLUME % LESS THAN 1.0 COMBINED IN ONE																					8.0
1168	TOTALS -	0.	0.	0.	0.	19.	48.	0.	5.	0.	3.	9.	1.	0.	0.	0.	14.	0.	0.	0.	0.	100.0

Volume DISTRIBUTION

SPECIES	Volume %	0.2-2.5	2.5-5.0	5.0-10.	10.- 20.	20.- 40.	40.- 80.	80.-500.
Si - -	13.3	8.	23.	32.	19.	9.	9.	0.
Ca - -	4.4	0.	6.	3.	21.	32.	12.	25.
Fe - -	10.1	2.	20.	17.	15.	14.	18.	15.
Si Al -	17.3	15.	33.	22.	16.	7.	5.	2.
Si Al K	18.0	13.	32.	18.	9.	12.	13.	2.
Si Al S	5.4	43.	27.	18.	8.	3.	0.	0.
OTHERS -	31.6	11.	16.	31.	29.	8.	5.	1.
TOTALS -	100.0	12.	23.	24.	19.	10.	8.	4.

Table 4-28. CCSEM Results of Washed Pittsburgh No. 8 ash, 1500C, 15%O2, SR=15.6, RST=0.718 s

AVERAGE SPECIES COMPOSITION

No.	SPECIES	C	O	Na	Mg	Al	Si	P	S	Cl	K	Ca	Ti	V	Cr	Mn	Fe	Ni	Cu	Zn	X	Vol %
146	Fe - -	0.	0.	0.	0.	0.	1.	0.	0.	0.	0.	0.	0.	0.	0.	0.	98.	0.	0.	0.	0.	10.2
154	Si - -	0.	0.	0.	0.	1.	97.	0.	1.	0.	1.	0.	0.	0.	0.	0.	0.	0.	0.	0.	0.	11.6
88	Ca - -	0.	0.	0.	0.	0.	1.	0.	3.	0.	0.	96.	0.	0.	0.	0.	1.	0.	0.	0.	0.	8.2
5	Al - -	0.	0.	0.	0.	100.	0.	0.	0.	0.	0.	0.	0.	0.	0.	0.	0.	0.	0.	0.	0.	0.7
10	Ca S -	0.	0.	0.	0.	0.	3.	0.	24.	0.	0.	72.	0.	0.	0.	0.	0.	0.	0.	0.	0.	0.6
159	Si Al -	0.	0.	0.	0.	40.	56.	0.	1.	0.	2.	0.	0.	0.	0.	0.	1.	0.	0.	0.	0.	15.2
24	Al Si -	0.	0.	0.	0.	52.	48.	0.	0.	0.	0.	0.	0.	0.	0.	0.	0.	0.	0.	0.	0.	1.4
7	Si S -	0.	0.	0.	0.	0.	76.	0.	23.	0.	0.	0.	0.	0.	0.	0.	0.	0.	0.	0.	0.	1.1
64	Si Al S	0.	0.	0.	0.	31.	48.	0.	13.	0.	3.	2.	2.	0.	0.	0.	1.	0.	0.	0.	0.	3.9
31	Si S Al	0.	0.	0.	0.	18.	46.	0.	23.	0.	3.	5.	1.	0.	0.	0.	2.	0.	0.	0.	0.	1.7
28	S Si Al	0.	0.	0.	0.	14.	28.	0.	44.	0.	2.	3.	2.	0.	0.	0.	6.	0.	0.	1.	0.	3.3
3	Si Fe Ca	0.	0.	0.	0.	5.	45.	0.	2.	0.	3.	20.	0.	0.	0.	0.	25.	0.	0.	0.	0.	0.8
33	Si Al Ca	0.	0.	0.	0.	29.	44.	0.	5.	0.	4.	13.	2.	0.	0.	0.	3.	0.	0.	0.	0.	3.4
13	Si Ca Al	0.	0.	0.	0.	14.	49.	2.	2.	0.	6.	25.	1.	0.	0.	0.	2.	0.	0.	0.	0.	0.8
4	Ca Al Si	0.	0.	0.	0.	32.	12.	0.	4.	0.	0.	49.	1.	0.	0.	0.	1.	0.	0.	0.	0.	1.2
14	Fe Si Al	0.	0.	0.	2.	12.	30.	0.	1.	0.	2.	0.	0.	0.	0.	0.	52.	0.	0.	0.	0.	0.8
31	Si Al Fe	0.	0.	0.	0.	30.	47.	0.	4.	0.	4.	3.	1.	0.	0.	0.	12.	0.	0.	0.	0.	4.2
13	Si Fe Al	0.	0.	0.	0.	23.	41.	0.	2.	0.	2.	4.	0.	0.	0.	0.	27.	0.	0.	0.	0.	1.1
178	Si Al K	0.	0.	0.	0.	29.	53.	0.	2.	0.	12.	1.	1.	0.	0.	0.	2.	0.	0.	0.	0.	17.2
8	Si K Al	0.	0.	0.	0.	18.	57.	0.	0.	0.	19.	2.	1.	0.	0.	0.	4.	0.	0.	0.	0.	1.1
4	Si Al Ti	0.	0.	0.	0.	26.	52.	0.	0.	0.	9.	0.	11.	0.	0.	0.	2.	0.	0.	0.	0.	0.6
8	Ca S Si	0.	0.	0.	1.	5.	10.	0.	22.	2.	0.	57.	1.	0.	0.	0.	2.	0.	0.	0.	0.	0.7
5	Ca Si S	0.	0.	0.	0.	7.	21.	0.	10.	0.	0.	61.	0.	0.	0.	0.	2.	0.	0.	0.	0.	0.7
8	S Si Ca	0.	0.	0.	0.	1.	27.	0.	46.	0.	5.	15.	2.	0.	0.	0.	3.	0.	0.	1.	0.	0.7
1	Si Ca S	0.	0.	0.	0.	13.	35.	0.	20.	0.	0.	28.	0.	0.	0.	0.	4.	0.	0.	0.	0.	0.5
9	Si Al Na	0.	0.	11.	0.	23.	65.	0.	1.	0.	0.	0.	0.	0.	0.	0.	0.	0.	0.	0.	0.	0.9
3	S Si Zn	0.	0.	0.	0.	1.	32.	0.	56.	1.	0.	0.	0.	0.	0.	0.	0.	0.	0.	10.	0.	0.7
111	ALL CATEGORIES WITH VOLUME % LESS THAN 1.0 COMBINED IN ONE																					6.2
1164	TOTALS -	0.	0.	0.	0.	19.	43.	0.	6.	0.	4.	13.	1.	0.	0.	0.	14.	0.	0.	0.	0.	100.0

Volume DISTRIBUTION

SPECIES	Volume %	0.2-2.5	2.5-5.0	5.0-10.	10.- 20.	20.- 40.	40.- 80.	80.-500.
Fe - -	10.2	4.	18.	18.	24.	24.	12.	0.
Si - -	11.6	12.	31.	23.	17.	14.	3.	0.
Ca - -	8.2	2.	12.	10.	13.	21.	28.	14.
Si Al -	15.2	17.	42.	20.	7.	4.	10.	0.
Si Al Fe	4.2	18.	66.	3.	0.	6.	6.	0.
Si Al K	17.2	11.	55.	9.	10.	12.	5.	0.
OTHERS -	33.4	22.	40.	13.	8.	9.	7.	
TOTALS -	100.0	15.	38.	14.	11.	12.	9.	2.

Table 4-29. CCSEM results of Washed Pittsburgh No. 8 ash, 1400C, 15%O2, SR=3.9, RST=0.994 s

AVERAGE SPECIES COMPOSITION

No.	SPECIES	C	O	Na	Mg	Al	Si	P	S	Cl	K	Ca	Ti	V	Cr	Mn	Fe	Ni	Cu	Zn	X	Vol %
68	Ca - -	0.	0.	0.	1.	0.	1.	0.	0.	0.	0.	96.	0.	0.	0.	0.	1.	0.	0.	0.	0.	5.4
127	Si - -	0.	0.	0.	0.	2.	95.	0.	0.	0.	2.	1.	0.	0.	0.	0.	0.	0.	0.	0.	0.	12.3
59	Fe - -	0.	0.	0.	0.	0.	1.	0.	0.	0.	0.	0.	0.	0.	0.	0.	99.	0.	0.	0.	0.	3.5
279	Si Al -	0.	0.	0.	0.	37.	57.	0.	0.	0.	3.	1.	1.	0.	0.	0.	1.	0.	0.	0.	0.	25.3
13	Al Si -	0.	0.	0.	0.	53.	47.	0.	0.	0.	0.	0.	0.	0.	0.	0.	0.	0.	0.	0.	0.	0.7
6	Si Fe -	0.	0.	0.	0.	1.	72.	0.	0.	0.	4.	1.	0.	0.	0.	0.	22.	0.	0.	0.	0.	0.6
8	Fe Si -	0.	0.	0.	0.	3.	17.	0.	0.	0.	0.	0.	0.	0.	0.	0.	79.	0.	0.	0.	0.	0.5
91	Si Al Ca	0.	0.	0.	0.	30.	48.	0.	0.	0.	3.	12.	2.	0.	0.	0.	5.	0.	0.	0.	0.	8.8
21	Ca Si Al	0.	0.	0.	0.	17.	26.	0.	0.	0.	0.	51.	2.	0.	0.	0.	3.	0.	0.	0.	0.	1.2
23	Si Ca Al	0.	0.	0.	0.	19.	47.	0.	0.	0.	1.	26.	2.	0.	0.	0.	5.	0.	0.	0.	0.	2.0
39	Fe Si Al	0.	0.	0.	0.	13.	29.	0.	0.	0.	2.	4.	2.	0.	0.	0.	49.	0.	0.	0.	0.	3.2
103	Si Al Fe	0.	0.	0.	0.	28.	50.	0.	0.	0.	5.	4.	2.	0.	0.	0.	11.	0.	0.	0.	0.	10.3
34	Si Fe Al	0.	0.	0.	0.	17.	45.	0.	0.	0.	4.	6.	2.	0.	0.	0.	25.	0.	0.	0.	0.	2.3
203	Si Al K	0.	0.	0.	0.	29.	57.	0.	0.	0.	8.	1.	1.	0.	0.	0.	3.	0.	0.	0.	0.	16.2
17	Si Al S	0.	0.	0.	0.	29.	49.	0.	14.	0.	3.	1.	2.	0.	0.	0.	2.	0.	0.	1.	0.	0.6
7	Si Fe Ca	0.	0.	0.	0.	15.	41.	0.	0.	0.	0.	19.	4.	0.	0.	0.	20.	0.	0.	0.	0.	1.1
4	Ca Si Fe	0.	0.	0.	0.	12.	29.	0.	0.	0.	2.	39.	2.	0.	0.	0.	16.	0.	0.	0.	0.	0.5
26	Si Al Ti	0.	0.	0.	0.	27.	54.	0.	0.	0.	4.	4.	9.	0.	0.	0.	2.	0.	0.	0.	0.	2.2
63	ALL CATEGORIES WITH VOLUME % LESS THAN 1.0 COMBINED IN ONE																					3.2
1191	TOTALS -	0.	0.	0.	0.	23.	52.	0.	0.	0.	3.	10.	1.	0.	0.	0.	10.	0.	0.	0.	0.	100.0

Volume DISTRIBUTION

SPECIES	Volume %	0.2-2.5	2.5-5.0	5.0-10.	10.- 20.	20.- 40.	40.- 80.	80.-500.
Ca - -	5.4	3.	25.	29.	18.	20.	5.	0.
Si - -	12.3	3.	11.	19.	42.	15.	10.	0.
Si Al -	25.3	8.	32.	29.	25.	4.	2.	0.
Si Al Ca	8.8	5.	26.	33.	31.	5.	0.	0.
Si Al K	16.2	8.	21.	23.	34.	11.	2.	0.
Si Al Fe	10.3	4.	28.	29.	34.	5.	0.	0.
OTHERS -	21.9	4.	7.	26.	30.	25.	8.	0.
TOTALS -	100.0	6.	21.	27.	31.	12.	4.	0.

Table 4-30. CCSEM Results of Washed Pittsburgh No. 8 Ash, 1400C, 15%O2, SR=3.9, RST=1.601 s

AVERAGE SPECIES COMPOSITION

No.	SPECIES	C	O	Na	Mg	Al	Si	P	S	Cl	K	Ca	Ti	V	Cr	Mn	Fe	Ni	Cu	Zn	X	Vol %
96	Fe - -	0.	0.	0.	0.	0.	2.	0.	0.	0.	0.	0.	0.	0.	0.	0.	97.	0.	0.	0.	0.	6.8
49	Ca - -	0.	0.	0.	0.	1.	3.	0.	1.	0.	0.	94.	0.	0.	0.	0.	1.	0.	0.	0.	0.	3.3
120	Si - -	0.	0.	0.	0.	2.	94.	0.	0.	0.	2.	1.	0.	0.	0.	0.	0.	0.	0.	0.	0.	12.6
22	Al Si -	0.	0.	0.	0.	51.	48.	0.	0.	0.	0.	0.	0.	0.	0.	0.	0.	0.	0.	0.	0.	1.5
204	Si Al -	0.	0.	0.	0.	36.	58.	0.	0.	0.	3.	1.	1.	0.	0.	0.	1.	0.	0.	0.	0.	18.6
131	Si Al Ca	0.	0.	0.	0.	29.	49.	0.	0.	0.	3.	13.	2.	0.	0.	0.	3.	0.	0.	0.	0.	12.4
24	Si Ca Al	0.	0.	0.	0.	16.	52.	0.	1.	0.	3.	23.	1.	0.	0.	0.	3.	0.	0.	0.	0.	2.3
22	Ca Si Al	0.	0.	0.	0.	15.	23.	0.	1.	0.	0.	57.	1.	0.	0.	0.	3.	0.	0.	0.	0.	1.7
224	Si Al K	0.	0.	0.	0.	29.	58.	0.	0.	0.	8.	1.	1.	0.	0.	0.	2.	0.	0.	0.	0.	19.7
96	Si Al Fe	0.	0.	0.	0.	30.	48.	0.	0.	0.	4.	4.	1.	0.	0.	0.	13.	0.	0.	0.	0.	8.4
22	Fe Si Al	0.	0.	0.	0.	12.	26.	0.	0.	0.	1.	3.	1.	0.	0.	0.	55.	0.	0.	0.	0.	2.0
18	Si Fe Al	0.	0.	0.	0.	17.	49.	0.	0.	0.	3.	5.	1.	0.	0.	0.	24.	0.	0.	0.	0.	0.9
9	Fe Si Ca	0.	0.	0.	0.	4.	28.	0.	0.	0.	1.	15.	2.	0.	0.	0.	50.	0.	0.	0.	0.	0.5
3	Fe Ca Si	0.	0.	0.	0.	16.	25.	0.	0.	0.	0.	26.	2.	0.	0.	0.	31.	0.	0.	0.	0.	0.6
26	Si Al Ti	0.	0.	0.	0.	27.	50.	0.	2.	1.	3.	3.	11.	0.	0.	0.	2.	0.	0.	0.	0.	2.3
10	Si Al Na	0.	0.	9.	0.	29.	59.	0.	0.	0.	1.	1.	0.	0.	0.	0.	0.	0.	0.	0.	0.	1.0
13	Si Al S	0.	0.	0.	0.	28.	48.	0.	11.	1.	5.	2.	1.	0.	1.	0.	3.	0.	1.	0.	0.	1.0
86	ALL CATEGORIES WITH VOLUME % LESS THAN 1.0 COMBINED IN ONE																					4.4
1177	TOTALS -	0.	0.	0.	0.	22.	52.	0.	1.	0.	4.	8.	1.	0.	0.	0.	11.	0.	0.	0.	0.	100.0

Volume DISTRIBUTION

SPECIES	Volume %	0.2-2.5	2.5-5.0	5.0-10.	10.- 20.	20.- 40.	40.- 80.	80.-500.
Fe - -	6.8	0.	0.	5.	47.	23.	12.	13.
Si - -	12.6	2.	23.	17.	43.	7.	4.	4.
Si Al -	18.6	7.	27.	32.	28.	5.	1.	0.
Si Al Ca	12.4	7.	20.	34.	37.	3.	0.	0.
Si Al K	19.7	5.	28.	37.	22.	6.	2.	0.
Si Al Fe	8.4	6.	15.	45.	29.	6.	0.	0.
OTHERS -	21.6	7.	17.	36.	27.	11.	1.	0.
TOTALS -	100.0	6.	21.	31.	31.	8.	2.	1.

Table 4-31. CCSEM Results of Washed Pittsburgh No. 8 Ash, 1400C, 15%O2, SR=3.9, RST=2.208 s

AVERAGE SPECIES COMPOSITION

No.	SPECIES	C	O	Na	Mg	Al	Si	P	S	Cl	K	Ca	Ti	V	Cr	Mn	Fe	Ni	Cu	Zn	X	Vol %
148	Si - -	0.	0.	0.	0.	2.	94.	0.	0.	0.	2.	1.	1.	0.	0.	0.	1.	0.	0.	0.	0.	12.7
69	Fe - -	0.	0.	0.	0.	1.	2.	0.	0.	0.	0.	0.	0.	0.	0.	0.	96.	0.	0.	0.	0.	4.6
38	Ca - -	0.	0.	0.	0.	0.	1.	0.	1.	0.	0.	97.	0.	0.	0.	0.	1.	0.	0.	0.	0.	3.2
23	Al Si -	0.	0.	0.	0.	52.	47.	0.	0.	0.	0.	0.	0.	0.	0.	0.	0.	0.	0.	0.	0.	2.1
242	Si Al -	0.	0.	0.	0.	33.	61.	0.	0.	0.	3.	1.	0.	0.	0.	0.	1.	0.	0.	0.	0.	22.9
9	Fe S -	0.	0.	0.	0.	0.	0.	0.	34.	0.	0.	0.	0.	0.	0.	0.	66.	0.	0.	0.	0.	0.6
7	Fe Si -	0.	0.	0.	0.	3.	18.	0.	0.	0.	0.	3.	2.	0.	0.	0.	74.	0.	0.	0.	0.	0.5
5	Ca Si -	0.	0.	0.	0.	2.	18.	0.	1.	0.	0.	79.	0.	0.	0.	0.	0.	0.	0.	0.	0.	0.6
108	Si Al Ca	0.	0.	0.	0.	28.	48.	0.	0.	0.	4.	12.	2.	0.	0.	0.	4.	0.	0.	0.	0.	8.8
29	Si Ca Al	0.	0.	0.	0.	17.	47.	0.	0.	0.	2.	24.	2.	0.	0.	0.	7.	0.	0.	0.	0.	2.6
21	Ca Si Al	0.	0.	0.	0.	15.	24.	1.	0.	0.	0.	56.	1.	0.	0.	0.	4.	0.	0.	0.	0.	1.8
214	Si Al K	0.	0.	0.	0.	29.	58.	0.	0.	0.	8.	1.	1.	0.	0.	0.	2.	0.	0.	0.	0.	19.8
79	Si Al Fe	0.	0.	0.	0.	29.	48.	0.	0.	0.	4.	5.	2.	0.	0.	0.	12.	0.	0.	0.	0.	7.4
23	Si Fe Al	0.	0.	0.	0.	16.	46.	0.	0.	0.	5.	6.	2.	0.	0.	0.	24.	0.	0.	0.	0.	1.7
18	Fe Si Al	0.	0.	0.	0.	12.	25.	0.	0.	0.	3.	4.	1.	0.	0.	0.	55.	0.	0.	0.	0.	1.0
25	Si Al Ti	0.	0.	0.	0.	27.	54.	0.	0.	0.	5.	3.	8.	0.	0.	0.	3.	0.	0.	0.	0.	2.5
5	Ca Si Fe	0.	0.	0.	2.	9.	22.	0.	0.	0.	0.	46.	3.	0.	0.	0.	18.	0.	0.	0.	0.	0.6
1	Fe K Si	0.	0.	0.	0.	6.	19.	0.	0.	0.	23.	8.	4.	0.	0.	0.	40.	0.	0.	0.	0.	0.6
9	Si Al Na	0.	0.	9.	0.	29.	59.	0.	0.	0.	3.	0.	0.	0.	0.	0.	0.	0.	0.	0.	0.	0.7
32	Si Al S	0.	0.	0.	0.	29.	52.	0.	12.	0.	3.	1.	1.	0.	0.	0.	2.	0.	0.	0.	0.	0.7
90	ALL CATEGORIES WITH VOLUME % LESS THAN 1.0 COMBINED IN ONE																					4.1
1196	TOTALS -	0.	0.	0.	0.	22.	53.	0.	1.	0.	4.	9.	2.	0.	0.	0.	9.	0.	0.	0.	0.	100.0

Volume DISTRIBUTION

SPECIES	Volume %	0.2-2.5	2.5-5.0	5.0-10.	10.- 20.	20.- 40.	40.- 80.	80.-500.
Si - -	12.7	4.	27.	25.	29.	11.	4.	0.
Fe - -	4.6	0.	0.	14.	29.	26.	30.	0.
Si Al -	22.9	8.	31.	25.	30.	4.	2.	0.
Si Al Ca	8.8	6.	31.	38.	19.	6.	0.	0.
Si Al K	19.8	4.	38.	29.	20.	6.	2.	0.
Si Al Fe	7.4	4.	23.	35.	31.	6.	1.	0.
OTHERS -	23.7	5.	11.	19.	39.	16.	7.	2.
TOTALS -	100.0	5.	25.	26.	29.	9.	5.	1.

Table 4-32. CCSEM Results of Washed Pittsburgh No. 8 Ash, 1400C, 15%O2, SR=3.9, RST=2.870 s

AVERAGE SPECIES COMPOSITION

No.	SPECIES	C	O	Na	Mg	Al	Si	P	S	Cl	K	Ca	Ti	V	Cr	Mn	Fe	Ni	Cu	Zn	X	Vol %
81	Fe - -	0.	0.	0.	0.	0.	1.	0.	0.	0.	0.	0.	0.	0.	0.	0.	98.	0.	0.	0.	0.	7.0
43	Ca - -	0.	0.	0.	0.	0.	1.	0.	1.	0.	0.	97.	0.	0.	0.	0.	1.	0.	0.	0.	0.	2.2
125	Si - -	0.	0.	0.	0.	1.	95.	0.	0.	0.	2.	1.	1.	0.	0.	0.	1.	0.	0.	0.	0.	11.5
195	Si Al -	0.	0.	0.	0.	38.	56.	0.	0.	0.	3.	1.	0.	0.	0.	0.	1.	0.	0.	0.	0.	16.8
11	Al Si -	0.	0.	0.	0.	51.	48.	0.	0.	0.	1.	0.	0.	0.	0.	0.	0.	0.	0.	0.	0.	0.8
8	Ca Si -	0.	0.	0.	0.	3.	23.	0.	1.	0.	0.	70.	0.	0.	0.	0.	3.	0.	0.	0.	0.	0.6
6	Fe Si -	0.	0.	0.	0.	2.	20.	0.	1.	0.	0.	1.	1.	0.	0.	0.	75.	0.	0.	0.	0.	0.8
120	Si Al Ca	0.	0.	0.	0.	30.	48.	0.	1.	0.	4.	11.	2.	0.	0.	0.	3.	0.	0.	0.	0.	8.6
30	Si Ca Al	0.	0.	0.	0.	17.	49.	0.	0.	0.	2.	27.	2.	0.	0.	0.	3.	0.	0.	0.	0.	1.5
25	Ca Si Al	0.	0.	0.	0.	14.	27.	0.	0.	0.	0.	54.	1.	0.	0.	0.	3.	0.	0.	0.	0.	2.6
252	Si Al K	0.	0.	0.	0.	29.	56.	0.	0.	0.	10.	2.	1.	0.	0.	0.	2.	0.	0.	0.	0.	26.3
87	Si Al Fe	0.	0.	0.	0.	28.	51.	0.	0.	0.	4.	3.	2.	0.	0.	0.	12.	0.	0.	0.	0.	5.4
18	Si Fe Al	0.	0.	0.	0.	15.	53.	0.	0.	0.	6.	3.	1.	0.	0.	0.	22.	0.	0.	0.	0.	1.8
19	Fe Si Al	0.	0.	0.	0.	12.	22.	0.	0.	0.	2.	1.	1.	0.	0.	0.	61.	0.	0.	0.	0.	0.9
15	Si Al Na	0.	0.	9.	0.	30.	58.	0.	1.	0.	1.	1.	0.	0.	0.	0.	0.	0.	0.	0.	0.	1.8
39	Si Al Ti	0.	0.	1.	0.	30.	47.	0.	0.	0.	4.	5.	10.	0.	0.	0.	4.	0.	0.	0.	0.	2.9
5	Ti Si Al	0.	0.	0.	0.	14.	28.	0.	0.	0.	5.	3.	46.	0.	0.	0.	4.	0.	0.	0.	0.	0.7
5	Ti Si Fe	0.	0.	0.	0.	10.	25.	0.	0.	0.	4.	5.	45.	0.	0.	0.	11.	0.	0.	0.	0.	0.8
2	Si Fe Ti	0.	0.	0.	0.	6.	42.	0.	2.	0.	6.	2.	19.	0.	0.	0.	24.	0.	0.	0.	0.	0.5
20	Si Al S	0.	0.	0.	0.	28.	49.	0.	12.	0.	5.	2.	1.	0.	0.	0.	3.	0.	0.	0.	0.	0.8
84	ALL CATEGORIES WITH VOLUME % LESS THAN 1.0 COMBINED IN ONE																					5.5
1190	TOTALS -	0.	0.	0.	0.	22.	51.	0.	1.	0.	4.	8.	2.	0.	0.	0.	12.	0.	0.	0.	0.	100.0

Volume DISTRIBUTION

SPECIES	Volume %	0.2-2.5	2.5-5.0	5.0-10.	10.- 20.	20.- 40.	40.- 80.	80.-500.
Fe - -	7.0	0.	1.	17.	46.	24.	12.	0.
Si - -	11.5	2.	9.	23.	47.	13.	5.	0.
Si Al -	16.8	5.	27.	34.	25.	7.	2.	0.
Si Al Ca	8.6	7.	24.	30.	28.	11.	0.	0.
Si Al K	26.3	3.	18.	24.	45.	8.	4.	0.
Si Al Fe	5.4	7.	35.	30.	6.	12.	3.	7.
OTHERS -	24.4	4.	15.	25.	36.	16.	4.	0.
TOTALS -	100.0	4.	18.	26.	36.	12.	4.	0.

4.4 MIT Drop Tube Furnace Produced Ash Samples

Mössbauer spectroscopic analysis was carried out on a series of ash samples produced by Taofang Zeng and Dr. Sarofim at MIT (Section 5). The beneficiated Pittsburgh No. 8 coal was combusted in their drop tube furnace under varying oxygen concentrations. As shown in Figure 4-11, the Mössbauer spectrum of this size segregated (< 75 micron) coal show substantial oxidation of pyrite. Non-size segregated beneficiated Pittsburgh No. 8 coal coal from PSI also showed substantial pyrite oxidation (Figure 4-4). However, the split between the two major peaks is sharper and the right side peak is better resolved in this size segregated coal due to lower amount of the ferric sulfate phase. Table 4-33 compares the results from the two size cuts. Mössbauer spectrum obtained at cryogenic temperatures showed the magnetic transition typical of the jarosite phase. The water soluble ferric sulfate phase was confirmed by the lack of this magnetic transition at cryogenic temperature. From these Mössbauer results, it appears that different size fractions of coal have different chemistry and their combustion behavior is expected to be different.

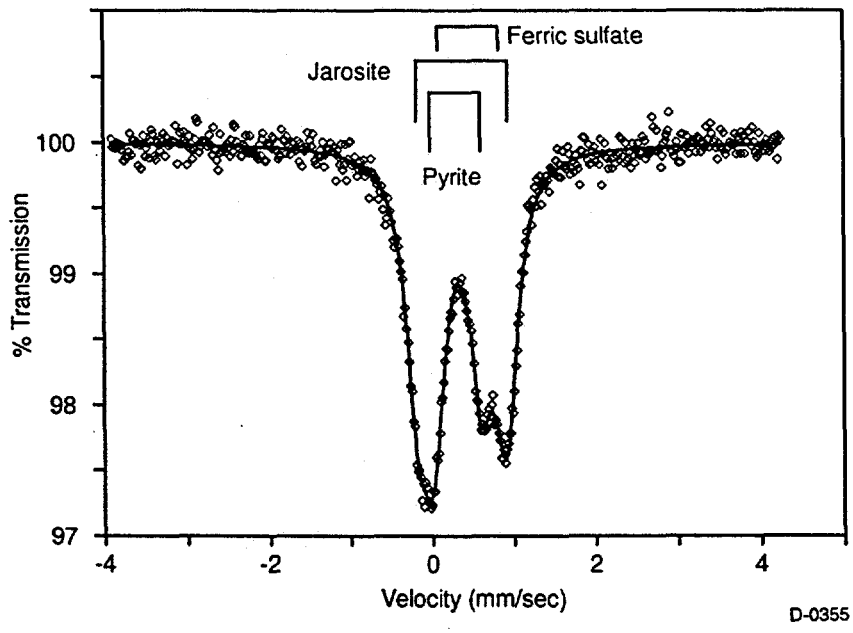

Figure 4-11. Mössbauer spectrum of size segregated (< 75 micron) beneficiated Pittsburgh No. 8 coal used by MIT group for drop tube furnace combustion experiments showing substantial amounts of pyrite oxidation products. (CFFLS No. 1218, MK No. 1834).

Because of the low coal feed rate (0.04g/min) the calculated stoichiometric ratio was much greater than one for all cases except the 0% oxygen case. Under equilibrium conditions, there should be sufficient oxygen to completely oxidize all iron present. However, due to short residence time (0.9 s) involved, the combustion is incomplete. This is clearly illustrated in the Mössbauer results shown in Table 4-34. It appears that large fraction of the residence time in this furnace is spent in coal particle heat-up. Since the experiment is carried out under super-stoichiometric conditions, coal particles either do not reach a high enough temperature or are quenched well before the combustion has progressed. At low oxygen concentrations (0 and 10%), pyrite undergoes decomposition and thereby produces pyrrhotite ($Fe_{1-x}S$) and iron metal. The ferric sulfate the just melts and does not appear to decompose. With increasing oxygen concentrations, we see formation of magnetite and its further oxidation to hematite. Also, with increasing oxygen partial pressure the Fe^{+++}/Fe^{++} ratio in the glassy phase increases.

Table 4-33. Mössbauer Spectroscopy Results of Beneficiated Pittsburgh No. 8 Coal: <75 Micron Size Segregated (MIT) and non-size Segregated (PSI).

MK#	CFFLS	Sample	Phases Present	I.S.	Q.S.	%Fe
1837	1219	0	Pyrite Clay Jarosite Ferric sulfate	0.31 1.19 0.37 0.47	0.58 2.40 1.14 0.56	3e+06
1838	1220	10	Pyrite Jarosite Ferric sulfate	0.30 0.37 0.47	0.62 1.12 0.74	4e+05

4.5 Mössbauer Analysis of University of Arizona's Drop Tube Furnace Tests

Washed Pittsburgh No. 8 coal was combusted in University of Arizona drop tube furnace under reducing conditions and large (5.5 s) residence times. The Mössbauer results of these ashes are shown in Table 4-35. This set of samples complement the set of ashes generated in PSI drop tube furnace (Tables 4-6 through 4-8). Even though the residence time was large, the samples exhibit considerable amounts of unreacted pyrite in the ash due to the lower stoichiometric ratio. For very low stoichiometric ratios (0.5), similar to PSI sample at SR=0.6 (Table 4-21), no oxide phase was observed. However, above SR=0.5, the Univ. of Arizona samples started showing magnetite, probably due to the longer residence times. All samples showed some pyrrhotite, indicating incomplete combustion of sulfur associated with Fe. With the increasing stoichiometric ratios, the amount of pyrite and pyrrhotite decreased and the amount of magnetite increased. However, even at the highest stoichiometric ratio of 0.65 no hematite was observed. Ash sample obtained at SR=0.65 contained 15% of iron in the pyrite phase.

4.6 Analysis of Silverdale Coal and Ashes

As a part of collaborative effort between this program and utility PowerGen in Great Britain, the Silverdale bituminous coal and its combustion products were investigated. The coal was obtained from National Power and was combusted in drop tube furnace tests at PSI. Fly ash, bottom ash and probe deposit samples were collected during field sampling at the PowerGen Ratcliffe station in October 1992 were provided by Imperial College for analysis.

4.6.1 Mössbauer Analysis

4.6.1.1 Mössbauer Analysis of PSI Drop Tube Furnace Produced Fly Ash Samples

Mössbauer results for the Silverdale coal drop tube furnace ashes are shown in Table 4-36. Combustion behavior of the Silverdale coal in PSI drop tube furnace tests was similar to that of the Pittsburgh No. 8 coals. Pyrrhotite and Fe^{++} (in glass) contents decreased, while magnetite and Fe^{+++} (in glass) contents increased with the increasing stoichiometric ratios.

Table 4-34. Beneficiated Pittsburgh No. 8, MIT DTF, 1650 K, 0.9 s Res. Time, 0.04g/min Coal Feed Rate, <75 Micron Coal Particle Size.

MK#	CFFLS	% O_2	S.R.	Phases Present	I.S.	Q.S.	H0	%Fe
1834	1218	Parent Coal		Pyrite Jarosite Ferric sulfate	0.30 0.37 0.47	0.62 1.12 0.74		41 42 16
1837	1219	0	0	Fe^{+++}/Jarosite γ Fe Metal Fe Metal $Fe_{1-x}S$ Fe Carbide	0.37 -0.08 -0.01 0.74 0.14	0.97 0 -0.09 0	 327 305 197	25 6 17 24 29
1838	1220	10	10	Fe^{++}/Glass Fe^{+++}/Glass γ Fe Metal Fe Metal Magnetite Magnetite $Fe_{1-x}S$	0.96 0.32 -0.06 -0.02 0.31 0.63 0.75	1.89 0.99 0 0 0 0	 328 486 448 299	19 28 2 8 17 15 11
1839	1221	30	29	Fe^{++}/Glass Fe^{+++}/Glass Magnetite Magnetite $Fe_{1-x}S$	0.86 0.39 0.35 0.65 0.67	2.33 0.95 0 0 0	 494 443 302	22 51 12 8 8
1841	1222	60	57	Fe^{++}/Glass Fe^{+++}/Glass α-Fe_2O_3 Magn.+Fe_2O_3	0.77 0.36 0.36 0.40	2.56 1.08 -0.08 -0.04	 496 427	11 66 9 14
1840	1223	100	96	Fe^{++}/Glass Fe^{+++}/Glass α-Fe_2O_3 Magn.+Fe_2O_3	0.73 0.35 0.37 0.39	2.74 1.17 -0.07 -0.05	 498 429	8 75 4 14
1842	1224	ASTM Ash		Fe^{+++}/Glass α-Fe_2O_3 α-Fe_2O_3	0.34 0.39 0.37	0.90 -0.08 -0.1	 514 494	7 55 39

Table 4-35. University of Arizona Drop Tube Furnace Generated Ashes of Washed Pittsburgh No. 8 Coal, 5.5 s Res. Time

MK#	CFFLS #	Stoichiometric Ratio/ Peak Furnace Temp (C)	Phases Present	I.S.	Q.S.	H0	%Fe
2120	95-107	0.40 / 1324	Fe^{++}/Glass	0.88	1.89		14
			Fe^{++}/Glass Pyrite	1.13	2.40		16
			$Fe_{1-x}S$	0.30	0.64		27
			$Fe_{1-x}S$	0.73	-0.08	309	31
				0.74	0.07	266	12
2122	95-108	0.52/1344	Fe^{++}/Glass	0.52	1.10		12
			Fe^{++}/Glass	1.12	2.29		24
			Pyrite	0.30	0.61		21
			Magnetite	0.26	0	495	9
			Magnetite	0.71	0	451	11
			$Fe_{1-x}S$	0.74	-0.05	302	23
2123	95-109	0.44/1356	Fe^{++}/Glass	1.08	2.14		26
			Pyrite	0.29	0.68		34
			$Fe_{1-x}S$	0.74	-0.06	309	26
			$Fe_{1-x}S$	0.84	0.21	262	14
2153	95-110	0.61/1325	Fe^{++}/Glass	1.05	2.13		29
			Fe^{+++}/Glass	0.35	0.73		22
			Magnetite	0.28	0	491	10
			Magnetite	0.53	0	455	7
			$Fe_{1-x}S$	0.75	-0.07	310	21
			$Fe_{1-x}S$	0.78	0.14	265	11
2125	95-111	0.58/1334	Fe^{++}/Glass	0.98	2.02		23
			Fe^{+++}/Glass	0.35	0.75		29
			Magnetite	0.27	0	495	9
			Magnetite	0.59	0	454	7
			$Fe_{1-x}S$	0.75	-0.06	307	27
			$Fe_{1-x}S$	0.35	0.55	266	5
2126	95-112	0.62/1328	Fe^{++}/Glass	1.01	2.11		27
			Fe^{+++}/Glass	0.38	0.40		21
			Magnetite	0.28	0	494	18
			Magnetite	0.57	0	453	13
			$Fe_{1-x}S$	0.72	-0.03	305	12
			$Fe_{1-x}S$	0.75	0.16	264	9
2127	95-113	0.52/1338	Fe^{++}/Glass	0.99	2.13		43
			Magnetite	0.20	0	484	8
			Magnetite	0.94	0	459	5
			$Fe_{1-x}S$	0.75	-0.07	305	15
			$Fe_{1-x}S$	0.66	0.04	268	9
			Pyrite	0.30	0.67		20

Table 4-35. University of Arizona Drop Tube Furnace Generated Ashes of Washed Pittsburgh No. 8 Coal, 5.5 s Res. Time (cont.)

MK#	CFFLS #	Stoichiometric Ratio/ Peak Furnace Temp (C)	Phases Present	I.S.	Q.S.	H0	%Fe
2128	95-114	0.65/1330	Fe^{++}/Glass	1.10	2.24		24
			Fe^{+++}/Glass	0.48	1.00		16
			Pyrite	0.31	0.63		15
			Magnetite	0.34	0	500	17
			Magnetite	0.66	0	450	12
			$Fe_{1-x}S$	0.71	-0.07	300	16

Table 4-36. Silverdale Coal and PSI Drop Tube Furnace Generated Ashes, 1500°C Furnace Set Point, 2.6 s Res. Time

MK#	CFFLS #	Stoichiometric Ratio	Phases Present	I.S.	Q.S.	H0	%Fe
1797	1206	COAL	Pyrite	0.30	0.59		84
			Jarosite	0.37	1.06		16
1827	1209	1.2	Fe^{++}/Glass	0.98	2.03		39
			Fe^{+++}/Glass	0.56	0.79		17
			Magnetite	0.29	-0.01	487	13
			Magnetite	0.64	-0.03	451	31
1826	1208	0.9	Fe^{++}/Glass	0.83	0.72		21
			Fe^{++}/Glass	1.18	2.05		26
			Fe^{++}/ Glass	0.84	1.83		24
			Magnetite	0.27	0.05	482	7
			Magnetite	0.68	-0.04	450	9
			$Fe_{1-x}S$	0.77	-0.05	301	13
1825	1207	0.6	Fe^{++}/Glass	1.10	2.22		22
			Fe^{++}/Glass	1.03	1.33		41
			$Fe_{1-x}S$	0.75	-0.08	309	30
			$Fe_{1-x}S$	0.71	0.05	270	7

4.6.1.2 Mössbauer Analysis of Ash Samples from Imperial College

Since the goal of this project is to study the effect of reducing stoichiometry on ash formation and deposition, the ash samples were collected during high, normal and low oxygen partial pressure conditions. Mössbauer results for these samples are reported in Table 4-37.

Table 4-37. Mössbauer spectroscopy results of samples collected during field sampling at the PowerGen Ratcliffe station. Silverdale coal was used during these tests. High,normal and low pO_2 levels correspond to 3.5,3.0 and 2.5% excess O_2 levels measured at the economiser outlet.

CFFLS/ MK#	Sample	Phases	I.S.	Q.S.	Hfs	%Fe
95-029	504/F	Fe^{++}/Glass	0.73	2.27		8
2019	Fly ash	Fe^{+++}/Glass	0.38	0.87		21
	Normal pO_2	α-Fe_2O_3	0.37	-0.10	513	16
		Magnetite	0.31	0	489	23
		Magnetite	0.58	0	451	32
95-030	510/F	Fe^{++}/Glass	0.86	2.26		15
2013	Fly ash	Fe^{+++}/Glass	0.44	0.83		18
	Low pO_2	α-Fe_2O_3	0.38	-0.10	511	10
		Magnetite	0.33	0	484	25
		Magnetite	0.56	0	452	22
		Magnetite	0.58	0.04	410	10
95-031	513/F	Fe^{++}/Glass	0.84	2.27		15
2020	Fly ash	Fe^{+++}/Glass	0.42	0.82		21
	High pO_2	α-Fe_2O_3	0.36	-0.10	512	8
		Magnetite	0.29	0	488	22
		Magnetite	0.60	0	451	34
95-032	572/S	Fe^{++}/Glass	0.72	2.15		10
2027	Bottom Ash	Fe^{+++}/Glass	0.38	0.95		21
	Normal pO_2	α-Fe_2O_3	0.36	-0.12	498	10
		Magnetite	0.28	0	483	14
		Magnetite	0.61	0	449	45
95-033	573/S	Fe^{++}/Glass	0.85	1.64		2
2018	Bottom ash	Fe^{+++}/Glass	0.30	1.11		21
	Low pO_2	α-Fe_2O_3	0.37	-0.11	504	45
		α-Fe_2O_3	0.37	-0.11	486	33
95-034	574/S	Fe^{++}/Glass	0.95	1.74		29
2036	Bottom ash	Fe^{+++}/Glass	0.40	0.72		19
	High pO_2	α-Fe_2O_3	0.37	-0.11	497	19
		Magnetite	0.35	0	470	13
		Magnetite	0.57	0	438	12
		Magnetite	0.59	0.01	392	8
95-035	526/D	Fe^{++}/Glass	0.58	2.27		2
2024	Probe deposit,	Fe^{+++}/Glass	0.34	0.98		15
	bulk, Normal pO_2	α-Fe_2O_3	0.37	-0.10	511	36
		Magnetite	0.33	0	487	21
		Magnetite	0.58	0	449	26

Table 4-37. Mössbauer spectroscopy results of samples collected during field sampling at the PowerGen Ratcliffe station. (cont.)

CFFLS/ MK#	Sample	Phases	I.S.	Q.S.	Hfs	%Fe
95-036 2010	539/D Probe deposit, bulk, Low pO_2	Fe^{++}/Glass Fe^{++}/Glass Fe^{+++}/Glass Magnetite Magnetite	1.02 0.90 0.49 0.17 0.79	2.15 1.54 -0.39 0 0	 480 450	40 32 10 7 11
95-037 2040	551/D Probe deposit, bulk, High pO_2	Fe^{++}/Glass Fe^{+++}/Glass Magnetite Magnetite	0.93 1.04 0.07 0.80	1.33 2.07 0 0	 466 451	31 53 6 10
	Probe deposit, bulk, Normal pO_2	No such sample from PowerGen/Imperial College				
95-038 2011	540/D Probe deposit, inner, Low pO_2	Fe^{++}/Glass Fe^{+++}/Glass α-Fe_2O_3 Magnetite Magnetite Magnetite	0.98 0.32 0.35 0.27 0.59 0.62	1.92 0.86 -0.11 0 0 -0.02	 512 485 458 432	9 8 31 23 18 11
95-039 2049	552/D Probe deposit, inner, High pO_2	Fe^{++}/Glass Fe^{++}/Glass Fe^{+++}/Glass α-Fe_2O_3 Magnetite Magnetite	1.07 0.90 0.49 0.37 0.28 0.62	2.86 1.87 0.62 -0.09 0 0	 515 487 451	3 14 9 6 20 48

There were significant differences between fly ash and bottom ash samples. Bottom ash shows the majority (78%) of iron in α-Fe_2O_3 while fly ash is enriched (57%) with magnetite. In both samples, the concentration of the ferric iron in glass is similar but the concentration of the ferrous iron in glass is much lower in the bottom ash (2%) than the fly ash (15%). This difference translates to an order of magnitude difference in the Fe^{++}/Fe^{+++} ratio, which would greatly affect the viscosity of the molten phase.

Probe deposit samples also show significant differences. Here also, the Fe^{+++}/Glass concentration is similar but Fe^{++}/Glass concentration is eight times higher in the bulk deposit (72%) than the initial deposit (9%). The inner (initial) deposit also shows higher concentrations of α-Fe_2O_3 (31%) and magnetite (52%) phases. These results suggest that the molten glass phase is <u>not</u> responsible for the deposit initiation.

4.6.1.3 Mössbauer Analysis of PSI Drop Tube Furnace Deposit Samples from Combustion of Silverdale Coal

To compare the ash formation and deposition behavior of the Silverdale coal in a power station field test with a laboratory drop tube furnace (with better controlled stoichiometric conditions) deposit samples were generated at PSIT. The PSIT deposit sample with the highest stoichiometric ratio (1.2) appears to have a composition closest to that of the fly ash sample collected under low pO_2 conditions during PowerGen field tests (Table 4-38).

Table 4-38. Mössbauer Spectroscopy Results for PSIT Lab Deposit Sample from Combustion of Silverdale Coal

CFFLS/ MK#	Sample	Phases	I.S.	Q.S.	Hfs	%Fe
95-040 2015	4/25A, PSIT deposit, SR=1.2	Fe^{++}/Glass Fe^{+++}/Glass Magnetite Magnetite Magnetite	0.91 0.30 0.30 0.67 0.38	2.00 1.14 0 0 -0.08	 487 454 362	7 19 32 25 17
95-041	4/25F, PSIT deposit, SR=0.9	Not enough sample to carry out Mössbauer Analysis				
95-042 2039	4/26C, PSIT dwposit, SR=0.6	Fe^{++}/Glass Fe^{+++}/Glass α-Fe_2O_3 superparamagnetic oxide	0.67 0.34 0.34 0.28	1.94 1.13 -0.11 0	 493 337	5 21 35 39

4.6.2 CCSEM Analysis

CCSEM analysis on Silverdale coal and three PSI drop tube furnace ashes from the Silverdale coal obtained at 0.6, 0.9 and 1.2 stoichiometric ratios are reported in Tables 4-39 through 4-42. As explained in the previous subsection, the ash samples contained a large amount of unburnt carbon. Therefore, all the ash samples were diluted with graphite and mounted with epoxy. With increasing stoichiometric ratio, we see reduction of Fe-S and Si-Al-S phases representing pyrrhotite and interaction of aluminosilicates with organic sulfur in the char. Also, increasing stoichiometric ratio shows an increase in the Fe-Si-Al phase, indicating interactions between iron and aluminosilicates to form ferric and ferrous glasses.

Table 4-39. CCSEM Analysis of Silverdale (Powergen) coal.

SAMPLE 1206 SILVERDALE coal (PSI)
RUN 1 DATE 25-JUN-94 SUMMARY 120 TOTAL 1199

AVERAGE SPECIES COMPOSITION

No.	MINERAL SPECIES	Na	Mg	Al	Si	P	S	Cl	K	Ca	Ti	Fe	Weight %
62	Quartz	0.	0.	0.	99.	0.	0.	0.	0.	0.	0.	0.	6.9
162	Kaolinite	0.	0.	44.	52.	0.	2.	0.	1.	0.	0.	0.	14.5
308	Illite	0.	0.	32.	53.	0.	2.	0.	9.	0.	1.	3.	22.0
1	K-Feldspar	0.	0.	18.	60.	0.	0.	0.	18.	0.	0.	3.	0.2
317	Misc. Silicates	0.	0.	33.	55.	0.	6.	1.	2.	0.	0.	2.	30.6
4	Elem. Sulfur	0.	0.	0.	5.	0.	90.	3.	0.	0.	0.	1.	0.1
189	Pyrite	0.	0.	0.	1.	0.	64.	0.	0.	0.	0.	35.	16.5
3	Ferrous Sulfate	0.	0.	1.	2.	0.	51.	0.	0.	0.	0.	46.	0.2
6	Gypsum	0.	0.	1.	3.	0.	45.	0.	0.	51.	0.	0.	0.3
25	Misc. sulf.	0.	0.	1.	7.	0.	50.	0.	0.	4.	0.	37.	1.3
13	Fe-rich	0.	0.	0.	1.	0.	0.	0.	0.	6.	0.	93.	1.1
22	Calcite	0.	0.	0.	0.	0.	0.	0.	0.	100.	0.	0.	1.6
20	Mixed Carbonate	0.	5.	0.	2.	0.	1.	0.	0.	62.	0.	28.	1.0
2	Ti-rich	0.	0.	4.	13.	0.	7.	0.	0.	0.	70.	6.	0.1
2	Quartz-Sulfate	0.	0.	3.	27.	0.	53.	9.	0.	0.	0.	4.	0.0
6	Sil-sulf	0.	0.	28.	37.	0.	24.	0.	2.	2.	0.	5.	0.4
13	Silicate-Pyrite	0.	0.	18.	27.	0.	36.	0.	1.	0.	0.	18.	1.7
33	Misc. Mixed	0.	0.	16.	29.	0.	20.	1.	2.	3.	2.	25.	1.4
1188	GRAND TOTALS	0.	0.	24.	45.	0.	15.	0.	3.	3.	0.	10.	100.0

WEIGHT DISTRIBUTION

Size Ranges (Microns)

MINERAL SPECIES	WT. %	0.2 2.5	2.5 5.0	5.0 10.0	10. 20.	20. 40.	40. 80.	80. 500.
Quartz	6.9	8.	68.	6.	1.	9.	7.	0.
Kaolinite	14.5	23.	45.	18.	8.	2.	4.	0.
Illite	22.0	11.	22.	7.	31.	16.	13.	0.
Misc. Silicates	30.6	42.	43.	4.	7.	3.	2.	0.
Pyrite	16.5	18.	11.	22.	3.	27.	19.	0.
MINOR MINERALS	9.4	22.	10.	12.	8.	20.	27.	0.
GRAND TOTALS	100.0	24.	32.	10.	11.	12.	10.	0.

Table 4-40. CCSEM Analysis of Silverdale (Powergen) Coal Ash, 1500 °C Furnace Set Point, 2.6 s Res. Time, Stoichiometric Ratio=0.6

SAMPLE 1207 PSI ASH SILVERDALE SR=0.6, 57.7% C (MADE TO 80%) IN EPOXY

AVERAGE SPECIES COMPOSITION

No.	SPECIES	C	O	Na	Mg	Al	Si	P	S	Cl	K	Ca	Ti	V	Cr	Mn	Fe	Ni	Cu	Zn	X	Vol %
83	Si - -	0.	0.	0.	0.	2.	93.	0.	1.	0.	2.	0.	0.	0.	0.	0.	2.	0.	0.	0.	0.	6.6
16	Ca - -	0.	0.	0.	0.	0.	1.	0.	4.	1.	0.	93.	0.	0.	0.	0.	0.	0.	0.	0.	0.	0.5
82	Si Al -	0.	0.	0.	0.	33.	59.	0.	2.	0.	4.	0.	0.	0.	0.	0.	2.	0.	0.	0.	0.	7.5
14	Al Si -	0.	0.	0.	0.	50.	46.	0.	0.	0.	3.	0.	0.	0.	0.	0.	1.	0.	0.	0.	0.	0.8
90	Fe S -	0.	0.	0.	0.	0.	1.	0.	35.	0.	0.	0.	0.	0.	0.	0.	64.	0.	0.	0.	0.	6.1
10	S Si -	0.	0.	0.	0.	1.	27.	0.	71.	0.	1.	0.	0.	0.	0.	0.	0.	0.	0.	0.	0.	1.0
250	Si Al K	0.	0.	0.	0.	31.	55.	0.	1.	0.	8.	0.	1.	0.	0.	0.	4.	0.	0.	0.	0.	24.3
39	Fe Si Al	0.	0.	0.	0.	14.	27.	0.	3.	1.	1.	1.	1.	0.	0.	0.	52.	0.	0.	0.	0.	2.9
200	Si Al Fe	0.	0.	0.	0.	29.	49.	0.	2.	0.	6.	1.	1.	0.	0.	0.	12.	0.	0.	0.	0.	20.0
28	Si Fe Al	0.	0.	0.	0.	21.	44.	0.	2.	0.	5.	2.	0.	0.	0.	0.	27.	0.	0.	0.	0.	2.8
16	Fe S Si	0.	0.	0.	0.	3.	9.	0.	26.	0.	0.	0.	0.	0.	0.	0.	63.	0.	0.	0.	0.	1.4
11	Fe Si S	0.	0.	0.	0.	6.	19.	0.	13.	0.	0.	0.	0.	0.	0.	0.	62.	0.	0.	0.	0.	0.8
11	S Si Fe	0.	0.	0.	0.	4.	24.	3.	54.	0.	2.	1.	1.	0.	0.	0.	12.	0.	1.	0.	0.	0.8
10	S Fe Si	0.	0.	0.	0.	3.	15.	1.	52.	1.	0.	1.	3.	0.	0.	0.	24.	0.	0.	0.	0.	1.2
8	Si Al Ti	0.	0.	0.	0.	25.	48.	0.	1.	0.	6.	1.	13.	0.	0.	0.	7.	0.	0.	0.	0.	1.4
4	Ti Si Al	0.	0.	0.	0.	15.	26.	0.	0.	0.	3.	1.	49.	0.	0.	0.	8.	0.	0.	0.	0.	0.8
56	S Si Al	0.	0.	0.	0.	16.	26.	0.	48.	1.	1.	2.	2.	0.	1.	0.	4.	0.	0.	0.	0.	5.4
79	Si Al S	0.	0.	0.	0.	28.	46.	0.	14.	0.	4.	2.	1.	0.	0.	0.	5.	0.	0.	0.	0.	5.3
34	Si S Al	0.	0.	0.	0.	20.	39.	0.	27.	1.	3.	1.	1.	0.	0.	0.	8.	0.	0.	0.	0.	1.9
11	S Al Si	0.	0.	0.	0.	18.	14.	0.	58.	5.	0.	0.	3.	0.	0.	0.	0.	0.	0.	1.	0.	0.8
3	Ca S Fe	0.	0.	0.	3.	0.	0.	0.	31.	0.	0.	43.	0.	0.	0.	0.	23.	0.	0.	0.	0.	0.8
104	ALL CATEGORIES WITH VOLUME % LESS THAN 1.0 COMBINED IN ONE																					6.6
1161	TOTALS -	0.	0.	0.	0.	21.	44.	0.	12.	0.	4.	3.	1.	0.	0.	0.	14.	0.	0.	0.	0.	100.0

Volume DISTRIBUTION

SPECIES	Volume %	0.2-2.5	2.5-5.0	5.0-10.	10.- 20.	20.- 40.	40.- 80.	80.-500.
Si - -	6.6	11.	18.	25.	24.	15.	7.	0.
Si Al -	7.5	6.	19.	9.	34.	18.	9.	5.
Fe S -	6.1	2.	7.	27.	36.	25.	3.	0.
Si Al K	24.3	4.	7.	17.	56.	14.	2.	0.
Si Al Fe	20.0	17.	42.	20.	18.	3.	0.	0.
S Si Al	5.4	19.	42.	28.	10.	1.	0.	0.
Si Al S	5.3	32.	45.	14.	7.	2.	0.	0.
OTHERS -	24.8	13.	25.	27.	20.	12.	2.	0.
TOTALS -	100.0	12.	24.	21.	29.	11.	2.	0.

Table 4-41. CCSEM Analysis of Silverdale (Powergen) Coal Ash, 1500 °C Furnace Set Point, 2.6 s Res. Time, Stoichiometric Ratio=0.9

SAMPLE 1208 PSI ASH SILVERDALE SR=0.9, 37.5% C (MADE TO 80%) IN EPOXY

AVERAGE SPECIES COMPOSITION

No.	SPECIES	C	O	Na	Mg	Al	Si	P	S	Cl	K	Ca	Ti	V	Cr	Mn	Fe	Ni	Cu	Zn	X	Vol %
16	Ca - -	0.	0.	0.	0.	2.	2.	1.	1.	2.	0.	92.	0.	0.	0.	0.	1.	0.	0.	0.	0.	1.5
84	Si - -	0.	0.	0.	0.	2.	92.	0.	1.	0.	3.	0.	0.	0.	0.	0.	2.	0.	0.	0.	0.	8.0
48	Fe - -	0.	0.	0.	0.	0.	2.	0.	3.	0.	0.	0.	0.	0.	0.	0.	94.	0.	0.	0.	0.	4.2
8	S - -	0.	0.	0.	0.	2.	0.	0.	95.	0.	0.	0.	1.	0.	1.	0.	0.	0.	1.	0.	0.	0.5
38	Fe S -	0.	0.	0.	0.	0.	0.	0.	27.	0.	0.	0.	0.	0.	0.	0.	73.	0.	0.	0.	0.	2.8
45	Si Al -	0.	0.	0.	0.	36.	57.	0.	1.	0.	4.	0.	0.	0.	0.	0.	2.	0.	0.	0.	0.	4.1
7	Al Si -	0.	0.	0.	0.	53.	47.	0.	0.	0.	0.	0.	0.	0.	0.	0.	0.	0.	0.	0.	0.	0.8
12	Fe Si -	0.	0.	0.	0.	2.	12.	0.	1.	0.	0.	0.	0.	0.	0.	0.	83.	0.	0.	0.	0.	0.6
268	Si Al K	0.	0.	0.	0.	31.	54.	0.	1.	0.	9.	0.	1.	0.	0.	0.	4.	0.	0.	0.	0.	26.8
55	Fe Si Al	0.	0.	0.	0.	13.	27.	0.	1.	0.	2.	2.	1.	0.	0.	0.	54.	0.	0.	0.	0.	4.3
277	Si Al Fe	0.	0.	0.	0.	28.	50.	0.	1.	0.	6.	2.	1.	0.	0.	0.	12.	0.	0.	0.	0.	24.6
45	Si Fe Al	0.	0.	0.	0.	20.	45.	0.	1.	0.	5.	2.	1.	0.	0.	0.	27.	0.	0.	0.	0.	3.9
7	Si Al Ti	0.	0.	0.	0.	25.	43.	0.	2.	0.	5.	1.	16.	0.	0.	0.	7.	0.	0.	0.	0.	0.6
14	Si Al Ca	0.	0.	0.	0.	29.	44.	0.	1.	0.	4.	15.	0.	0.	0.	0.	6.	0.	0.	0.	0.	1.1
3	Al Si Ca	0.	0.	0.	0.	39.	25.	0.	2.	0.	1.	17.	2.	0.	0.	0.	13.	0.	0.	0.	0.	0.6
5	Si Fe K	0.	0.	0.	0.	5.	70.	0.	0.	0.	9.	1.	2.	0.	0.	0.	14.	0.	0.	0.	0.	0.5
58	Si Al S	0.	0.	0.	0.	26.	47.	0.	14.	0.	6.	1.	1.	0.	0.	0.	5.	0.	0.	0.	0.	4.6
26	Si S Al	0.	0.	0.	0.	16.	40.	0.	28.	1.	3.	2.	1.	0.	0.	0.	7.	0.	0.	0.	0.	1.2
34	S Si Al	0.	0.	0.	0.	14.	26.	1.	48.	1.	2.	2.	0.	0.	1.	1.	3.	0.	0.	0.	0.	1.6
13	S Si Fe	0.	0.	0.	0.	3.	17.	1.	59.	2.	2.	3.	1.	0.	0.	0.	11.	0.	1.	0.	0.	0.9
7	Fe S Si	0.	0.	0.	0.	8.	17.	0.	25.	0.	1.	2.	0.	0.	0.	0.	46.	0.	0.	0.	0.	0.5
112	ALL CATEGORIES WITH VOLUME % LESS THAN 1.0 COMBINED IN ONE																					5.9
1182	TOTALS -	0.	0.	0.	0.	21.	46.	0.	6.	0.	5.	3.	1.	0.	0.	0.	16.	0.	0.	0.	0.	100.0

Volume DISTRIBUTION

SPECIES	Volume %	0.2-2.5	2.5-5.0	5.0-10.	10.- 20.	20.- 40.	40.- 80.	80.-500.
Si - -	8.0	5.	19.	27.	22.	18.	9.	0.
Fe - -	4.2	1.	0.	15.	38.	26.	21.	0.
Si Al -	4.1	3.	16.	26.	20.	24.	11.	0.
Si Al K	26.8	4.	14.	21.	36.	19.	6.	0.
Fe Si Al	4.3	2.	8.	18.	32.	32.	9.	0.
Si Al Fe	24.6	16.	31.	28.	20.	5.	1.	0.
Si Al S	4.6	22.	52.	26.	0.	1.	0.	0.
OTHERS -	23.5	13.	21.	27.	19.	15.	5.	0.
TOTALS -	100.0	9.	21.	25.	25.	15.	5.	0.

Table 4-42. CCSEM analysis of Silverdale (Powergen) coal ash, 1500 °C furnace set point, 2.6 sec res. time, stoichiometric ratio=1.2

SAMPLE 1209 PSI SILVERDALE ASH SR=1.2, 14.7% C (MADE TO 80%) IN EPOXY

AVERAGE SPECIES COMPOSITION

No.	SPECIES	C	O	Na	Mg	Al	Si	P	S	Cl	K	Ca	Ti	V	Cr	Mn	Fe	Ni	Cu	Zn	X	Vol %
97	Si - -	0.	0.	0.	0.	1.	96.	0.	0.	0.	1.	0.	0.	0.	0.	0.	1.	0.	0.	0.	0.	10.7
51	Fe - -	0.	0.	0.	0.	1.	2.	0.	1.	0.	0.	1.	0.	0.	0.	0.	95.	0.	0.	0.	0.	3.8
13	Ca - -	0.	0.	0.	0.	0.	3.	0.	1.	0.	0.	92.	0.	0.	0.	0.	3.	0.	0.	0.	0.	1.5
16	Al Si -	0.	0.	0.	0.	51.	47.	0.	0.	0.	2.	0.	0.	0.	0.	0.	0.	0.	0.	0.	0.	1.5
68	Si Al -	0.	0.	0.	0.	35.	58.	0.	0.	0.	4.	1.	1.	0.	0.	0.	2.	0.	0.	0.	0.	5.6
9	Fe Si -	0.	0.	0.	0.	3.	14.	0.	0.	0.	0.	0.	0.	0.	0.	0.	82.	0.	0.	0.	0.	0.5
4	Fe S -	0.	0.	0.	0.	0.	0.	0.	13.	0.	0.	0.	0.	0.	0.	0.	87.	0.	0.	0.	0.	0.6
5	S Si -	0.	0.	0.	0.	3.	33.	0.	61.	0.	0.	0.	0.	0.	0.	0.	3.	0.	0.	0.	0.	0.7
72	Fe Si Al	0.	0.	0.	0.	14.	28.	0.	0.	0.	2.	2.	2.	0.	0.	0.	52.	0.	0.	0.	0.	6.4
304	Si Al Fe	0.	0.	0.	0.	27.	50.	0.	1.	0.	6.	2.	1.	0.	0.	0.	12.	0.	0.	0.	0.	23.1
6	Al Si Fe	0.	0.	0.	0.	39.	34.	0.	0.	0.	2.	10.	3.	0.	0.	0.	12.	0.	0.	0.	0.	0.7
57	Si Fe Al	0.	0.	0.	0.	21.	42.	0.	1.	0.	5.	2.	1.	0.	0.	0.	29.	0.	0.	0.	0.	4.3
244	Si Al K	0.	0.	0.	0.	31.	55.	0.	0.	0.	8.	0.	1.	0.	0.	0.	4.	0.	0.	0.	0.	23.1
2	Ca Fe Si	0.	0.	0.	0.	9.	20.	0.	0.	0.	0.	49.	0.	0.	0.	0.	22.	0.	0.	0.	0.	0.5
17	Si Al Ca	0.	0.	0.	0.	29.	43.	0.	1.	0.	3.	12.	4.	0.	0.	0.	8.	0.	0.	0.	0.	1.4
20	Si Al S	0.	0.	0.	0.	23.	48.	0.	14.	1.	2.	1.	1.	0.	1.	0.	6.	0.	0.	0.	0.	1.6
8	S Si Al	0.	0.	0.	0.	11.	30.	0.	53.	0.	2.	0.	0.	0.	1.	0.	3.	0.	0.	0.	0.	1.3
6	Si S Al	0.	0.	0.	0.	16.	40.	0.	19.	7.	9.	0.	0.	0.	0.	0.	9.	0.	0.	1.	0.	0.6
7	Fe S Si	0.	0.	0.	0.	1.	7.	0.	25.	0.	0.	0.	0.	0.	0.	0.	67.	0.	0.	0.	0.	0.6
12	Si S Fe	0.	0.	0.	0.	2.	44.	0.	26.	6.	1.	0.	1.	0.	0.	0.	18.	0.	1.	0.	0.	1.2
8	S Si Ti	0.	0.	0.	0.	0.	26.	0.	58.	0.	0.	3.	11.	0.	0.	0.	2.	0.	0.	0.	0.	0.6
5	S Cl Si	0.	0.	0.	0.	1.	17.	2.	46.	24.	1.	0.	2.	1.	0.	1.	2.	0.	0.	3.	0.	0.5
9	Si S Cl	0.	0.	0.	0.	1.	48.	0.	28.	15.	3.	0.	0.	2.	0.	0.	0.	1.	0.	3.	0.	1.2
4	S Si Cl	0.	0.	0.	0.	0.	27.	0.	36.	19.	0.	9.	0.	0.	0.	0.	9.	0.	0.	0.	0.	0.6
124	ALL CATEGORIES WITH VOLUME % LESS THAN 1.0 COMBINED IN ONE																					7.4
1168	TOTALS -	0.	0.	0.	0.	20.	49.	0.	5.	1.	5.	4.	1.	0.	0.	0.	15.	0.	0.	0.	0.	100.0

Volume DISTRIBUTION

SPECIES	Volume %	0.2-2.5	2.5-5.0	5.0-10.	10.- 20.	20.- 40.	40.- 80.	80.-500.
Si - -	10.7	1.	11.	12.	51.	15.	10.	0.
Si Al -	5.6	5.	21.	11.	29.	23.	11.	0.
Fe Si Al	6.4	2.	8.	7.	50.	24.	9.	0.
Si Al Fe	23.1	7.	34.	32.	20.	8.	0.	0.
Si Fe Al	4.3	7.	17.	16.	38.	19.	3.	0.
Si Al K	23.1	2.	10.	30.	42.	15.	2.	0.
OTHERS -	26.8	4.	11.	24.	40.	17.	3.	0.
TOTALS -	100.0	4.	17.	24.	37.	15.	4.	0.

4.6.3 XAFS Analysis

As shown in Figure 4-12, Fe K-edge XANES data were collected for selected PowerGen fly and bottom ash samples. However, as discussed later in this report, we are unable currently to deconvolute the XANES spectra to quantify the contributions of various phases to the features of the spectra.

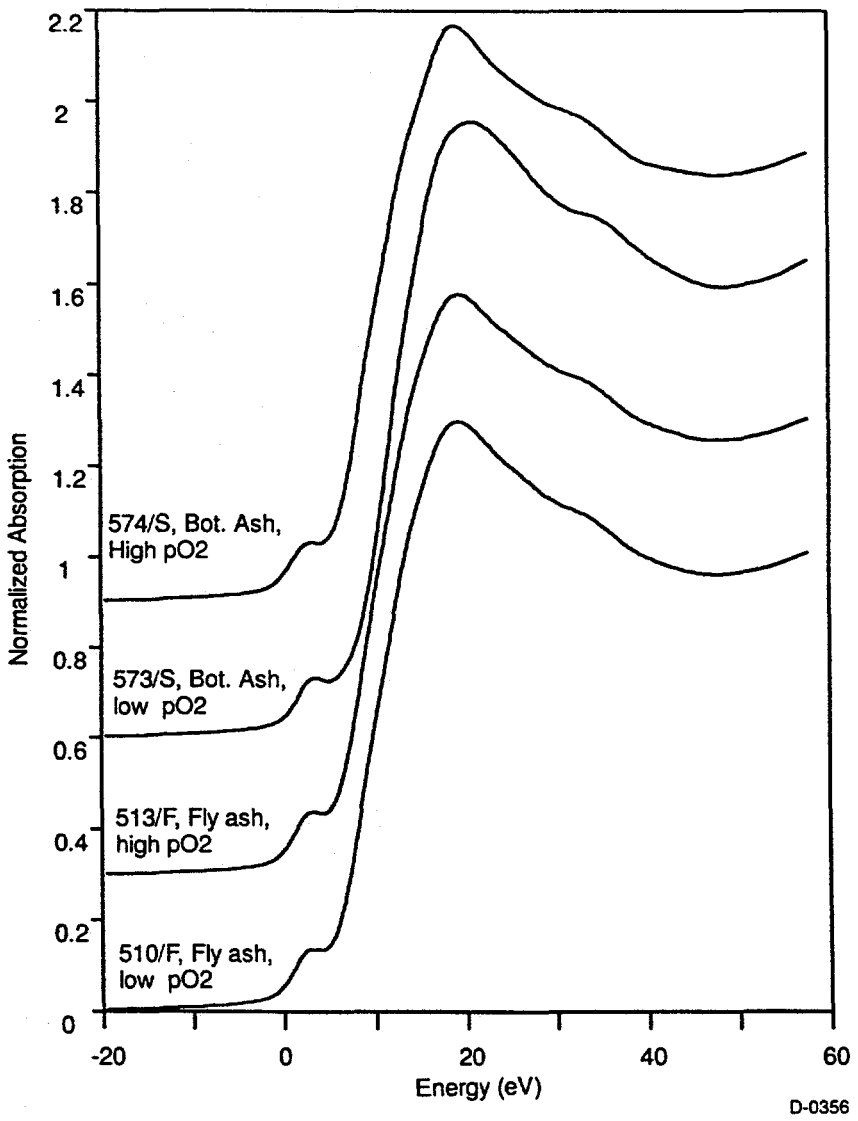

Figure 4-12. Fe K edge XANES of selected fly and bottom ash samples collected during PowerGen field test using Silverdale coal.

Figure 4-13 shows Ca-K edge XANES of some standard compounds. Wollastonite is a triclinic mineral form of $CaSiO_3$ and its spectra appears similar to that of a $CaSiO_3$ chemical compound (obtained from Alfa/Aesar chemicals). Stilbite is an aluminosilicate mineral of the zeolite family with a composition of $(Ca,Na)_3Al_5(Al,Si)Si_{14}O_{40}\cdot 15H_2O$. Figure 4-14 shows Ca-K edge XANES of the selected ash samples collected under high and low oxygen partial pressure conditions. XANES spectra features of all ash samples appear to show combinations of XANES spectral features of calcium silicate, calcium alumino-silicate and calcium sulfate. Samples collected under higher oxygen partial pressure show a better defined

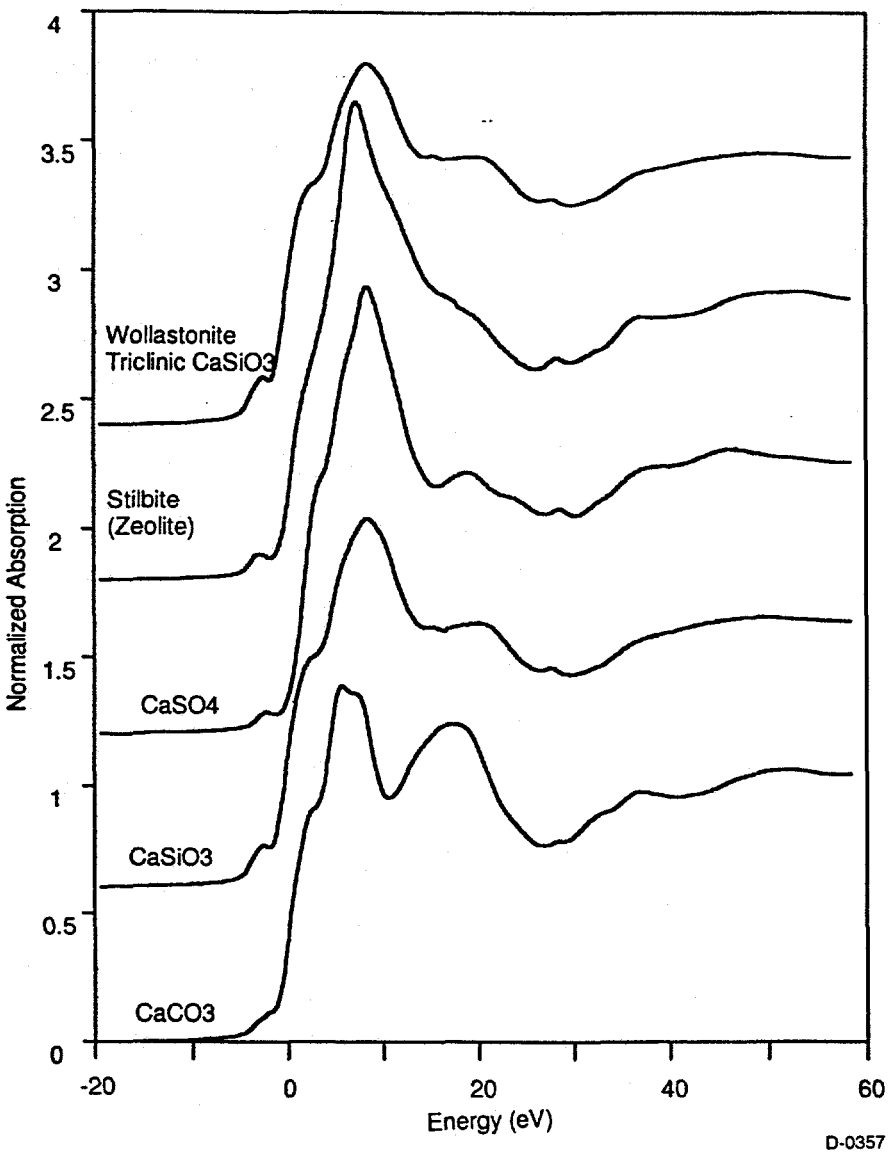

Figure 4-13. Ca K edge XANES of standard compounds and minerals.

preedge peak and a more pronounced shoulder on the main peak indicating presence of higher amounts of calcium silicate. Unlike Fe (obtained by Mössbauer Spectroscopy) data, Ca K edge XANES spectra of bulk and inner deposits do not show any significant differences. We are currently experimenting with derivatives of these spectra in an attempt to bring out the structural differences between the samples more clearly.

Figure 4-15 shows Ca K edge XANES of the three PSIT droptube furnace Silverdale samples. It appears that the combustion conditions have negligible effect on the distribution of the forms of calcium in the deposit. The preedge peak and the shoulder on the low energy side of the main peak are more pronounced in PSIT deposits than in the PowerGen field test which would suggest that the partial pressure of oxygen in the PSIT tests is higher. However, unlike the PowerGen field test, these features do not change with different stoichiometric ratios.

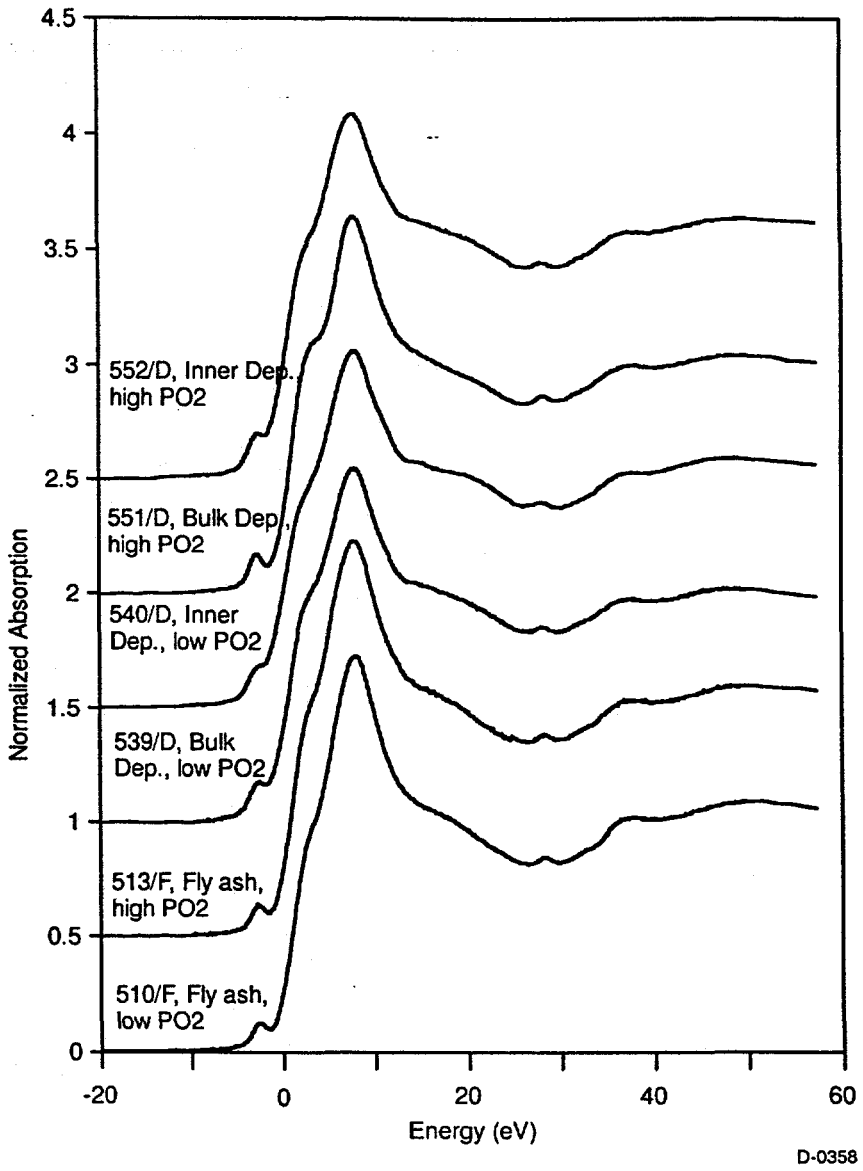

Figure 4-14. Ca K edge XANES of flyash and deposit samples collected during field test at the PowerGen Ratcliffe Station burning Silverdale coal.

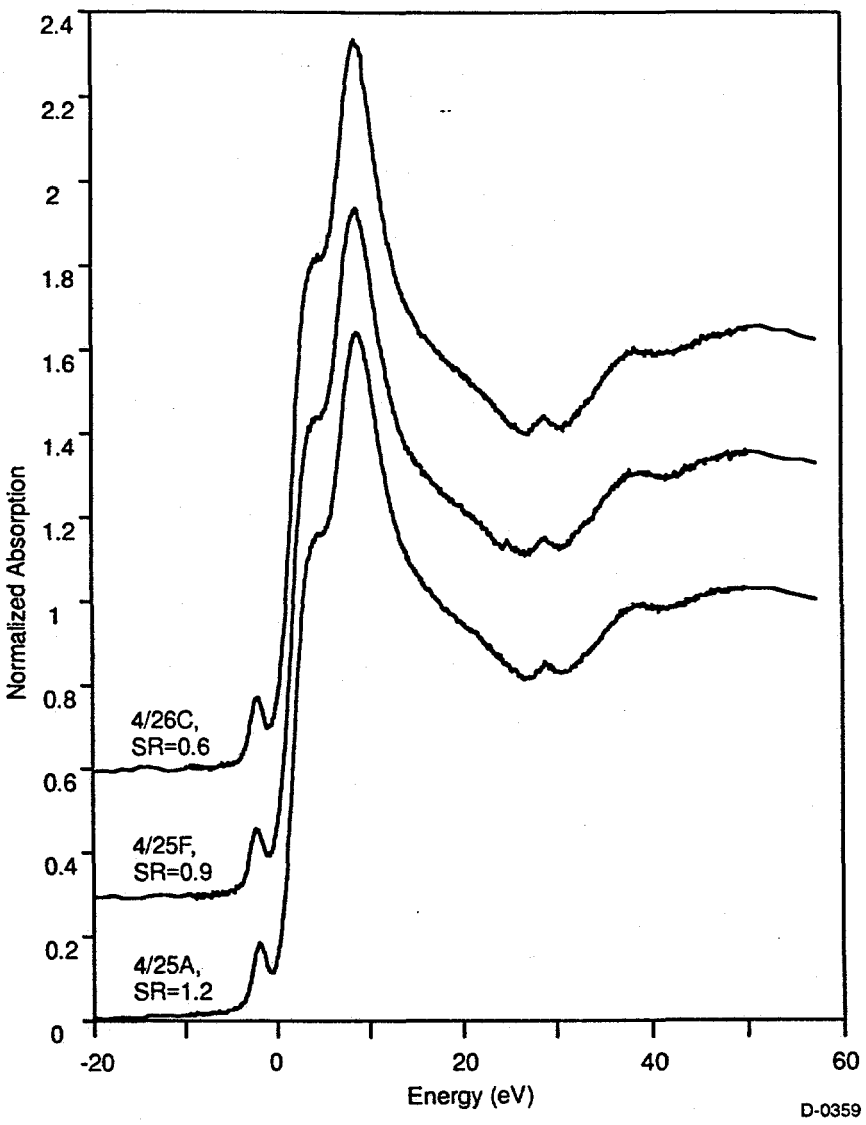

Figure 4-15. Ca K edge XANES of drop tube furnace deposits samples generated using Silverdale coal.

4.7 *In situ* XAFS Furnace

As part of our efforts to better understand how minerals interact during the combustion process PSI, in conjunction with the University of Kentucky (UK) and the Division of Applied Sciences (DAS) at Brookhaven National Laboratory, has designed and constructed a combustion test facility to collect XAFS data in-situ. The facility, the only system of its type in the world, consists of an auger type powder feeder, an entrained flow reactor, a six-way cross, and an ash collection system. The use of the facility in beamline X-19A of the National Synchrotron Light Source, allows in-situ measurements (XAFS) to be made of the ash immediately after the ash exits the reactor. Therefore, this system allows measurements to be made at high temperatures and oxidizing conditions without the introduction of potentially confounding effects during quenching of the samples.

Figure 4-16 is a schematic diagram of the furnace system designed and built by PSIT/UKy during previous DoE funded programs for *in situ* XAFS investigations of iron and calcium phases during coal combustion. It is designed to be separable into top and bottom sections so that it can be wheeled into the experimental hutch and reassembled. The drop tube furnace is designed for one standard cubic foot per minute (scfm) total gas flow and one to 10 g/min of reactant feed rate. The input gas can be a mixture of two gases (nitrogen and oxygen) to produce varying oxidizing/reducing combustion conditions. About 80% of the total gas flow (primary air) is preheated to about 900 K before being injected to the diffuser, while the remaining 20% of gas flow is used to entrain the utility grind reactant (coal or mineral) from the auger feeder. The diffuser, at the top of the furnace, is designed to thoroughly mix the primary and feeder air and to distribute the solid particles uniformly across the entire flow cross section in the alumina retort of the furnace. The 30 in. long, 3 in. i.d. alumina retort is electrically heated to achieve up to 1500 K wall temperature with a constant temperature zone of 20 in. At one scfm gas flow rate and 1500 K gas temperature the residence time of the coal particle is about 2.5 s which is sufficient to achieve complete combustion of utility grind coal particles. A conical ceramic venturi at the exit of the furnace reduces the outlet gas stream diameter from 3 in. to 1 in. diameter before it enters the six-way cross.

Figure 4-17 is a cut-away view of the six-way cross, which is designed to allow the X-ray beam and the detectors full access to the combustion product stream. During the assembly, the 6-way cross is aligned with respect to the X-ray beam so that a thin X-ray beam passes the center of the cross without touching any of the walls. On a water cooled port, either a solid state X-ray detector with 0.003 in. thick beryllium window or a fluorescence ionization chamber (design is similar to Lytle detector) is mounted orthogonal to both the X-ray beam and the ash stream. Helium gas is purged through the X-ray inlet and exit ports as well as the detector port toward the center of the cross to reduce x-ray attenuation and to inhibit fly ash particles from flowing outward toward windows. A port across from the detector port is used for an ash deposition probe. A boron nitride (BN) disk is placed at 45 deg to all major axes (X-ray beam, ash stream and detector) to optimize both the collection efficiency and the X-ray signal. After the six-way cross the ash and exit gas stream is cleaned and the gas flow rate is monitored (to check for any leaks) before venting it to the exhaust. Since the experiment is carried out inside the experimental hutch, where personnel are not allowed when the X-ray beam is on, the entire operation of the furnace is remotely controlled and several safety features were installed for emergency shutdown.

The *in situ* XAFS furnace was designed and built by PSI in January 1993 under a separate contract. After testing it was disassembled and moved to Brookhaven National Laboratory. In February 1993 it was moved to the beamline X-19A and tested with pure pyrite and with tailings from a Kentucky No. 9 coal washing plant. It was then stored at NSLS till next set of experiments.

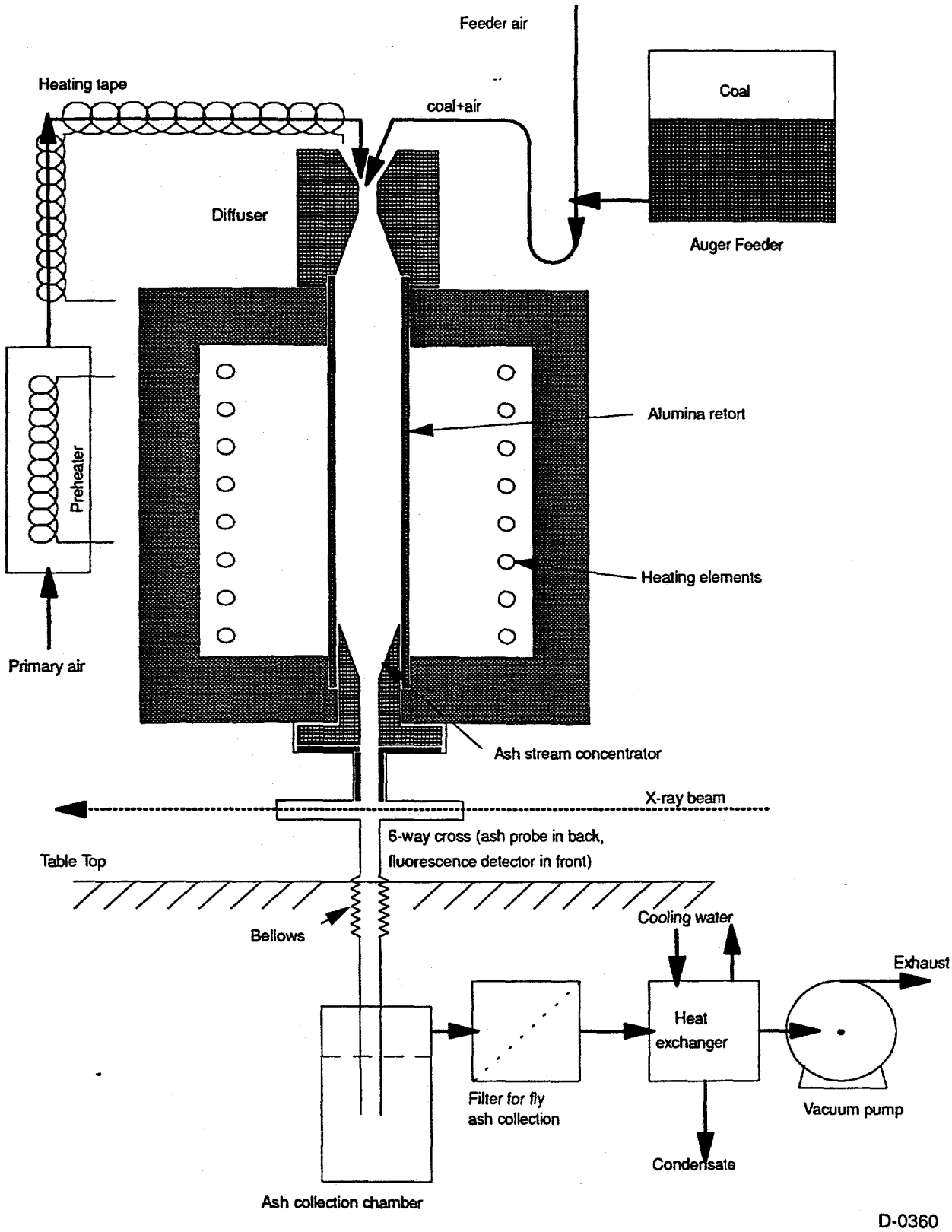

Figure 4-16. Schematic of in-situ XAFS furnace system.

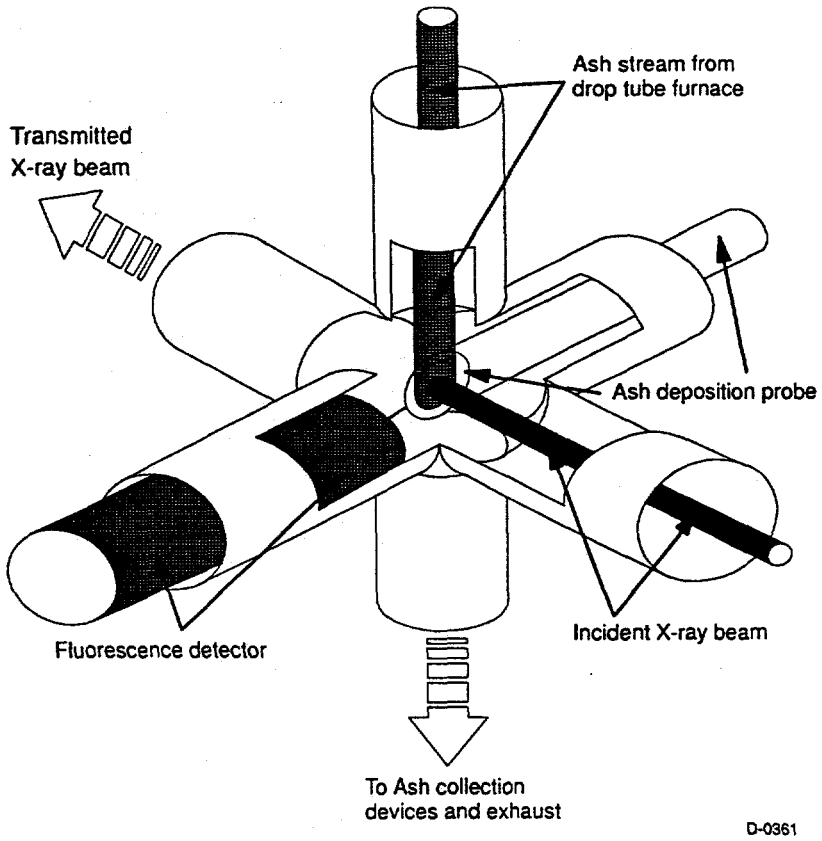

Figure 4-17. Cut-away view of 6-way cross used for in-situ XAFS observation of ash stream and ash deposits.

Preliminary In situ combustion test at NSLS

Table 4-43 indicates the experimental conditions for the preliminary *in-situ* experiments.

Table 4-43. Experimental matrix for August 1993 *in situ* XAFS experiment.

Sample	Feed Rate (g./min)	Furnace Temp., °C	% O_2	Substrate Temp., °C	Approximate Stoichiometric Ratio #
Pyrite	1	1300	20	460	8
Pyrite	1	1300	14	520	5
Pyrite	1	1300	5	560	2
KY No. 9	2	1100	20	400	2
KY No. 9	4	1300	20	480	1
KY No. 9	4	1400	20	500	1
KY No. 9	6	1500	20	650	0.6
KY No. 9	6	1500	5	700	0.2

Precise value unavailable because of feeder fluctuations.

Pyrite

Figure 4-18 shows Fe K-edge XANES of deposit formed while pyrite was fed at 1g./min feed rate to the furnace at 1300°C. The deposition probe temperature was about 460°C. Air was used for the primary air supply and for the pyrite feed stream. The initial deposit (bottom spectra in the figure) showed less oxidation as compared to the outer deposit (middle spectra). Pyrite feed was then stopped and hot air was allowed to pass over the deposit to monitor further transformations in the deposit. After 2 h of 'aging' the XANES spectra of the deposit did not indicate any further changes in the deposit (top spectra).

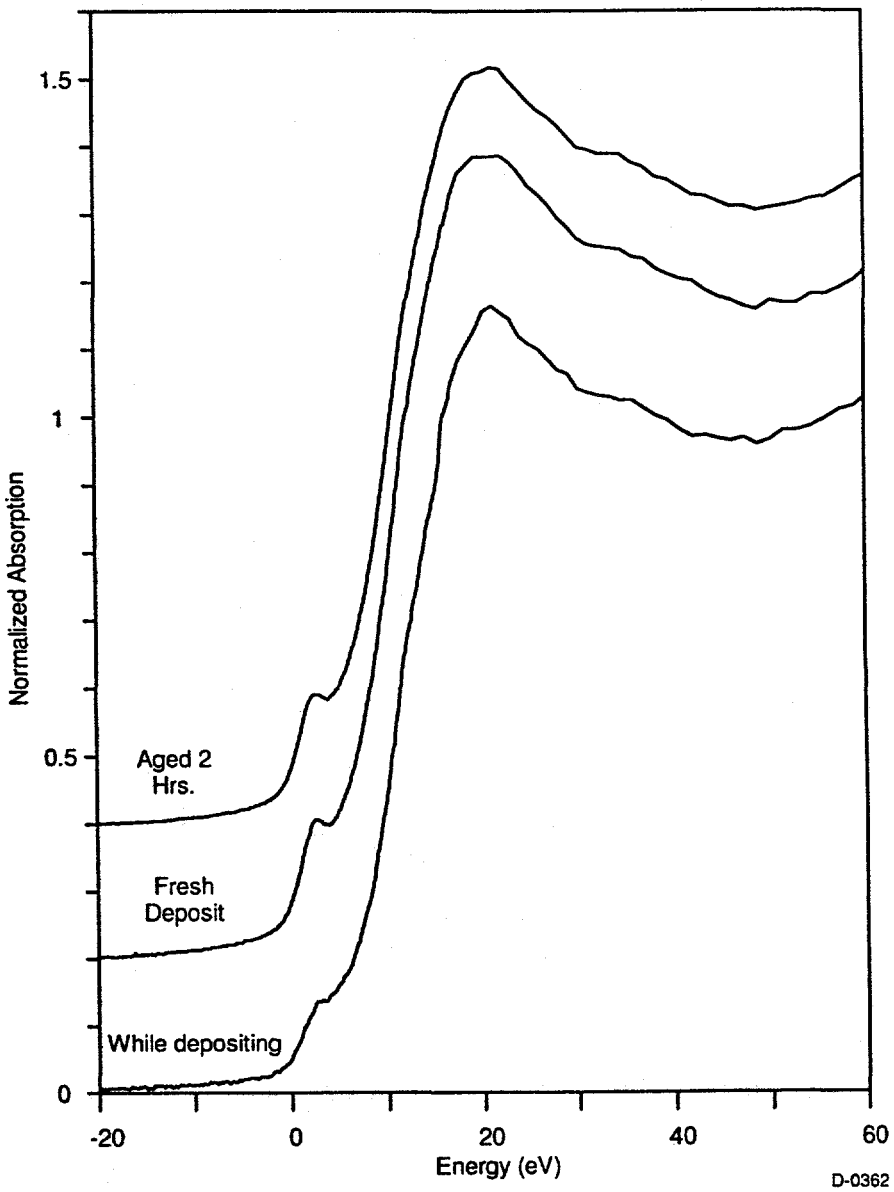

Figure 4-18. Fe K edge *in situ* XANES of pyrite deposit. Furnace set point 1300°C, 25% oxygen, substrate temperature of 450°C.

The oxygen partial pressure was reduced to 5% by substituting nitrogen for feeder air and by mixing nitrogen with the primary air. The bottom spectra in Figure 4-19 shows Fe XANES of the deposit collected at 1300 °C furnace temperature and 5% oxygen partial pressure. Under reducing conditions, pyrite does not oxidize completely but forms what may be an Fe-oxysulfide phase. The pre-edge peak in the spectra indicates the onset of iron oxide phase formation. When the partial pressure of oxygen was increased to 14%, the pre-edge peak was better defined. In fact, the spectrum for 14% oxygen partial pressure is very similar to that collected at 20% oxygen partial pressure (see Figure 4-18).

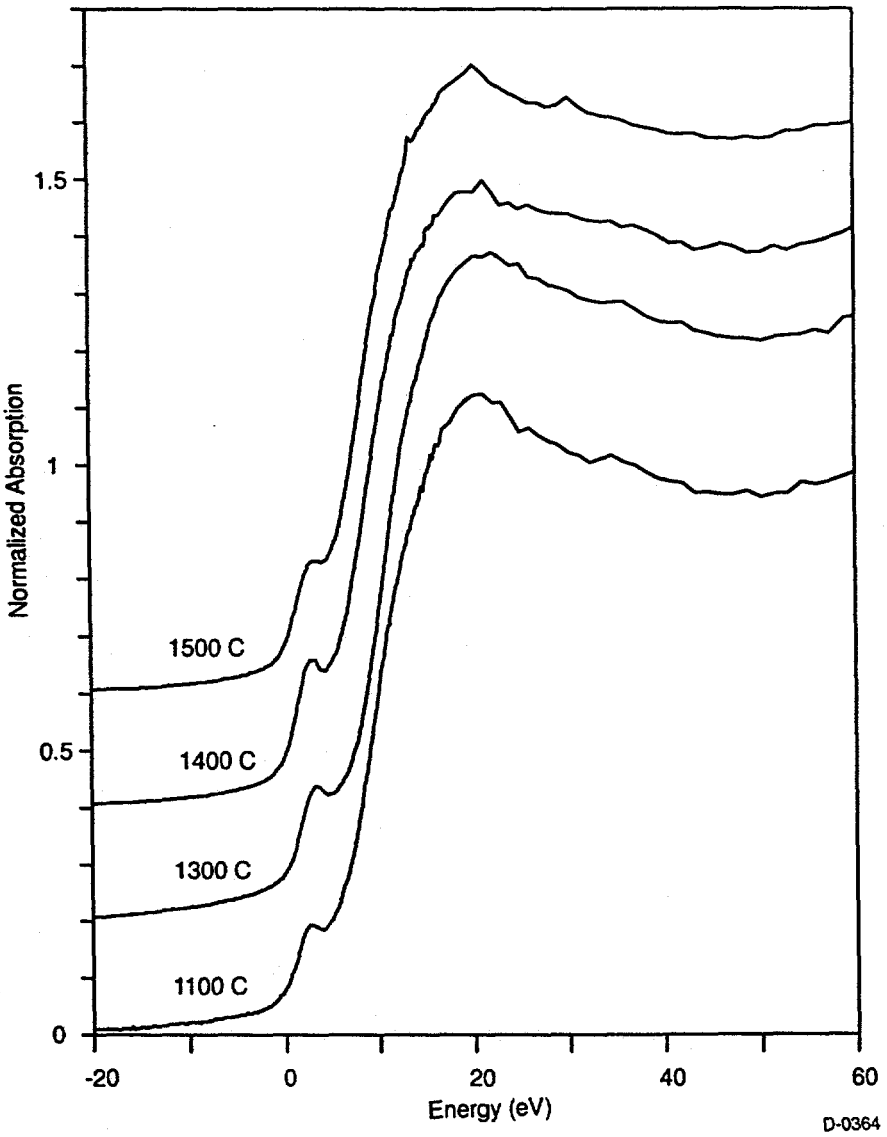

Figure 4-19. Fe K edge *in situ* XANES of pyrite deposit. Furnace set point 1300°C, substrate temperatures for 5 and 14% O_2 conditions are noted in the figure.

Kentucky No. 9 coal

Figure 4-20 shows a series of XANES spectra collected at 20% oxygen partial pressure and at varying furnace temperature settings. The spectra are quite similar to each other, but show subtle

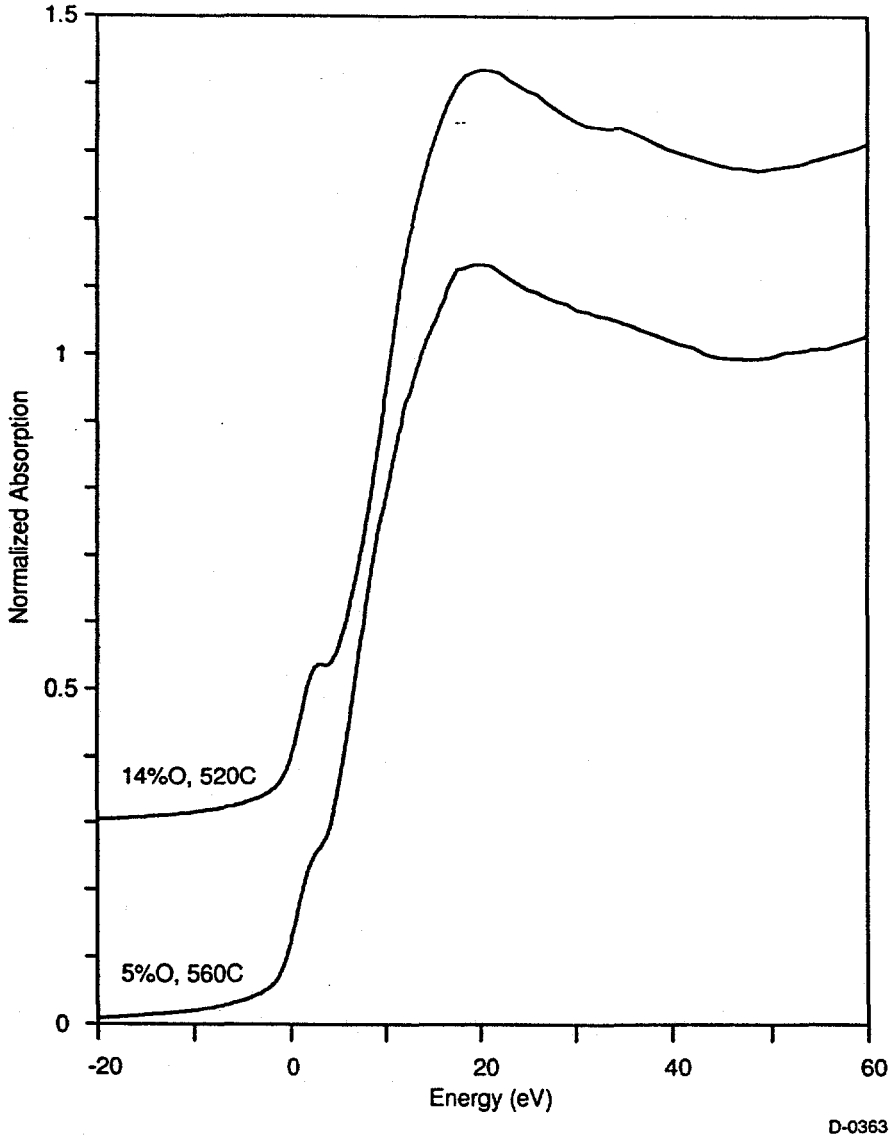

Figure 4-20. Fe K edge *in situ* XANES of deposit of Kentucky No. 9 coal at various furnace temperature settings. 20% oxygen, 6g/min feed rate.

differences in the pre-edge feature. The spectrum is also similar to that of the deposit obtained when pure pyrite was fed to the furnace.

Figure 4-21 is a comparison between XANES spectra obtained for Kentucky No. 9 coal under oxidizing (20% O) and reducing (5% O) operating conditions at 1500 °C furnace set point. Just like pure pyrite feed (Figure 4-19) at lower oxygen partial pressures iron does not completely oxidize but appears to be incorporated in an oxide-sulfide mixture. This phase is quite sticky and easily forms an initial deposit. During this experiment, a substantial amount of this highly viscous slag phase was deposited in the alumina retort and plugged up the ash stream concentrator at the bottom of the furnace. At longer residence times, even under reducing conditions, this slag transformed into a very tenacious deposit and was impossible to remove.

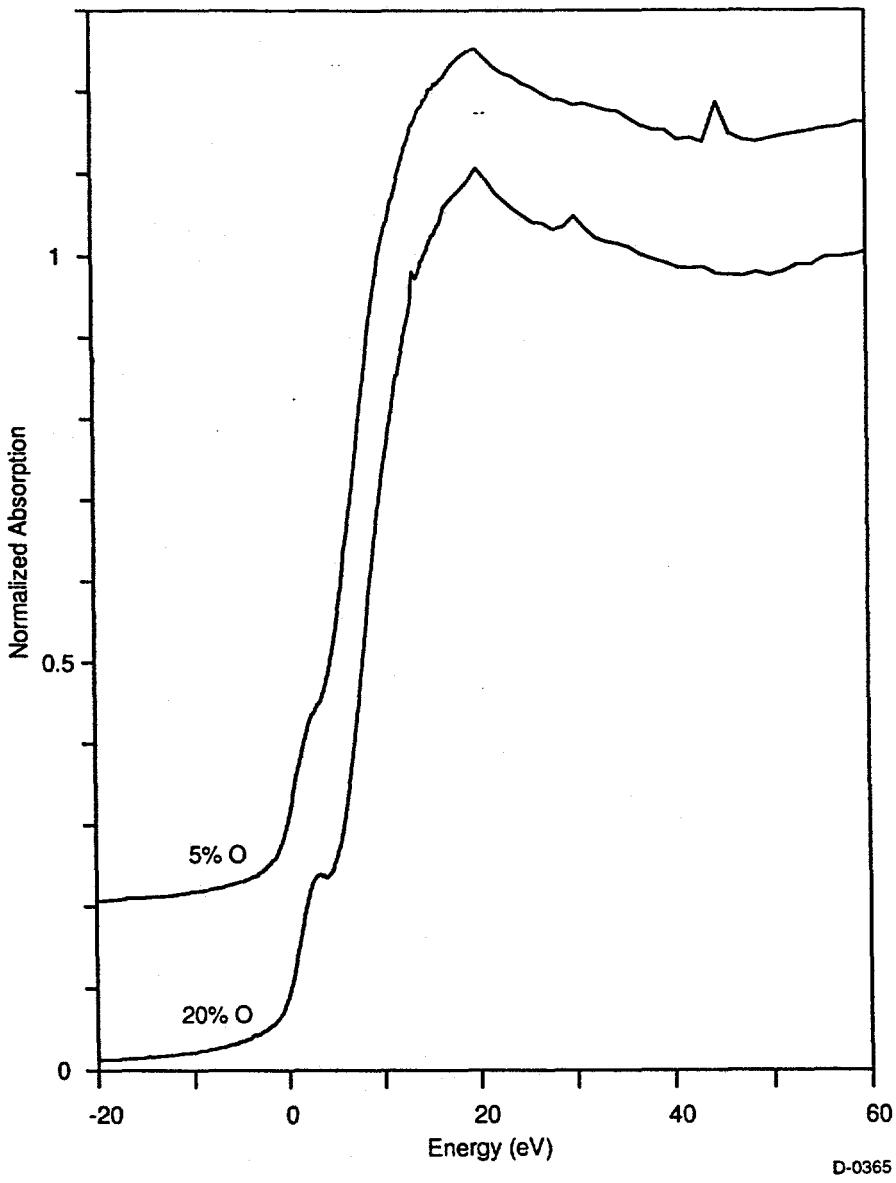

Figure 4-21. Fe K edge *in situ* XANES of deposit of Kentucky No. 9 coal. 6g/min feed rate, 1500°C furnace set point.

In situ combustion test with washed Pittsburgh No. 8

In early March 1994, a preliminary test of the *in situ* XAFS combustor was carried out off-line to replace a broken furnace retort and to perform scheduled maintenance. The entire air transfer line was replaced. The condenser after the 6-way cross developed a water leak and was removed from the exhaust air flow path. The exhaust air was cooled in the ash filters to room temperature and did not pose any problem to the poly-flow tubing. In late March, at the start of our beam-time allotment, we installed a new laser alignment system to align a laser beam coincident to the X-ray beam. The furnace parts were then brought into the X-19A hutch and assembled. Prior to the run, a new "Lytle" type fluorescence x-ray

detector was designed and built at the Univ. of Kentucky. It was installed in the water-cooled port instead of the solid state Ge detector.

Since the washed Pittsburgh No. 8 coal was tested in various tasks of this project, it was selected for testing for *in-situ* XAFS combustion experiments. In order to achieve a uniform feed rate and to facilitate complete combustion, this coal was sieved to <75 μm size fraction and this fine fraction of coal was used for the combustion experiments. Table 4-44 shows the experimental matrix used to observe the effect of variation in the stoichiometric ratios and temperatures on the ash deposit formation. The coal feed rate was maintained at one gram per minute for all experimental conditions. Though the furnace is designed to handle one SCFM gas flow, the flow rate was reduced to increase residence time and to achieve complete combustion. The output oxygen concentration was measured at one of the ports of the six-way cross with an oxygen analyzer mounted on suction pyrometer. The accuracy of the analyzer was reported to be ±1%.

Table 4-44. Experimental matrix for March 1994 *in situ* XAFS experiment.

Stoichiometric Ratio (Calculated)	Total Gas Flow	Preheated Gas Flow		Feeder Gas Flow		Input O_2 Conc. (Calc.)	Output O_2 Conc. (Measured)
	SCFM	Air SCFM	N_2 SCFM	Air SCFM	N_2 SCFM		Error: ±0.01
Furnace Temp. setting - 1300 °C							
2.45	0.75	0.6		0.15		0.21	0.15
0.9	0.5	0.274	0.03		0.2	0.115	0.05
0.7	0.5		0.3	0.2		0.09	0.032
Furnace Temp. setting - 1400 °C							
1.6	0.5	0.3		0.2		0.21	0.125
0.9	0.5	0.274	0.03		0.2	0.115	0.01
0.7	0.5		0.3	0.2		0.09	0.015

In our previous experiments, we had noted that it was difficult to form of a deposit layer on the boron nitride (BN) substrate. Since mullite probes are routinely used for deposition studies in utility furnaces, we decided to use deposition probes made out of 3/8 in. dia. rods of alumina (containing less than 100 ppm iron). As shown in Figure 4-22, Fe K edge XANES of the alumina probe indicated presence of a substantial amount of Fe impurity in the alumina probe material. However, from the absolute signal and the signal/noise ratio values, it was evident that the Fe signal from the deposit on top of the probe overwhelms this signal. Since the Fe K-edge XANES from both the probe and the deposit were quite similar, it is impossible to correct for this signal contamination. Since a blank BN substrate does not give any Fe K-edge signal, we used BN substrates for about half the experiments.

The ionizing gas in the fluorescent ion chamber used as a detector is separated from the furnace with 6 μm thick Mylar film. Slight variations in the furnace pressure causes fluorescence ion chamber pressure to fluctuate, which in turn, gives rise to noise in the signal. These pressure fluctuations were less at lower gas flow rate through the furnace. Coal feed rate fluctuations with each rotation of the auger

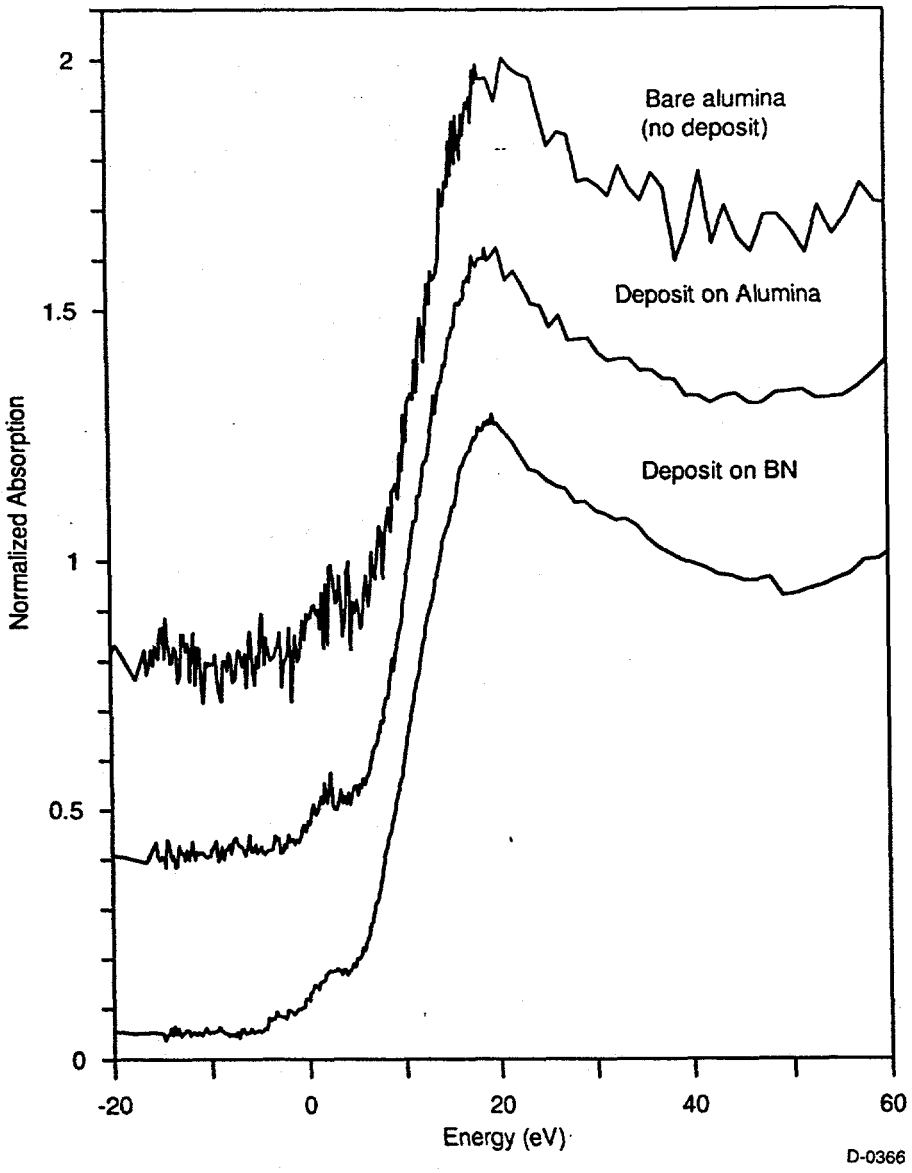

Figure 4-22. Fe K edge XANES of deposits on alumina and BN substrates. Deposits obtained from combustion of Pittsburgh No. 8 coal at 1400°C with stoichiometric ratio of 0.9.

feeder causes micro lumps of coal being injected into the furnace. When these lumps of coal burn, the furnace pressure fluctuates and the XAFS signal is noisier. If we turn the feeder off, the noise is considerably lower than when the feeder is on. To reduce the noise due to feed rate fluctuations, we lowered the feed rate to one g/min from the designed feed rate of four g/min. We also collected several sets of data for a given furnace condition and averaged the XAFS spectra to improve the signal to noise.

Figures 4-23 and 4-24 K-edge XANES of Pittsburgh No. 8 coal deposits obtained for furnace temperature settings of 1300 and 1400°C respectively. The coal feed rate was maintained at one g/min. The XANES spectra for all six of the conditions studied appear similar. The spectra indicate presence of iron oxide and iron in aluminosilicate glassy phase. Under more oxidizing conditions (S.R.=2.5 at 1300 °C and S.R.=1.6 at 1400 °C), there is more complete combustion of mineral matter and the resulting ash has very high viscosity. These high viscosity ash particles have lower sticking efficiency and are swept

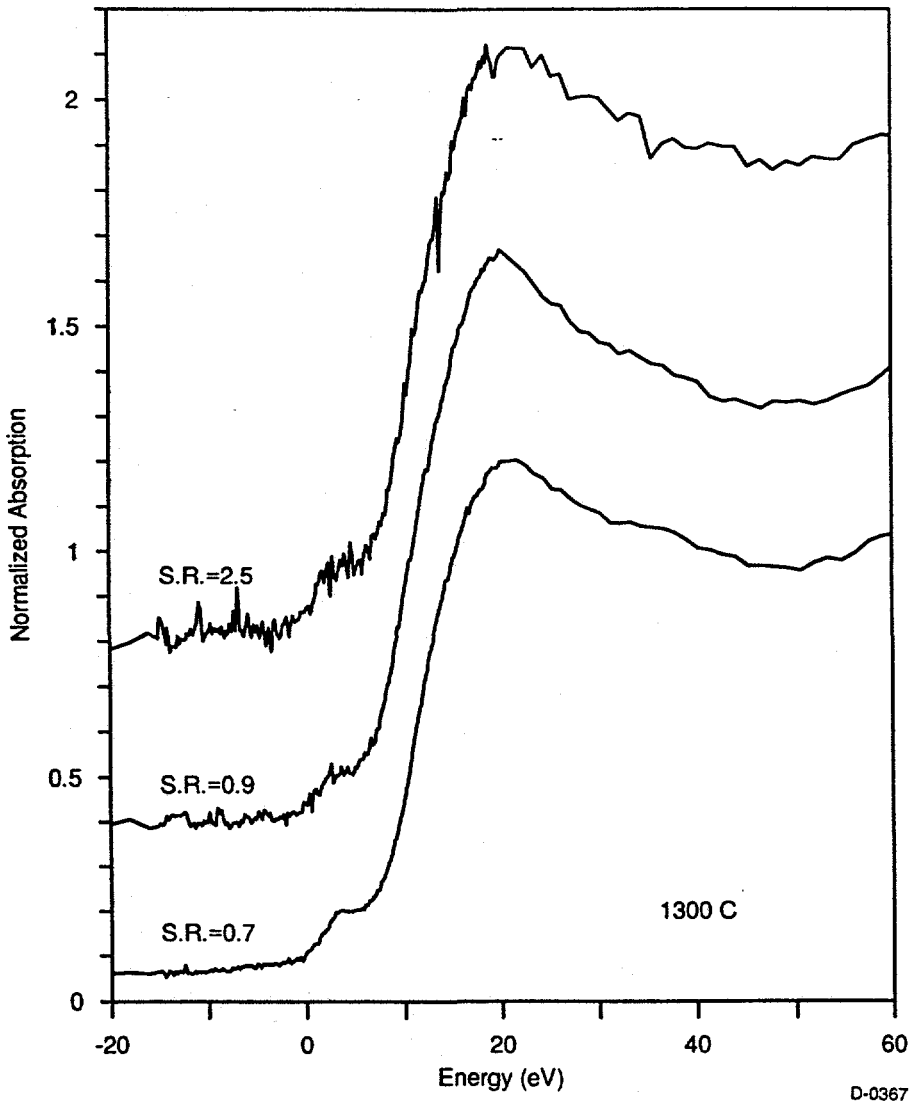

Figure 4-23. Fe K edge XANES of Pittsburgh No. 8 coal deposits obtained at different stoichiometric ratio. 1 g/min coal feed rate at 1300°C furnace setting.

away with the gas stream. Because of the choking of the gas stream in the center of the 6-way cross due to ash deposition probe, the surface gas flow rate on the probe is high and it carries with it any loose ash particles. Thus under these conditions, the effective amount of sample on the deposition probe is reduced and the signal quality deteriorates.

Several times during the experiment, we noticed an increase in the differential furnace pressure drop indicating a blockage to air flow. Usually, this was due to clogging of the Balston filter used as a fine ash trap. Some char from this ash trap was analyzed later for carbon content. Even for the highest stoichiometric ratio (2.45) we noticed substantial (about 50%) carbon content in the ash. This suggests that the combustion is incomplete in all the cases.

We were planning to collect deposits on alumina deposition probes for further analysis with Mössbauer Spectroscopy. However, the ash viscosity was apparaently too high to have enough stickiness

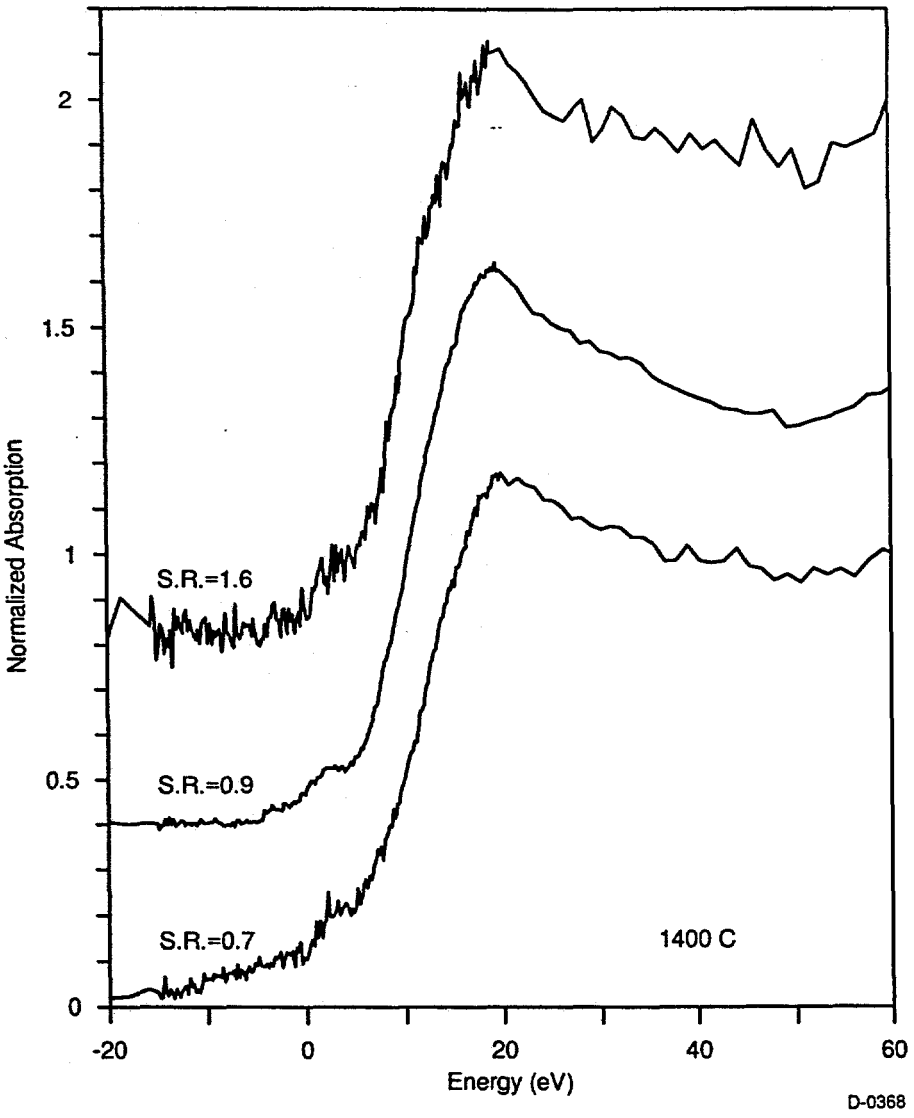

Figure 4-24. Fe K edge XANES of Pittsburgh No. 8 coal deposits obtained at different stoichiometric ratios. 1 g/min coal feed rate at 1400°C furnace setting.

to form a good deposit. We measured the gas temperature at the center of the six-way cross with a suction pyrometer. The gas temperature was between 600 and 700 °C for all the furnace conditions. This temperature is too low to form a good deposit.

Near the end of the run, we switched the coal in the feeder to Black Thunder coal. A helium air-path was created between the incident beam (I_0) ion chamber and the incident beam port of the 6-way cross to reduce X-ray beam attenuation. The monochromator was slewed to Ca K-edge energy and we tried to collect Ca K-edge XANES data on the deposit. We were unable to notice any edge jump in XAFS data. The possible reasons for this can be any one of the following: (1) excessive attenuation in the beam path, (2) low Ca concentration in the deposit, (3) attenuation of the X-ray signal in the detector windows and a thin soot layer on the window.

Combustion test using in situ XAFS furnace at BNL (February 1995)

Early in 1995 a number of experiments were performed off-line with the in-situ XAFS reactor. These experiments, utilizing Pittsburgh No. 8 seam coals, were then repeated in the PSIT entrained flow reactor (EFR). This study was designed to test the operation of the in-situ reactor, and collect data on iron transformations under various conditions. Specifically, the goals of this effort were to:

(1) test and modify the in-situ XAFS reactor for its improved operation in X-19A;
(2) compare operational parameters (eg; carbon burnout) of in-situ reactor with those from PSIT's entrained flow reactor;
(3) conduct experiments for assessment of the sensitivity of iron phase distributions to combustion conditions.

The on-site tests were carried out in DAS Building 815, Room D-2 from January 22, 1995 through January 26, 1995. The PSIT EFR experiments were performed in February, 1995. The ash samples collected at both facilities were analyzed for their carbon content and sent to the University of Kentucky for static XAFS and Mössbauer analysis. Each activity is discussed on more detail in the following sections.

On-site tests with in-situ XAFS reactor

The purposes of the on-site tests were to:

(1) test a low flow rate powder feeder in order to minimize the feed fluctuation;
(2) modify the in-situ reactor to increase the inlet gas temperature; and
(3) perform combustion experiments with Pittsburgh No. 8 coal and collect samples for static XAFS and Mössbauer analysis.

All the objectives were successfully accomplished. Samples collected were later analyzed using Mössbauer and XAFS analysis methods for iron transformation behavior. A brief description of the tests follows.

A low-flow rate powder feeder designed for pharmaceutical industry (Powder Feed Dynamics, Inc., Beechwood, OH, model XV-RD) was rented and tested for future in-situ XAFS experiments. Whereas the operating principle is the same as that of our AccuRate feeder, several additional design features made the feeder acceptable for applications requiring low and steady feed rates. Preliminary tests of the feeder conducted by the vendor using our Pittsburgh No. 8 coal suggested a promising performance.

The feeder was first calibrated with parent Pittsburgh No. 8, washed Pittsburgh No. 8, and size-segregated (<63 um) parent Pittsburgh No. 8 coals. The coal feed rate at a given rpm (revolution per minute) setting of the auger was reproducible. For example, the feed rates of washed Pittsburgh No. 8 coal measured three times at 200 rpm were 1.68, 1.76, and 1.76 g/min. The feeder with the weight and size of about 150 lb and 1.5 ft x 1.5 ft x 2 ft was placed on the floor next to the reactor during the test. The test range was 0.1 to 3 g coal/min. Visual observation of the char and/or flyash stream in the six-way cross strongly indicated a substantial decrease in coal feed fluctuation and a steadier feeder performance than in the case of our AccuRate feeder. Burning coal and glowing hot fly ash stream was recorded on a videotape through one of the 6-way cross ports.

During the test, the heating coil inside the preheater failed. The air preheating system was, therefore, modified. A new 8-ft, 220V, 960W heating tape was first wrapped around the preheater. An

additional 3-ft, 1/2-in. diameter stainless steel tubing wrapped with the same type of heating tape was then connected to the preheater. The gas feed line between the preheater and the diffuser was also wrapped with a heating tape. The diffuser was wrapped with glass wool insulation materials. The gas temperature obtained at the diffuser inlet was around 500°C. Notice that 40% of the total air into the reactor entrains coal and is maintained at room temperature. This room-temperature, coal-laden air is mixed with the preheated air in the diffuser.

A simple energy balance for a mixture of 40% room air and 60% 500°C air results in a temperature of around 300°C. The diffuser temperature, however, was between 300 and 750°C. The diffuser temperature strongly depended on the coal feed rate. At a relatively high coal feed rate, the diffuser temperature reached 750°C indicating that coal particles were burning inside the diffuser and releasing heat.

Combustion experiments for iron transformation were carried out with washed Pittsburgh No. 8 coal. The test matrix was as follows:

Wall temperature = 1400°C	Stoichiometric Ratio = 10
	Stoichiometric Ratio = 2
	Stoichiometric Ratio = 1.2
Wall temperature = 1200°C	Stoichiometric Ratio = 10
	Stoichiometric Ratio = 1.2

The total air flow rate was fixed at 1 scfm (standard cubic foot per minute). The stoichiometric ratio was varied by varying the coal feed rate from 0.3 to 2.7 g/min. For each of the conditions, ash samples were collected from the six-way cross using a 3/8-in. tubing bent at the tip, as well as from the bottom of the reactor. Ash samples from the ash collection system were burned out in a muffle furnace under flowing oxygen to determine the carbon content.

In order to re-evaluate the operability of the reactor for in-situ XAFS in X-19A, the reactor was tested for about 2 h with no interruptions using washed Pittsburgh No. 8 coal. No operational difficulties were experienced. The reactor was then tested at a rather extreme condition. When the feed rate of 4 g/min was maintained for a high-ash-content, parent Pittsburgh No. 8 (ash content = 27%) coal, the ceramic venturi piece before the 6-way cross was partially clogged after 2 hr operation.

Testing of the in-situ XAFS reactor at various conditions suggests that given proper attention to the coal properties, experimental conditions and the reactor system, safe and reliable operations in X-19A for XAFS analysis can be made for an extended period of time.

Combustion experiments with PSIT Entrained Flow Reactor

One of the goals of this test was to compare the iron transformations observed in the in-situ XAFS reactor with those observed in a similar, well characterized, laboratory reactor that has been used in several other DoE sponsored studies. Therefore, the combustion experiments with the washed Pittsburgh No. 8 coal were repeated in the PSIT entrained flow reactor.

In these experiments the coal, washed Pittsburgh No. 8, was fed into the top of the PSIT entrained flow reactor with an AccuRate powder feeder (the pharmaceutical powder feeder was returned to the owner prior to beginning the PSIT experiments). The coal was burned under the same conditions as used

in the in-situ XAFS reactor testing, outlined in the previous section. At each combustion condition ash samples were collected at the exit of the reactor using a nitrogen quenched probe. In addition, to explore the effect of allowing the ash to cool at a slower rate (eg; no quenching) as would be the case in the XAFS reactor, total filter ash samples were also collected at the exit of the reactor. All of the ash samples were burned out under flowing oxygen to determine the carbon content. Samples were also sent to the University of Kentucky for analysis.

Comparison of Carbon Burnout in the In-situ XAFS and PSIT Entrained Flow Reactors

In order to compare the combustion characteristics of the two entrained flow reactors, ash samples from each experiment were burned out under flowing oxygen to determine the amount of residual carbon in the ash. In general the ash from the in-situ XAFS reactor had a higher carbon content than the ash from the corresponding PSIT experiment. Uncooled data from the PSIT experiment suggest that the samples collected in the nitrogen quenched probe may be lower in carbon content than the ash in the reactor. Contamination of the 'uncooled' sample from residual carbon present in the total-filter collection system from prior experiments (with a non-coal fuel), however, may have occurred.

The Effect of Combustion Environment on Iron Transformations in washed Pittsburgh No. 8

Examination of the Mössbauer spectroscopy data (Table 4-45) reveals some differences between the two facilities in the iron phase distribution. All samples generated at PSIT demonstrated higher fractions of iron in the glassy phases than did samples generated under identical conditions at Brookhaven, despite PSIT samples generally having *lower* concentrations of carbon. The combination of better burnout and higher fraction of iron in the glassy phases suggest that the PSIT generated samples had higher particle temperatures. This effect of temperature can also be seen in the temperature data for each stoichiometric ratio. In general the fraction of iron in the glassy phase is lower in the low temperature experiments. This trend is consistent with data in the literature (Bool, 1995) and may be due to the higher coalescence rates between clays and pyrite at high temperatures.

Reasons for the differences in particle temperature between the two facilities, as suggested by the differences in iron-glass partitioning and char burnout, may be due to slight differences in the temperature profile in each reactor. In the in-situ XAFS furnace the maximum gas temperature is approximately 125°C lower than the furnace setpoint (see users manual for facility). In the PSIT entrained flow reactor the maximum temperature is approximately 50°C lower than the furnace setpoint. The high temperature zone of the PSIT reactor is also slightly longer than that of the in-situ XAFS reactor.

For all samples, the Fe^{+3}/Fe^{+2} phase distribution was similar between the facilities with the exception of the lowest temperature, lowest S.R. runs. PSIT data for this 1200°C, SR=1.2 run are consistent with data obtained at other conditions. Both furnaces show similar trends of increasing amounts of ferrous iron in glass and the magnetite/hematite ratios with decreasing stoichiometric ratios.

Figures 4-25 and 4-26 compare Fe K edge XANES data for ash samples produced in PSI and BNL tests at furnace set points of 1400 and 1200°C respectively. XANES and EXAFS data do not show any dramatic changes with changing combustion condtions. However, when we take third derivative of the XANES, then systematic changes are observed. Figure 4-27 shows the Fe K-edge XANES of some standard compounds. It is difficult to assign various phases (as seen by Mössbauer spectroscopy) to the features of the XANES in Figures 4-25 and 4-26 However, as shown in the Figure 4-28, the third derivatives clearly bring out minor differences in the features of the white line of the XANES spectra. Figure 4-29 shows third derivatives of the Fe K-edge XANES of some of the drop tube furnace generated

Table 4-45. Mössbauer Spectroscopy results of ashes from combustion of DOE washed Pittsburgh No. 8 coal. Samples 1 through 5 were obtained with BNL *in situ* XAFS combustor and samples 6 through 12 were obtained with PSIT combustor.

CFFLS/ MK#	Sample	Phases	I.S.	Q.S.	Hfs	%Fe
95-091 2067	No. 1, BNL 1200 °C, SR=1.2, %C=41	Fe^{++}/Glass Fe^{+++}/Glass α-Fe_2O_3 Magnetite Magnetite	0.97 0.34 0.36 0.28 0.65	1.92 0.77 -0.09 -0.01 -0.02	 515 490 458	3 4 56 20 17
95-092 2068	No. 2, BNL 1200 °C, SR=2, %C=21	Fe^{+++}/Glass α-Fe_2O_3 Magnetite Magnetite	0.34 0.36 0.33 0.53	0.95 -0.20 -0.07 -0.02	 515 492 453	9 78 8 5
95-093 2069	No. 3, BNL 1200 °C, SR=10, %C=24	Fe^{+++}/Glass α-Fe_2O_3 Magnetite Magnetite	0.30 0.36 0.59 0.34	0.96 -0.09 0.03 -0.07	 516 456 492	7 74 8 11
95-094 2070	No. 4, BNL 1400 °C, SR=10, %C=25	Fe^{+++}/Glass α-Fe_2O_3 Magnetite Magnetite	0.33 0.36 0.29 0.66	0.96 -0.10 -0.04 -0.01	 515 490 457	10 61 14 15
95-095 2071	No. 5, BNL 1400 °C, SR=1.2, %C=74	Fe^{++}/Glass Fe^{+++}/Glass α-Fe_2O_3 Magnetite Magnetite	1.13 0.32 0.36 0.66 0.25	2.00 0.88 -0.08 0 0	 5e+08 	16 14 31 23 16
95-049 2041	No. 6, PSIT 1200°C, SR=10,%C=2	Fe^{+++}/Glass α-Fe_2O_3 α-Fe_2O_3	0.30 0.36 0.30	0.91 -0.11 -0.08	 515 477	17 64 19
95-048 2042	No. 7, PSIT 1200°C, SR=2, %C=4	Fe^{+++}/Glass α-Fe_2O_3 Magnetite Magnetite	0.31 0.37 0.33 0.56	0.99 -0.11 -0.06 -0.04	 512 490 452	18 48 20 14
95-047 2043	No. 8, PSIT 1200°C, SR=1.2, %C=60	Fe^{++}/Glass Fe^{+++}/Glass α-Fe_2O_3 Magnetite Magnetite	0.98 0.22 0.39 0.26 0.67	1.34 0.49 -0.12 0 0	 515 489 456	33 6 8 20 33

Table 4-45. Mössbauer Spectroscopy results of ashes from combustion of DOE washed Pittsburgh No. 8 coal (cont.)

CFFLS/ MK#	Sample	Phases	I.S.	Q.S.	Hfs	%Fe
95-050 2048	No. 9, PSIT 1400 °C, SR=10, %C=2	Fe^{+++}/Glass α-Fe_2O_3 α-Fe_2O_3	0.32 0.37 0.37	1.16 -0.10 -0.08	 515 494	19 59 22
95-052 2044	No. 10, PSIT 1400 °C, SR=2, %C=3	Fe^{++}/Glass Fe^{+++}/Glass Magnetite Magnetite	0.68 0.39 0.31 0.62	2.33 0.97 0 0	 490 454	6 21 40 33
95-051 2046	No. 11, PSIT 1400 °C, SR=1.2, %C=39	Fe^{++}/Glass Fe^{++}/Glass Magnetite Magnetite Magnetite	0.80 1.03 0.27 0.67 0.77	0.79 1.92 0 0 0	 488 456 307	29 26 13 29 3
95-053 2047	No. 12, PSIT 1400 °C, SR=2, %C=17 unquenched total filter	Fe^{++}/Glass Fe^{+++}/Glass α-Fe_2O_3 Magnetite Magnetite	0.71 0.39 0.37 0.30 0.61	2.34 0.92 -0.08 0 0	 514 492 454	6 17 15 33 29

ash samples. Third derivatives of the XANES of samples exhibiting similar composition (as measured by Mössbauer spectroscopy) are similar. We are developing methodology deconvolute the features of third derivatives of XANES and assign them to the individual forms of Fe present.

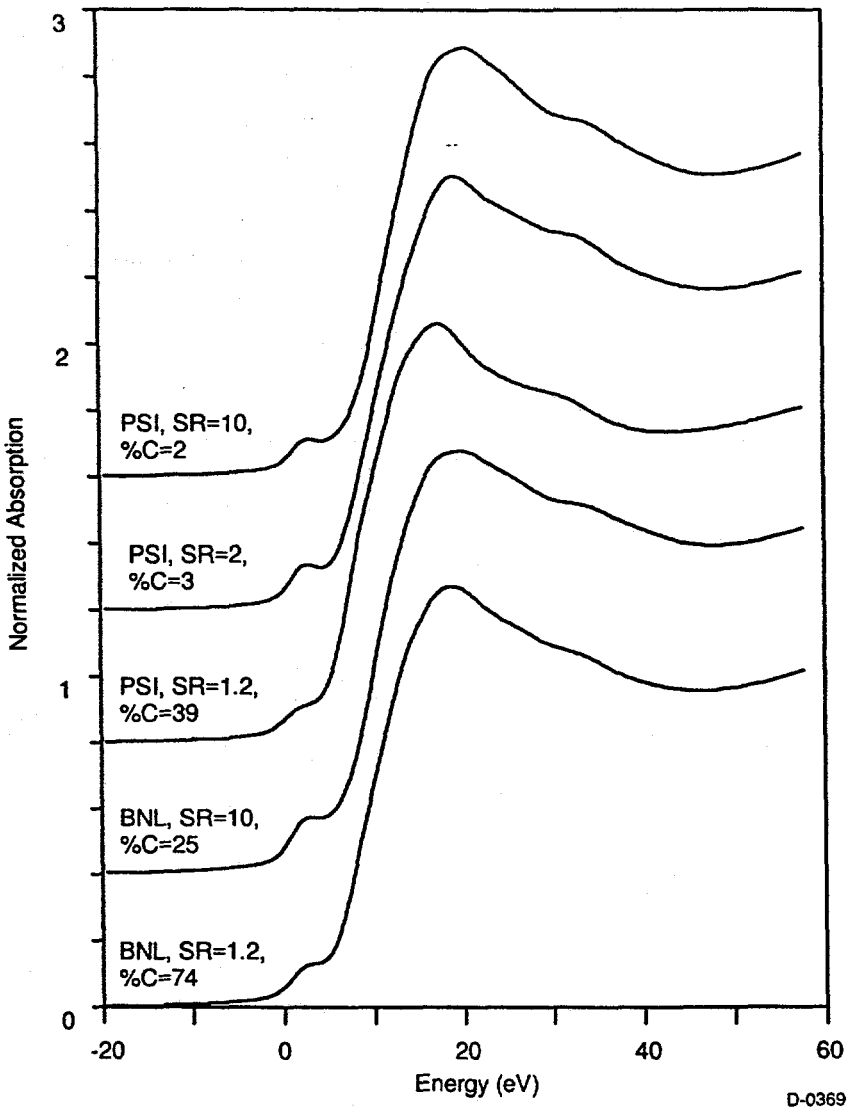

Figure 4-25. Fe K edge XANES of PSI and BNL drop tube furnace generated ash samples for washed Pittsburgh No. 8 coal. Furnace temperature set point = 1400°C.

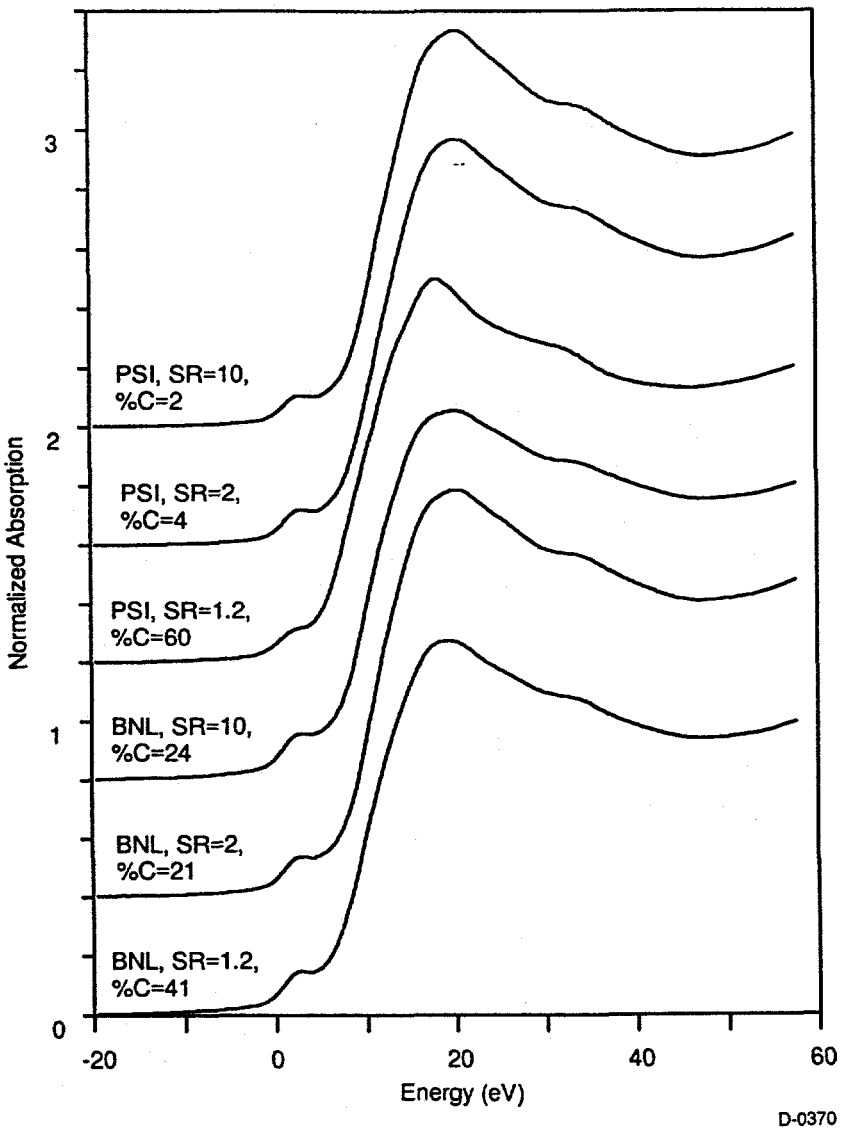

Figure 4-26. Fe K edge XANES of PSI and BNL drop tube furnace generated ash samples for washed Pittsburgh No. 8 coal. Furnace temperature set point = 1200°C.

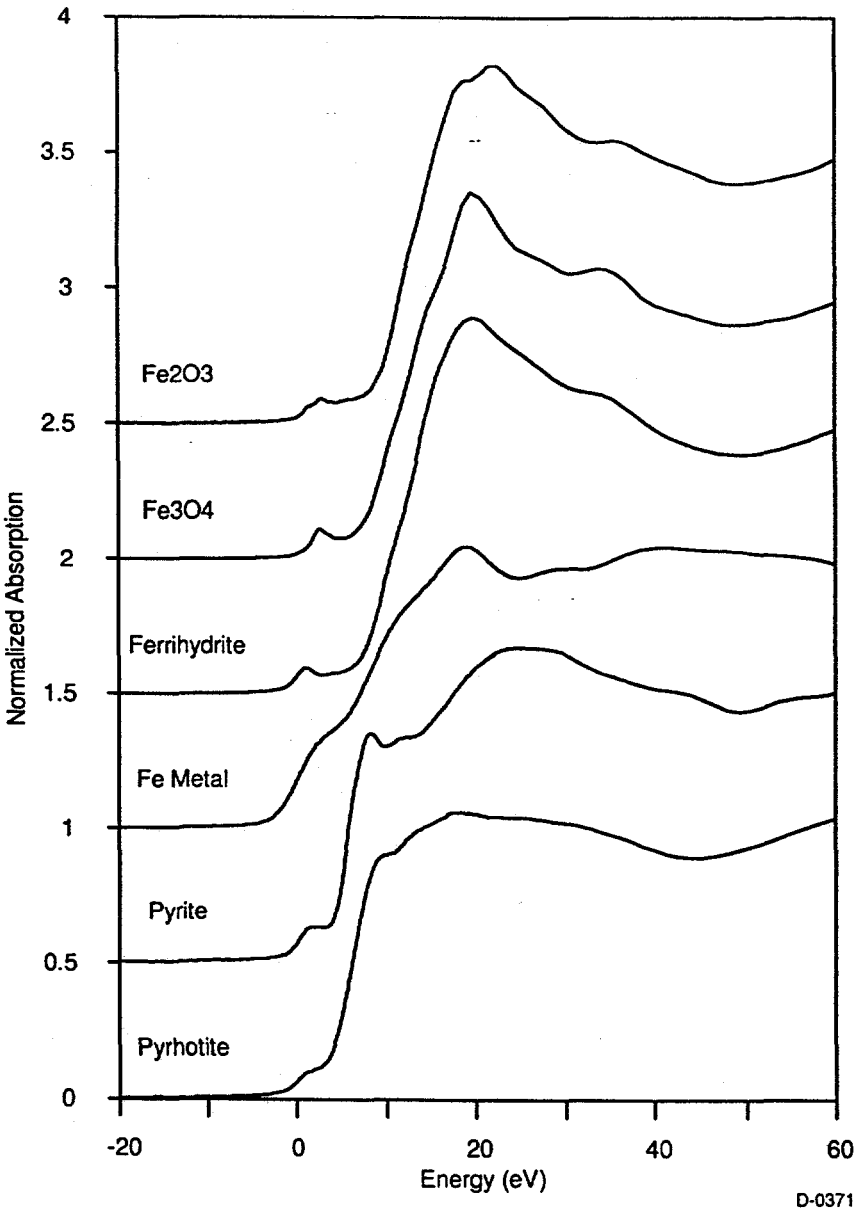

Figure 4-27. Fe K-edge XANES of several standard compounds.

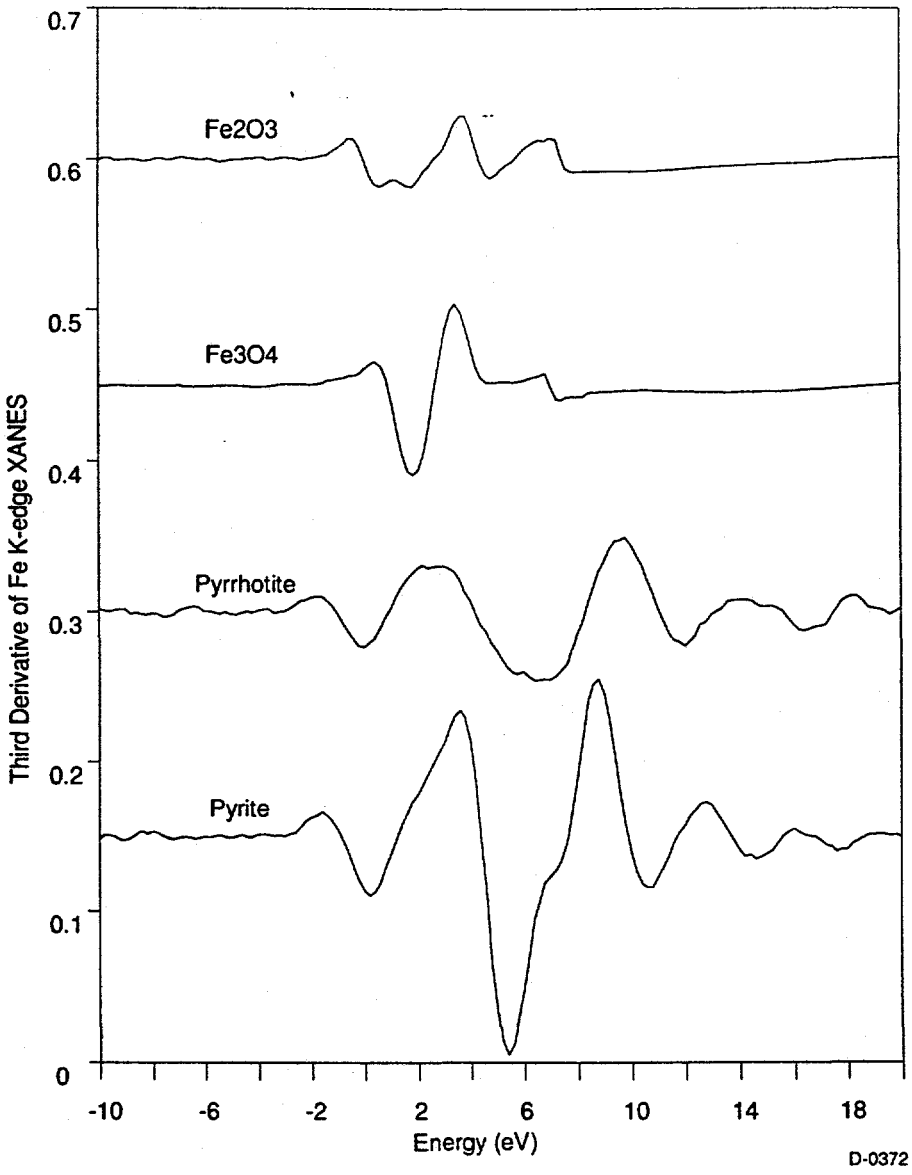

Figure 4-28. Third derivatives of Fe K-edge XANES of several standard compounds.

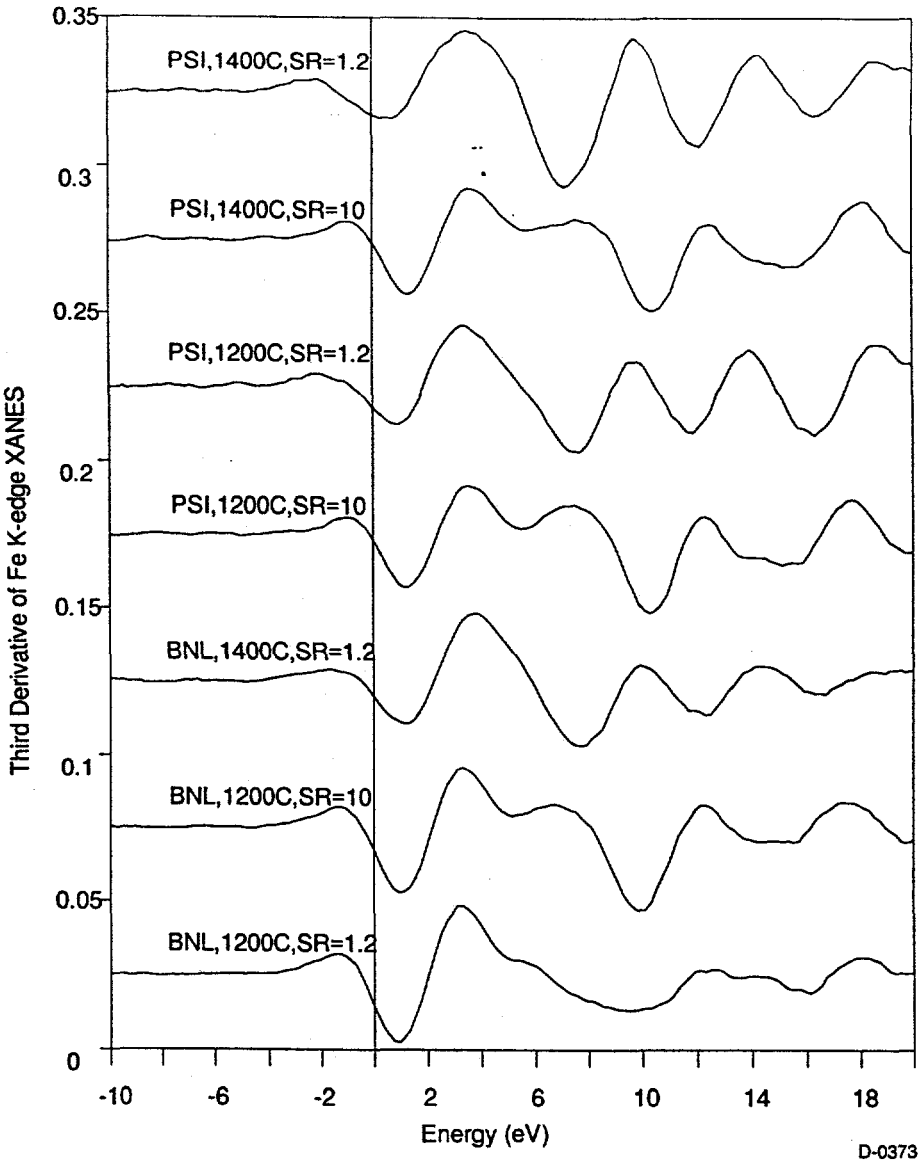

Figure 4-29. Third derivatives of Fe K-edge XANES of drop tube furnace generated ash samples. XANES are shown in Figure 4-25 and 4-26.

4.8 References

1. J.J. Helble et al., Transformations of Inorganic Coal Constituents in combustion systems, Final Report - DOE Contract No.DE-AC22-86PC90751, 1992.

2. F.E. Huggins, D.A. Kosmack, G.P. Huffman, R.J. Lee; Coal Mineralogies by SEM Automatic Image Analysis, *Scanning Electron Microscopy*, SEM Inc., (1980), 531-540.

3. G.P. Huffman, et al., *The Impact of Ash Deposition on Coal Fired Plants*, Proc. of Engr. Found. Conf., Ed:J. Williamson and F. Wigley, (1993), 409-423.

4. N. Shah, G.P. Huffman, F.E. Huggins, A.D. Shah, *Transformations and Ash Deposition during Combustion,* Proc. Engr. Found. Conf., Ed: S.A. Benson, (1992) 179-190.

5. G.P. Huffman, F.E. Huggins, Mössbauer Studies of Coal and Coke: Quantitative Phase Identification and Direct Determination of Pyritic and Iron-Sulfide Sulfur Content, *Fuel*, 57, (1978), 592-604.

6. X-ray Absorption: Principles, Applications, Techniques of EXAFS, SEXAFS and XANES, Ed: D.C. Koningsberger, R. Prins, John Wiley & Sons, (1988).

7. G.P. Huffman, F.E. Huggins, N. Shah, A. Shah, *Prog. In Energy & Comb. Sc.*, 16(4), (1990), 243-251.

SECTION 5

TASK 5.3: FUNDAMENTAL COMBUSTION STUDY OF MINERAL INTERACTION AND ASH VAPORIZATION UNDER REDUCING CONDITIONS

(Massachusetts Institute of Technology)

5. FUNDAMENTAL COMBUSTION STUDY OF MINERAL INTERACTION AND ASH VAPORIZATION UNDER REDUCING CONDITIONS

This task was designed to explore the fundamental mechanisms governing mineral transformations, specifically those of iron-bearing minerals, during the combustion process. This task utilized a drop tube reactor to combust coal particles under very well controlled conditions. Experiments were performed with a beneficiated Pittsburgh No. 8 coal. This coal was selected for additional analysis due to its higher iron content. Extensive experiments were performed to extract information on the transformations of major mineral minerals, with particular emphasis placed on the iron species, over a wide range of oxygen concentrations.

In the experiments, the atmosphere in the furnace was set to a specific value by adjusting the flow rates of oxygen and nitrogen. The coal particles react with oxygen at constant furnace temperature. The product gas loaded with fine ash particles was passed to a cascade Andersen impactor where ash particles were segregated into ten groups ranging from greater than 10 microns to less than 0.43 microns. Inductively Coupled Plasma (ICP) spectroscopy was used to determine the concentrations of aluminum, silicon, calcium, magnesium, iron, sodium and potassium for each sample. Iron speciation was measured using Mössbauer spectroscopy.

For a given coal combustion conditions determine the transformations of minerals. Of the major elements sodium and potassium have the highest potential for vaporization, while aluminum is the least volatile. As the concentration of oxygen in the reactor increases, more elements will vaporize. The effect of oxygen concentration can be explained by the increase in combustion temperature with increasing oxygen concentration. If the combustion temperature is known, the vaporization of the mineral constituents at the temperature and gas concentration in the char particle can be predicted by assuming equilibrium. For ash particles with sizes greater than 1 micron, the particle size distribution can be explained by the coalescence of molten matter at the char surfaces. If the minerals do not melt and coalesce on the char surface, the size distribution of the fly ash will resemble that of the original minerals. The coalescence of mineral inclusions is very complicated, and is still being studied.

The fate of iron is therefore determined by two simultaneous mechanisms: vaporization and coalescence. Furthermore, iron once vaporized will react with vaporized silicon oxide to form iron glass in the boundary layer surrounding the particle. The measurement of significant amounts of magnetite and hematite in the submicron ash particle shows that the vaporized iron will react with oxygen, but that once the submicron particle is formed (by condensation), the reaction rate decreases. For larger ash particles (> 1 micron), iron containing particles will coalesce with other elements to form glass if there is sufficient silicates, or to form magnetite or hematite if there is not enough silicate in the mineral melt.

The effects of oxygen concentrations are to; (1) determine the combustion temperature for a given furnace temperature and coal type, and (2) determine the oxidation of iron compounds. In coal combustion the effect of oxygen concentration is to increase the combustion temperature. Higher temperatures and higher oxygen concentrations in the post flame will favor the formation of Fe (III)/glass and hematite. If the coal combustion temperature is lowered by using a staged coal burner, the iron will tend to form Fe (II)/glass and magnetite.

5.1 Experimental Apparatus and Procedures

5.1.1 Drop-tube Furnace

Combustion experiments were performed on a drop-tube furnace allowing for well-defined combustion. The furnace, shown in Figure 5-1, is composed of three major components: the feeding system, the reaction zone, and the collection system. In the feeding system coal particles were entrained by a carrier gas and uniformly fed into the electrically-heated furnace.

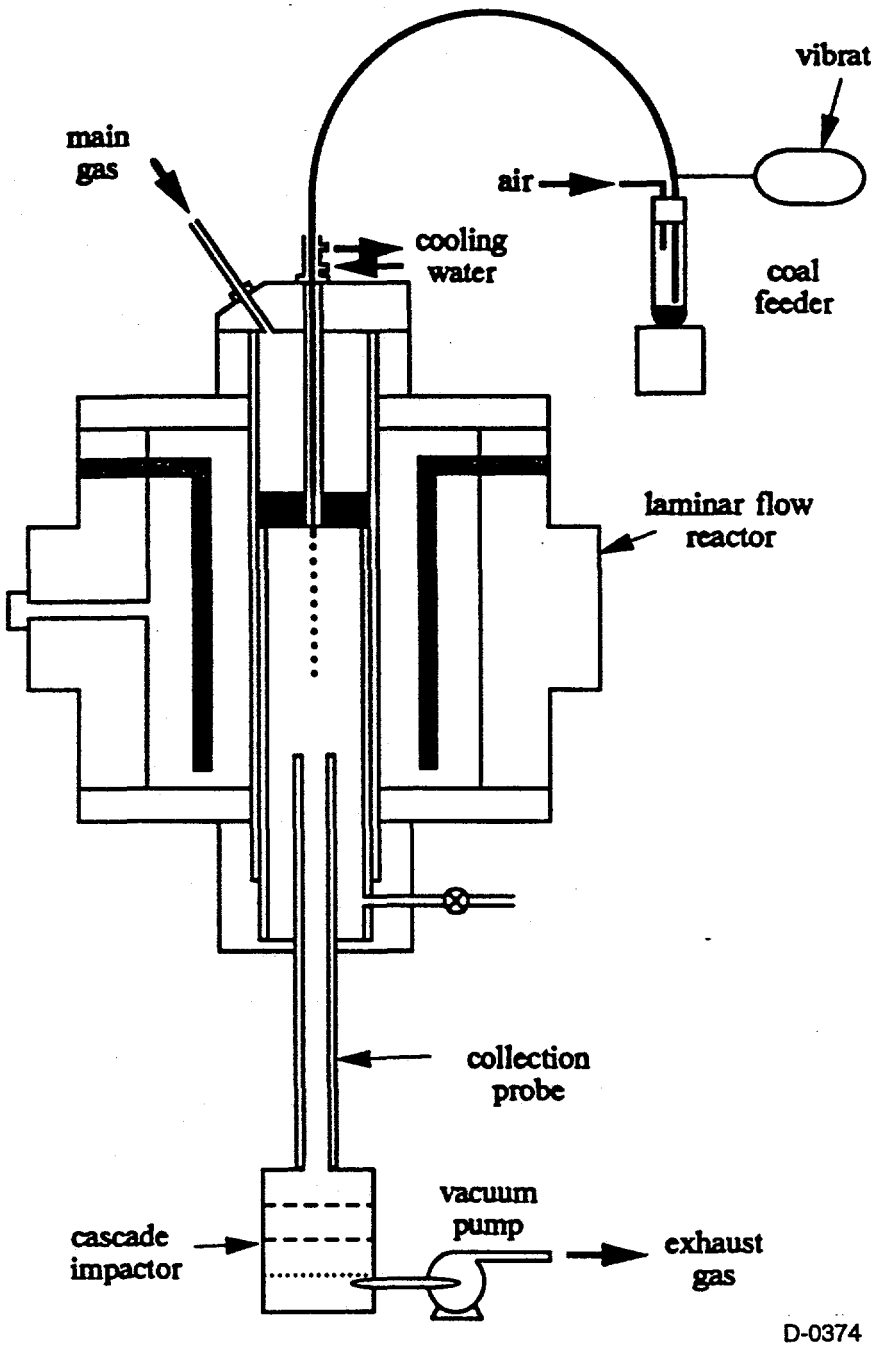

Figure 5-1. Schematic diagram of the MIT drop-tube furnace.

The reaction zone is an alumina tube 430 mm long x 50 mm inner diameter, which is heated by a graphite heater. By adjusting the current, the furnace temperature can easily be adjusted. Although the total length of the heated section was 430 mm, the first 120 mm were used to preheat the main gas stream. The residence time of sample particles in the hot zone can be calculated for different particle sizes and furnace temperatures.

At the exit of the drop tube, the particle laden gas was passed into a copper, water cooled, collection probe. The ash particles were quenched (in the collection probe) by the addition of a quench gas. A cascade impactor was used to collect and segregate the ash particles. The impactor was an on-line particle size analyzer, see Table 5-1 for size ranges, in which a particle laden aerosol jet impinges on the plates and are deposited on the greased aluminum foil substrates. The impactor was MARK II 20-800 non-viable ambient particle sizing sampler by Andersen 2000, Inc., and was combined with an impactor preseparator.

Table 5-1. Size Classification - MIT Cascade Impactor

Stage	pre-separator	1	2	3	4	5	6	7	final	filter
Particle (μm)	>10	9.0-10	5.8-9.0	4.7-5.8	3.3-4.7	2.1-3.3	1.1-2.1	0.65-1.1	0.43-0.65	0.04-0.43

After each run, ten samples of segregated ash particles were obtained. By using ICP, the elemental distribution with particle size was determined. By using Mössbauer spectroscopy, the distribution of iron phases was measured.

5.1.2 ICPES

The instrument used for sample analysis was a Plasma 40 ICP (Inductively Coupled Plasma Emission Spectrometry), manufactured by Perkin-Elmer (Norwalk, Connecticut). The Plasma 40 ICP performs sequential multi-element analyses samples (digested solutions) by atomic emission spectroscopy. Samples are introduced through a capillary tube and nebulized into a fine aerosol which is then injected into an argon-supported inductively coupled plasma. The high temperature of the plasma breaks down the sample and promotes atomic and ionic transitions which are observable at ultraviolet and visible wavelengths. A monochromator then isolates the characteristic wavelength for each desired elements. The emission intensity is then measured to determine the concentration of the element of interest.

5.1.3 Mössbauer Spectroscopy

The Mössbauer technique is a gamma ray technique based on Mössbauer effects of the resonant absorption and emission of gamma rays. Since its discovery in 1958, Mössbauer spectroscopy has found wide applications in element analyses. In coal analysis, Mössbauer spectroscopy is used to measure the relative amounts of iron-bearing minerals in coal such as pyrite, jarosite and iron-bearing clays, and the oxidation products: pyrhotite, magnetite and hematite (Huffman and Huggins, 1978, 1981). Some of Mössbauer analyses in this section of report were carried out in the University of Kentucky, and some were performed in the National Magnet Lab at MIT.

5.2 Calibration for the System and Analytical Tools

5.2.1 Furnace Testing

The furnace was rebuilt for these experiments and the collection probe was replaced by a new design. The furnace was exhaustively tested for leaks, and the new flow meters were calibrated. When the flow rate was low (less than 5ml/min), a bulb method was applied. When the flow rate was high (greater than 6 ml/min), a wet standard test meter was used.

Before running a combustion experiment, the mass closure of ash in the furnace was carefully calibrated. A size fraction of the Black Thunder coal, between 106 and 126 microns, was fed into the furnace at ambient temperatures. The probe, preseparator and cascade impactor described above were used to collect the coal. Several repetitions were performed, typical results were as follows:

The coal fed in: 1.34977g
The coal collected: 1.19185g
To give recovery rate of 1.19185/1.34977 = 88.3%

As mentioned by Graham (1991), a good recovery for this system is near 90%.

The collection efficiency was also measured at combustion conditions using Al_2O_3 power. The results were as follows:

Operation condition: T=1650K, total flow rate=30l/min
Test sample: Al_2O_3 power with diameter $\leq$ 200 μm
Sample fed = 2.554g
Sample captured = 2.1522g
Recovery rate = 2.1522/2.554 = 84.6%

In addition to using Al_2O_3 power as a test sample, the ash in the coal was also used to test the mass balance. For example, using the ASTM procedure, the ash content for the beneficiated Pittsburgh #8 coal was found to be 4.61%. This coal was tested for mass balance under combustion conditions:

Operational condition: T = 1650 K, 100% O_2 (30 l/min)
Sample: 0.063 mm $\leq d_p \leq$ 0.075 mm
Coal fed = 0.6888g
Ash captured = 0.02799g
Collection efficiency = 0.02799/(0.6888*4.61%) = 88.1%

This recovery rate was repeatable.

5.2.2 ICPES

ICPES (Inductively Coupled Plasma Emission Spectroscopy) can measure elements with concentrations at the ppm level. The elements to be analyzed by ICPES were K, Na, Ca, Mg, Fe, Al, Ti, and Si. The operating conditions and wavelength of ICPES analysis are listed in Table 5-2.

Table 5-2. ICPES Operating Conditions and Wavelength

Argon flow rate (l/min): 2.4 to 3.5							
Wavelength (nm)							
Al	Fe	Ca	Mg	K	Na	Ti	Si
396.125	238.204	393.366	279.533	766.49	589.592	334.941	251.611

First, we calibrated the ICPES with multielement standard solutions which were prepared by using the standard atomic emission reference solutions. The calibrated results are summarized in Table 5-3. Calibration repeat showed less than 0.1% deviation. To use ICPES, the samples to be analyzed were dissolved by using an HF solution with water added to generate a solution with concentration measurable by the ICP.

Table 5-3. Calibration of ICPES

Fe	AV	599.5	SD	4.9	CV	0.8
Si	AV	3179.0	SD	202.2	CV	6.4
Mg	AV	1313.0	SD	4.2	CV	0.3
Ti	AV	1207.5	SD	10.6	CV	0.9
Ca	AV	3341.0	SD	17.0	CV	0.5
Al	AV	872.0	SD	2.8	CV	0.3
Na	AV	7199.5	SD	87.0	CV	1.2
K	AV	2170.0	SD	11.3	CV	0.5
Fe	CC	1.0000	SLOPE	1988.8077	INT	675.5377
Si	CC	0.9997	SLOPE	681.7288	INT	3464.5195
Mg	CC	1.0000	SLOPE	96250.265	INT	1257.4453
Ti	CC	1.0000	SLOPE	8605.7695	INT	1160.1920
Ca	CC	1.0000	SLOPE	81573.132	INT	2889.4453
Al	CC	1.0000	SLOPE	373.3192	INT	864.8459
Na	CC	0.9978	SLOPE	83576.789	INT	8469.6416
K	CC	0.9993	SLOPE	80.1154	INT	2167.4038

Where AV = average intensity of signals
SD = standard deviation
CV = coefficient of variation
CC = correlation coefficient
SLOPE = slope of the correlation line
INT = intercept of the correlation line

5.2.3 Mössbauer Spectroscopy

In addition to analyzing some iron-bearing minerals at the University of Kentucky, analyses were carried out by using Mössbauer Spectroscopy in the National Magnet Laboratory at MIT because of the proximity of the facility. The use of MIT facility to analyze the iron-bearing coal particle or ash particle was facilitated by using the samples which were analyzed by the University of Kentucky for comparison. Figure 5-2 and Figure 5-3 are the calibration results, which are in good agreement with the results by the University of Kentucky.

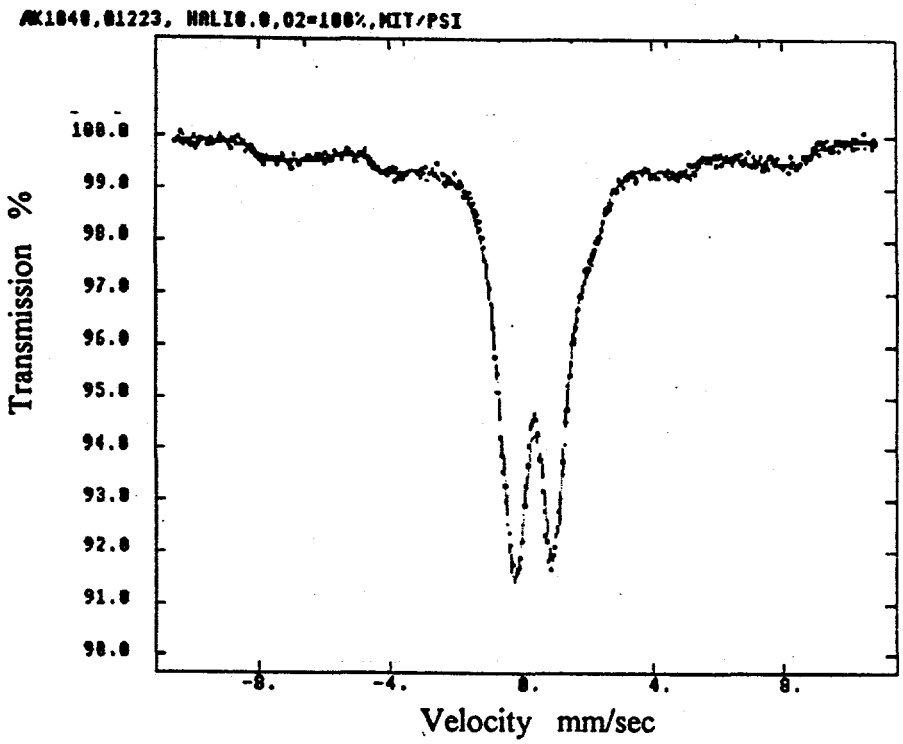

U. of K. results (%)

Fe++/glass	8
Fe+++/glass	75
α-Fe_2O_3	4
Fe_3O_4+Fe_2O_3	13

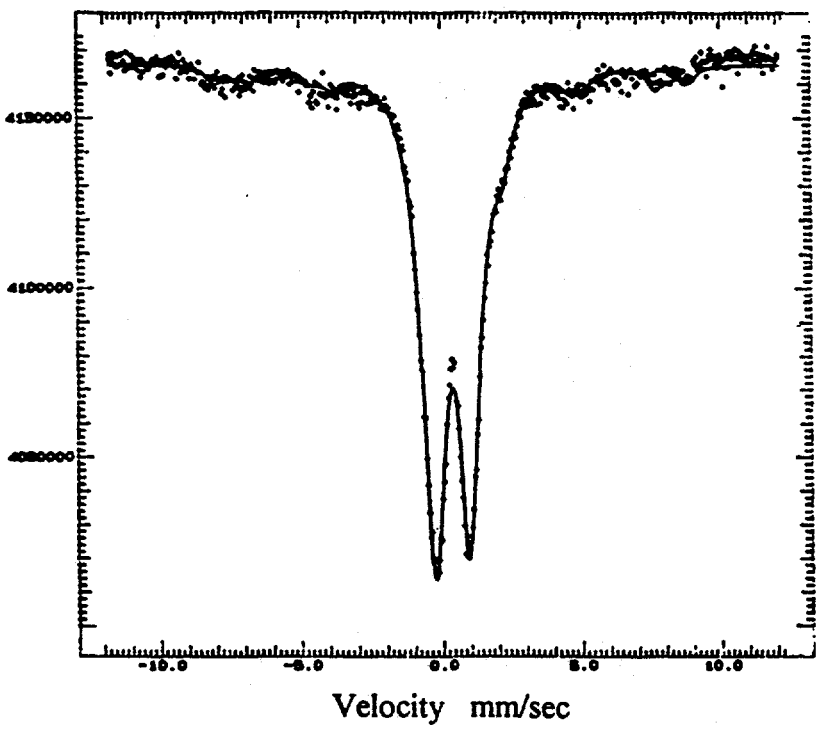

MIT results (%)

Fe++/glass	9.9
Fe+++/glass	79.1
α-Fe_2O_3	3.8
Fe_3O_4+γ-Fe_2O_3	7.2

D-0375

Figure 5-2. Calibration of Mössbauer at MIT

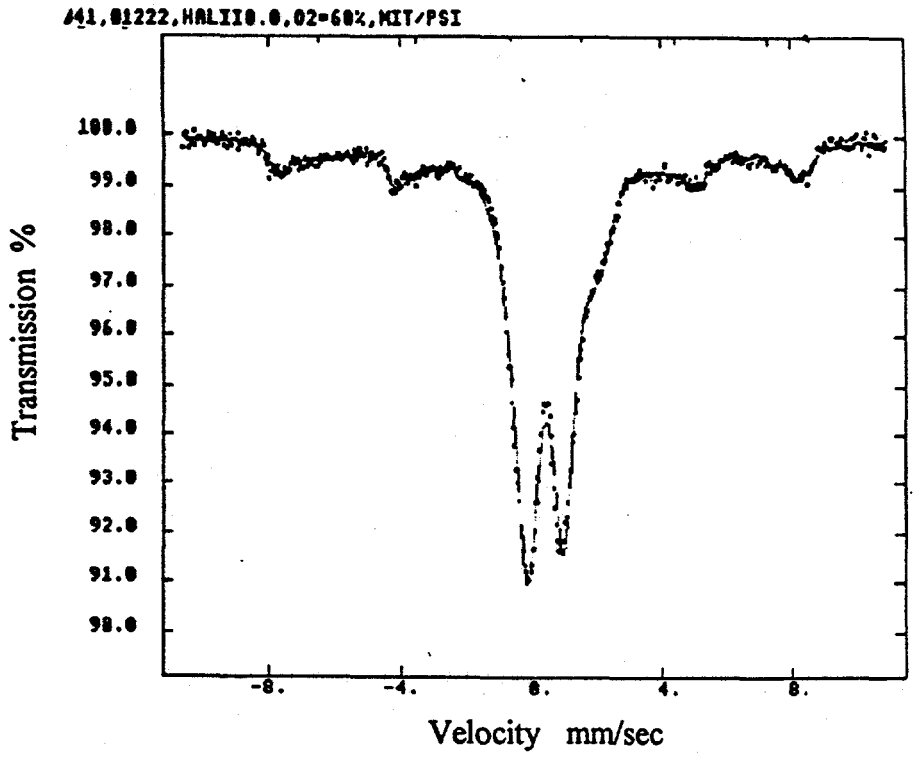

U. of K. results (%)

Fe++/glass	11
Fe+++/glass	66
α-Fe_2O_3	9
Fe_3O_4+Fe_2O_3	14

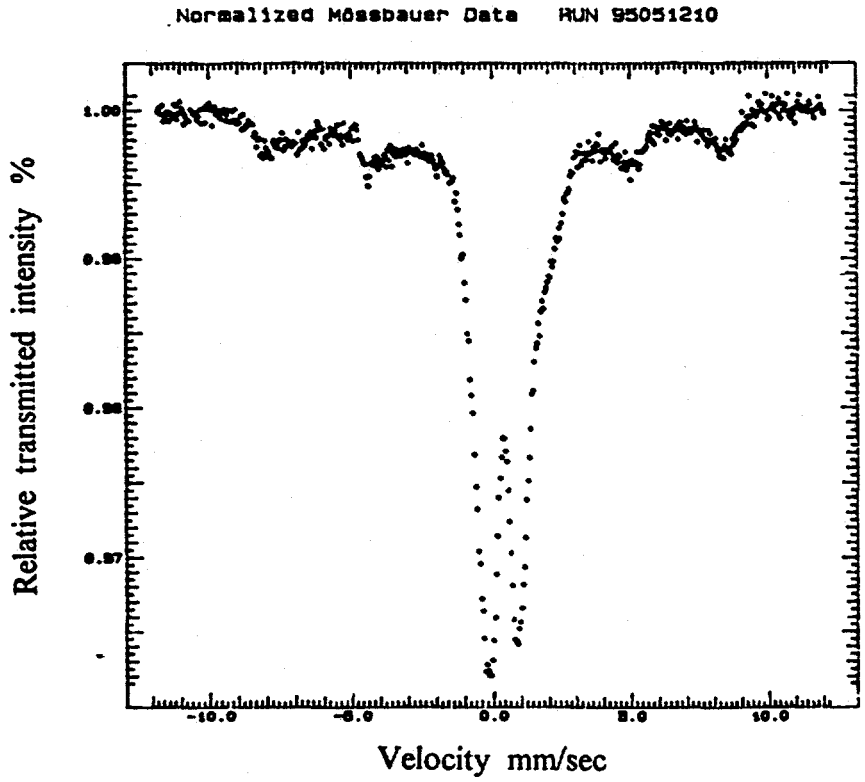

MIT results (%)

Fe++/glass	10.4
Fe+++/glass	67.7
α-Fe_2O_3	9.8
Fe_3O_4+Fe_2O_3	12.1

D-0376

Figure 5-3. Calibration of Mössbauer at MIT with sample # 1222.

5.3 Experimental Results and Discussion

The experimental results can be classified into three classes: the photomicrographs of the samples obtained in the furnace; the distributions of mineral elements by ICP; the distributions of different iron states by Mössbauer spectroscopy. The experiments performed in this study were carefully designed to reveal the transformation of minerals, especially the iron-bearing minerals.

5.3.1 Ash Morphology

SEM

Figure 5-4 is an ash SEM (Scanning Electron Microscopy) micrograph from previous researchers (Quann and Sarofim, 1986). The white spheres are ash particles, while those with irregular shape and darker color are char. As we know, there are two limiting models to describe coal combustion. These include: the shrinking char particle oxidation model with a constant density (representative of a lignite char), and the model for combustion at constant diameter and decreasing density (representative of bituminous char). Correspondingly, for the first model, ash will come to the char surface and form a separate particle as char burns out. This mode yields particles similar to Figure 5-4. For the latter model mineral inclusions will remain at the original positions and form a shell around the char particle. Those two models determine the char combustion rate and the transformation of minerals. When calculations are made to predict the combustion rates and mineral transformation, identifying the combustion mode is the first step.

Optical microscopy picture for ash particles

Figure 5-5 are the color pictures for ash particles with different size. The pictures were obtained using an optical microscope. The microscope is a WILD M8 Stereomicroscope with WILD MPS 55/51 photoautomat. The microscope can display a stereo-picture of the sample. The ash particles in Figure 5-5 were obtained under: 100 O_2 , $T_{furnace}$ = 1650K, reaction time ≈ 0.2 seconds (calculated and shown later). The colors of the particles change from the black of the biggest particles (> 10 μm) to the red of the smallest particle (<0.43 μm). The red color suggests that the particles may contain Fe (III). The black color suggests that the particles have a lot of unburnt char.

5.3.2 Distributions of Mineral Elements with ICP

The following results are for the beneficiated No. 8 Pittsburgh coal. The operating conditions were as follows:

Coal: beneficiated Pittsburgh #8
Residence time: 0.9 s
Coal feeding rate: 0.08 g/min
O_2 concentration in the main gas: 0 to 100%
Particle size distribution (shown in Figure 5-19): nominal 63/75 μm
Furnace wall temperature: 1650 K
Main gas: 6 l/min

The samples were dissolved in HF solution in order to be analyzed by the ICP. Since HF solution can only dissolve inorganic materials, carbon was removed from the char/ash samples collected by the cascade impactor. Here carbon was removed by the standard ASTM procedure: (ASTM standard number D3174 [1984]).

Figure 5-4. SEM picture for ash particle.

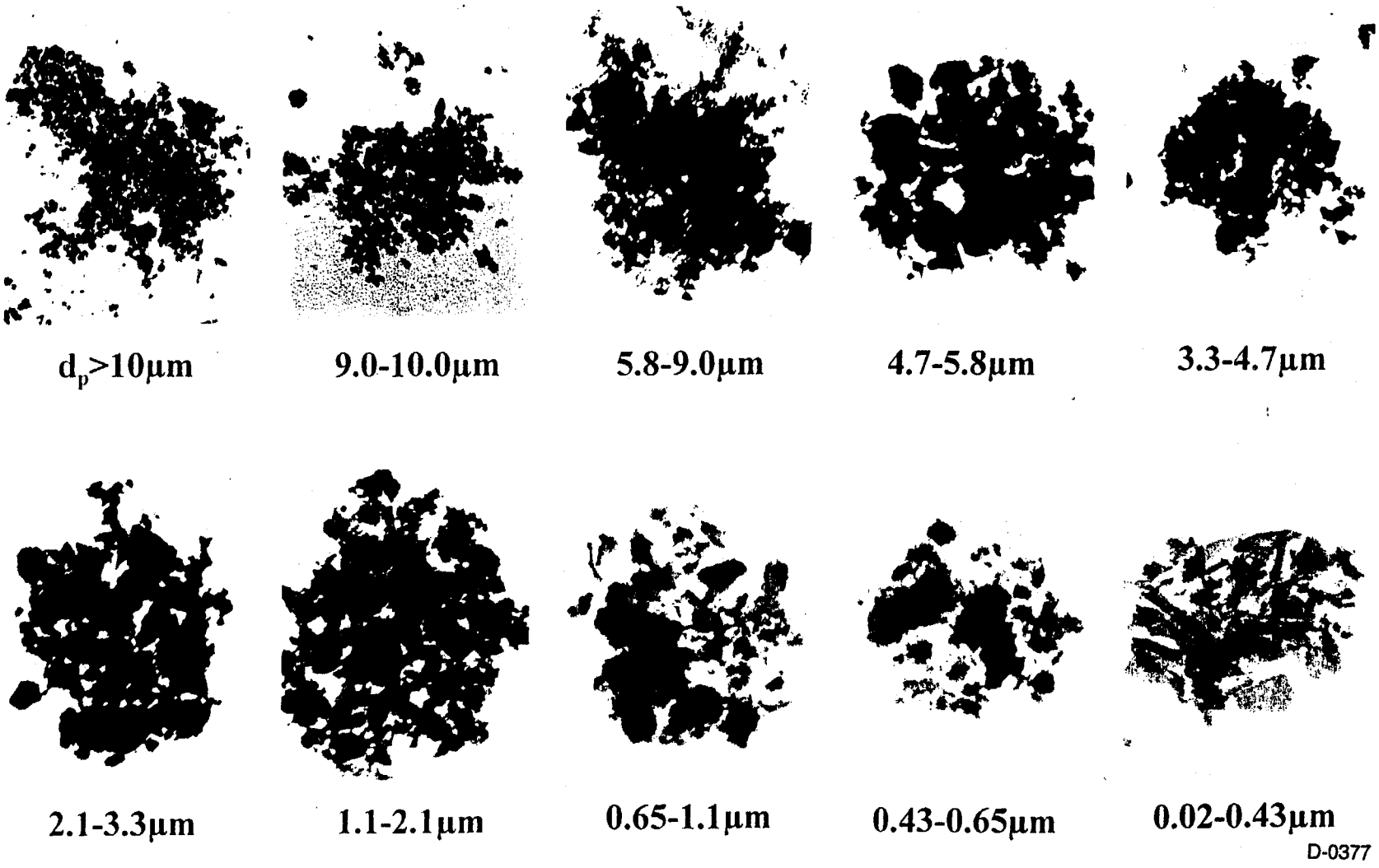

Figure 5-5. Microscopy picture for ash particles with different size.

Distribution of Coal and Char

A sieve was used to remove the parent coal particles with size greater than 75 μm. The coal particle size distribution (psd) is shown in Figure 5-6. The psd of the devolatilized char ($T_{furnace}$ = 1650 K) is also shown in Figure 5-6. It can be seen that the size of the devolatilized char particle is less than that of the parent coal - indicating that the coal particles shrink during devolatilization. Further, the devolatilized material forms very small soot particles.

Ash Distribution with 0% O_2

Figure 5-7 shows the ash particle size distribution for coal devolatilized under pure nitrogen. As seen in this figure most of the minerals remain in the largest size fraction (stage 1). Very little ash was found on stages 6 through the after filter, suggesting that little or no mineral vaporization occurred during devolatilization. This result is consistent with prior work that demonstrated that inorganic species do not begin to vaporize appreciably until the temperature exceeds 1650 K.

Ash Distribution with 60% O_2

The ash psd generated by combustion at 1650 K and 60% O_2 is shown in Figure 5-7. This ash psd suggests that a significant fraction of the ash remains in the largest size cuts (the preseparator through Stage 4). This is likely due to the fact that there was significant unburned carbon in these experiments. Therefore the minerals associated with the unburned char will the captured in the largest size fractions. This figure also demonstrates the onset of inorganics vaporization as evidenced by the ash present in the smallest size cuts.

Ash Distribution with 100% O_2

The trend noted above continued with the ash from the 100% O_2 (Figure 5-8). In this case, about one-third of the ash collected is found on stage 10 (filter holder). According to Wibberly and Wall (1986) and Wall (1992), particles with size between 0.02 μm and 0.2 μm are formed by heterogeneous/homogeneous nucleation and subsequent coalescence of vaporized inorganic species. The samples on the after filter should therefore be oxidized ash only. The fact that so much ash was vaporized is due to the high combustion temperature at 100% O_2.

Ash Mass Percentage in Char Particles

Figure 5-9a to c show the ash mass percentage distribution (ie: the fraction of ash in each particle). These plots indicate that the ash contains significant unburned char and that the carbon content in the particles decreases as the concentration of O_2 in the main gas increases. Figure 5-9c shows that the ash mass percentages on each stage are nearly identical (9 to 12%). This indicates that the ash distribution of the parent coal is uniform and is independent of coal particle size.

Iron Percentage in Char

Figure 5-10 shows the percentage of iron on each stage (including unburned char). The smallest size cut, the final filter, is very iron rich. This stage also contains little or no carbon. The high concentration of iron in the fume suggests that this element is more likely to vaporize under these conditions than other mineral species. It is also interesting to note that the iron percentage on the final filter (100 % O_2) is identical to that on the final stage (60 % O_2) and stage 7 (30% O_2). This trend suggests that the

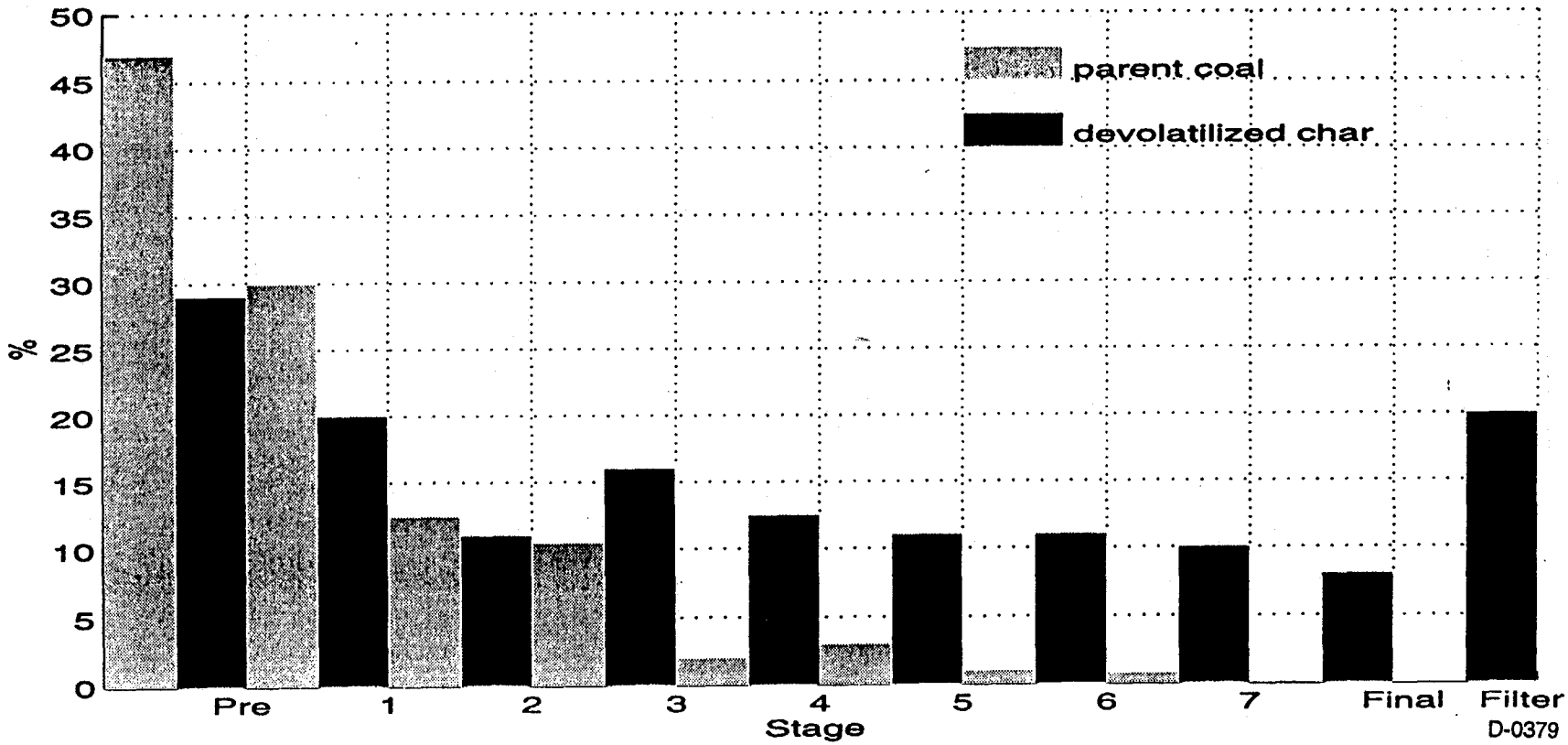

Figure 5-6. Mass distribution of coal used in experiments.

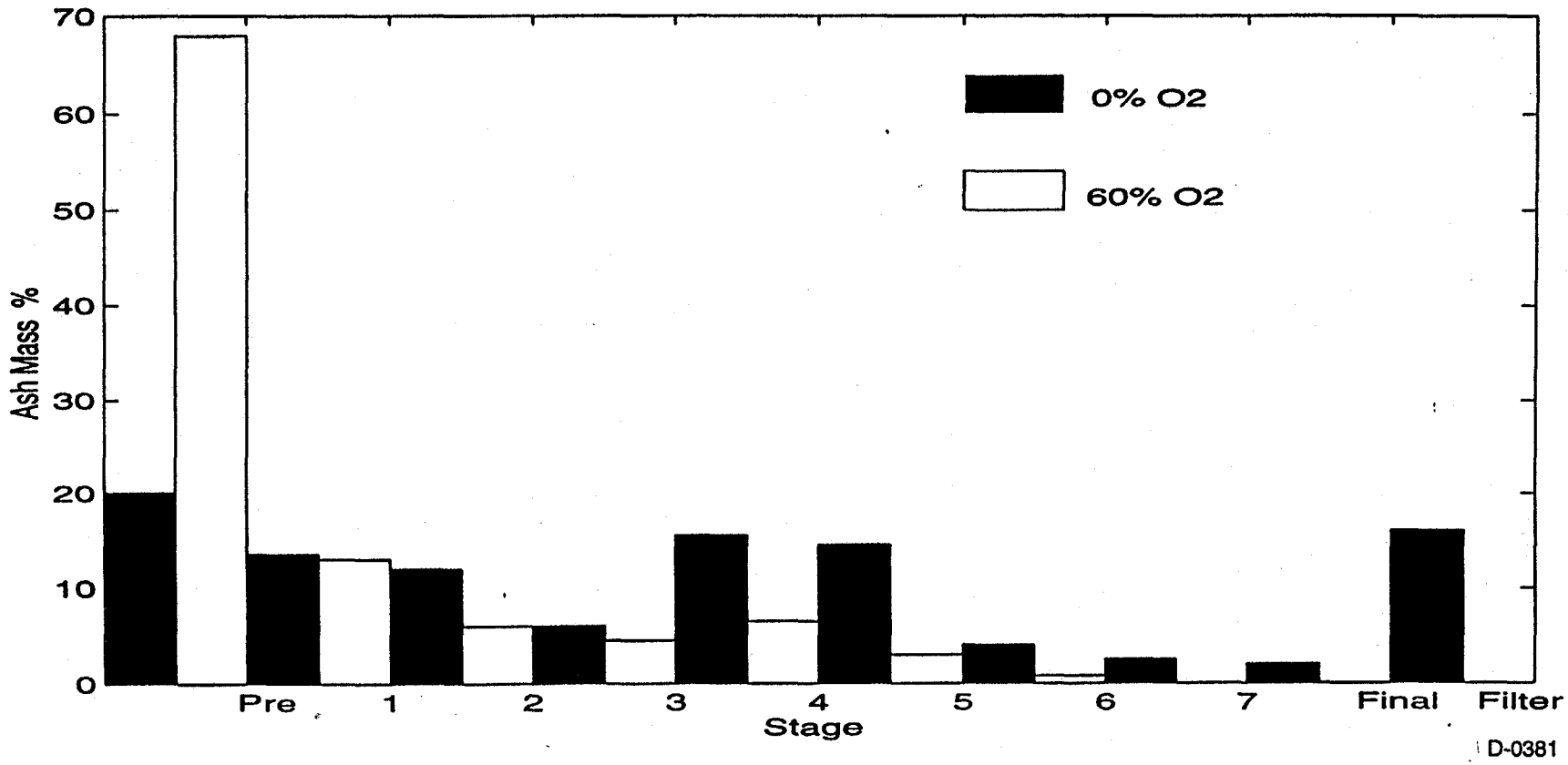

Figure 5-7. Ash distribution at 0% O_2 and 60% O_2.

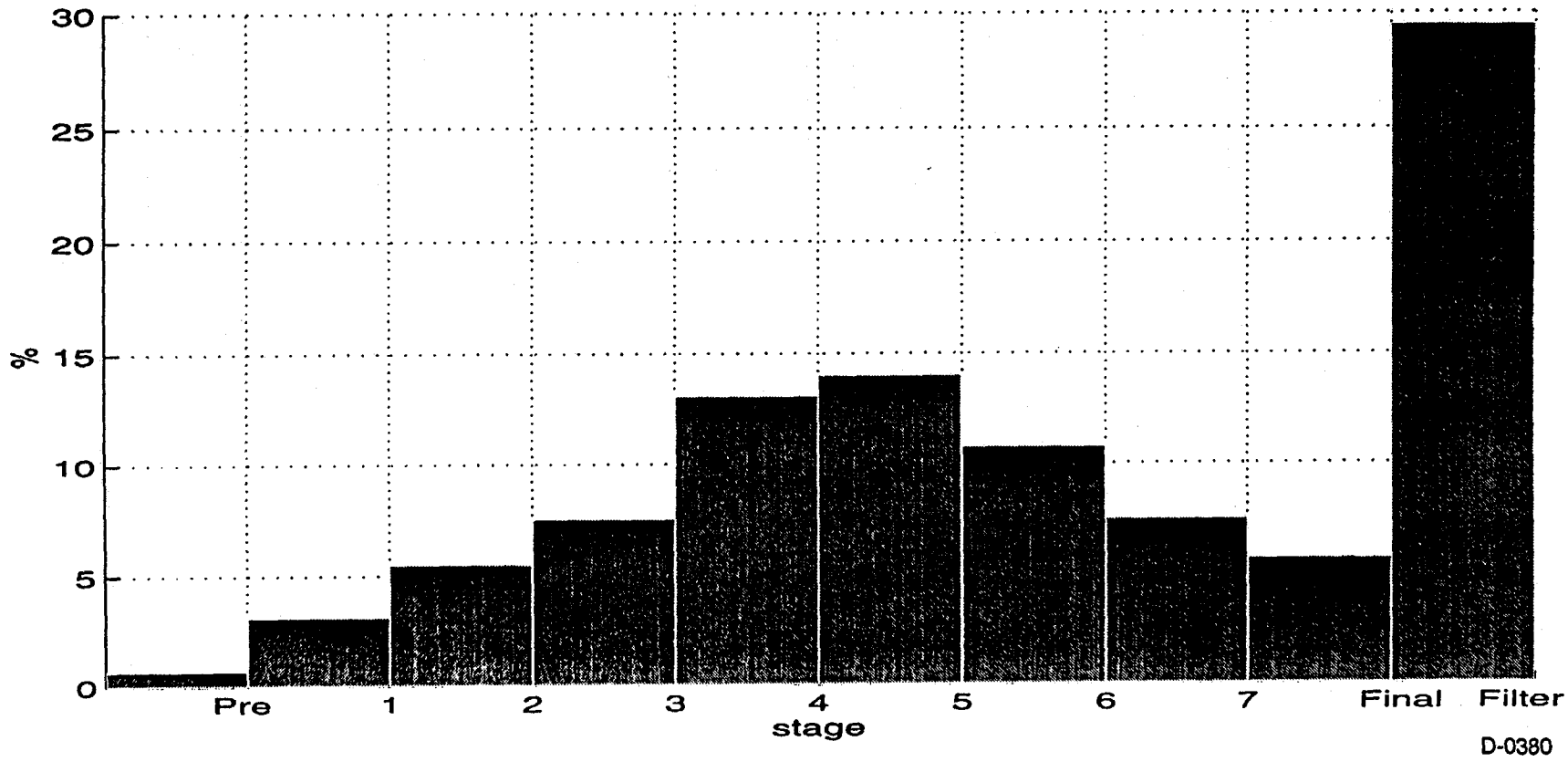

Figure 5-8. Ash distribution at 100% O_2.

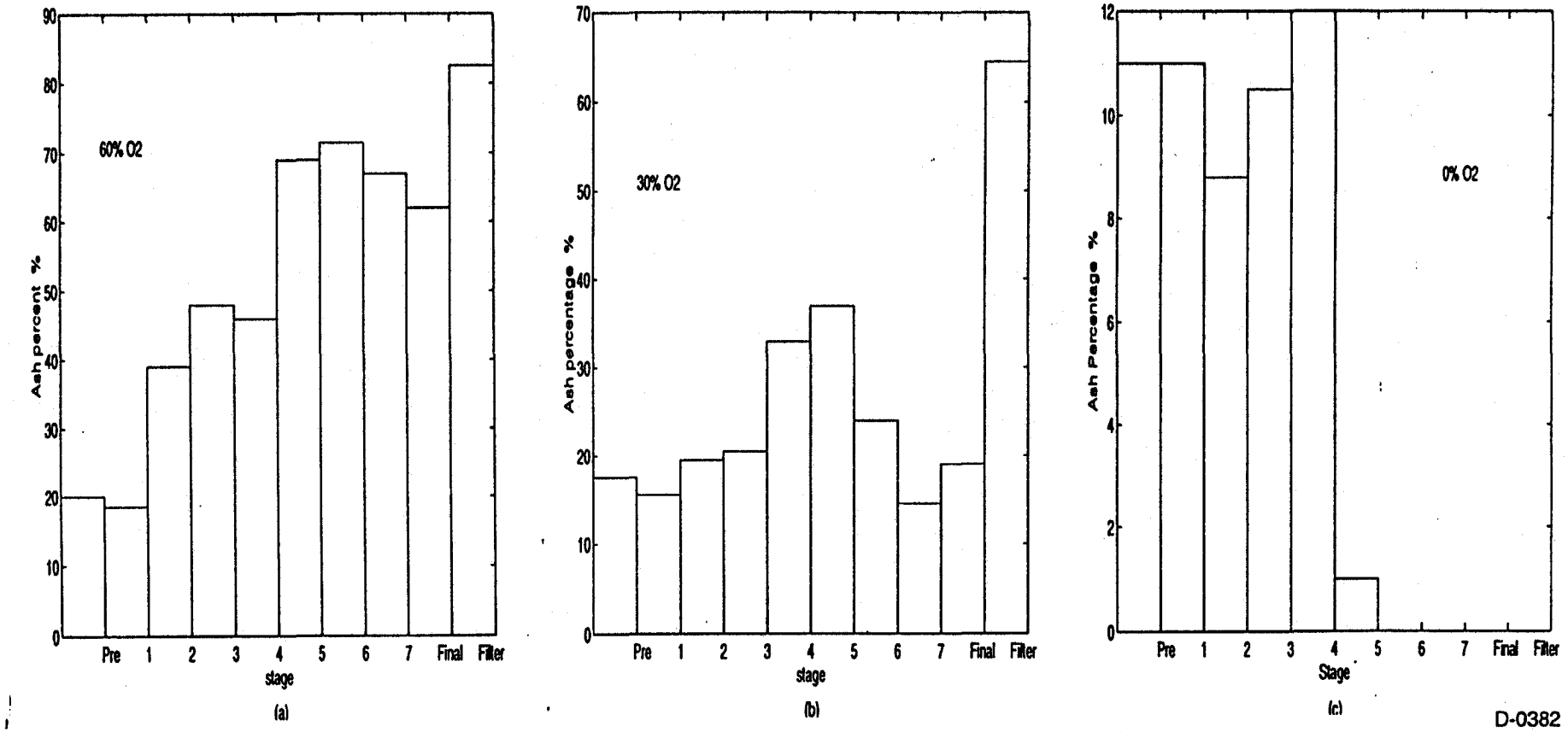

Figure 5-9. Ash mass percentage in char.

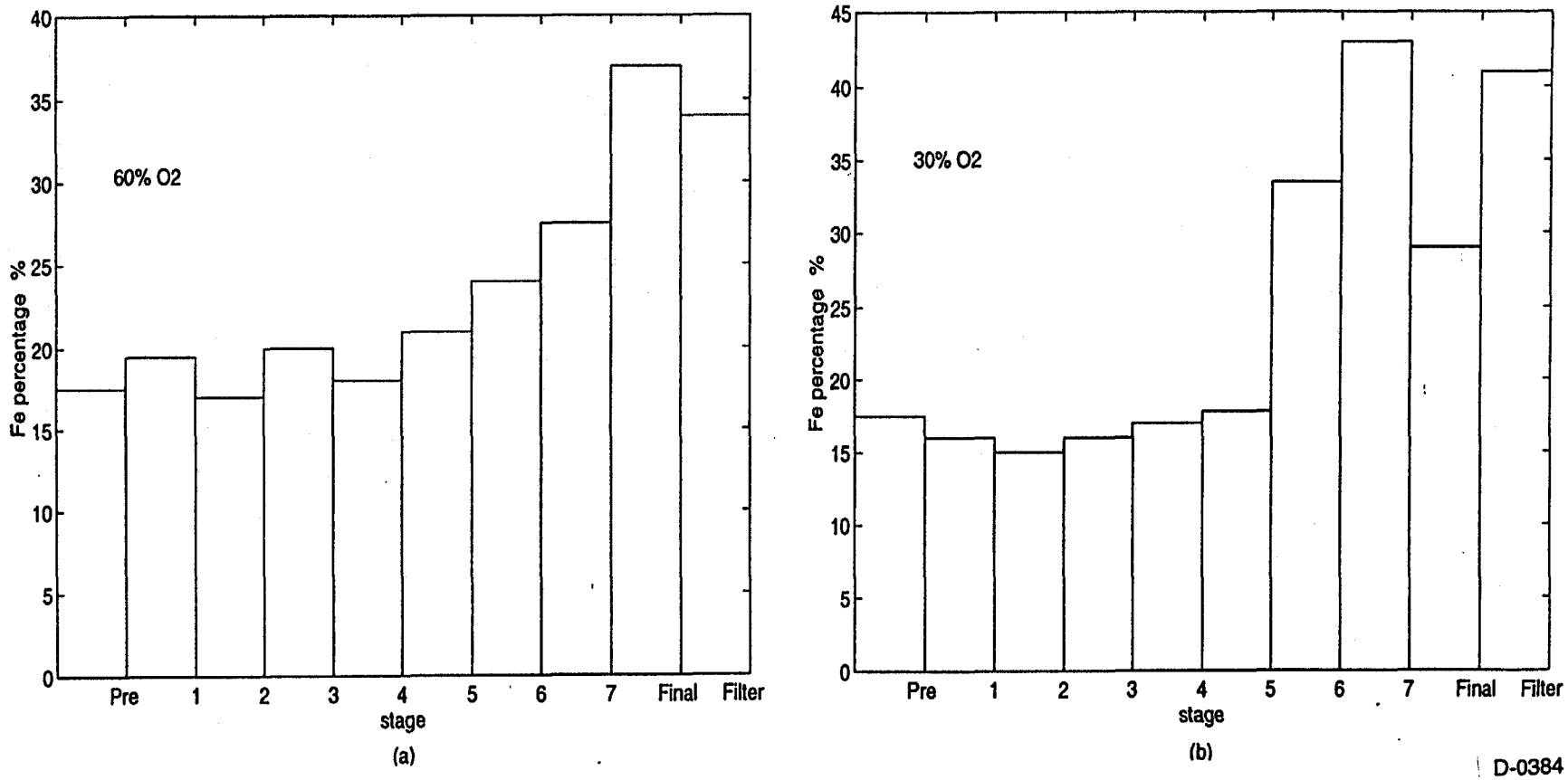

Figure 5-10 Iron concentration distribution.

subsequent nucleation/condensation of the iron vapor may also be dependent on the oxygen concentration. This effect was not explored further.

Composition of Ash

Figure 5-11 shows the composition of the ash resulting from combustion experiments conducted in both 60 and 30 % O_2. As can be seen from the figure, the concentration of iron increases as particle size decreases in both cases. The concentration of aluminum increases as particle size decreases until stage 4, below which it decreases as particle size decreases suggesting that transformation of aluminum is mainly by coalescence into in larger particles. It is difficult to vaporize aluminum embodied in the minerals as clay. Potassium , in contrast, was only observed on the after filter, suggesting that much of it had vaporized and recondensed.

Elemental Size Distributions

Figure 5-12a to g show the concentration distributions (unburned char included) of the major elements versus impactor stage for different conditions. The amount of Na was too low to be detected by the ICP. The vaporization order was K > Fe > Si > Mg > Ti > Ca > Al for this coal. At 30% O_2 , except for the after filter, the fraction of each element decreased as particle size decreased. At 60% O_2 , the fractions of elements decrease from the preseparator to stage 3; the concentrations on stage 4 or 5 are, however, much higher than those on stage 3. Concentrations (% of each element per stage) decrease from stage 4 to 8 . Combining this with the ash mass percentage in char in Figure 5-10, we can see that the ash-particle size distribution is mainly dependent upon the burnout of char. When the results are reported on a carbon-free basis, the ash-particle size distribution will approach the distribution of that for 100% O_2.

5.3.3 Iron Speciation (Mössbauer)

The transformations of iron species was the major focus of this work. As discussed in the previous section, the iron distribution was obtained using ICPES. In this section, results from Mössbauer spectroscopy are presented to show chemical transformation of iron under different combustion conditions.

Iron Distribution under Different Combustion Conditions

Table 5-4 shows the iron distributions for beneficiated Pittsburgh No. 8 coal for the following conditions: $T_{furnace}$ =1650K, residence time = 0.9 s, coal feed rate = 0.08 g / min, $d_p \leq 75$ μm. The analyses were made at the University of Kentucky. The table shows that the iron compounds in the parent coal are pyrite: FeS_2 and jarosite: $(Na, K)Fe_3(SO_4)_2(OH)_6$. Since very little is known about jarosite, it is assumed that jarosite has the same properties as pyrite. Under heating (for 0 % O_2), pyrite and jarosite are changed into Fe-metal, pyrrhotite, and iron carbide as expected (Asaki etc. 1985; Srinivasachar, 1985).

Under oxidation conditions, pyrite / jarosite is changed into magnetite(Fe_3O_4) and hematite (Fe_2O_3). Figures 5-13 and 5-14 show that more iron is changed into Fe / glass as the concentration of O_2 increases. Reactions accounting for the transformation that may occur under oxidation include the following:

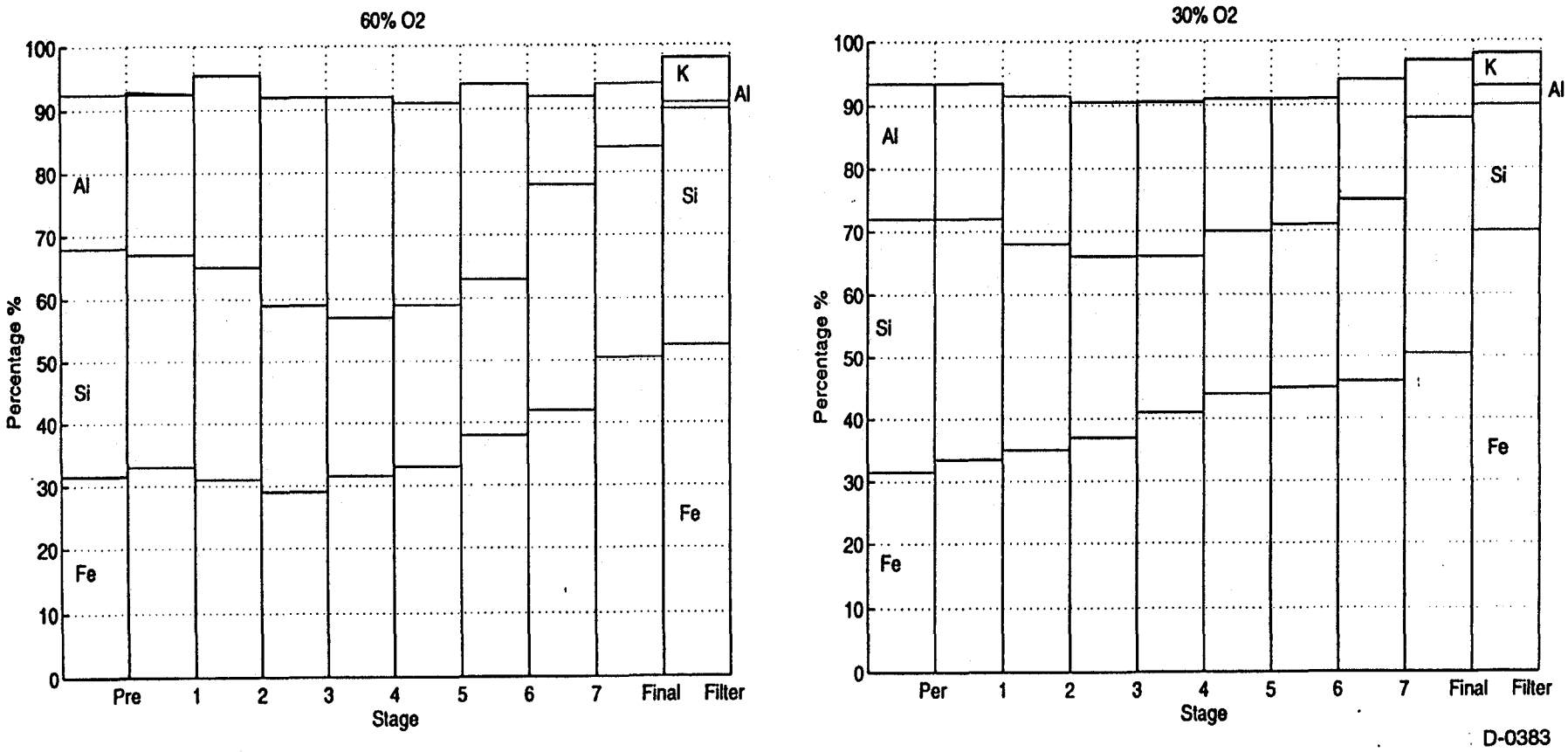

Figure 5-11. Ash composition distribution

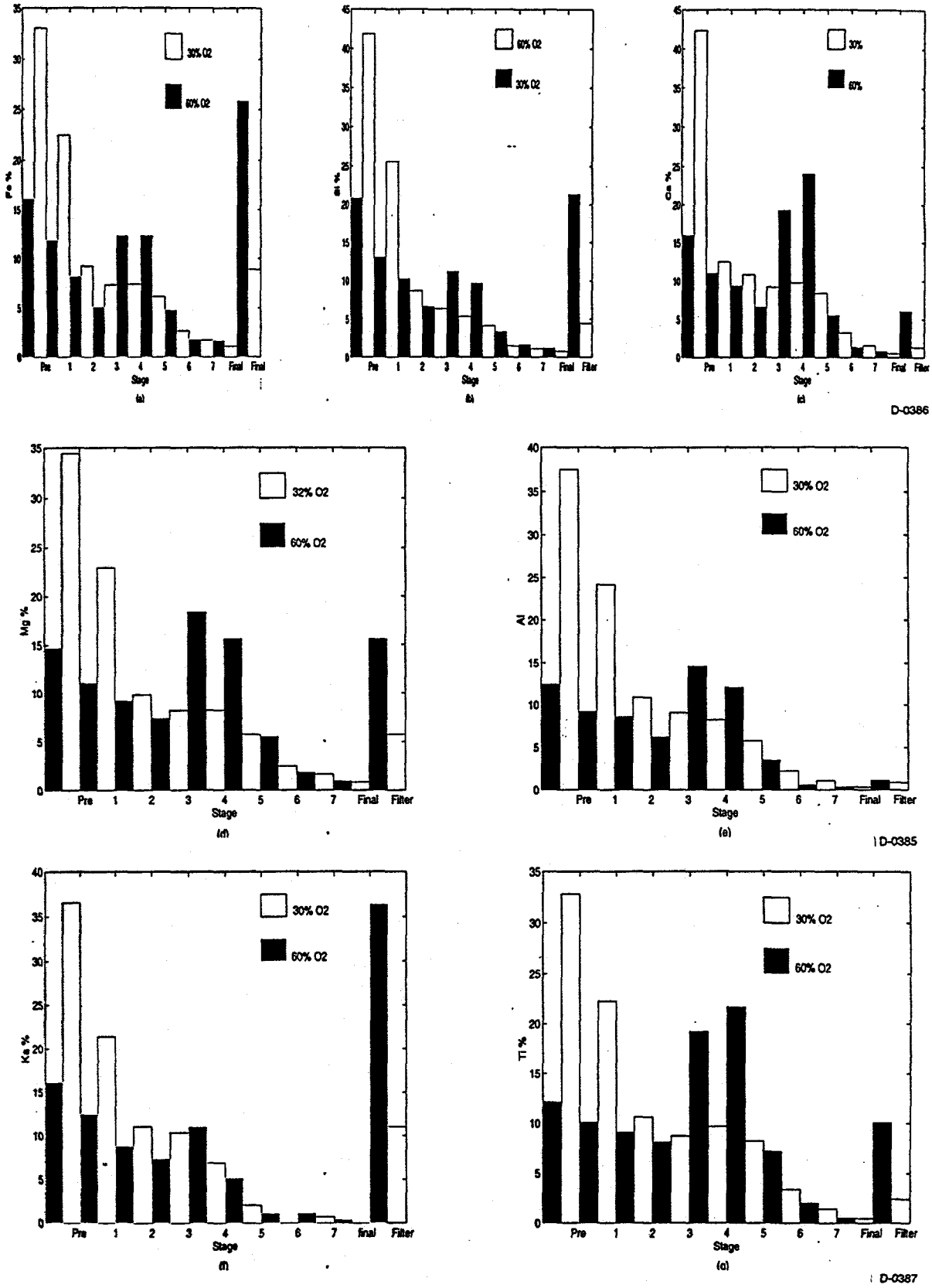

Figure 5-12. Elemental concentration

$Fe_2S \rightarrow FeS + S_2$
$FeS \rightarrow Fe + S_2$
$Fe + O_2 \rightarrow FeO$
$FeO + O_2 \rightarrow Fe_3O_4$
$FeO + SiO_2 \rightarrow$ Fe (II) / glass
$Fe_3O_4 + O_2 \rightarrow Fe_2O_3$
Fe (II) / glass + $O_2 \rightarrow$ Fe (III) / glass
$Fe_2O_3 + SiO_2 \rightarrow$ Fe (III) / glass

Table 5-4. Iron Distribution under Different Combustion Conditions

% O_2	Phase Present	I.S.	Q.S.	HO	%Fe
parent coal	pyrite	0.33	0.56		41
	jarosite	0.38	1.06		50
0	Fe (III) / jarosite	0.37	0.97		25
	γ Fe Metal	-0.08			6
	Fe Metal	-0.01	0	327	17
	Fe_{1-x} S	0.74	-0.09	305	24
	Fe Carbide	0.14	0	195	29
10	Fe (II) / glass	0.96	1.89		19
	Fe (III) / glass	0.32	0.99		29
	γ Fe Metal	-0.06			2
	Fe Metal	-0.02	0	328	8
	Magnetite	0.31	0	486	17
	Magnetite	0.63	0	448	15
	Fe_{1-x} S	0.75	0	299	11
30	Fe (II) / glass	0,86	2.33		22
	Fe (III) / glass	0.39	0.95		51
	Magnetite	0.35	0	494	12
	Magnetite	0.65	0	443	8
	Fe_{1-x} S	0.67	0	302	8
60	Fe (II)/ glass	0.77	2.56		11
	Fe (III)/ glass	0.36	1.08		66
	α-Fe_2O_3	0.36	-0.08	496	9
	Magn.+ Fe_2O_3	0.40	-0.08	427	4
100	Fe (II)/ glass	0.73	2.74		8
	Fe (III)/ glass	0.35	1.17		75
	α-Fe_2O_3	0.37	-0.07	498	4
	Magn.+ Fe_2O_3	0.39	-0.05	429	14
ASTM Ash	Fe (III)/ glass	0.34	0-.90		7
	α-Fe_2O_3	0.39	-0.08	514	55
	α-Fe_2O_3	0.37	-0.1	494	39

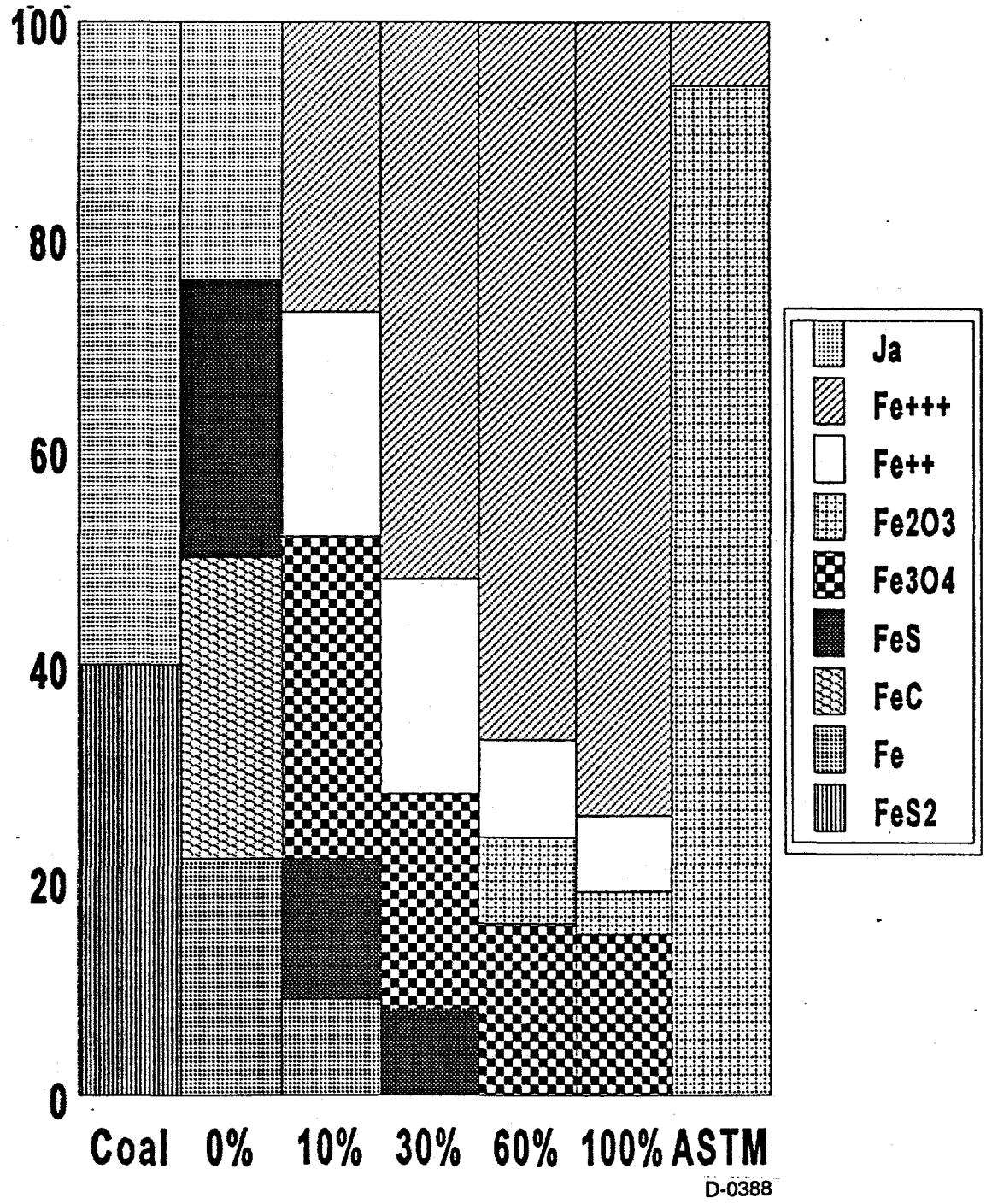

Figure 5-13. Iron speciation in ash as a function of O_2 concentration.

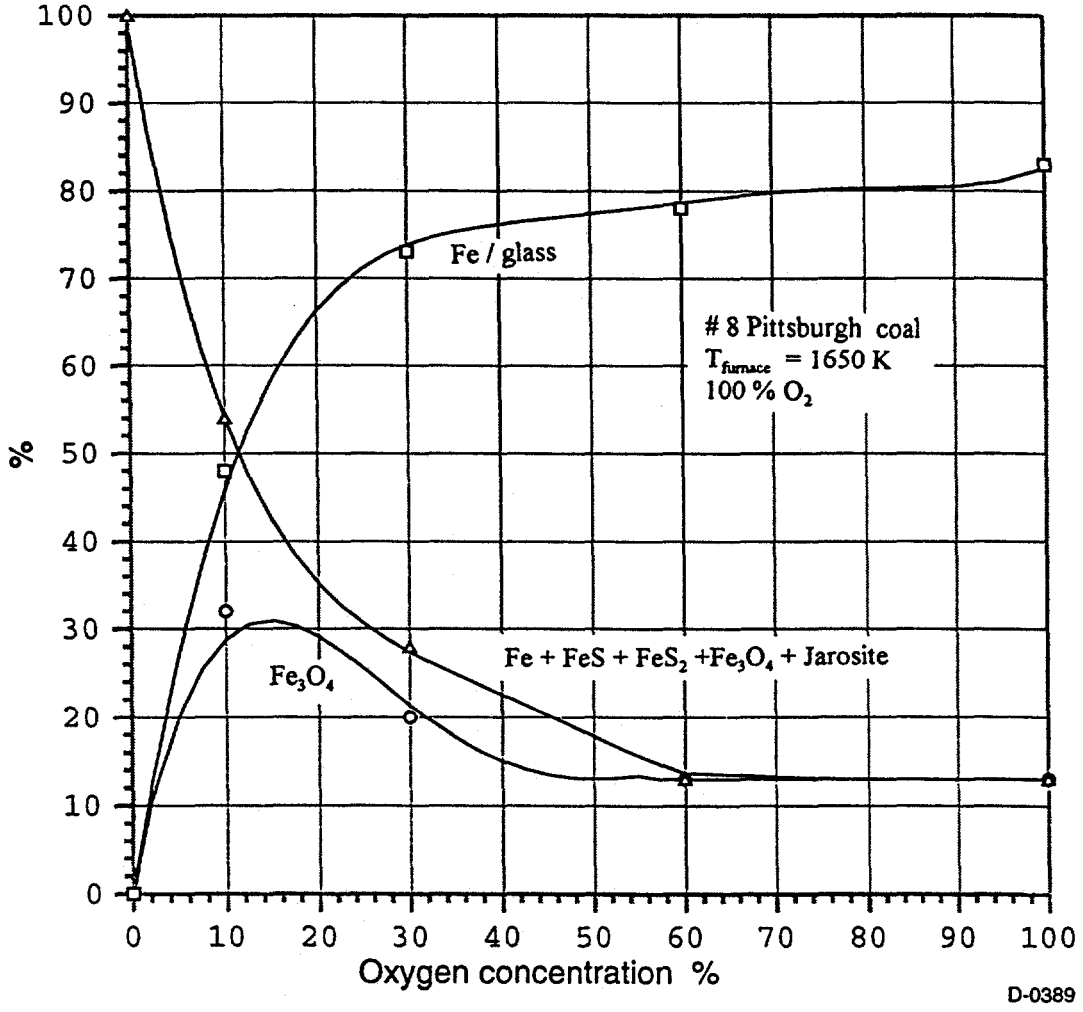

Figure 5-14. Iron conversion as a function of O_2 concentration.

Based upon the reactions in the literature and sintering, Bool et al. (1995) proposed a coalescence model to predict the fate of iron during coal combustion. With this model they obtained good predictions on the partitioning of iron between different compounds. This work addresses additional mechanistic considerations particularly relating to vaporization, CO formation, and oxidation in the particle boundary layer as this will determine the O_2 concentration at the char particle surface.

Table 5-5. Iron Distribution in Size Cuts at 100% O_2, T_∞=1650 K

Stage	Size Range (μm)	Composition	Percentage
Preseparator	>10	$^{Fe\ (II)}$/ glass	18
		$^{Fe\ (III)}$/ glass	34
		Fe_3O_4+ γ-Fe_2O_3	14
		α-Fe_2O_3	28
		Fe-metal	2
		$Fe_{1-x}S$	4
1	9.0-10	$^{Fe\ (II)}$/ glass	20
		$^{Fe\ (III)}$/ glass	60
		Fe_3O_4+ γ-Fe_2O_3	4
		α-Fe_2O_3	15
		Fe Carbide	1
4	3.3-4.7	$^{Fe\ (II)}$/ glass	13
		$^{Fe\ (III)}$/ glass	78
		Fe_3O_4+ γ-Fe_2O_3	6
		α-Fe_2O_3	3
6	1.1-2.1	$^{Fe\ (II)}$/ glass	11
		$^{Fe\ (III)}$/ glass	71
		Fe_3O_4+ γ-Fe_2O_3	8
		α-Fe_2O_3	1
		Fe-metal	3
		$Fe_{1-x}S$	5
		Fe Carbide	1
Final	0.43-0.65	$^{Fe\ (II)}$/ glass	2.9
		$^{Fe\ (III)}$/ glass	60.0
		Fe_3O_4+ γ-Fe_2O_3	28
		Fe-metal	3.7
		$Fe_{1-x}S$	3.8
		Fe Carbide	1.0
Filter Holder	0.04-0.43	$^{Fe\ (II)}$/ glass	2.3
		$^{Fe\ (III)}$/ glass	66.3
		Fe_3O_4+ γ-Fe_2O_3	19.9
		Fe-metal	5.1
		$Fe_{1-x}S$	6.4

Figure 5-15 shows that the Fe (III)/Fe (II) ratio in the glass increases as the oxygen concentration increases. Higher O_2 favors the oxidation of Fe (II) to Fe (III) in the glass and Fe vaporization. Iron in glass formed via vaporization should only be Fe (III). Figure 5-16 shows the relationship between carbon conversion (x) and O_2 concentration. It can be seen that at $T_{furnace}$ = 1650 K, the conversion of carbon is not complete.

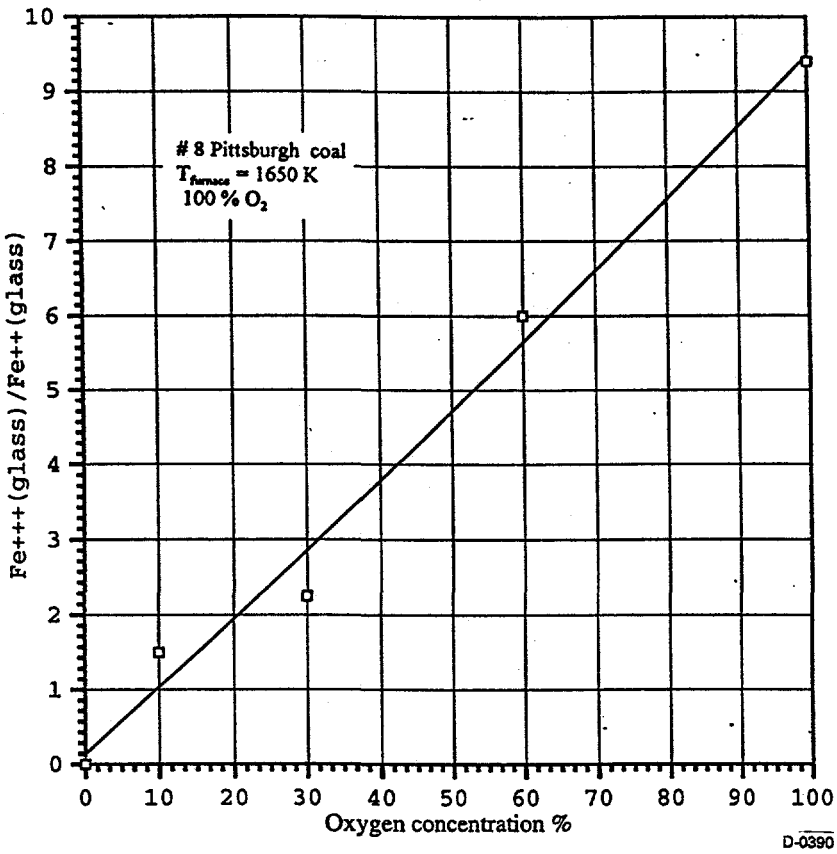

Figure 5-15. Iron oxidation state in glassy ash as a function of O_2 concentration.

Iron Distribution in Different Size Particles

Under typical combustion conditions there are several mechanisms that may control the partitioning of ash into various size ranges. These mechanisms include vaporization, coalescence, and mineral fragmentation. By analyzing the particle size distribution of ash it is generally possible to determine which size ranges are formed by a specific mechanism. For example, Figures 5-16 and 5-17 show that the iron in the ash is generally found in three discrete size ranges. Iron found in the submicron fume vaporized and subsequently nucleated/condensed. Particles in the 1.1 to 10 μm range are generally formed by coalescence. Finally, those particles greater than 10 μm are primarily unburned char. The mass in this last size range is small in these experiments and can be neglected (see Figure 5-18). Therefore, for this coal iron either vaporizes or coalesces with other minerals.

The hypothesis that the particles in the 1.1 to 10 μm range are formed by coalescence is borne out by the fact that almost all of the iron in these particles is found in the glassy phase - indicating coalescence of 'pure' iron species, such as pyrite, with other minerals,. such as clays. The oxidation of the iron in the glassy particles has been shown to be controlled by oxygen diffusion through the molten particle (Bool, 1995).

The iron states in submicron particles are generally Fe (III) in a glass and compounds of Fe_3O_4 and Fe_2O_3. The presence of iron oxides suggests that only part of iron can react with silicate since there is not

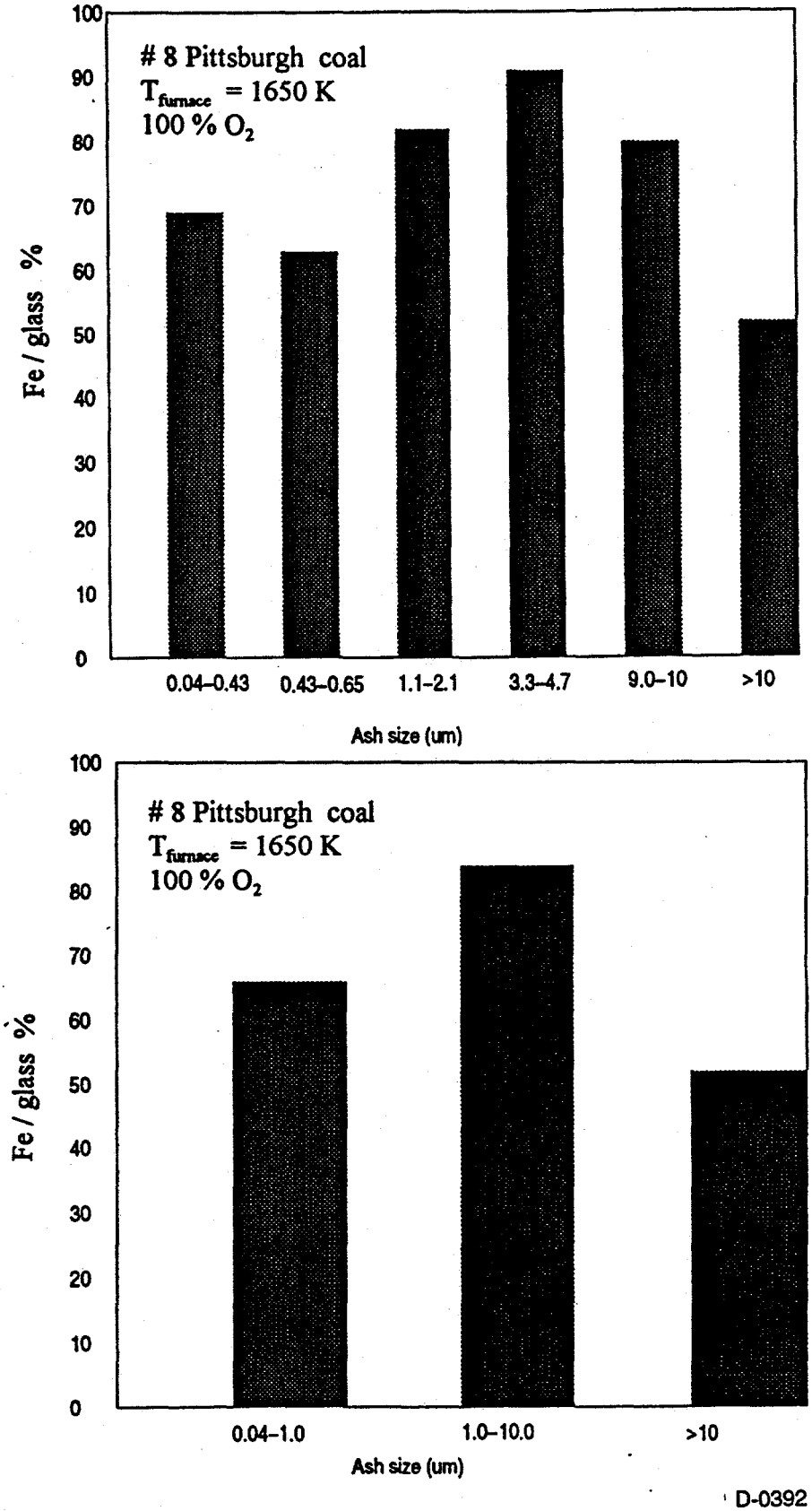

Figure 5-16. Fraction of Fe in glassy phase in each size range.

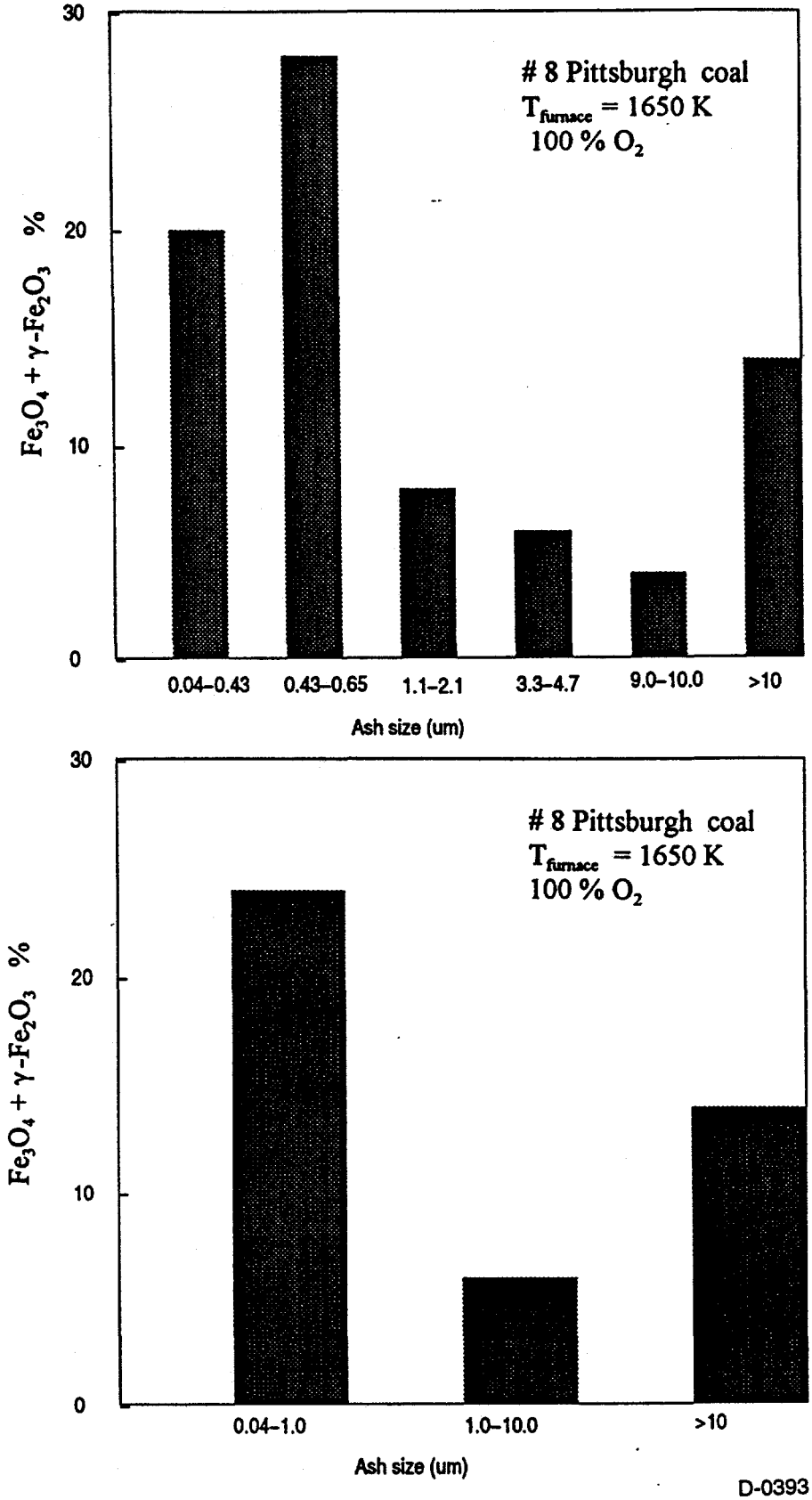

Figure 5-17. Fraction of Fe in oxide phases in each size range.

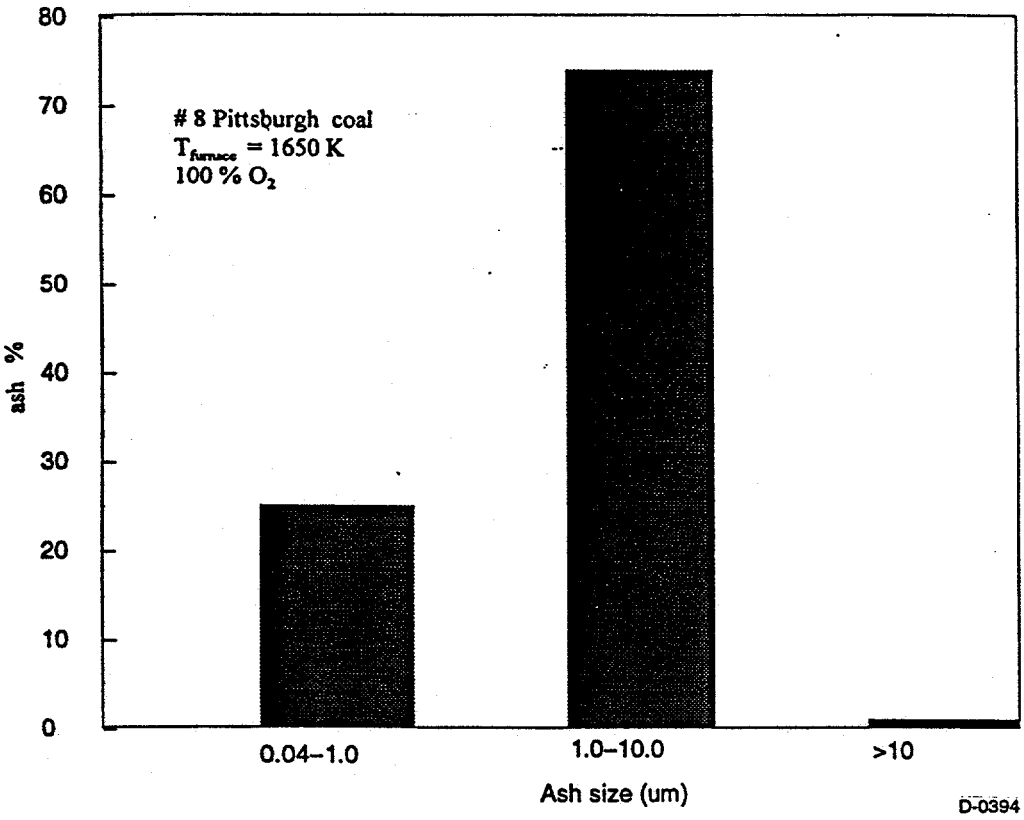

Figure 5-18. Ash mass distribution.

enough silicate to react with the iron for this coal. The reactions between iron vapor and other minerals are homogeneous and are controlled by the concentrations of the reactants and reaction time in the gas phase.

5.4 Modeling

The primary difference between pyrite transformations for excluded pyrite and pyrite in coal particle are the combustion temperature and environment. However the combustion temperature and environment for the particle are generally not easy to measure. In this section, some basic calculations were performed to obtain these parameters for further model development.

5.4.1 Estimation of Combustion Kinetics for Coal

5.4.1.1 Transport Properties of Reacting Gas

It is well known that the combustion of the char particle can be classified into three regions: region I - kinetically controlled combustion, region II - diffusively controlled combustion, and in region III - kinetically and diffusively controlled combustion. In region I the char reacts with oxygen in the whole particle, in region II oxygen penetrates into the particle to some depth. Under typical combustion conditions, char combustion takes place in region III. Therefore, the gas transport properties are essential to this study.

The Diffusion Coefficient for O_2 - N_2

The main components of the reacting gases surrounding the particle are CO, CO_2, O_2 and N_2. The dominant gases in this system are O_2 and N_2. Therefore, diffusion between the gases can be taken as O_2 - N_2. We can calculate the diffusion coefficient according to Lienhard(1987):

$$D_{o_2\text{-}N_2} = \frac{(1.83583\times10^{-7})T^{3/2}}{p\sigma_{AB}^{2}\Omega_D}\sqrt{\frac{1}{M_A}+\frac{1}{M_B}} \tag{5-1}$$

where p = 1 atm, $\sigma_{AB} = 3.5785$, $\Omega_D = 0.6558$, $M_A = 32$, $M_B = 28$ at T = 2000 K, $D_{O2\text{-}N2} = 5.024 \times 10^{-4}$ m/s. At other temperatures:

$$\frac{D(T)}{D(2000)} = \left(\frac{T}{2000}\right)^{\frac{3}{2}} \tag{5-2}$$

Density of Reacting Gas

We take the gas as an ideal gas, so:

$$P = \rho R T$$

or:

$$\rho = \frac{P}{RT} \tag{5-3}$$

5.4.1.2 Estimation for Reaction Time

The momentum equation for char particle in gas:

$$m\frac{dV}{dt} = mg - 3\pi\mu d(V - V_g) - \frac{m}{\rho}\rho_a g \tag{5-4}$$

$$\frac{dV}{dt} = g - \frac{3\pi\mu d(V - V_g)}{m} - \frac{\rho_a}{\rho}g \tag{5-5}$$

The pathway of the particle in our reactor is composed of two sections. The first section is the vertical path from the coal feeder to the reaction zone. The second section is the reaction zone. For the first section, the vertical length is 0.57m. The cross-section-area of the feed pipe is:

$$S = \frac{\pi}{4}D^2 = \frac{\pi}{4}(0.3175\times10^{-2})^2 = 7.9168\times10^{-6}m^2 \tag{5-6}$$

and the feed flow rate is:

$$Q = 150 \text{ ml/min} = 2.5\times10^{-6} \text{ m}^3/\text{s}. \tag{5-7}$$

Therefore the velocity of gas is:

$$V_g = Q/S = 0.31578 \text{ m/s}. \tag{5-8}$$

The initial condition for the particle is:

$$V(t=0) = V_g. \tag{5-9}$$

By using MAPLE, we can easily calculate:

$$V(z = 0.57 \text{ m}) = 0.5224 \text{ m/s for } d_p = 75\ \mu\text{m}. \tag{5-10}$$

For the second section (the reactor zone), the flow rate of the main gas is:

$$Q = 6 \text{ l/min} = 0.1\times10^{-3} \text{ m}^3/\text{s}. \tag{5-11}$$

The cross-sectional area of the furnace is:

$$S=\frac{\pi}{4}(2\times2.54\times10^{-2})^2=2.0268\times10^{-3}\text{m}^2. \tag{5-12}$$

The furnace temperature is 1650 K, therefore:

$$V_g=\overline{V}_{gas}=\frac{(0.1\times10^{-3})\times\frac{1650}{300}}{2.0268}=0.271\text{m/s}. \tag{5-13}$$

The length with T_{wall} = 1650 K is 3.5 inches or 0.0889 m.

When the particle is very small, it will follow the gas streamlines in the furnace. In this case, the reacting time for the particle is:

$$\frac{L}{\overline{V}_{gas}} = 0.33 \text{ s}. \tag{5-14}$$

When the mass of the particle does not change or decreases slightly (corresponding to low carbon conversion), we can simply integrate Eq. (5-5) to obtain V (t). Then we can calculate $\overline{V}_p = 0.518$, so the reaction time for the particle is:

$$\frac{L}{\overline{V}_p} = 0.17 \text{ s.} \tag{5-15}$$

5.4.1.3 Estimation of Chemical Kinetics for Char Combustion

The calculation of char oxidation rates is a fundamental part of coal combustion research. There are numerous articles on this topic. However, as the focus of this program is the iron transformations so we will simplify the carbon burnout analysis by acknowledging that the char combustion is essentially carbon oxidation. The reactions for carbon oxidation are as follows:

$$C + O_2 \rightarrow CO_2 \tag{5-16}$$

$$C + 1/2\ O_2 \rightarrow CO \tag{5-17}$$

$$C + CO_2 \rightarrow 2\ CO. \tag{5-18}$$

The reaction rates for these reactions can be written as:

$$\frac{dm(a)}{dt} = K_{oa}(\rho_s Y_{o,s})^{n_a} \exp\left(-\frac{E_a}{RT_p}\right)\frac{M_{co_2}}{M_{o_2}} \tag{5-19}$$

$$\frac{dm(c)}{dt} = K_{oc}(\rho_s Y_{co_2,s}) \exp\left(-\frac{E_c}{RT_p}\right) \tag{5-21}$$

$$\frac{dm(b)}{dt} = K_{ob}(\rho_s Y_{o,s})^{n_b} \exp\left(-\frac{E_b}{RT_p}\right)\frac{M_{co}}{\frac{1}{2}}M_{o_2}. \tag{5-20}$$

In a previous study, the kinetic parameters have been determined for solid pure carbon particle (Zeng and Fu, 1995):

$$\begin{aligned} &K_{oa} = 3500,\ n_a = 0.88,\ E_a = 113000 \\ &K_{0b} = 1.05\text{x}10^6,\ n_b = 0.64,\ E_b = 180000 \\ &K_{0c} = 10^8,\ E_c = 270000 \end{aligned} \tag{5-22}$$

The difference between the solid pure carbon particle and the coal particle is that the coal particle has porosity within the particle. As mentioned in Section 5.4.1.1, when the coal burns in region I and II, the porosity may increase the reaction area, while in region III, the porosity may not effect the reaction area or may decrease the reaction area. For example, Hecker et al. [1992] found that the intrinsic reaction rate of partially burned out char at high temperatures decreases with burnout level. For simplification we take the kinetic parameters as constants. This can be achieved by multiplying a constant K to the expressions for reaction rates of solid pure carbon particle. This constant K represents an empirical fit to describe the difference between combustion of a pure solid carbon particle and combustion of a given coal.

$$\frac{dm_{char}}{dt} = K[K_{oa}(\rho_s Y_{o,s})^{n_a}\exp(-\frac{E_a}{RT_p}) + K_{ob}(\rho_s Y_{o,s})^{n_b}\exp(-\frac{E_b}{RT_p}) + K_{oc}(\rho_s Y_{co_2,s})\exp(-\frac{E_c}{RT_p})] \quad (5\text{-}23)$$

Temperature measurements of solid pure particle (Zeng, 1995) and of a pulverized coal particle (Timothy, 1982) showed that the combustion temperature of particles were constant during combustion. Therefore, we can take the combustion processes to be quasi-steady. We can then write the energy equation for the particle as follows:

$$Q_a K\frac{dm_a}{dt} + Q_b K\frac{dm_b}{dt} - Q_c K\frac{dm_c}{dt} = -\lambda_a\frac{dT}{dr} + \epsilon\sigma(T^4{}_p - T^4{}_g) \quad (5\text{-}24)$$

The particle diameter can be computed from:

$$\frac{d(\rho\frac{4}{3}\pi r^3)}{dt} = -\frac{dm}{dt} \quad (5\text{-}25)$$

By solving the equations governing the species and temperature distributions surrounding the particle, we can obtain the oxygen concentration on the particle surface in terms of the combustion temperature (Zeng, 1995, Makino, 1986). Thus we can predict mass loss of the particle. The conditions for this simulation are:

Furnace temperature (T_g) = 1650 K	Bulk oxygen concentration ($Y_{0\infty}$) = 10 %
Particle diameter (d_p) = 75 μm	Reaction time = 0.2 s (from Section 6.2)
Carbon conversion = 41 %	Coal type = Pittsburgh #8 (cleaned)

By adjusting K, we can fit the predictions for combustion under a single set of conditions with the experimental results. Therefore we obtain:

$$K = 0.2 \quad (5\text{-}26)$$

These equations, using K=0.2, were then able to successfully predict combustion of this coal under other conditions.

5.4.2 Prediction of Combustion Processes

Using the method described in Subsection 5.4.1 (with K = 0.2), we can predict the combustion process under other combustion conditions, as long as combustion is still in region III. Typical results are shown in Figures 5-19 to 5-22. These figures show that the combustion is near region III since the surface oxygen concentration is of the order of 1%. While CO_2 is present on the char surface, the dominant gas is CO.

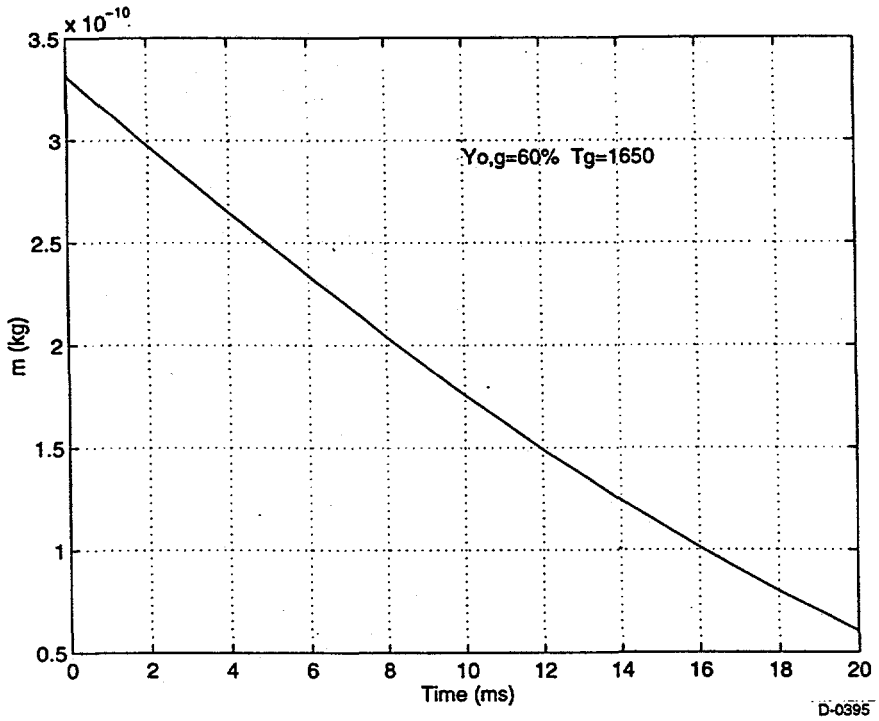

Figure 5-19. Char mass as a function of time.

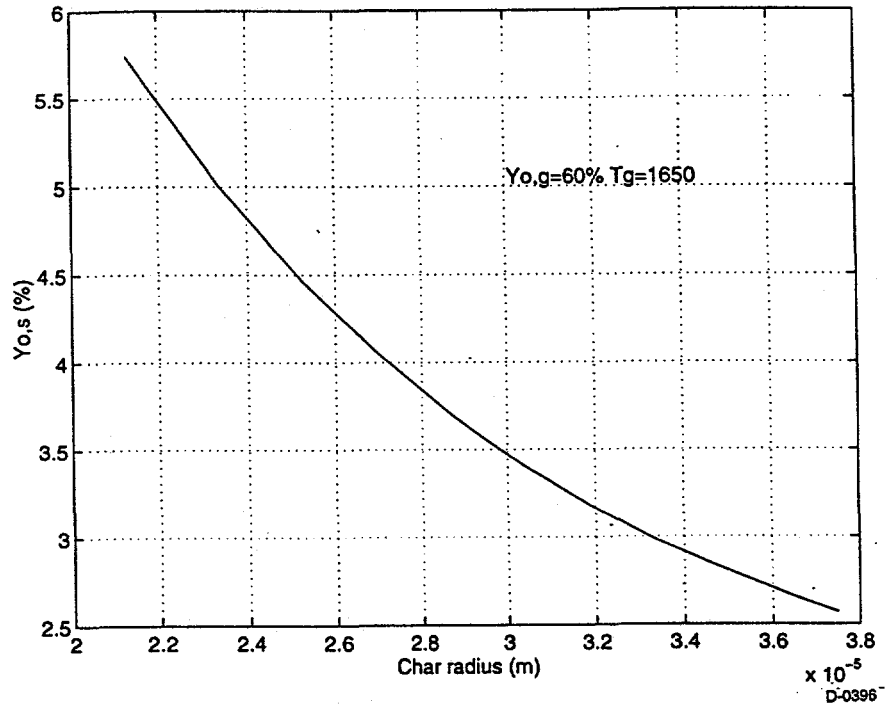

Figure 5-20. O_2 concentration on char surface as a function of particle size.

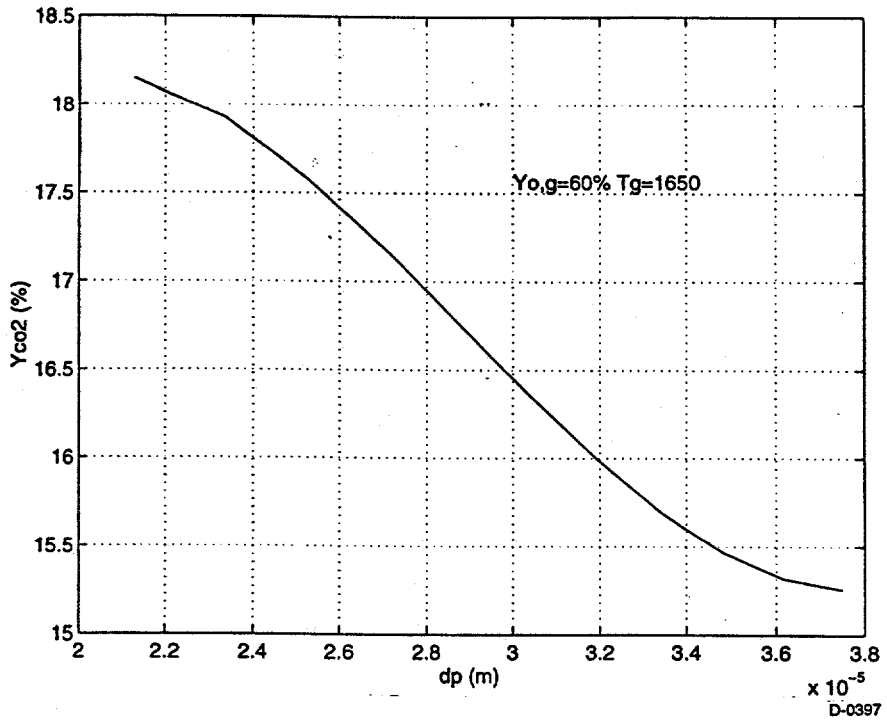

Figure 5-21. CO_2 concentration on char surface as a function of particle size.

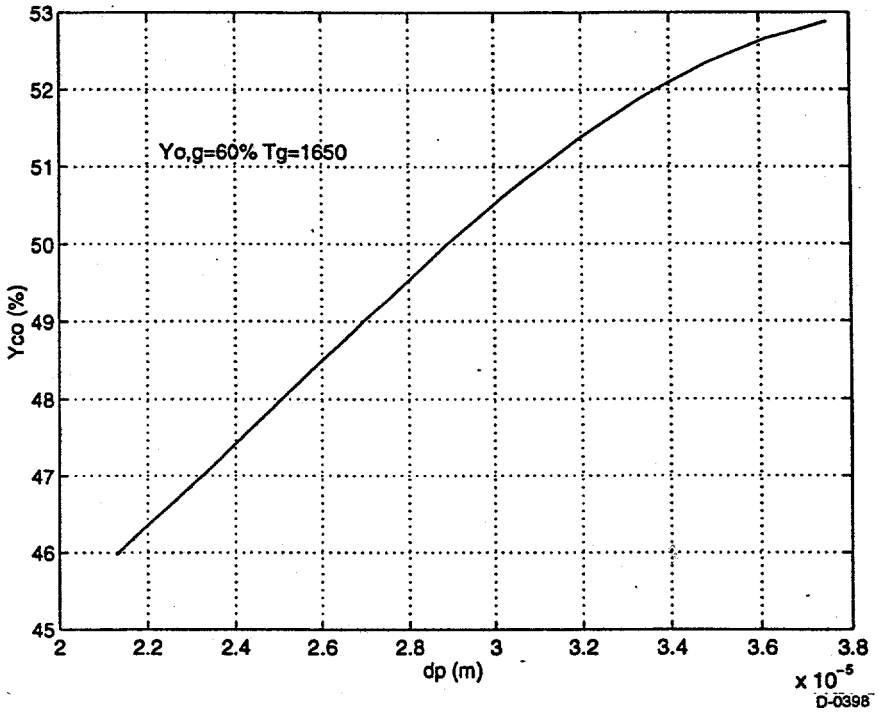

Figure 5-22. CO concentration on char surface as a function of particle size.

5.4.3 Vaporization of Iron

As part of the broader modeling effort, the vaporization rates of iron during coal combustion were calculated based on the results described in 5.4.1. and 5.4.2.

5.4.3.1 Reducing Mechanism

It is generally believed that refractory oxides, such as SiO_2 and CaO, are much more difficult to vaporize than the corresponding volatile suboxide or metal. As shown in the previous section, CO dominates for the environment on the particle surface: the concentration of CO is more than 50 times than that of O_2. Therefore it is likely that the refractory oxides can be reduced to the more volative forms if any reaction with gases exists. For iron it is assumed that the reduction occurs via the following reaction:

$$FeS + CO \leftrightarrow COS + Fe\ (gas) \tag{5-27}$$

This reaction is assumed to be at equilibrium at the surface of each inclusion within the char particle (Quann,1982). The partial pressure of Fe at the inclusion surface is determined from the equilibrium constant K_e and the local gas compositions:

$$K_e = \frac{P^e Pcos}{aPco} \tag{5-28}$$

where a is the activity of FeS, which is set equal to 1. Since there is no other source of COS, the concentration of COS is taken to be that of Fe. Therefore the concentration of Fe can be calculated by the following equation:

$$P^e = Pcos = (\ Ke\ Pco\ )^{1/2} \tag{5-29}$$

5.4.3.2 Calculation Strategy

The method to calculate the vaporization rates of Fe is based upon the work by Quann (1982) and is described briefly here. If ρ_I is the number density of inclusions in a single coal particle, then the vapor mole fraction profile, x_m, with respect to the coal particle's internal radial coordinate is:

$$cD_e \nabla^2 x_m + \rho_I V_I^i(r) = 0 \tag{5-30}$$

where V^i_I is the vaporization rate for a single inclusion and is approximately given by:

$$V^i_I = 4\pi r_i c D_e (x^e_m - x_m) \tag{5-31}$$

where x^e_m is the equilibrium mole fraction of the vapor at the inclusion surface, D_e is the effective diffusivity for Knudsen diffusion in the char pore, and r_r is the radius of inclusions. Equation (5-31) is valid when the inclusions are embedded in an isotropic porous medium with pore size much less than the inclusion size.

During combustion inclusions initially embedded in the coal matrix will be exposed during burnout. The contribution of these surface inclusions to the total vaporization from the char is neglected. As discussed in Subsection 5.3.4.2, the surface inclusions will coalescence with silicate to form Fe/ glass or be oxidized. The number of inclusions, N_I, within the char is given by:

$$N_I = \theta\left(\frac{r_p}{r_i}\right)^3 \tag{5-32}$$

where θ is the inclusion volume fraction in the char and r_p is the char radius. During combustion N_I decreases and θ and ρ_I remain constant. Here the model of constant char density is used. The parameter r_p can be calculated with the method in 5.4.2. The boundary conditions are:

$$\begin{aligned} r = 0: &\frac{dx_m}{dr} = 0 \\ r = r_p: &-4\pi r_p^2 c D_e \frac{dx_m}{dr}\Big|_{r=r_p} = 4\pi r_p D_o \alpha x^s_m \end{aligned} \tag{5-33}$$

The factor α, a correction for Stefan flow, is:

$$\alpha = [1 - \exp(-\frac{D_o}{D_m}\ln(1 + x^b_o))]^{-1} \ln(1 + x^b_o) \tag{5-34}$$

where, D_m, D_o, and x_o^b are gas diffusivity of the inorganic vapor , diffusivity of oxygen, and the mole fraction of O_2. Equation (5-30) is analogous to diffusion and reaction in a porous catalyst pellet, with the Thiele modulus:

$$\phi = (3\theta)^{1/2} r_p / r_i. \tag{5-35}$$

The total instantaneous rate of vaporization V_c (moles/sec) from a single char particle is determined from:

$$V_c = 4\pi r^2_p c D_e \frac{dx}{dr}\Big|_{r=r_p} = 4\pi r_p c D_{O_2} \alpha x^s_m \tag{5-36}$$

with the vapor mole fraction at the char surface:

$$x^s_m = \frac{\frac{D_e}{\alpha D_o}\left(\frac{\phi}{\tanh\phi} - 1\right)}{1 + \frac{D_e}{\alpha D_o}\left(\frac{\phi}{\tanh\phi} - 1\right)} x^e_m \tag{5-37}$$

The effectiveness factor is:

$$\eta = \frac{3}{\phi}\left[\frac{1}{\tanh\phi} - \frac{1}{\phi}\right]\left[1 + \frac{D_e}{\alpha D_o}\left(\frac{\phi}{\tanh\phi} - 1\right)\right]^{-1} \qquad (5\text{-}38)$$

where η is the ratio of the total vaporization rate of Fe (with particles interacting and with external diffusion control) over the vaporization rate of N_I isolated ash droplets in the char. The instantaneous rate can be re-expressed as

$$V_c = \eta\, N_I\, V^{ni} \qquad (5\text{-}39)$$

where V^{ni}_I is the vaporization rate for a single noninteracting inclusion:

$$V^{ni}_I = 4\,\pi\, r_i\, c\, D_e\, x^e_m \qquad (5\text{-}40)$$

For a given combustion environment the combustion temperature and the gas constituents can be calculated as discussed in the previous section. Then the equilibrium constant, Ke, can be calculated, and the concentration of Fe vapor can be computed. From this, the instantaneous vaporization rate can be obtained. By integrating the instantaneous rate, the total Fe vaporized can be obtained.

5.4.3.3 Calculation Results

Figures 5-23 and 5-24 show typical calculation results. As shown in the figures, we have estimated that the partial pressure of Fe on the particle surfaces, and the vaporization rates, change with time (eg: char particle size). The calculated total Fe vaporized is in good agreement with the experimental data.

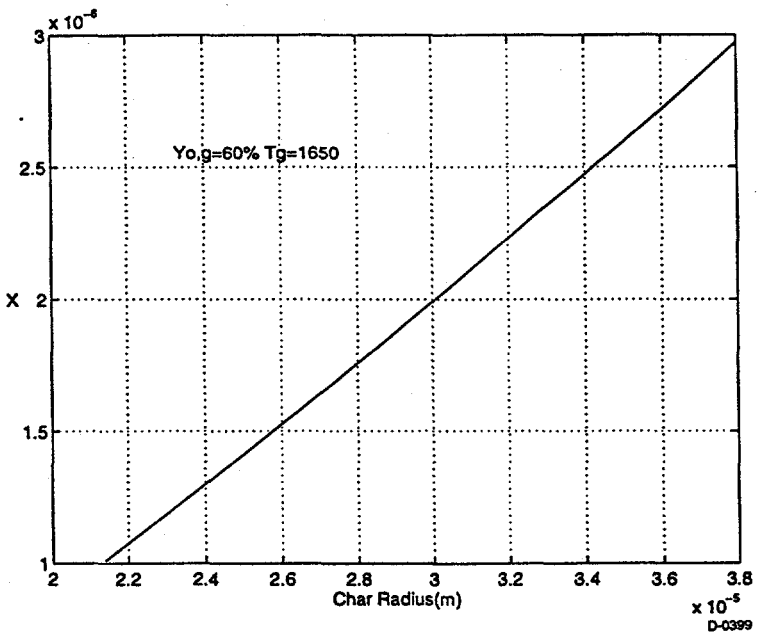

Figure 5-23. Iron vapor mole fraction at char surface as a function of particle size.

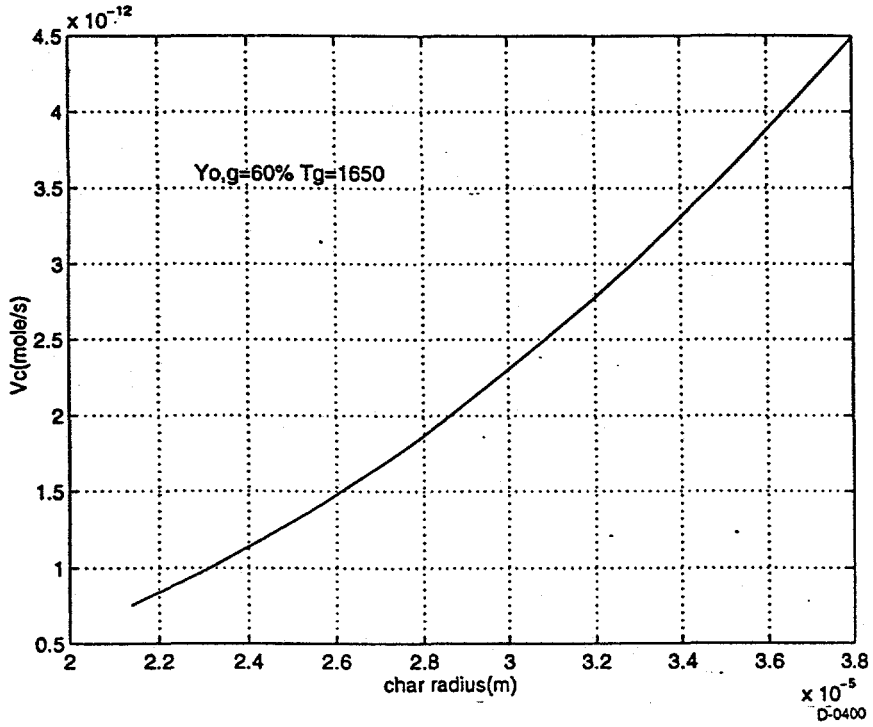

Figure 5-24. Iron vaporization rate as a function of particle size.

These results indicate that the iron vaporization rates can be predicted. The Fe vapor will react with O_2 and Si vapor in the boundary layer near the char particle to form Fe/glass or Fe oxides. In order to estimate the composition of the Fe/glass and iron oxide in the submicron particles there is a need for additional reaction kinetic parameters for the relevant reactions. The iron distribution in the larger particles with size $\geq 1\mu m$ is due to the coalescence with silicates to form Fe/ glass (Bool, 1995) or reaction with O_2 to form Fe oxides, see Section 6 for a discussion of this model.

5.5 References

Asaki, Z., Mosi, S., Ikeda, M. and Kondo, Y., Oxidation of pyrhotite particles falling through a vertical tube, Metallurgical Transactions (B) 16B, pp.627-638, 1985.

Barta, L.E., Horvath,F., Beer, J.M., and Sarofim, A.F.,Variation of mineral matter distribution in individual pulverized coal particles: application of the 'URN' model, Twenty-third Symposium (International) on Combustion, The Combustion Institute, pp.1289-1296, 1990.

Baxter, L.L., Char fragmentation and fly ash formation during pulverized-coal combustion, Combust. Flame 90, pp.174-184, 1992.

Baxter, L.L. and Mitchell, R.E., The release of iron during the combustion of Illinois No.6 coal, Combust. Flame 88, pp.1-14, 1992.

Bool, L.E., Peterson, T.W. and Wendt, J.O.L., The partitioning of iron during the combustion of pulverized coal, Combust. Flame 100, pp.262-270, 1995.

Bool, L.E., Helble, J.J., Iron oxidation sate and its effect on ash particle stickiness, Eng. Found. Conference on Application of Advanced Technology to Ash Related Problems in Boilers, Waterville Valley, NH, July 1995.

Gallagher, N.B., Bool, L.E., Wendt, J.O.L. and Peterson, T.W., Alkali metal partitioning in ash from pulverized coal combustion, Combust. Sci. and Tech. 74, pp.211-221, 1990.

Graham, K.A., Submicron ash formation and interaction with sulfur oxides during pulverized coal combustion, PhD thesis, MIT, 1991.

Hecker, W.C., McDonald, K. M., Reade, W., Swensen, M. R. and Cope, R. F.,Effects of Burnout on Char Oxidation Kinetics, Twenty-Fourth Symposium (International) on Combustion / The Combustion Institute, 1992, pp. 1225-1231.

Helble, J.J. and Bool, L.E., Fundamental study of ash formation and deposition, Quarterly Report to DoE, PSI-1178, 1995 .

Helble, J.J. and Sarofim, A.F. , Influence of char fragmentation on ash particle distribution, Combust. Flame 76, pp.183-196, 1989.

Helble, J.J., Neville, M. and Sarofim, A.F., Aggregate formation from vaporized ash during pulverized coal combustion, Twenty-first Symposium (International) on Combustion, The Combustion Institute, pp.411-417, 1986.

Huffman, G.P., Huggins, F.E., Levasseur, A.A., Chow, O., Srinivasachar, S. and Mehta, A.K., Investigation of the transformations of pyrite in a drop tube furnace, Fuel 68, pp.485-490, 1989.

Huffman, G.P., Huggins, F.E. and Dunmyre, G. R., Investigation of the high-temperature behaviour of coal ash in reducing and oxidizing atmospheres, Fuel 60, pp.585-597, 1981.

Huffman, G.P. and Huggins, F.E., Mössbauer studies of coal and coke: quantitative phase identification and direct determination of pyritic and iron sulphide sulphur content, Fuel 57, pp. 592-604, 1978.

Kang, S.G., Helble, J.J., sarofim, A.F. and Beer, J.M., Time-resolved evolution of fly ash during pulverized coal combustion, Twenty-second Symposium (International) on Combustion, The Combustion Institute, pp.231-238, 1988.

Kaufherr, N., Shenasa, M. and Lichtman, D., X-ray photoelectron spectroscopy studies of coal fly ashes with emphasis on depth profiling of submicronmeter particle size fractions, Environ. Sci. Technol. 19, pp.609-614, 1985.

Kauppinen, E.I. and Pakkanen, B.F., Coal combustion aerosol: A field study, Environ. Sci. Technol. 24, pp.1811-1818, 1990.

Kerstein, A.R. and Edward, B.F., Percolation model for simulation of char oxidation and fragmentation time histories, Chem. Eng. Sci. 42, pp.. 1629-1634, 1987.

Lienhard, J. H., A Heat Transfer Textbook, 2nd edition, Prentice Hall, Englewaood Cliffs, 1987, p. 531.

Makino, A. and Law, C. K., Quasi-Steady and Transient Combustion of a Carbon Particle: Theory and Experimental Comparisons, Twenty - First Symposium (International) on Combustion, The Combustion Institute, 1986, pp. 183-191.

Markowski, G.R. and Filby, R., Trace element concentration as a function of particle size in fly ash from a pulverized coal utility boiler, Environ. Sci. Technol.. 19, pp.796-804, 1985.

Neville, M. and Sarofim, A.F., The stratified composition of inorganic submicron particles produced during coal combustion, Nineteeth Symposium (International) on Combustion, The Combustion Institute, pp.1441-1449, 1982.

Neville, M., Quann, R.J., Haynes, B.S. and Sarofim, A.F. , Vaporization and condensation of mineral matter during pulverized coal combustion, Eighteenth Symposium (International) on Combustion, The Combustion Institute, pp. 1267-1274, 1980.

Quann, R.J. and Sarofim, A.F., A scanning electron microscopy study of the transformations of organically bound metals during lignite combustion, Fuel 65, pp.40-46, 1986.

Quann, R. J. and Sarofim, A.F., Vaporization of Refractory Oxides During Pulverized Coal Combustion, Nineteenth Symposium (international) on Combustion / The Combustion Institute, 1982 , pp. 1429-1440.

Sarofim, A.F. and Helble, J.J., Mechanisms of ash formation and deposit, Quarterly report to DoE, PSI-1178SR-703, 1993.

Sarofim, A.F., Howard, J.B. and Padia, A.S., The physical transformation of the mineral in pulverized coal under simulated combustion conditions, Combust. Sci. Technol. 16, pp.187-204, 1977.

Senior, C.L. and Flagan, R.C., Synthetic chars for the study of ash vaporization, Twentieth Symposium (International) on Combustion, The Combustion Institute, pp. 921-929, 1984.

Srinivasachar, S., Helble, J.J. and Boni, A.A., Mineral behavior during coal combustion 1. pyrite transformations, Prog. in Energy Combust. Sci. 16, 281-292, 1990.

Srinivasachar, S. and Boni, A.A., A kinetic model for pyrite transformations in a combustion environment, Fuel 68, pp.829-836, 1989.

Timothy, L. D., Sarofim, A. F. and Beer, J. M. , Characteristics of single particle coal combustion, Nineteenth Symposium (International) on Combustion / The Combustion Institute, 1982, pp. 1123-1130.

Wall, T.F., Mineral matter transformations and deposition in pulverized coal combustion, Twenty-fourth Symposium (International) on Combustion, The Combustion Institute, pp.1119-26, 1992.

Wibberly, L.J. and Wall, T.F., An investigation of factors affecting the physical characteristics of fly ash formed in a laboratory scale combustor, Combust. Sci. Technol. 48, pp.177-190, 1986.

Zeng Taofang and Fu Weibiao , The ratio CO/CO2 of carbon oxidation on a burning carbon surface, Combust. Flame (accepted for publication), 1995.

SECTION 6

TASK 5.2: PULVERIZED COAL COMBUSTION STUDIES UNDER REDUCING CONDITIONS IN A CONTINUOUS, SELF-SUSTAINED LABORATORY SCALE REACTOR

(University of Arizona)

This work performed under this task consisted of two major efforts. The first effort was to model the fate of iron during coal combustion. Early in this program a model was developed to describe the partitioning of iron during pulverized coal combustion. This model was described in earlier quarterly reports and in the literature (Bool et al, 1995). Later in the program modifications were to better define, or eliminate, the two fit parameters of the original model. Both versions of the model were based on the premise that pyrite (FeS_2) decomposes to pyrrhotite ($Fe_{0.877}S$) early in the combustion process. The pyrrhotite is involved in competing processes leading to iron in the flyash particles as iron oxide and iron ions captured in silicate glass. Remaining pyrrhotite might also be found in the flyash, especially if the coal was burned under substoichiometric conditions. This section describes a kinetic model of the transformation processes including oxidation of solid and liquid pyrrhotite, crystallization of magnetite, and capture of iron ions in silicate glass. A distinction between the behavior of the inherent and extraneous iron is made within the kinetic model.

Another major part of this effort was the design and setup of a number of fundamental experiments to collect more data on iron partitioning. A drop tube aerosol reactor was designed and constructed for combustion of pulverized coal under well controlled conditions. A major portion of this work was the construction of a new feed system, which allows quasi-constant feed rates down to 4 g/h. After characterizing and testing the drop tube reactor a number of experiments were performed with an Illinois No. 6 and a Pittsburgh No. 8 coal.

6.1 Iron Partitioning Model

The model discussed here was developed by L. Bool (1993) early in this program. The model was then modified by the authors to better describe the crystallization process and to better understand the significance of the two fit parameters in the original model. Bool and others found that iron in ash particles from pulverized coal combustion occurs primarily as iron oxide (as magnetite, Fe_3O_4 or hematite, Fe_2O_3,), or as ions captured in a silicate glass (both Fe (II) and Fe (III)). Bool then derived a pathway for this partitioning, in which a distinction is made between the extraneous iron, and the inherent iron . In ash from extraneous iron-bearing minerals there is typically no appreciable amount of other species. On the other hand, ash from inherent iron typically contains other species and is normally found as ash agglomerates. Both the extraneous and the inherent iron-containing species in coals occur predominantly as pyrite (FeS_2), which undergoes a decomposition to pyrrhotite ($Fe_{0.877}S$) at 800K-900K.

The extraneous pyrrhotite immediately starts to oxidize, building an iron oxide shell around a pyrrhotite core. If the particle temperature exceeds 1356K the pyrrhotite begins to melt. We then have to consider the particles as Fe-O-S droplets. As long as sulfur is remaining within this melt, oxidation continues. After all the sulfur has been removed, crystallization of magnetite out of the Fe-O-melt takes place. This crystallization occurs as long as the temperature reaches, or is below, 1600 K, and the temperature gradient is negative. During crystallization, the assumption is made that the temperature remains constant. If the particle temperature subsequently exceeds 1870 K, the magnetite melts, and will crystallize again when the temperature falls below 1600 K. In order to simplify the model, two assumptions are made. The first is that extraneous pyrite does not interact with other ash particles. Secondly, the fragmentation of the pyrrhotite will be neglected.

For the inherent pyrite the model assumes that the pyrite decomposes to pyrrhotite and melts while inside the carbon matrix. As the char burns away, pyrrhotite begins to oxidize and Fe-O-S-melts occur on the char surface. Then the possibility of Fe-O-S-melts or Fe-O-melts contacting silicate melts (which occur at temperatures over 1258 K) on the surface of the char particles increases with decreasing char surface. If no contact occurs between these particles, iron oxide forms out of an Fe-O-S-melt following the same

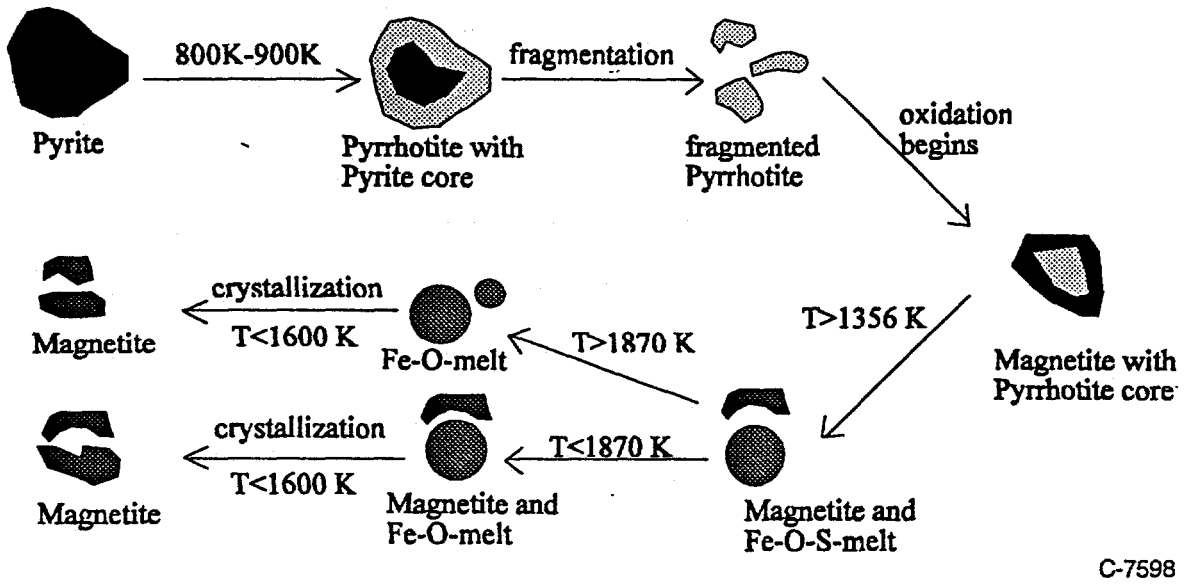

Figure 6-1. Pathways for the behavior of extraneous pyrite.

pathways as described for the extraneous pyrite. Otherwise, if these particles contact each other, iron ions start to diffuse into the silicate particle. This process, where the iron ions are moving into the glassy matrix, and become later on part of the solidified glass, is defined as 'glass capture'. If the temperature is below 1600 K and the temperature gradient is negative, a competition between crystallization and diffusion occurs, in which both processes consume ionic iron. The original model neglected the potential for iron oxide crystallization from the silicate melt - assuming the melt formed an iron-containing glass. However, as the presence of iron oxide crystals in the melt may dramatically affect its deposition behavior, this issue must be addressed in more detail. One important parameter controlling glass formation is the rate of quenching. If the quench rate is very fast, crystallization within the glassy matrix will not take place. Otherwise, iron oxide might crystallize within the glassy matrix.

Based on these pathways, a kinetic model was developed, describing the important steps of the discussed mechanism. These are: oxidation of solid pyrrhotite, oxidation of a Fe-O-S-melt, crystallization of magnetite, and glass capture. This leads to the determination of the iron partitioning between iron oxide and iron in glassy phases. Additional information that is critical to the success of the model is the particle time-temperature history and the char burnout rate.

6.1.1 Time-Temperature-History

The gas time-temperature-history is a major environmental variation for all processes occurring in coal combustion. The time-temperature history is dependent on the furnace design, furnace operating conditions, and the coal characteristics. Therefore, for the purposes of this model the measured gas temperature profile was fitted to the following equation:

$$T_g = a_1 \cdot \exp(-a_2 \cdot (t + a_4)) \cdot (1 - \exp(-a_3 \cdot (t + a_4))) + a_5 \quad . \qquad (6\text{-}1)$$

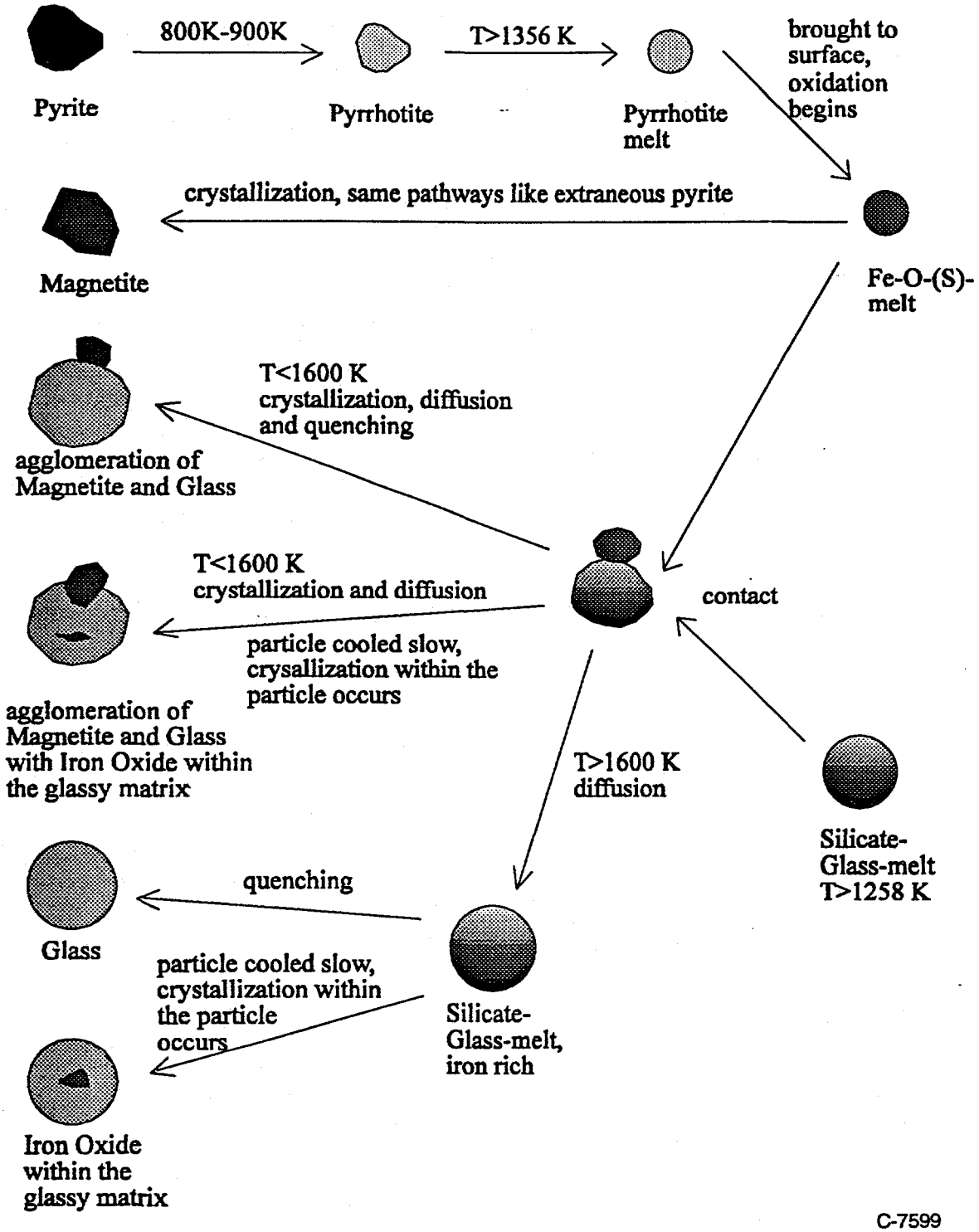

Figure 6-2. Pathways for the behavior of inherent pyrite.

This function was used by Bool (1993) and Gallagher (1992). The first parameter, a_1, sets the peak, a_2 determines the rise, and a_3 the drop of the temperature. The offset a_4 and the constant a_5 are responsible for the temperature at the start (time zero).

The second important temperature is that of the char particle. It was assumed that the temperature is the same throughout the particles. Therefore, the char particle temperature is also the temperature of the inherent pyrite. Taking into account conduction, radiation, and reaction terms for the char burnout, the energy balance leads to (Bool, 1993):

$$\frac{dT_{char}}{dt} = \frac{A_{char} \cdot (h_{char} \cdot (T_g - T_{char}) + \sigma \varepsilon (T_w^4 - T_{char}^4)) + \Delta H_c \frac{dm_{char}}{dt}}{c_{p,char}\, m_{char}} . \qquad (6\text{-}2)$$

Correlations for the heat of the reaction ΔH_c , the specific heat capacity $c_{p,char}$, the wall temperature T_w and the particle emissivity ϵ were given by Gallagher (1992). σ is the Stefan-Boltzmann-constant. The radius of the char particles R_{char} is given by Eq. (6-13). By assuming a constant density of the char for each coal, the particle mass might be calculated by assuming spherical particles, and the gradient is given by Eq. (6-9). The heat transfer coefficient h_{char} is given by Bool (1993) taken from work by Jorgensen (1981). It is based on the mean film temperature, taking into account the radius of the char particle and a reference temperature $T_{ref=298\,K}$.

$$\Delta H_c = \frac{1}{12} \cdot \left(106462 + 3.4332\, T_{char} + 0.00126\, T_{char}^2 + \frac{891788}{T_{char}} \right) \left[\frac{kJ}{kg} \right] \qquad (6\text{-}3)$$

$$c_{p,char} = \frac{1}{12} \cdot \left(16.873 + 0.004773 \cdot T_{char} - \frac{854107.2}{T_{char}^2} \right) \left[\frac{kJ}{kg \cdot K} \right]$$

$$T_w = 0.98 \cdot T_g;\ \varepsilon = 0.8;\ \sigma = 5.78 \cdot 10^{-8} \left[\frac{W}{m^2 \cdot K^4} \right] \qquad (6\text{-}4)$$

$$h_{char} = \frac{0.0242 \left[\frac{W}{m \cdot K} \right]}{R_{char}[m]} \cdot \left(\frac{T_g + T_{char}}{2\, T_{ref}} \right)^{0.75} . \qquad (6\text{-}5)$$

When char combustion is complete, the ash temperature might still be above 1600 K. Therefore, the time-temperature-history of the ash may be important for the partitioning of the inherent iron after burnout. Equation (6-3) becomes:

$$\frac{dT_{ash}}{dt} = \frac{A_{ash} (h_{ash} (T_g - T_{ash}) + \sigma \varepsilon (T_w^4 - T_{char}^4))}{c_{p,ash}\, m_{ash}} \qquad (6\text{-}6)$$

where the ash mass is the mass of ash particles formed from the char. The radius and the temperature of the char in Eq. 6-5 have to be replaced by the radius of a mean ash particle and the temperature of the ash to determine h_{ash}. Both ash mass distributions and ash particle size distributions for different coals are given by Bool (1993). The specific heat capacity might vary within wide ranges depending on the composition of the ash particles, but the composition of the ash for the coals of interest was determined by Foster Wheeler Development Corp. and given by Bool (1993). Therefore the mean specific heat capacity can be calculated based on a weighted average of the specific heat of the components.

The last temperature which is important for the model is the temperature of the extraneous pyrite and its products. As noted above, it is assumed that the extraneous pyrite will not interact with other minerals. Therefore, the state of oxidation and crystallization is a function of time without influence on the partitioning. In order to achieve a kinetic model which gives a complete description of the iron behavior during combustion, the formation of magnetite from extraneous pyrite is included. This makes it necessary to determine the time-temperature-history of the extraneous particles. An energy balance for the oxidation of solid pyrrhotite is given by Scrinivasachar et al. (1989):

$$\frac{dT_p}{dt} = \frac{A_p\left(h_p\left(T_g - T_p\right) + \sigma\,\varepsilon\left(T_w^4 - T_{char}^4\right)\right) + \Delta H_r \dfrac{dN_{O_2,R}}{dt}}{c_{p,Fe_{0.877}S}\, m_{Fe_{0.877}S}} \tag{6-7}$$

where the heat of the reaction was found to be $\Delta H_r = -201.24$ kJ/(mole O_2), and the specific heat capacity should be constant at $c_{p,Fe_{0.887}S} = 0.6534$ kJ/(kg·K) . The other values and correlations are the same as given for the char particle energy balance, except the heat transfer coefficient given by Eq. (6-5), where the radius and the temperature of the char particle have to be replaced by the radius and the temperature of the pyrrhotite particle. The radius of a pyrrhotite particle is given later in this section by Eq. (6-45), and the particle mass (particles assumed to be spheres) might then be calculated by taking into account the density of solid pyrrhotite, given by Raask (1985) to be $\rho_{Fe_{0.887}S} = 4600$ kg/m^3. The radius gives as well the surface area of the particle.

As the pyrrhotite melts at 1356 K, the melting and the oxidation result in a period where the particle temperature is constant. This period is assumed to be short and is therefore neglected. After melting, oxidation of the Fe-O-S-melt droplet takes place. Srinivasachar et al. (1989) found the same heat balance with $\Delta H_r = 190.1$ kJ/(mole O_2) and $c_{p,Fe\text{-}O\text{-}S} = 1.1669$ kJ/ · K); this value is calculated at 1800 K. The radius of the extraneous Fe-O-S-melt particles is given by Eqs. (6-52) and (6-53). That of the inherent melt particles is given by Eq. (6-103). The density is taken to be the arithmetic mean of the density of magnetite and pyrrhotite, giving $\rho_{Fe\text{-}O\text{-}S} = 4359.5$ kg/m^3. These values lead to the particle mass and the surface area.

As all the sulfur is consumed and the char burned away, the Fe_3O_4-melt droplet begins to cool depending on the gas temperature. As in the earlier energy balance, the full equation then reduces to:

$$\frac{dT_P}{dt} = \frac{A_p\left(h_p\left(T_g - T_p\right) + \sigma\,\varepsilon\left(T_w^4 - T_P^4\right)\right)}{c_{p,Fe\text{-}O_4}\, m_{Fe\text{-}O}} \,. \tag{6-8}$$

The specific heat of a Fe_3O_4-melt is again given by Srinivasachar et al. (1989) as $c_{p,Fe_3O_4}=0.9015 kJ/(kg \cdot K)$. The radius of the inherent magnetite melt particles is discussed later and given by Eq. (6-102), and for the extraneous particles by Eqs. (6-52) and (6-53) at the time all the sulfur is consumed. The density of a magnetite melt is taken to be that of a Fe-O-melt, found in Slag Atlas (1981) to be $\rho_{Fe_3O_4(l)} = 4719$ kg/m^3.

Finally, if the droplet reaches 1600 K, the temperature again remains constant until a solid magnetite particle is formed due to the heat of crystallization. If the particle temperature never exceeds 1600 K, it is assumed that the crystallization takes place as soon as oxidation of the melt is complete.

6.1.2 Char Burnout

For the determination of the behavior of the inherent pyrite, it is very important to know the char burnout rate. Char burnout determines when a molten pyrrhotite particle is exposed on the surface of the char particle, and is also a major variable for the contact of Fe-O-(S)-melts and silicate melts on the surface.

The char burnout starts at a temperature of approximately 600 K. Hurt and Mitchell (1992) found in an empirical study the following function for the char burnout rate:

$$\frac{dm_{char}}{dt} = -K_c \exp\left(\frac{-E_c}{R\,T_{char}}\right) A_{char}\, p_{O_2,s}^{0.5} \qquad (6\text{-}9)$$

where the rate is depending on the char temperature, the char surface area, and the partial oxygen pressure on the surface. The parameters E_c and K_c were given as a function of the weight percentage of carbon in the coal.

$$E_c = -0.02487 + 1.486 \cdot 10^{-3}\{\text{wt\%C}\}\,[\text{kJ/kmole}] \qquad (6\text{-}10)$$

$$K_c = \frac{1}{\sqrt{98100}} \exp\left(28 - 0.758 \cdot \{\text{wt\%C}\} + \frac{E_c}{R \cdot 1750\text{K}}\right) \left[\text{kg}/(\text{m}^2 \cdot \text{s} \cdot \text{Pa}^{0.5}\right] \ . \qquad (6\text{-}11)$$

The change of the char particle radius can be calculated from Eq. (6-9) by replacing the mass with the product of the density (assumed to be constant) and the volume. This gives:

$$\frac{dm_{char}}{dt} = \frac{d}{dt}\left(\rho_{char}\frac{4}{3}\pi R_{char}^3\right) = \rho_{char} A_{char} \frac{dR_{char}}{dt} \qquad (6\text{-}12)$$

$$\Rightarrow \frac{dR_{char}}{dt} = -\frac{K_c}{\rho_{char}} \exp\left(\frac{-E_c}{R\,T_{char}}\right) p_{O_2,s}^{0.5} \tag{6-13}$$

where the starting value $R_{char,0}$ is given for different coals by Bool (1993). The partial oxygen pressure on the surface of the char particle was also found by Bool (1993). He assumed a steady state between oxygen transport and oxygen consumption, and CO as the reaction product, leading to

$$C + \frac{1}{2} O_2 \rightarrow CO \tag{6-14}$$

$$A_{char} \cdot \frac{D_g}{R_{char}} \cdot \frac{p_{O_2} - p_{O_{2s}}}{R \cdot T_g} = -\frac{1}{2 \cdot M_c} \cdot \frac{dm_{char}}{dt} \tag{6-15}$$

where D_g is the diffusion coefficient for the diffusion through the gaseous boundary layer and M_c the molecular weight of carbon. Based on this equation, the surface oxygen concentration is given by Eqs. (6-16) through (6-19).

$$p_{O_{2,s}} = \left(\frac{1}{2A}\left(-B + \sqrt{B^2 - 4A \cdot C}\right)\right)^2 [Pa] \tag{6-16}$$

$$A = \frac{2 D_g M_C}{R_{char} R \cdot T_g} \left[kg/(m^2 \cdot s \cdot PA)\right] \tag{6-17}$$

$$B = K_c \exp\left(\frac{-E_c}{R\,T_{char}}\right) \left[kg/(m^2 \cdot s \cdot Pa^{0.5})\right] \tag{6-18}$$

$$C = -A \cdot p_{O_2} \; [kg/(m^2 \cdot s)] \tag{6-19}$$

where the diffusion D_g coefficien is given by Jorgensen (1981) with a reference temperature of $T_{ref} = 1800$ K:

$$D_g = 4.26 \cdot \left(\frac{T_{char} + T_g}{2 \cdot T_{ref}} \right)^{1.75} \; [m^2/s] \; . \qquad (6\text{-}20)$$

This diffusion coefficient was determined during Jorgensen's work on pyrite transformation. It describes the diffusion of oxygen through a gaseous boundary layer to a pyrite particle and was fitted to data achieved in that work. Thus it is difficult to say if this approach fits for the diffusion of oxygen through a gaseous boundary layer to a char particle, as it is assumed here, and was assumed by Bool (1993). The partial pressure of oxygen in the main stream was also given by Bool (1993). He assumed that the main substances existing as gas in the stream are O_2, H_2O, CO and CO_2. This leads to:

$$p_{O_2} = \frac{N_{O_2}}{N_{O_2} + N_{H_2O} + N_{CO} + N_{CO_2}} \cdot p = \frac{N_{O_2}}{N_t} \cdot p \qquad (6\text{-}21)$$

where p is the pressure in the combustor and N are the moles. It was now assumed that the oxygen consumption by char burnout is much larger than oxygen consumption by other sources (ie: pyrite oxidation). During char burnout, an equilibrium between CO and CO_2 exists:

$$CO + \frac{1}{2} O_2 \leftrightarrow CO_2 \; . \qquad (6\text{-}22)$$

The forward and backward reaction rates, R_f and R_b, were given by Dryer et al. (1973) and by Westbrook et al. (1981) respectively:

$$R_f = 3.8 \cdot 10^{17} V_g \exp\left(-\frac{E_{CO}}{R T_g} \right) \cdot \left(\frac{N_{CO}}{V_g} \right) \left(\frac{N_{H_2O}}{V_g} \right)^{0.25} \cdot \left(\frac{N_{O_2}}{V_g} \right)^{0.5} \; [kmole/s] \qquad (6\text{-}23)$$

$$R_b = 1 \cdot 10^{14} V_g \cdot \exp\left(-\frac{E_{CO}}{R T_g} \right) \cdot \left(\frac{N_{CO_2}}{V_g} \right) \cdot [kmole/s] \qquad (6\text{-}24)$$

$$V_g = \frac{N_t R \cdot T_g}{p} \; [m^3]$$

$$E_{CO} = 167367 \; [kJ/kmole] \; ; \left(\frac{N}{V_g} \right) \; [mole/cm^3] \; . \qquad (6\text{-}25)$$

This leads to the balances for O_2, CO and CO_2, taking into account the relation for the char burnout (9) (Bool, 1993):

$$\frac{dN_{O_2}}{dt} = \frac{1}{2 \cdot M_c} \cdot \frac{dm_{char}}{dt} + \frac{1}{2}\left(R_b - R_f\right) \tag{6-26}$$

$$\frac{dN_{CO}}{dt} = \frac{1}{M_c} \cdot \frac{dm_{char}}{dt} + \frac{1}{2}\left(R_b - R_f\right) \tag{6-27}$$

$$\frac{dN_{CO_2}}{dt} = \left(R_f - R_b\right) . \tag{6-28}$$

Finally, we have to determine the moles of water in the gas. We assume that all the water (moisture) included in the coal vaporizes rapidly. Therefore, the moles of water in the stream are equivalent to the moles of water in the coal, which were determined for the coals of interest by Foster Wheeler Development Corp. and given by Bool (1993).

6.1.3 Oxidation of a Solid Pyrrhotite Particle

A detailed model describing the kinetics of this process was given by Srinivasachar et al. (1989). He supposed a model for pyrite oxidation which was also used by Bool (1993). The reaction he used to describe pyrite oxidation is:

$$\frac{3}{0.877} Fe_{0.877}S(s) + \left(2 + \frac{3}{2 \cdot 0.877}\right) O_2(g) \rightarrow Fe_3O_4(s) + \frac{3}{0.877} SO(g) . \tag{6-29}$$

Based on this reaction rate, and data in the literature, Srinivasachar (1989) developed a rate equation for oxidation of solid pyrite. Although this model fits the experimental data well, a change is suggested in rate equation to take into account the geometry of the process. Using the shrinking core model given by Smith (1990), we derived an equation similar to the equation given by Srinivasachar et al. (1989), with a different overall rate coefficient (including the reaction rate and the mass transfer rates). This equation may yield a more reasonable overall rate, with a better approach for the determining mass transfer coefficient in the condensed phases. This may provide more information that the fit proposed by Srinivasachar (1989) who found a linear function between gas and solid mass transfer, which he fitted within the temperature ranges of interest.

In the shrinking core model, the particles are assumed to be spheres. The solid reactant is placed in the core and the solid product building a shell around it. If we look at the oxygen transport and consumption in this process, we can distinguish three rates: the rate for the external diffusion (gaseous boundary layer), the rate for the diffusion through the iron oxide shell of the particle, and the reaction rate.

Assuming that the reaction occurs at the boundary of iron oxide shell and pyrrhotite core yield the following equation:

$$-\frac{dN_{O_2,R}}{dt} = A_p k_g (C_s - C_p) = A_c D_{sl} \cdot \left(\frac{\partial C}{\partial r}\right)_{r=R_c} = A_c k \cdot C_c \qquad (6\text{-}30)$$

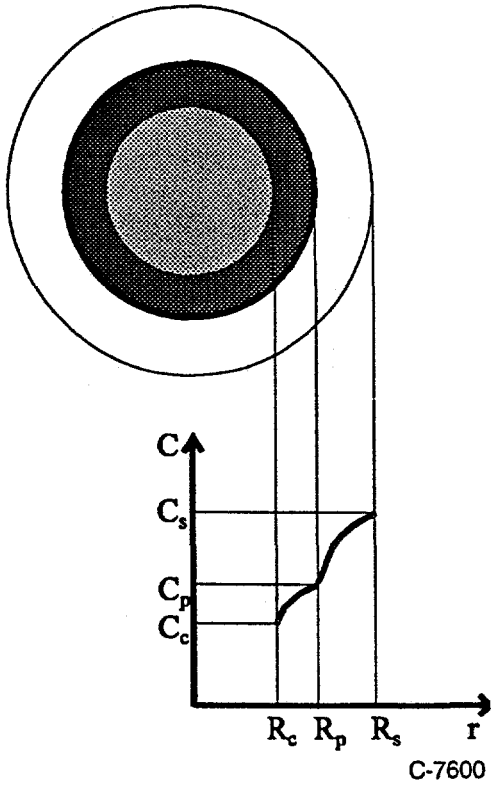

Figure 6-3. Shrinking core model.

where the first term describes the external diffusion, the second term the diffusion through the shell, and the last term the reaction. The variable $N_{O_2,R}$ is used instead of N_{O_2} to indicate this is not the over-all oxygen consumption, which was discussed for char burnout, but only the oxygen consumption for this particular reaction. This variable is used for the calculation here and has no influence on the model. The index 's' stands for stream, 'p' for particle surface and 'c' for core surface. The surface areas are described with 'A', the concentrations with 'C', k_g is the gas mass transfer coefficient, D_{sl} the diffusion coefficient for the diffusion through the solid layer, and k the reaction rate. To get the concentration gradient, Smith (1990) assumes a pseudo-steady-state for the diffusion through the product. This leads to:

$$\frac{\partial C}{\partial t} = 0 = \frac{D_{sl}}{r^2} \cdot \left(\frac{\partial}{\partial r} \cdot r^2 \cdot \frac{\partial C}{\partial r}\right) \qquad (6\text{-}31)$$

Taking into account the boundary conditions, which are given by the concentrations on the surface of the particle and the core, we receive:

$$C(r) = \frac{C_p R_p (r - R_c) + C_c R_c (R_p - r)}{r \cdot (R_p - R_c)} \quad . \tag{6-32}$$

Deriving that equation referring to r at $r = R_c$ brings:

$$\left(\frac{\partial C}{\partial r}\right)_{r+R_C} = \frac{R_p (C_p - C_c)}{R_c \cdot (R_p - R_c)} \quad . \tag{6-33}$$

Substituting into the main Eq. (6-30) leads to two equations for C_c, C_p and C_s,. Therefore, we are able to eliminate C_p and find a relation between C_c and C_s.

$$C_c = \frac{C_s}{1 + \left(\frac{R_c}{R_p}\right)^2 \cdot \frac{k}{k_g} + \left(1 - \frac{R_c}{R_p}\right) \cdot \frac{k \cdot R_c}{D_{sl}}} \quad . \tag{6-34}$$

This equation for the oxygen transport and consumption rate can then be inserted into the reaction rate part of the main Eq. (6-30). By taking into account the stoichiometries, we can also determine rates for iron oxide formation and pyrrhotite consumption. The concentration of oxygen in the stream is given by the ideal gas law (Eq. 6-38).

$$-\frac{dN_{O_2,R}}{dt} = \frac{4 \cdot \pi \cdot R_c^2 \cdot C_s}{\frac{1}{k} += \frac{1}{k_g} \cdot \left(\frac{R_C}{R_p}\right)^2 + \frac{R_c}{D_{sl}} \cdot \left(1 - \frac{R_c}{R_p}\right)} \tag{5-35}$$

$$\frac{dN_{Fe_3O_4}}{dt} = -\frac{\alpha}{\beta} \cdot \frac{dN_{O_2,R}}{dt} \tag{6-36}$$

$$\frac{dN_{Fe_{0.877}S}}{dt} = \frac{1}{\beta} \cdot \frac{dN_{O_2,R}}{dt}$$

$$\alpha = \frac{0.877}{3} \; ; \; \beta = \frac{2 \cdot 0.877}{3} + \frac{1}{2} \tag{6-37}$$

$$C_s = \frac{p_{O_2}}{R \cdot T_g} \,. \tag{6-38}$$

Equations for k and k_g were proposed by Srinivasachar et al. (1989) and used by Bool (1995). The reaction rate constant k follows an Arrhenius equation:

$$k = k_o \cdot \exp\left(\frac{-E_s}{R \cdot T_p}\right) \tag{6-39}$$

where the activation energy E_s was found to be $1.5 \cdot 10^5$ kJ/kmole and the constant k_0 was found to be $5 \cdot 10^7$ m/s. For the gas phase mass transfer coefficient, k_g, the Sherwood number was assumed to be 1, and the diffusion coefficient was found by Jorgensen (1981) to follow a Fuller-type correlation. This leads to:

$$k_g = \frac{D_g}{R_p} = \frac{1}{R_p} \cdot D_{RE} \left(\frac{T_p + T_g}{2 \cdot T_{RE}}\right)^{1.75} \tag{6-40}$$

where the reference diffusion coefficient D_{RE} was given to be $4.26 \cdot 10^{-4}$ m²/s at a reference temperature T_{RE} of 1800 K. The mean particle radius is defined as that of the pyrrhotite particle at time zero, and the radius of the core is given by the decrease of pyrrhotite as a differential function in time, leading to a system of differential equations:

$$\frac{dN_{Fe_{0.877}S}}{dt} = \frac{\rho_{Fe_{0.877}S}}{M_{Fe_{0.877}S}} \cdot \frac{d}{dt}\left(\frac{4}{3} \cdot \pi \cdot R_c^3\right) = \frac{\rho_{Fe_{0.877}S}}{M_{Fe_{0.877}S}} \cdot 4 \cdot \pi \cdot R_c^2 \cdot \frac{dR_c}{dt} \tag{6-41}$$

$$\Rightarrow \frac{dR_c}{dt} = \frac{M_{Fe_{0.877}S}}{\rho_{Fe_{0.877}S}} \cdot \frac{1}{\beta} \cdot \frac{C_s}{\frac{1}{k} + \left(\frac{R_c}{R_p}\right)^2 \cdot \frac{1}{k_g} + \left(1 - \frac{R_c}{R_p}\right) \cdot \frac{R_c}{D_{sl}}} \tag{6-42}$$

where the density of solid pyrrhotite $\rho_{Fe_{0.877}S} = 4600$ kg/m³ is given by Raask (1985) and $M_{Fe_{0.877}S}$ is the molecular weight of pyrrhotite. The diffusion coefficient D_{sl} for oxygen, diffusing through a porous solid layer of iron oxide, has to be found. Because we have to deal within a wide temperature range (850K to 1356K), we shall try to find the diffusion coefficient as a function of the temperature, probably fitting an Arrhenius equation. The initial condition for the core radius is the extraneous pyrite particle radius.

The decomposition of pyrite is given by the equation:

$$FeS_2(s) = \frac{1}{0.877}\,Fe_{0.877}S(s) + \left(1 - \frac{1}{2\cdot 0.877}\right) S_2(g) \qquad (6\text{-}43)$$

as found by Srinivasachar (1989). Therefore, the mass of pyrrhotite is related to the mass of pyrite by:

$$m_{Fe_{0.877}S} = \frac{1}{0.877}\cdot\frac{M_{Fe_{0.877}S}}{M_{pyr}}\cdot m_{pyr}\ . \qquad (6\text{-}44)$$

This result leads to the pyrrhotite radius:

$$R_{Fe_{0.877}S} = \left(\frac{1}{0.877}\cdot\frac{M_{Fe_{0.877}S}}{M_{pyr}}\cdot\frac{\rho_{pyr}}{\rho_{Fe_{0.877}S}}\right)^{1/3}\cdot R_{ext,pry}\ . \qquad (6\text{-}45)$$

where the mean radius of the extraneous pyrite particles $R_{ext,pyr}$ is given for different coals by Bool (1993).

6.1.4 Oxidation of a Fe-O-S-Melt

A description of the oxidation kinetics occurring is again given by Srinivasachar et al. (1989) and also used by Bool (1993). The reaction is assumed to be the same as that occurring in solid state, with the difference that the pyrrhotite (and magnetite) are molten. Therefore:

$$\frac{3}{0.877}Fe_{0.877}S(\ell 1) + \left(2 + \frac{3}{2\cdot 0.877}\right) O_2(g) \rightarrow Fe_3O_4(\ell 1) + \frac{3}{0.877}SO(g)\ . \qquad (6\text{-}46)$$

Again the reaction is divided into three steps: external diffusion, diffusion through a liquid boundary layer, and a reaction rate. We are therefore able to take a similar approach to that of the shrinking core model (assuming no recirculation in the melt):

$$\frac{dN_{O_2,R}}{dt} = A_R\,k_g\left(C_2 - C_R\right) = A_{R-\delta}\cdot D_{11}\left(\frac{\partial C}{\partial r}\right)_{r=R-\delta} = A_{R-\delta}\,k\cdot C_{R-\delta} \qquad (6\text{-}47)$$

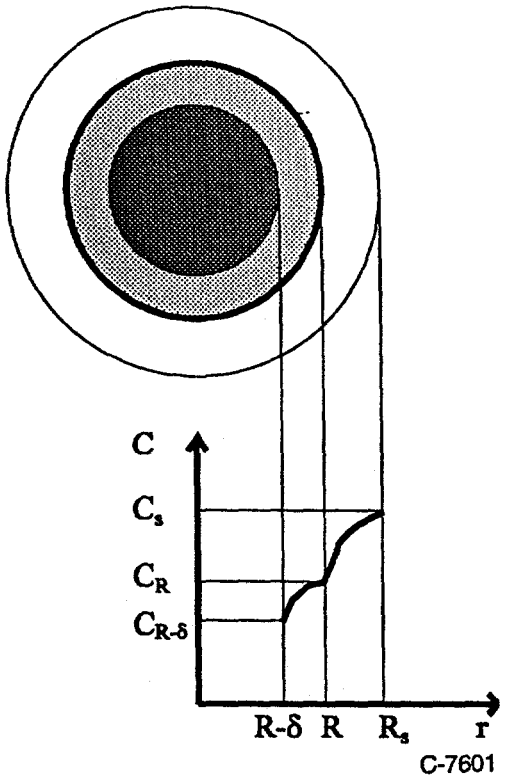

Figure 6-4. Oxidation of a Fe-O-S-melt.

where δ is the thickness of the liquid boundary layer and R the radius of the droplet, assumed as a sphere. For δ, an approach defining a linear relation between radius and boundary layer thickness is proposed:

$$\delta = K_1 \cdot R \tag{6-48}$$

where $0<K_1<0.1$ should be the range for the constant. Assuming now again a pseudo-steady-state diffusion, this time through the liquid boundary layer, we find:

$$\left(\frac{\partial C}{\partial r}\right)_{r=R-\delta} = \frac{C_R - C_s}{K_1 \cdot R \cdot (1-K_1)} \; . \tag{6-49}$$

From the analysis presented earlier for the shrinking core model, we derive an equation for the oxygen consumption:

$$-\frac{dN_{O_2,R}}{dt} = \frac{4 \cdot \pi \cdot R^2 \cdot (1-K_1)^2 \cdot C_s}{\frac{1}{k} + \frac{1}{k_g} \cdot (1-K_1)^2 + \frac{R}{D_{11}} \cdot K_1 (1-K_1)} \; . \tag{6-50}$$

The rates for iron oxide formation and for pyrrhotite consumption are also given as described in the previous section. Now we take into account a variable droplet radius in place of a variable particle radius:

$$\frac{M_{Fe_{0.877}S}}{\rho_{Fe_{0.877}S(1)}}\cdot\frac{dN_{Fe_{0.877}S}}{dt}+\frac{M_{Fe_3O_4}}{\rho_{Fe_3O_4(1)}}\cdot\frac{dN_{Fe_3O_4}}{dt}=\frac{d}{dt}\left(\frac{4}{3}\cdot\pi\cdot R^3\right)=4\cdot\pi\cdot R^2\cdot\frac{dR}{dt} \tag{6-51}$$

$$\Rightarrow \frac{dR}{dt}=\left[\frac{M_{Fe_3O_4}}{\rho_{Fe_3O_4(\ell)}}\cdot\frac{\alpha}{\beta}-\frac{M_{Fe_{0.877}S}}{\rho_{Fe_{0.877}S(\ell)}}\cdot\frac{1}{\beta}\right]\cdot\frac{C_s\cdot(1-K_1)^2}{\frac{1}{k}+(1-K_1)^2\cdot\frac{1}{k_g}+(1-K_1)\cdot K_1\cdot\frac{R}{D_{11}}}\cdot \tag{6-52}$$

This leads again to a differential equation system, where α, β and C_s are given in the previous section, and k and k_g again are determined by the Eqs. (6-39) and (6-40) given by Srinivasachar et al. (1989). For the inherent Fe-O-S-melt, the particle temperature T_p in Eqs. (6-39) and (6-40) has to be replaced by either the char temperature or the ash temperature. The density of liquid magnetite is taken to be that of an Fe-O-melt found in Slag Atlas (1981) to be $\rho_{Fe_3O_4(1)} = 4719$ kg/m^3. The density of liquid pyrrhotite was estimated to be $\rho_{Fe_{0.877}S(1)} = 4000$ kg/m^3. D_{11} is the effective diffusion coefficient for oxygen diffusing through a liquid boundary layer of an Fe-O-S-melt, which has to be found. Here again we have to deal within a wide temperature range, and to achieve a relation between the temperature and the diffusion coefficient should be the goal. The starting value for the extraneous pyrrhotite particle radius is that of the core radius at the melting point, multiplied with the cube root of the ratio of liquid to solid pyrrhotite density Eq. (6-53), to take into account the expansion caused by the change of state.

$$R_{Fe_{0.877}S,ex}=\left(\frac{\rho_{Fe_{0.877}S}}{\rho_{Fe_{0.877}S(1)}}\right)^{1/3}\cdot R_c \qquad \left[(T_p = 1356K)\right]. \tag{6-53}$$

For the inherent pyrite particles, the progress of the reaction is different for each particle, depending on when they were exposed. Therefore, we are not able to take into account the change of the particle radius with time, but have to find a mean radius. This mean radius is taken as the arithmetic mean between a pure pyrrhotite melt particle and the corresponding pure magnetite melt particle, given by Eq. (6-53). The change caused by iron diffusing into silicate melts and by contraction due to partial crystallization was neglected.

6.1.5 Crystallization of Magnetite

To this point, much of the work described was similar to the original model given by Bool (1993). However, in the original model no attempts were made to quantify the iron oxide crystallization step. To address this issue, the crystallization behavior of magnetite melts under combustion conditions was modeled.

Crystallization out of slag melts is, in most practical situations, determined by crystal growth (Turkdogan, 1985). This is due to the large number of impurities in the melts, which are related to the

nature of coals and their ashes. These impurities cause heterogeneous nucleation, resulting in very fast nucleation rates. Therefore, in this model the nucleation rate is neglected. During crystallization, the heat of crystallization and the cooling of the particle are assumed to balance - yielding a constant equilibrium temperature. This constant temperature yields a constant concentration of nuclei in the melt. These nuclei have the size of the critical nucleus, which is determined by the temperature and the degree of supercooling.

6.1.5.1 Crystal Growth

Mullin (1990) found that the driving force for crystal growth in metal melts is the temperature difference between the melting temperature, which occurs at the surface of the crystal, and the temperature of the supercooled melt, leading to the equation:

$$\frac{dm}{dt} = Kg \cdot A \cdot (T^* - T)^n \qquad (6\text{-}54)$$

where Kg is an overall mass transfer coefficient, A is the crystal surface area, (T* - T) the temperature difference, and n an exponent. Mullin (1990) gives $1.5 < n < 2.5$. Therefore, n is assumed to be 2. Heat transfer during crystallization can be modeled as:

$$\frac{dq}{dt} = h \cdot A \cdot (T^* - T) = \Delta H_c \cdot \frac{dm}{dt} \qquad (6\text{-}55)$$

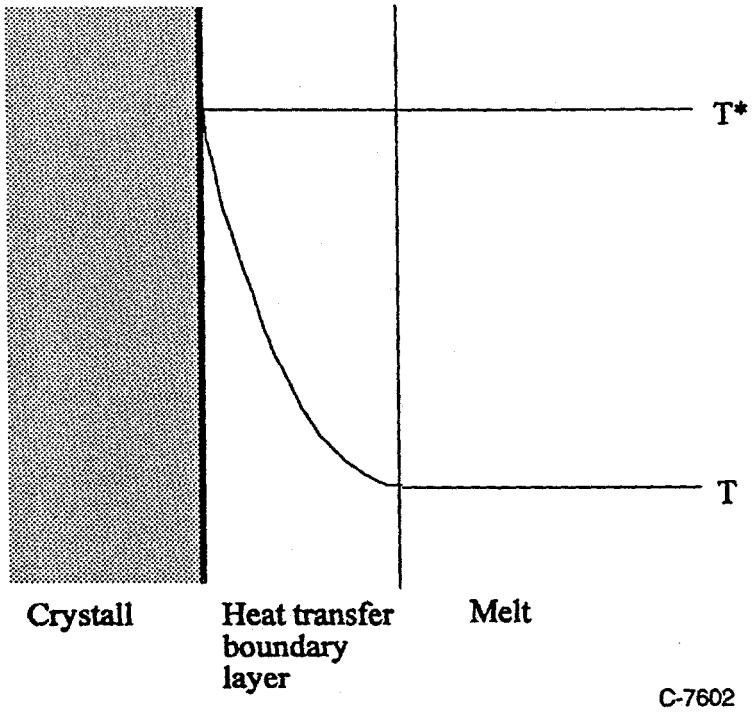

Figure 6-5. Crystallization from melts.

where h is the over-all heat transfer coefficient and ΔH_c the crystallization enthalpy. This equation yields:

$$K_g = \frac{h}{(T^* - T)^{n-1} \cdot \Delta H_c} = \frac{h}{(T^* - T) \cdot \Delta H_c} \quad (5\text{-}56)$$

Assuming the crystal is a sphere with radius R, and that $h = k/\delta$, where k is the heat conductivity coefficient of molten magnetite, and δ the thickness of the effective heat transfer boundary layer (assumed to $\delta = \alpha \cdot R$) we obtain:

$$\frac{dm}{dt} = \frac{4 \pi k R (T^* - T)}{\alpha \cdot \Delta H_c} \quad (5\text{-}57)$$

Remembering that magnetite melts at 1870K, that crystallization of magnetite starts at 1600K, and that the temperature is assumed to be constant during crystallization, the temperature difference is 270K. The crystallization enthalpy is assumed to equal the melt enthalpy which was found to be $\Delta H_c = 164.4$ kJ/kg (Saxena et. al., 1993). The thermal conductivity in this temperature range was estimated to be k=30W/(m°K) (Rohsenow et. al., 1985). A typical crystal radius should be $R = 5 \cdot 10^{-7}$m, and the factor for the thickness of the boundary layer might be estimated with α=0.5. This thick boundary layer is reasonable, because there is nearly no relative velocity between the crystal and the melt within the droplet (the viscosity of the melt is high), leading to heat transfer governed by conduction. There is also a large temperature gradient, which increases the boundary layer. These values lead to an approximation of the growth rate of: $dm/dt = 6.2 \cdot 10^{-7}$ kg/s. To get a better understanding of this result, we divide it by the particle volume $V = (4/3) \cdot \pi \cdot R^3$ and the density of solid magnetite (given by Raask (1985) as $\rho Fe_3O_4 = 5140$ dg/m^3). This leads to a crystallization time constant of: $\tau_c = 2.3 \cdot 10^8$ [1/s], which we will use to compare crystallization and diffusion rate in the next section.

As said before, the crystals are assumed to be spheres. Thus, we are able to determine the particle radius as a function of time:

$$m = \rho_{Fe_3O_4} \cdot \frac{4}{3} \cdot \pi \cdot R^3 \Rightarrow \frac{dm}{dt} = 4 \cdot \pi \cdot R^2 \cdot \rho_{Fe_3O_4} \cdot \frac{dR}{dt} \quad (5\text{-}58)$$

$$\frac{dR}{dt} = \frac{k \cdot (T^* - T)}{\alpha \cdot \rho_{FeE_3O_4} \cdot \Delta H_c} \cdot \frac{1}{R} \quad (6\text{-}59)$$

$$R(t) = \sqrt{\frac{2 \cdot k \cdot (T^* - T)}{\alpha \cdot \rho_{Fe_3O_4} \cdot \Delta H_c} \cdot t + R_0^2} \quad (6\text{-}60)$$

where R_0 is the radius at time zero, which should be the radius of a critical crystal nucleus. This leads to:

$$\frac{dm}{dt} = \frac{4 \cdot \pi \cdot k \cdot (T^* - T)}{\alpha \cdot \Delta H_c} \cdot \sqrt{\frac{2 \cdot k \cdot (T^* - T)}{\alpha \cdot \rho_{Fe_3O_4} \cdot \Delta H_c} \cdot t + R_0^2} \qquad (5\text{-}61)$$

as an equation for the rate of crystal growth of one magnetite crystal out of a Fe-O-melt. The crystallization rate for the total melt is then given by:

$$\frac{dm_{Fe_3O_4,cryst}}{dt} = n_{nuc} \cdot m_{Fe_3O_4(1)} \cdot \frac{4 \cdot \pi \cdot k \cdot (T^* - T)}{\alpha \cdot \Delta H_c} \cdot \sqrt{\frac{2 \cdot k \cdot (T^* - T)}{\alpha \cdot \rho_{Fe_3O_4} \cdot \Delta H_c} \cdot (t - t_0) + R_0^2} \qquad (6\text{-}62)$$

where t_0 is the time at which for the first time the temperature is below 1600 K, the sulfur is completely oxidized and the particle temperature gradient is negative.

For the inherent Fe-O-melt particles the difficulty, again, arises that each particle is brought to the surface at a different time. This leads to different conversion times for each particle. Because of the dependence of Eq. (6-62) on the starting time, we have to find a mean crystallization rate for the total mass of inherent Fe-O-melt, exposed between t_0 and t. To do this, we integrate Eq. (6-62) from t_0 to t, and divide the result by the difference of t and t_0. This leads to:

$$\frac{dm_{Fe_3O_4,cryst}}{dt}(inh) = n_{nuc} \cdot \frac{m_{Fe_3O_4(1)}}{t - t_0} \cdot \frac{4}{3} \cdot \pi \cdot \rho_{Fe_3O_4} \left(\frac{2 \cdot k \cdot (T^* - T)}{\alpha \cdot \rho_{Fe_3O_4} \cdot \Delta H_c} \cdot (t - t_0) + R_0^2 \right)^{3/2} . \qquad (6\text{-}63)$$

The starting time t_0 might be taken as the difference between the time, where the particle temperature is for the first time below 1600 K (t*) and accompanied by a negative temperature gradient, and the time step size made by the algorithm, which solves the differential equation system, in this step ($t_0 = t^* - \Delta t_{alg}$).

6.1.5.2 Nucleation

It can be seen in the Eq. (6-62) and (6-63), that the critical crystal nucleus radius R_0 is very important for the crystallization rate. It is also very important to know the number of nuclei n_{nuc} within one kg Fe-O-melt. In classical nucleation theory, the radius of the critical nucleus is given by:

$$R_o = \frac{2 \sigma \cdot T^*}{\rho_{Fe_3O_4(1)} \cdot \Delta H_c \cdot (T^* - T)} \qquad (5\text{-}64)$$

(Mullin 1993), where σ is the surface energy of the melt droplet. The surface energy for Fe-O-melts is given in Slag Atlas (1981) to be $\sigma = 5.84 \cdot 10^{-4}$ kJ/m^2, leading to an estimation of the crystal growth rate to a critical radius of $R_0 = 10^{-8}$m. The number of crystals per kilogram of melt is given by Sloan and McGhie (1988) to be:

$$n_{nuc} = \frac{n}{\rho_{Fe_3O_4}} \cdot \exp\left(-\frac{\Delta G}{k \cdot T} \right) \qquad (6\text{-}65)$$

where k is the Boltzmann-constant, ΔG the excess free energy for the nucleation of the critical nucleus, and n the number of molecules per unit volume in the nucleus. The molecular volume of magnetite is given by Saxena et al. (1993), and the number of molecules per unit volume can then be determined by dividing the Avogadro-constant with the molecular volume. This leads to $n = 1.3527 \cdot 10^{28}$ [1/m^3]. The excess free energy for heterogeneous nucleation is given by Mullin (1993) to be:

$$\Delta G_c = \Phi \frac{4}{3} \pi \sigma \cdot R_0^2 \qquad (6\text{-}66)$$

where Φ is a function of the wetting angle Θ between the heterogeneous surface and the nucleus.

$$\Phi(\Theta) = \frac{1}{4} \cdot (2 + \cos(\Theta)) \cdot (1 - \cos(\Theta))^2 \ . \qquad (6\text{-}67)$$

The heterogeneous surface can be either solid or liquid, as found by Zell and Mutaftschiev (1968). The impurities which might contact the melt are the other ash particles, which are glassy melts, oxide melts, or solidified oxides. The oxides which occur in addition to magnetite in coal ashes are MgO, CaO and Al_2O_3, all of which have a melting point above 2300K. Thus, we might expect these oxides to be at least partially solidified when crystallization of magnetite occurs. The estimation of a main contact angle is difficult because of these various possibilities. But the wetting angle between these oxides and an oxide melt should be small. In Slag Atlas (1981) a wetting angle of twenty degrees for the contact between a Al_2O_3-CaO-SiO_2-melt and MgO-crystals is given. Therefore, the wetting angle is estimated to be Θ=20°. This value has to be used carefully, because its influence on the calculation of the number of nuclei is large. Taking into account this value, we estimate $\Delta G = 7.10922 \cdot 10^{-22}$ kJ. This leads to an estimation of $n_{nuc} = 2.778 \cdot 10^{10}$ [1/kg]. Therefore, in one typical Fe-O-melt droplet with the radius $R = 7 \cdot 10^{-6}$ m the number of nuclei is: $n_{nuc,droplet} = 0.2$. Finally, we can estimate a rate constant for the nucleation. The classical nucleation rate is determined by:

$$\frac{dn_{nuc}}{dt} = \frac{A}{\rho_{Fe_3O_4}} \cdot \exp\left(\frac{\Delta G}{k \cdot T} \right)] \qquad (5\text{-}68)$$

as can be found in Mullin (1993). He also gives $A = 10^{19}$ [1/(m^3 · s)] as an estimation for the constant. Multiplication of this rate with the mass of a critical nuclei ($m_{nuc} = (4/3) \cdot \pi \cdot R_0^3 \cdot \rho_{Fe_3O_4}$) leads to a time constant $\tau_{nuc} = 4.42 \cdot 10^{-19}$ [1/s] for the nucleation rate. This is very much smaller than the time constant for the crystallization rate, suggesting that the crystallization is governed by nucleation. There are two possible explanations for this contradiction of the previous assumption of a very fast nucleation rate. The first is given by Mullin (1993), who noted a lack of success of the classical nucleation theory in explaining the behavior of real systems, and that empirical relationships are often the only ones that can be justified. The second possibility is, that some of the pyrrhotite is oxidized on the surface of the char particles in solid state. As the char burnout starts at 600 K, the assumption that at least some solid magnetite is present on

the char particle surface before the pyrrhotite is molten seems reasonable. This might lead to solid magnetite particles within the Fe-O-(S)-melt as long as the particle temperature does not exceed 1870 K, the magnetite melting point. Thus, nucleation would not be necessary for the crystallization process. However, the results presented above for the nucleation rate constant suggest that further analysis is required.

6.1.6 Glass Formation

Slag melts are often described by two different theories (Slag Atlas, 1981). The first, called the molecular theory, is based on classical chemistry and rests on the assumption that liquid slags are composed of individual oxides, sulphides or fluorides. This would lead to definite iron-silicates in slags, which might be described with chemical formulas giving a stoichiometric ratio between iron and silicon. The most powerful argument against this theory is the experimental data showing high electrical conductivity of molten slags. These experiments have led to the theory that molten slag consist of ions.

Because of the high ratio of silicate impurities in coals, these ionic melts contain a high percentage of SiO_4^{4-}-anions, which are well known as very good glass former (Slag Atlas, 1981 and Vogel, 1979). Other glass forming anions in molten slags are for instance AlO_3^{3-} and $Fe_2O_5^{4-}$. These anions are able to polymerize by delivery of oxygen, building a network which is responsible for the huge increase in viscosity of slag melts with decreasing temperature. This network might be cracked by big cations like K^+ and Ca^{2+}. Therefore, these cations are called 'network modifiers'. Cations which might either replace silicon within the network or crack the network are called 'intermediate oxides', those are Fe^{2+}, Mg^{2+} and Mn^{2+}. Concentration gradients within a molten slag droplet should cause diffusion, resulting in a homogeneous mixture. However, as the molten particle is only in the furnace for short times it is likely that glassy particles are heterogeneous mixtures of ions.

The experimental results for the six coals investigated by Bool (1993) show that approximately 31 wt-% extraneous iron oxide is formed during coal combustion, while 37 wt-% inherent iron oxide is formed and 32 wt-% of the iron were found as iron captured in glass. It was also found that the stoichiometric ratio had a major influence on iron oxide formation. Bool's model predicted that decreasing the stoichiometric ratio dramatically increases the iron remaining as unoxidized pyrrhotite, while the fraction of iron captured in glass remained nearly constant. His results with the Kentucky #11 coal show that varying the stoichiometric ratio between 1.0 and 0.8 supports the prediction of the model, while a variation between 0.8 and 1.32 leads to a significant decrease of the iron captured in glass with decreasing stoichiometric ratio. This decrease might be due to the lower gas temperatures in these experiments. The peak gas temperature is 1713 K for the stoichiometric ratio 1.32 experiment, and 1390 K for the stoichiometric ratio 0.8 experiment. Although the model agrees with the experimental data, additional data are required to fully understand the effect of stoichiometric ratio on the iron partitioning.

Bool (1993) proposed a mathematical model for glass formation based on a determined stoichiometric ratio between iron and silicate in glass:

$$FeO + y\ \text{Silicate} \rightarrow (1+y)\ \text{Glass} \qquad (6\text{-}69)$$

$$Fe_{0.877}S + y\ \text{Silicate} \rightarrow (1+y)\ \text{Glass} \qquad (6\text{-}70)$$

The silicates might be illite, kaolinite or quartz. He also suggests the glass formation rate can be determined by the equation

$$\frac{dU}{dt} = X_g \cdot M_g \qquad (6\text{-}71)$$

where X_g stands for the probability of contact between iron and silicate particles and M_g for the rate at which molten iron and molten silicate particles in contact sinter. This rate is given by

$$M_g = \frac{Dg}{r_{sil}} \cdot \rho_{sil} \cdot A_{sil} \cdot \qquad (6\text{-}72)$$

Although his model fits existing data well, the use of the fit parameter y requires more study. This fit parameter has a major influence on the simulation results, as shown by varying this parameter during test runs. The discussion above suggests that there is no determinable ratio between iron and silicate existing within molten slag. Therefore this parameter may not mirror true slags. In order to explore replacements for this parameter, modifications were made to the original model. Further, the original glass formation rate was re-examined to better understand the fit parameter associated with the mixing rate M_g.

The original model was based on the assumption that capturing of iron in glassy phases occurs only if both the iron and the silicate are molten (no solid phase sintering). Taking into account the melting points of silicates and pyrrhotite, which were found by Bool (1993) to be 1258 K and 1356 K, that the peak gas temperature of all the experiments made by Bool (1993) is higher than 1390 K, and that the peak char particle temperature should be between 100 K and 300 K higher than the peak gas temperature, it is reasonable to expect molten Fe-O-S and silicate particles on the surface of the char particles.

The experimental evidence presented by Bool (1993), achieved by the use of Transmission Electron Microscopy, show that particles of crystalline material embedded in a glassy matrix are rare in the ash. He found predominantly large glassy particles containing Si, Al, Ca, K, and Fe, and also large particles of beam stable material, which were almost pure Fe. The first type of particles represents the iron captured in glass, and the second type the iron oxide. Because of this results, the possibility of crystallization of magnetite within the glass is neglected, as in the original model.

6.1.6.1 Neck Growth and Coalescence

When a particle of molten silicate glass and a molten Fe-O-S particle contact each other on the surface of a char particle during char burnout, they will immediately start to build a neck.

The neck growth between two fused ash particles is described by Raask (1985) with a formula found by Frenkel in early sintering work. Frenkel's formula determines the time needed to build a neck with a diameter x, depending on the radius of the particles R:

$$t = \frac{2 \cdot \mu}{3 \cdot \gamma} \cdot R \cdot \left(\frac{x}{R}\right)^2 \qquad (6\text{-}73)$$

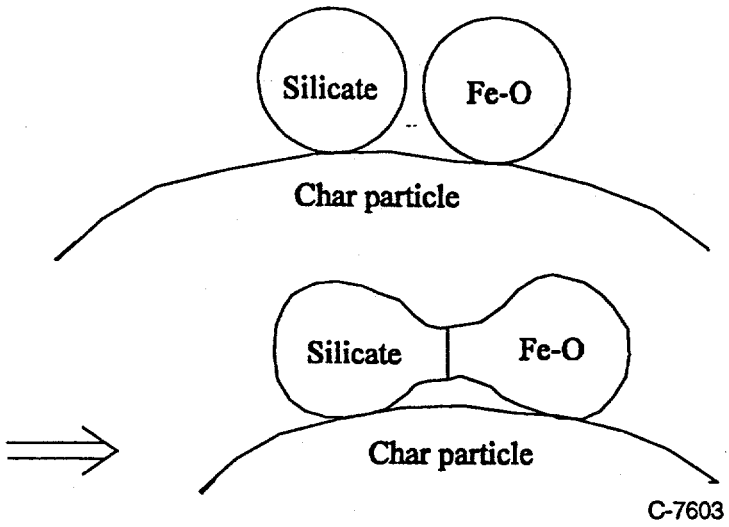

Figure 6-6. Contact between silicate and iron oxide melt on char surface.

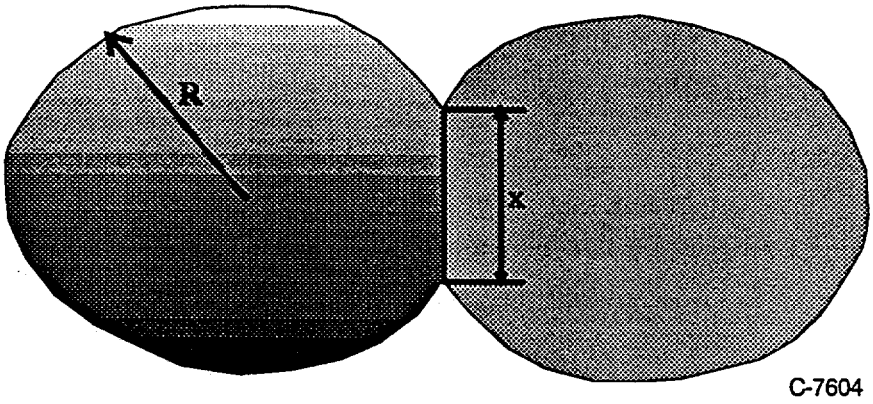

Figure 6-7. Neck between two fused ash particles.

where μ is the viscosity and γ the surface tension. This formula is applicable for $x/R < 0.3$. The surface tension of molten slags was found by Raask (1985) to vary within 0.25 N/m and 0.4 N/m, giving a mean value of $\gamma = 0.32$ N/m. The viscosity is more difficult to estimate because of its exponential increase with decreasing temperatures, and because of the strong dependence on composition, as can be seen in Turkdogan (1983). To get a reasonable value for the comparison of glass capture rate and crystallization rate, we take a slag viscosity at 1600 K. For a slag with 40 wt% SiO_2 and 40 wt-% FeO a viscosity of approximately $\mu = 0.3$ N · s/m^2 can be found in Slag Atlas (1981). This stands in strong contrast to Raask (1985), who found slag viscosity in the range of 1000 N · s/m^2. The reasons for that difference are different measurement methods, and different states of the particles. While the values in Slag Atlas (1981) are given for liquid slags, Raask (1985) gives values for solid ash particles with a molten layer, which he measured by applying Frenkels formula. The value given by Slag Atlas is taken, because temperature gradients within the particles have been neglected in this model, leading to complete liquid particles. Assuming a mean particle radius of silicate and iron oxide particles of $R = 7 \cdot 10^{-6}$ m from data given by Bool (1993), we find a time of $t = 4 \cdot 10^{-7}$s for the neck growth up to $x/R = 0.3$. This suggests that coalescence occurs very quickly. However, it is not possible to neglect coalescence time. Therefore the assumption is made that the Frenkel equation can be applied until full coalescence is reached, and that it

can also be applied for spherical droplets with different radius. For the time of the coalescence process, the radii are assumed to remain constant. Full coalescence should be reached when $x = 2 \cdot \min (R_{sil}, R_{Fe\text{-}O\text{-}S})$, and from then on x is assumed to remain constant. The Frenkel equation leads, for example, to a time for full coalescence of $t = 1.75 \cdot 10^{-5}$ s. This might be too fast, as we would expect the coalescence rate to decrease during this process, but the error should be negligible. Thus, we have the equations:

$$\left(\frac{x}{R_{min}}\right)^2 = \frac{3}{2} \cdot \frac{\gamma}{\mu \cdot R_{min}} \cdot t \qquad (6\text{-}74)$$

$$R_{min} = \min \left(R_{sil}, R_{Fe\text{-}O\text{-}S}\right) \quad . \qquad (6\text{-}75)$$

A very short coalescence time was also found by Beér et al. (1992) by work on their model of the agglomeration of fly ash particles on the char surface during char burnout.

6.1.6.2 Diffusion

A diffusive process is proposed for the description of the glass capture of iron. Considering the high viscosity of silicate melts, which is due to the network formation by SiO_4^{4-}-anions, the assumption is made, that iron ions diffuse into the glassy melt through the phase boundary between the silicate and the Fe-O-S droplet, while the SiO_4^{4-}-anions remain within the network. This diffusion of iron cations might occur as soon as a molten silicate droplet contacts a Fe-O-S-melt droplet, not depending on whether the oxidation of the pyrrhotite is complete and crystallization takes place or not. Fick's second law of diffusion and the boundary conditions lead to the following mathematical description:

$$\frac{\partial C}{\partial t} = D_I \cdot \frac{\partial^2 C}{\partial z^2} \qquad (6\text{-}76)$$

$$C(t=0,z)=0 \qquad [1] \qquad (6\text{-}77)$$

$$C(t,z=0)=C_o \qquad [2] \qquad (6\text{-}78)$$

$$\frac{\partial C}{\partial z}(t,z\rightarrow\infty)=0 \qquad [3] \qquad (6\text{-}79)$$

where D_I is the diffusion coefficient, and the concentration of iron ions at the phase boundary C_0 is taken to be pseudo-constant. Although there are some doubts about the boundary conditions, this should be a

reasonable approach to describe the problem. The solution for this differential equation and boundary conditions is given by Crank (1975):

$$C(z,t) = C_0 \cdot \mathrm{erfc}\left(\frac{z}{2 \cdot \sqrt{D_I \cdot t}}\right) \quad . \tag{6-80}$$

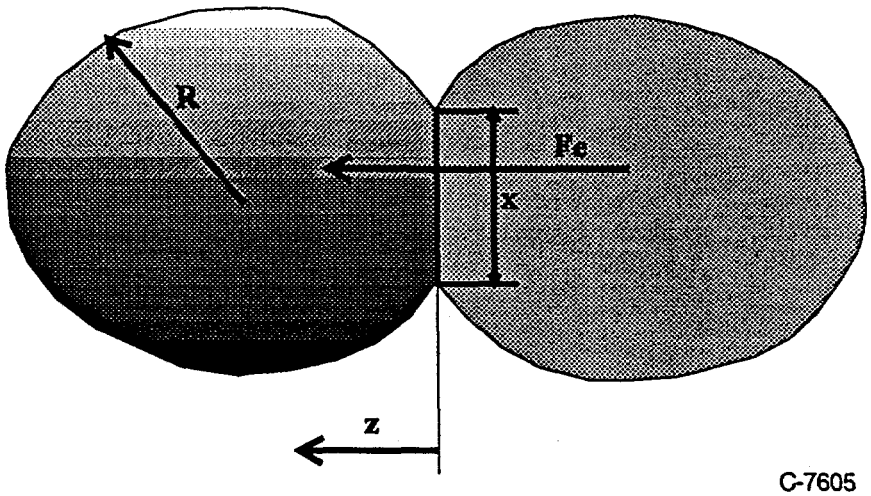

Figure 6-8. Diffusion of iron in glassy silicate particle.

Deriving this equation at z=0 gives the concentration gradient at the phase boundary:

$$\frac{\partial C}{\partial z}(z=0,t) = \frac{C_0}{\sqrt{\pi \cdot D_I \cdot t}} \quad . \tag{6-81}$$

The rate for the iron capture is then given by:

$$\frac{dm_{Fe}}{dt} = M_{Fe} \cdot \pi \cdot x^2 \cdot D_I \cdot \frac{\partial C}{\partial z}(z=0,t) = M_{Fe} \cdot C_0 \cdot \left(\frac{x}{R}\right)^2 \cdot R^2 \cdot \sqrt{\frac{\pi \cdot D_I}{t}} \tag{6-82}$$

where M_{Fe} is the molar weight of iron. It is obvious that this equation delivers an infinite result for t=0. Therefore, the coalescence time can not be neglected, and the neck ratio, x/R, is replaced by the Frenkel equation. This leads to:

$$\frac{dm_{Fe}}{dt} = \frac{3}{2} \cdot \frac{\gamma}{\mu} \cdot R_{min} \cdot M_{Fe} \cdot C_0 \cdot \sqrt{\pi \cdot D_I \cdot t} \qquad \frac{x}{R_{min}} \leq 2 \tag{6-83}$$

$$\frac{dm_{Fe}}{dt} = 4 \cdot R_{min}^2 \cdot M_{Fe} \cdot C_0 \cdot \sqrt{\frac{\pi \cdot D_I}{t}} \qquad \frac{x}{R_{min}} = 2 \quad . \tag{6-84}$$

The change of the radius with time is not taken into account here. Both radii are assumed to be constant during coalescence, and x is assumed to be constant after that. It can be seen that the radius of the smaller particle before the contact, and the diffusion coefficient, are important variables for the glass capture rate. The diffusion coefficient has an exponential relation to the temperature, thus the particle temperature plays a major role as well. By taking into account an Arrhenius-type function for the dependence of the diffusion coefficient on the temperature, the activation energy might be assumed as the activation energy for iron ions diffusing in glass, which is given by Turkdogan (1983, as cited by Bool (1993), to be E_I = 104535.7 kJ/kmole.

$$D_I = D_{I0} \cdot \exp\left(-\frac{E}{R \cdot T_{char}}\right) \quad . \tag{6-85}$$

To find the factor D_{I0}, a reference value, taken at a reference temperature, is needed. Nowok et al. (1990) gave a formula for the dependence of the diffusion coefficient on viscosity and surface tension:

$$D = \frac{\gamma \cdot L}{\mu} \tag{6-86}$$

The relation is exponential, as can also be seen in Slag Atlas (1981). Therefore, the surface tension can be taken as constant, and we might again use the value given by Raask (1985) γ = 0.32 N/m. This leads to:

$$D_{I0} = R_{min} \cdot 2759.11 \text{ m/s} \tag{6-87}$$

and we might then write:

$$\frac{dm_{Fe}}{dt} = \frac{3}{2} \cdot D_I \cdot M_{Fe} \cdot C_0 \cdot \sqrt{\pi \cdot D_I \cdot t} \qquad \frac{x}{R_{min}} \leq 2 \tag{6-88}$$

$$\frac{dm_{Fe}}{dt} = 4 \cdot R_{min}^2 \cdot M_{Fe} \cdot C_0 \cdot \sqrt{\frac{\pi \cdot D_I}{t}} \qquad \frac{x}{R_{min}} = 2 \quad . \tag{6-89}$$

Finally, the concentration of iron within an Fe-O-S-melt has to be determined. By taking into account the concentration of iron in a pure pyrrhotite melt and in a pure magnetite melt, we find C_0 depending on the progress of oxidation:

$$C_0 = (1 - w) \cdot \frac{0.877 \cdot \rho_{Fe_{0.877}S(1)}}{M_{Fe_{0.877}S}} + \frac{3 \cdot \rho_{Fe_3O_4(1)}}{M_{Fe_3O_4}} \qquad (6\text{-}90)$$

$$w = \frac{N_{Fe_3O_4(1)}}{N_{Fe_3O_4(1)} + N_{Fe_{0.0877}S(1)}} \qquad (6\text{-}91)$$

where w is the ratio of magnetite in the particle, and the mole magnetite and pyrrhotite melt exposed at time t are given by the mass balances (129) and (130). The density of liquid magnetite is assumed to be the same as that of liquid iron oxide melt, which is given in Slag Atlas (1981) to be $\rho_{Fe_3O_4(1)} = 4719$ kg/m^3. The density of solid pyrrhotite $\rho_{Fe_{0.877}S(s)} = 4600$ kg/m^3 is given by Raask (1985), and taking into account that value the density of liquid pyrrhotite is estimated to be $\rho_{Fe_{0.877}S(1)} = 4000$ kg/m^3.

It is interesting to note that the model developed here based on a more fundamental analysis yields a rate equation very similar to the original model. In the original model all of the concentration and diffusion terms were incorporated into a global fit parameter for the mixing rate. This analysis suggests a method for estimating the value of this fit parameter from fundamental materials properties. Additional modifications are discussed in subsequent sections.

6.1.6.3 Glass Formation Rate Compared to Crystallization Rate

In order to compare the proposed glass formation rate with the crystallization rate discussed earlier, we estimate a pseudo-time constant and compare that to the time constant of the crystallization rate. To do this, we divide the equation for the glass capture rate by the mass of an iron oxide droplet.

$$\tau = \frac{1}{\frac{4}{3} \cdot \pi \cdot R^3 \cdot \rho} \cdot \frac{dm_{Fe}}{dt} \quad . \qquad (6\text{-}92)$$

The values for the temperature and the radius are again assumed to be T = 1350K and $R_{min} = 7 \cdot 10^{-6}$m, as they were for describing the neck growth. To estimate the concentration at the phase boundary, it is assumed that a pure magnetite melt exists, thus:

$$C_0 = \frac{3 \cdot \rho}{M_{Fe_3O_4}} \quad . \qquad (6\text{-}93)$$

This leads to a value for the diffusion coefficient of $D = 7.5 \cdot 10^{-6}$ m^2/s and to pseudo-time constants of:

$$\tau = \frac{27}{8} \cdot \frac{M_{Fe}}{M_{Fe_3O_4}} \cdot \frac{D}{R^3} \cdot \sqrt{\frac{D \cdot t}{\pi}} \qquad t \leq 1.75 \cdot 10^{-5}\ s \tag{6-94}$$

$$\tau = 9 \cdot \frac{M_{Fe}}{M_{Fe_3O_4}} \cdot \frac{1}{R} \cdot \sqrt{\frac{D}{\pi \cdot t}} \qquad t \geq 1.75 \cdot 10^{-5}\ s \tag{6-95}$$

This gives a maximum time constant for $t = 1.75 \cdot 10^{-5}$s of $\tau = 3.5 \cdot 10^{5}$ [1/s]. Compared to the crystallization time constant of $\tau_c = 2.3 \cdot 10^{8}$[1/s], this value is smaller by a factor of a thousand. The experimental results of Bool (1993) show that neither glass capture nor crystallization should be dominant. However, taking into account that these time constants are estimates, and that glass capture occurs when crystallization does not (particle temperature over 1600 K or positive particle temperature gradient), these values are reasonable. Parameters not considered in this comparison are the probability and the number of contacts between Fe-O-S-melt and silicate melt particles, and the number and size of crystal nuclei in the Fe-O-melt. These parameters have a strong influence on the competition between crystallization and glass capture.

6.1.6.4 Contact Between Molten Iron Oxide and Glass Particles

In the examined coals, the weight percentage of silicon oxide and iron oxide in the ash varies within a wide range. The ratio of silicon oxide is between 21.6 wt-% and 50.6 wt-%, and the ratio of iron oxide between 6.1 wt-% and 22.4 wt-% of the ash. Thus, the probability and the number of contacts between molten iron oxide and silicate glass particles depends strongly on the coal, and the number of particles exposed on the char surface. Because this contact occurs on the surface of the char particle, we might regard the problem as two dimensional, where the cross surface areas of the particles and the char surface area are the determining geometric factors.

6.1.6.4.1 The Probability of Contact

In the original model Bool (1993) proposed a function for the probability of contact, in which the cross surface area occupied by Fe-O-S-melts on the char surface is divided by the surface area not occupied by Fe-O-S-melts. Although this function mirrors the physical situation, it may underpredict the true contact probability. This function has a maximum during char burnout, and decreases after burnout. This trend is reasonable for the original model of the glass formation, because he assumed a reaction with a definite stoichiometry (given by the fit parameter y) between the Fe-O-S-melt and the silicate melt particles. Therefore, after a contact occurred a silicate particle is "used", and not available for another contact. In the modification suggested here, a silicate particle is available for contact as long as it is molten. This assumption leads to a problem with the boundary condition of the differential equation describing the diffusion of Fe into the silicate Eq. (6-77). In this equation the assumption is made that the concentration of iron within the silicate is zero at the moment contact occurs. As long as the maximum iron content in the glass is relatively low, this assumption is reasonable.

The mass of silicate and pyrrhotite exposed at time t is given by:

$$m_{sil} = v_{sil} \cdot \frac{4}{3} \cdot \pi \cdot \rho_{char} \left(R_{char,0}^3 - R_{char}^3 \right) \tag{6-96}$$

$$m_{Fe_{0.877}S} = v_{pyr} \cdot \frac{1}{0.877} \cdot \frac{M_{Fe_{0.877}S}}{M_{pyr}} \cdot \frac{4}{3} \cdot \pi \cdot \rho_{char} \left(R_{char,0}^3 - R_{char}^3 \right) \tag{6-97}$$

where v_{sil} and v_{pyr} are the mass fractions of silicate and pyrite in the coal, and $R_{char,0}$ is the mean radius of the char particles before the combustion. Note this is similar to the balance proposed in the original model. By neglecting the influence of coalescence on the number of particles, the number of silicate and Fe-O-S-melt particles on the surface might be estimated by dividing the total mass with the mean particle mass. This leads (for the silicate) to:

$$n_{sil} = \frac{3}{4} \cdot \frac{m_{sil}}{\rho_{sil} \cdot \pi \cdot R_{sil}^3} \tag{6-98}$$

where the mean radius, R_{sil}, is given for different coals by Bool (1993) and the density ($\rho_{sil} = 3000$ kg/m^3) might be estimated from values given by Turkdogan (1983). To estimate the number of Fe-O-S-melt particles is more difficult because of the occurring reaction and the different times particles are exposed. The mass, density and radius of Fe-O-S-melt particles lie between those of pure pyrrhotite and pure magnetite melts. The mass of a pure pyrrhotite melt is given by Eq. (6-97), and the mass of the corresponding pure magnetite melt is found by taking into account the reaction stoichiometry (Eq. 6-46). We might then take the mass of the Fe-O-S-melt to be the difference between the mean value of these two extremes and the crystallized magnetite. It is reasonable to neglect the loss of melt mass caused by the glass capture at this point, because the growth of the silicate glass mass was neglected as well.

$$m_{Fe_3O_4(l)} = \frac{M_{Fe_3O_4}}{\frac{3}{0.877} M_{Fe_{0.877}S}} \cdot m_{Fe_{0.877}S} \tag{6-99}$$

$$m_{Fe-O-S} = \frac{1}{2} \cdot m_{Fe_{0.877}S} \cdot \left(1 + \frac{0.877 \cdot M_{Fe_3O_4}}{3 \cdot M_{Fe_{0.877}S}} \right) - m_{Fe_3O_4,cryst} \quad . \tag{6-100}$$

The density of the Fe-O-S-melt was taken as the arithmetic mean of the densities of liquid pyrrhotite and magnetite, leading to a value of $\rho_{Fe-O-S} = 4359.5$ kg/m^3. Referring to the particle radius, the radius of a pyrrhotite particle is given by:

$$R_{Fe_{0.877}S} = \left(\frac{1}{0.877} \cdot \frac{M_{Fe_{0.877}S}}{M_{FeS_2}} \cdot \frac{\rho_{pyr}}{\rho_{Fe_{0.877}S(l)}} \right)^{1/3} \cdot R_{in\cdot pyr} \qquad (6\text{-}101)$$

where the mean values for the radius of the inherent pyrite particles are given for different coals by Bool (1993). The radius of the corresponding magnetite melt particle is then given by:

$$R_{Fe_3O_4} = \left(\frac{M_{Fe_3O_4}}{\frac{3}{0.877} \cdot M_{Fe_{0.877}S}} \cdot \frac{\rho_{Fe_{0.877}S(l)}}{\rho_{Fe_3O_4(l)}} \right)^{1/3} \cdot R_{Fe_{0.877}S} \qquad (6\text{-}102)$$

where the change of the particle radius due to partial crystallization is neglected. The radius of the Fe-O-S-melt particles might again be taken as the mean of these two:

$$R_{Fe\text{-}O\text{-}S} = \frac{R_{Fe_{0.877}S}}{2} \cdot \left(1 + \left(\frac{0.877}{3} \cdot \frac{M_{Fe_3O_4}}{M_{Fe_{0.877}S}} \cdot \frac{\rho_{Fe_{0.877}S(l)}}{\rho_{Fe_3O_4(l)}} \right)^{1/3} \right) \qquad (6\text{-}103)$$

With these relations for the mass and the radius, and with the value for the density, we are now able to estimate the number of Fe-O-S-melt particles on the surface:

$$n_{Fe\text{-}O\text{-}S} = \frac{3}{4} \cdot \frac{m_{Fe\text{-}O\text{-}S}}{\rho_{Fe\text{-}O\text{-}S} \cdot \pi \cdot R^3_{Fe\text{-}O\text{-}S}} \cdot \qquad (6\text{-}104)$$

By knowing know how many silicate and Fe-O-S-melt particles are on the char surface, the probability of contact is given by the cross surface area covered by these particles within the area where contact might occur, divided by this area. Thus, the geometric problem might be regarded as that of small spheres of different sizes placed on a big sphere.

If the char radius is R, the radius of the silicate and Fe-O-S-melt particles R_1 and R_2, with R_1 = max (R_{sil}, $R_{Fe\text{-}O\text{-}S}$) , and the contact radius R*, we find by using the cosine rule:

$$\frac{(R+R_2)^2 + (R_1+R_2)^2 - (R+R_1)^2}{2\,(R_1+R_2)(R_1+R_2)} = \cos(\alpha_2) = \frac{(R+R_2)^2 + R_2^2 - (R^*)^2}{2 \cdot R_2 \cdot (R+R_2)} \cdot \qquad (6\text{-}105)$$

This gives us the radius of the contact area R*:

$$R^* = \sqrt{(R+R_2)^2 + R_2^2 - \frac{R_2}{R_1+R_2} \cdot ((R+R_2)^2 + (R_1+R_2)^2 - (R+R_1)^2)} \; . \qquad (6\text{-}106)$$

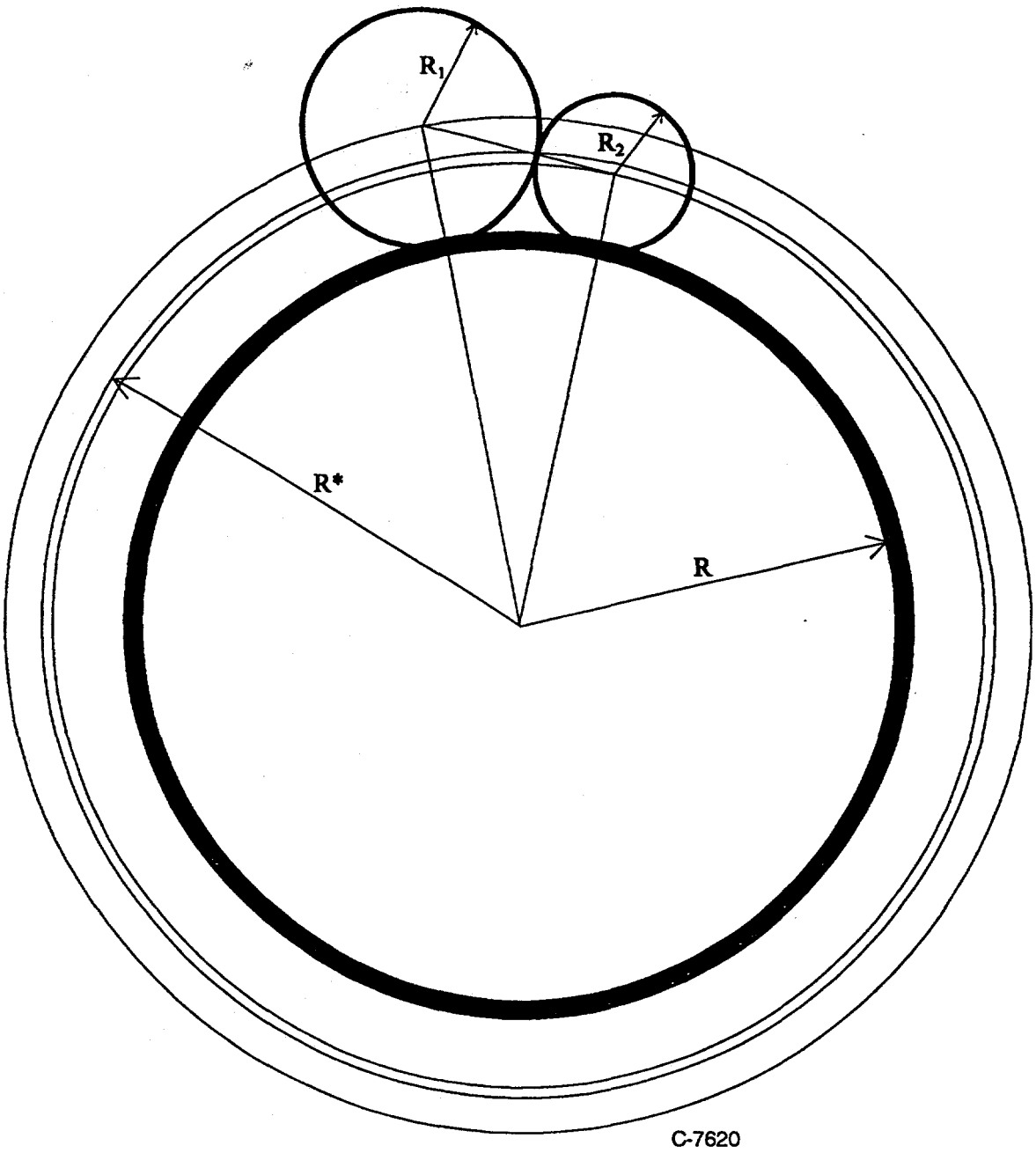

Figure 6-9. Radius of contact area.

Thus, the contact area is given by $A^*=4\cdot\pi\cdot(R^*)^2$. To calculate the part of this area occupied by a single spherical particle, we have to find the segment of the contact sphere occupied by it.

The segments are determined by their heights h_1 and h_2 and the radii r_1 and r_2. To get equations for these lengths, first the angles α_1 and α_2 have to be found, which are given by the cosine rule:

$$\cos(\alpha_1) = \frac{(R^*)^2 + R_1^2 - (R + R_1)^2}{2 \cdot R_1 \cdot R^*} \tag{6-107}$$

$$\cos(\alpha_2) = \frac{(R + R_2)^2 + R_2^2 - (R^*)^2}{2 \cdot R_2 \cdot (R + R_2)} \; . \tag{6-108}$$

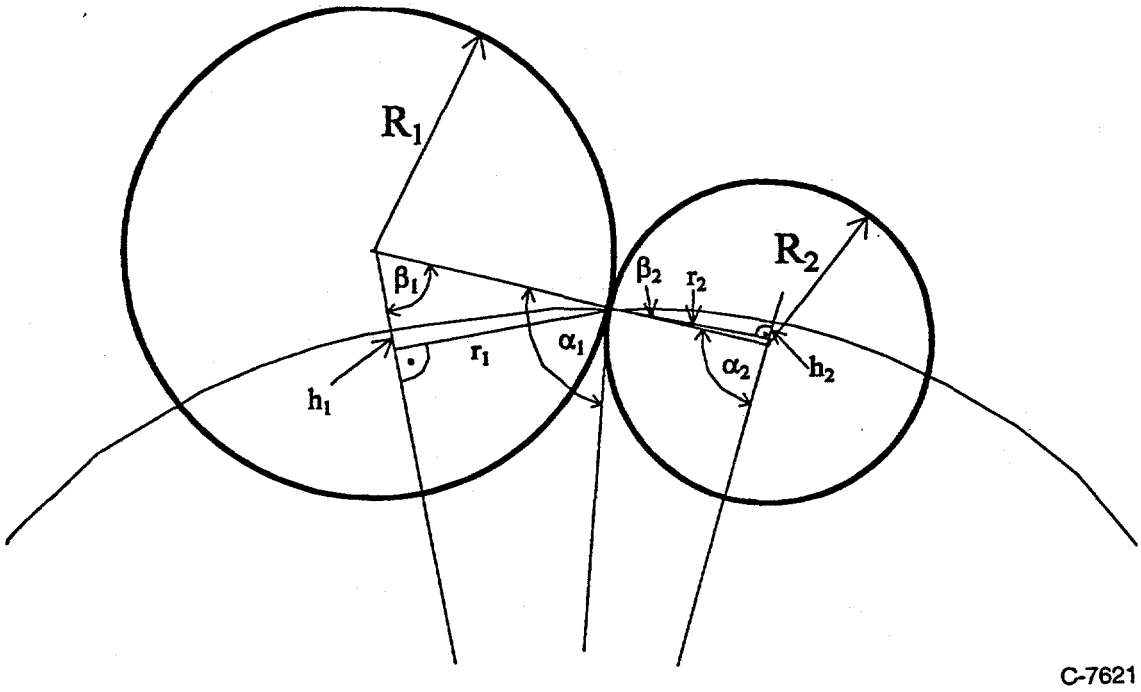

Figure 6-10. Radius and height of the contact sphere segments.

The angle β_1 is then determined by the sine rule and the angle β_2 is the difference between α_2 and the right angle.

$$\sin(\beta_1) = \sin(\alpha_1) \cdot \frac{R^*}{R + R_1} \tag{6-109}$$

$$\beta_2 = \alpha_2 - 90° \tag{6-110}$$

This gives finally the radii and the heights by taking into account angle functions:

$$r_1 = R_1 \cdot \sin(\beta_1) \tag{6-111}$$

$$h_1 = R^* - (R + R_1 \cdot (1 - \cos(\beta_1))) \tag{6-112}$$

$$r_2 = R_2 \cdot \cos(\beta_2) \tag{6-113}$$

$$h_2 = R^* - (R + R_2 \cdot (1 + \sin(\beta_2))) \tag{6-114}$$

The areas of the sphere segment tops are the given by $A = 2 \cdot \pi \cdot r \cdot h$ (Dubbel, 1990) and therefore the area occupied by the spheres is:

$$A_{oc} = 2\pi \cdot (n_1 r_1 h_1 + n_2 r_2 h_2) \tag{6-115}$$

where n_1 is the number of the particles with bigger size and n_2 the number of those with smaller size. This leads to the function for the probability of contact between silicate and Fe-O-S-melt particles:

$$\Theta = \frac{n_1 r_1 h_1 + n_2 r_2 h_2}{2 \cdot (R^*)^2} . \tag{6-116}$$

If the value given by this function exceeds one, it is taken to be one.

6.1.6.4.2 The Number of Contacts

In the last section the probability of contact was considered. This contact probability tells us how likely it is for contact to occur. Now we must address the number of contacts, (if the probability of contact is one). Therefore we have to examine the ratio of the surface area of the silicate and the Fe-O-S melt particles to the total ash surface area. Similar to the function derived in the original model this describes blocking of contact by the residual ash particles (ash particles which are neither Fe-O-S-melt nor silicate melt).

To examine this effect, we consider the problem to be that of spherical particles with equal size arranged to give the closest possible packing. The mean radius of all ash particles R_{ash}, which is given for different coals by Bool (1993), is then taken to determine a hypothetical number of particles:

$$n_{sil,h} = \frac{3}{4} \cdot \frac{m_{sil}}{\pi \cdot \rho_{sil} \cdot R_{ash}^3} \tag{6-117}$$

$$n_{Fe-O-S,h} = \frac{3}{4} \cdot \frac{m_{Fe-O-S}}{\pi \cdot \rho_{Fe-O-S} \cdot R_{ash}^3} \tag{6-118}$$

$$n_{res\ ash,\ h} = \frac{3}{4} \cdot \frac{m_{ash} - m_{sil} - m_{Fe-O-S}}{\pi \cdot \rho_{ash} \cdot R_{ash}^3} \quad . \tag{6-119}$$

For closest possible packing a hypothetical Fe-O-S-melt particle is surrounded by six other particles - yielding six possible contacts. Thus, the mean number of contacts between a single Fe-O-S-melt particle and silicate melt particles is given by:

$$n_{con,\ 1} = 6 \cdot \frac{n_{sil,\ h}}{N_{sil,\ h} + n_{Fe-O-S,\ h} = n_{res,\ ash,\ h} - 1} = 6 \cdot \frac{n_{sil,\ h}}{n_{total} - 1} \tag{6-120}$$

and the total number of contacts is:

$$n_{con} = \frac{6 \cdot n_{Fe-O-S,\ h} \cdot n_{sil,\ h}}{n_{total} - 1} \tag{6-121}$$

This function takes into account the effect of the ratio of the amount of iron oxide and silicate in the ash. The number of contacts is high, if the ratios of silicate and iron oxide within the ash are high and almost equal. It is low, if the ratios are low and one ratio is much bigger than the other. For instance, if within a total of 100 particles 40 are iron oxide and 40 are silicate particles, the number of contacts is 97. If now just 30 silicate particles and 5 iron particles are in there, the number of contacts is 9. Qualitatively this is similar to the approach taken by Bool (1993) in the original model. However, this new approach may provide a better quantitative description of the process.

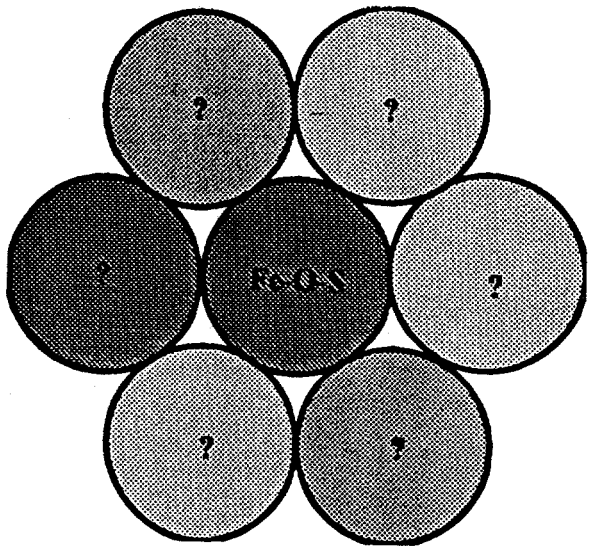

Figure 6-11. Order of highest possible particle density.

6.1.6.5 The Glass Capture Rate

Combining the rate of glass formation for a single contact, the probability of contact, and the number of contacts, we receive:

$$\frac{dm_{Fe}}{dt} = \Theta \cdot n_{con} \frac{3}{2} \cdot D_I \cdot M_{Fe} \cdot C_0 \cdot \sqrt{\pi \cdot D_I \cdot (t - t_0)} \qquad \frac{x}{R_{min}} \leq 2 \tag{6-122}$$

$$\frac{dm_{Fe}}{dt} = \Theta \cdot n_{con}\, 4 \cdot R_{min}^2 \cdot M_{Fe} \cdot C_0 \cdot \sqrt{\frac{\pi \cdot D_I}{t - t_0}} \qquad \frac{x}{R_{min}} = 2 \tag{6-123}$$

where Θ is given by equation (116), n_{con} by equation (121), and where t_0 is the time at which the contact occurs. The ratio for the neck growth is given by the Frenkel equation, and taken to be constant if the calculated ratio x/R_{min} exceeds 2:

$$\left(\frac{x}{R_{min}}\right)^2 = \frac{3}{2} \cdot \frac{D_I}{R_{min}^2} \cdot (t - t_0) \tag{6-124}$$

$$R_{min} = \min \left(R_{sil}, R_{Fe\text{-}O\text{-}S}\right) . \tag{6-125}$$

Because the equations depend on the time at which contact occurs, we have to find a mean value for all contacts which have happened up to time t. This might be done by taking into account the earliest possible contact time, which is the time the temperature exceeds 1356 K, to be t_0. Then we might integrate from this time to the actual time t, and divide the result by the time interval $t-t_0$. This leads to:

$$\frac{dm_{Fe,\ glass}}{dt} = \Theta \cdot n_{con}\ D_I \cdot M_{Fe} \cdot C_0 \cdot \sqrt{\pi \cdot D_I \cdot t - t_0} \qquad \frac{x}{R_{min}} = \leq 2 \tag{6-126}$$

$$\frac{dm_{Fe,\ glass}}{dt} = \Theta \cdot n_{con}\ 8 \cdot R_{min}^2 \cdot M_{Fe} \cdot C_0 \cdot \sqrt{\frac{\pi \cdot D_I}{t - t_0}} \qquad \frac{x}{R_{min}} = 2 \tag{6-127}$$

$$\left(\frac{x}{R_{min}}\right)^2 = \frac{3}{4} \cdot \frac{D_I}{R_{min}^2} \cdot (t - t_0)\ . \tag{6-128}$$

These are the final equations for the glass capture rate, describing the diffusion of inherent iron into silicate glass melts. These equations allow for an estimate of the glass formation rate from fundamental material properties. Unfortunately these properties are not always available. Therefore, a fit parameter may still be required

For example, in both versions of the model if the probability and the number of contacts after the available area occupied by ash particles exceeds the contact area, the glass formation rate may no longer be a two dimensional problem, but a three dimensional problem. This situation increases the probability and the numbers of contact. In addition, the assumption was made that the concentration of iron in the silicate particles is initially zero for each contact. In reality, it will probably not be zero. This initial iron content may slow the glass capture. Finally, in the modified model the assumption was made that the Frenkel equation can be applied until full coalescence is reached. However, this is simply an estimate. In general, however, both the original and modified model provide a reasonable description of glass formation during the combustion process.

6.1.7 Mass Balance Systems

In this section, the results of the previous sections are combined to form the mass balances. The extraneous and the inherent material are discussed separately to give a better overview.

6.1.7.1 Mass Balances for Extraneous Pyrite

The initial mass of extraneous pyrrhotite is given by Eq. (6-44). Oxidation of the solid pyrrhotite was found to start between 800 K and 900 K, thus the mean temperature of 850 K was used. The mass of the pyrrhotite decreases, due to oxidation, as shown by Eq. (6-37). The mass of solid magnetite

correspondingly increases, Eq. (6-36). In both equations, the oxygen consumption rate has to be replaced by Eq. (6-35).

As the temperature exceeds the pyrrhotite melting point of 1356 K, the magnetite shell of the particle is cracked due to the expansion caused by the change of state and probably dissolved into the resulting Fe-O-S melt. The rates for the increase of molten magnetite and the decrease of pyrrhotite within the Fe-O-S-melt are again given by the Eqs. (6-36) and (6-37), where the oxygen consumption rate has now to be replaced by Eq (6-50) if the particle temperature of the extraneous pyrite exceeds 1870 K.

As all the pyrrhotite is consumed, there are two possibilities. Either the temperature gradient is positive or the temperature is between 1600 K and 1870 K, both leading to a phase with constant values for the mass of Fe-O-melt and solid magnetite. Another possibility is a temperature below 1600 K, and a negative temperature gradient. This leads to the direct onset of crystallization as soon as oxidation is complete. The increase of solid magnetite mass and the decrease of magnetite melt mass due to crystallization are then given by Eq. (6-62).

6.1.7.2 Mass Balances for the Inherent Material

Although char burnout begins at approximately 600 K, the assumption was made in the modified model that the solid state oxidation of pyrrhotite on the char surface can be neglected (it was included in the original model). As the char temperature exceeds 1356 K, the first Fe-S-melt mass is given by Eq. (6-97). From that point on, the mass of the pyrrhotite in the melt is determined by:

$$m_{Fe_{0.877}S(1)} = m_{Fe_{0.877}S} - \frac{\frac{3}{0.877} \cdot M_{Fe_{0.877}S}}{M_{Fe_3O_4}} \cdot \left(M_{Fe_3O_4(1)} + m_{Fe_3O_4,cryst} + \frac{M_{Fe_3O_4}}{M_{Fe}} \cdot m_{Fe,\ glass} \right) \qquad (6\text{-}129)$$

where the exposed pyrrhotite mass $m_{Fe_{0.877}S}$ for each time step is given by Eq. (6-97). At the time the particle temperature exceeds 1356 K, the mass of magnetite in the melt starts to grow, due to oxidation. The Eqs. (6-36) and (6-50) describe the increase of molten magnetite mass ($m_{Fe_3O_4}$) caused by the reaction. The mass of magnetite in the melt is then determined by:

$$m_{Fe_3O_4(1)} = m_{Fe_3O_4} - m_{Fe_3O_4,\ cryst} - \frac{M_{Fe_3O_4}}{M_{Fe}} \cdot M_{Fe,\ glass} \cdot \qquad (6\text{-}130)$$

Glass capture also occurs as soon as the particle temperature exceeds 1356 K. The increase of the mass of iron captured in glass is given by the Eqs. (6-126) and (6-127). Finally, the mass of crystallized magnetite (initially zero) starts to grow when the temperature drops below 1600 K, and the temperature gradient is negative. The increase of the solid inherent magnetite mass is then given by Eq. (6-63).

6.1.8 Model Validation

A means by which to validate a portion of the modified model was developed. This was done using the FORTRAN program of the original model, and changing the dependencies of the glass capture rate. The glass capture rate given by Bool (1993) is:

$$\frac{dm_{glass}}{dt} = G_k \cdot \exp\left(-\frac{E_g}{R \cdot T_{char}}\right) \cdot A_{glass} \cdot X_g \,. \qquad (6\text{-}131)$$

In the original model the product of A_{glass} and X_g (X_g stands for the probability of contact including the decrease at the end of the burn due to less molten particles) behaved like the product of the probability of contact and the number of contacts found in this work. The exponential dependency of Eq. (6-131) has the same exponent as the dependency of the diffusion coefficient D_I. Thus, our additional analysis has shown that Bool's fit parameter G_k includes the dependencies of the time, the radius, and the iron concentration in the melt of Eqs. (6-126) and (6-127). Therefore, the original fit parameter may be calculated from fundamental data by:

$$G_k = V \cdot C_0 \cdot \sqrt{\exp\left(-\frac{E_g}{R \cdot T_{char}}\right) \cdot (t - t_0)} \qquad \frac{x}{R_{min}} \le 2 \qquad (6\text{-}132)$$

$$G_k = V \cdot 8 \cdot R_{min}^2 \cdot C_0 \cdot \sqrt{\exp\left(\frac{E_g}{R \cdot T_{char}}\right) \cdot \frac{1}{(t - t_0)}} \qquad \frac{x}{R_{min}} = 2 \qquad (6\text{-}133)$$

$$\left(\frac{x}{R_{min}}\right)^2 = \frac{3}{4} \cdot \frac{D_I}{R_{min}^2} \cdot (t - t_0) \qquad (6\text{-}134)$$

where C_0 is a constant, which was optimized to be $1.45 \cdot 10^{13}$. Taking the fraction of iron in slag causing phases (iron in glass and remaining pyrrhotite) and comparing the results of the model with the new glass capture rate to the results of the original model developed by Bool (1993), and to the experimental data found by Bool (1993), the following conclusions are obtained:

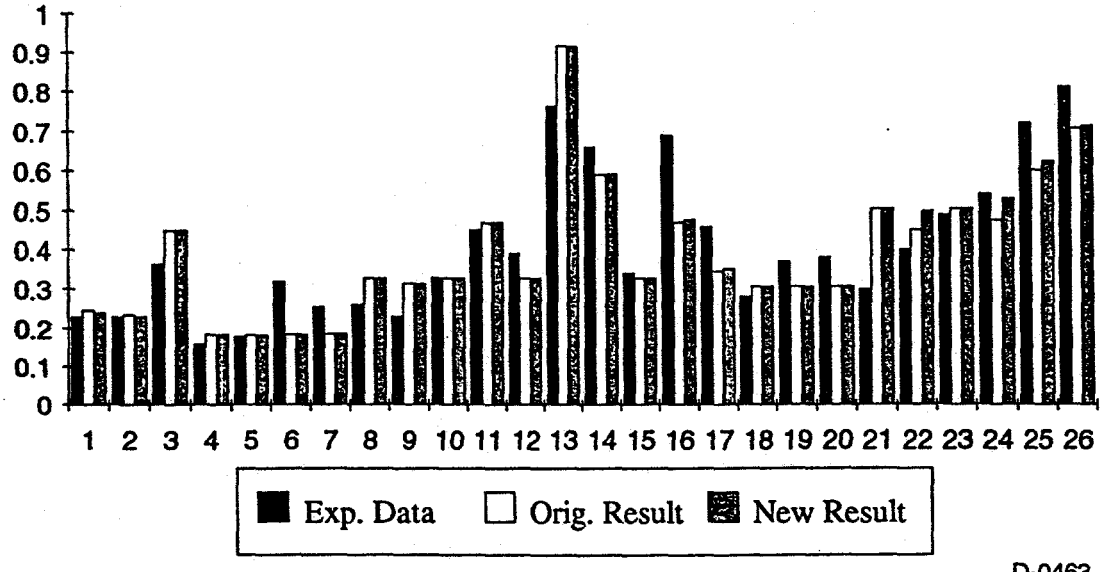

Figure 6-12. Comparison of results.

- Out of 26 simulated 'burns', 18 are not affected by this change of the glass formation rate. Their ratio of iron in slag-causing phases varies within 0.2%. This result is encouraging, because good correlation with the data is still achieved, after the more detailed version of the glass capture rate was inserted in the old model.

- Seven burns were affected positively. Over all 26 burns, the average error was reduced from 0.072 to 0.0695, and the error of the least squares was reduced from 0.2217 to 0.2125.

Table 6-1. Comparison of Results

#	Run ID	Coal Name	Exp. Data	Orig. Result	New Result	Absolute Error
1	Run 67	Kentucky #9	0.23	0.247	0.241	0.011 / -0.006
2	Run 68	Kentucky #9	0.23	0.235	0.231	0.001 / -0.004
3	Run 69a	Kentucky #9	0.363	0.449	0.45	0.087 / +0.001
4	Run 21	Illinois #6	0.16	0.185	0.185	0.025 / 0
5	Run 47b	Illinois #6	0.18	0.184	0.183	0.003 / -0.001
6	Run 47h	Illinois #6	0.32	0.185	0.185	0.135 / 0
7	Run 70b	Illinois #6	0.256	0.186	0.186	0.070 / 0
8	Run 27	Kentucky #11	0.26	0.328	0.328	0.068 / 0
9	Run 56c	Kentucky #11	0.23	0.314	0.312	0.082 / -0.002
10	Run 56f	Kentucky #11	0.33	0.328	0.328	0.002 / 0
11	Run 57	Kentucky #11	0.45	0.469	0.471	0.021 / +0.002
12	Run 58	Kentucky #11	0.39	0.328	0.328	0.062 / 0
13	Run 72	Kentucky #11	0.763	0.917	0.916	0.153 / -0.001
14	Run 73b	Kentucky #11	0.66	0.589	0.591	0.069 / -0.002
15	Run 73e	Kentucky #11	0.34	0.328	0.328	0.012 / 0
16	Run 74c	Kentucky #11	0.69	0.47	0.477	0.213 / -0.007
17	Run 74e	Kentucky #11	0.458	0.345	0.352	0.106 / -0.007
18	Run 22	Beulah Lignite	0.28	0.306	0.306	0.026 / 0
19	Run 48b	Beulah Lignite	0.37	0.306	0.306	0.064 / 0
20	Run 48f	Beulah Lignite	0.38	0.306	0.306	0.074 / 0
21	Run 32	Upper Freeport	0.3	0.503	0.503	0.203 / 0
22	Run 35	Upper Freeport	0.4	0.45	0.496	0.096 / +0.046
23	Run 71	Upper Freeport	0.486	0.503	0.503	0.017 / 0
24	Run 23	Eagle Butte	0.54	0.474	0.529	0.011 / -0.055
25	Run 61	Eagle Butte	0.72	0.599	0.623	0.097 / -0.024
26	Run 64	Eagle Butte	0.812	0.707	0.712	0.100 / -0.005
		Average Error		0.072	0.0695	
		Least Squares		0.2217	0.2125	

- One burn was affected negatively (burn R35). This may be due to experimental error or to the influence of the pyrite radius. The coal used in this burn, the Upper Freeport, is the coal with by far the largest pyrite and silicate particles of all six coals examined by Bool (1993). It is also the only coal where ash fragmentation was found by the researchers at Physical Sciences Inc., as cited by Bool (1993). Thus, mineral fragmentation might not be neglected, as it was in the model. By taking the radius to be 1/3 of the original ash particle radius, as the data from Physical Sciences Inc. would suggest, a clear improvement was made.

Overall, a slight positive effect on the results of the program was obtained. By taking into account that the influence of the fit parameter y (describing the ratio of iron and silicate in glassy particles) used by Bool (1993) is a critical portion of the program, a big improvement could not be expected. The results lead to the conclusion that the new dependencies for the glass capture rate (time, radius, concentration of iron in melt, correction of the temperature influence) are reasonable. This analysis demonstrates further that the original model provides a good description of iron partitioning during combustion. In addition, the modifications implemented here provide a better description of the importance of the original fit parameters, and lead to a method of estimating the fit parameters based on fundamental properties.

6.2 Design and Setup of Experiments

During pulverized coal combustion, the possibility exists for vaporization and subsequent nucleation of inorganic matter. Alkali vapors contribute to slagging, fouling, and corrosion problems, as found by Gallagher (1992). They also participate in submicron particle emissions, as do toxic vapors containing e.g. arsenic or mercury. In order to minimize and to control such emissions, the fundamental mechanisms of their formation will be examined in future work. In a first step, experiments with a drop tube aerosol reactor will be conducted. Particle size distributions will be collected, and used to collect evidence for mechanisms such processes as vaporization and subsequent heterogeneous condensation. Furthermore, the aerosol formed will be sampled and chemically analyzed.

The second goal of the experiments is to collect more data on the iron partitioning, especially for the substoichiometric cases. Ash samples will be conducted and examined by Mössbauer analysis. The data will be compared to model results, and the model given by Bool (1993) might be improved.

This part of this section deals with the experimental setup and design. It is described how to test and how to operate the equipment. A recipe for a base case experiment is given.

6.2.1 Experimental and Analytical Equipment

The goal of the experimental design is to burn pulverized coal at bench scale under well controlled environmental conditions. The furnace was designed such that the residence time in the middle heating section is approximately 3 s - comparable to residence times in industrial furnaces. For this residence time, a feed gas stream (carrying the coal particles) of about 8 l/min is needed. Using electrical heaters, wall temperatures of 1150°C can be reached. This leads coal particle to temperatures between 1300°C and 1500°C.

Due to the bench scale, small coal feed rates (between 2 g/h and 10 g/h) are used. The feed gas consists of nitrogen and air, or oxygen. This allows for adjustment of the stoichiometric ratio with the air or the oxygen, and for adjustment of the total feed gas stream independent of the stoichiometric ratio. For safety during the substoichiometric experiments, the entire system is sealed except the exhaust.

To collect more data on iron partitioning, fly ash for Mössbauer analysis is drawn out of the furnace with a vacuum pump and collected on a filter. Particle size distributions in the range of the vaporized material are determined using a TSI Inc. Scanning Mobility Particle Sizer (SMPS).

This section describes the components of the system, and the complete experimental setup.

6.2.1.1 The Drop Tube Aerosol Reactor

The main part of the drop tube aerosol reactor is a quartz tube with a length of 1067 mm and an inner diameter of 41.9 mm. The choice of quartz for the furnace material is convenient because of its thermal stability in the expected wall temperature ranges, its minimal thermal expansion properties, and its low thermal conductivity.

The outlet of the furnace tube is closed with a water cooled stainless steel sleeve, sealed with two Viton O-rings. The water cooling is necessary because the O-rings break down at temperatures over 200°C, and it is sufficient to keep the temperatures below this value because the outlet is outside of the heating zone.

The probe rod for the ash particle size analysis sample is inserted through the sleeve, and also sealed with a Viton O-ring. This probe rod is adjustable, so that particle samples might be collected at different heights (and therefore different residence times) in the furnace. The probe rod is normally connected to the Electrostatic Classifier of the Scanning Mobility Particle Sizer (SMPS).

The sleeve has four outlets for the exhaust, of which one is used to take a second particle sample. This is done by applying a vacuum pump, which draws the particles with the exhaust air out of the furnace. The flow induced by the vacuum pump can be controlled by adjusting a valve placed on the pump. The particles are first passing a water cooled metal tube, and then collected in an impactor after-filter of a cascade impactor. This impactor after-filter sample is collected for the Mössbauer analysis. However, it is possible to change the arrangement such, that the impactor after-filter is connected to the probe rod and the Electrostatic Classifier is connected to the outlet. The other three exhaust outlets are connected to the laboratory fume hood.

The upper end of the quartz tube was first sealed with a Number 8.5 rubber stopper. This was assumed to be sufficient because the inlet is 203 mm outside of the heating zone, and therefore the temperature should be low enough for the rubber stopper. The rubber stopper would have had the advantage of high flexibility. As the inlet for the feed gas stream (which carrys the coal particles), a stainless steel pipe with an outer diameter of 6.35 mm was forced through the rubber stopper. This pipe was connected to the feed system. However, it was found that the rubber stopper was releasing gases during the combustion process, which might influence the combustion and the particle size distribution scanned with the Scanning Mobile Particle Sizer (SMPS). Therefore, a special quartz tube, with an upper end made from quartz glass as well, which allows a direct connection to the quarter inch pipe coming from the feed system was designed and applied.

6.2.1.1.1 Furnace Heating

Three sections of insulated, cylindrical, electric heating elements with an inner diameter of 76.2 mm and an outer diameter of 165.1 mm are placed around the middle part of the quartz tube. The top and the bottom sections have lengths of 152.4 mm, and the middle section a length of 304.8 mm. The

three sections are currently connected to a single 240 volt AC variable power supply. However, use of one power supply for each section may provide better control over the temperature profile.

To measure the wall temperature as an indicator for steady state, ten Cole-Parmer type K thermocouples were placed on the quartz tube in the heating zone. These thermocouples are connected to a Cole-Parmer 12-channel scanning JTEK thermocouple thermometer, which is connected to a printer for automatic print out of the temperature profile in adjustable time steps. The distance between each thermocouple is 50.8 mm, starting at 101.6 mm from the bottom of the heating zone.

The part of the tube between the lower heater and the steel sleeve is air-cooled by applying two fans, while the part between the upper heater and the upper end is air-cooled by the use of one fan. Figure 6-13 shows the furnace and heating system schematic.

6.2.1.1.2 Feed System

The design of the feed system turned out to be very difficult and caused several weeks of project delay. Finally, a system consisting of a Plexiglas cylinder and piston, and a syringe pump was constructed, as shown in Figure 6-14. The arrangement is horizontal, with the cylinder having an inner diameter of 15 mm and the piston an outer diameter of 14.98 mm. To prevent leakage, an O-ring is placed on the piston at 6.35 mm from the top. The end of the cylinder is closed with a Plexiglas sheet. Close to the end of the cylinder, two holes were drilled in a vertical arrangement. The upper one has a 0.16 mm opening, where the gas stream, consisting of nitrogen and air or nitrogen and oxygen, enters the cylinder with high velocity. The lower one has a 6.35 mm opening, through which the feed stream, consisting of the gas stream and the coal particles, leaves the cylinder. The syringe pump pushes the piston forward at a constant rate, and thus the coal to the opening. The current geometry of the feed system provides the possibility of feeding up to 15 g of coal. The feed stream can be varied to cover the range of 2 g/h to 10 g/h.

The feed gas stream is a mixture of either nitrogen and air, or nitrogen and oxygen. The nitrogen flow is adjusted with a Matheson stainless steel float flowmeter type 604, and the air or oxygen stream with either an Aalborg flowmeter type GFM-1700, or a Matheson glass float flowmeter type 604 (depending on the stoichiometric ratio).

6.2.1.1.3 The Probe Rod

The probe rod is designed not only for collecting the particles, but also for quickly quenching and diluting the particle stream with nitrogen. Dilution of the sample minimizes the particle-particle interactions, forces the nucleation of vaporized material, and stops the oxidation. Sufficient dilution is also necessary to prevent supersaturation, subsequent nucleation, and condensation of water if water vapor is present in the sample. The nitrogen is added to the sample through a 6.35 mm outer diameter, porous stainless steel pipe. The sample and the dilution nitrogen is pulled through the probe rod by the vacuum pump from the ash particle size distribution analysis tool (Scanning Mobility Particle Sizer, SMPS), or by the vacuum pump connected to the impactor after-filter. Cooling of the rod is provided by a two channel surrounding water jacket. The probe rod was designed to be small in outer diameter (12.7 mm), and big in inner diameter (3.175 mm), so that the deformation of the streamline is small. Figure 6-15 shows a schematic of the particle collection system utilized.

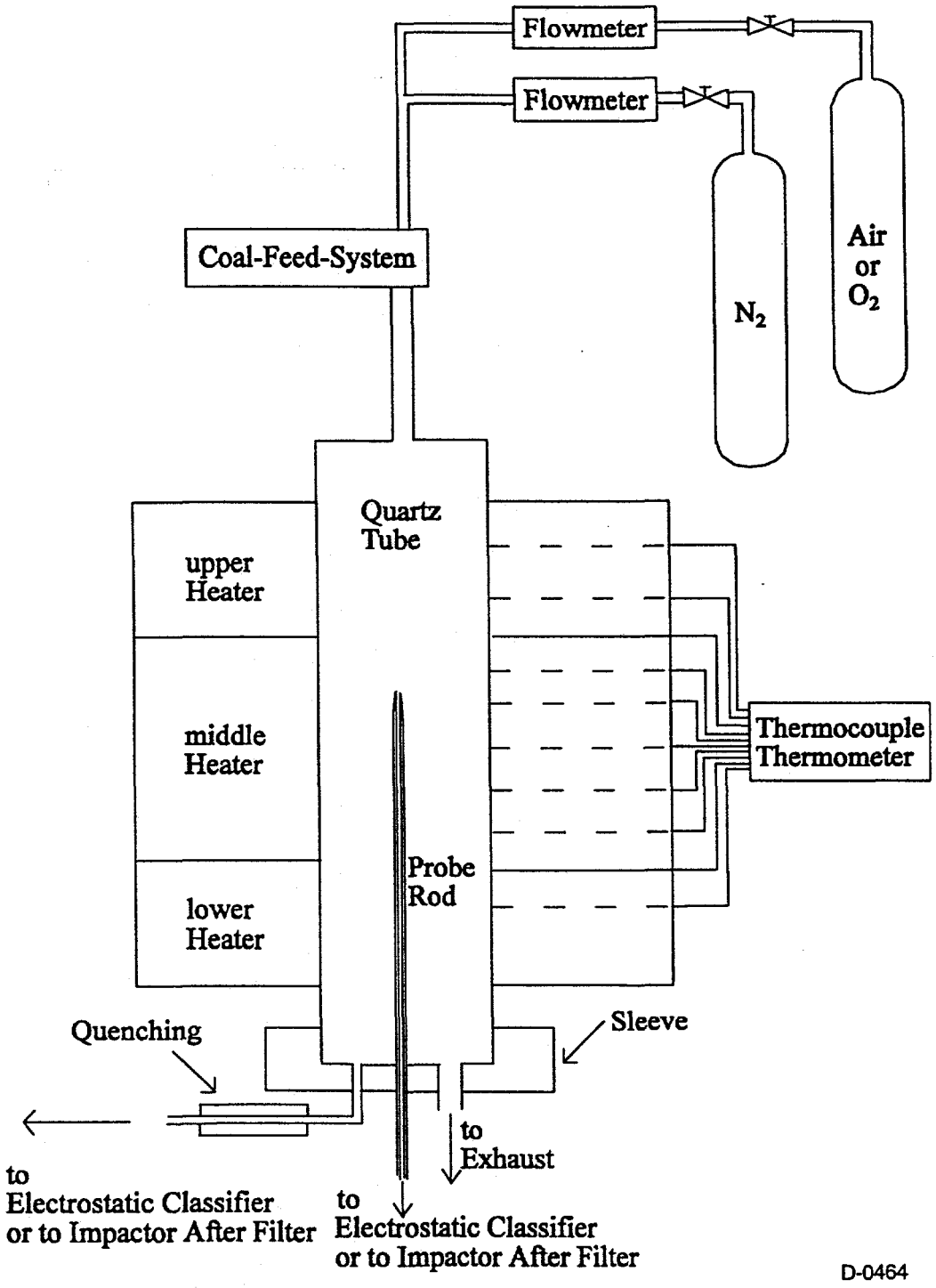

Figure 6-13. Furnace and heating system schematic.

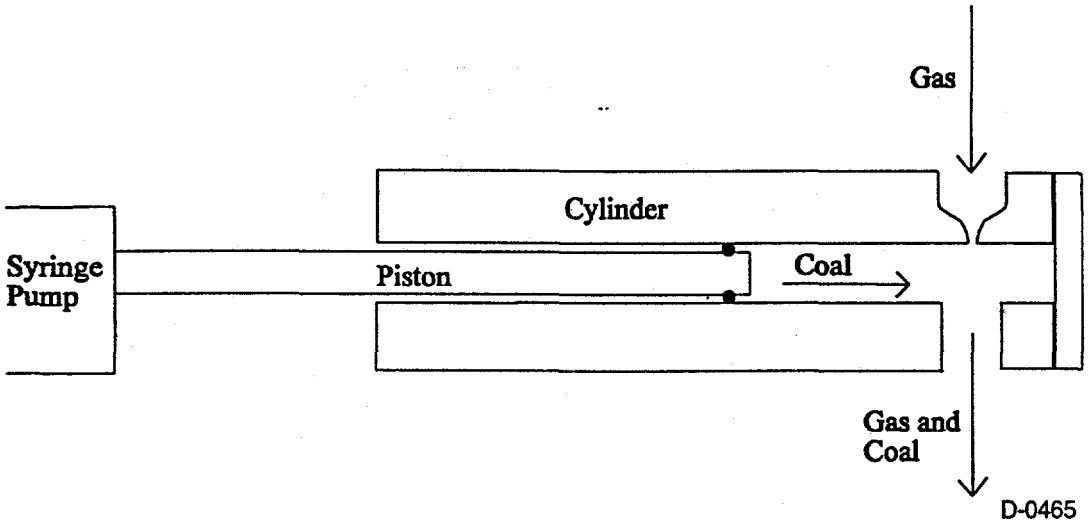

Figure 6-14. Feed system.

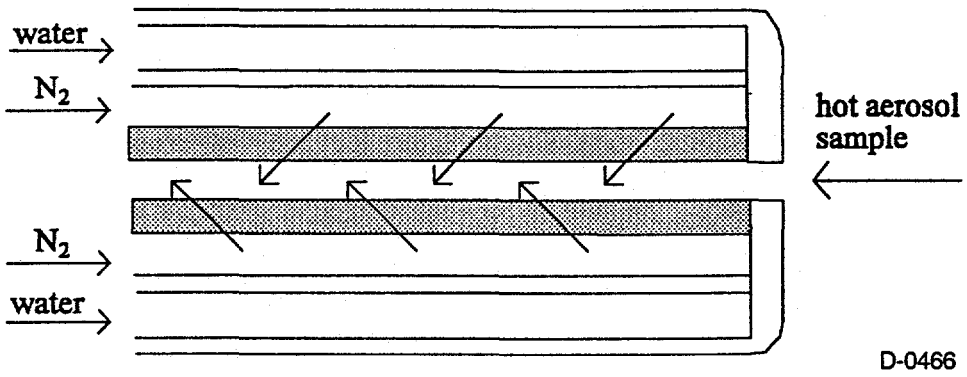

Figure 6-15. Probe rod for ash particle size distribution sample.

The probe rod has two cooling water inlets and two dilution nitrogen inlets close to its lower end. This gives a better distribution than a single inlet. The nitrogen flows are adjusted with a Matheson glass float flowmeter type 602 and a combined Matheson glass and stainless steel float flowmeter type 602.

6.2.1.2 The Scanning Mobility Particle Sizer

The Scanning Mobility Particle Sizer (SMPS) provides the possibility to measure particle size distributions in the range of 10 nm to 394 nm. These small particles represent the condensation products of volatile matter released during the combustion process. The SMPS (Figure 6-16) consists of three main parts, the Electrostatic Classifier (TSI Incorporated Model 3071), the Ultrafine Condensation Particle Counter (TSI Incorporated Model 3025) and the microcomputer (Gateway 2000).

The Electrostatic Classifier is used to classify the particles according to their size, while the Condensation Particle Counter counts the number of particles of each size. The Particle Counter is connected to the Microcomputer, which analyzes the data using a software packet delivered by TSI with the Particle Counter and the Electrostatic Classifier.

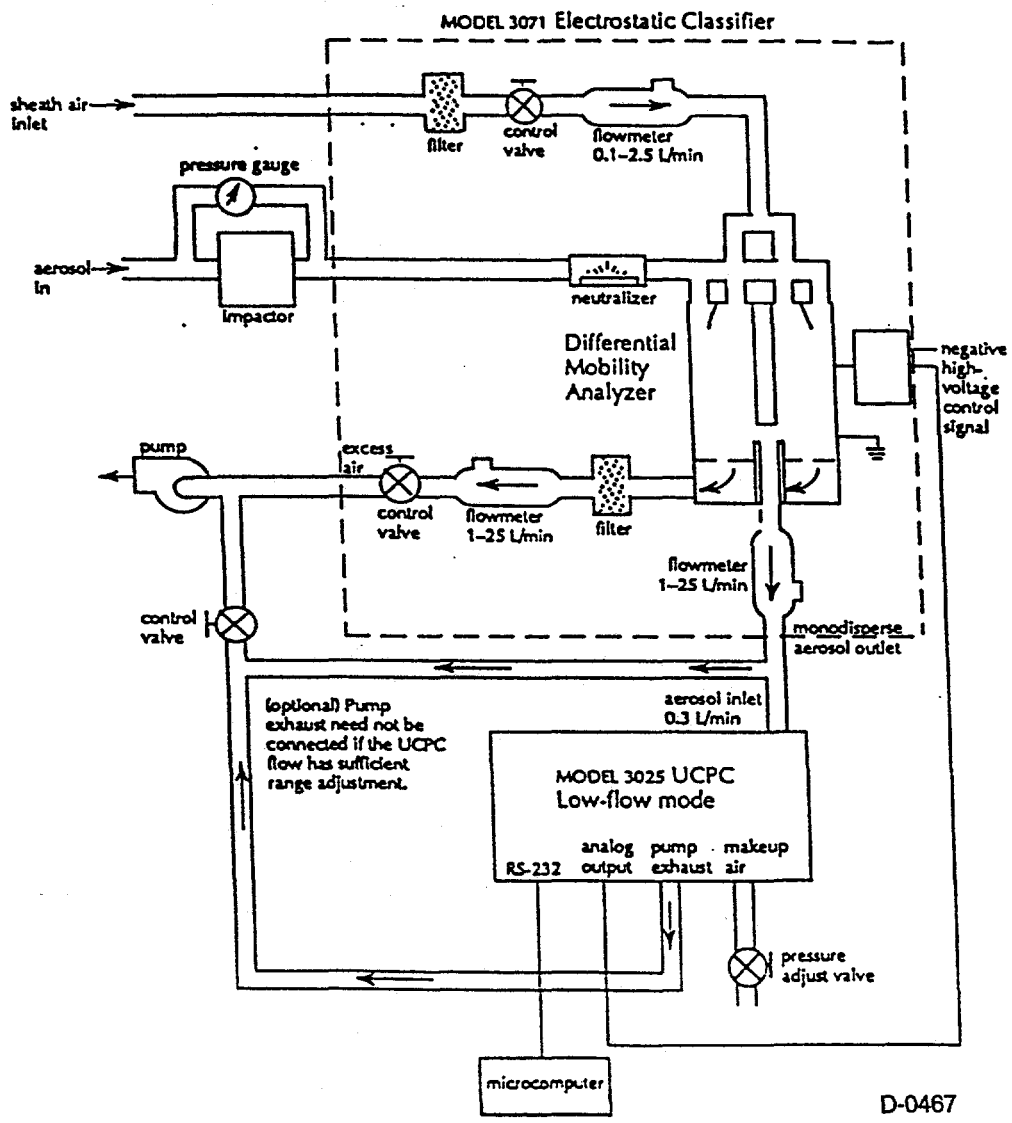

Figure 6-16: Schematic of the size distribution analysis tool (underpressure mode)[1]

The system can be run in underpressure or overpressure mode. In overpressure mode, air is forced through the system by an aerosol source (under pressure) and compressed air. However, for these experiments the underpressure mode was used. Air is drawn through the system by a vacuum. As can be seen in Figure 6-16, an impactor is needed to remove the large particles which carry more than a single charge. A vacuum pump is used to run the system in underpressure mode.

[1]Taken out of the Instruction Manual of the 'Ultrafine Condensation Particle Counter', TSI Incorporated, Model 3025

6.2.1.2.1 The Electrostatic Classifier

The principle of electrostatic classifying is based on the relationship between electrical mobility and particle size. The particles are first exposed to a gaseous medium containing bipolar ions, which are produced by a radioactive source (Kr-95). Particles and ions will then collide due to the thermal motion of the ions. In time, an equilibrium state is attained where the particles carry a bipolar charge given by the Boltzmann law. This charge is normally distributed according to the particle size. Small particles in equilibrium with bipolar ions carry low elementary charge (e.g. all particles with a diameter of 0.01 μm carry between -1 and 1 elementary charge units), while the charge of bigger particles is distributed over wider ranges of elementary charge units. Thus, the amount of singly charged particles (particle with an elementary charge unit of -1 or 1) is related to the total amount of particles of these size by this distribution.

The electrical mobility of a singly charged particle is a monotonically decreasing function of the particle size. The charged particles are passed through an annular metal cylinder, between which negative dc voltage is applied (see Figure 6-17). This causes particles of positive polarity to be attracted to the metal cylinder. Highly charged particles, and singly charged particles with high electrical mobility, will be captured on the upper part of the cylinder, while those with lower electrical mobility, and the ones with negative polarity, will be carried along with the main outlet flow. Only those singly charged particles with the correct electrical mobility, and hence particle size, will be attracted to the slit at the end of the cylinder. Thus, the particles are classified by changing the dc voltage of the cylinder within this range, such that the singly charged particles of each class are drawn through the slit.

6.2.1.2.2 The Condensation Particle Counter

In the Condensation Particle Counter (Figure 6-18), the particles are first enlarged by a condensing vapor, and then optically counted. When vapor surrounding a particle reaches a certain degree of supersaturation, it begins to condense onto the particle. This is called heterogeneous condensation. For a given saturation ratio, vapor can condense onto particles only if they are large enough, leading to a critical particle diameter. The higher the saturation ratio is, the smaller the critical diameter. Thus, by forcing a certain saturation ratio, particles from a certain size upwards are enlarged. The particles are surrounded by the liquid to form droplets with a diameter of several micrometers.

After their enlargement, the particles pass through a lighted viewing volume where they scatter light. The scattered-light pulses are sensed by a photodetector and converted into electrical pulses. The electrical pulses are then counted and their rate (calculated) is a measure of the particle concentration.

6.2.1.2.3 The Microcomputer and the Software

The microcomputer used was a Gateway 2000, equipped with a 486 microprocessor, Microsoft DOS version 6.20, Microsoft Windows for Workgroups version 3.11, and a mouse. The SMPS software package is designed to run under Microsoft Windows, and provides pull down menus, dialog boxes, and the use of a mouse. The software delivers many different representations of particle size distributions, e.g. the distribution of the number distribution size, in the form of histograms, or tables.

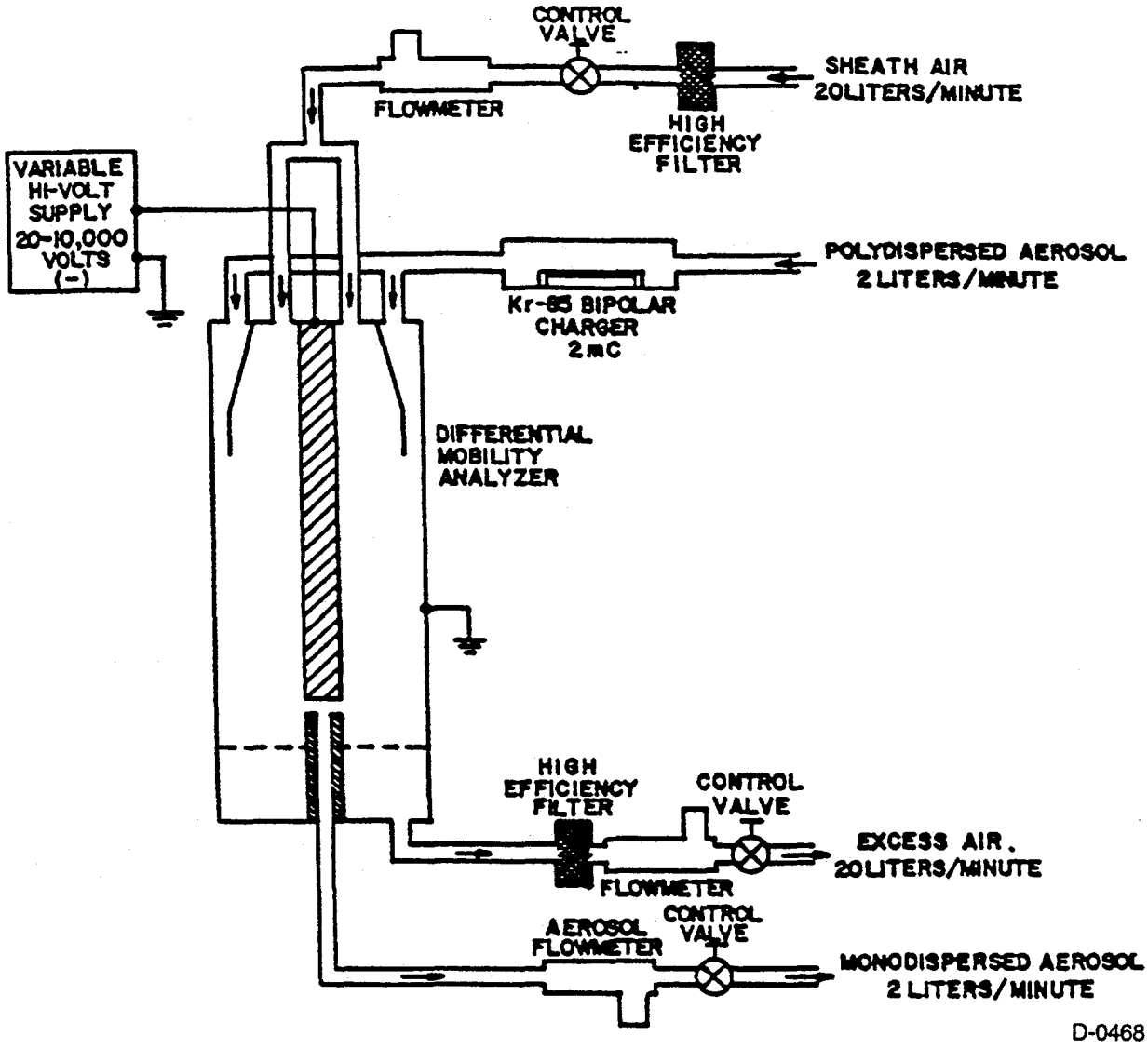

Figure 6-17: Schematic diagram of the Electrostatic Classifier[2]

6.2.1.3 Mössbauer Analysis

As the analytic tool to determine the iron partitioning of a sample, Mössbauer analysis is used (in conjunction with Dr. Roy Emrick, University of Arizona). This method is based on an effect found by the German physicist R.L. Mössbauer, who was awarded the Nobel Prize for his work. The Mössbauer effect is alternatively known as recoil-free nuclear resonance absorption. Resonance absorption occurs if a system absorbs a quantum of energy equal to the difference between two of its energy states. By passing γ-radiation through the sample, and measuring the amount absorbed as a function of the γ-beam energy, a curve with characteristic absorption peaks for each compound is obtained. The chemical state of the iron in the glass might then be determined, as well as the oxide forms, by finding these characteristic peaks.

[2]Taken out of the Instruction Manual of the 'Electrostatic Classifier', TSI Incorporated, Model 3071

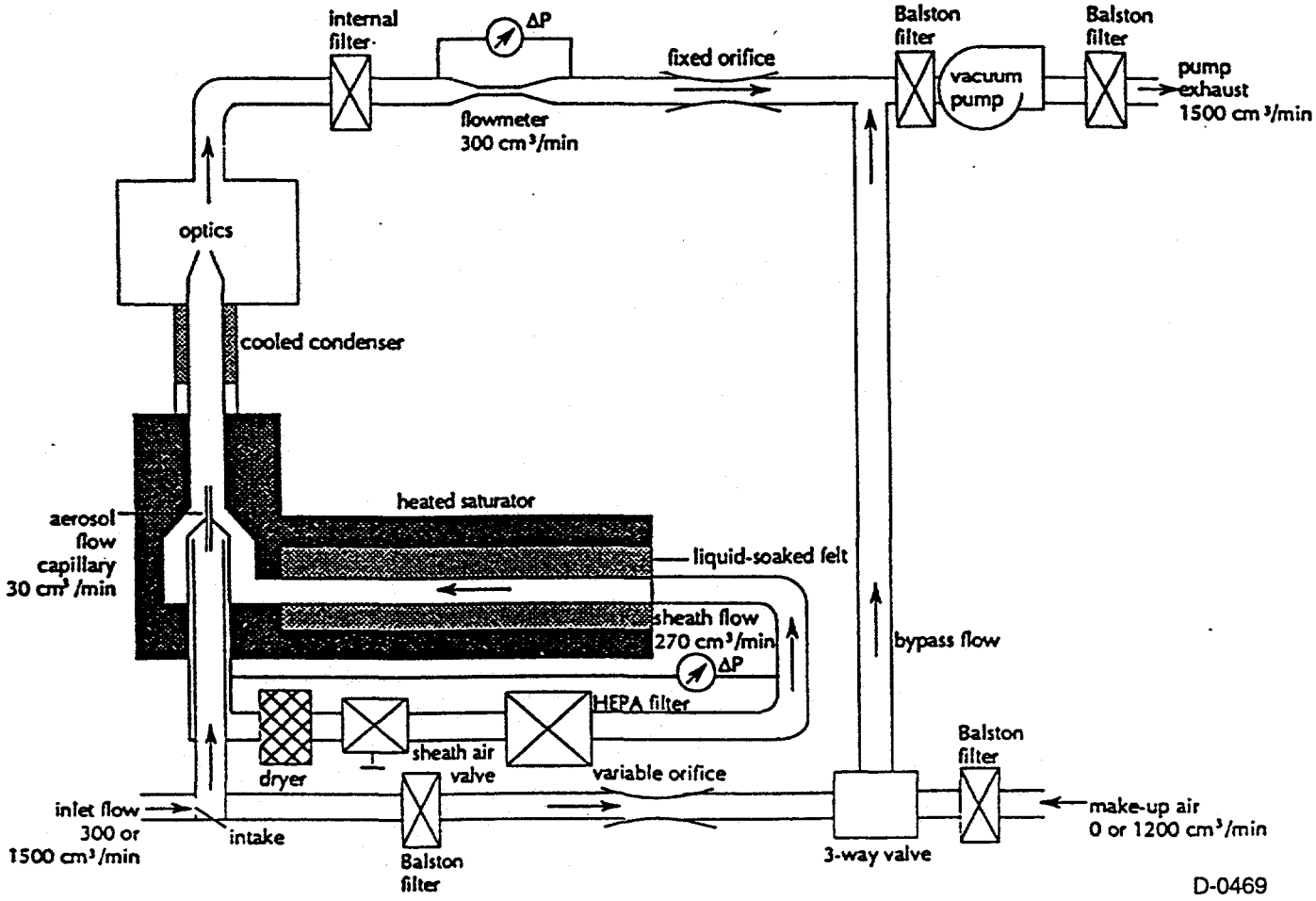

Figure 6-18: Flow schematic of the Condensation Particle Counter[3]

The fraction of each compound is given by dividing the area under its peak with the area under all the peaks. For additional information see Vértes et al. (1979).

Using this technique, a relatively large sample of approximately 0.5 g is mounted in a thin layer on a filter paper, and fixed with DEFT Polyurethane spray (DEFTHANE). Because a relative large sample is needed for this analysis, only the iron distribution in the ash as a whole (no size classified information) can be obtained. This ash sample is drawn out of the furnace during the combustion process by a vacuum pump, and collected on the impactor after-filter of a Delron Research Products Co. cascade impactor model DCI-5. Initially, the complete impactor was connected to the furnace outlet. By doing this, particle size distributions between 0.25 μm and 4 μm should be obtained, while the sample for the Mössbauer analysis was to be collected on the first impactor stage (because many particles with diameters bigger than four microns were expected). However, it was found that the impactor jets clogged very quickly, probably due to a bounce-off problem. The full impactor was then replaced with just the after-filter-collecting a total filter sample for Mössbauer analysis.

---

[3] Taken out of the Instruction Manual of the 'Ultrafine Condensation Particle Counter", TSI Incorporated, Model 3025

The data files from Dr. Emrick's facility were transformed and computed with software developed by Dr. Emrick. The data was smoothed over ten points in order to better determine peak location. The values were normalized by dividing them with the first value (channel 6) to receive transmission percent. The channels correspond to the particle velocity following Eq. (6-135), which was found by Bool (1993) from calibrations with metallic iron.

$$\text{velocity} = 0.03852 \cdot \text{channel\#} - 9.83511 \text{ [mm/s]} \qquad (6\text{-}135)$$

For the quantitative analysis, the unsmoothed data was used. The program needs the peak locations as inputs. The locations of the magnetite and hematite peaks can be seen in Bool (1993) or Vértes et al. (1979). The peak doublet, which is caused by iron ions captured in glass, is also to be found in Bool (1993).

6.2.2 Operating the System

Several tests and experiments were carried out to check and characterize the components of the system, and to determine a method to run the complete system. Main points were testing and improving the new feed system, testing the Scanning Mobility Particle Sizer, conducting temperature profiles, and identifying and solving problems associated with running the complete system. In this section, operation of the feed system, and testing of the Scanning Mobility Particle Sizer are discussed. A general experimental procedure for operating the complete system is given. Furthermore, the influence of the gas stream and combustion conditions on temperature profiles is discussed.

6.2.2.1 Operating the Feed System

The main problems associated with the feed system are that the piston might get stuck and the coal feed is very "puffy" instead of (quasi-)constant. To prevent these problems, experiments with the feed system were carried out, leading to the handling instructions documented here.

It is very important that the piston and the cylinder are dry and clean before the coal is filled in the cylinder. Special attention should be given to the connectors for the gas and the feed stream, since moisture often remains there. The piston's O-ring has to be checked for damage and then smeared with a dry lubricant such as Mr. Zip Extra Fine Graphite. Initially, vacuum grease was used instead of graphite. It was found that the grease interacted with the coal, forming a sticky paste, making it more likely that the feed system stuck during the experiment.

The coal should be kept dry. This prevents stickiness leading to agglomeration, which also causes problems. If large agglomerates within the pulverized coal can be seen, it is useful to screen the coal. It was found that the feed system works well if the coal particles are smaller than 150 μm. However, attention has to be paid to ensure that the screened out coal particles are not different in composition than the remaining coal, (e.g. that predominantly ash particles are screened out).

The pulverized coal should be added to the cylinder by placing the cylinder vertically and inserting a funnel in the end of it (the opening for the piston). When the coal is poured in, the gas inlet and the feed stream outlet should remain open. This causes some coal to flow out again, but keeps the coal inside the cylinder loose. The coal should be poured into the cylinder until the cylinder is completely filled. Then, keeping the cylinder vertical, the piston is used to push the coal out until the piston is half way inside of the cylinder. If problems occur pushing the coal out, there is a strong chance that the feed system will get stuck. In this case, the procedure should be aborted, everything cleaned and dried, and started again at the

beginning. If no problems occur, the gas inlet and the feed outlet were sealed with caps, and the weight of cylinder, piston, caps and coal was determined. The weight without coal is 0.392 kg, so the coal mass can easily be calculated.

Afterwards, the cylinder/piston assembly has to be placed in the syringe pump, using one of the three possible places, (normally the third counting from the regulators upwards). The fixing hook of the syringe pump is placed in the groove at the end of the cylinder and adjusted. The other end of the cylinder should be fixed with a clamp. The clamp is connected to the grating. The board on which the syringe pump is fixed is also connected to the grating. The cylinder must be fixed straight in piston, and straight to the syringe pump as well.

To adjust the feed stream with the regulators of the syringe pump, the grams coal in the system are compared to the length coal-containing part of the cylinder. Therefore, the linear speed for the wanted feed rate is found. The regulators are set on a 60 ml syringe, and on X1 in the range ml/hour. Then, following calibration data, the flow rate to adjust at the syringe pump is given by:

$$\text{flow rate setting} = \frac{\text{linear speed [cm/hour]}}{0.17577} \qquad (6\text{-}136)$$

Finally, the cap from the feed stream outlet is removed and the pipe to the furnace connected. Then, the cap from the gas stream inlet is removed, and the gas stream connected. This often leads to a first big puff of coal entering the furnace (carrying about one gram of coal). The syringe pump is then turned on. While the piston moves the first centimeter the coal is more compacted than pushed out. This leads to a relatively small amount of coal being fed during this time. Afterwards, the feed stream becomes quasi-constant. The smoothness depends strongly on the feed gas stream. If a feed gas stream of 2 l/min is used, the system puffs with a frequency between ten seconds and one minute. If a feed gas stream of 8 l/min is used (corresponding to a flow of 10 cm/s in the furnace) puffing is not to be seen.

After use, the cylinder and piston should be cleaned by first blowing the remaining coal particles out with pressure air, and then washing with water. Stronger washing substances like acetone should not be used, because they affect the Plexiglas. To achieve a completely clean system, and especially to ensure that no coal remains in the groove under the O-ring, the O-ring has to be taken off and cleaned separately.

6.2.2.2 Testing the Scanning Mobility Particle Sizer

With the goal to obtain a set of base case data, cigarette smoke from cigarettes of the brand 'KOOL' was sampled with the Scanning Mobility Particle Sizer. The system was run in underpressure mode, and the 459 nm impactor nozzle was applied. The delay times were set to tf = 3.8 s and to td = 3.9 s, and charge correction was not used. The aerosol flow was set to 0.6 l/min, and the sheath air and excess air flow to 6 l/min. This corresponds in the meter range of 10 V with values given by the flowmeters of 2.82 for the monodisperse aerosol, 2.98 for the excess air, and 2.9 for the sheath air. The pressure gauge, as the aerosol inlet flowmeter, showed a value of 27 cm of water. The scan uptime and downtime were set to 60 s and 15 s respectively.

The collected distributions showed a peak of the number of particles at midpoint diameters between 160 nm and 200 nm, while a minimum in the smaller size ranges could be seen (Figure 6-19 and

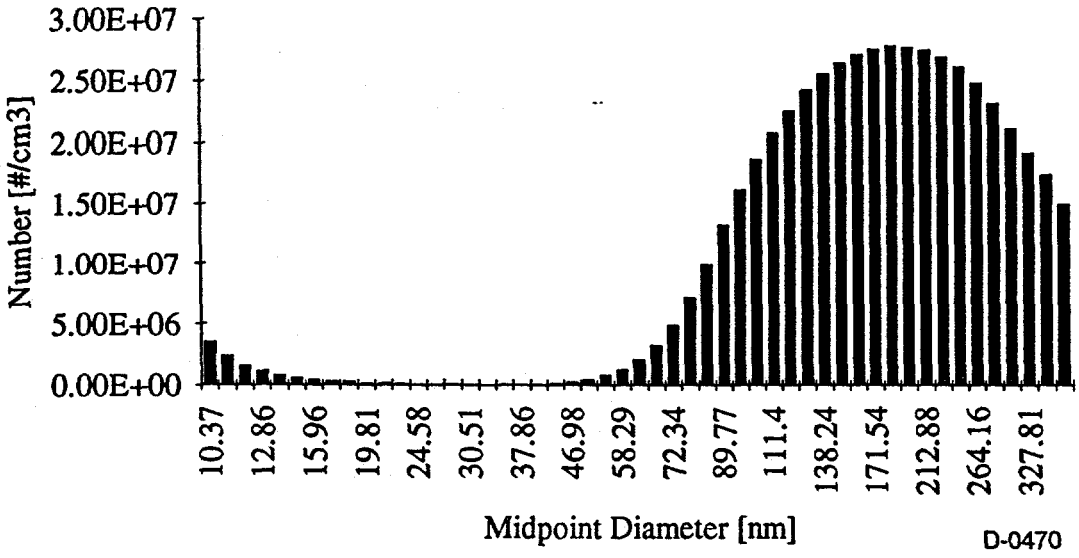

Figure 6-19: Typical cigarette smoke particle number distribution

Table 6-2). Because of the regularity of the distributions, and the simple experimental procedure, it is easy to test the Scanning Mobility Particle Sizer.

Table 6-2: Typical Cigarette Smoke Particle Distributions

Channel	Midpoint Diameter	Number	Surface	Volume
17	10.37	3511500	1185500000	2048200000
18	11.14	2407900	938710000	1742800000
19	11.97	1658100	746400000	1489300000
20	12.86	1219100	633760000	1358800000
21	13.82	838110	503150000	1159200000
22	14.86	643860	446360000	1105100000
23	15.96	478450	383030000	1019100000
24	17.15	333790	308590000	882270000
25	18.43	307300	328070000	1007900000
26	19.81	182360	224810000	742240000
27	21.29	147130	209450000	743130000
28	22.88	122780	201850000	769570000
29	24.58	76296	144840000	593440000
30	26.42	89026	195170000	859290000
31	28.39	45272	114610000	542250000
32	30.51	41440	121150000	615950000
33	32.78	41835	141230000	771640000
34	35.23	48851	190440000	1118100000
35	37.86	63021	283720000	1790000000
36	40.68	92254	479610000	3251700000

Table 6-2: Typical Cigarette Smoke Particle Distributions (cont.)

Channel	Midpoint Diameter	Number	Surface	Volume
37	43.71	173960	1044300000	7608800000
38	46.98	288930	2003000000	15682000000
39	50.48	466510	3734700000	31422000000
40	54.25	851520	7872200000	71174000000
41	58.29	1336200	14265000000	1.3859E+11
42	62.64	2096300	25844000000	2.6982E+11
43	67.32	3264800	46479000000	5.2147E+11
44	72.34	4971500	81731000000	9.8539E+11
45	77.47	7201800	1.3672E+11	1.7714E+12
46	83.54	9925100	2.1759E+11	3.0294E+12
47	89.77	13314000	3.3705E+11	5.0428E+12
48	96.47	16239000	4.7475E+11	7.6329E+12
49	103.66	18721000	6.3202E+11	1.0919E+13
50	111.4	20849000	8.128E+11	1.5091E+13
51	119.71	22652000	1.0198E+12	2.0346E+13
52	128.64	24266000	1.2615E+12	2.7047E+13
53	138.24	25584000	1.5359E+12	3.5387E+13
54	148.55	26458000	1.8343E+12	4.5414E+13
55	159.63	27144000	2.1731E+12	5.7817E+13
56	171.54	27576000	2.5494E+12	7.2888E+13
57	184.34	27826000	2.9707E+12	9.127E+13
58	198.1	27719000	3.4172E+12	1.1282E+14
59	212.88	27526000	3.9187E+12	1.3903E+14
60	228.76	26937000	4.4284E+12	1.6884E+14
61	245.82	26148000	4.964E+12	2.0338E+14
62	264.16	24860000	5.45E+12	2.3995E+14
63	283.87	23235000	5.8823E+12	2.7831E+14
64	305.05	21143000	6.181E+12	3.1426E+14
65	327.81	19250000	6.4987E+12	3.5506E+14
66	352.27	17484000	6.8162E+12	4.0019E+14
67	378.55	15016000	6.76E+12	4.265E+14
Totals		16340000	2.02E+12	9.4814E+13

Generally, the flowmeters of the Electrostatic Classifier should be watched carefully, because they were found to be very sensitive. Their values for zero flow should be compared regularly to the calibration data. If these values differ more than 0.05 V in the 10 V range, the Electrostatic Classifier has to be opened, and the flowmeter sensors have to be cleaned with acetone.

6.2.2.3 General Experimental Procedure

At the beginning of each experiment the electrical heaters were turned on. The regulator was set between forty and fifty percent of maximum output voltage, which corresponds to 112 V and 140 V, respectively. The voltage was increased with increasing gas feed stream to reach maximum temperatures of about 1100°C.

The probe rod was inserted, the cooling water turned on, and the fans switched on. After about one hour, a maximum wall temperature in the middle section of 950°C was reached. At this point, the gas streams were set and connected. The vacuum pumps were switched on, yielding the complete flow pattern in the furnace.

During the last phase of heating up, furnace 'air' samples with the Scanning Mobility Particle Sizer were taken. If particles were detected during this period, their source was identified and eliminated. For instance, when the rubber stoppers were used to seal the top of the tube, the experiment was delayed until the rubber stopper stopped emitting gas.

To indicate steady state operation the wall temperatures were used. Steady state was reached when the temperatures did not change more than 10°C in about half an hour. The wall temperature profile has a maximum in the middle section, and falls on both ends of the tube. If this profile is not measured by the thermocouples, then most likely the thermocouples measuring unexpected values are wrongly placed (for instance not pushed all the way through the heater to the outside of the glass tube).

After a steady state temperature profile was achieved, the feed system was prepared, connected, and the coal feed started. The temperature profile was not substantially affected by the burning coal, rising a maximum of 20°C from the values reached at steady state without feed. After the initial feed puff, the filter paper in the impactor after-filter was changed, and the nozzle and impactor plate of the Scanning Mobility Particle Sizer were cleaned. From then on, particle size distributions were collected with the Scanning Mobility Particle Sizer. If special events occurred, the notefile of the Scanning Mobility Particle Sizer was used to note them. Furthermore, they were written down on the computer printout, which showed the wall temperatures and the experimental time. After the coal feed was completed, the vacuum pumps and the heat were turned off. Then, the feed system was disconnected, and the feed and dilution gas turned off.

For cooling down a time of about 2 to 3 h is needed. During this period the feed system, the probe rod, and the impactor plate and nozzle of the Scanning Mobility Particle Sizer were cleaned. The pipes through which feed stream or sample air flows were also cleaned by the use of pressure air. The filter paper was removed out of the impactor after-filter and stored in a sample container. A backup of the data collected with the Scanning Mobility Particle Sizer was saved to floppy disk. As the quartz tube reached temperatures below 100°C, the water cooling was shut down, and the fans were switched off. The quartz tube was removed from the heaters. A close look was given the deposits on the tube wall before the tube was cleaned with acetone. The ash deposit in the sleeve was placed in a sample container, and the sleeve cleaned with pressure air.

6.2.2.4 Temperature Profiles

To characterize the reactor and determine the relation between the gas temperatures in the tube and the tube wall temperatures (outside) a 91.44 cm long Cole-Parmer thermocouple probe type K was inserted from the bottom into the glass tube. This was done by using the opening for the probe rod of the sleeve,

and inserting the thermocouple through a hole in a number 0 rubber stopper fixing the thermocouple probe and sealing the opening. The thermocouple probe was moved from one position of a wall temperature thermocouple to the next, starting at the lowest position (the bottom thermocouple is placed 101.6 mm from the bottom of the heating zone, the difference between two thermocouples is always 50.8 mm). At each position, the measured temperature was allowed to reach a steady state, before the value and the corresponding wall temperature were noted. Between two and three minutes were normally required to come to a steady state.

When the highest position was reached, the thermocouple was left there until the start of the next measurement. It was then moved down from position to position. This method was chosen to prevent noticeable temperature gradients in the furnace caused by the thermocouple probe. The wall temperature profile indicated no effect of the thermocouple probe. During the measurements, special attention was paid so that the thermocouple probe was placed close to the centerline, and did not touch the inside of the tube wall.

Two types of experiments were performed. The goal of the first ones was to explore the effect of the gas stream on the temperatures. The goal of the second ones was to measure gas temperatures during coal combustion.

Because the probe rod could not be inserted, the flow pattern in the furnace was slightly different from the flow pattern during 'normal' experiments. However, the device used to collect the fly ash sample was switched on to get as close as possible to actual conditions.

6.2.2.4.1 Dependency on the Gas Stream

Temperature profiles were measured for gas flowrates of 2, 4, 6 and 8 liters/mine. No coal was burned in the furnace during these experiments. The gas utilized was pure nitrogen, except for the measurement at 8 liters/min. For this condition a gas stream consisting of 4 liters oxygen and 4 liters nitrogen/min was used. The furnace temperature was set so that the peak wall temperature was between 1050 °C and 1060 °C.

Temperature differences from 10°C to 70°C were observed between gas and wall temperature in the middle heating section. As expected, with increasing the gas flowrate resulted in gas temperature decreases. The temperature differences between wall and gas also increase. The big difference between wall and gas temperature at the top is due to the gas stream inlet, and the air cooling of the upper part of the tube. The low temperature difference at the bottom (which is reversed for the gas streams of two and four liters per minute) is due to the water cooled sleeve, and the air cooling of the lower part of the tube.

6.2.2.4.2 Temperature Profiles During Burn

The setup of the experiment was similar to those of the base case experiment). The coal burned was the Illinois #6, and the feed gas stream consisted of 4 l/min pure nitrogen and 4 l/min pure oxygen. The temperatures were a little lower than during the base case experiments to avoid the danger of overheating the thermocouple probe. Thus, the peak wall temperature before the start of the burn was adjusted to be similar to the peak wall temperature during the measurement of the temperature profiles for a gas stream of 8 l/min.

Table 6-3. Temperature Profiles [°C]

Gas Stream		Bottom	2	3	4	5	6	7	8	9	Top
2 l/min	Gas	927.5	955.5	995.3	1017	1026	1013	994.5	952	902.1	826.4
	Wall	920.3	977.5	1007	1031	1059	1035	1029	974.9	945.5	928.4
4 l/min	Gas	921	943.6	981.4	1001	1013	994.5	972.8	943.5	891.9	814.9
	Wall	915	970.6	988.1	1024	1051	1026	1021	967.9	936.5	913.3
6 l/min	Gas	933.6	945.6	970.6	997.4	1010	975.2	957.3	943.3	894.3	783.5
	Wall	942.8	985.8	1008	1032	1057	1028	1021	965	936.4	906.4
8 l/min	Gas	917.8	932.5	967.4	1002	992.1	973.6	942.4	894.4	853.3	772.4
	Wall	929.6	980.4	1007	1034	1056	1027	1018	954.4	916.8	891.1

Table 6-4. Differences Between Gas and Wall Temperature [°C]

Gas Stream	Bottom	2	3	4	5	6	7	8	9	Top
2 l/min	-7.2	22	11.7	14	33	22	34.5	22.9	43.4	102
4 l/min	-6	27	6.7	23	38	31.5	48.2	24.4	44.6	98.4
6 l/min	9.2	40.2	37.4	34.6	47	52.7	63.7	21.7	42.1	122.9
8 l/min	11.8	47.9	39.6	32	63.9	53.4	75.6	60	63.5	118.7

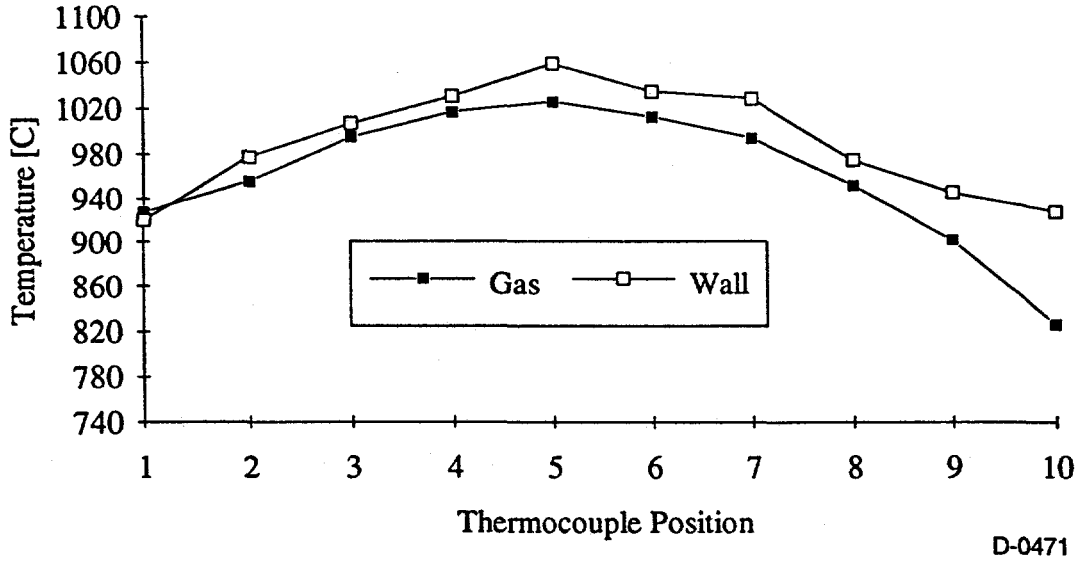

Figure 6-20. Profiles for gas stream of 2 l/min.

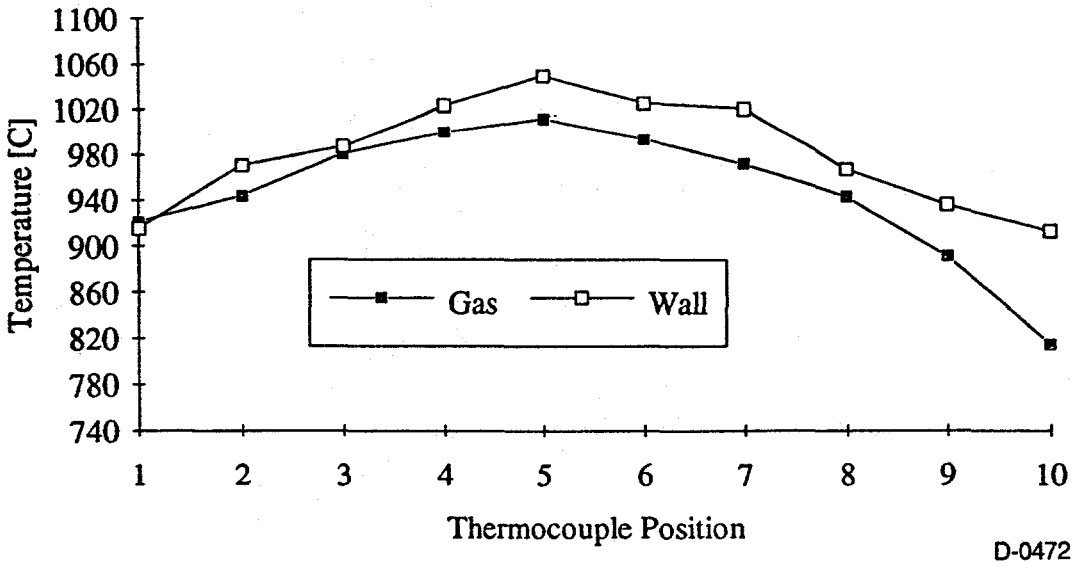

Figure 6-21. Profiles for gas stream of 4 l/min.

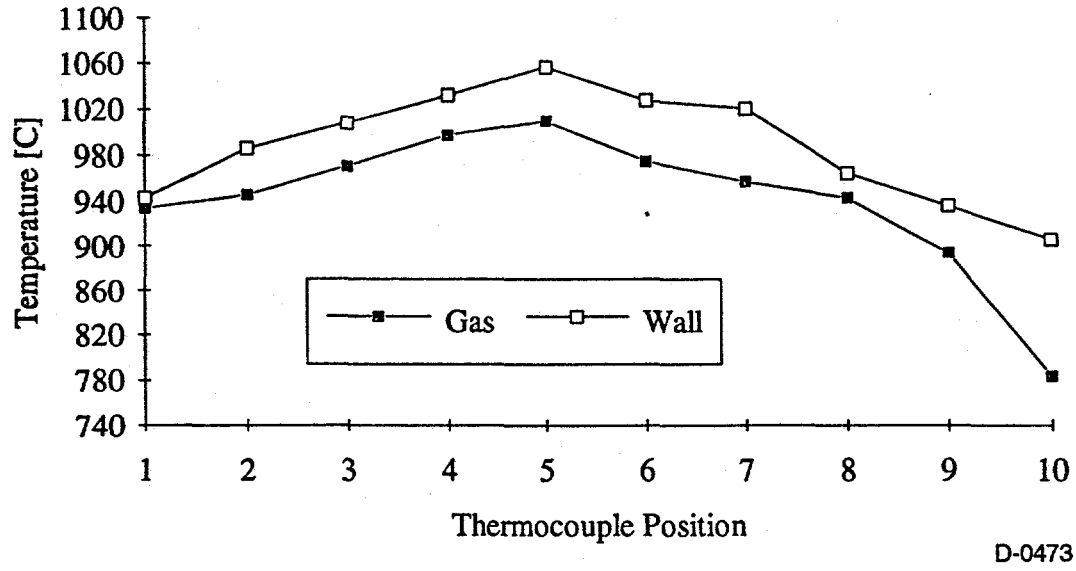

Figure 6-22. Profiles for gas stream of 6 l/min.

Three gas temperature scans were made during the experiment. First the thermocouple probe was moved up, then down, and finally up again. The temperatures during the first scan were higher than subsequent scans. This was due to the heating of the system caused by the initial coal pulse (as discussed in previous sections).

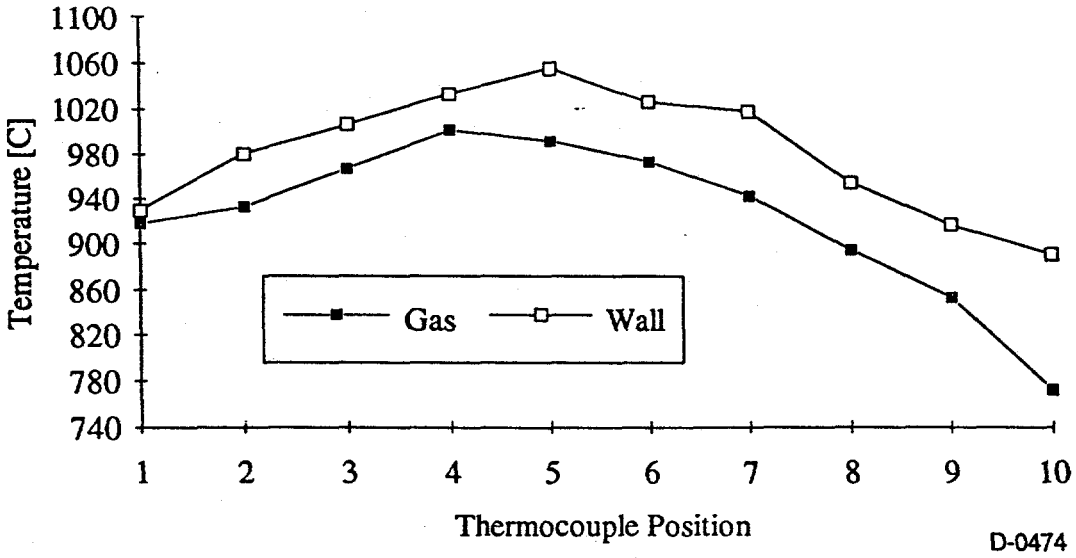

Figure 6-23. Profiles for gas stream of 8 l/min.

Table 6-5: Temperature profiles during burn [°C]

		Bottom	2	3	4	5	6	7	8	9	Top
Scan #1	Gas	947	955.5	994.7	1017	1027	1017	965.4	929.7	881.9	782.6
	Wall	963.3	989.6	1024	1051	1075	1064	1031	990.3	959.2	916.2
Scan #2	Gas	917.9	936	987.8	1000	1009	998.1	978.9	917.9	875.5	776.7
	Wall	923.6	967.3	1009	1037	1065	1048	1033	987.3	956	913.5
Scan #3	Gas	916.9	939.4	987.6	994.5	1005	1004	968.6	932.6	882.7	782.8
	Wall	922.4	966.4	1006	1037	1065	1046	1031	993.6	958.8	909
Mean	Gas	927.3	943.6	990	1004	1014	1006	971	926.7	880	780.7
	Wall	936.4	974.4	1013	1042	1068	1053	1032	990.4	958	912.9
Difference		9.167	30.8	22.97	37.83	54.7	46.3	60.7	63.67	77.97	132.2

The results show that the influence of the burning coal is very small. The mean temperature differences are similar to those found for a gas stream of 8 l/min without burning coal while gas and wall temperatures are between 10 and 30°C higher. The peak gas temperature is to be found at the fifth thermocouple instead of the fourth.

6.2.3 Base Case Experiment

To achieve a repeatable experiment for testing the system, and to compare the obtained data to data obtained by Bool (1993) in his experiments with the down fired laboratory scale combustor, a base case experiment was carried out.

6.2.3.1 Setup of the Experiment

The base case experiment followed the general experimental procedure outlined previously. Because of its small coal particle sizes the Illinois #6 coal was used. It was found by screening the coal

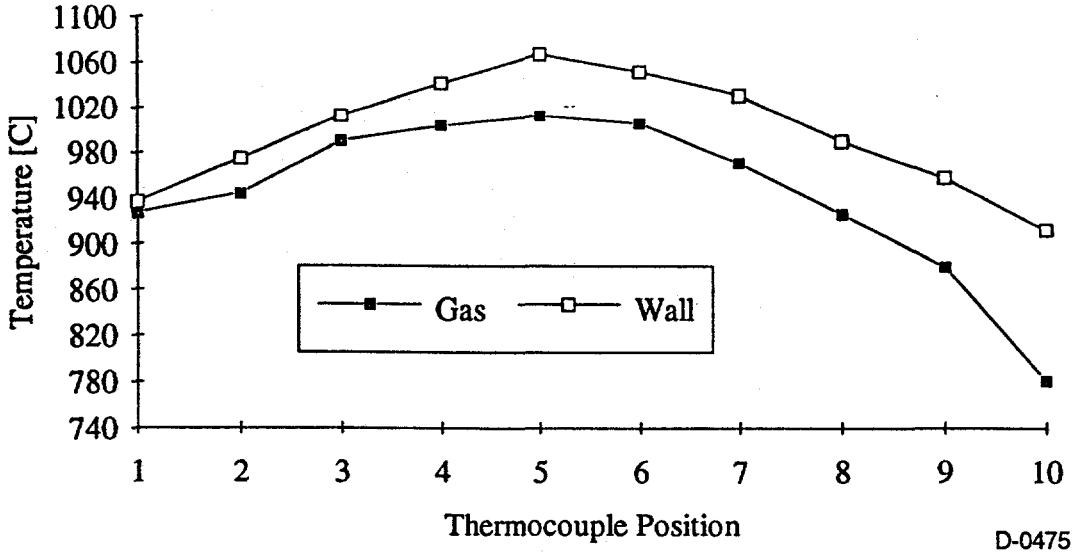

Figure 6-24: Mean temperature profiles during burn.

that all particles were smaller than 150 μm. Therefore, the coal was easy to feed. The coal has a low ash content of 8.62%, 42.15% fixed carbon, 35.92% volatile matter, and contains 13.31% moisture (proximate analysis by Foster Wheeler Co.). The ash analysis shows a high silicate and a high iron content (46.1% silica oxide and 20.5% iron oxide, analysis by Foster Wheeler Co.). The coal is one of the six coals examined by Bool (1993), allowing a comparison of the results.

The feed gas flow was set to 8 l/min, consisting of 4 l/min pure oxygen and 4 l/min pure nitrogen. The dilution nitrogen flows were set to 0.3 l/min for the upper nitrogen inlet of the probe rod, and 0.1 l/min for the lower one. According to the aerosol inlet stream of the SMPS of 0.6 l/min, the resulting dilution was two parts nitrogen on one part furnace air.

The regulator for the electrical heaters was set to 42 percent. The resulting wall temperature profile at the steady state before the beginning of the coal feed was about 980°C - 1020°C in the upper section, 1080°C in the middle section, and 1000°C - 910°C in the lower section. The value for the syringe pump flow rate setting was set to a coal feed rate of 4 g/h. This corresponds to a high stoichiometric ratio of 69, chosen to ensure that complete combustion occurs. The feed rate allowed three hours of coal feed. A steady state of the temperature profile, and the feed stream, was reached after about half an hour, and remained so for 2.15 hours. The temperature profile during this steady state phase was 1000°C - 1050°C in the upper section, 1100°C - 1120°C in the middle section, and 1030°C - 940°C in the lower section of the heating zone.

The Scanning Mobility Particle Sizer was set to 5 scans per sample, giving 29 samples during the feeding phase of the experiment. Charge correction was not used, and the delay times were set to tf = 3.8 s and td = 3.9 s. The aerosol inlet flow and the monodisperse aerosol outlet flow were set to 0.6 l/min, corresponding to a pressure gauge value of 27 cm water, and flowmeter value of 2.82 (10 V range). The sheath air and the excess air flow were set to 6 l/min, giving flowmeter values of 2.9 and 2.98, respectively (10 V range). The scan uptime was set to 60 s, and the downtime to 15 s.

6.2.3.2 Data

The typical particle size distributions sampled with the Scanning Mobility Particle Sizer showed a peak in the numbers of particles between 40 nm and 55 nm, and a minimum between 12 nm and 18 nm. The peak concentrations were between $1.7 \cdot 10^7$ and $1.9 \cdot 10^7$ particles per cubic centimeter. It is important to note that the given values are the values for the diluted aerosol stream (dilution of two parts nitrogen on one part furnace air), indicating that the concentration within the furnace was three times that high).

Table 6-6: Typical Particle Distributions of Base Case Experiment

Channel	Midpoint Diameter	Number	Surface	Volume
17	10.37	5.03E+06	1.70E+09	2.93E+09
18	11.14	2.68E+06	1.05E+09	1.94E+09
19	11.97	1.55E+06	6.96E+08	1.39E+09
20	12.86	9.98E+05	5.19E+08	1.11E+09
21	13.82	7.60E+05	4.56E+08	1.05E+09
22	14.86	7.54E+05	5.23E+08	1.29E+09
23	15.96	8.72E+05	6.98E+08	1.86E+09
24	17.15	1.12E+06	1.04E+09	2.96E+09
25	18.43	1.53E+06	1.63E+09	5.01E+09
26	19.81	2.08E+06	2.57E+09	8.48E+09
27	21.29	2.81E+06	4.01E+09	1.42E+10
28	22.88	3.69E+06	6.07E+09	2.32E+10
29	24.58	4.64E+06	8.81E+09	3.61E+10
30	26.42	5.76E+06	1.26E+10	5.56E+10
31	28.39	7.13E+06	1.80E+10	8.54E+10
32	30.51	8.60E+06	2.51E+10	1.28E+11
33	32.78	1.03E+07	3.46E+10	1.89E+11
34	35.23	1.21E+07	4.71E+10	2.77E+11
35	37.86	1.37E+07	6.16E+10	3.89E+11
36	40.68	1.54E+07	8.00E+10	5.42E+11
37	43.71	1.65E+07	9.93E+10	7.23E+11
38	46.98	1.72E+07	1.20E+11	9.36E+11
39	50.48	1.74E+07	1.39E+11	1.17E+12
40	54.25	1.73E+07	1.60E+11	1.44E+12
41	58.29	1.70E+07	1.81E+11	1.76E+12
42	62.64	1.64E+07	2.02E+11	2.11E+12
43	67.32	1.55E+07	2.21E+11	2.48E+12
44	72.34	1.46E+07	2.40E+11	2.89E+12
45	77.74	1.34E+07	2.55E+11	3.30E+12
46	83.54	1.22E+07	2.67E+11	3.72E+12
47	89.77	1.07E+07	2.71E+11	4.05E+12
48	96.47	8.98E+06	2.62E+11	4.22E+12

Table 6-6: Typical Particle Distributions of Base Case Experiment (cont.)

Channel	Midpoint Diameter	Number	Surface	Volume
49	103.66	7.27E+06	2.45E+11	4.24E+12
50	111.4	5.77E+06	2.25E+11	4.18E+12
51	119.71	4.52E+06	2.04E+11	4.06E+12
52	128.64	3.51E+06	1.82E+11	3.91E+12
53	138.24	2.68E+06	1.61E+11	3.70E+12
54	148.55	2.08E+06	1.44E+11	3.57E+12
55	159.63	1.63E+06	1.30E+11	3.46E+12
56	171.54	1.27E+06	1.18E+11	3.37E+12
57	184.34	9.77E+05	1.04E+11	3.21E+12
58	198.1	7.74E+05	9.54E+10	3.15E+12
59	212.88	6.05E+05	8.62E+10	3.06E+12
60	228.76	4.89E+05	8.05E+10	3.07E+12
61	245.82	3.90E+05	7.40E+10	3.03E+12
62	264.16	3.13E+05	6.86E+10	3.02E+12
63	283.87	2.54E+05	6.42E+10	3.04E+12
64	305.05	2.18E+05	6.36E+10	3.23E+16
65	327.81	1.72E+05	5.82E+10	3.18E+12
66	352.27	1.46E+05	5.70E+10	3.35E+12
67	378.55	1.28E+05	5.75E+10	3.63E+12
Totals		9.74E+06	1.15E+11	3.00E+12

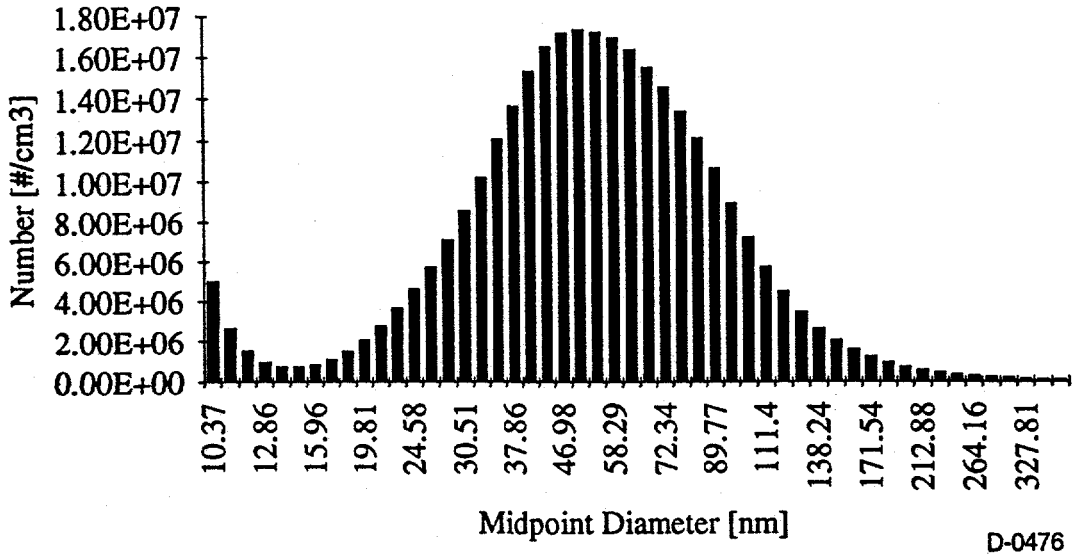

Figure 6-25: Typical particle number distribution of base case experiment.

The ash samples collected in the impactor after-filter were analyzed using Dr. Emrick's Mössbauer spectroscopy facilities. The Mössbauer spectra showed peaks quite similar to those found by analyzing an

ash trap sample of Run 47 (Bool, 1993). This run was chosen for comparison because the coal burned in the down fired laboratory scale combustor was also the Illinois #6. The six characteristic hematite peaks can be seen at velocities of about -8 mm/s, -4.5 mm/s, -1 mm/s, 2 mm/s, 5 mm/s and 8.5 mm/s, while the iron in glass caused the peak doublet 0 mm/s and 2 mm/s (Bool, 1993). Some of the many magnetite peaks are nearly identical with the hematite peaks, which leads to overlapping. Thus, two or three overlapping peaks are only to be seen as one peak.

A first quantitative analysis of a base case experiment sample (using the software developed by Dr. Emrick) delivered eighty percent iron oxide, and twenty percent iron in glass. This result is similar to the result of run 47b (Bool, 1993).

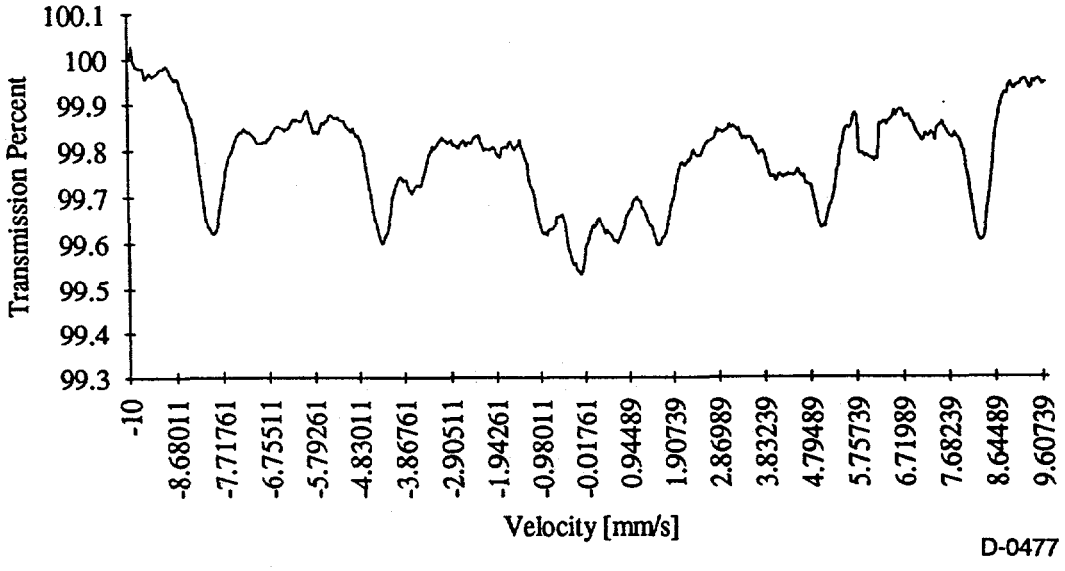

Figure 6-26: Mössbauer spectrum of base case experiment.

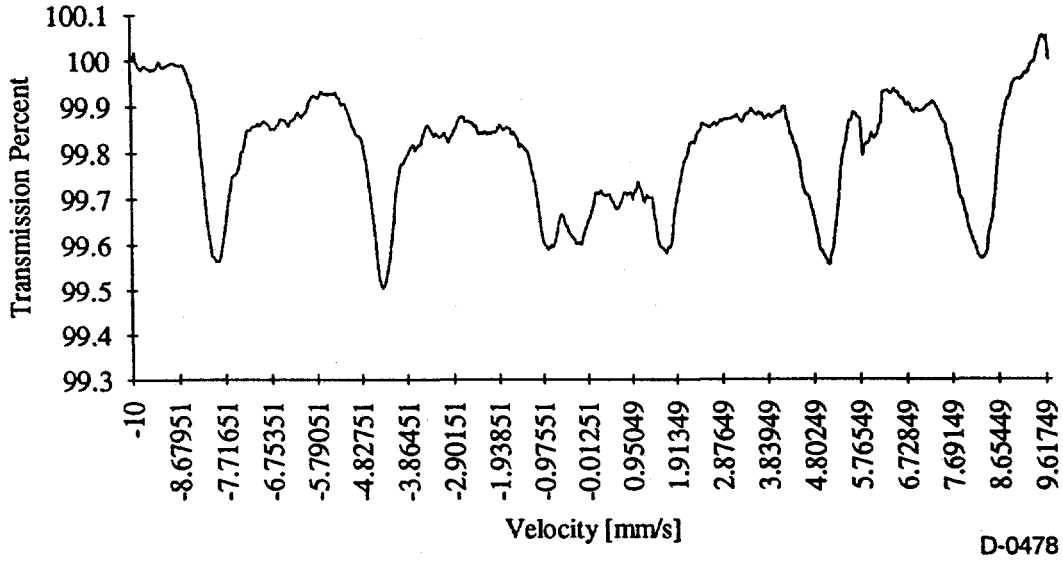

Figure 6-27: Mössbauer spectrum of ash trap sample from Run 47 (Bool, 1993).

6.3 Experiment with the washed Pittsburgh No. 8

Once the furnace was completely characterized as described in the previous sections an series of experiments were performed with the washed Pittsburgh No. 8. These experiments followed the procedure described above. In addition the coal ash was analyzed for carbon content. This analysis and the iron distributions are discussed below.

Coal Ash Analysis

The coal ash was analyized two ways. The first method was for carbon content. Since the drop tube furnace has problems with incomplete combustion, the stoichiometric ratio was determined by coal burnout. The initial and final carbon content of the coal was determined, and the coal burnout was determined by doing a carbon mass balance. The amount of burnout was calculated, and this was assumed to be the stoichiometric ratio.

The coal ash was also sent to the University of Kentucky to determine the iron phases that were present in the ash. The data from the Pittsburgh #8 coal is presented in Table 1.

Results

The samples that were analyized show a large amount of unreacted pyrite in the coal ash. This is due to the low stoichiometric ratios that were used. However, for a stoichiometric ratio of 0.65, 15% pyrite was still observed in the ash. For the lower stoichiometric ratios, (below 0.5) no oxide was present in the ash. Large percentages of pyrrhotite was present in all of the samples. The percent of pyrrhotite present decreased and the percent of magnetite increased as the stoichiometric ratio increased. None of the samples contained hematite.

Table 6-7. Mössbauer Data from Washed Pittsburgh No. 8 Experiments

Mossbauer Analysis						
SR	Peak Temp (oC)	% Fe^{++} Glass	% Fe^{+++} Glass	% Magnetite	% $Fe_x S$	% Pyrite
0.40	1324	30	0	0	43	27
0.44	1356	26	0	0	40	34
0.52	1338	43	0	13	24	20
0.52	1344	36	0	20	23	21
0.58	1334	23	29	16	32	0
0.61	1325	29	22	17	32	0
0.62	1328	27	21	31	21	0
0.65	1330	24	16	29	16	15

6.4 References

Baxter, L.B. and Mitchell, R.E.; "The Release of Iron During the Combustion of Illinois No. 6 Coal"; *Combustion and Flame*; 88, 1992

Beér, J.M.; Kang, S.; Sarofim, A.F., Graham, K.A.; "Fundamental Studies of Mineral Matter Vaporization and Residual Ash Formation" in: "Transformations of Inorganic Coal Constituents in Combustion Systems"; Final Report, U.S. Department of Energy Contract No. DE-AC22-86PC90751, Pittsburgh Energy Technology Center, Pittsburgh, PA, 1992

Bool, L.E.; "The Partitioning of Iron During the Combustion of Pulverized Coal"; PhD Dissertation, Department of Chemical Engineering, University of Arizona, 1993

Borio, R.W. and Levasseur, A.A.; "Coal Ash Deposition in Boilers" in: Vorres, K.S. (Editor); *Mineral Matter and Ash in Coal*, American Chemical Society, Washington DC, 1986

Crank, J.; *The Mathematics of Diffusion*; Oxford University Press, Oxford, 1975

Dryer, F.L.; Glassmann, I.; "High Temperature Oxidation of CO and "; *Fourteenth (International) Symposium on Combustion*; The Combustion Institute, Pittsburgh, PA, 1973

Dubbel - Taschenbuch für den Maschinenbau; Prepared by W.Beitz and K.-H. Küttner; Springer-Verlag, Berlin, 1990

Gallagher, N.B.; "Alkali Metal Partitioning in Ash from Pulverized Coal Combustion"; PhD Dissertation, Department of Chemical Engineering, University of Arizona, 1992

Hinds, W.C.; *Aerosol Technology*; John Wiley & Sons Inc., New York, 1982

Hurt, R.H. and Mitchell, R.E.; "On Combustion Kinetics of Heterogeneous Char Particle Populations"; *The Twenty Fourth International Symposium on Combustion*; Sidney, Australia, June 5-10, 1992

Jorgensen, R.F.A.; "On Maximum Temperatures Attained During Single-Particle Combustion of Pyrite"; *Transactions (Section C)*, The Institution of Mining and Metallurgy, 90, 1981

Metals Handbook, Ninth Edition, Vol. 11, "Failure Analysis and Prevention", American Society for Metals, 1986

Mullin, J.W.; *Crystallization;* Butterworth & Co. (Publishers) Ltd, London ,1993

Nowok, J.W.; Benson, S.A.; Jones, M.L.; Kalmanovitch, D.P.; "Sintering Behavior and Strength Development in Various Coal Ashes"; *Fuel*, 69, 1990

Raask, E.; *Mineral Impurities in Coal Combustion*; Hemisphere Publishing Corp., New York, 1985

Rohsenow, W.M.; Hartnett, J.P.; Ganic, E.N.; *Handbook of Heat Transfer Fundamentals*; McGraw-Hill Book Company, New York, 1985

Saxena, S.K.; Chatterjee, N.; Fei, Y.; Shen, G.; *Thermodynamic Data on Oxides and Silicates*; Springer-Verlag, Berlin, 1993

Scrinivasachar, S.; Boni, A.A.; "A Kinetic Model for Pyrite Transformations in a Combustion Environment"; *Fuel,* 68, 1989

Slag Atlas; Prepared by the Committee for Fundamental Metallurgy, Düsseldorf, 1981

Sloan, G.J. and McGhie, A.R.; *Techniques of Melt Crystallization*; John Wiley & Sons Inc., New York, 1988

Smith, J.M.; *Chemical Engineering Kinetics*; McGraw-Hill Book Company, New York, 1990

Turkdogan, E.T.; *Physiochemical Properties of Molten Slags and Glasses*; The Metals Society, London, 1983

Vértes, A.; Korecz, L.; Burger, K.; *Mössbauer Spectroscopy*; Elsevier Scientific Publishing Company, Amsterdam, 1979

Vogel, W.; *Glaschemie*; VEB Deutscher Verlag für Grundstoffindustrie, Berlin, 1979

Westbrook, C.K.; Dryer, F.L.; "Simplified Reaction Mechanisms for the Oxidation of Hydrocarbon Fuels in Flames"; *Combustion Science and Technology*, 27, 1981

Zell, J. and Mutaftschiev, B.; "Nucléation sur la Surface d'un Fluide de Petites Dimensions"; *Journal of Crystal Growth*; No.3 and 4, 1968

SECTION 7

TASK 2: FUNDAMENTAL STUDY OF ASH FORMATION AND DEPOSIT INITIATION UNDER REDUCING CONDITIONS
(PSI Technologies)

7. FUNDAMENTAL STUDY OF ASH FORMATION AND DEPOSIT INITIATION UNDER REDUCING CONDITIONS

In this work two types of experiments were performed to assess the effect of unburned, or partially burned, char on ash stickiness. In the first set of experiments a coal was combusted under fuel lean conditions using the PSIT entrained flow reactor (EFR) described later. Ash stickiness and carbon content measurements were taken at various residence times in the EFR. The second set of experiments consisted of tests with a suite of five coals combusted in the EFR under various stoichiometric ratios. As in the earlier experiments, ash stickiness and carbon content measurements were performed for each coal at each stoichiometric ratio. The data from these two experiments were used to determine what effect residual carbon has on ash stickiness and whether the source of the residual carbon (short residence times under fuel lean combustion or reducing stoichiometries) plays a role in the carbon's effect on ash stickiness.

7.1 Description of Facilities

As noted above, the measurements in this work were performed utilizing the PSIT entrained flow reactor shown schematically in Figure 7-1. Coal or synthetic ash particles were fed into the top of the reactor using either an AccuRate auger-type dry materials feeder or a syringe pump. The particles were carried into the swirl stabilized section with transport gas (either oxygen or nitrogen) at a typical flow rate of 4.2 standard liters per minute (slpm). At the top of the swirl stabilized section, the coal (or synthetic ash) and transport gas were mixed with the remaining combustion gases. These gases consisted of oxygen and nitrogen, mixed to achieve the desired stoichiometric ratio. The coal-gas mixture was then concentrated in a venturi and rapidly expanded to disperse the coal across the entire tube cross-section. From the swirl stabilized section the coal-gas mixture entered the laminar flow reactor. This reactor consists of an externally heated 3.375 in. (8.57 cm) inner diameter mullite tube approximately 62 in. (1.57m) long. There are three independently controlled temperature zones.

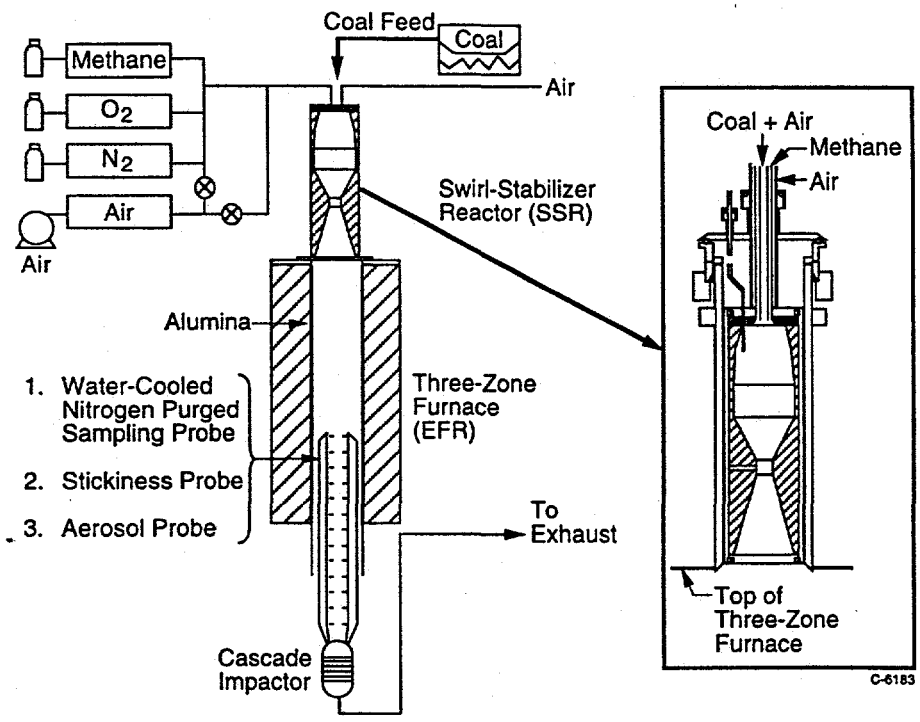

Figure 7-1. PSIT entrained flow reactor (EFR).

For the deposition measurements, the particle-laden gas stream entered the deposition test section, consisting of a conical converging section at the exit of the EFR, where the flow area was reduced to approximately 5 cm^2. Two deposition probes (uncooled mullite tubes) were placed perpendicular to the direction of the flow. The deposition probes were placed in the conical section such that the velocity of the approaching particles was either 1 m/s (top probe) or 5 m/s (bottom probe), although for high gas flowrate experiments (greater than 28 slpm) only 5 m/s samples can be collected. These velocities yield particle kinetic energies consistent with those of particles approaching the waterwall tubes in coal fired boilers (Srinivasachar et al, 1990). Particles that did not adhere to the tubes were collected on a quartz filter for analysis. To avoid deposit shedding, or erosion of loose deposits by the unburned char, sampling times were kept to the minimum required to collected a measurable deposit. The mass collection efficiency, defined as the mass of particles collected by the probe divided by the mass of particles approaching the probe, was determined from the mass change of each probe, the mass collected on the after filter, the projected area of the probe, and the cone cross sectional area at the tube location.

As part of each experiment ash samples were collected at the exit of the reactor (with the deposition test section removed) using a water-cooled particle sampling probe. Particle-laden flue gas was drawn into the sampling probe and mixed with room temperature nitrogen to quench the char combustion. In some cases these samples were burned out under flowing oxygen in a tube furnace to determine the amount of carbon in the ash. Ash samples were sent to the University of Kentucky for CCSEM and Mössbauer analysis.

7.1.1 Characterization of PSIT Entrained Flow Reactor (EFR)

Many of the experiments performed in this program used reactor configurations and operating conditions not previously explored at PSI. These new configurations included increased gas flow in the reactor and insertion of a coal injection probe. New operating conditions included deeply reducing combustion stoichiometries (stoichiometric ratio 0.6). As the effect of these new configurations/operating conditions on gas temperatures in the reactor was unclear, efforts were made to characterize the reactor under many of these configurations/operating conditions.

Temperature measurements were made with two different types of probes; a modified particle injection probe, and a suction pyrometer. The modified injection probe consisted of a particle injection probe with a thermocouple inserted down the center. The thermocouple bead was shielded from the wall radiation by an open platinum foil cylinder suspended from the ceramic thermocouple protector. By using the platinum foil cylinder, gas was allowed to flow around the bead, but radiation from the wall was minimized. The injection probe was inserted in one of three locations, corresponding to approximately 30.5, 58.4, and 86.4 cm from the top of the reactor (the same locations used in subsequent experiments, see Subsection 7.2). At each location the thermocouple was extended in small increments, with temperature measurements recorded at each position. In order to quantify the quenching effect of the injection probe, the probe was insulated with 1/8 in. thick Inswool-HP ceramic fiber paper. The probe was then fully inserted in the reactor, and the temperature measurements repeated. The gas temperatures in the lower half of the reactor were also measured using a suction pyrometer. The pyrometer was inserted in increments upwards from the bottom of the reactor, with temperature measurements taken at each location. Both probes used type R thermocouples.

Effect of Furnace Setpoint and Gas Flowrate:

The first two experiments were designed to determine the effect of the furnace setpoint and gas flowrate on the reactor temperature profile. These experiments used furnace setpoints of 1300° and 1500°C and gas flowrates of 1, 2.5, and 4 SCFM (28.3, 70.8, and 113.2 slpm). For these experiments the N_2-quenched sampling probe was also inserted approximately 25 cm into the bottom of the reactor. The temperature profiles, Figures 7-2 and 7-3, were measured using only the modified injection probe described above. The effect of gas flowrate was relatively small, but non-negligible. As expected, increasing the furnace setpoint caused a corresponding increase in the gas temperature. The peak gas temperatures were approximately 50 and 100°C less than the furnace setpoint for the lowest and the highest flowrates, respectively. The N_2-quenched probe and the fully inserted injection probe caused a significant drop in the gas temperature in the lower part of the furnace. This effect was explored in the next set of measurements.

Effect of N_2 Quenched Probe and Fully Inserted Injection Probe:

The effect of both the N_2-quenched probe and the fully inserted injection probe can be seen in Figure 7-4. The furnace temperature profile in the absence of both probes can be seen in Figure 7-5. In this case the peak temperature in the lower section of the reactor is approximately 50°C below the setpoint. When the injection probe was fully inserted, the peak temperature decreased by approximately 150°C. Addition of the N_2-quenched probe caused another 100°C decrease. However, when the N_2-quenched probe was removed and the injection probe insulated with a ceramic fiber insulation, the lower-reactor temperatures are very similar to those obtained in the absence of both probes.

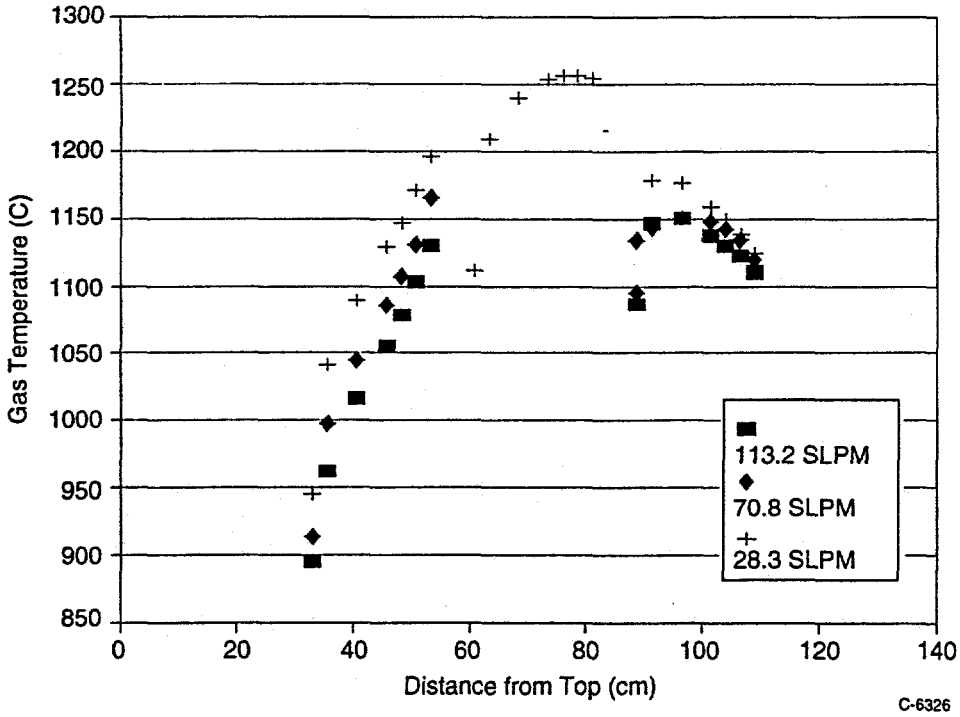

Figure 7-2. PSI entrained flow reactor temperature profile (setpoint: 1300°C with quenched probe).

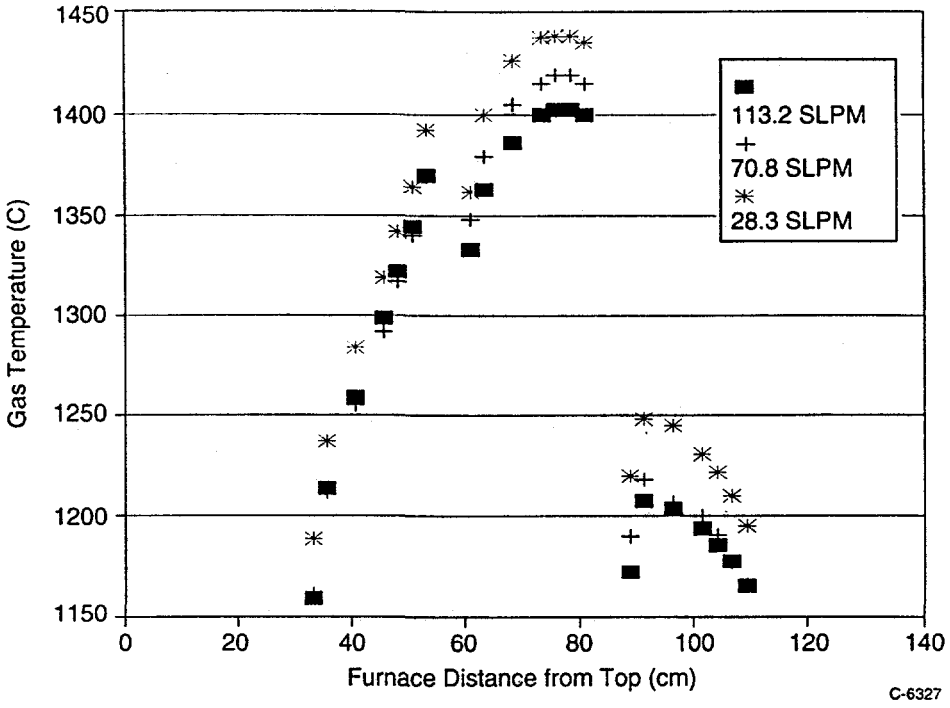

Figure 7-3. PSI entrained flow reactor temperature profile (setpoint: 1500°C with quenched probe).

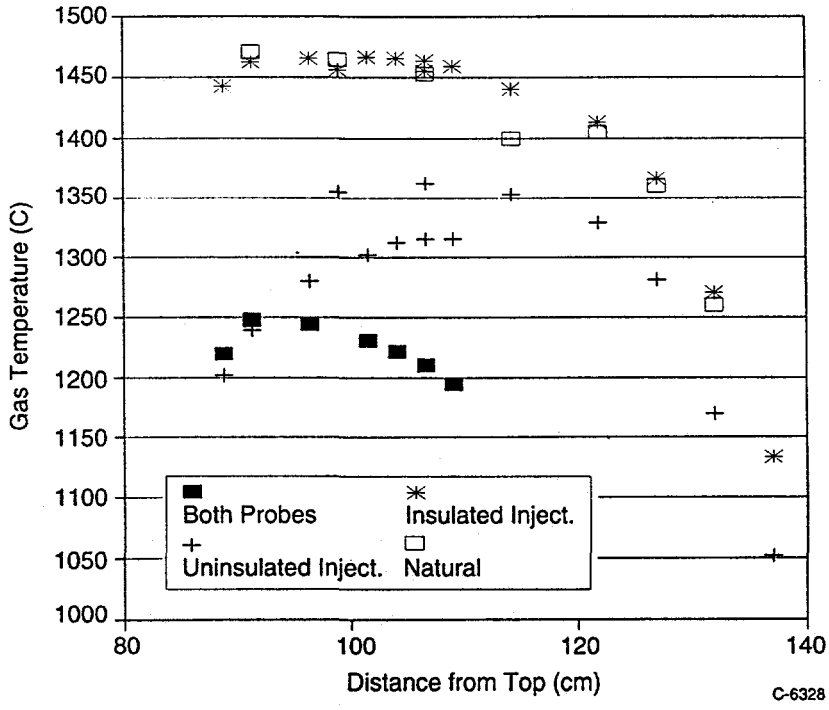

Figure 7-4. PSI entrained flow reactor temperature profile - effect of quench and injection probes.

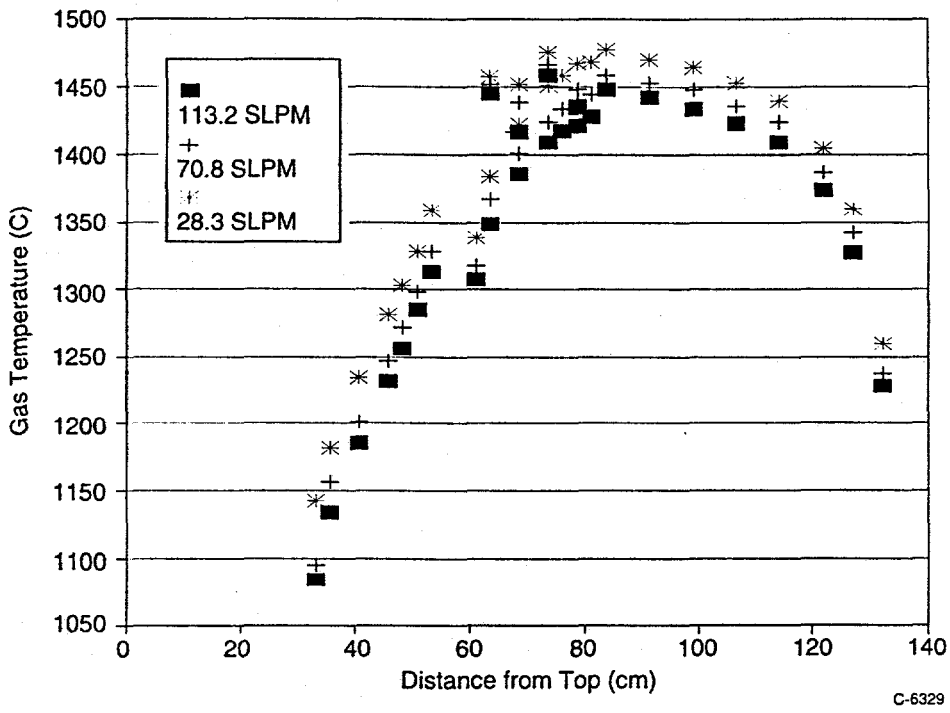

Figure 7-5. PSI entrained flow reactor temperature profile - no probes.

The data from these measurements suggest that the gas temperature profile is similar for experiments at different gas flowrates. However, for those experiments where the injection probe was fully inserted, the probe had to be insulated to avoid significant decreases in reactor gas temperatures.

7.2 Short Residence Time Experiments

One of the important questions addressed in this work is the effect of sub-stoichiometric combustion conditions on ash deposition behavior. One of the effects of substoichiometric conditions is the presence of residual carbon and unoxidized, or only partially oxidized, pyrite in the ash. Several experiments were performed to explore the effect of these components on ash stickiness. These experiments focused on the stickiness of ash at short residence times. Although the experiments were all carried out under fuel lean conditions, the presence of carbon and partially oxidized pyrite in the ash at short residence times is similar to that obtained by combustion of the coal under reducing conditions.

For these experiments the coal, washed Pittsburgh No. 8 (obtained from DOE/PETC), was fed at 0.6 g/min into the reactor using the injection probe. The combustion gas consisted of 15% oxygen, balance nitrogen. In order to control the fractional conversion of pyrite, and the amount of carbon in the ash, the residence time was varied between 0.25 and 2.9 s by varying injection probe location and gas flowrates. Table 7-1 outlines the conditions used to achieve each residence time. As seen in the table, the furnace setpoint was reduced for the lower flowrate. This was to ensure that the gas temperature (as measured with a thermocouple) in the deposition test section remained constant between the two different gas flowrates.

Table 7-1. Reactor Conditions and Configurations for Short Residence Time Experiments

Setpoint (°C)	Flow (slpm)	Injection Location (cm from top)	Residence Time (seconds)
1500	113.2	86.4 58.4 30.5 0.0	0.25 0.40 0.55 0.72
1400	28.3	86.4 58.4 30.5 0.0	0.99 1.60 2.21 2.87

7.2.1 Short Residence Time Experiments - Effect of Residence Time on Ash Stickiness

At each of the residence times outlined in Table 7-1 ash deposition tests were performed as discussed in Section 7.1. The particle velocities at the point of impaction were kept constant at 1 and 5 m/s, although for the high gas flowrate experiments only 5 m/s samples could be collected. Ash samples were collected using the nitrogen-quenched probe. These samples were then analyzed for carbon content to determine the fractional burnout at the point (residence time) of deposition.

The data from these experiments can be seen in Figure 7-6. In this figure both the fraction of fixed carbon remaining and the ash collection efficiency are plotted as a function of time. The *fixed* carbon, or unburned char, remaining was calculated using the proximate analysis for this coal and assuming that devolatilization was complete. This parameter was used to determine the fractional char burnout. From the plot we can see that the collection efficiency increased dramatically between 0.25 and 0.400 s, with a maximum occurring at approximately 1 s. The collection efficiency continues to increase substantially after burnout is essentially complete (0.55 s). These data, and the data in Figure 7-7 suggest that high

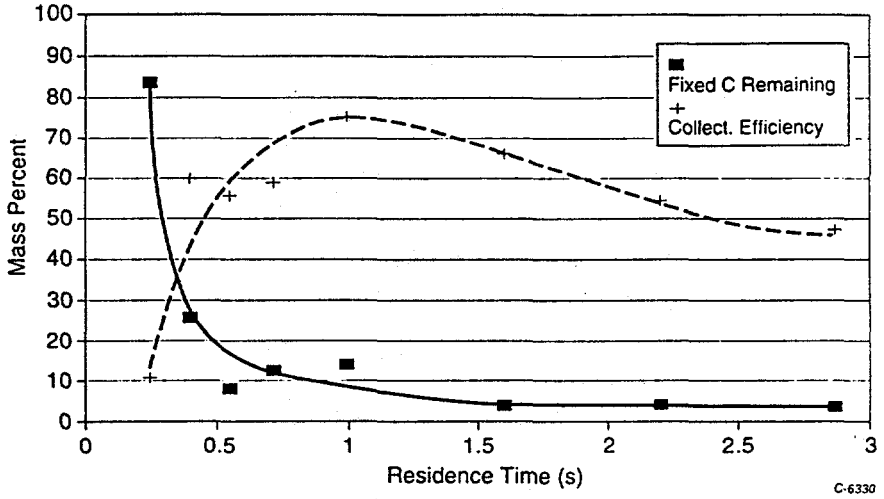

Figure 7-6. Burnout and stickiness comparison - washed Pittsburgh #8 (DOE).

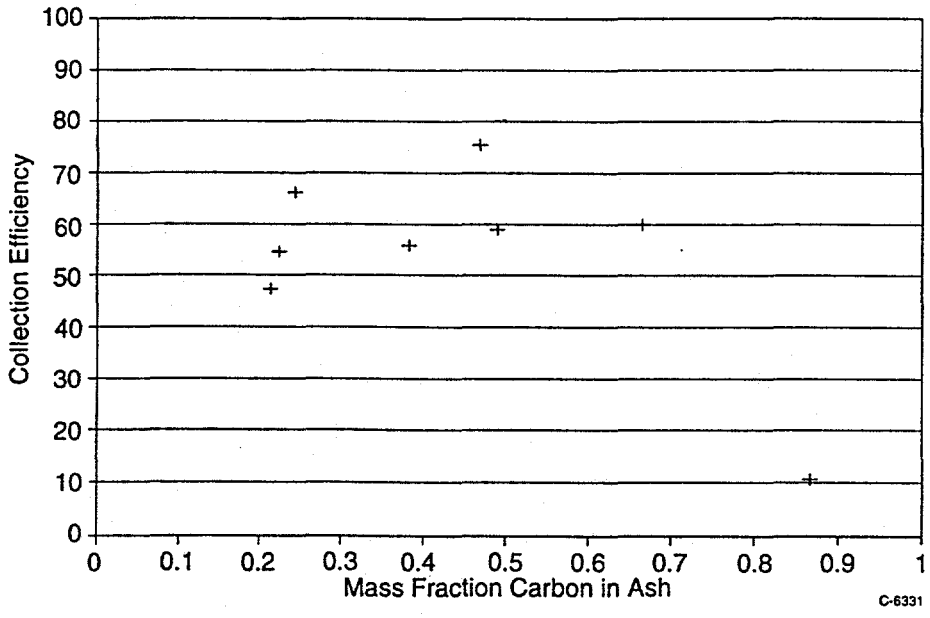

Figure 7-7. Collection efficiency versus carbon content (washed Pittsburgh #8 (DOE)).

carbon contents, indicative of low char burnout, may dramatically affect ash stickiness. Below a critical value, approximately 70% for this coal, the carbon content has little or no effect on ash stickiness.

7.2.2 Short Residence Time Experiments - Effect of Residence Time on Iron Partitioning

Ash samples from the short residence time experiments were analyzed by Mössbauer spectroscopy at the University of Kentucky. The goal of this analysis was to determine whether unoxidized, or only partially oxidized iron species affect the ash deposition at short residence times. The data presented in Table 7-2 indicate that the ash from the shortest residence time (0.25) contained appreciable amounts of sticky iron phases (pyrrhotite and Fe(II) glass). The ash collection efficiency data, however, are lowest for this residence time. This result suggests that the presence of unburned char at short residence times may be more important than the presence of sticky iron particles in controlling ash stickiness at short residence times.

The information in Table 7-2 raises an interesting point about the oxidation rate of iron in glass. Immediately after the char is completely combusted, one would expect the Fe(II) state in the glass to be dominant, or at least be present. However, the data in Table 7-2 suggest that this is not the case. One possible explanation is that the oxidation rate of Fe(II) in the glass is strongly temperature dependent. For the first four residence times the furnace setpoint was 1500°C. The data for these residence times, with the exception of the shortest residence time, indicate that the Fe(II) in the glassy phase is completely oxidized. For the last four residence times the gas temperature was decreased by approximately 100°C. Although the iron-containing glass particles remained in the reactor for a longer period of time, a significant fraction of the iron in the glassy phase was still present as Fe(II). The data further show that the Fe(II) oxidized to Fe(III) at longer residence times. As the iron oxidation state in glass is suspected to play an important role on ash stickiness, additional work was performed to better understand Fe(II) oxidation (see Subsection 7.5).

Table 7-2. Iron Partitioning in Ash as a Function of Residence Time

Residence Time (s)	Iron as Oxide (wt%)		Iron in Glass (wt%)	
	Fe_3O_4	Fe_2O_3	Fe^{2+}	Fe^{3+}
0.25*	66	-	12	14
0.40	41	47	-	12
0.55	50	40	-	11
0.72	26	64	-	10
0.99	30	41**	10	19
1.60	77	-	7	16
2.21	23	51**	9	20
2.87	11	71**	-	18

*Contained 8% FeS.
**Includes magnetite.

Comparing the collection efficiency data presented in the previous section with the data in Table 7-2 supports the premise that iron partitioning plays an important role in the post-burnout ash stickiness. In Figure 7-6 the ash stickiness increases between 0.72 and 0.99 s. This increase may be due to the fact that the fraction of iron in the glassy ash particles, and the fraction as Fe(II) increases due to the changes in temperature between the two experiment. Further, as the Fe(II) in the glassy ash particles decreases so does the ash stickiness. This effect of Fe(II) oxidation on ash stickiness is discussed in more detail in Subsection 7.5.

7.3 Baseline Experiments - Coal Combustion Under Reducing and Oxidizing Conditions

As part of this program a number of experiments were performed to explore the effect of reducing conditions on ash particle stickiness. In these experiments each of the five program coals was combusted in the entrained flow reactor (EFR), discussed in Subsection 7.1, under both fuel lean and fuel rich conditions. The experimental conditions for each coal were:

- stoichiometric ratios of 0.6, 0.9, and 1.2 - all coals
- stoichiometric ratio of 0.7 and 0.8 - washed Pittsburgh No. 8 and Black Thunder
- coal feedrate of 3.5 g/min
- furnace gas flowrate of 1 scfm
- furnace setpoint (wall temperature) of 1500°C.

In these experiments, the stoichiometric ratio was varied by changing the oxygen feed into the furnace as shown in Table 7-3. At each condition, three deposition samples and two nitrogen-quenched ash samples were collected. Both quench probe samples were analyzed for residual carbon and one sample of each set was sent to the University of Kentucky for CCSEM and Mössbauer analysis.

Table 7-3. Experimental Conditions for Baseline Experiments

Coal	Stoichiometric Ratio	Po_2 (atm)
washed Pittsburgh No. 8	1.2	0.27
	0.9	0.20
	0.8	0.18
	0.7	0.16
	0.6	0.14
run-of-mine Pittsburgh No. 8	1.2	0.20
	0.9	0.15
	0.6	0.10
cleaned Pittsburgh No. 8	1.2	0.28
	0.9	0.21
	0.6	0.14
Silverdale	1.2	0.23
	0.9	0.18
	0.6	0.12
Black Thunder	1.2	0.19
	0.9	0.14
	0.8	0.12
	0.7	0.11
	0.6	0.09

7.3.1 Effect of SR on Carbon Burnout and Ash Stickiness

The effect of stoichiometric ratio on carbon burnout can be seen in Figure 7-8. There was relatively little fixed carbon remaining for all coals at the highest stoichiometric ratio. However, as the stoichiometric ratio was decreased the fraction of fixed carbon remaining increased dramatically for the four bituminous coals. The exception to this trend was the Black Thunder coal. For this coal the of fraction fixed carbon remaining was approximately constant for all of the stoichiometric ratios studied. The high carbon conversion, even at the lowest stoichiometric ratio, for this coal may have been due to the formation of a highly reactive open char or gasification of the fixed carbon by the high moisture content.

The ash collection efficiencies (Figures 7-9 through 7-13) were found to follow the same trend as the carbon burnout for the various stoichiometric ratios - similar to the observed trend in the short residence time experiments. For example, Figure 7-14 shows a comparison of the ash collection efficiencies at 5 m/s gas velocity for the bituminous coals. This figure, and Figures 7-9 through 7-13, show that the ash stickiness increases with increasing stoichiometric ratio. This figure also demonstrates that the British coal showed a trend similar to that of the other bituminous coals - indicating that coals of similar rank and ash composition will show similar deposition trends independent of the source of the coal. The ash stickiness for the Black Thunder coal, however, did not increase with increasing stoichiometric ratio. This is also consistent with the observed carbon burnout trend for this coal.

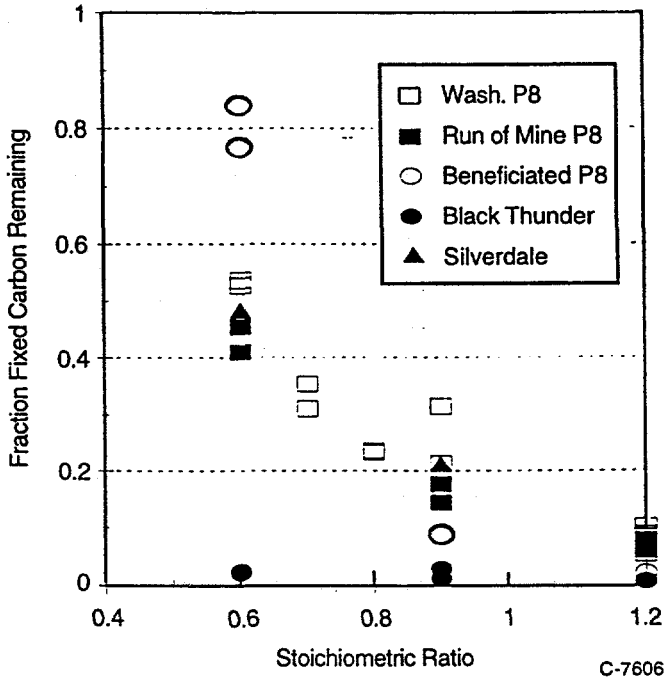

Figure 7-8. Effect of stoichiometric ratio on carbon burnout - 2.6 s residence time.

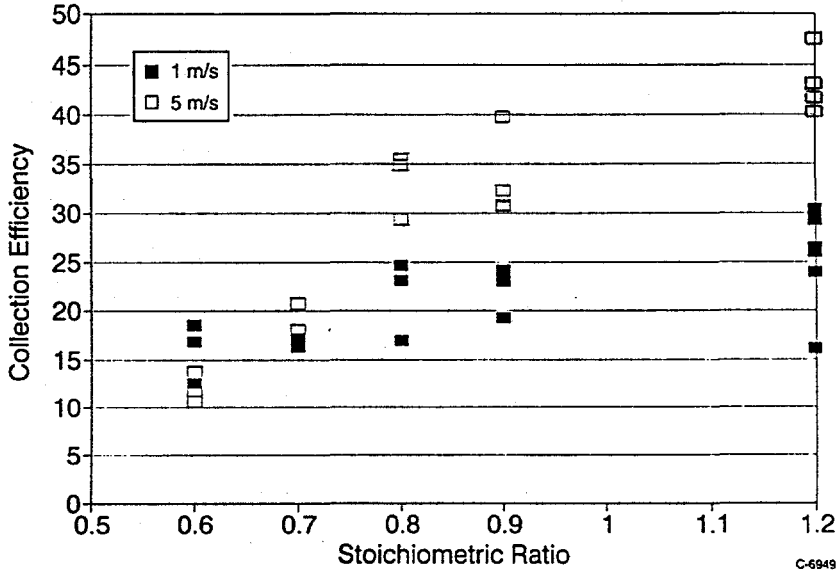

Figure 7-9. Effect of Stoichiometric ratio on ash collection efficiency - washed Pittsburgh No. 8.

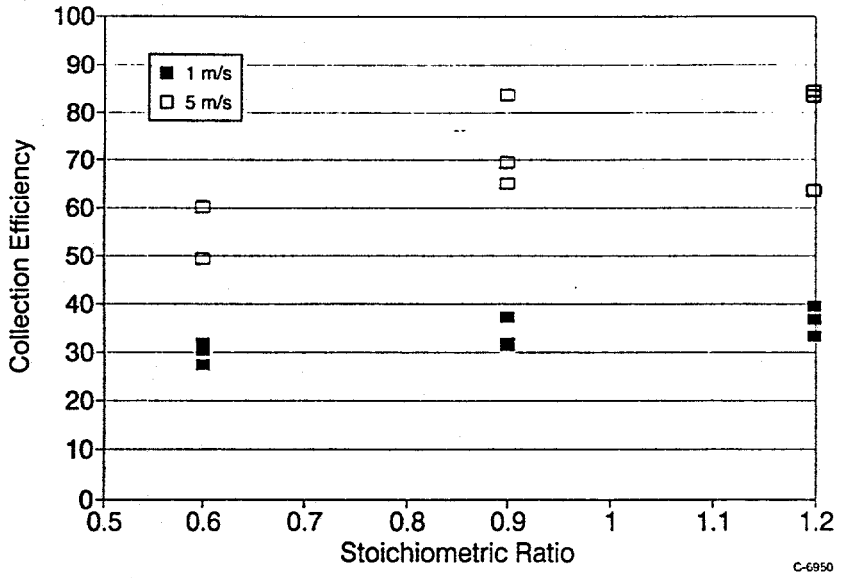

Figure 7-10. Effect of Stoichiometric ratio on ash collection efficiency - run-of-mine Pittsburgh No. 8.

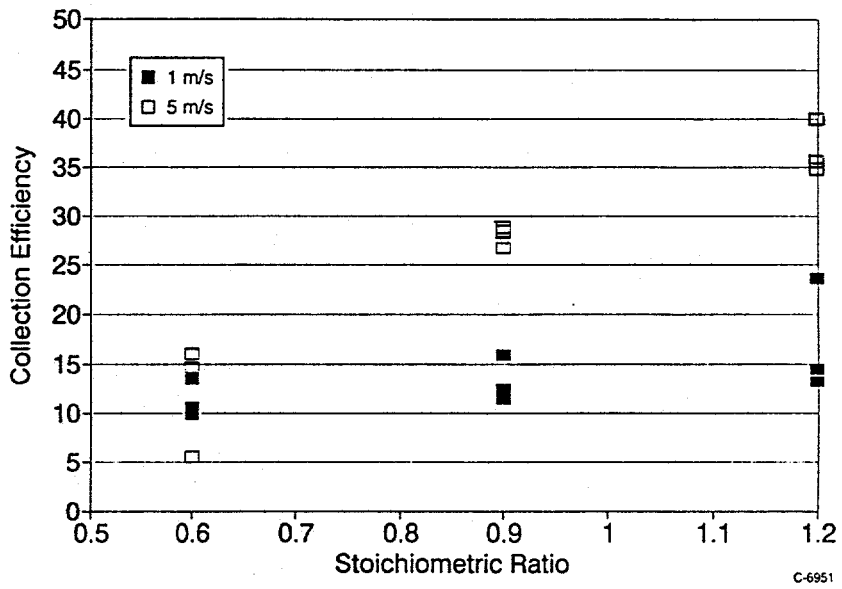

Figure 7-11. Effect of Stoichiometric ratio on ash collection efficiency - cleaned Pittsburgh No. 8.

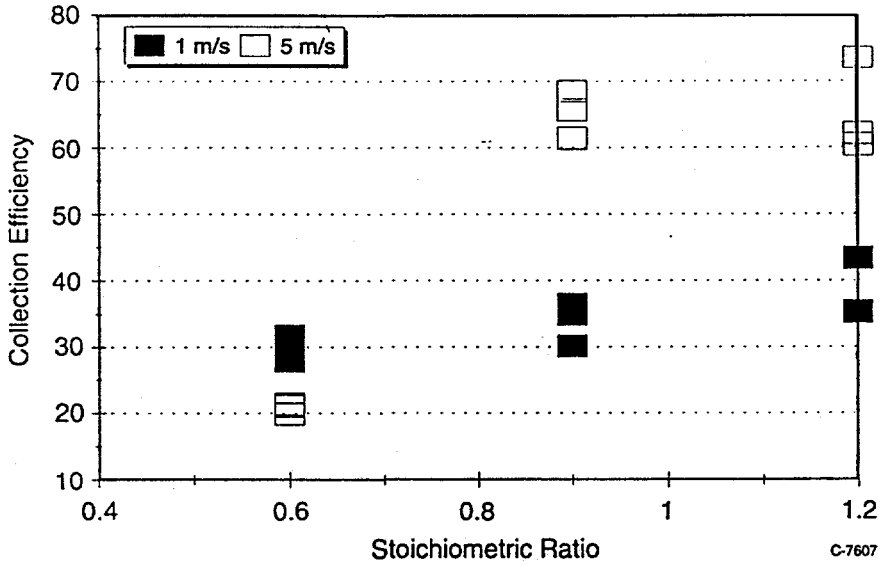

Figure 7-12. Effect of Stoichiometric ratio on ash collection efficiency - Silverdale.

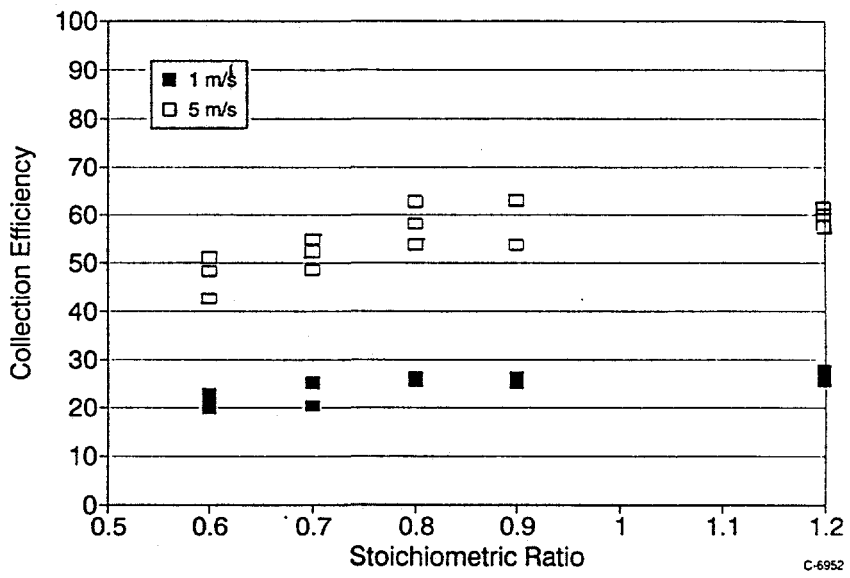

Figure 7-13. Effect of Stoichiometric ratio on ash collection efficiency - Black Thunder .

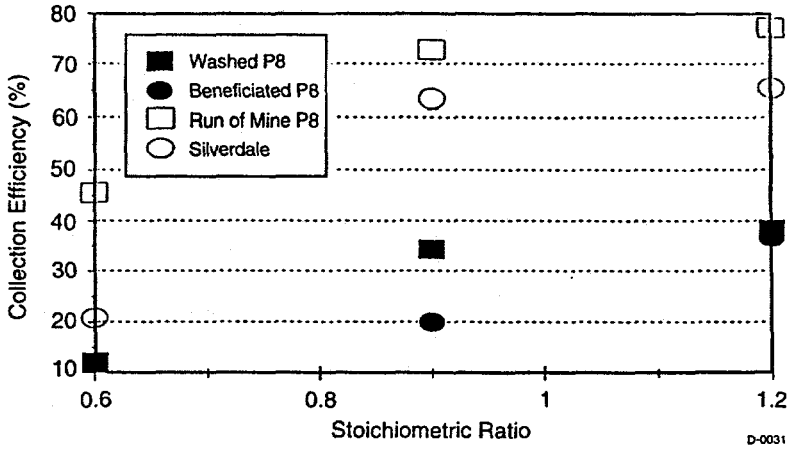

Figure 7-14. Ash collection efficiencies for bituminous coals.

In order to ensure that the results shown in Figures 7-9 through 7-13 were not caused by lower particle temperatures in the substoichiometric ratio experiments, due to lower oxygen partial pressures in these experiments, an additional experiment was performed with the washed Pittsburgh No. 8 to explore the effect of char particle temperature on ash particle stickiness. The furnace setpoint for this experiment was decreased to 1400°C to match predicted particle temperatures in previous substoichiometric combustion experiments. All of the other experimental variables were those used in the earlier experiment at stoichiometric ratio of 1.2. As can be seen from the data in Table 7-4, the collection efficiency did not change appreciably between the two experiments (note: the data in Table 7-4 are repeat measurements at each condition). Therefore, the increase in collection efficiency with stoichiometric ratio was due to other factors, including the presence of carbon at the lower stoichiometric ratios.

Table 7-4. Collection Efficiencies for Stoichiometric Ratio 1.2 Experiments with Washed Pittsburgh No. 8.

Setpoint: 1400 °C		Setpoint: 1500 °C	
1 m/sec	5 m/sec	1 m/sec	5 m/sec
30.4	50.5	16.2	30.0
26.5	40.3	29.3	43.1
26.0	47.4	24.3	41.7

7.3.2 Effect of Stoichiometric Ratio on Ash Impaction and Adhesion Efficiencies

In the previous sub-section we presented data on the collection efficiency of ash as a function of stoichiometric ratio for various coals. This collection efficiency was defined, simply, as the fraction of the ash approaching the substrate that is collected. Therefore, the collection efficiency is a function of the *impaction* efficiency and the *adhesion* efficiency of the ash. The impaction efficiency, defined as the fraction of particles approaching a target that contact the target, is a function of particle size, density, and velocity. The adhesion efficiency, or the fraction of particles contacting the target that stick, has been

shown to be a function of the ash viscosity (Boni et al, 1991). Both of these parameters are discussed below:

Impaction efficiency:

The impaction efficiency of particles approaching cylindrical targets has been studied in detail and can be predicted based on the Stokes number of the particle. The impaction efficiencies were calculated for the two tube locations used in the baseline experiments and can be seen in Figure 7-15. The mass average impaction efficiency of the four program coals, and the Silverdale bituminous coal, were shown in Figure 7-14. For comparison, the ash particle size distribution (psd) for these coals is shown in Figure 7-16. As the psd of all ashes, except that of the washed Pittsburgh No. 8, are very similar below 20 μm, it is not surprising that the calculated impaction efficiencies are also similar. The ash psd generated from combustion of the washed Pittsburgh No. 8, on the other hand, is much smaller - resulting in a lower average impaction efficiency.

It is important to note that the impaction efficiencies discussed above were calculated based on CCSEM analysis of the collected ash. This is important because the CCSEM analysis determines the size distribution of the minerals, but not of particles containing carbon *and* minerals (eg; partially burned char). Therefore, when there is little or no residual carbon in the ash, such as the high stoichiometric ratio experiments, the measured ash psd is representative of the overall (ash plus carbon) particle size distribution. However, when there is significant unburned char, as in the lower stoichiometric ratio experiments, the true size distribution of the particles approaching the tubes is larger than the measured ash psd. For this reason the impaction and adhesion efficiencies were not calculated for the lower stoichiometric ratios.

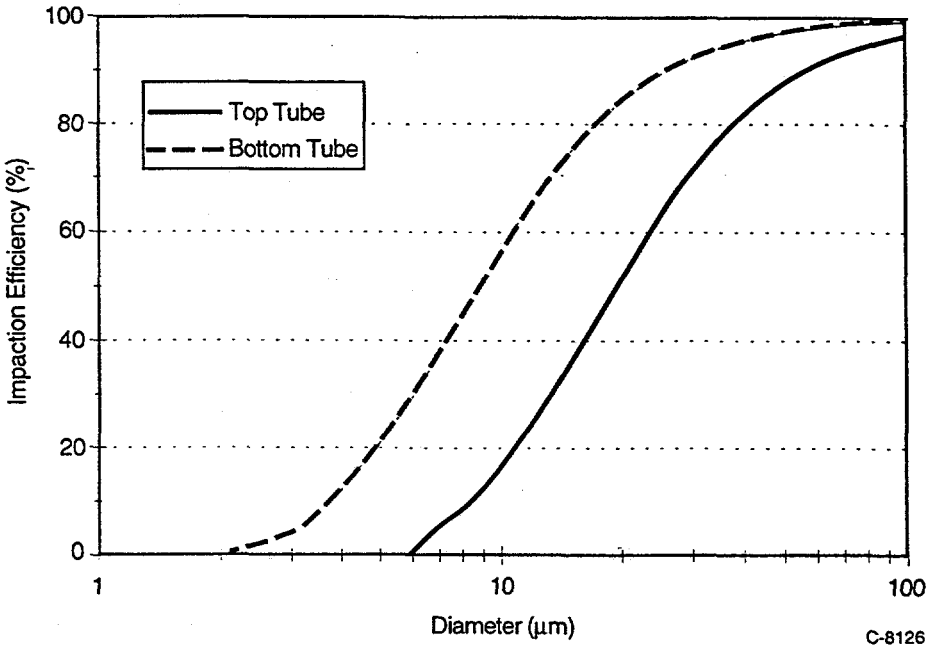

Figure 7-15. Particle impaction efficiencies.

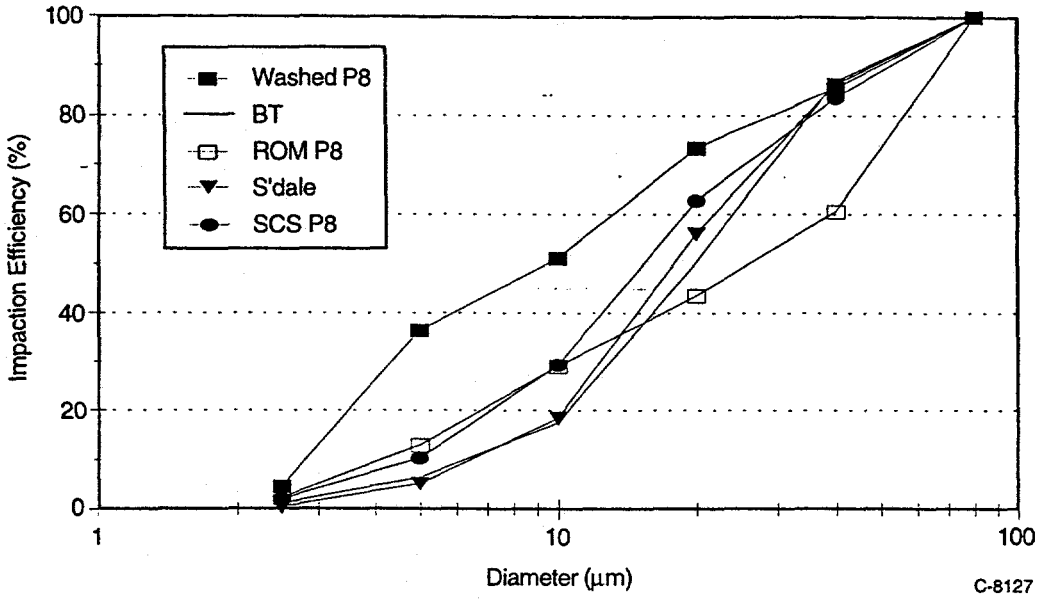

Figure 7-16. Mass average impaction efficiency for program coals.

Adhesion efficiencies:

Once the impaction efficiency is known it is possible to calculate the adhesion efficiency for the baseline experiments. The adhesion efficiency is simply the collection efficiency (measured) divided by the impaction efficiency (calculated, using measured ash psd data). Previous work has suggested that the particle viscosity plays a major role in determining the particle's adhesion efficiency. Work by Srinivasachar and coworkers (1990) showed that below a critical ash viscosity all of the impacting ash particles adhered to the surface. Above this critical value the particles tended to bounce off the impaction substrate.

To test whether this idea of a critical viscosity is substantiated by the data collected in the baseline experiments, the adhesion efficiency for each experiment was calculated using two different critical viscosity values: $1x10^5$ poise and $1x10^7$ poise. This covers most of the critical viscosity range proposed by Boni et al (1990) for adhesion of ash particles. The ash adhesion efficiency was calculated using the CCSEM data file *for the ash* and using the steps described below:

1) the composition and size of a particle is read from the CCSEM file
2) the impaction efficiency for that size particle is calculated as described in the previous section
3) the viscosity for a particle of that composition at the deposit temperature is calculated
4) if the particle viscosity is greater than μ_{crit} the adhesion efficiency is 0, otherwise the adhesion efficiency is 100%.

The volume average adhesion efficiencies were calculated for each critical viscosity by determining the volume of particles that would have impacted the substrate (step 2) and the volume of particles that would have adhered to the substrate (step 4). The ash adhesion efficiency is then given by the volume that adheres divided by the volume that impacts the substrate. Figures 7-17 and 7-18 shows the calculated and

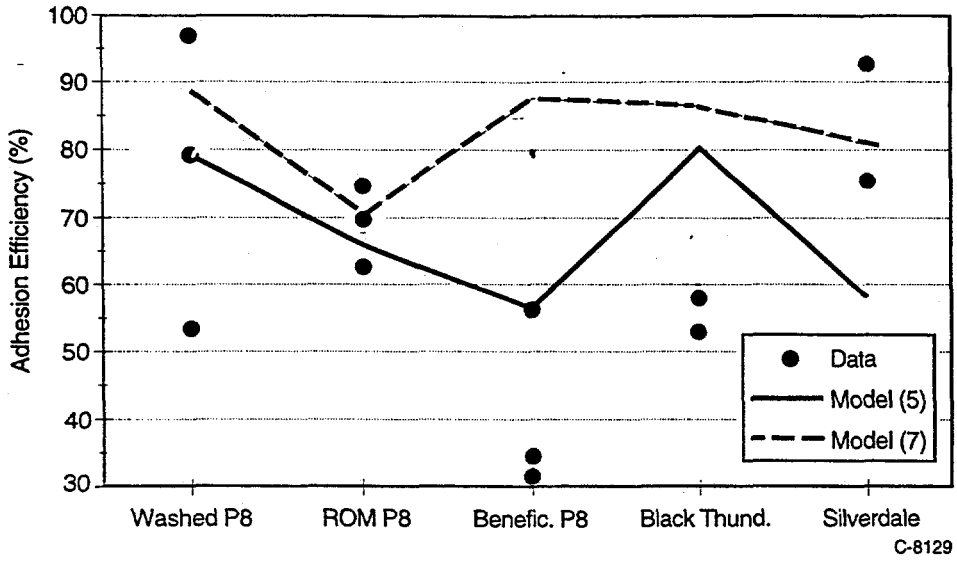

Figure 7-17. Model and data for upper tube. (5) indicates a critical viscosity of 10^5 poise; (7) indicates 10^7 poise.

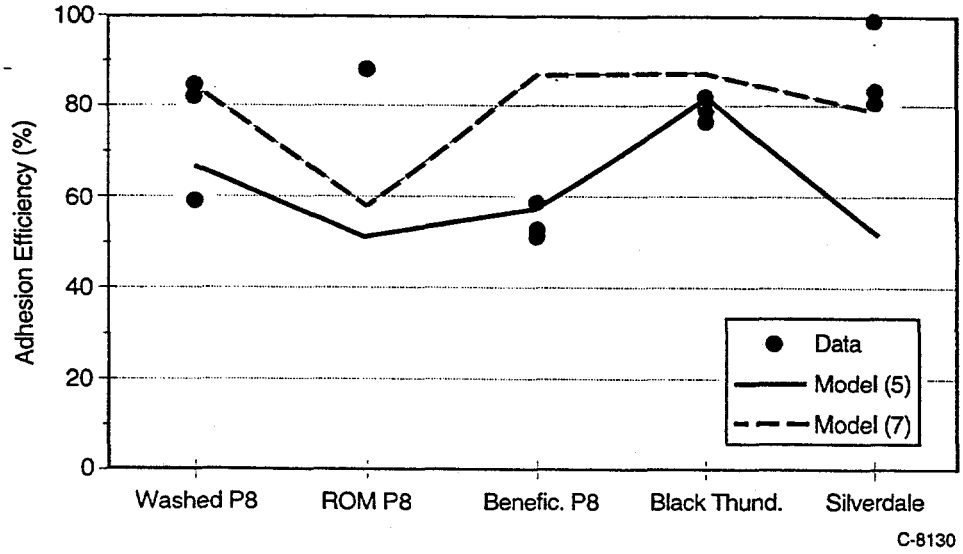

Figure 7-18. Model and data for lower tube. (5) indicates a critical viscosity of 10^5 poise; (7) indicates 10^7 poise.

measured adhesion efficiencies. For the lower velocity (upper tube) the predicted adhesion efficiencies fit the measured efficiencies reasonably well, with the exception of the beneficiated Pittsburgh No. 8 and the Black Thunder. However, there was a fairly large experimental error in some of the measurements, as evidenced by the large spread in measured adhesion efficiency values. For the higher velocity (upper tube) the fit was also reasonably good. Therefore, the data collected in the baseline experiments are consistent with the critical viscosity model.

7.3.3 Baseline Experiments - Fe-Al-Si Interactions Under Reducing Conditions (CCSEM)

As part of this program, ash samples collected during the baseline experiments (Helble et al, 1994b) were analyzed by CCSEM. These samples were collected at different stoichiometric ratios using the various program coals. Since many of the samples were collected under reducing conditions, they contained significant amounts of unburned carbon. This unburned carbon initially presented problems for the CCSEM analysis. To minimize these problems, the ash samples were mounted in epoxy and cross sectioned (similar to the procedure used for the raw coal). Because of the problems associated with this technique for ash, some care should be taken in using the data for quantitative analysis. The Fe-Al-Si interactions identified by the CCSEM results and a comparison to those presented earlier by Mössbauer analysis will be discussed here.

Figures 7-19 through 7-21 show the ternary Fe-Al-Si plots, from CCSEM, for the Pittsburgh No. 8 coals and ash samples collected from these coals at three different stoichiometric ratios. As can be seen from the figures, there are not any major differences in the mode of Fe-Al-Si interaction between the three stoichiometric ratios for any of the coals. In general, the line of intermediate compositions between the pure iron corner and the 'pure' aluminosilicate clay boundary suggests that the major iron containing species interact with these clay species during combustion to form particles of varying iron contents. Although the *mode* of Fe-Al-Si interaction was found to be constant for all the conditions studied, the *degree* of Fe-Al-Si interaction varied slightly for different conditions and different coals. For example, ash from the washed and run of mine Pittsburgh No. 8 coals had more iron oxide under fuel lean conditions (SR = 1.2) than was seen under fuel rich conditions. This trend was reversed, however, for the beneficiated Pittsburgh No. 8 coal. Although this may seem contradictory, it demonstrates that there are at least two major factors controlling the Fe-Si-Al interactions for these coals: (1) the degree of mineral coalescence (related to the degree of carbon burnout) and (2) the amount of extraneous iron present in the pulverized coal.

Previous work (Bool et al., 1995) has demonstrated that Fe-Al-Si particles are formed when ash particles coalesce during burnout. The particles can consist of either agglomerates of 'pure' iron and 'pure' aluminosilicate particles or they can be single glassy particles containing the three species. Based on this work, the degree of interaction is controlled by both the degree of burnout (and therefore the degree of ash coalescence) and the amount of extraneous iron. The extraneous iron does not interact with other species during combustion - resulting in 'pure' iron species particles (e.g., iron oxide).

For the data presented here, the presence of significant amounts iron oxide under fuel lean conditions suggests that there is significant extraneous iron for at least two of the coals. This is substantiated for the run of mine Pittsburgh No. 8 which was found to contain approximately 77% of the pyrite as extraneous pyrite (Section 4). For the beneficiated Pittsburgh No. 8 the fraction of iron as pyrite and siderite (which would result in iron oxide) is much lower. Coalescence with any iron oxide formed (assuming relatively low extraneous pyrite concentrations) will therefore result in fewer particles identified as iron oxide by CCSEM - as seen in the data.

Under the most reducing condition the degree of Fe-Al-Si interaction should be lowest for all these coals. This is due to the high amount of unburned carbon, and, therefore, unexposed ash. In addition, under reducing conditions any pyrite may not be completely oxidized - resulting in a lower number of particles found in the 'pure' iron corner (recall that the results are on a oxygen free basis, whereas sulfur is included). The data presented here for all coals are consistent with these qualitative predictions.

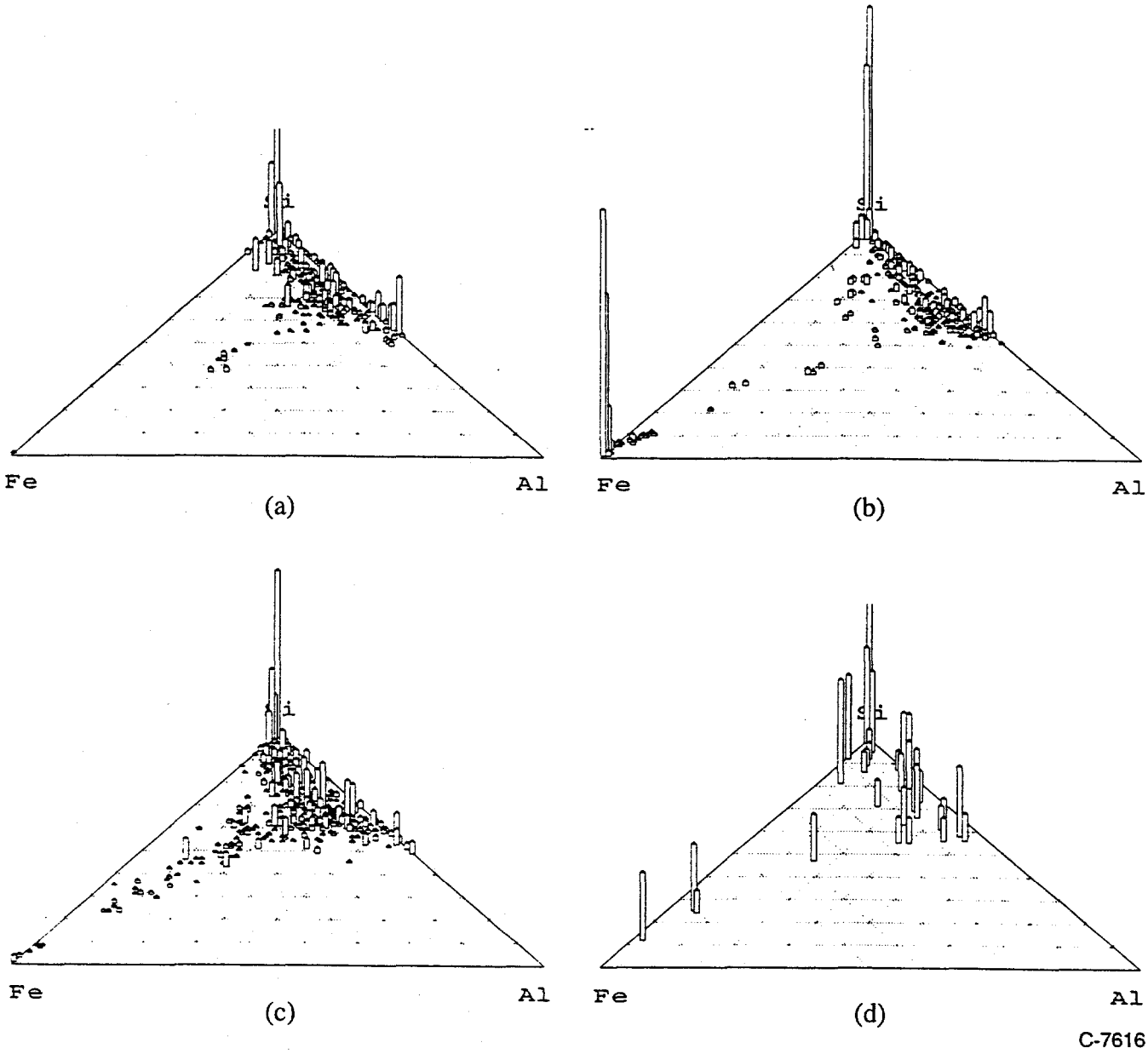

Figure 7-19. Fe-Al-Si ternary diagram (volume%) for run-of-mine Pittsburgh No. 8: (a) raw coal; (b) ash from SR=1.2; (c) ash from SR=0.9; (d) ash from SR=0.6.

Although the CCSEM analysis presented in the previous figures suggests that there is a large number of Fe-Si-Al particles, it is not possible to distinguish completely between the agglomerated particles discussed above and Fe-Al-Si melts. However, Mössbauer analysis of these ashes (Section 4) can distinguish between these two cases. For the coals discussed here, a significant amount of the iron is contained in glassy particles. This suggests that the aluminosilicate particles sinter with the iron-rich particles, and the iron bearing clays melt to form glasses.

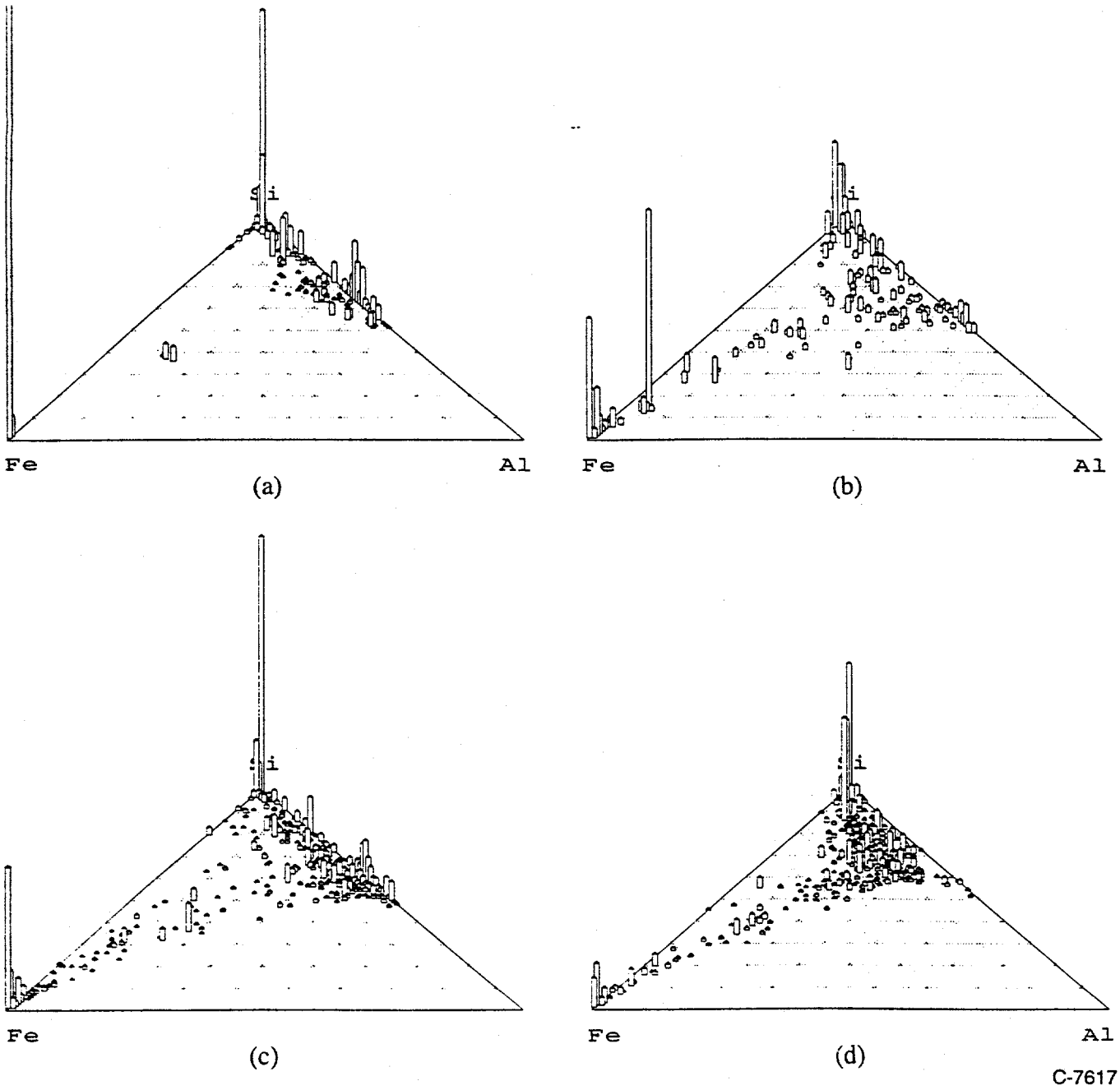

Figure 7-20. Fe-Al-Si ternary diagram (volume%) for washed Pittsburgh No. 8: (a) raw coal; (b) ash from SR=1.2; (c) ash from SR=0.9; (d) ash from SR=0.6.

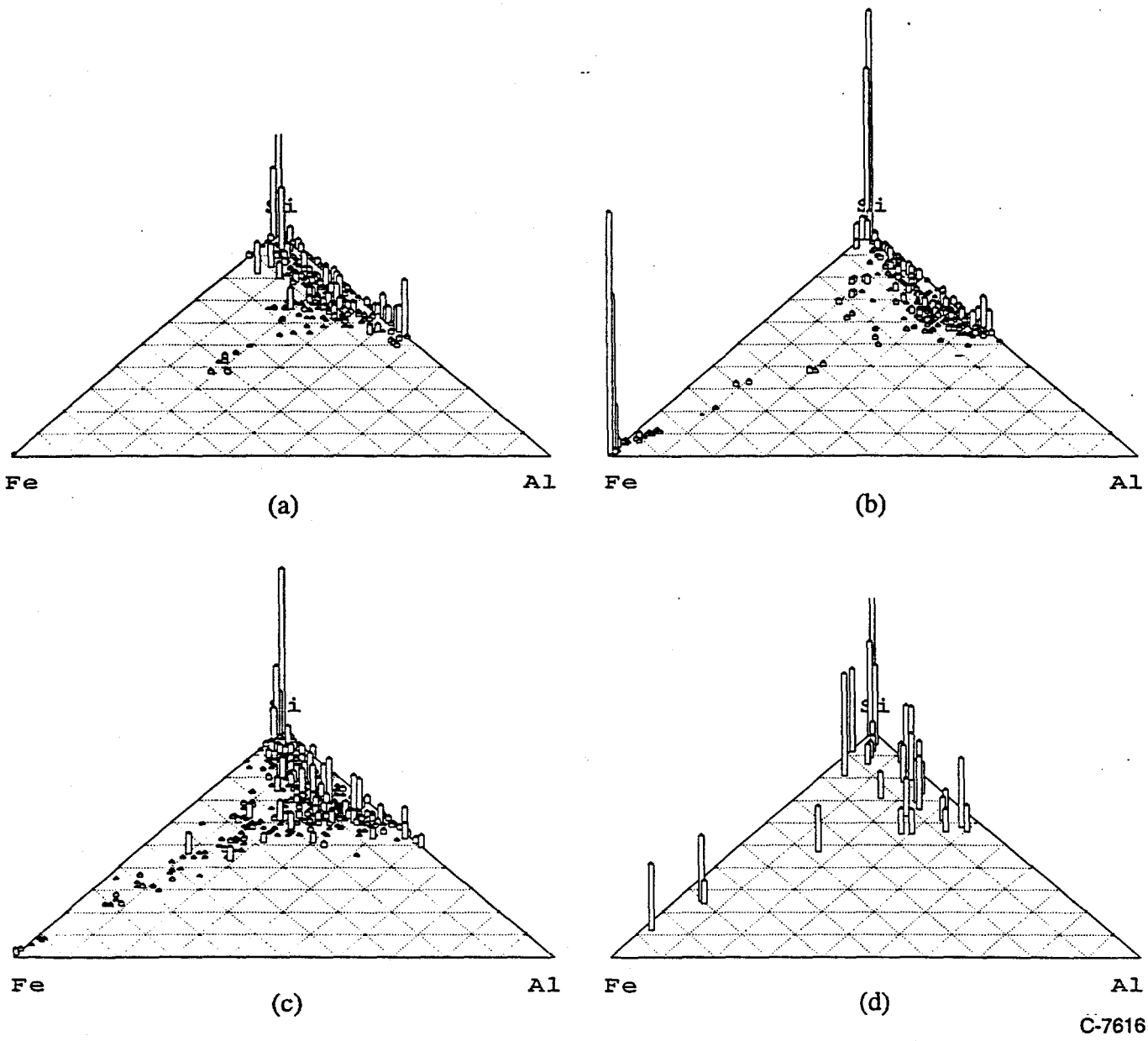

Figure 7-21. Fe-Al-Si ternary diagram (volume%) for beneficiated Pittsburgh No. 8: (a) raw coal; (b) ash from SR=1.2; (c) ash from SR=0.9; (d) ash from SR=0.6.

7.3.4 Baseline Experiments - Ca-Al-Si Interactions Under Reducing Conditions (CCSEM)

The data in Figures 7-22 through 7-25 illustrate the Ca-Al-Si interactions during burnout for each of the four program coals. In the run-of-mine and washed Pittsburgh No. 8 coals the calcium and aluminosilicates exist as essentially pure species (eg; no significant Ca-Al-Si phases are present in the coal). However, coalescence between these species begins early in the burnout process, as shown by the significant amount of intermediate, Ca Al Si containing, phases present in the low stoichoimetric ratio ash for these two coals. The coalescence increases with stoichiometric ratio for these coals. This trend is not observed for the beneficiated Pittsburgh No. 8 (Figure 7-24). In this coal no significant interaction occurs under any conditions. This lack of interaction may be due to the relatively low calcium concentration in this coal (see Section 3). The Black Thunder coal, in contrast, contained a significant amount of calcium, some of which was contained in clays. This coal showed significant Ca-Al-Si interaction at all the conditions studied, probably due to the high carbon burnout at all conditions.

7.4 The Effect of Carbon on Ash Stickiness

One of the effects of burning a coal under reducing stoichiometries is an increase in the carbon content of ash approaching heat exchange surfaces. Although the role carbon plays in determining ash stickiness under reducing conditions is unclear, it may serve to decrease the effective stickiness of the ash by physically preventing sticky ash particles from coming in contact with the heat exchange surfaces.

Data from the short residence time experiments and the baseline experiments with the washed Pittsburgh #8 coal are presented in Figure 7-26. In these experiments the collection efficiency and carbon content samples were collected independently. In order to illustrate the widest variability in collection efficiency for each condition, the data extremes for collection efficiency are plotted. As suggested in Section 7.3 the data indicate that there is a critical carbon content, below which carbon content has little or no effect on ash stickiness. Above this critical value, however, the ash stickiness (collection efficiency) decreases with increasing carbon content. For the washed Pittsburgh #8 coal, this critical value is approximately 60 to 70% carbon in the ash. Another coal that shows the same trend is the beneficiated Pittsburgh #8, as shown in Figure 7-28. For this coal the critical value is approximately 50%. The other study coals, however, did not exhibit this trend. For the run-of-mine Pittsburgh #8, Figure 7-27, and the Black Thunder sub-bituminous coal, Figure 7-30, there is no apparent effect of carbon content. For these coals, there are other factors that must be considered including rapid carbon conversion and the presence of extraneous ash.

In order to test our understanding of the role of carbon in ash stickiness, a simple model was created. If the carbon simply "gets in the way" of molten ash particles when the char contacts heat exchange surfaces, then there should be some critical point (as suggested by the data) when there is sufficient ash on the char surface for a particle to stick. After this critical point has been reached, the ash stickiness is only slightly dependent on carbon content. If this analysis is correct, then the effective ash stickiness should depend on the amount of ash exposed and the stickiness of the ash. Therefore, a preliminary model can be written:

$$\eta_{effective} = \eta_{ash} \cdot X_c \qquad (7\text{-}1)$$

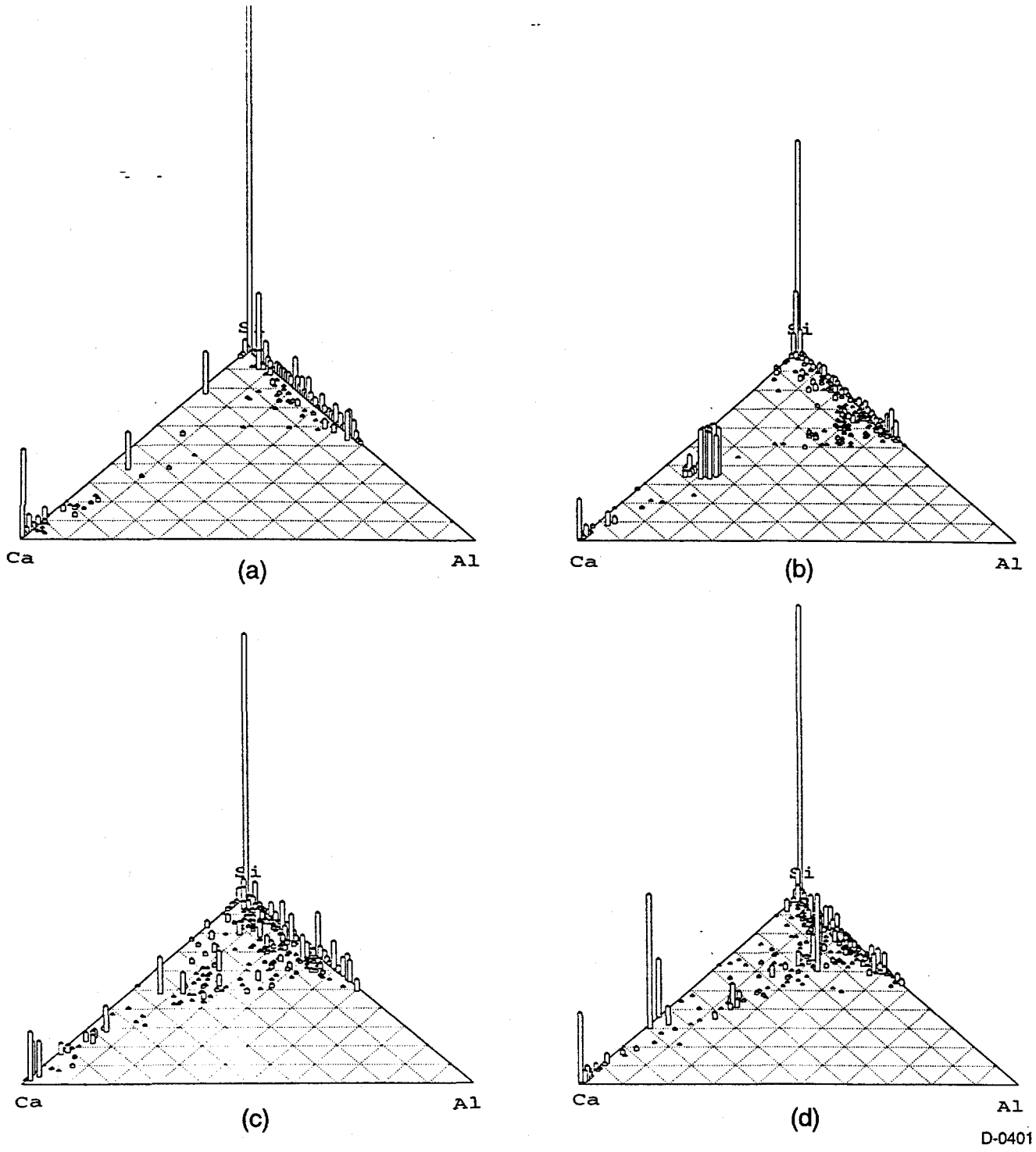

Figure 7-22. Ca-Al-Si ternary diagram (volume%) for run-of-mine Pittsburgh No. 8: (a) raw coal; (b) ash from SR=1.2; (c) ash from SR=0.9; (d) ash from SR=0.6.

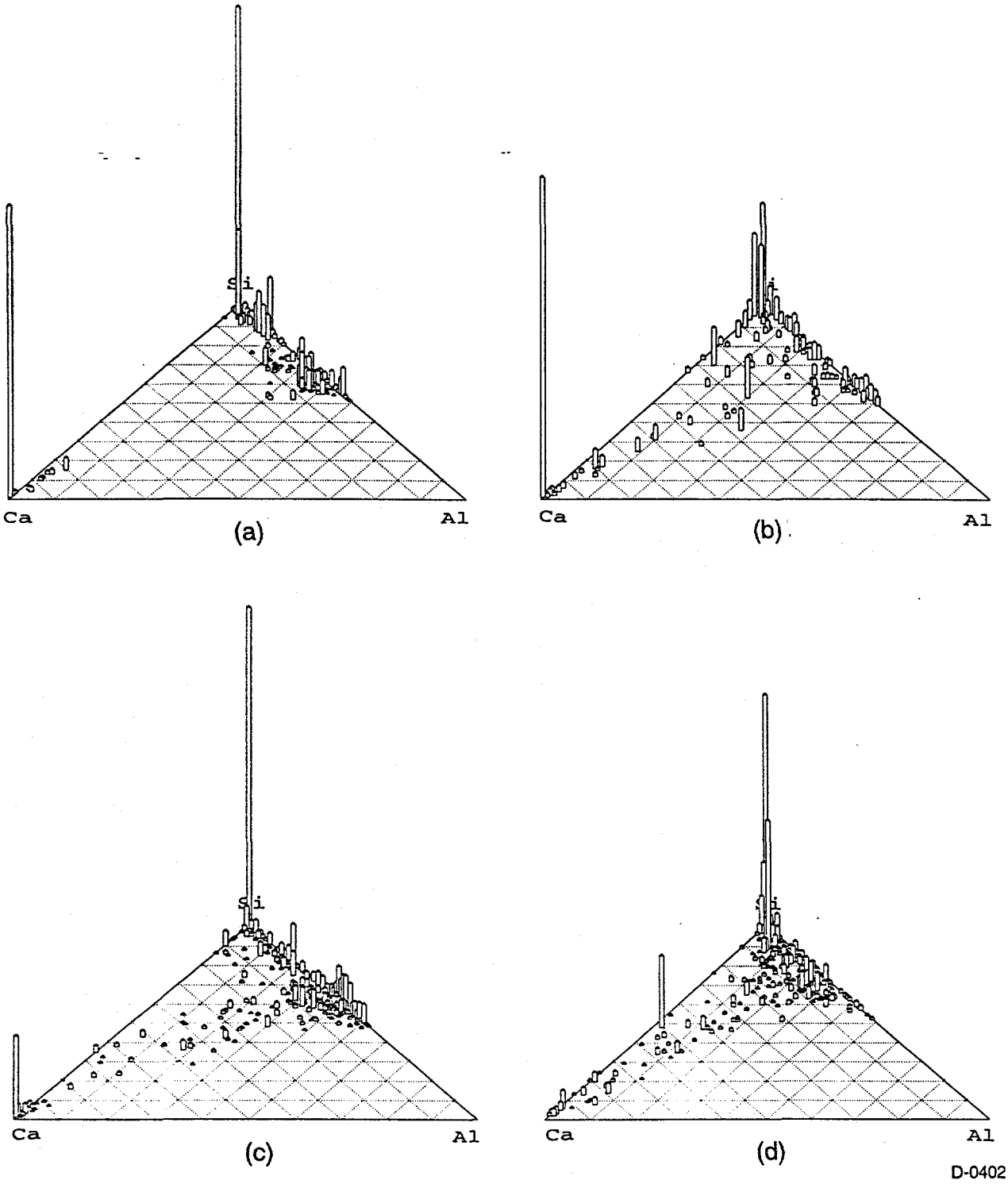

Figure 7-23. Ca-Al-Si ternary diagram (volume%) for washed Pittsburgh No. 8: (a) raw coal; (b) ash from SR=1.2; (c) ash from SR=0.9; (d) ash from SR=0.6.

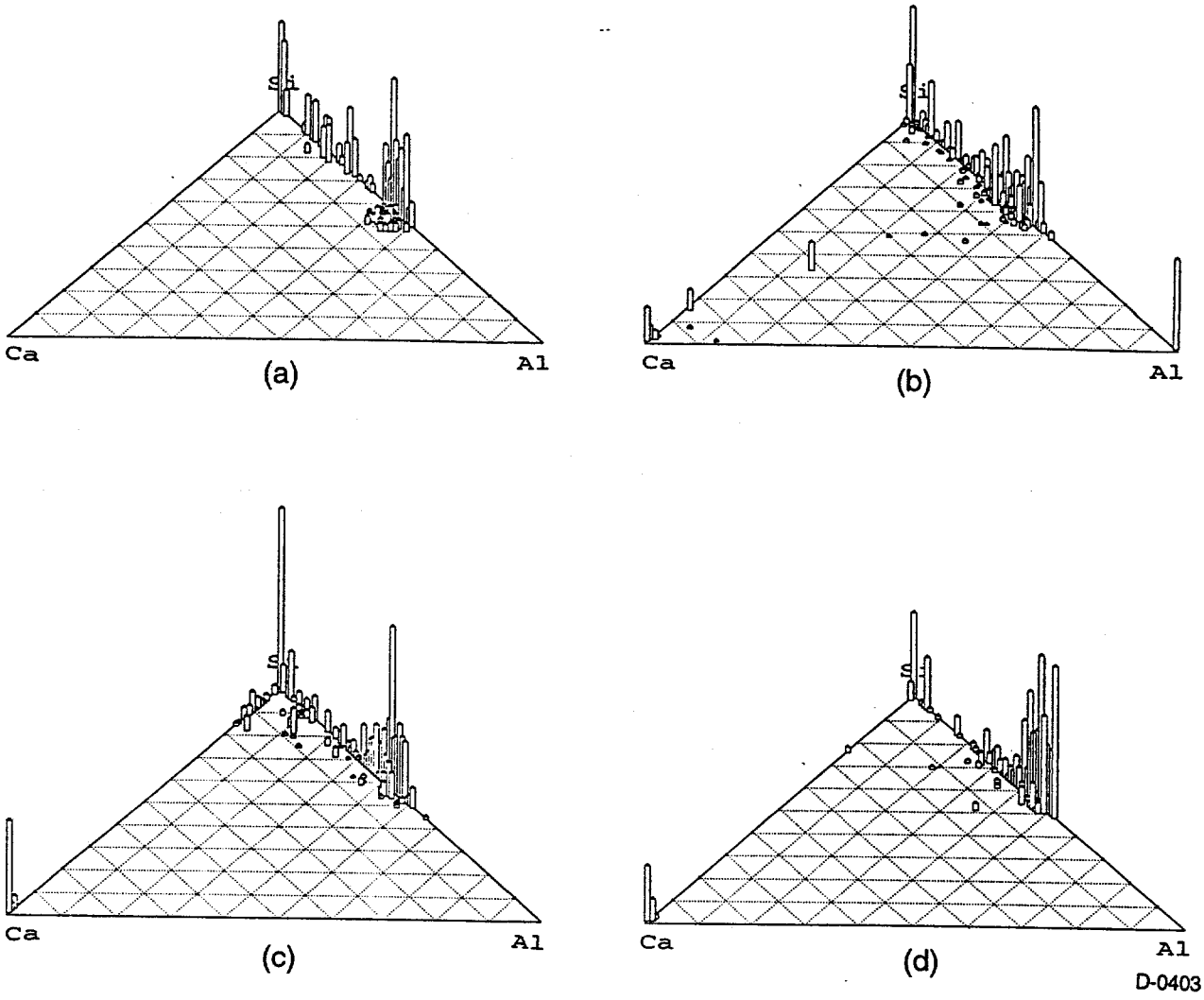

Figure 7-24. Ca-Al-Si ternary diagram (volume%) for beneficiated Pittsburgh No. 8: (a) raw coal; (b) ash from SR=1.2; (c) ash from SR=0.9; (d) ash from SR=0.6.

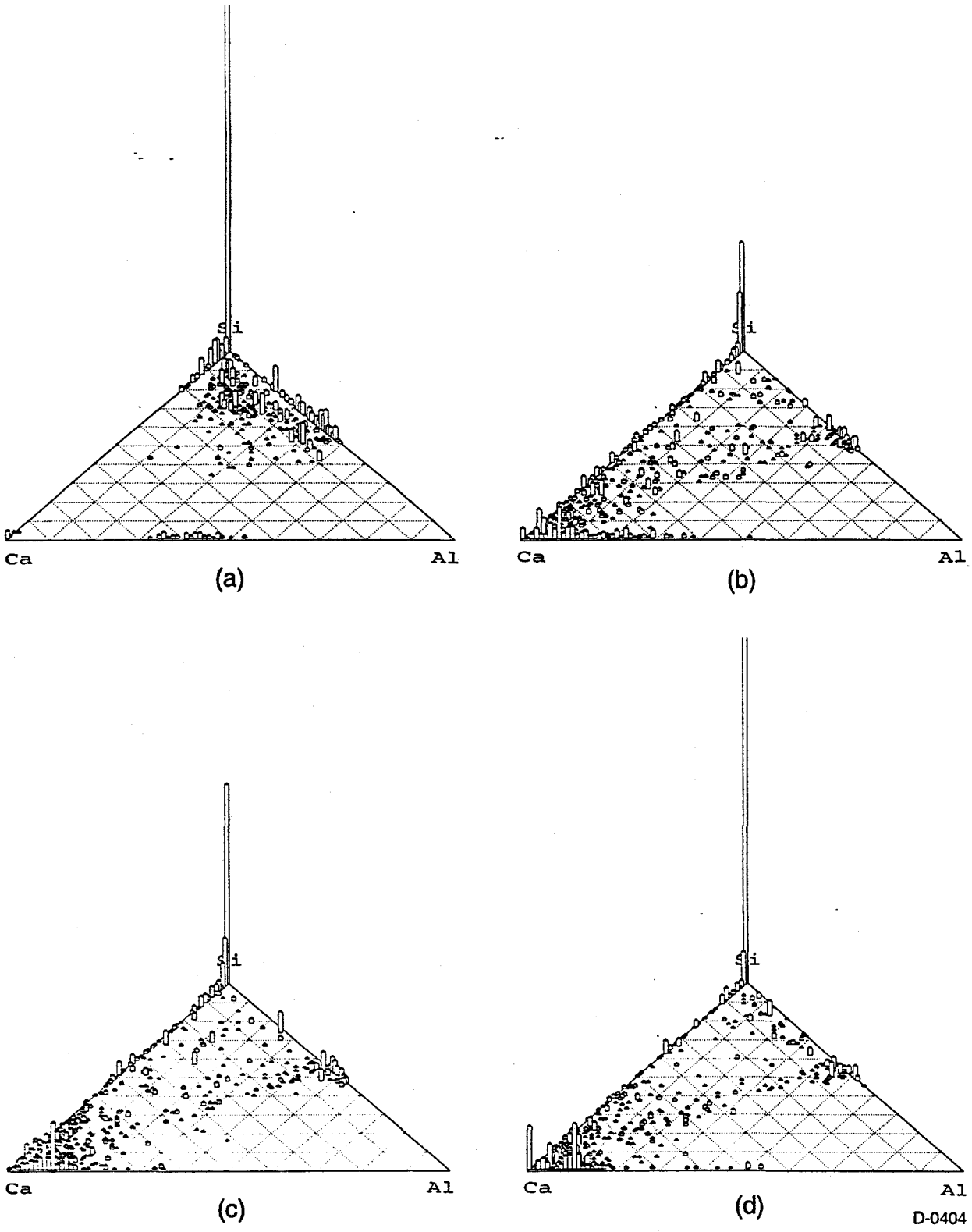

Figure 7-25. Ca-Al-Si ternary diagram (volume%) for Black Thunder: (a) raw coal; (b) ash from SR=1.2; (c) ash from SR=0.9; (d) ash from SR=0.6.

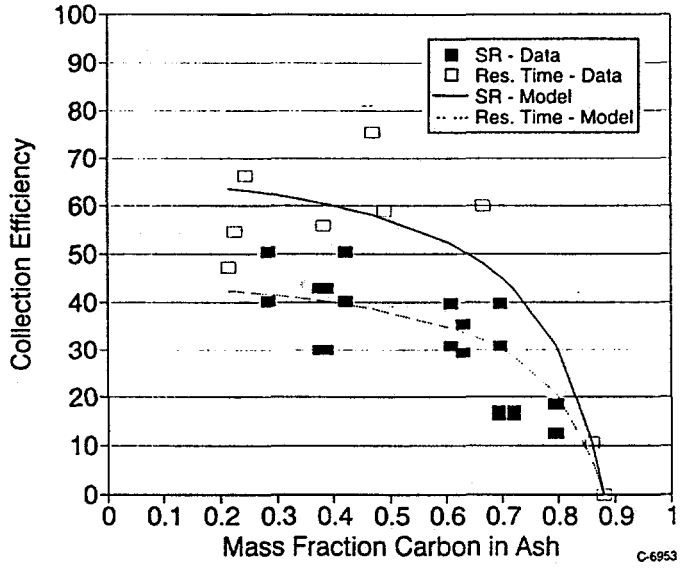

Figure 7-26. Collection efficiency vs. carbon content - washed Pittsburgh No. 8.

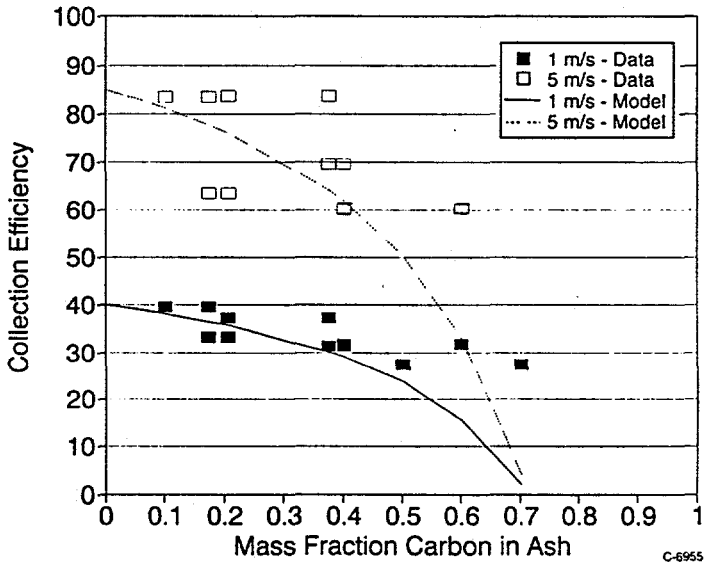

Figure 7-27. Collection efficiency vs. carbon content - run-of-mine Pittsburgh No. 8.

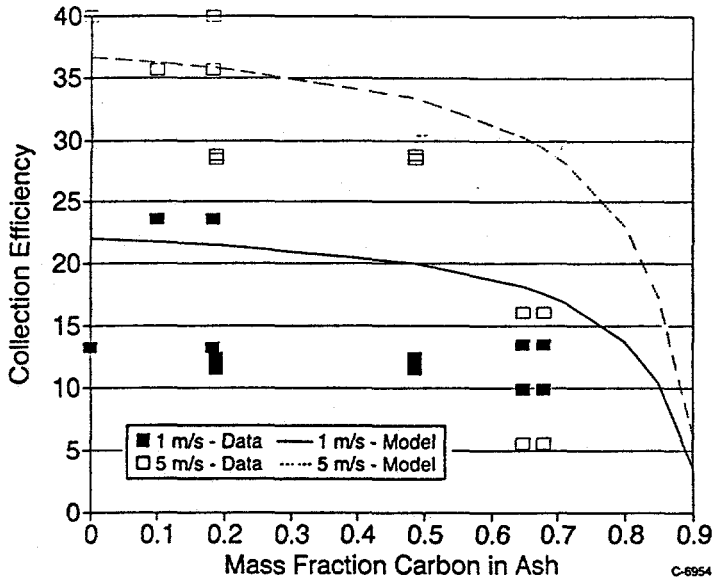

Figure 7-28. Collection efficiency vs. carbon content - beneficiated Pittsburgh No. 8.

where $\eta_{effective}$ is the effective collection efficiency, η_{ash} is the ash collection efficiency (given by the maximum collection efficiency at the lowest carbon content), and X_c is the fraction of the char burned away (calculated from the proximate analysis and the carbon content in the ash).

The values for η_{ash} are given in Table 7-5. The model curves are shown in Figures 7-26 through 7-30. This simple model fits the data reasonably well for all coals except for the high ash run-of-mine Pittsburgh #8 coal. The discrepancy for this coal may be due to the simplicity of the model. This model does not consider the presence of extraneous minerals and therefore may underpredict the stickiness in some cases. Further modifications on this preliminary model may help increase the quality of fit for the other coals as well.

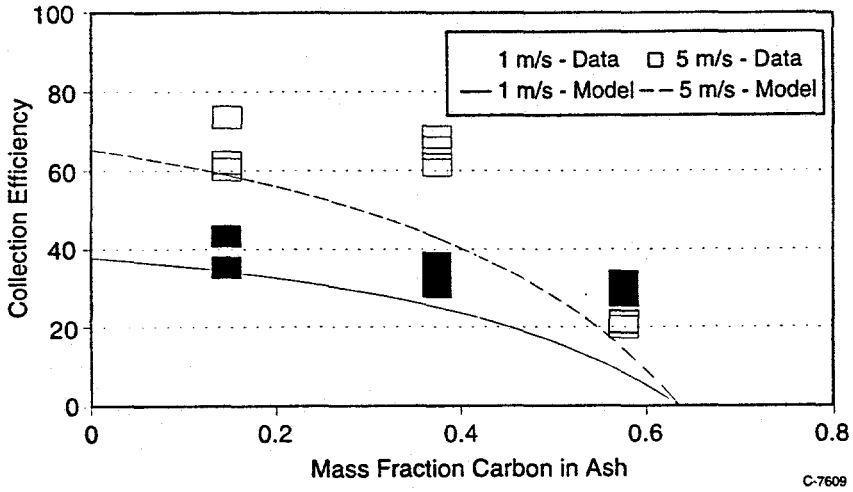

Figure 7-29. Collection efficiency vs. carbon content - Silverdale.

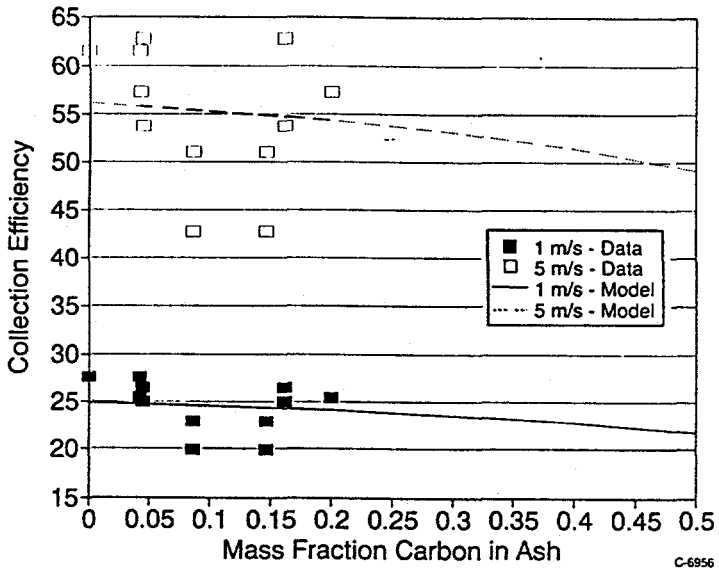

Figure 7-30. Collection efficiency vs. carbon content - Black Thunder.

Table 7-5. Collection efficiencies for carbon-free ash.

Coal	1 m/s (%)	5 m/s (%)
Pittsburgh #8 (run-of-mine)	40	63
Pittsburgh #8 (beneficiated)	24	40
Black Thunder	28	84
	Residence Time Experiments (%)	Baseline Experiments (%)
Washed Pittsburgh #8	75	50

7.5 Synthetic Ash Experiments

To gain a better understanding of the role of iron in controlling ash deposition under reducing conditions, a number of experiments were performed to measure the adhesion efficiency of iron containing glassy ash particles. To avoid the particle-to-particle variations in ash composition and iron oxidation state typical of coal ash, two synthetic ashes, with identical compositions, were used in these experiments. Each synthetic ash was produced by a commercial laboratory from a homogeneous melt containing iron (II) oxide, silica, alumina, and potassium oxide (see Table 7-6). By producing the synthetic ashes from homogenous melts, particle to particle variations in composition were avoided. The resulting glasses were then pulverized to a particle size distribution approximating that of coal fly ash. As shown in Figure 7-31. the size distributions of the two samples measured by the Malvern technique were similar, with mass mean diameters of 28 and 30 μm for glass 1 and glass 2, respectively.

Table 7-6. Composition Specifications for Iron Containing Glass

Oxide	Weight %
SiO_2	51
Al_2O_3	21
FeO	20
K_2O	8

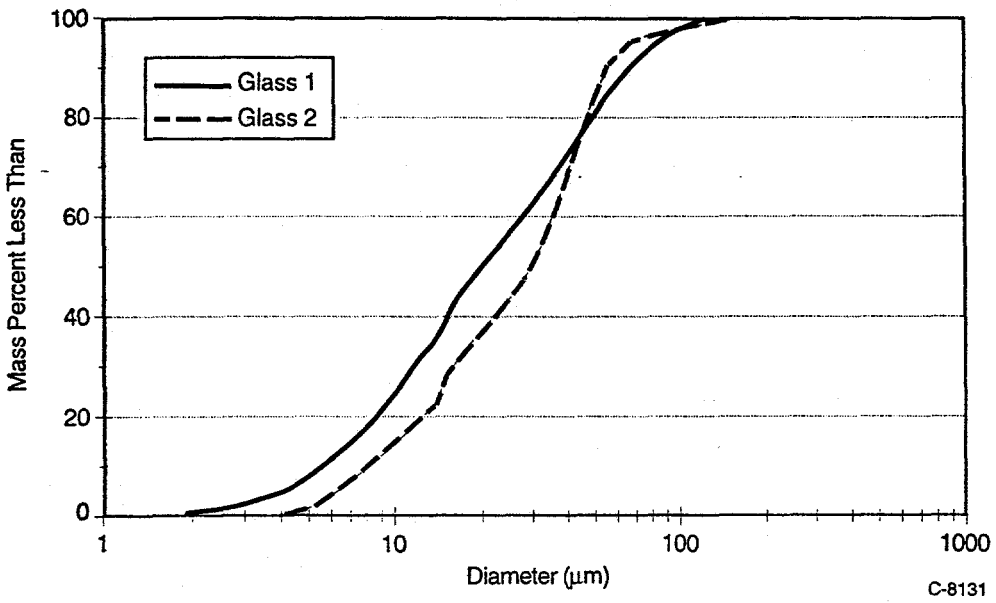

Figure 7-31. Particle size distributions for glasses.

Samples of each glass were analyzed by Mössbauer spectroscopy and by Fe(II) titration to measure the percentages of Fe(II) and Fe(III) present. Although the iron was expected to be present exclusively as FeO, the initial Mössbauer analysis indicated that both glasses also contained metallic iron. The FeO titration, however, indicated the glasses each contained approximately 19.5% FeO by weight, the target amount. To resolve this discrepancy, samples of the glasses were examined for total iron concentration by atomic absorption spectroscopy. The total iron analyses (18.64% and 19.95%) agreed with both the manufacturing specifications and the FeO titration. It was therefore concluded that the Mössbauer indication of metallic iron was incorrect; all of the iron in the each glass was initially in the Fe(II) state.

Deposition experiments were performed over a range of temperatures and carrier gas compositions as shown in Table 7-7. In the first set of experiments one of the glasses was passed through the EFR under pure nitrogen at gas temperatures between 900 and 1400°C. For the second set of experiments the oxygen concentration was set at 20% and the furnace setpoint again varied from 900 to 1400°C. Similar experiments were also performed under 100% oxygen. The experiments were repeated at selected conditions with the second glass sample. At each condition ash collection efficiency at gas velocities of 1 and 5 m/s was determined using the deposition apparatus described above. In addition, particle samples were collected at the exit of the EFR using a nitrogen-quenched probe for three different residence times (for use in the modeling effort). The residence time was controlled by either changing the gas flow rate or by

Table 7-7. Experimental Conditions

	Data Set		
	1	2	3
Furnace Setpoint Temperatures (°C)	900 1000 1150 1300 1400	1000 1150 1300 1400	1000 1150 1300 1400
O_2 Concentration (Mole %)	0	20	100
Glass Used	Glass 1* Glass 2	Glass 2	Glass 1* Glass 2

*Measurements only made at 1400°C for this glass

injecting particles into the lower section of the EFR. Selected samples were then analyzed by FeO titration to determine the conversion of Fe(II) to Fe(III).

The results of the deposition measurements are shown in Figure 7-32 and Figure 7-33. Both the temperature and the iron oxidation state (as affected by the gas composition) play a major role in determining the collection efficiency of the ash. In almost all cases the collection efficiency increases with increasing temperature. This increase however, is much more pronounced for the pristine glasses (all iron present as Fe(II)). When the iron in the glass is oxidized to Fe(III), as occurs at the higher oxygen concentrations, the collection efficiency decreases by a factor of 2 to 4. This decrease in collection efficiency is likely due to the increase in particle viscosity associated with the conversion of Fe(II) to Fe(III). As shown in Figure 7-34, measurement of the post-experiment iron oxidation state in selected samples suggests that very little conversion of Fe(II) to Fe (III) is required to cause the observed decrease

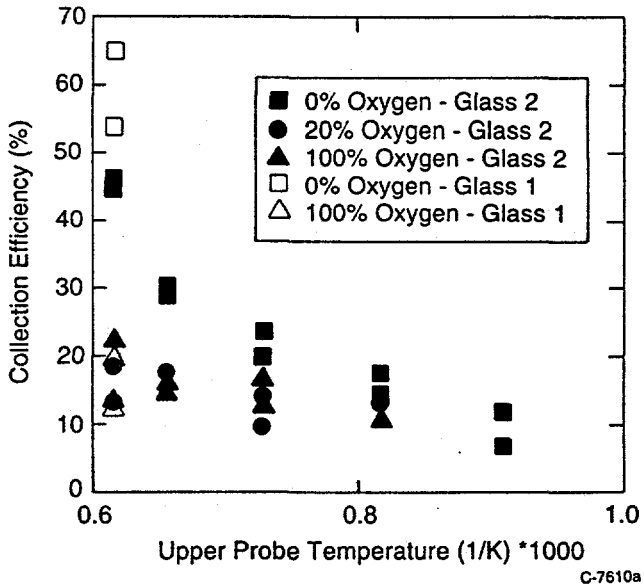

Figure 7-32. Glass stickiness as a function of particle temperature (1 m/s).

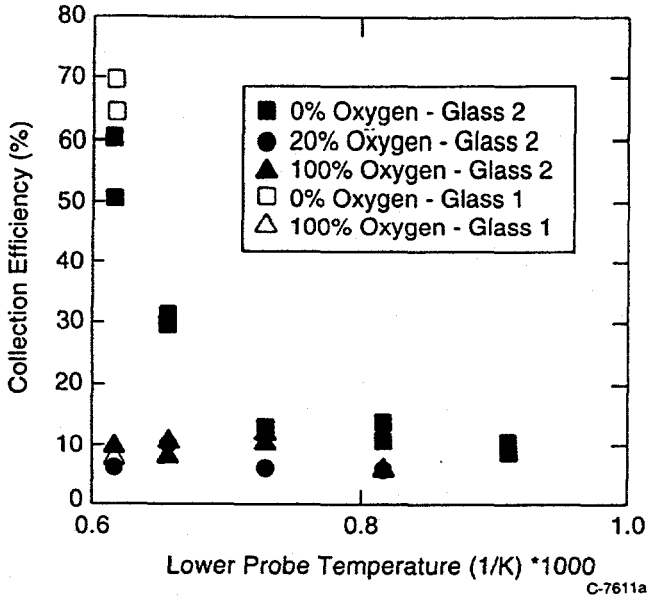

Figure 7-33. Glass stickiness as a function of particle temperature (5 m/s).

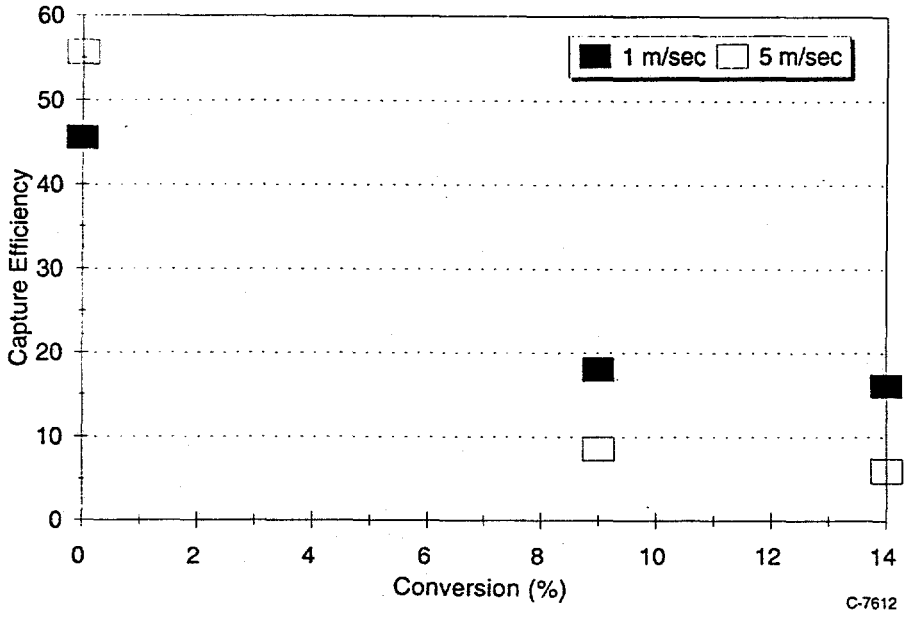

Figure 7-34. Effect of Fe(II) oxidation on particle stickiness.

in ash stickiness. These measured values are based upon the bulk concentration of Fe(III); concentrations at the particle surface are likely higher.

The conversion of Fe(II) to Fe(III) for the two glasses is shown in Figure 7-35 as a function of the percentage of oxygen in the bulk gas. The data for glass 2, measured at 1400°C and oxygen concentrations of 0, 20, and 100%, suggest that the conversion is independent of oxygen concentration. For glass 1 measurements were only made at oxygen concentrations of 0 and 100%. These data are included in Figure 7-28. Although both glasses were of the same composition, the Fe(II) conversion was slightly higher for

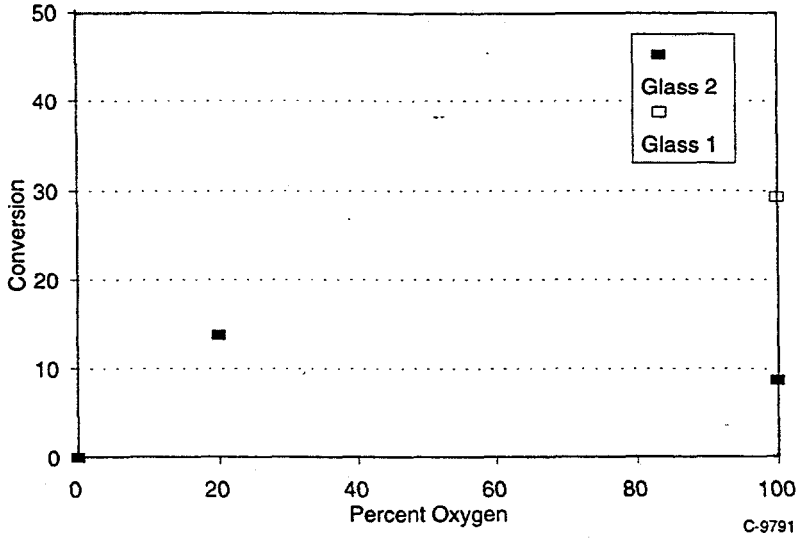

Figure 7-35. Effect of gas composition on oxidation of iron in glassy particles.

glass 1. This difference may be attributed to the fact that glass 1 was slightly smaller than glass 2 - increasing the reaction rate as discussed later. At approximately 2.9 s, 100% oxygen, and a furnace setpoint of 1400°C the conversion ranged between 9 and 28%. Additional experiments (data not shown) indicated that the conversion was 0% at lower gas temperatures (1150°C) under 100% oxygen. The independence of conversion from oxygen concentration suggests that the oxidation of the iron in glass is limited by melt diffusion.

To test the hypothesis that melt diffusion controls the oxidation of iron in glassy ash particles, a simple model was developed. It was assumed that the oxygen concentration in the melt (C_o) at the gas-liquid boundary was constant, and equaled some fraction of the oxygen solubility in the melt. The model further assumed that the glass droplets were static as they oxidized. Oxygen transport was therefore assumed to occur by diffusion alone - no convective transport by liquid recirculation takes place inside the particle. By making this assumption it was possible to use a shrinking core model to describe the oxidation of iron in the glass particles. This mechanism is described schematically in Figure 7-36. Oxygen diffuses through the molten glass containing Fe(III) (defined as Fe_2O_3) to the reaction interface where it reacts as follows:

$$-\frac{dV}{dt} = \frac{b\ 4\ \pi\ D_e\ C_0}{\left(\frac{1}{r_c} - \frac{1}{R}\right)\ \rho_b} \qquad (7\text{-}2)$$

The reaction rate is then defined by Eq. (7-2), where V is the volume of unreacted glass, and r_c and R are the radii of the unreacted core and the particle, respectively. D_e is the effective diffusivity (the diffusivity of oxygen through the melt) and is a function of temperature as described later. C_0 is the concentration of oxygen in the melt at the surface of the particle, b is the stoichiometric conversion, and ρ_b is the concentration of Fe(II) (FeO) in the unreacted glass. When we substitute the definition of the

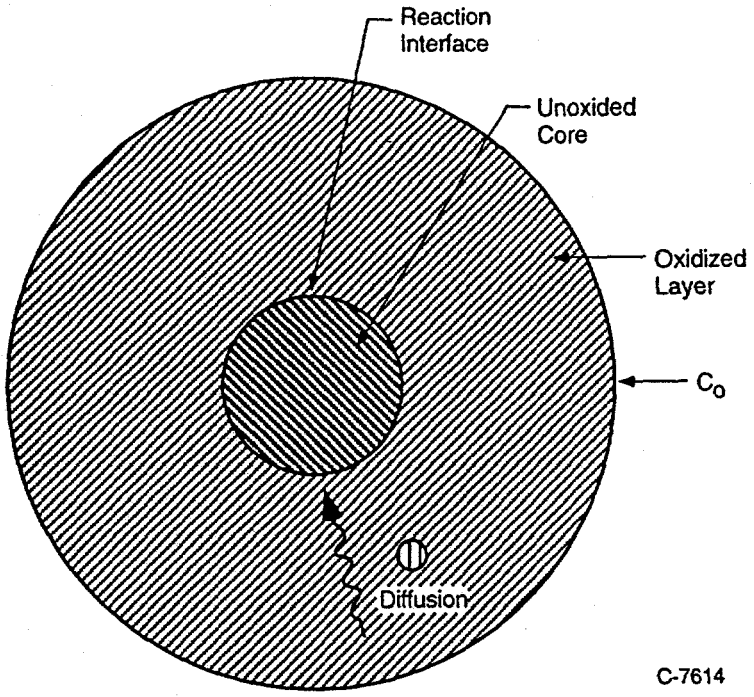

Figure 7-36. Schematic diagram of glass oxidation model.

conversion (X_b), Eq. (7-3), we obtain an equation that describes the conversion of Fe(II) in glass as a function of time (Eq. (7-4)).

$$X_b = 1 - \frac{V}{V_0} = 1 - \left(\frac{r_c}{R}\right)^3 \tag{7-3}$$

$$\frac{dX_b}{dt} = \frac{3\ b\ D_e\ C_0}{\rho_b\ R^2}\left(\frac{(1-X_b)^{1/3}}{1-(1-X_b)^{1/3}}\right) \tag{7-4}$$

The necessary parameters were either calculated or obtained from the literature. For example, the FeO concentration (approximately 0.00738 mol/cc) was determined from the Fe(II) mass fraction in the glass. The oxygen concentration (C_o) was defined as a fraction of the oxygen solubility in molten glass, 7.2×10^{-4} g/cc, or 2.2×10^{-5} mol/cc, as presented by Cable (1961) for the 1400°C particle temperature considered here. The oxygen solubility was assumed to be independent of temperature. The oxygen diffusivity (D_e) was obtained from the data of several investigators compiled by Turkdogan (1983) for oxygen diffusion in a $CaO\text{-}Al_2O_3\text{-}SiO_2$ melt. The temperature dependence of the oxygen diffusivity can be modeled with an Arrhenius type equation (Turkdogan, 1983):

$$D_e = D_{e_0} \exp\left(-\frac{A}{T}\right) \tag{7-5}$$

The constants are approximately:

$$D_{e_0} = 1.3283 \times 10^3 \quad [cm^2/sec]$$
$$A = 3.50 \times 10^4 \quad [K].$$

Because there is very little heat generated by the iron oxidation, the temperature of the glassy particles can be assumed to equal the gas temperature. For the entrained flow reactor described above the gas temperature profile was fitted in three segments as a function of residence time in the furnace. The three segments consisted of a linear heating zone (from room temperature to peak gas temperature), a flat constant temperature zone (maintained at the peak gas temperature), and a linear cooling zone (from peak gas temperature to exit temperature).

The model was integrated numerically to determine the Fe(II) conversion as a function of the particle residence time for two model extremes; 0.1 and 0.9 times the oxygen saturation. The results from these simulations are shown in Figure 7-37. The data included on this plot were collected at various residence times under conditions of a furnace setpoint equal to 1400°C and a gas composition of 100% O_2. Qualitative agreement between experimental data and the model is indicated, suggesting that melt diffusion is the limiting mechanism. The trend shown by the experimental data suggests that the oxygen solubility may increase with temperature. At the shortest residence time the measured conversion was very similar to that predicted for 10% of the maximum oxygen saturation at the surface of the particle. At the longest residence time the measured value was similar to that predicted for 90% of the maximum saturation. In our experiments the gas temperature, and therefore the particle temperature, is still fairly low (less than the peak value) at the residence time of the first measurement. Therefore, the oxygen solubility may be lower at these lower temperatures. At longer residence times the particle temperatures are higher - therefore the mean oxygen solubility may be higher. However, more experimental data and a better value for the temperature dependence of the oxygen solubility in aluminosilicate melts are required to test this hypothesis and to assess the quantitative agreement between the model and the data.

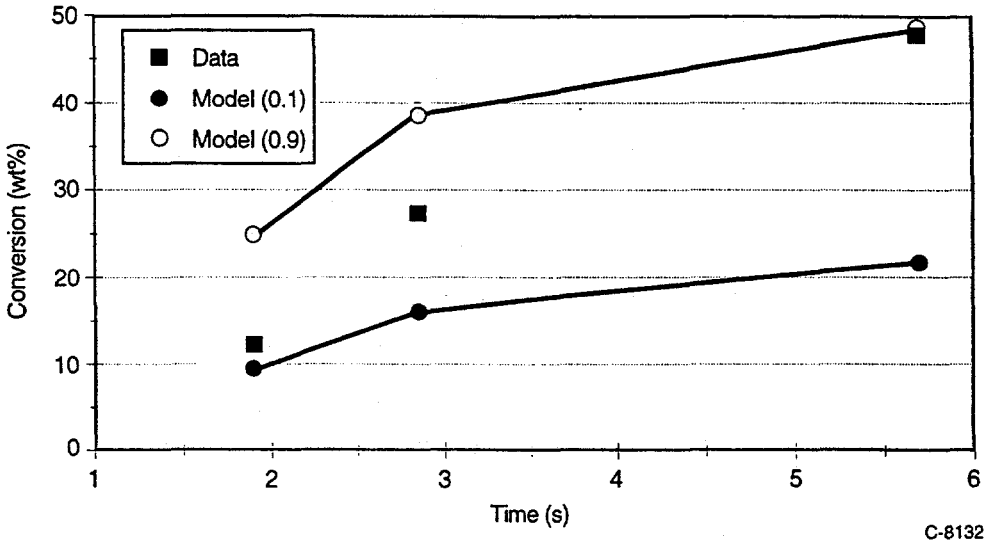

Figure 7-37. Results of iron-in-glass oxidation model.

7.6 Effect of Coal Weathering on Iron-Fume Formation

Early in this program a model was developed to predict the partitioning of iron during coal combustion (see discussion in Section 6 of this report). One of the primary assumptions made during the development of this model was that iron fume does not form under typical combustion conditions (Bool et al, 1995). This assumption was based on data obtained in the University of Arizona self-sustained test furnace and presented by Boni et al. (1990), Helble et al. (1992), and Bool (1993). However, other investigators (Baxter and Mitchell, 1992) have suggested that substantial amounts of iron fume are generated under normal combustion conditions from a chemical reaction process (i.e., a path other than iron vaporization). The lack of iron fume formation observed in the Arizona, PSI, and MIT experiments was attributed by Baxter and Mitchell to surface oxidation (i.e., weathering) of the coal and pyrite prior to combustion.

In their experiments, Baxter and Mitchell (1992) used size-classified samples of a pristine Illinois No. 6 coal (Penn State Coal Sample Bank) and combusted them in a drop tube facility under dilute phase conditions (each particle burning as a single particle). The mean gas temperature was approximately 1610 K and oxygen mole percentages were maintained at either 6 or 12%. The simulated flue gas also contained approximately 16% water and 2% CO_2 with the balance N_2. The diameter of the coal particles ranged from 75 to 125 μm. Ash was collected on Nuclepore polycarbonate filters at residence times between 47 and 117 μs. By using several inorganic species as tracers, Baxter and Mitchell were able to estimate the overall mass loss at each residence time. They also estimated the mass loss for each of the major species. This analysis suggested that a significant fraction of the iron (approaching 40 to 60 %) was lost immediately after devolatilization. They postulated that this iron may have formed small (<1 μm) particles by a mechanism other than vaporization. It was further postulated that the iron was lost to the system by passing through the micrometer-sized pores in the filter.

In order to better understand the importance of iron fume formation under typical combustion conditions, a number of experiments were performed at PSIT to determine the extent of iron fume formation and to capture the <1 μm iron particles suggested by Baxter and Mitchell. To remove the potential confounding effect of pyrite weathering, the experiments were performed utilizing pristine Illinois No. 6 coal samples obtained from Dr. L.L. Baxter, Sandia National Laboratory and the Penn State University Coal Bank. The experiments with these coals were designed to simulate the earlier experiments by Baxter and Mitchell:

Furnace setpoint:	1500°C (gas temperature approx. 1450°C)
Gas flowrate:	1 scfm
Coal feedrate:	0.13 g/min
Oxygen conc.:	6% oxygen
Particle size:	Sandia coal sample (originally from Penn State): 63/45 μm Penn State University Coal Bank Sample: <200 mesh, dry sieved to a fraction that was <125 μm used for experiments.
Residence time:	2.9 sec.

Analysis of the Sandia coal sample by Mössbauer spectroscopy indicated that all of the iron was present in pyrite or clay minerals. No evidence for pyrite oxidation was found. The iron distribution based upon form of sulfur analysis, using Sandia values for the iron content of different coal size fractions, indicated that 71 to 102% of the iron was pyritic. The existence of a range results from a lack of data on the iron concentration in the PSI sub-sample.

Because Baxter and Mitchell (1992) showed a higher iron loss at 6% oxygen, this value was chosen for our experiments. The low coal feedrate (SR of approximately 13) was selected so that the oxygen concentration would be relatively constant - as was the case in the earlier experiments. Two minor differences existed between our conditions and those of Baxter and Mitchell (1992). First, only nitrogen and oxygen were present in the gas stream in our system (other than the minor amounts of CO_2 and water generated by combustion of the coal particles). Second, residence times in our system were longer than those of Baxter and Mitchell (1992). Our conditions were chosen to maximize overlap with previous experiments conducted in the PSI facility using other coals. In addition, although our gas temperature is slightly higher than that used by Baxter and Mitchell, the net effect on the coal *particle* temperatures is negligible.

For each experiment size, classified ash samples were collected with a nitrogen-quenched probe and a cascade impactor. The measured ash mass distribution can be seen in Figure 7-38. This plot shows that there is very little ash less than 1μm (plates 5 through the after filter) - suggesting that little or no fume forms for this particular coal. In addition, analysis of the selected samples (Table 7-8) suggests that less than 1% of the iron collected is less than 1 μm. This small amount of fume is indicative of much lower levels of iron loss than the 40 to 60 % iron loss observed by Baxter and Mitchell. Our data therefore support the conclusion that iron loss leading to iron fume formation is not a major pathway for iron transformations under typical combustion conditions.

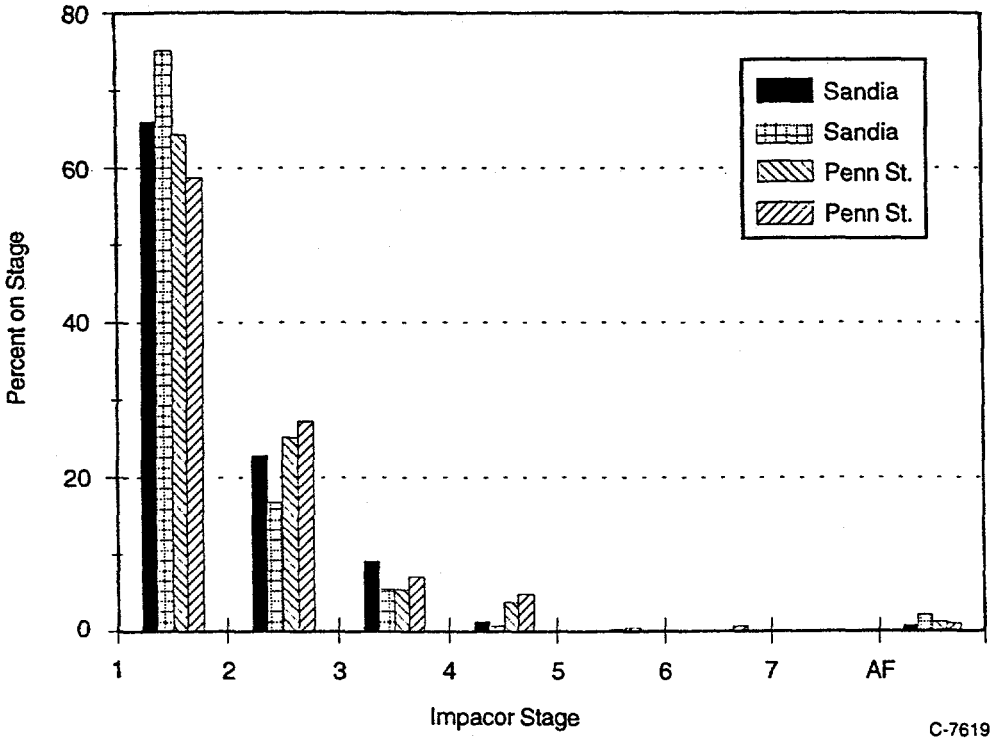

Figure 7-38. Ash mass distributions for pristine Illinois No. 6 experiments.

Table 7-8. Iron Analysis of Selected Ash Samples (wt% as Element)

Impactor Stage	Sandia Sample (Run A)	Sandia Sample (Run B)	Penn St. Univ. Sample (Run A)
1	2.44	7.38	7.31
2	1.32	1.91	4.50
3	—	0.83	—
4	—	0.21	—
5	—	—	—
6	—	—	—
7	—	—	—
AF	—	0.023	0.079

7.7 References

Bool, L.E., Peterson, T.W., Wendt, J.O.L, "The Partitioning of Iron During the Combustion of Pulverized Coal.", ***Comb. and Flame***, 100, 262-270, 1995.

Boni et al.,"Transformations of Inorganic Coal Constituents on Combustion Systems", Phase I Final Report, U.S. DoE Contract No. DE-AC22-86PC90751, Pittsburgh Technology Center, Pittsburgh, PA, 1990.

Bool, L.E., "The Partitioning of Iron During the Combustion of Pulverized Coal", Ph.D. Dissertation, University of Arizona, 1993.

Baxter L.L. and Mitchell, R.E., "The Release of Iron During the Combustion of Illinois No. 6 Coal", *Comb. and. Flame* **88**, p.1-14, 1992.

Helble et al, "Transformations of Inorganic Coal Constituents on Combustion Systems", Phase II Final Report, U.S. DoE Contract No. DE-AC22-86PC90751, Pittsburgh Technology Center, Pittsburgh, PA, 1992.

Srinivasachar, S., Helble, J.J., Boni, A.A., "An Experimental Study of the Inertial Deposition of Ash Under Coal Combusion Conditions", *Proc. of Twenty Third Symposium on Combustion*, The Combustion Institute, Pittsburgh, 1305-1312, 1990.

Turkdogan, E.T., "Physiochemical Properties of Molten Slags and Glasses", 1st Ed., The Metals Society, London, England,1983.

SECTION 8

TASK 4: ENGINEERING MODEL FOR ASH FORMATION
(PSI Technologies)

8. ENGINEERING MODEL FOR ASH FORMATION

During this program several modifications were made to the Engineering Model for Ash Formation (EMAF). This model, developed at PSIT as part of other DoE funded programs, was designed to predict the size and composition distributions of fly ash generated during combustion under *fuel lean* conditions. The model uses coal particle size distributions, coal mineral composition and size distributions derived from computer controlled scanning electron microscopy (CCSEM), bulk ash content, volatile fraction, and swelling indices as inputs to generate ash particle size and composition distributions. By accounting for particle-to-particle variations in mineral content, size, and composition, and by including phenomena such as char fragmentation and limited mineral coalescence, the model provides a physically realistic analog of the processes involved in fly ash formation.

Modifications to the original version of EMAF were performed to describe the effects of char fragmentation and fuel rich combustion on fly ash formation. A complimentary, stand alone, model was also developed to predict the formation of submicron aerosols during combustion. Predictions made with the modified EMAF were then compared to eperimental data compliled in this program and others. The following sections provide a description of the model, a discussion of each EMAF modification, or sub-model development, and comparisons with experimental data.

8.1 Description of Model

As noted, our model predicts ash particle size and composition distributions based upon coal properties. The key features of the model are a mineral redistribution routine to simulate the variability of the mineral content of individual coal particles and a mineral interaction routine to simulate the transformation of the distributed minerals into ash particles during combustion.

During combustion, ash particles are produced from extraneous mineral particles and from mineral inclusions contained in mainly carbonaceous particles. Thus the first step in our approach to modeling ash formation is the generation of a set of coal particles whose individual mineral inventories fluctuate in amount and composition in a fairly realistic way. In principle, CCSEM analysis could provide this information exactly, but until CCSEM data are routinely available for the compositions and sizes of the mineral inclusions found in a large number of individual coal particles, an alternative means for generating this information must be used. The mineral redistribution procedure fills this need in our model.

8.1.1 Mineral Redistribution Model

Mineral redistribution models have been developed by several researchers and used in attempts to predict ash size and composition. Charon et al. (1990) applied Monte Carlo methods to simulate the random distribution of minerals among a set of coal particles. Barta et al. (1992) developed an analytical "Urn Model" based on Poisson statistics for determining the (joint) size and chemical composition distribution for the mineral inclusions based on CCSEM data. They then used a random coalescence model to calculate the ash distributions. Wilemski et al. (1992) used a composite method that combines Poisson statistics for distributing the smallest minerals among the smallest coal particles with a Monte Carlo method for handling all of the larger minerals and coal particles. Ash distributions were predicted in the full and no coalescence limits. Zygarlicke et al. (1992) are developing an expert system using a large data base of measured ash properties to derive "mixing rules" for coal mineral properties to predict the ash size and composition distributions.

In our model, the mineral redistribution procedure is performed using a composite method that combines straightforward Monte Carlo techniques with Poisson statistics. First, a discrete representation of the coal particle size distribution is generated by subdividing the distribution into a sequence of (generally) 10 μm wide size ranges. The number of coal particles assigned to each size range is directly proportional to the volume fraction of coal found experimentally in that range. These baseline numbers are chosen to ensure that at least one mineral particle of each size and type is present in each coal size range, except where size restrictions apply. Next, a discrete representation of the mineral population is generated. The mineral matter is imagined to be subdivided into idealized particles of different sizes and types. These "particles" are then randomly distributed among the computer coal "particles" just as if one were randomly tossing balls of different sizes and colors into a set of boxes of different sizes. In our procedure, the mineral particles are assumed to be of six different diameters (2, 4, 8, 16, 30, and 60 μm) and seven different types (quartz, kaolinite, illite or montmorillonite, miscellaneous silicates, pyrite, calcite and/or gypsum, and others).

As an example of results generated using this procedure, consider an Illinois 6 bituminous coal. There are roughly 10^8 coal particles in the representation with 7×10^7 in the 10 μm range and about one thousand particles in the largest size (160 μm) range. For the mineral particle representation, the simulation produces 4.9×10^8 particles of 2-μm diameter and another 6×10^7 particles of all of the larger sizes combined.

In practice it is impractical to use these large numbers. Instead, a small number of coal particles ranging from several tens to thousands is used in each size range with an appropriately reduced mineral population. Some care is needed in selecting these sizes in order to preserve the statistical significance of the results. Generally smaller numbers are used for the largest coal size ranges and the value is gradually increased as the coal size decreases. Thus the mineral redistribution is actually performed on a scaled set of coal particles for each size range whose number is usually much smaller than the baseline value in order to make the simulation feasible on computers with modest memory and speed capabilities. After the mineral redistribution is performed over the reduced sample for each size range, the ash is produced and analyzed, and the results are rescaled to values representative of the original sample size. The results are judged adequate when they are insensitive to the scaling factors.

When the average number of mineral inclusions of a particular size and type is expected to be large per coal particle the redistribution of mineral particles is handled using Poisson distributions. When the average is small, the mineral redistribution is performed with standard Monte Carlo methods. The rationale for these differences is to reduce the computer memory and time requirements to a reasonable level.

Since the volume fraction of the minerals in coal is small (around 0.1) and since the coal particles are typically much larger than the minerals, the random placement of all of the mineral particles results in a smaller fraction of excluded minerals compared to what is experimentally observed. To remedy this, measured excluded and included mineral size distributions are used when available, and only included minerals are randomly distributed among the coal particles.

8.1.2 Ash Formation Modes

With a complete inventory available for the mineral content of each coal particle in the simulated coal particle size distribution, the composition and size distributions of ash produced during combustion are then predicted in accordance with the char fragmentation and mineral coalescence behavior expected during combustion. Ash particles are produced during combustion by the transformations and interactions

of the mineral inclusions within a coal particle. Organically bound elements are assumed to coalesce with the included ash, with the amount adding to any particular ash particle proportional to the surface area of that particle. Each extraneous mineral particle is assumed to form one ash particle.

There are three principal modes for generating ash distributions: 1) In the "no coalescence" mode, each mineral inclusion is assumed to produce one ash particle. 2) In the "full coalescence" mode, the minerals in each coal particle are assumed to coalesce fully, producing one ash particle per coal particle. 3) In the "char fragmentation" mode, which applies to cenospheric chars, ash particles are formed by the coalescence of inclusions that have high probabilities of encountering each other as the censospheric char shell burns away.

The generation of ash under the "full coalescence" and "no coalescence" modes was addressed by Wilemski et al., (1992). The algorithm discussed here was developed primarily to treat ash formation from cenospheric char particles. However, it is also applicable to non-cenospheric char particles for which it predicts nearly full coalescence. The approach that we have taken is a direct outgrowth of many of the ideas developed by Kang (1991) in his Ph.D thesis. In the following sections we describe the basic ideas underlying the computation of the number and sizes of ash particles released from the char particle. Then we indicate in general terms how the ash release algorithm operates in the present mineral redistribution code. Finally, results are presented for several coals.

8.2 EMAF Modification - Effect of Char Fragmentation

8.2.1 Ash Release from Cenospheric Char Particles

During the pyrolysis and devolatilization of pulverized bituminous coal, many coal particles become plastic and deform into thin-walled cenospheres due to high internal gas pressure. We assume that most of the initial mineral content of each coal particle is retained in or on the cenosphere shell. During the subsequent burnout of the cenospheric char particle, the shell becomes thinner and weaker. Any large pores (blowholes) in the shell will lead to lateral burning of the shell and further weaken it. As the char matrix shrinks, mineral inclusions trapped within are brought into contact. If the inclusions are molten, they may then coalesce. Eventually, the shell either burns out fully or breaks into a number of fragments. Either way, the coalesced mineral inclusions are released, producing ash particles whose size and composition are determined by the mineral inclusions found within localized sections of the shell or in the shell fragments. In our model, we assume complete coalescence for each pair of contacting mineral inclusions. We also account for chemical transformations affecting different minerals when computing the chemical composition of the resulting ash particle.

The mineral redistribution code provides us with a discrete set of coal particles of known mineral content giving us the capability of generating ash particles from each coal particle. In order to determine the number and size of the mineral inclusions that coalesce during burnout we adapt the ideas of Kang (1991) whose approach was analogous to that used to treat molecular collisions in the kinetic theory of gases. The basic idea is that as the cenosphere shell burns and becomes thinner, mineral inclusions at the edges of the shell are brought into contact with other inclusions that become exposed as the char burns away. If we assume that all such contacts result in coalescence, we need only estimate the number of such "collisions" for each mineral inclusion in order to calculate the final size of the ash particle released.

The number of mineral inclusions of diameter D_j contacted by a larger mineral inclusion of diameter D_i can be estimated by computing the volume encompassed by these two inclusions as the shell burns out and multiplying this volume by the number density of minerals of size j in the shell. As sketched

in Figure 8-1, this volume is proportional to the effective "collision cross-section" of the two inclusions times an effective thickness δ_e of the cenosphere. The volume of inclusion i should also be subtracted from the volume swept out because the "collision partners" (the size j inclusions) are excluded from char occupied by the size i inclusion. Similarly, in computing the number density of mineral inclusions of a given size in the cenosphere, the shell volume should be corrected for the volume of all larger mineral inclusions. Smaller mineral inclusions are obviously excluded from the shell volume occupied by the larger minerals, effectively increasing their number density in the remaining carbon matrix.

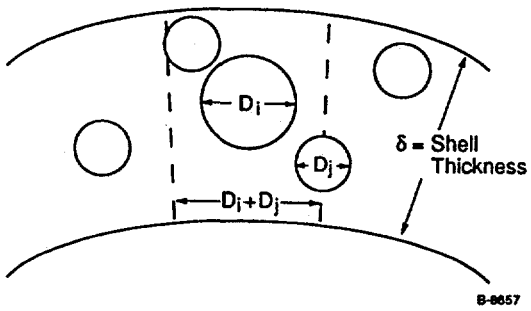

Figure 8-1 Two-dimensional schematic of interaction region swept out by mineral inclusions of diameter D_i and D_j during burnout. Only inclusions whose centers lie within the circular cross section of diameter $D_i + D_j$ will be intercepted by the larger mineral inclusion.

We next consider how to determine the cenosphere shell thickness δ, an important parameter strongly influencing ash formation. We imagine the char particles to be spherical shells with uniform thickness δ as shown in Figure 8-2. The value of δ is found using a volume conservation argument involving the following coal particle properties: initial unswollen volume V, swelling index S, swollen particle diameter D_O, diameter of inner spherical cavity D_I, porosity of the shell ϕ, and the volatile fraction of mineral-free coal matrix f_v. This last parameter is related to the more familiar volatile weight fraction of the coal, f, through the relation $f = f_v(1-\phi_M)$, where ϕ_M is the volume fraction of mineral in the coal. To obtain δ, we first equate the volume of the swollen char particle ($S^3V = \pi D_O^3/6$) to the sum of the mineral volume V_M, the residual "carbon" volume $(V-V_M)(1-f_v)$, the volume of the inner cavity $\pi D_I^3/6$, and the shell

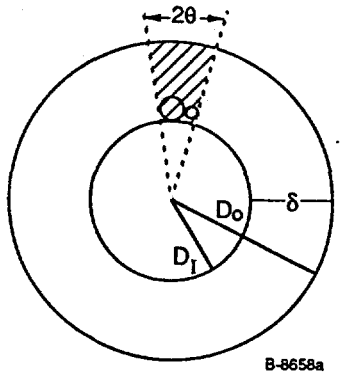

Figure 8-2. Two-dimensional illustration of conical volume swept out by two mineral inclusions due to spherical shape of char particle.

pore volume formed during devolatilization $\phi\pi(D_O^3-D_I^3)/6$. The resulting equation is then solved for the ratio $\gamma=D_I/D_O$ which, in turn, yields δ through the definition, $\delta=D_O(1-\gamma)/2$. The expression for γ is

$$\gamma^3 = 1 - S^{-3}(1 - f_v + f_v V_M/V)/(1-\phi)\,, \tag{8-1}$$

which shows that δ depends most strongly on S, f_v, and ϕ. The behavior of δ predicted by this simple model is discussed later.

The effective length, δ_e is related to δ, the thickness of the cenosphere shell, but its specific value depends on two principal considerations. First, δ_e should reflect the radial dimension of the shell volume containing all of the mineral inclusions destined to end up as a single ash particle. Clearly, δ is an upper bound for this value. A smaller value is possible if the shell contained a sizeable fraction of pores large enough to disengage any ash particle encountering such a pore. Kang (1991) has shown that the separation length can be estimated from the formula

$$L_s = (2/3)D_p(1-\phi_p)/\phi_p\,, \tag{8-2}$$

where D_p is the diameter of the pore encountered by the ash particle and ϕ_p is the porosity associated with those pores. Obviously, in most situations, D_p must exceed the ash particle diameter in order for the ash particle to be released. As discussed later, δ is typically 10 to 30% of D_O, that is, between 1 and 3 μm for the smallest coal particles and between 20 and 60 μm for the largest. Mineral inclusions larger than δ will not undergo coalescence for geometric reasons unless they are captured within the cenosphere interior - a special case. Purely geometric considerations imply that for mineral inclusions occupying a substantial fraction of the shell thickness, for example those with $D_i>\delta/3$, it is unlikely that large pores with $D_p>D_i$ will be found between the mineral inclusion and the shell boundaries often enough to effect significant ash release. Thus, for this case we must have $L_s\approx\delta$. In larger coal particles, smaller mineral inclusions will be captured efficiently by larger mineral inclusions precluding their release by intercepting a smaller pore. Again, we have $L_s\approx\delta$. Finally, if we consider small mineral inclusions (D = 2.5 μm) in small coal particles (D_O = 10 to 20 μm), we find from Eq. (8-2) (with D_p = 2.5 μm and ϕ_p = 0.2) that L_s = 6.7 μm, a value larger or, at best, comparable to δ. Thus we conclude that δ is a suitable initial estimate for the separation length. A second consideration addressed by Kang (1991) concerns the effect of the geometry of the spherical shell on the coalescence process. As burning proceeds, inclusions initially too far apart to coalesce in a linear burning geometry can approach each other as the spherical particle shrinks. Thus additional volume is consumed bringing more mineral inclusions together. The situation is illustrated in Figure 8-2. Kang (1991) estimated a conical correction factor for this effect by taking the shell volume times the ratio of the mineral inclusion cross-sectional area to the total area of the spherical surface at the inner ash separation distance. In this case, that corresponds to the inner surface of the cenosphere.

A more general result can be found by computing the fraction of the total shell volume occupied by the cross-hatched "interaction" region in Figure 8-2. This fraction equals $(1-\cos\theta)/2$ where $\sin\theta = (D_i+D_j)/(D_i+D_j+D_I)$. This result reduces to that obtained by Kang (1991) when $D_I >> (D_i+D_j)$, but in the opposite limit, for very small values of D_I, it yields the volume of the hemisphere for the interaction volume. This implies that two ash particles per coal particle will form in this limit. Thus, in this limit the shell fragmentation model yields results that are very close to the full coalescence limit.

8.2.2 Description of Ash Release Algorithm

To implement the above description of ash release in the engineering model computer code, the following procedure is used. The initial stages of the calculation are carried out using the mineral redistribution code described above. After the mineral inventory of each coal particle is established, the ash release procedure is begun. In the present version of the code, to simplify the bookkeeping involved, coal particles are analyzed in order of largest to smallest, followed by the analysis of all excluded mineral particles. To compute the ash released from a given coal particle, the code first calculates δ and the number densities of the different sized mineral inclusions. The final preliminary step involves calculating the average numbers of various sized mineral inclusions that coalesce into a single ash particle.

The next step determines the fate of all mineral inclusions whose diameter exceeds δ. These are placed into the excluded mineral category on the grounds that they would be released from the char during burnout with little or no coalescence with smaller inclusions. After this step only minerals smaller than δ are left in the shell. These minerals are then combined to form ash particles in a sequential process beginning with the largest mineral inclusions, since these occupy the largest volume of char.

The mineral inclusions of each size to be combined with a given inclusion are selected randomly (averages are used if the numbers are large), and the inventory of mineral sizes and types is adjusted at each step. After the smallest mineral inclusions have been added, organically bound inorganics are added in proportion to the char volume "consumed" in forming this ash particle. The ash particle is then analyzed to determine its size and composition, and the results are stored to await statistical analysis after all ash particles have been treated. When inclusions of a given size are exhausted in the shell, mineral inclusions of the next smaller size are then considered as the seed particles for the accumulation of the remaining smaller mineral inclusions. In this way, a sequence of ash particles of descending size is generated from each coal particle. Figure 8-3 schematically illustrates the ash generation procedure from a cenospheric char particle.

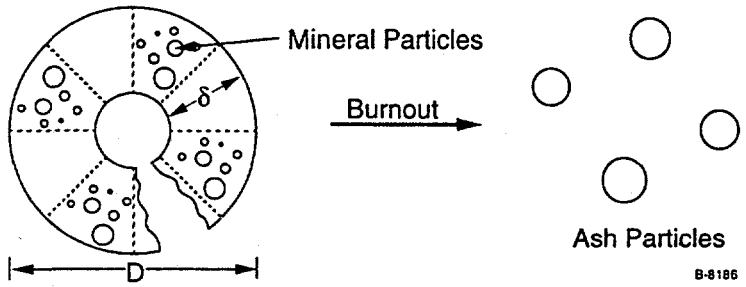

Figure 8-3. Schematic representation of ash particle formation and release from a cenospheric char particle. Minerals within the dashed sectors come into contact and coalesce during burnout. Only four ash particles are shown, although many hundreds may be produced from the larger coal particles.

8.2.3 Model Predictions - Parametric Study and Comparison with Experimental Data

Behavior of Shell Thickness Based Upon Coal Properties

To investigate the dependence of δ predicted by Eq. (8-1) and its influence on the calculated ash size distribution, a number of calculations were performed using the characteristics of a nominal Illinois No. 6 bituminous coal. For baseline properties, we assumed a mineral content of 10 wt%, a shell porosity,

ϕ, of 15%, and a volatile weight percent of 60, which yields $f_v \approx 0.63$ after renormalizing for the mineral volume. Figure 8-4 shows how δ varies with ϕ for four values of the shell porosity. Only for S=1 and as ϕ approaches f_v is the variation significant. In this case, the increasing shell porosity consumes so much of the total particle volume that the inner cavity is forced to shrink substantially to conserve volume. For other values of S, the increased size of the particle permits δ to remain a small fraction of the particle diameter despite the increase in ϕ. Figure 8-5 shows how δ depends on f. The behavior is similar to that in Figure 8-4. For S>1, not much variation is evident. The results for f<0.15 may be unphysical since it is not clear how the excess porosity would be created in such a low volatile coal. For S=1 the sharp transition to a noncenospheric char is seen as f drops just below the value of ϕ. The explanation is the same as that provided for Figure 8-4. A limitation of the model is the independence of the parameters f and ϕ. It is thus possible to specify values ϕ>f such that the physically impossible results $\gamma<0$ and $\delta > D_o/2$ occur. In such a case, the noncenospheric limit is always assumed to hold. Figure 8-6 shows how δ depends on S for four different values of f with ϕ held at 0.15. The most significant influence is seen to occur as S approaches one for the smaller values of f. The approach to the noncenospheric limit is also seen when f=0.15.

Finally in Figure 8-7, the dependence of δ on the unswollen coal particle diameter D is shown. For this plot, the average value of δ was obtained for each 10 μm wide size cut of an ensemble of coal particles whose sizes ranged from 10 to 160 μm and whose fluctuating mineral contents were determined using the mineral distribution model described earlier. For this exercise, no excluded mineral particles were allowed. All of the curves were calculated with the volatile weight fraction f equal to 0.6. The shell porosity was varied from 15 to 65%. Three of the curves were computed with S=1; S=1.1 was used for the remaining curve. From the figure, we see that the two lower porosity, nonswelling cases show little dependence of δ on D. The highest porosity nonswelling case shows the strongest dependence, the thickest shells, and the transition to noncenospheric chars for the larger coal particles. The thicker shells are the result of the large value of the porosity as discussed for Figure 8-4. Since the shells are so thick,

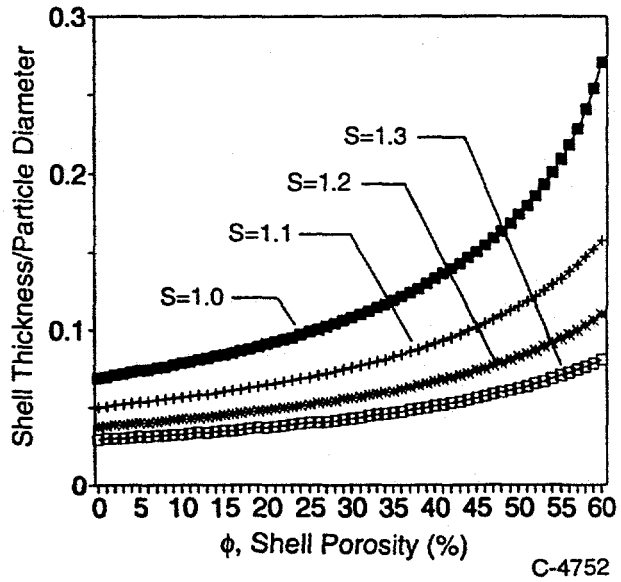

Figure 8-4. Shell thickness vs shell porosity. 60 wt% volatiles, 10 wt% mineral.

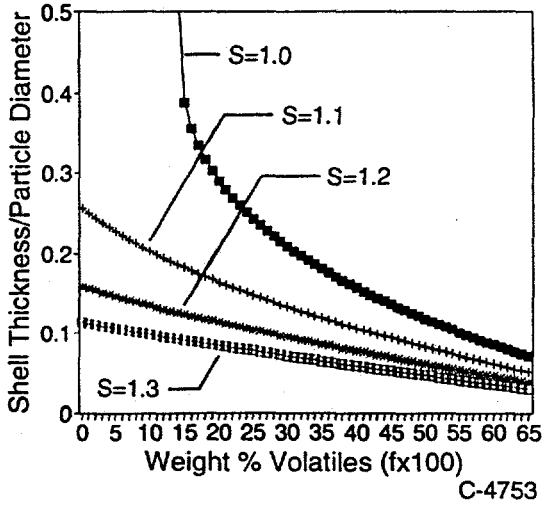

Figure 8-5. Char shell thickness vs volatile wt%. 15% char porosity, 10 wt% mineral.

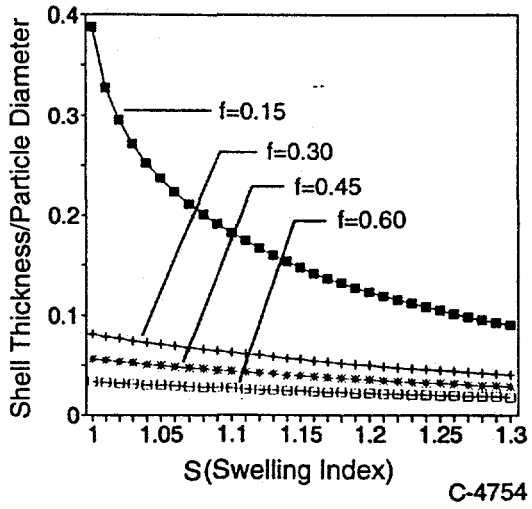

Figure 8-6. Shell thickness vs swelling index. 15% shell porosity, 10 wt% mineral.

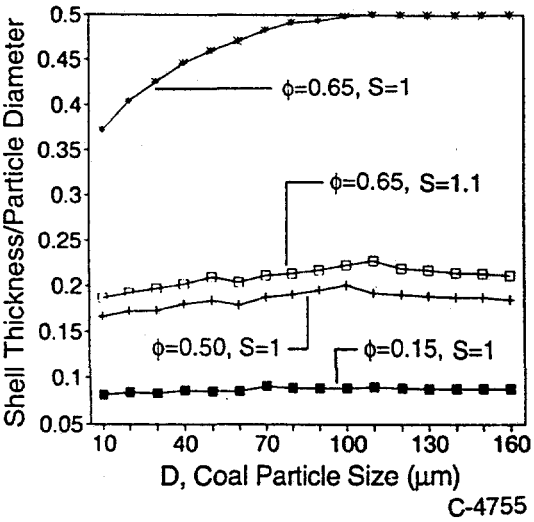

Figure 8-7. Shell thickness vs particle size. 60 wt% volatiles, 10 wt% mineral, ϕ and S are porosity and swelling factor respectively.

the value of δ is more sensitive to the mineral content of the coal particles than is true in the thin shell regime. In this case, with mineral inclusions randomly distributed, the smaller coal particles receive less than the average amount of mineral matter because minerals larger than the coal particle cannot be placed in that size range. Thus as the average mineral content increases with increasing coal particle size, the shell thickens to accommodate the additional volume until it equals the particle radius. The other highest porosity curve shows what happens when the particle is allowed to swell somewhat (S=1.1). In this case, the additional particle volume readily accommodates the added mineral content, and the shell thickness is considerably smaller and shows much less variation with D.

The influence of the shell thickness on ash formation can be inferred from the ash size distributions predicted by the char fragmentation/mineral coalescence model described above. The results are

shown in Figure 8-8 on a cumulative volume percent basis. The upper curve corresponds to the mineral distribution and the no coalescence limit. The lowest curve depicts the full coalescence results. All but one of the remaining curves are for nonswelling (S=1) conditions. Only the highest porosity nonswelling case, for which the thickest shells occurred, is seen to approach the full coalescence results. The remaining cases, including the only swelling high porosity case, all cluster near the no coalescence limit. Some deviation from this limit is seen for the smaller sizes.

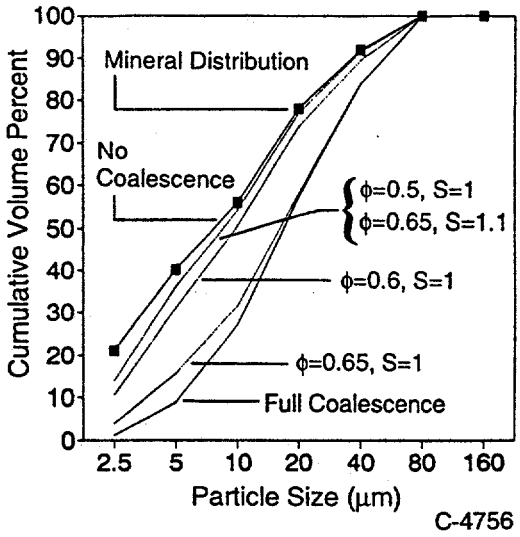

Figure 8-8. Mineral and ash size.

This indicates that some of the smallest mineral particles have coalesced with the largest. The results are very sensitive to small changes in porosity or swelling index for the given value of f. An indication of the degree of coalescence is given in Figure 8-9 which shows the average number of mineral particles used per ash particle as a function of D. For the thin shell cases the number never exceeds five, whereas for the thick shell case the number rapidly grows into the thousands. An indicator of the degree of char fragmentation, inversely related to the Figure 8-9 results, is given in Figure 8-10 where the number of ash particles per coal particle is plotted versus D. Here the thick shell and full coalescence results are indistinguishable along the x-axis. The thin shell chars first start producing substantial numbers of ash particles at about 50 μm. The thin shell results lie closer to the no coalescence results as δ diminishes, but for the cases studied there was always some coalescence evident in the larger coal particles.

Comparison of Predictions with Experimental Data

In order to evaluate the performance of the modified EMAF, several simulations were performed to predict the ash composition and particle size distributions (psd) for specific coals. These predictions were then compared to ash data from droptube experiments or field measurements for these coals. The coals included six bituminous coals, including two non-U.S. coals, a sub-bituminous coal, and a lignite. The results of these simulations are described in this section.

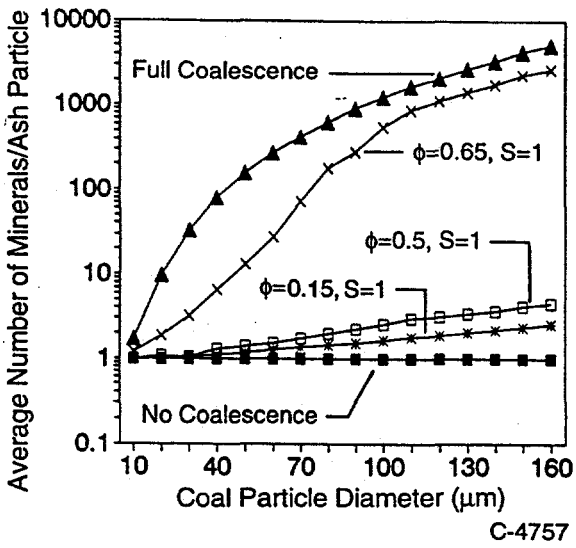

Figure 8-9. Number of minerals per distributions.

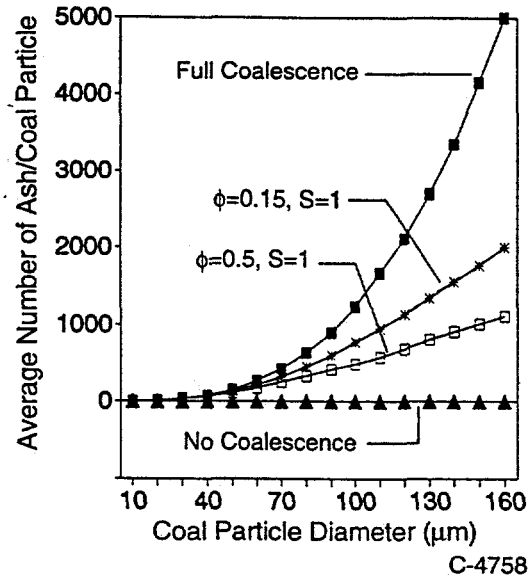

Figure 8-10. Number of ash vs coal particle size. 60 volatile wt%, 10 wt% mineral.

The mineral composition and size distributions, from CCSEM, used as model inputs for each coal were based on more detailed distributions presented elsewhere (Boni et al., 1990). In order to simplify the modelling process, only the major minerals were used as inputs. However, in many cases more minerals were included in these simulations than in previous EMAF simulations (Helble et al., 1993). As the original mineral size distributions (Boni et al., 1990) did not include a category for the unidentified, or mixed species, the size distributions for this category were estimated from the overall mineral size distribution and the distribution of all other species. Other important inputs, such as ASTM ash analysis, were used as originally presented.

For each of the simulations a char combustion pattern was assumed, based on the coal type (see Table 8-1). For example, based on the current knowledge of char formation mechanisms for American coals, the lignite and the sub-bituminous coals were assumed to burn without forming cenospheres (swelling parameters set to 1, no fragmentation allowed). For the first two U.S. bituminous coals both mechanisms were used to explore the behavior of the model. The remaining U.S. bituminous coals were assumed to form cenospheres during devolatilization. Field data on ash particle size and composition distributions for two non-U.S. coals were provided to PSI by the Aerosol Technology Group of VTT Technical Research Center of Finland. As no information regarding the behavior of the two non-U.S. coals was provided to PSI, two calculations were performed with each coal -- first assuming cenosphere formation and later assuming no cenosphere formation. The results for each simulation are discussed below.

Table 8-1 Assumed Burnout Mechanisms for Simulations

Coal	Mechanism
Illinois 6 bituminous	No cenosphere formation Cenosphere formation
Pocahantas bituminous	No cenosphere formation Cenosphere formation
Beulah lignite	No cenosphere formation
Eagle Butte sub-bituminous	No cenosphere formation
Kentucky 11 bituminous	Cenosphere formation
Upper Freeport bituminous	Cenosphere formation
Polish bituminous	No cenosphere formation Cenosphere formation
South African bituminous	No cenosphere formation Cenosphere formation

Illinois No. 6 Bituminous Coal:

Figure 8-11 shows the results for the cleaned Illinois #6 compared with the model predictions for the full (no cenosphere formation/fragmentation) coalescence limit and for extensive char fragmentation. The full coalescence results fail to describe the experimental behavior, whereas the fragmentation results are highly acceptable. The lack of coalescence in the experimental ash is not surprising when we consider that the cleaning process removes about half of the included mineral from the parent coal. Relative abundances of the major ash categories are shown in Figure 8-12. Again, the fragmentation results are in substantially better agreement with the experimental results with the exception of the iron-rich ash particles.

Pocahontas Bituminous Coal:

Results for the Pocahontas coal are compared in Figure 8-13. The experimental ash distribution shows that a high degree of coalescence has occurred. Therefore the model was first run in the full coalescence limit. Surprisingly, the full coalescence limit (Model-1 in Figure 8-13) overpredicts the ash in

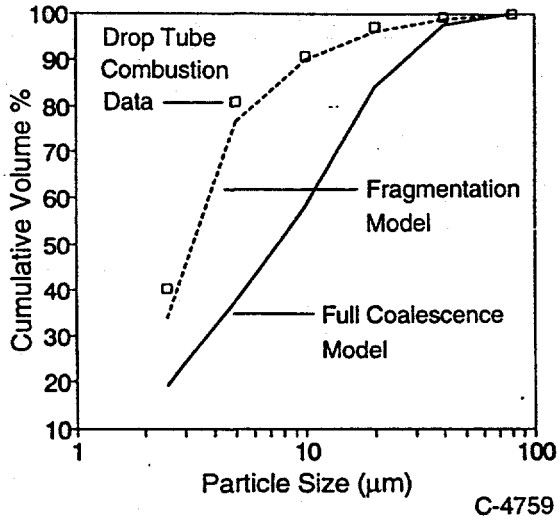

Figure 8-11. Ash size distributions for Illinois No. 6 cleaned coal.

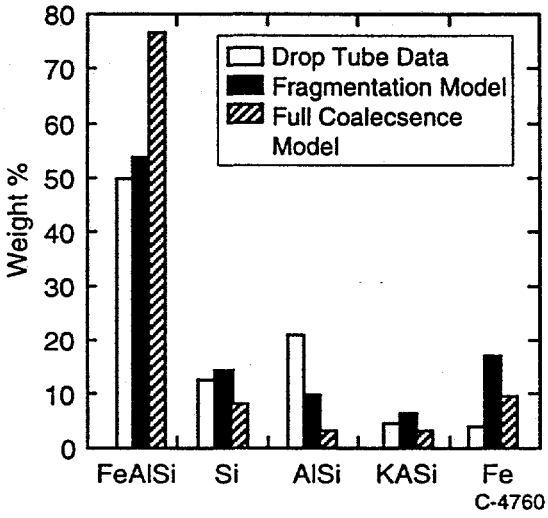

Figure 8-12. Ash composition for Illinois No. 6 cleaned coal.

the two finest size ranges and underpredicts the ash in the largest size range. Since the full coalescence limit predicts the coarsest possible ash distribution for a given mineral distribution, these discrepancies strongly suggest that the assumption of a random mineral distribution may be at fault. In a random distribution, the number of minerals placed in each coal size range is directly proportional to the volume fraction of the coal in that size range. In the Pocahontas coal, 40% of the volume is found in the 10 μm coal particles. Thus, 40% of the 2, 4, and 8 μm mineral particles would be allocated to this coal size. If just 2-μm minerals are considered, and these are uniformly distributed in the bulk coal on a simple cubic lattice, the average interparticle distance would be about 11 μm. This agrees with the result of the random distribution which places about one such small mineral inclusion per 10 μm coal particle. On the other hand, knowing that mineral-rich veins occur in unground coal, we might anticipate on statistical grounds that the small coal particles would be largely mineral free, that significant amounts of extraneous minerals would be produced, and that only the larger coal particles would contain significant numbers of mineral inclusions.

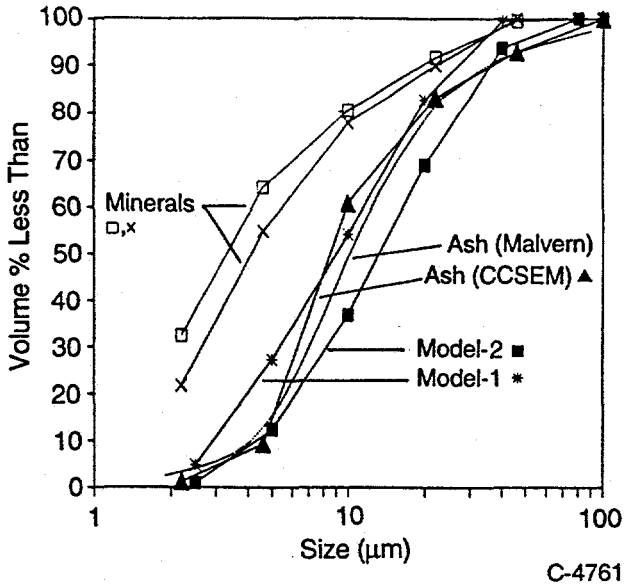

Figure 8-13. Mineral and ash size distributions for Pocahontas coal.

To test the effect of such a nonrandom mineral distribution on the fly ash distribution, we modified the mineral distribution scheme to allocate to the smallest coal size range only a specified fraction of the minerals that would otherwise be randomly placed in it. The nonallocated minerals were proportionately redistributed over the larger coal sizes thus enhancing their share of the mineral loading. Since we had no CCSEM data available regarding the distribution of extraneous minerals, we were forced to rely on simple volume exclusion tests to generate excluded minerals. This procedure results in no excluded 2, 4, or 8 μm minerals which is likely to be incorrect. However, the experimental ash distribution provides an upper bound for the amount of extraneous mineral in these sizes if we assume that all ash of these sizes was formed from extraneous mineral matter. The small amount of ash observed below 5 μm indicates that at least the 2 and 4 μm minerals were mainly included within carbonaceous coal particles. When the modified mineral distribution procedure was used with the 10 μm coal particles receiving only 5% of the random mineral allotment, the full coalescence results (not shown) now underpredicted the ash in the three smallest size ranges as well as in the largest size. This seemed to indicate that a small degree of char fragmentation could be responsible for the finer ash. We thus ran the model in the fragmentation mode (Model-2 in Figure 8-13) with parameters chosen to produce very thick shells: δ/D ranged from 0.4 to 0.49 as D varied from 10 to 130 μm. With these parameters the model generated 3 to 4 ash particles per coal particle from the larger (90 to 130 μm) coal particles and 5 or 6 ash particles for each smaller coal particle (20 to 80 μm). Only one out of ten of the mineral-deficient 10 μm coal particles produced an ash particle. The resulting ash size distribution is seen in the figure to be quite accurate for the largest and two smallest size ranges; the intermediate size ranges are either under- or overpredicted significantly.

Beulah Lignite Coal

In previous model evaluations (Helble et al., 1993), EMAF was used to simulate the behavior of primarily bituminous coals during combustion, with only one lignite tested. In order to test the applicability of the model for a wider range of coals, simulations were performed for a North Dakota lignite (Beulah). The mineral composition and size distributions for this coal can be seen in Tables 8-2 and 8-3. Kaolinite and pyrite represent 33.0% and 28.6% of the mineral mass, respectively. The unidentified, or mixed, species represent 14.3% (silicates) and 11.0% (other minor minerals). Most of the silicate species were very finely divided, while pyrite consisted of fairly large particles.

Table 8-2. Mineral Species Composition: Beulah Lignite

Mineral Species	Wt%	Elemental Composition (mole%)										
		Na	Mg	Al	Si	S	Cl	P	K	Ca	Ti	Fe
Quartz	13.2				97	1				1	1	
Kaolinite	33.0			42	52	2	1		1	1	1	1
Misc. silicates	14.3			30	57	3	1		2	3	2	2
Pyrite	28.6		1		1	66					2	31
Misc. mixed	11.0	2	4	12	15	24	4	2	3	20	15	6

Table 8-3. Mineral Size Distribution (μm) for Beulah Lignite.

Mineral	<2.5 (wt%)	2.5-5 (wt%)	5-10 (wt%)	10-20 (wt%)	20-40 (wt%)	>40 (wt%)
Quartz	11	11	17	23	19	18
Kaolinite	42	7	9	13	12	17
Mix. silicates	73	6	7	7	7	0
Pyrite	1	1	3	12	26	56
Misc. Mixed*	16	13	8	11	12	40
Total	27	7	8	13	16	30
*Estimated from other minerals and total mineral distribution.						

For these simulations the coal was assumed to devolatilize without forming cenospheres. Figure 8-14 shows a comparison between the ash particle size distribution (psd) from PSI droptube experiments and the predicted ash psd for two simulations. In the full coalescence case all of the minerals are assumed to coalesce (1 ash particle produced per coal particle or excluded mineral). In the partial coalescence case

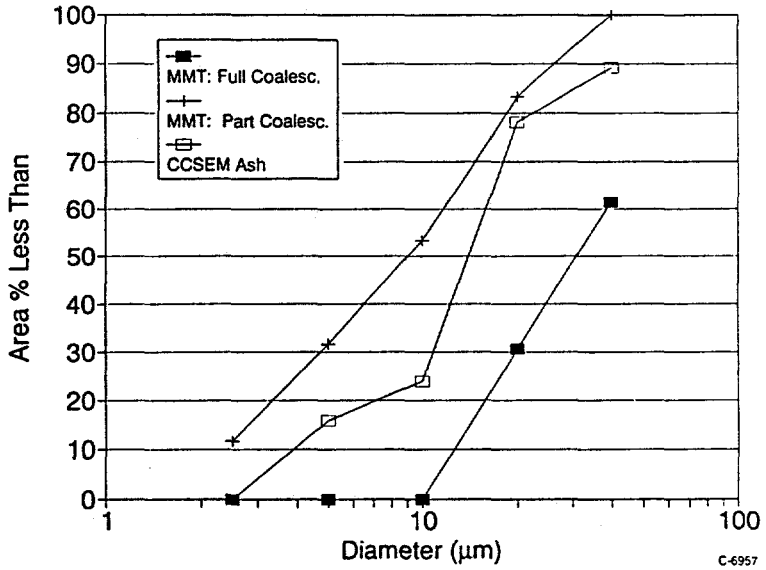

Figure 8-14. Ash psd: model versus data -- Beulah lignite - no cenospheres.

quartz and kaolinite do not melt or coalesce. For the full coalescence simulation all of the resulting ash particles were greater than 10 μm. The partial coalescence simulation resulted in a much finer ash distribution due to the formation of one ash particle for each quartz and kaolinite particle. The measured ash psd was bounded by the two simulations. This suggests that full coalescence does not take place, perhaps due to minerals not melting. Char fragmentation is another, although less likely (Helble et al., 1993), possibility.

Figure 8-15 presents a comparison between the predicted and measured ash compositions. In both the model and the CCSEM analysis each ash type is categorized based on the three highest elemental concentrations. In addition, the concentration bounds are placed so that if only one or two elements dominate (eg; there is no second element greater than 10% or third element greater than 6%), a second (or third) element is not selected. For example, a quartz particle would contain primarily Si (oxygen-free basis) and would be categorized as "Si".

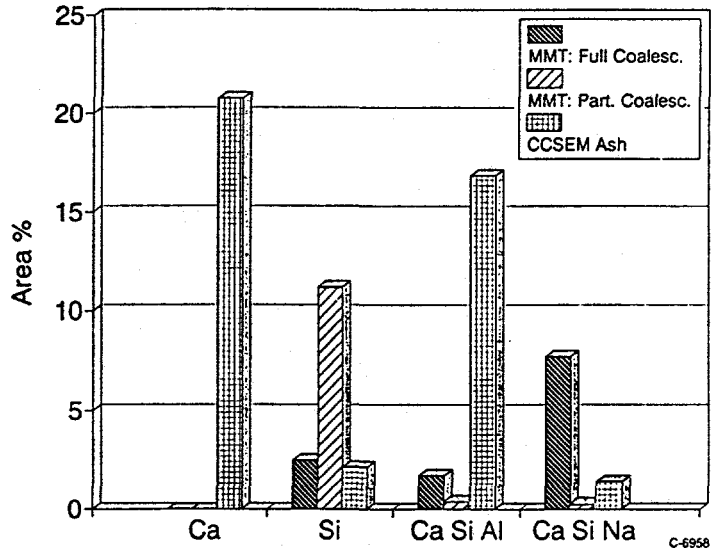

Figure 8-15. Ash composition: model versus data -- Beulah lignite - no cenospheres.

The predicted and measured category compositions for the Beulah Lignite can be seen in Table 8-4. Most of the categories compare reasonably well between the measured and predicted values. However there were no "Ca" particles in the predictions. In addition, the measured composition of the "Ca Si Al" category is enriched in Ca as compared to the predictions. Both of these points are discussed in more detail below.

The area percent (from CCSEM) of all particles in each composition category is shown in Figure 8-15. For example, the Si category represents the area percent of all particles that contain primarily silicon (probably quartz). As seen in Figure 8-15, the EMAF full coalescence predictions agree reasonably well with the measurements for this category. Due to the assumption that quartz does not coalesce in the partial coalescence simulation, the amount of ash in the Si category is overpredicted in this case. For the Ca and Ca-Si-Al categories the model predicts values much lower than measured. The Ca-Si-Na category is bounded by the two model predictions.

Table 8-4. Average Category Compositions for EMAF Predictions and Data: (Beulah Lignite - No Cenosphere Formation)

	Category	Na	Mg	Al	Si	K	Ca	Ti	Fe	Other
EMAF	Ca*				74.0					
(Full)	Si	0.7	0.6	0.7	23.2		2.6	1.0	0.2	
	Ca Si Al	12.7	10.8	16.1	22.4	0.8	30.3	2.6	3.4	0.1
	Ca Si Na	15.9	13.2	7.7		0.4	36.0	1.5	2.8	0.1
EMAF	Ca*									
(Partial)	Si				98.0		1.0	1.0		
	Ca Si Al	12.2	10.3	14.6	26.8	1.3	29.9	2.8	2.0	0.1
	Ca Si Na	16.0	13.4	10.1	18.6	0.9	37.3	2.0	1.8	
CCSEM	Ca	1.0	4.0	2.0	4.0		82.0	2.0	3.0	2.0
	Si	3.0		1.0	92.0		2.0	1.0		1.0
	Ca Si Al	4.0	3.0	15.0	21.0		52.0	2.0	2.0	
	Ca Si Na	16.0	4.0	12.0	24.0		39.0	1.0	3.0	

*no particles found

Some of the differences between the predicted and measured ash composition can be attributed, in part, to the CCSEM analysis of the ash. Because CCSEM is primarily a *surface* analysis technique, rather than a bulk technique, compositions reported by CCSEM are strongly affected by species present on the surface, but in lower concentrations in the bulk (surface enriched). The EMAF, however, predicts the *bulk* particle compositions. Therefore, direct comparison of the two results may be misleading for those coals with significant surface enrichment. For example, the simulations discussed above predicted a much lower calcium concentration in the ash (the Ca category) than was reported by CCSEM. This may be due to the high fraction of organically bound calcium - leading to significant surface enrichment of this species. Therefore, in this case, the model predictions may represent a more realistic measure of the bulk ash composition than do CCSEM surface measurements. Sectioned CCSEM - analysis of the particle cross-sections - could be used to provide a better comparison with the bulk ash composition provided by EMAF.

Eagle Butte -- Sub-bituminous Coal

Another test of the model's flexibility was the simulation with the Eagle Butte sub-bituminous coal. The mineralogy for this coal is dominated by quartz (see Tables 8-5 and 8-6). This mineral represents 41.7% of all minerals. Silicate species (including quartz) represent approximately 70% of the mineral matter. Unidentified and mixed species represent 29% of the minerals. These minerals were fairly evenly distributed throughout the measured size ranges (Table 8-5).

The simulations for this coal also were based on the assumption that no char cenospheres form during devolatilization as shown in earlier work (Helble et al., 1993). The predicted and measured ash psd can be seen in Figure 8-16. As can be seen from this figure, the measured ash psd is again bounded by the two simulations. These simulations again represent coalescence of all minerals and coalescence of selected minerals, as in the previous simulation. However, for these simulations it was assumed that siderite, calcite, and kaolinite did not coalesce (calcite and siderite were not present in the previous coal). The quartz in this coal contained significant impurities, lowering the melting point. Therefore the quartz was allowed to coalesce for this coal but not for the previous coal. Again the full coalescence simulation

Table 8-5. Mineral Species Composition. Eagle Butte Sub-bituminous

Mineral Species	Wt%	Elemental Composition (mole%)										
		Na	Mg	Al	Si	S	Cl	P	K	Ca	Ti	Fe
Quartz	41.7			1	96				1	1	1	1
Kaolinite	13.5	1		41	52	1	1		1	2	2	1
Illite	2.1			28	53	1	2		10	3	2	2
Misc. silicates	13.5	1	2	20	50	2	2		3	6	2	4
Pyrite	4.2			1		60				2		36
Fe-rich (siderite)	4.2			1	3	2		2	1	4	2	85
Ca-rich (calcite)	3.1	1		1	3	4	1	1	3	84	1	5
Misc. mixed	15.6	1	2	22	15	8	4		4	28	8	4

Table 8-6. Mineral Size Distribution for Eagle Butte Sub-bituminous

Mineral	<2.5 μm (wt%)	2.5-5 μm (wt%)	5-10 μm (wt%)	10-20 μm (wt%)	20-40 μm (wt%)	>40 μm (wt%)
Quartz	21	10	20	17	20	12
Kaolinite	9	10	31	17	22	11
Mix. silicates	37	16	18	8	5	16
Pyrite	9	7	22	30	28	3
Misc. Mixed*	26	10	18	12	11	22
Total	100	23	21	15	16	15

*Estimated from other minerals and total mineral distribution, siderite, calcite, and montmorillite assumed to have same distribution.

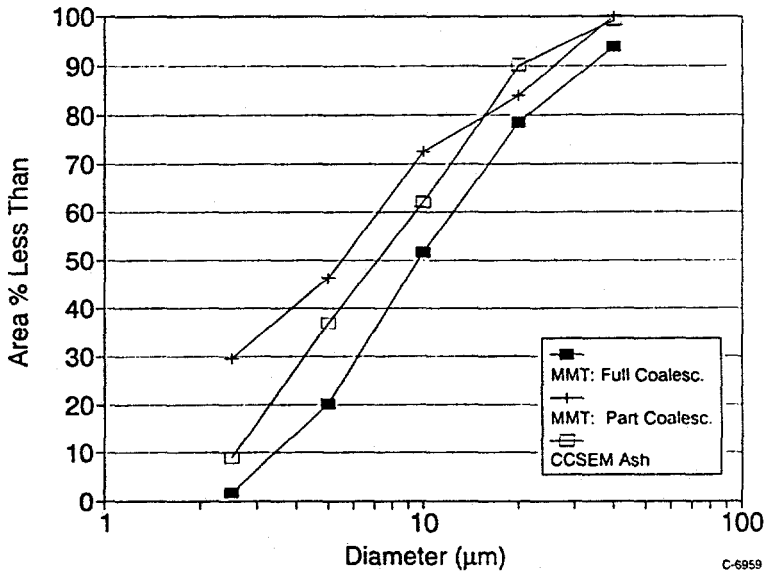

Figure 8-16. Ash psd: model versus data -- Eagle Butte - no cenospheres.

results in a coarser distribution than was reported by CCSEM. The partial coalescence case resulted in a finer distribution but contained more particles in the larger size ranges than was measured.

A comparison of the predicted and measured ash composition is shown in Figure 8-17 The EMAF overpredicts the amount of ash in the Si and Si Al Ca categories, while underpredicting the the Ca and Ca Al Si category. The average category compositions for the Eagle Butte (Table 8-7) agree reasonably well between the measured and predicted values, with the exception of the "Ca Al Si" category. The measured composition for this category is also enriched in Ca as compared to the predicted, suggesting that the surface bias may have caused a slight discrepancy for this coal as well.

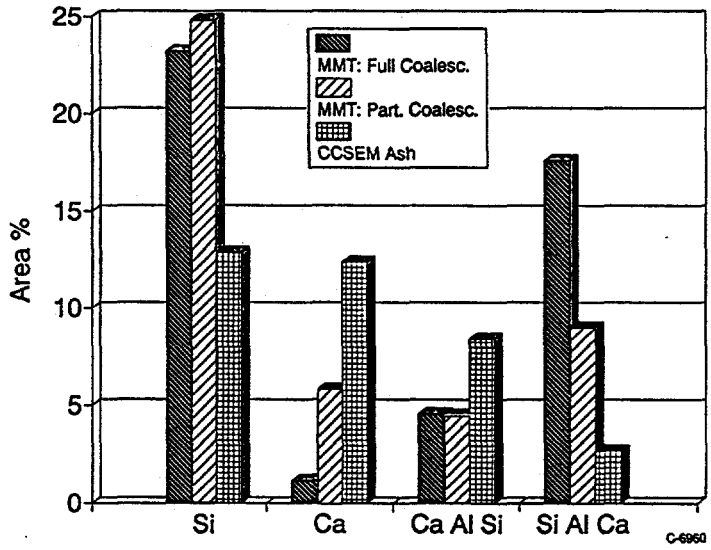

Figure 8-17. Ash composition: model versus data -- Eagle Butte - no cenospheres.

Table 8-7. Average Category Compositions for EMAF Predictions and Data: (Eagle Butte - No Cenosphere Formation)

	Category	Na	Mg	Al	Si	K	Ca	Ti	Fe	Other
EMAF (Full)	Si	0.5	0.6	2.5	89.1	1.1	2.9	1.1	2.1	0.1
	Ca	1.2	0.2	1.7	4.7	3.0	82.8	1.1	5.3	
	Ca Al Si	1.6	2.7	25.1	18.9	4.5	32.8	8.9	5.4	0.1
	Si Al Ca	2.2	2.7	22.4	52.4	2.4	10.8	2.3	4.8	
EMAF (Partial)	Si	0.8	1.0	2.1	89.2	1.1	3.1	1.1	1.5	0.1
	Ca	1.0		1.0	3.1	3.1	85.7	1.0	5.1	
	Ca Al Si	1.9	3.1	25.1	18.8	4.6	32.8	9.0	4.8	
	Si Al Ca	2.1	3.2	19.8	55.4	3.3	9.6	2.4	4.2	
CCSEM	Si				97.0		2.0			1.0
	Ca		5.	6.0	3.0		81.0		4.0	1.0
	Ca Al Si		2.0	20.0	12.0		60.0	1.0	4.0	1.0
	Si Al Ca	1.0		30.0	48.0	2.0	17.0	1.0	1.0	

Kentucky No. 11 Bituminous Coal

As part of an evaluation of the initial version of EMAF (Helble et al., 1992) simulations were performed using this coal. Therefore, the Kentucky No. 11 and the Upper Freeport coal were also included in this evaluation. Pyrite represents a large fraction of the mineral matter in the Kentucky No. 11 (Table 8-8). The pyrite is evenly distributed in the individual size ranges (Table 8-9), but there is a large fraction in the larger (>20μm) size ranges. Illite and the miscellaneous silicate categories represent a significant fraction of the silicate species.

Table 8-8. Mineral Species Composition: Kentucky No. 11 Bituminus

Mineral Species	Wt%	Elemental Composition (mole%)										
		Na	Mg	Al	Si	S	Cl	P	K	Ca	Ti	Fe
Quartz	20.0			3	94				1		1	
Kaolinite	9.0			40	51	3			2	2	2	2
Illite	17.0			28	54	3			10	1	2	4
Misc. silicates	25.0			21	61	2			11	2	2	4
Pyrite Fe-rich (siderite) Ca-rich (calcite)	26.0			2	3	63			1		1	33
Misc. mixed	3.0			11	30	11	4	3	6	14	17	6

Table 8-9. Mineral Size Distribution for Kentucky No. 11 Bituminous

Mineral	<2.5 μm (wt%)	2.5-5 μm (wt%)	5-10 μm (wt%)	10-20 μm (wt%)	20-40 μm (wt%)	>40 μm (wt%)
Quartz	19	25	23	16	12	5
Kaolinite	33	16	28	12	6	4
Illite	34	24	21	8	9	4
Mix. silicates	26	14	20	15	14	11
Pyrite	10	9	14	14	21	33
Misc. Mixed*	35	0	0	8	23	0
Total	24	15	18	13	15	16
*Estimated from other minerals and total mineral distribution.						

The EMAF simulations assumed that all coal particles greater than 10 μm formed cenospheres during devolatilization, as shown in earlier work with a similar coal (Helble et al., 1993). In the simulations with the unmodified version of EMAF, the model overpredicted the amount of fine ash and overpredicted the amount of very large particles. In the simulations discussed here, Figure 8-18, this pattern was repeated but to a lesser degree.

The ash composition predictions, Figure 8-19, were also similar to those of the earlier simulations. The model overpredicted the interaction between iron and illite, overpredicting the Si-Al-Fe category and underpredicting the Si-Al-K category. The Si and Si-Al categories are in reasonable agreement. The category compositions (not shown) are also in good agreement.

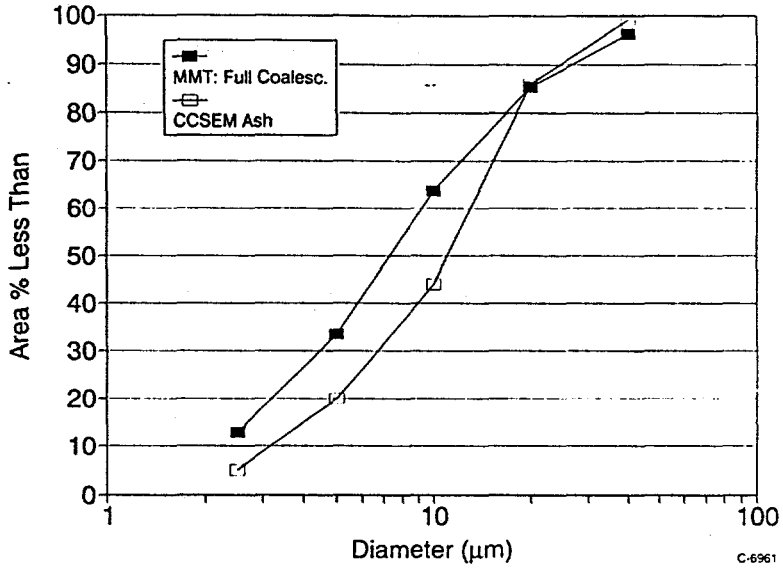

Figure 8-18. Ash psd: model versus data -- Kentucky No. 11 - cenospheres.

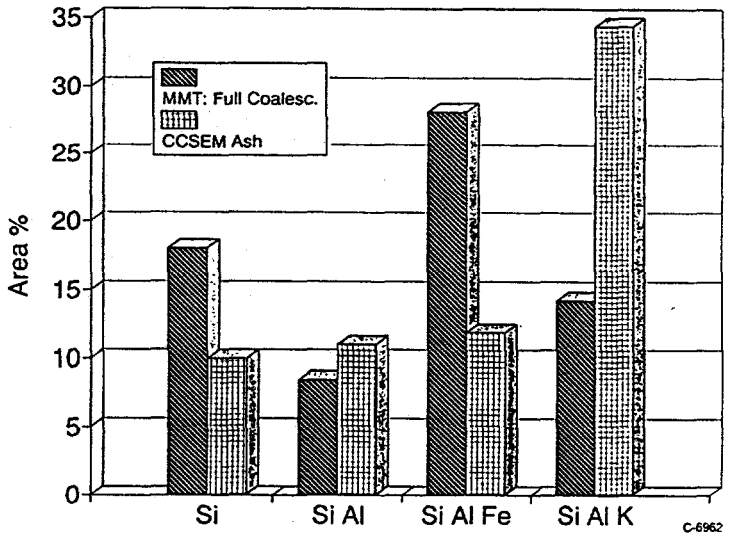

Figure 8-19. Ash composition: model versus data -- Kentucky No. 11 - cenospheres.

It is somewhat unusual to have the ash composition comparisons suggest that the model overpredicts the amount of ash coalescence, but the model also overpredicts the amount of ash in the small sizes. This combination suggests that random placement of the small minerals may be inaccurate, or the coal psd may have been incorrectly measured (Helble et al., 1992).

Upper Freeport -- Bituminous Coal

The Upper Freeport coal was also included in this study to compare the effects of the previously described modifications to EMAF. The mineral matter composition and psd for this coal can be seen in Tables 8-10 and 8-11. Similar to the previous coal, Si-Al-K species (illite and miscellaneous silicate)

Table 8-10. Mineral Species Composition: Upper Freeport Bituminous

Mineral Species	Wt%	Elemental Composition (mole%)										
		Na	Mg	Al	Si	S	Cl	P	K	Ca	Ti	Fe
Quartz	10.5			2	93				1	1	1	1
Kaolinite	7.4	1	1	38	49	2	3		2	2	1	1
Illite	36.8	1	1	28	51	1	2		12	2	2	3
Misc. silicates	20.0	1	1	20	57	2	1		7	1	2	10
Pyrite	18.9		1	2	4	59				1	1	33
Misc. mixed	6.3	1	3	13	30	12	8	2	9	7	10	10

Table 8-11. Mineral Size Distribution for Upper Freeport

Mineral	<2.5 μm (wt%)	2.5-5 μm (wt%)	5-10 μm (wt%)	10-20 μm (wt%)	20-40 μm (wt%)	>40 μm (wt%)
Quartz	8	14	26	20	26	6
Kaolinite	15	9	15	25	19	16
Illite	10	10	13	11	12	44
Mix. silicates	12	16	15	21	12	23
Pyrite	4	2	13	13	14	54
Misc. Mixed*	6	10	16	11	11	46
Total	9	10	15	15	14	36
*Estimated from other minerals and total mineral distribution.						

comprise a significant fraction of the mineral matter. Other major minerals include pyrite, quartz, and kaolinite. Unidentified, mixed, species comprise 6% of the minerals. In general the minerals in this coal are evenly distributed throughout the size ranges, although pyrite, illite, and miscellaneous mixed occur primarily in the largest size range (>40 μm).

The Upper Freeport was also simulated assuming all coal particles greater than 10 μm form cenospheres during devolatilization. Figure 8-20 shows a comparison between the model predictions and the measured ash psd. In the previous simulations the unmodified EMAF predicted the <10-μm psd reasonably well. However, above this size the model underpredicted the intermediate size range. In the simulation with the modified EMAF, the model almost exactly predicted the ash psd. Most of the ash composition categories (Figure 8-21) also agree with the measurements for this coal. Only the Si-Al and Si-Al-Fe are underpredicted by the model. The category compositions (not shown) are also in good agreement.

Polish Bituminous Coal

In order to further test EMAF for non-American coals, simulations were made for a Polish bituminous coal. The mineral composition and size distribution for this coal can be seen in Tables 8-12 and 8-13. Major silicate minerals include quartz, illite, and mixtures of other silicates (miscellaneous silicate). Carbonates, including calcite, represent approximately 9% of the mineral matter. Other species, including unidentified phases, comprise 12% of the minerals.

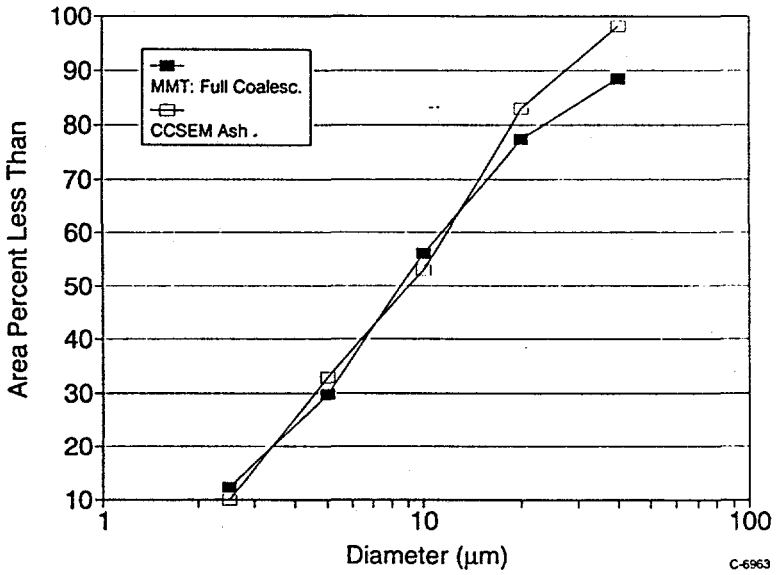

Figure 8-20. Ash psd: model versus data -- Upper Freeport -- cenospheres.

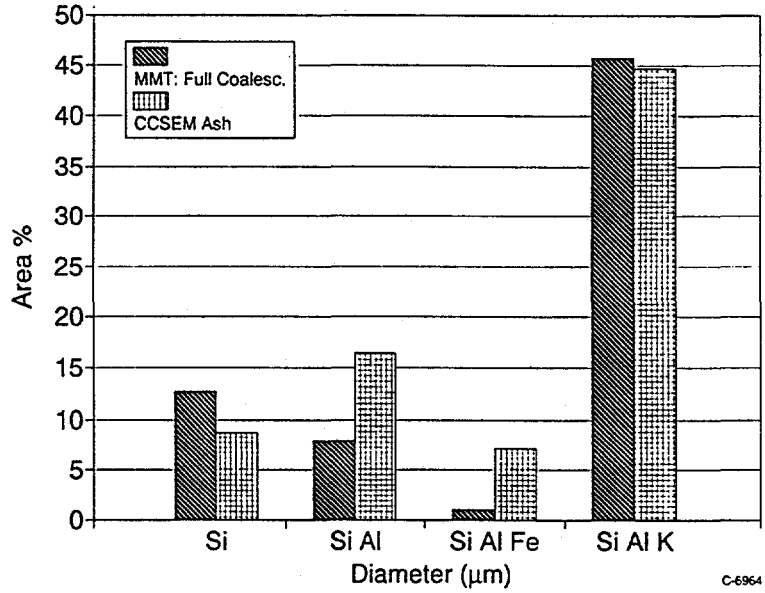

Figure 8-21. Ash composition: model versus data -- Upper Freeport -- cenospheres.

Table 8-12. Mineral Species Composition: Polish Bituminous

Mineral Species	Wt%	Elemental Composition (mole%)										
		Na	Mg	Al	Si	S	Cl	P	K	Ca	Ti	Fe
Quartz	10.0				99				1			
Illite	32.0			26	56	2			12	1	1	2
Misc. silicates	27.0			20	59	2			11		2	4
Pyrite	7.0			1		65						34
Fe-rich (siderite)	3.0			2	2					2		94
Ca-rich (calcite)	2.0		1							96		3
Mixed carbonates	7.0		1		1	1		1		79		17
Misc. mixed	12.0			20	34	11	1	6	7	19	4	8

Table 8-13. Mineral Size Distribution for Polish Bituminous

Mineral	<2.5 μm (wt%)	2.5-5 μm (wt%)	5-10 μm (wt%)	10-20 μm (wt%)	20-40 μm (wt%)	>40 μm (wt%)
Quartz	12	25	16	17	6	24
Illite	19	26	19	24	6	6
Mix. silicates	24	24	24	13	7	9
Pyrite	16	47	6	8	1	14
Siderite	17	25	7	11	18	22
Calcite	15	52	4	4	11	13
Mixed carbonates	12	8	17	40	9	14
Misc. Mixed*	15	39	6	7	12	15
Total						

*Estimated from other minerals and total mineral distribution.

As previously discussed, no information was given to PSI regarding the behavior of this coal during devolatilization. Therefore, simulations were performed assuming cenospheres formed, and assuming no cenospheres formed. In the initial simulations (Figures 8-22 and 8-23), it was assumed that the coal did not swell during devolatilization. The mineral coalescence was divided into three different categories: full coalescence (all minerals coalesce), partial coalescence (selected minerals do not coalesce), and 1-ash per mineral (no minerals coalesce). The minerals not allowed to coalesce under the partial coalescence category, quartz and mixed carbonates, were selected based on the mineral composition and their known behavior in combustion systems. For example, pure quartz has a very high melting point and therefore would not likely form viscous melts to coalesce with other minerals. Illite, with a lower melting point, would be more likely to melt and coalesce.

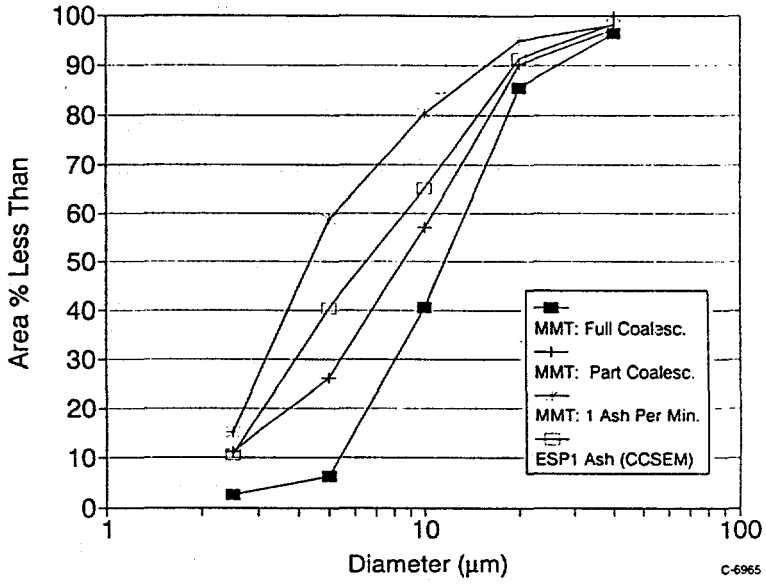

Figure 8-22. Ash psd: model versus field data -- Polish bituminous -- no cenospheres.

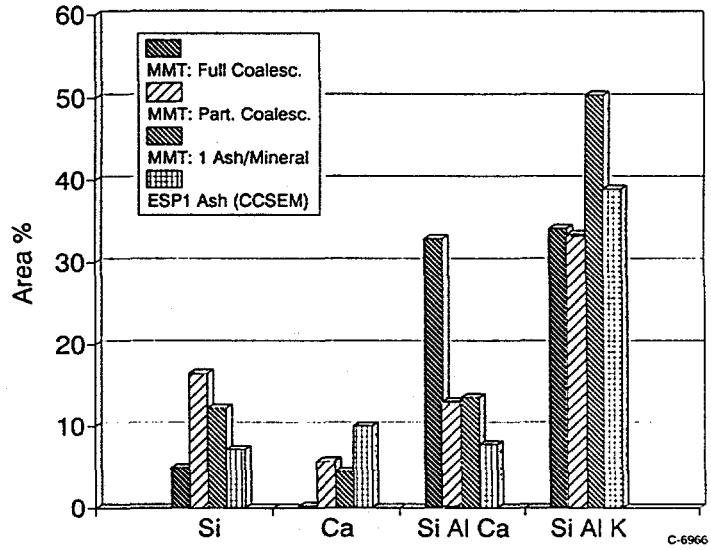

Figure 8-23. Ash composition: model versus field data -- Polish bituminous -- no cenospheres.

As seen in Figure 8-22, the EMAF predictions for full coalescence and 1-ash per mineral bound the psd from the first electrostatic precipitator (ESP1, assumed to contain most of the ash mass). The partial coalescence prediction agreed fairly well with the measured ash psd. The predicted ash composition for partial coalescence, Figure 8-23, also agreed fairly well with VTT's measurements.

A second set of simulations was performed assuming the Polish bituminous coal reacted similarly to typical American bituminous coals. For this set of simulations, the coal was assumed to swell and form cenospheres during devolatilization. Only the full coalescence and partial coalescence categories described above were included.

Predictions from the second set of simulations can be seen in Figures 8-24 and 8-25. The agreement between predicted and measured ash composition and psd is better than the previous case. The pure calcium fraction is again underpredicted in all model simulations. The opposite is true for the Si-Al-Ca category. This discrepancy is likely due to calcium enrichment on the surface of larger particles.

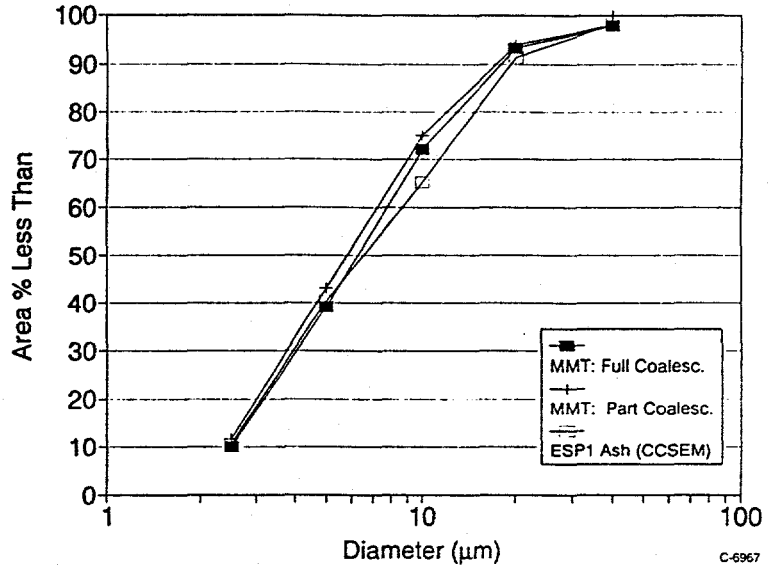

Figure 8-24. Ash psd: model versus field data -- Polish bituminous -- cenospheres.

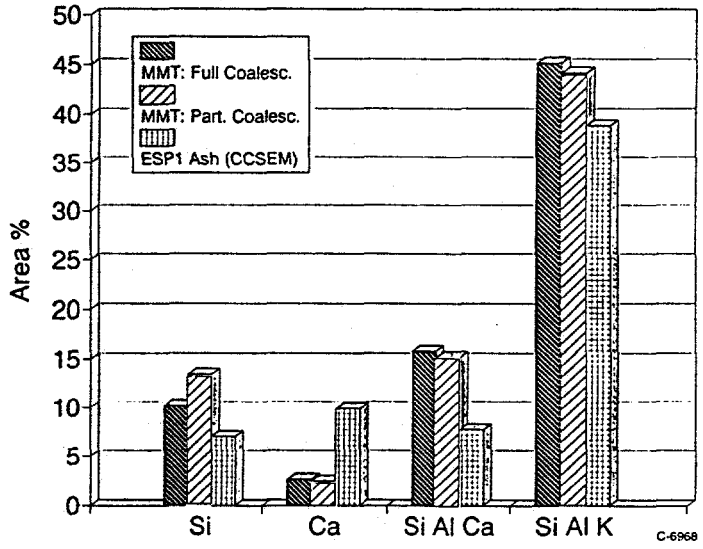

Figure 8-25. Ash composition: model versus field data -- Polish bituminous -- cenospheres.

South African Bituminous Coal

The mineral size and composition information for the South African bituminous coal can be seen in Tables 8-14 and 8-15. This coal contained a large amount of kaolinite, representing almost all of the silicates. Other important minerals included quartz, illite, calcite, and pyrite. Approximately 7.4% of the minerals consisted of minor minerals.

Table 8-14. Mineral Species Composition: South African Bituminous

Mineral Species	Wt%	Elemental Composition (mole%)											
		Na	Mg	Al	Si	S	Cl	P	K	Ca	Ti	Fe	Ba
Quartz	7.3			1	93	1					4	1	1
Kaolinite	61.5			43	51	1	1		1	1	1	1	
Illite	3.2	1	1	35	48	2	1	1	8	1	1	1	1
Misc. silicates	6.7			32	53	2	1	1	2	4	2	4	
Pyrite	3.3			1	1	69					1	28	
Ca-rich (calcite)	7.4		9	1	2	4	1	1	1	79	1	1	1
Misc. mixed	7.4		4	21	27	5	2	5	2	19	4	7	4

Table 8-15. Mineral Size Distribution (μm) for South African Bituminous

Mineral	<2.5 μm (wt%)	2.5-5 μm (wt%)	5-10 μm (wt%)	10-20 μm (wt%)	20-40 μm (wt%)	>40 μm (wt%)
Quartz	18	35	14	14	6	13
Kaolinite	17	49	17	13	4	0
Illite	30	60	9	1	0	0
Mix. silicates	37	16	18	8	5	16
Pyrite	15	38	19	17	6	5
Calcite	15	30	16	16	11	12
Misc. Mixed*	35	44	7	10	4	0
Total						

*Estimated from other minerals and total mineral distribution.

The initial simulations were similar to those for the Polish bituminous coal. For the partial coalescence category, kaolinite and calcite were not allowed to coalesce. In this coal, the quartz contained significant amounts of impurities (Table 8-14) causing the mineral to melt at a much lower temperature. Therefore, quartz was allowed to coalesce for this coal, unlike the simulations with the Polish coal.

The ash psd predictions can be seen in Figure 8-26. The EMAF predicted distributions agreed reasonably well with the measured (from the first ESP) distribution. Again, the measured psd was bounded by the two model extremes. The partial coalescence case best agreed with the data. For the ash composition predictions (Figure 8-27), the ash was dominated by the Si-Al category, arising from the extremely high kaolinite content. The partial coalescence case best predicted the amount measured in this category, and in the Si category.

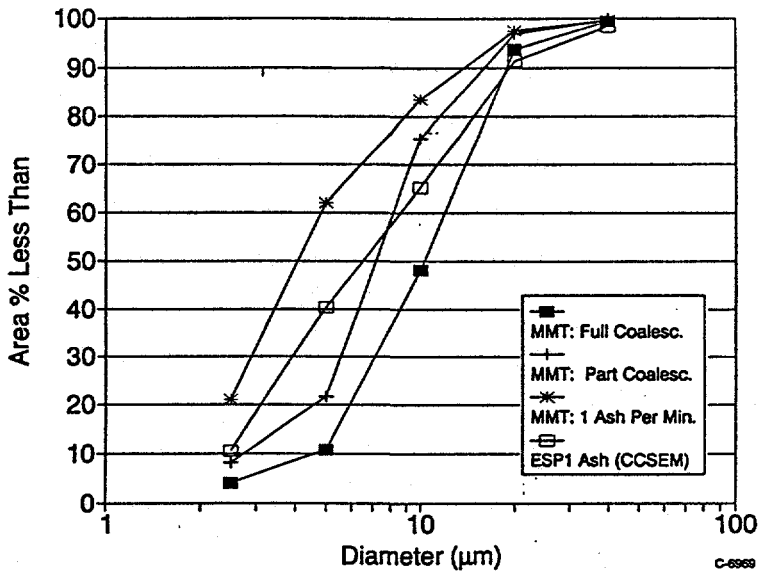

Figure 8-26. Ash psd: model versus field data -- South African bituminous -- no cenospheres.

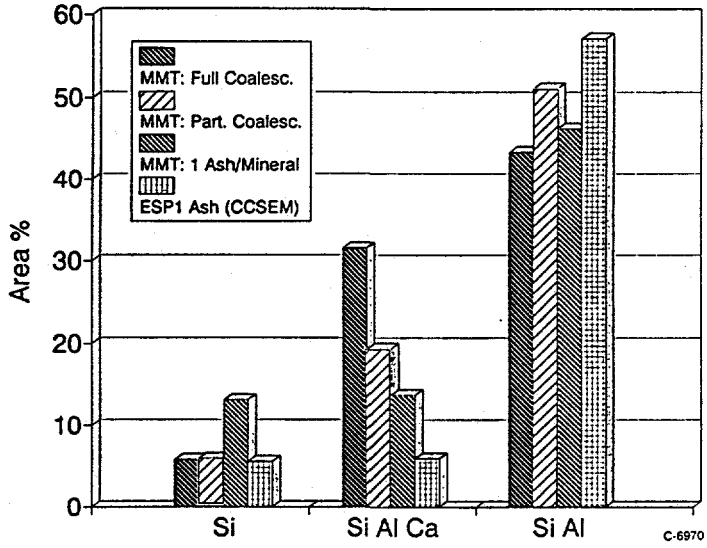

Figure 8-27. Ash composition: model versus field data -- South African bituminous -- no cenospheres.

Figures 8-28 and 8-29 show the results of the second set of simulations, assuming cenosphere formation during devolatilization. The predicted ash psd agreed reasonably well with the field data, as did the composition predictions. As mentioned previously, the over-prediction of the Si-Al-Ca phase is likely due to calcium surface enrichment. In general, the agreement between prediction and data was better assuming cenosphere formation, than for the previous case (no cenosphere formation).

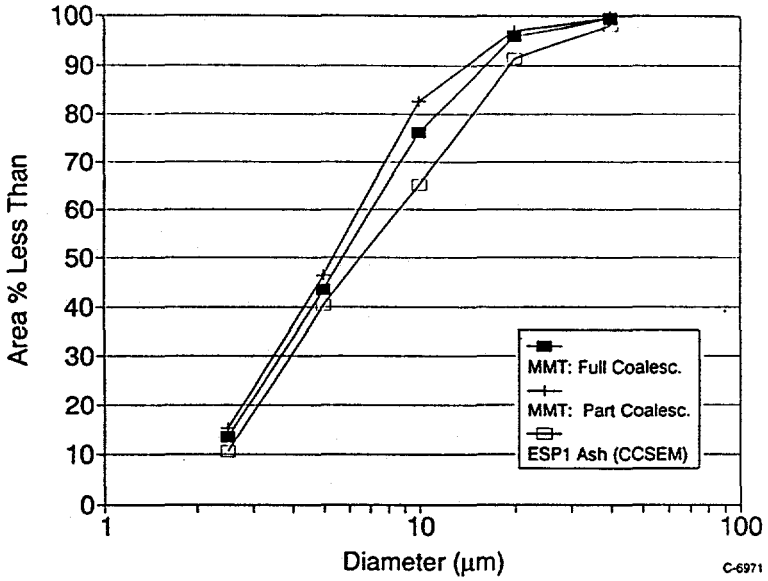

Figure 8-28. Ash psd: model versus field data -- South African bituminous -- cenospheres.

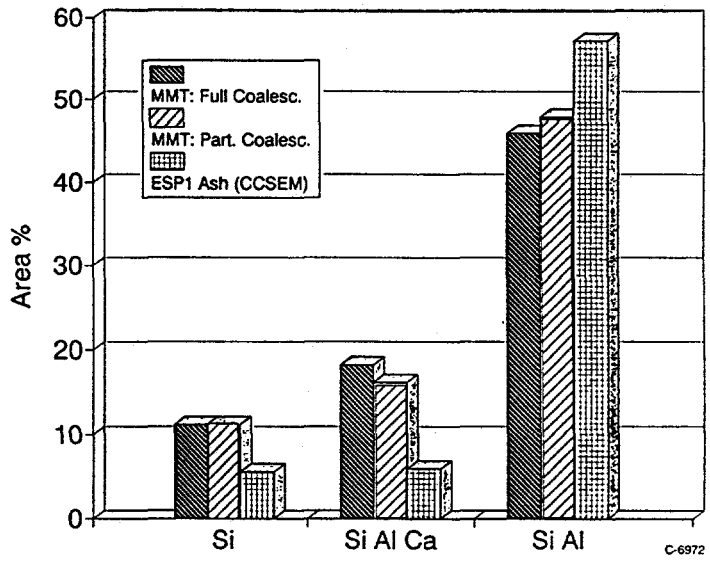

Figure 8-29. Ash composition: model versus field data -- South African bituminous -- cenospheres.

8.3 Submicron Aerosol Formation Model

One of the goals of this work is to incorporate an aerosol formation submodel into the engineering model for ash formation (EMAF). The first step toward this goal, development of a simple model describing submicron ash formation, was completed in the last quarter. Much of the development of this model was completed under separate DoE funding as part of the program "Advanced Analytical Methods for Selection of Coal and Coal Blends," contract number DE-FG02-92ER81376. Modifications to the model to make it suitable for incorporation into EMAF have been conducted under this program. A description of the complete sub-model, including discussion of development work that occurred under the other DoE contract, is included here for completeness.

As part of this submodel development, the question was asked -- what does the submicron ash look like? VTT has observed two modes, ultrafine and intermediate. The ultrafine mode has been observed by other people making measurements of fly ash from coal-fired power plants (Schmidt et al., 1976; McElroy et al, 1982). Schmidt et al. used an EAA and they observed a peak at about 0.12 μm and a broad peak from 0.2 to 0.5 μm. McElroy et al. report EAA data from 0.01 to 0.3 μm and low pressure impactor data from 0.3 μm and up. Therefore the model needs to address both the formation of ultrafine ash and intermediate ash.

8.3.1 Ultrafine Ash Mode

The ultrafine mode can be ascribed to a vaporization-condensation mechanism. Taking into account all the observations mentioned above, the ultrafine mode has a peak (mass distribution) of 0.07 to 0.15 μm. The variation in the diameter is mostly due to the combustion conditions; coal type is a second order effect. This can be seen in the data of McElroy et al. (1982) Six power plants of different designs were sampled. All but one were burning western sub-bituminous coals (see Table 8-16). Using data on NO emissions versus submicron mass loading, the effect of combustion conditions can be seen clearly (Figures 8-30 and 8-31).

Table 8-16. Summary of Data of McElroy et al.

Boiler	Coal Ash Content (wt% dry)	Total Mass Loading (g/m^3)	% Mass with D < 2 μm)	% Mass in Submicron Mode	Submicron Peak Diameter (μm)
360-MW, front wall fired, sub-bituminous coal	11	10.5	7	0.3	0.1
540-MW, tangential fired, Eastern bituminous coal	20	9.5	4	0.2	0.08
530-MW, opposed wall fired, sub-bituminous coal	12	6.4	4	1.3	0 .14
113-MW, roof fired, sub-bituminous coal	9	3.4	8	2.2	0.14
360-MW, tangential fired, sub-bituminous coal	10	2.3	20	0.9	0.095
25-MW, front wall fired, sub-bituminous coal	4	1.7	8	0.5	0.075

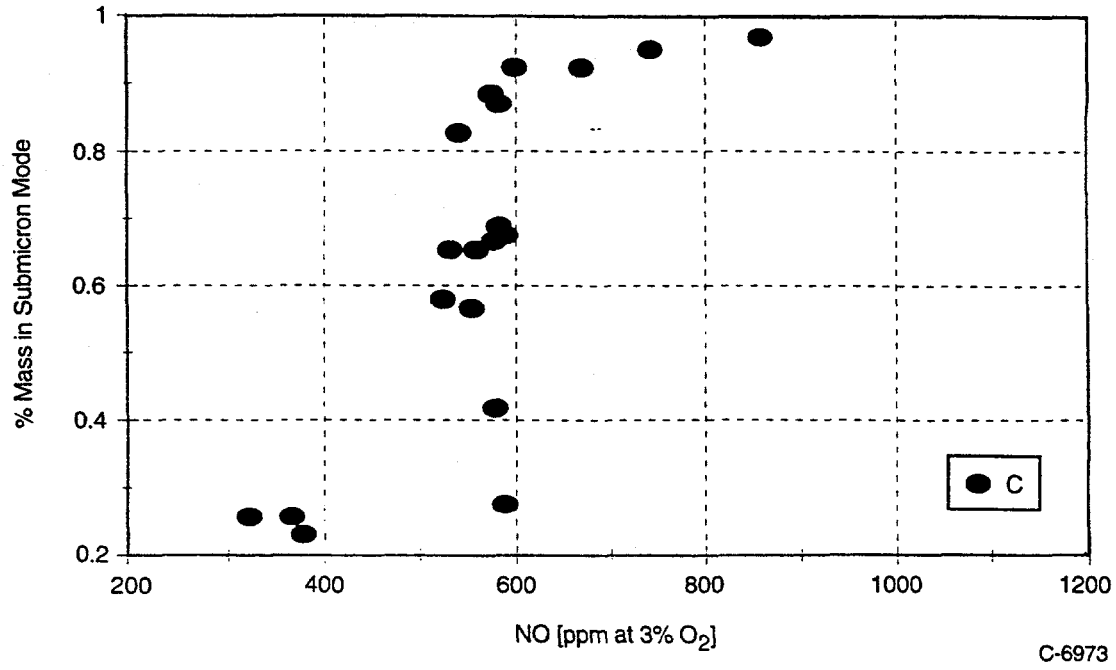

Figure 8-30. Mass loading in submicron mode (data of McElroy et al.).

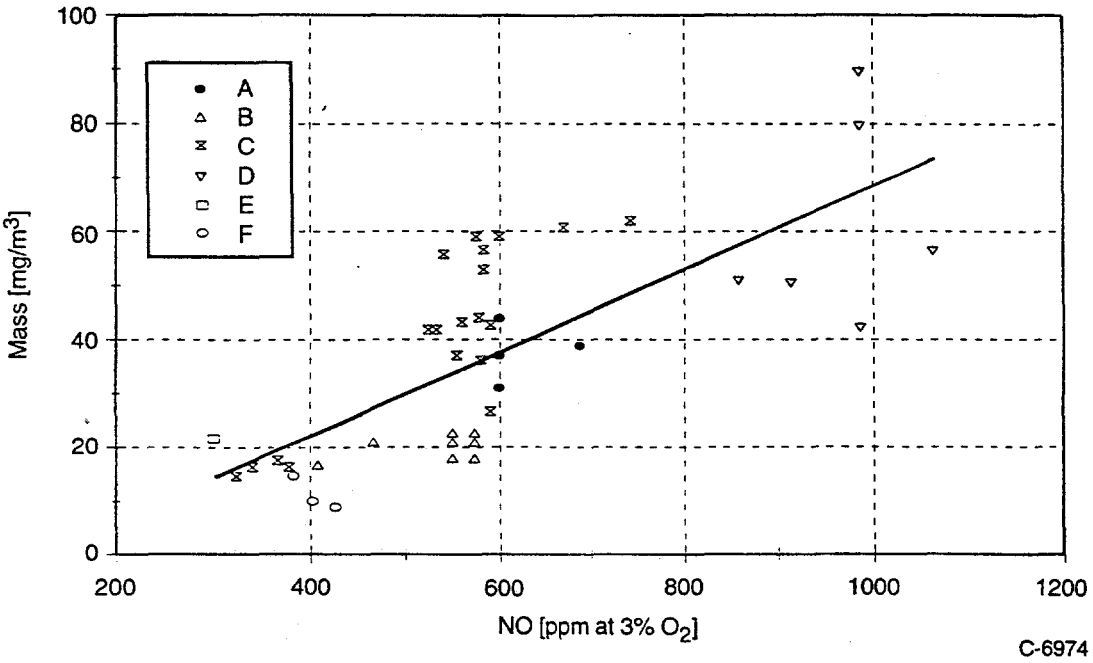

Figure 8-31. Mass loading in submicron mode (data of McElroy et al.).

Data are given on the mass loading of submicron aerosol as a function of NO content in the exhaust gas (Figure 8-30). Since NO is related to the peak combustion temperature, Figure 8-30 shows that the combustion conditions have a strong effect on the amount of mass in the ultrafine mode. The type of coal and furnace design do not seem to have a strong influence on the amount of ash in the ultrafine mode. Although, it should be noted that while this data set represents most types of boilers (except cyclone-fired), five out of six of the coals are Western sub-bituminous coals. The single Eastern coal fits

the same trend, however. Figure 8-31 shows slightly better correlation ($r^2 = 0.57$) between NO and the percentage of ash in the ultrafine mode.

It should be noted that Schmidt et al. (1976) saw an increase in the amount of submicron aerosol when one burner was taken out of service (a simulated low NO_x condition). Microscopic analysis of the fly ash showed much more carbon in the fine aerosol with a burner out of service.

Thus, we can use a characteristic temperature in the furnace to predict the mass of ash which vaporizes to form the utltrafine aerosol mode. We should be able to develop one correlation for all furnace types as a preliminary prediction of vaporization. However, the work by Quann (1982) and others at MIT has shown that different coals show different amounts of ash vaporized when burned under the same combustion conditions. This will probably be a second order effect except for low rank coals containing a lot of sodium; for lignites, Quann and Sarofim (1982) saw 3 to 9% of the ash appear in the submicron mode and attributed this to the high sodium content of these coals.

What about the composition of the ultrafine mode? The most complete dataset is found in Quann and Sarofim (1982). They studied eight coals, two lignites, two sub-bituminous coals, and four bituminous coals. Most were burned at 1750 K in 20% O_2 which corresponds to a particle temperature of 2000 to 2100 K. The amount of material in the submicron ash (<0.5 μm final filter sample) was 0.9 to 1.7 % of the ash for the bituminous coals, 1 to 3% of the ash for the sub-bituminous coals, and 3 to 9% of the ash for the lignites. The very high vaporization rates for the lignites and one of the sub-bituminous coals seems to be due to large amounts of sodium in the coal. Certainly, the bituminous coals are pretty much the same in terms of the amount of ash vaporized. We probably should treat vaporization differently for coals of different ranks.

Based on the data at 1750 K/20% O_2, we can make some generalizations about coals of different rank.

Bituminous coals. The submicron modes is primarily a silicate with very little aluminum. From 0.5 to 1.5% of SiO_2 vaporizes, but only 0.1 to 0.15% of the Al_2O_3 vaporizes. The SiO_2 content of the submicron aerosol is 20 to 40%. It contains less than 2% Al_2O_3. The other constituents of the submicron mode are FeO (2 to 8% vaporized), MgO (1 to 4% vaporized), K_2O (2 to 12% vaporized), and Na_2O (25 to 40% vaporized).

Sub-bituminous coals. The submicron mode consists primarily of MgO and Na_2O with minor (<10 wt%) amounts of SiO_2, FeO, and CaO. Mg and Na are organically bound in these coals and are fairly volatile. Thus it is not surprising that they make up most of the submicron mode.

Lignite. The composition of the submicron mode is similar to that for the sub-bituminous coals, mostly Na_2O and MgO with some CaO and FeO. More iron seems to vaporize in these lignites, however. From 6 to 14% of the iron ends up in the submicron mode. The form of iron may be different in these lignites than in the sub-bituminous coals.

Vaporization of individual oxides was modeled by Quann (1982). Vaporization was assumed to proceed via formation of a reduced species, for example,

$$SiO_{2(c)} + CO \Leftrightarrow SiO + CO_2 \tag{8-3}$$

And the partial pressure of SiO is equal to

$$P_{SiO} = (a_{SiO_2} K_{eq} P_{CO})^{1/2} \tag{8-4}$$

where a_{SiO_2} is the activity coefficient and K_{eq} is the equilibrium constant.

For elements that are found in discrete mineral inclusions, internal diffusion resistance dominates the vaporization process and the ratio of the fraction vaporized to the burnout time is given by

$$\frac{f_v}{t_b} = \frac{9 M_i c D_e x_i^{eq}}{\sqrt{3\Theta}\rho_i r_I r_o} \tag{8-5}$$

where the subscript I denotes the mineral inclusion and the subscript i denotes properties of the metal oxide species. The initial char particle diameter is r_o. This assumes a Thiele modulus of about 10. The approximation has removed the influence of char pore structure.

For atomically dispersed elements such as Ca and Mg in low rank coals, vaporization is controlled by external diffusion and

$$\frac{f_v}{t_b} = \frac{3\alpha c D_o M_i x_i^{eq}}{\Theta \rho_i r_o^2} \tag{8-6}$$

where α takes into account Stefan flow effects resulting from diffusion-controlled combustion.

As long as we can calculate the equilibrium vapor pressure of the species, we can estimate the vaporization rates. The species of interest are SiO_2, CaO, MgO, FeO, Na_2O, and K_2O.

The simple equilibria between CO and CO_2 can be used (see Eq. (8-3)) for each metal species of interest, assuming that oxygen diffusing to the char particle surface is completely consumed and that CO is the only product of combustion. In this case, the bulk oxygen concentration, $P_{O_2 b}$, will determine the concentration of CO at the surface

$$P_{COs} = 2P_{O_2 b} / \left(1 + P_{O_2 b}\right) \tag{8-7}$$

The bulk oxygen concentration can be calculated by assuming that all the volatiles burn first.

Instead of calculating f_v/t_B from first principles, we will use the reported value at a reference temperature from the data of Quann (1982). The equations are

$$f_V/t_B = (f_v/t_B)_r (x_i/x_{ir}) (r_{or}/r_o) \quad (8\text{-}8)$$

for mineral particles and

$$f_V/t_B = (f_v/t_B)_r (x_i/x_{ir}) (r_{or}/r_o)^2 \quad (8\text{-}9)$$

for organically-bound elements. The subscript r denotes the reference condition. Quann's data were generated with a gas temperature of 1750 K and various oxygen partial pressures. The reference condition will be at an oxygen partial pressure (bulk) of 0.2. Two types of coal will be used, Illinois No. 6 bituminous coal and Montana Savage lignite. The activity of the various oxides in the ash will change depending on the composition of the ash. The activity coefficient is contained in the above equations, so it is best to use bituminous coal reference conditions when calculating vaporization from bituminous coals and low rank reference condition for low rank coals. Table 8-17 gives the reference conditions for both coals. The values of f_V/t_B were calculated by two different methods. For Si, Fe, Ca, and Mg data on the amount of each element vaporized (in μg/g coal burned) and on the burnout times was used to calculate the quantity. For Al, Na, and K the amount of element vaporized was calculated from the composition of the bulk ash and submicron fume.

Table 8-17. Reference Conditions for Vaporization Calculations

Coal Rank	Illinois No. 6 Bituminous	Montana Savage Lignite
r_o (μm)	26.5	30.5
T_p (K)	2186	2000
f_V/t_B (s^{-1}) Total ash	0.6	1.65
Si	0.4	0.3
Al	0.04	0.05
Fe	0.5	4.0
Ca	0.04	0.58
Mg	0.74	10.51
Na	12.8	21.33
K	4.0	4.82

The equilibrium constants used were curvefits from JANAF data over a temperature range of 1500 to 2500 K as shown in Table 8-18.

To test the calculation of f_V/t_B, calculated values at other temperatures were compared with data reported by Quann (based on μg/g coal burned). The calculated values for individual elements were normalized to the amount of *inherent* mineral matter in the coal to be consistent with Quann's calculation of the fraction vaporized. In the low rank coal, Na, Mg, and Ca were not normalized because these elements are organically bound. Tables 8-19 and 8-20 compare the calculated to the reported numbers.

Table 8-18. Equilibrium Constants for Vaporization of Metals

$\ln(K) = a + 10^4\ b/T$	a	b
$SiO_{2(l)} + CO \rightarrow SiO + CO_2$	18.6621	-5.9507
$Al_2O_{3(l)} + CO \rightarrow 2AlO + CO_2$	38.2805	-16.7937
$FeO_{(l)} + CO \rightarrow Fe + CO_2$	11.0258	-4.42495
$CaO_{(l)} + CO \rightarrow Ca + CO_2$	10.1895	-5.1918
$MgO_{(l)} + CO \rightarrow Mg + CO_2$	11.8032	-4.5773
$Na_2O_{(l)} + CO \rightarrow 2Na + CO_2$	17.7349	-2.8271
$K_2O_{(l)} + CO \rightarrow 2K + CO_2$	19.1685	-2.1940

Table 8-19. Calculation of f_V/f_B for Illinois No. 6 (44% Inherent Mineral Matter)

T_p (K)	2457	2439
	f_V/t_B (s^{-1}) calculated (reported)	
Total ash	3.5 (3.5)	8.1 (14.0)
Si	4.0 (4.4)	10.6 (22.7)
Al	9.0	108.9
Fe	3.3 (4.7)	6.8 (8.7)
Ca	0.3 (0.17)	0.8 (2.7)
Mg	5.2 (3.6)	11.4 (11.4)
Na	82.9	141.3
K	22.2	34.6
NOTE: Al not used to calculated total ash vaporized.		

There is generally agreement within about 50% for Si, Fe, Ca, and Mg. The total amount of ash vaporized is predicted well, with an average error of about 20%. The calculated amount of aluminum vaporized is very high and there are no data available to check these numbers. Since aluminum does not vaporize extensively, it is reasonable to omit aluminum from the calculation of the total ash vaporized (as has been done here). Relatively large amounts of sodium and potassium are predicted to vaporized; alkali vaporization will be discussed below.

Table 8-20. Calculation of fv/fB for Montana Lignite (73% Inherent Mineral Matter)

T_p (K)	2190	2364
	f_v/t_B (s^{-1}) calculated (reported)	
Total ash	10.1 (9.6)	25.0 (17.0)
Si	1.8 (3.3)	5.7 (8.0)
Al	5.0	96.5
Fe	17.0 (13.7)	39.8 (17.9)
Ca	3.0 (8.2)	8.3 (27.5)
Mg	48.0 (42.2)	118.6 (77.8)
Na	94.1	173.5
K	18.6	30.7
NOTE: Al not used to calculated total ash vaporized.		

Silicates interact with sodium during combustion and this can effect the amount of sodium that vaporizes and ultimately condenses in the submicron fume. In an earlier DoE- funded mineral matter transformation study, a correlation was made between the amount of acid soluble sodium in the coal divided by the amount of silica in the ash and the fraction of sodium found in the submicron ash as shown in Figure 8-32. (Gallagher, 1992). These data were taken in the University of Arizona furnace on the a number of coals (including the Loy Yang Australian coal) at stoichiometric ratios of 1.2 to 1.3. The relationship between the fraction of sodium vaporized (f_{Na}) and the ratio of acid soluble Na to SiO_2 (x) was determined to be

$$f_{Na} = \begin{cases} 0.01, & x < 0.05 \\ 0.347427 + 0.4013384x + 0.111283x^2, & x \geq 0.05 \end{cases} \qquad (8\text{-}10)$$

The amount of potassium appearing in the submicron ash was not correlated with the parameter x (as defined above). However, the amount of potassium vaporized was correlated with the amount of sodium vaporized ash shown in Figure 8-33 This relationship is given by

$$f_K = 0.007706 + 0.615746 f_{Na} \quad . \qquad (8\text{-}11)$$

These correlations should give results which agree with the calculations using Quann's data as a reference. At first glance, the amount of alkali species vaporized reflected in Quann's data seems high relative to Gallagher's data. It should be noted that the bulk oxygen concentrations, particle diameters and gas temperatures are very different between the two experiments. Also, Quann used a narrow range of coal particles while Gallagher burned a utility grind with a volume median diameter of about 25 μm. We can try, however, to compare the two data sets by choosing appropriate particle temperatures and bulk oxygen concentrations.

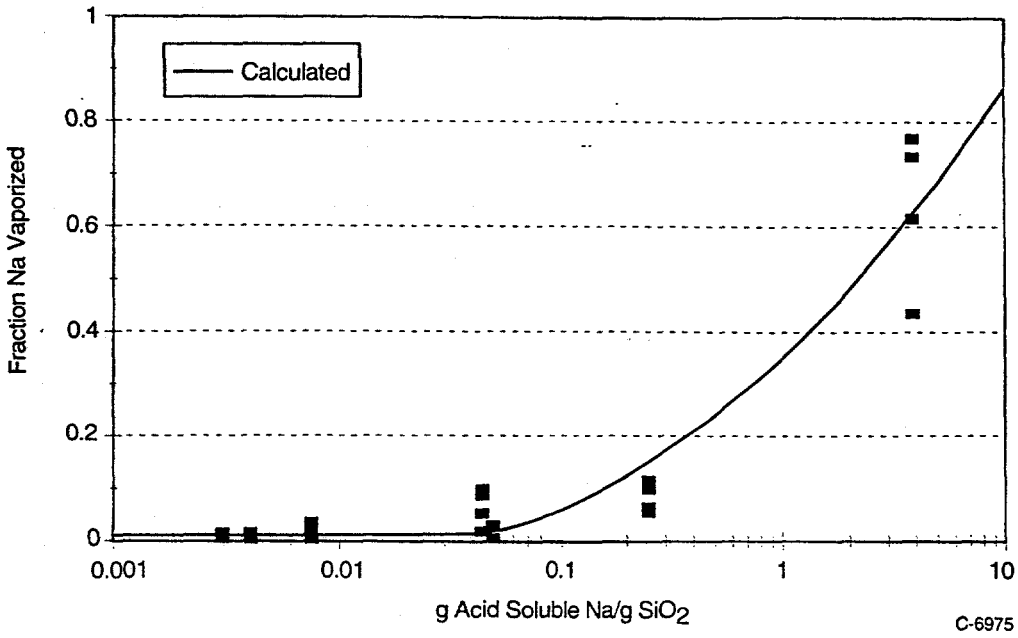

Figure 8-32. Fraction of Na vaporized for several coals (Gallagher, 1992).

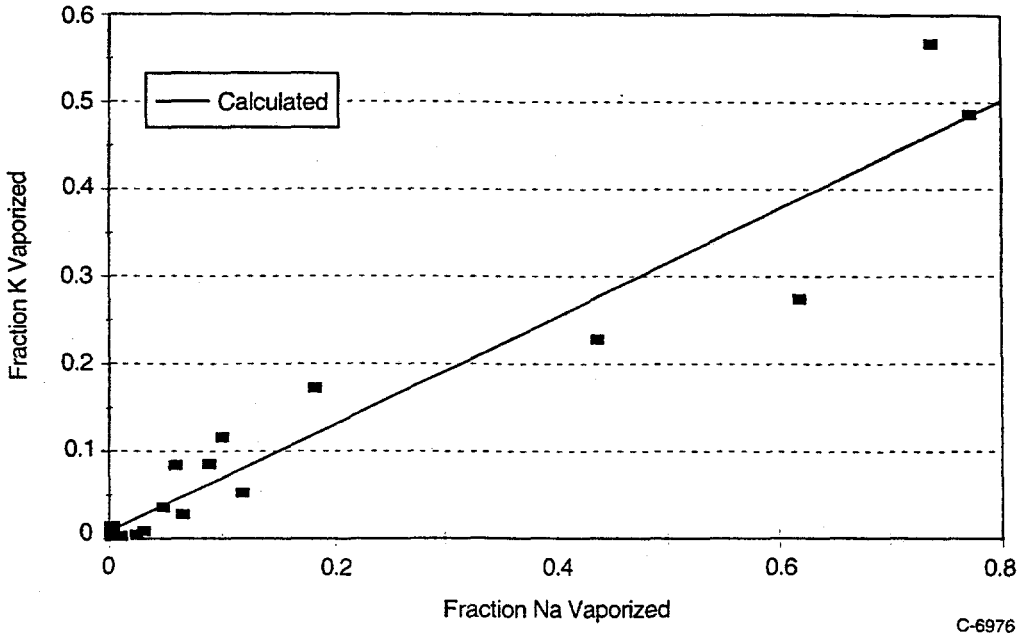

Figure 8-33. Correlation of Na and K vaporized (Gallagher, 1992).

Two coals were chosen for the comparison, Illinois No. 6 and Beulah (North Dakota) lignite because they were burned in both investigations. The ratios of the acid soluble sodium to total silica for these two coals are 0.05 and 0.35, respectively. The results of the comparison are summarized in Table 8-21. The particle temperature was assumed to be 1700 K, based on the range of calculated particle temperatures in Bool's (1993) thesis. These particle temperatures indicate a bulk oxygen concentration of approximately 0.05 atm, based on correlations between particle temperature and bulk oxygen concentration. The char burnout time is calculated from the relationship.

Table 8-21. Comparison of Sodium and Potassium Vaporization Calculated by Two Methods

Coal	% Na Vaporized		% K Vaporized	
	Quann Data	Gallagher Data	Quann Data	Gallagher Data
Illinois No. 6	2.1	1.5	1.0	1.9
Beulah lignite	18.1	18.7	5.4	12.3

$$d_o^2/t_B = 0.0138 \ln\left[1+X_{O_2}^b\right] \quad (8\text{-}12)$$

For a particle diameter of 25 μm and a bulk oxygen concentration of 0.05 atm, the char burnout time is calculated to be 9.3 ms.

The equations developed by Quann can be used to calculate the fraction of sodium and potassium vaporized at conditions other than the reference conditions. The reference value of f_v/t_B for these two elements should be calculated from the correlations determined from the work of Gallagher.

The following quantities will be needed as input to calculate the fractional vaporization rates and composition of the ultrafine mode:

- burnout time (calculated from temperature, radius,and oxygen concentration)
- particle temperature (calculated from gas temperature and oxygen concentration)
- equilibrium constants for vapor pressures (as fn. of T_p)
- initial char particle radius
- bulk oxygen concentration (calculated from volatile content)
- coal rank.

The self-preserving aerosol model can be used to calculated the size distribution (Flagan and Friedlander, 1978). Initially, let us neglect scavenging of small particles by large (supermicron particles). The total volume of aerosol is constant and equal to the amount of material vaporized:

$$V = f_v M_{ash} \quad (8\text{-}13)$$

where M_{ash} is the ash loading in g/m^3. The initial number of particles is therefore

$$N(0) = \frac{6V}{\pi D_o^3} \quad (8\text{-}14)$$

where D_o is the initial particle diameter which can be calculated from nucleation theory. The initial diameter can be estimated to be one or two molecules since the saturation ratio is generally large. The rate of decay of the number distribution is given by

$$\frac{dN}{dt} = -\frac{1}{2}\left[\frac{3}{4\pi}\right]^{1/6}\left[\frac{6kT}{\rho_p}\right]^{1/2}\left[\frac{p}{RT}\right] I_1 V^{1/6} N^{11/6} \qquad (8\text{-}15)$$

The size distribution is calculated from N(t) and V as

$$n = \left[\frac{N^2}{V}\right]\Psi(\eta) \qquad (8\text{-}16)$$

where $\eta = vN/V$. The function $\Psi(\eta)$ is tabulated by Friedlander (1977).

To make the calculation, we will assume that nucleation and coagulation happen on much faster time scales than those on which the gas temperature is changing. That is, we will impose a temperature-temperature history on the gas. For example, Flagan and Friedlander used the following temperature history to simulate the boiler: T = 1800 K for 0.5 s, T = 1800 to 1400 K (FEGT) over 1 s, and T = 1400 K to 425 K over 2 s.

The quantities needed to calculate the aerosol size distribution are:

- burnout time (calculated from temperature, radius,and oxygen concentration)
- gas temperature and residence time profile in the furnace (including FEGT)
- gas temperature at inlet to ESP
- fraction of ash mass vaporized
- total mass loading of ash.

8.3.2 Intermediate Mode

Unfortunately, CCSEM analysis does not provide information on particles less than approximately 1 μm. From measurements made by a European group, VTT, (Joutensaari et al., 1993), we believe that this mode does exist. The aerosol appears to consist of dense spheres which would suggest that the intermediate mode is not the product of a vaporization-condensation process. Instead, this mode may result from fine minerals in the coal. These have been observed via TEM (Hurley and Shobert, 1992) in sub-bituminous coals.

The approach taken here is somewhat simplified but does produce results that appear realistic. However, some refinement will be needed. The size distribution of minerals from eleven coals of various rank were examined. When the mineral distribution is calculated (examples in Figures 8-34 through 8-36), the largest number of minerals is found in the smallest size bin of approximately 1 to 2.5 μm.

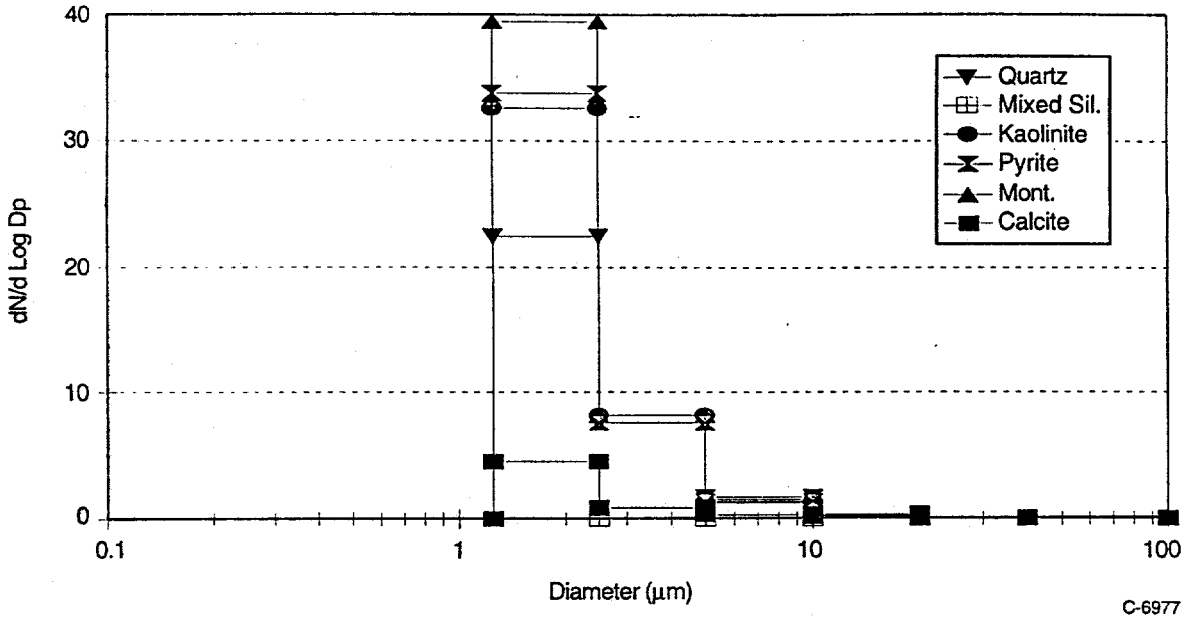

Figure 8-34. Illinois No. 6 minerals.

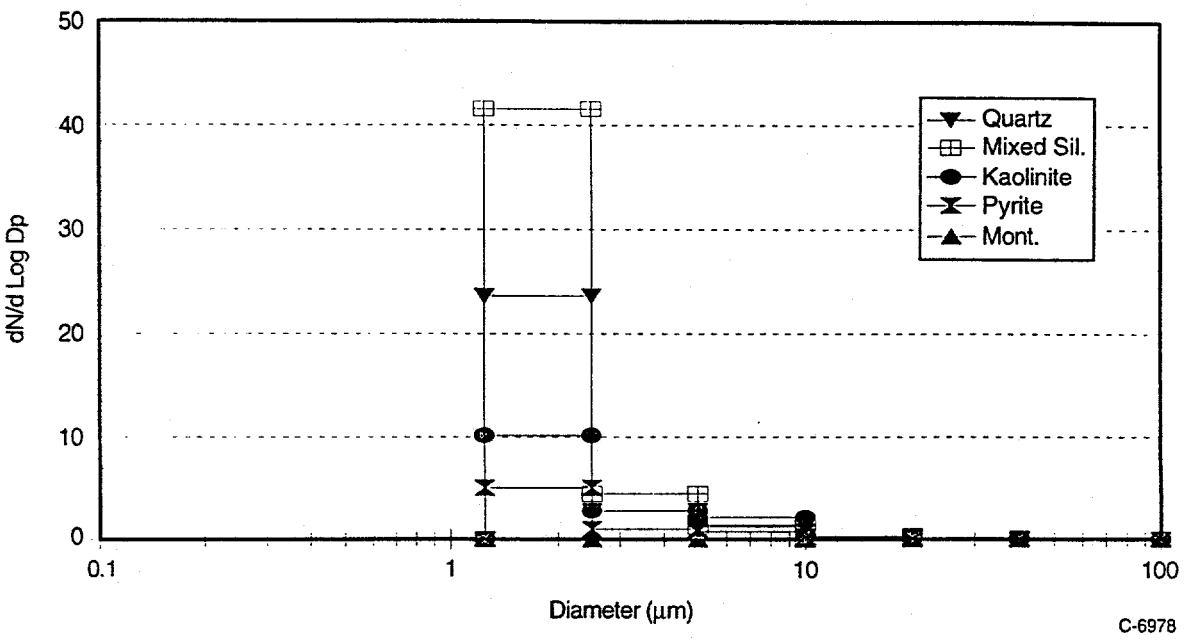

Figure 8-35. Eagle Butte minerals.

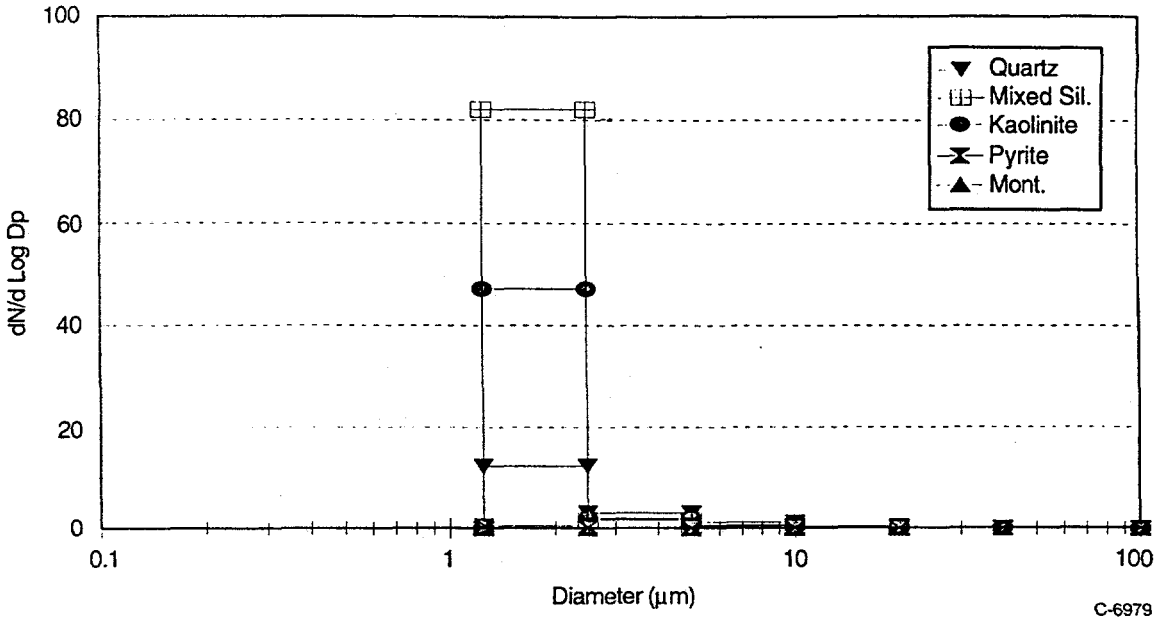

Figure 8-36. Beulah minerals.

The number of submicron minerals is approximated by assuming that the number distribution (on a log Dp basis) is symmetric about the 1 to 2.5 μm size range. The sizes chosen for the bins are 0.156 to 0.313, 0.313 to 0.625, and 0.625 to 1.25 μm. If the number distribution denoted by n(Dp) is the number of minerals between Dp and Dp + dDp then my assumption is equivalent to

$$\begin{aligned} n(0.625) &= n(1.25) \\ n(0.313) &= n(2.5) \\ n(0.156) &= n(5) \end{aligned} \qquad (8\text{-}17)$$

The calculation will be performed for each mineral class and then summed over all mineral classes. The mass distribution, $n_m(Dp)$ is then calculated for each mineral class of the submicron mode as

$$n_m(Dp) = \rho(\pi/6)Dp^3 n(Dp) \quad . \qquad (8\text{-}18)$$

The entire mass distribution is then renormalized. The only point of comparison available is the Polish coal for which VTT measured the ash size distribution (Joutensaari et al, 1993). The result of the calculation is given in Table 8-22.

Once the amount of submicron minerals has been predicted, how do you transform that into ash? Based on VTT's observation of the intermediate mode, we assume that some of the ultrafine minerals are released from the char during devolatilization and char combustion. These minerals melt but do not otherwise interact.

Table 8-22. Mineral Mass Distribution for Polish Coal (Submicron Calculated)

Mineral (wt%)	0.16-0.31 µm	0.31-0.63 µm	0.63-1.25 µm	1.25 2.5 µm	2.5-5 µm	5-10 µm	10-20 µm	20-40 µm	40-80 µm	>80µm	Total
Quartz	0	0.005	0.139	1.1	2.3	1.5	1.6	0.6	0.6	1.7	9.4
Illite	0.0002	0.016	0.731	5.8	8.0	5.8	7.4	1.8	1.8	0	31.5
Misc. sil	0.0002	0.012	0.784	6.3	6.3	6.3	3.4	1.8	2.1	0.3	27.2
Carbonates	0	0.001	0.101	0.8	0.54	1.1	2.7	0.6	0.5	0.5	6.9
Others	0.0001	0.012	0.778	6.2	6.0	4.5	4.2	1.9	0.8	0.5	25.0
Total	0.0006	0.045	2.53	20.3	23.1	19.3	19.3	6.8	5.8	2.9	100.

If we assume that *all* the submicron minerals are released during combustion, we can calculate the mass distribution in Figure 8-37 (The total ash mass loading at 7% excess O_2 was calculated to be 10.2 g/Nm^3; VTT reports 6 g/Nm^3.) The calculated submicron mass distribution is the right order of magnitude as compared to VTT's measured size distribution. Note that if all submicron minerals are released, the calculated ash psd contains 2.6% of the ash mass less than 1.25 μm and VTT reported 1.9% mass less than 1 μm.

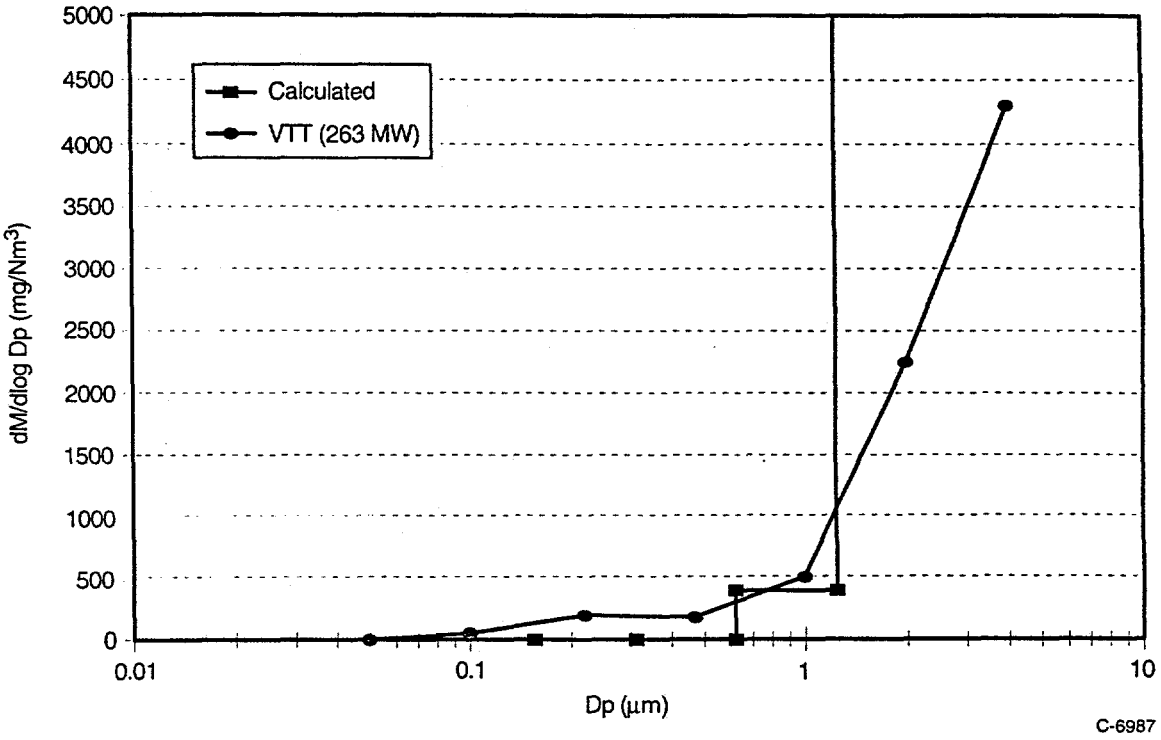

Figure 8-37. Calculated and measured submicron psd.

This agreement between the amount of submicron ash calculated here and that reported by VTT is deceptive, for two reasons. First, it is probably not realistic to assume that all the submicron minerals are released during combustion; some will probably coalesce with larger minerals in the char particle. Second, the evidence from American coals suggests that vaporization contributes a substantial fraction of the submicron aerosol. In laboratory tests (Quann and Sarofim, 1982) and field tests (McElroy et al., 1982) the mass in the submicron aerosol has been shown to be a function of combustion conditions which has always been interpreted to mean that the submicron aerosol is the product of a vaporization-condensation mechanism.

In VTT's experience with the Polish coal, the ultrafine (vaporization-condensation) mode does not contribute any significant amount of mass. However, many researchers assume that most of the mass in the submicron mode is a product of vaporization. Therefore we suggest that submicron coal minerals may contribute to the submicron ash *in addition to vaporized material.* In other words, the fine minerals represent the lower limit on the mass of submicron aerosol, in the limit of low temperatures and little vaporization.

8.4 Engineering Model for Ash Formation - Modifications for Reducing Conditions

One of the major goals in this program was to modify the Engineering Model for Ash Formation (EMAF) to incorporate ash formation behavior that is unique to reducing environments. Previous experimental work in this program at PSIT and MIT has shown that the degree of carbon burnout plays a major role in mineral matter transformations during combustion under reducing environments and in deposition characteristics (e.g. stickiness) of the resulting ash. Therefore in order to use EMAF to model the ash size distribution and composition distributions for combustion under reducing conditions it was necessary to modify the model to account for the presence of unburned char. This modification was accomplished by developing a kinetic submodel, based on information in the literature, to predict the fraction of unburned char in each particle size range. The modified EMAF was then used to simulate combustion of each of the program coals under stoichiometric ratios of 0.6, 0.9, and 1.2. These simulations were then compared with experimental data for these coals and conditions, obtained as part of this program (Section 7).

8.4.1 Kinetic Burnout Submodel

The kinetic submodel used here is similar to that discussed elsewhere (Bool et al., 1995, Helble et al 1992). In this submodel, the fractional burnout of char in a given size range is calculated by simultaneously solving for the burnout of all the size ranges present in the coal. For example, a coal with a particle size distribution ranging from 10 μm to 120 μm is divided into 12 size bins. The kinetic submodel then simultaneously solves the 12 rate equations describing burnout in the individual size bins. By simultaneously solving for the oxygen, carbon monoxide, and carbon dioxide concentrations, the submodel predicts which particles burn out first, and as a result predicts the degree of burnout for all size ranges.

The char burnout relation used, Eq. 8-19, was taken from Hurt and Mitchell (1992). According to this empirical study, the global char burnout rate is a function of the char external surface area (SA_{char}) and

$$\frac{d(CHAR)}{dt} = -K_c \exp\left(\frac{-E_c}{RT_p}\right) SA_{char} (P_{O_{2s}})^{1/2} \qquad (8\text{-}19)$$

the char particle temperature (T_p). To simplify the kinetic submodel, the char burnout temperature is set equal to the gas temperature - a reasonable assumption for substoichiometric combustion. The gas temperature profile used in these calculations was that presented in Quarterly Report Number 3. The burnout rate was assumed to be proportional to the square root of the surface oxygen partial pressure (Po_{2s}). Finally, the global rate constants were determined empirically (by fitting to data from several coals) to be a function of the coal carbon content (%C, ash and H_2O free) as shown in Eqs. 8-20 and 8-21 (Hurt et al, 1992), where T_{ref} here is equal to K.

$$E_c = -5.945 + 0.355(\%C) \qquad (8\text{-}20)$$

$$\ln K_c = (2.80 + 0.0758(\%C)) - \left(\frac{E_c}{T_{ref} R}\right) \qquad (8\text{-}21)$$

It should be noted that Hurt et al. (1992) found that the lower rank coals burned in the diffusion limited regime. This fact was taken into account during the derivation of the parameters in Eqs. (8-20) and (8-21). Therefore, the model allows lower rank coals to burn much faster than the bituminous coals.

In the kinetic submodel the combustion product is assumed to be CO. The CO is then oxidized to CO_2 in the bulk gas phase according to Eq. (8-22). The global forward and

$$CO + 1/2\ O_2 \rightleftharpoons CO_2 \tag{8-22}$$

reverse reaction rates, R_f and R_b, shown in Eqs. (8-23) and (8-24), are those presented by Dryer et al (1973) and Westbrook et al (1981) respectively.

$$R_f = 3.8x10^{14}\ V_g \exp\left(\frac{-E_{CO}}{\mathbf{R}\ T_g}\right)\ [CO]\ [H_2O]^{1/4}\ [O_2]^{1/2} \tag{8-23}$$

$$R_b = 1x10^{11}\ V_g \exp\left(\frac{-E_{CO}}{\mathbf{R}\ T_g}\right)\ [CO_2] \tag{8-24}$$

The species concentrations are determined from the number of moles of each species in the system and the gas volume (from Eq. (8-25)). Mole balances for O_2, CO, CO_2 are shown in Eqs. (8-26) through (8-28). Finally, the surface partial pressure of oxygen is determined by assuming a steady state between oxygen transport and consumption (see Eq. (8-29)).

$$V_g = \frac{n_t\ \mathbf{R}\ T_g}{p} \tag{8-25}$$

$$\frac{d\{O_2\}}{dt} = \frac{1}{24}\left(\Sigma\frac{d(CHAR)}{dt}\right) + \frac{1}{2}(R_b - R_f) \tag{8-26}$$

$$\frac{d\{CO\}}{dt} = -\frac{1}{12}\left(\Sigma\frac{d(CHAR)}{dt}\right) + (R_b - R_f) \tag{8-27}$$

$$\frac{d\{CO_2\}}{dt} = R_f - R_b \tag{8-28}$$

$$\left(\frac{D}{r_c}\right)\left(\frac{P_{O_2}-P_{O_{2s}}}{R\,T_g}\right) = \frac{-k_c}{24}\exp\left(\frac{-E_c}{R\,T_p}\right)(P_{O_{2s}})^{1/2} \qquad (8\text{-}29)$$

Because there is no simple means to take into account the coal devolatilization, we assumed that devolatilization has taken place before the char begins to burn. The initial amounts of each of the gaseous species are determined from the coal mass, the stoichiometric ratio, and the fraction of volatile matter.

A typical burnout distribution is shown in Figure 8-38 for the washed Pittsburgh No. 8 examined in this program. This plot shows that as the stoichiometric ratio is increased, the small particles burn out before the larger particles. This result is reasonable given that during the shorter residence time required to completely burn the small particles, the particles experience oxygen rich conditions. However, as these small particles burn the oxygen is largely consumed - resulting in fuel rich conditions. The burnout of the larger particles is therefore prolonged because they combust primarily under fuel rich conditions. Figure 8-39 shows a comparison between the fraction carbon in the ash predicted by the kinetic submodel and that measured as part of the experimental procedure. The data shown here are for the three Pittsburgh No. 8 program coals (i.e. run-of-mine, washed, and beneficiated). There is reasonable agreement between the data and the predictions, but further comparisons with a wider range of coals and conditions are required to fully validate the submodel.

The output of this kinetic submodel is then used in EMAF to define the fraction of minerals in each simulated coal particle that is **not** exposed to the outer char particle surface during the combustion process. These minerals will generally maintain the same size and composition, since they cannot interact with other minerals. The remaining minerals are assumed to coalesce and interact with other minerals; this is the approach taken in the original version of EMAF for super-stoichiometric combustion conditions. Based on these mechanisms, the model predicts the size and composition distributions of the ash.

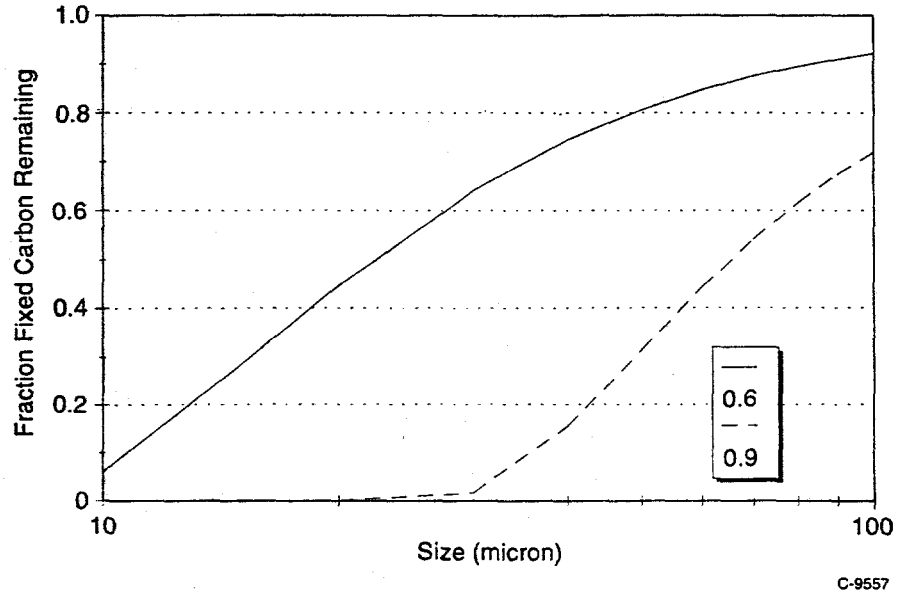

Figure 8-38. Fractional burnout by size - DOE Pittsburgh No. 8.

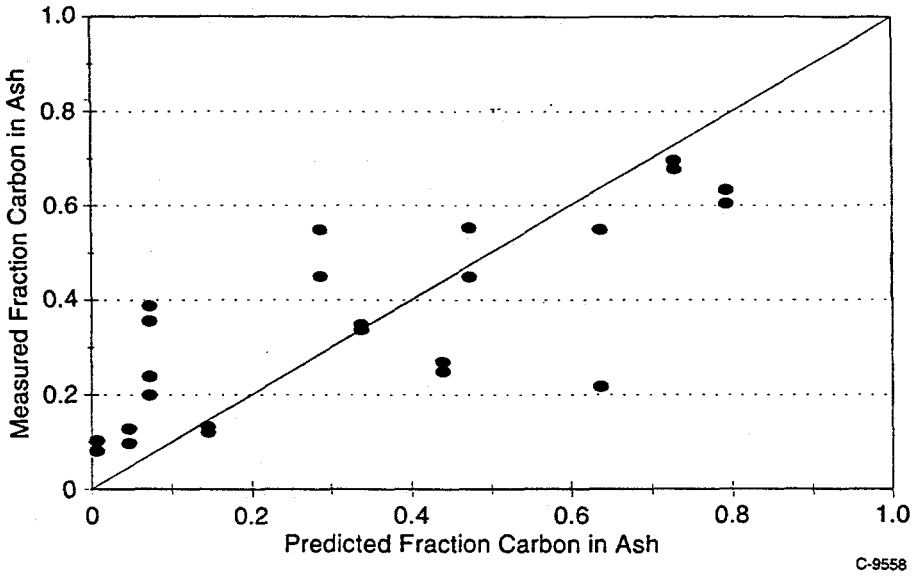

Figure 8-39. Burnout predictions for program coals - carbon content from deposition samples.

Figures 8-40 and 8-41 illustrate the predicted changes in ash size and composition as a function of stoichiometric ratio for the run-of-mine Pittsburgh No. 8. On one extreme is the 1 ash per mineral case, which would match those conditions where very little char burnout has taken place, such as low residence times or stoichiometric ratios. The other extreme is the completely burned out case (SR=1.2). The model predicts a smooth transition of ash mass to the larger sizes with increasing stoichiometric ratio - indicating an increase in ash coalescence with stoichiometric ratio. This increase in coalescence is also evident in the composition predictions (Figure 8-39). The minerals are initially (on an oxygen, carbon, and hydrogen free basis): Si Al K, Si, Si Al, and lesser amounts of Si Al Fe and Si Al Ca. As these minerals coalesce,

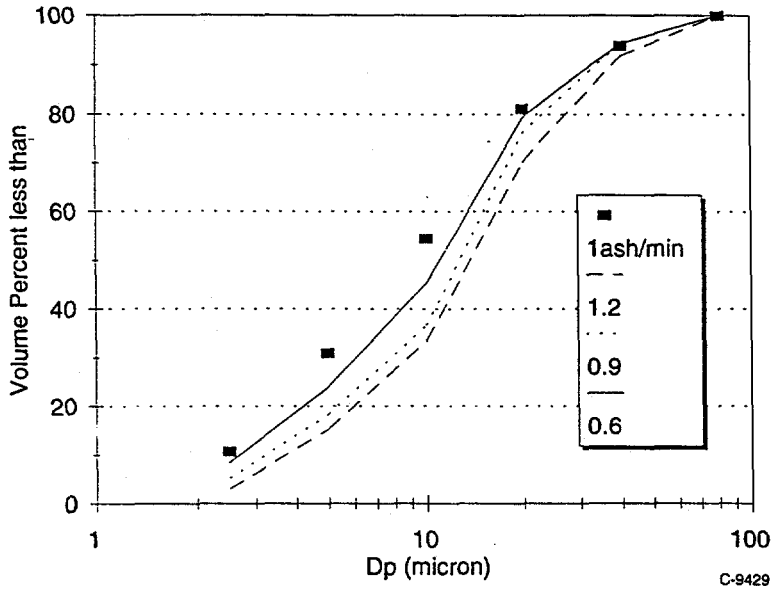

Figure 8-40. Predicted ash PSD as a function of stoichiometric ratio. Mineral size distribution (1 ash/min) shown for comparison. Coal: ROM Pittsburgh No. 8.

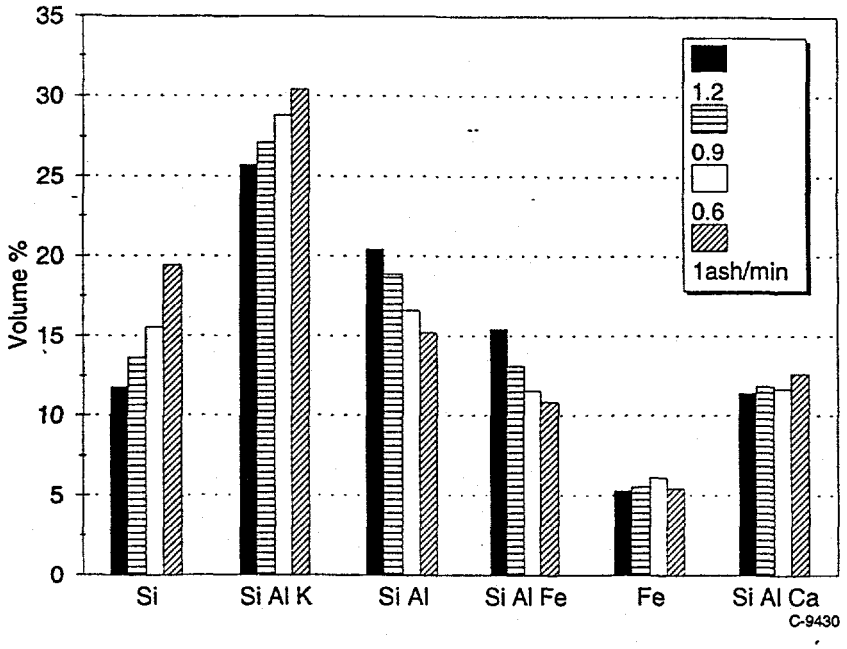

Figure 8-41. Model prediction for ash composition - ROM Pittsburgh No. 8.

the amounts of Si (quartz) and Si Al K (illite) decrease, while the amount of Si Al increases. This is due to the fact that the product of Si and Si Al K mixing has a lower K content and is put in the Si Al category by EMAF. There is also evidence of increased Fe - silicate coalescence as a function of stoichiometric ratio (burnout), which is qualitatively consistent with the experimental data for this coal.

8.4.2 Comparison of EMAF Predictions and Experimental Data

Once the modifications were complete a number of simulations were performed to predict ash size and composition distributions for each of the program coals burned under stoichiometric ratios of 0.6, 0.9, and 1.2. The mineral size and compositions used as inputs for these simulations were based on the CCSEM measurements of the raw coal, discussed in Section 4. The predictions were then compared with the experimental data obtained using the PSIT entrained flow reactor (Section 7). The simulations for each coal, and comparision with the experimental data, are discussed below.

Washed Pittsburgh No. 8:

Data from the combustion experiments with this coal are shown in Figure 8-42. These data suggest that significant mineral fragmentation occurs during combustion of this coal at the higher, (0.9 and 1.2) stoichiometric ratios. However, the measured ash size distribution for the 0.6 stoichiometric ratio is similar to that of the original coal, suggesting that very little mineral-mineral interaction occurrs at the low stoichiometries. Either very little char burnout occurred, or the lower particle temperatures associated with combustion under fuel rich conditions inhibited mineral coalescence. The predicted ash psd for this coal, Figures 8-43 through 8-45, indicate that the model overpredicts the degree of mineral interactions for the stoichiometric ratios of 1.2 and 0.9. However, this overprediction is consistent with the mineral fragmentation noted in the experimental data as EMAF currently does not include **mineral** fragmentation. The ash psd predictions for the lowest stoichiometric ratio are in good agreement with the data. This agreement validates, at least qualitatively, the kinetic approach taken to model decreased mineral interaction due to reduce char burnout at lower stoichiometric ratios.

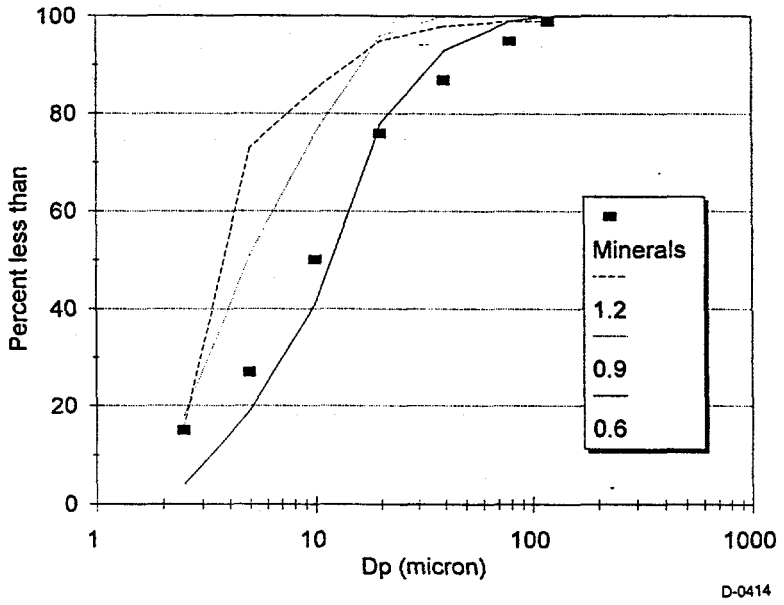

Figure 8-42. Measured ash psd (CCSEM) - washed Pittsburgh No. 8

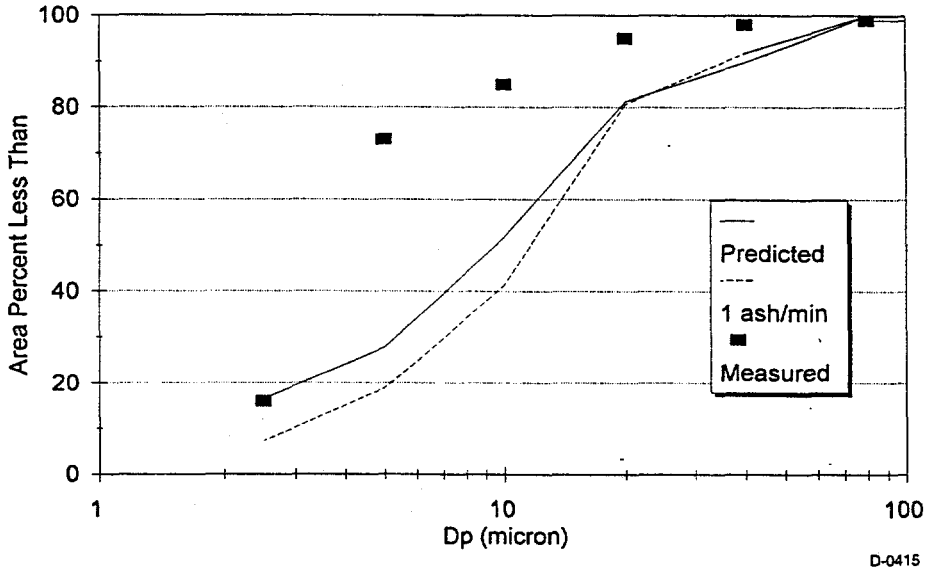

Figure 8-43. Comparison of measured and predicted ash psd - washed Pittsburgh No.8, SR=1.2

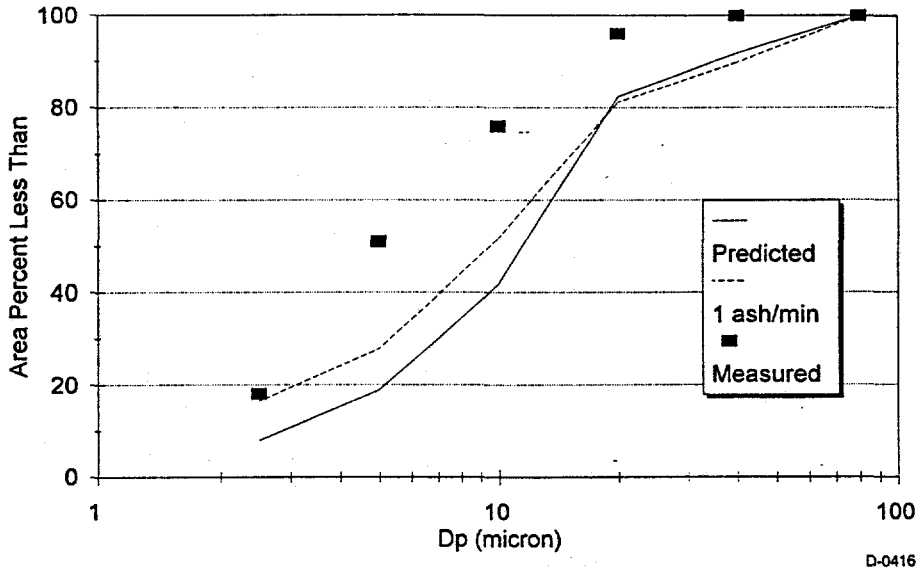

Figure 8-44. Comparison of measured and predicted ash psd - washed Pittsburgh No.8, SR=0.9.

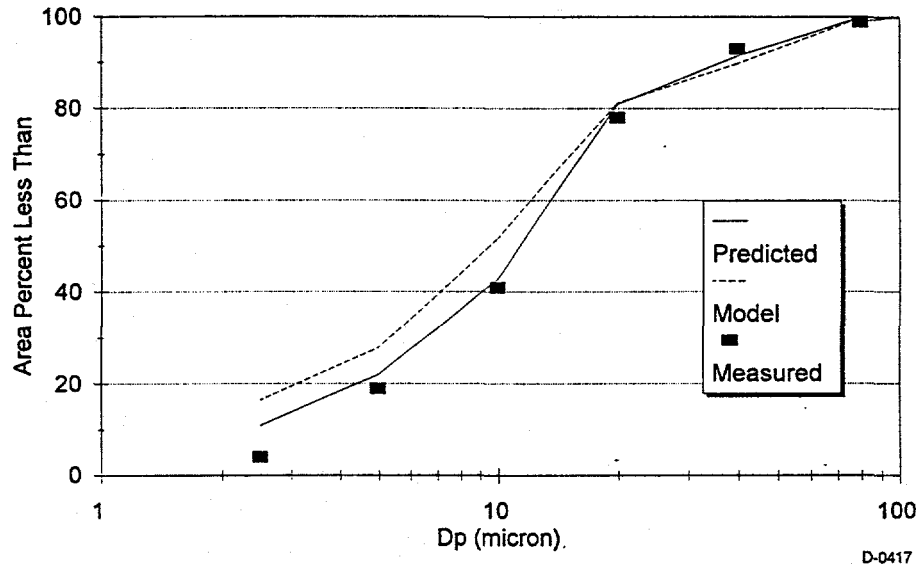

Figure 8-45. Comparison of measured and predicted ash psd - washed Pittsburgh No.8, SR=0.6

The predicted, and measured, ash composition distributions for this coal can be seen in Figures 8-46 through 8-48. The data on these figures represent the volume percent of ash that exists in a given composition range. In all cases the percent ash predicted as Si was similar to the measured value. However, there were significant discrepancies between the model predictions and the measurements the remaining five composition categories. These discrepancies are probably due to differences between the coal analysis and the ash analysis. Comparison of the pyrite content of this coal as measured by CCSEM and that measured by Mössbauer show that the CCSEM significantly over-measures the pyrite. Further the CCSEM misses, or incorrectly identified, a significant fraction of the illite. As the model predictions are based on the coal CCSEM analysis, it is not surprising that the model underpredicts the amount of ash in the Si Al K category (it is assigned to the Si Al category in the model) while overpredicting the ash in the pure Fe category. However, the model agrees with the *trends* in the data (Figure 8-49).

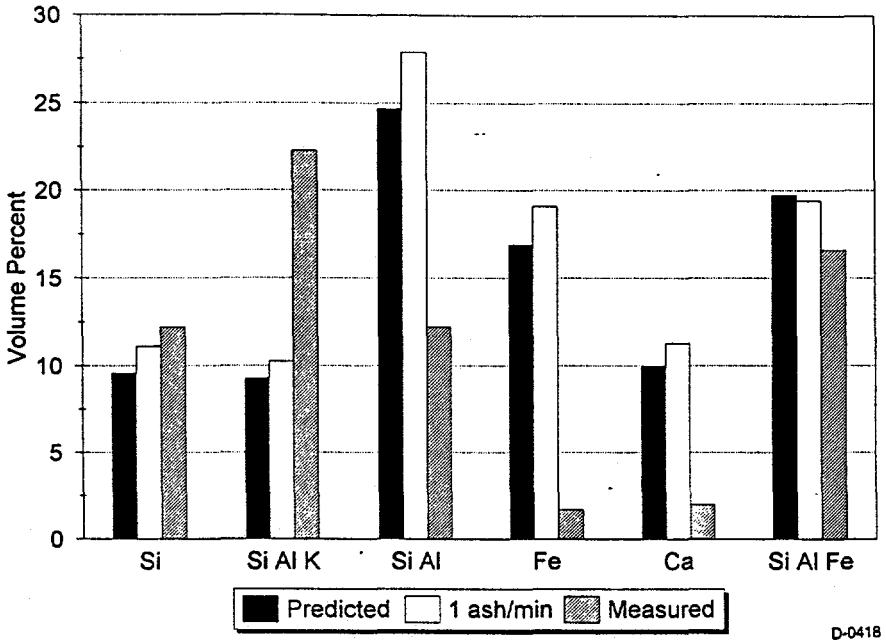

Figure 8-46. Comparison of measured and predicted ash composition - washed Pittsburgh No.8, SR=1.2

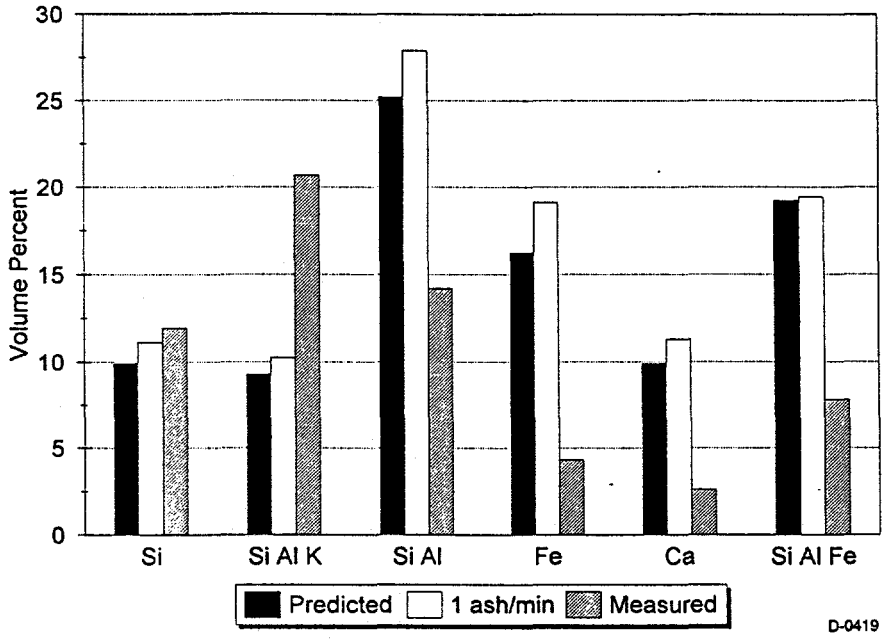

Figure 8-47. Comparison of measured and predicted ash composition - washed Pittsburgh No.8, SR=0.9

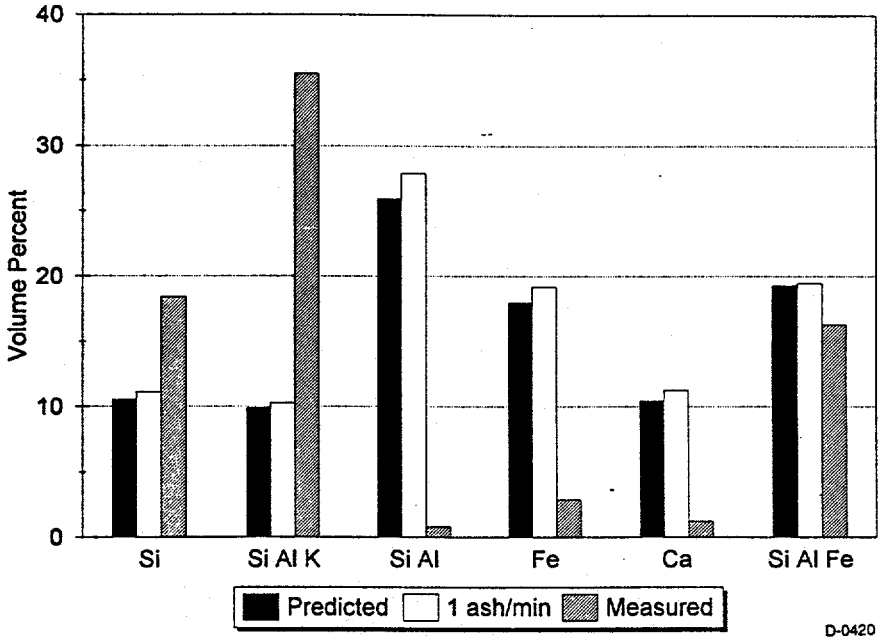

Figure 8-48. Comparison of measured and predicted ash composition - washed Pittsburgh No.8, SR=0.6

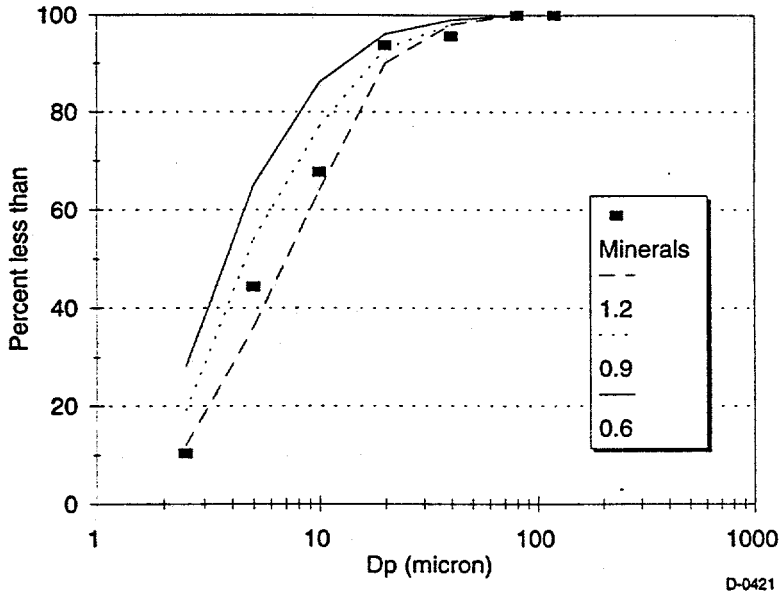

Figure 8-49. Measured ash psd (CCSEM) - beneficiated Pittsburgh No. 8.

In general the data for this coal show fewer 'pure' mineral compounds in the ash as compared to the model. For example, in many cases the model predicts the presence of pure Ca or Fe particles. These particles are not present in the ash. Therefore, the model seems to underpredict the degree of coalescence between included minerals. This conclusion would seem to contradict the psd data discussed above. However, it possible that the increase in the ash psd gain due to coalescence of inherent minerals is 'swamped out' by the decrease due to mineral fragmentation.

Beneficiated Pittsburgh No. 8:

Unlike the data from the previous coal, the ash psd data for the beneficiated Pittsburgh No. 8 indicated that little mineral coalescence or fragmentation occurred (Figure 8-49). This lack of mineral coalescence is reflected in the model predictions (Figures 8-50 through 8-52). In general the model predictions were in very good agreement with the measured ash psd for each condition. Many of the predicted ash composition categories, Figures 8-53 through 8-55, were also in agreement with the data. However, the overprediction of the Fe category and the underprediction of the Fe Si Al category suggest that the model may be slightly underpredicting the degree of mineral interaction. The presence of an Fe Ca Si category in the model is due to the need to combine all of the minor mineral species into a single

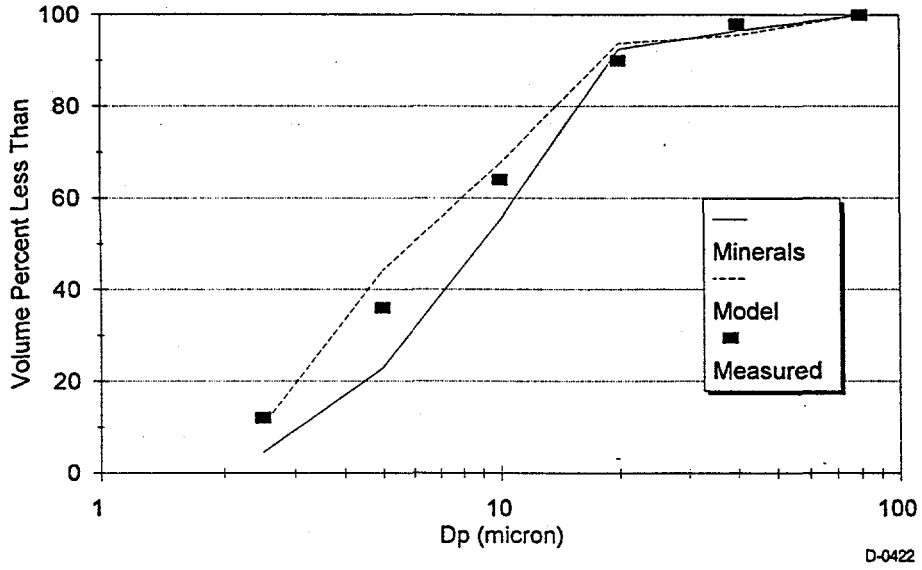

Figure 8-50. Comparison of measured and predicted ash psd - beneficiated Pittsburgh No. 8, SR=1.2.

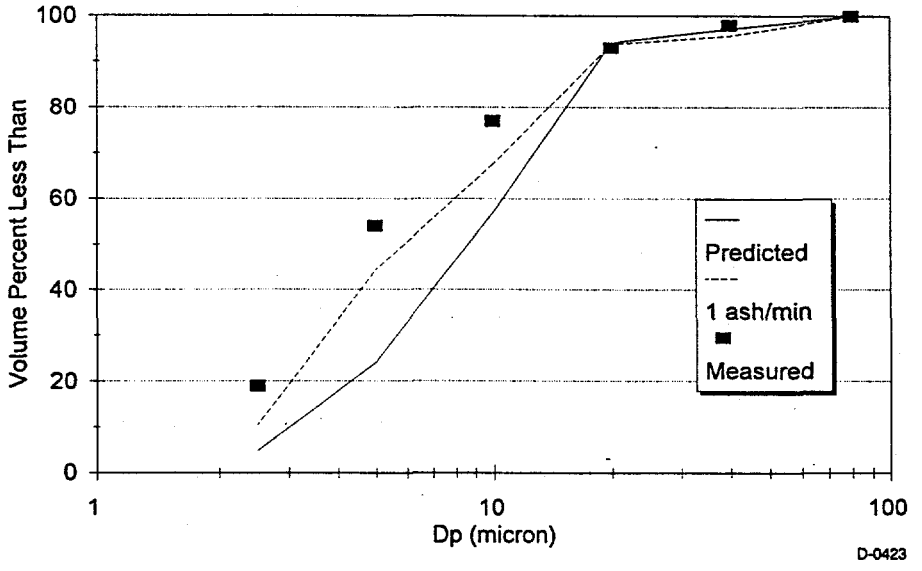

Figure 8-51. Comparison of measured and predicted ash psd - beneficiated Pittsburgh No. 8, SR=0.9.

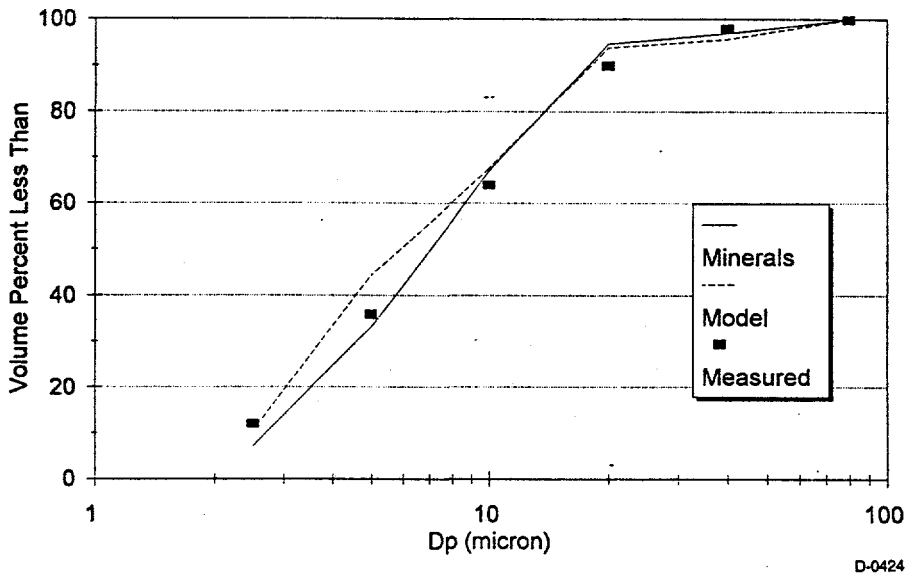

Figure 8-52. Comparison of measured and predicted ash psd - beneficiated Pittsburgh No. 8, SR=0.6.

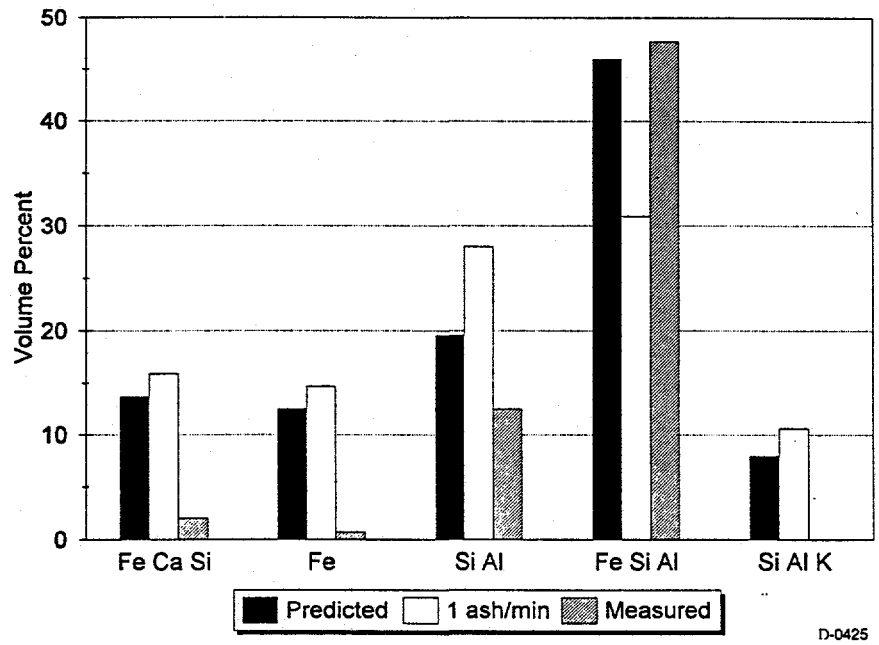

Figure 8-53. Comparison of measured and predicted ash composition - beneficiated Pittsburgh No. 8, SR=1.2.

category, misc. mixed, in the model. The model treats this category as a mineral with the stated composition. However, it is likely that there are no particles with the composition specified as "misc. mixed".

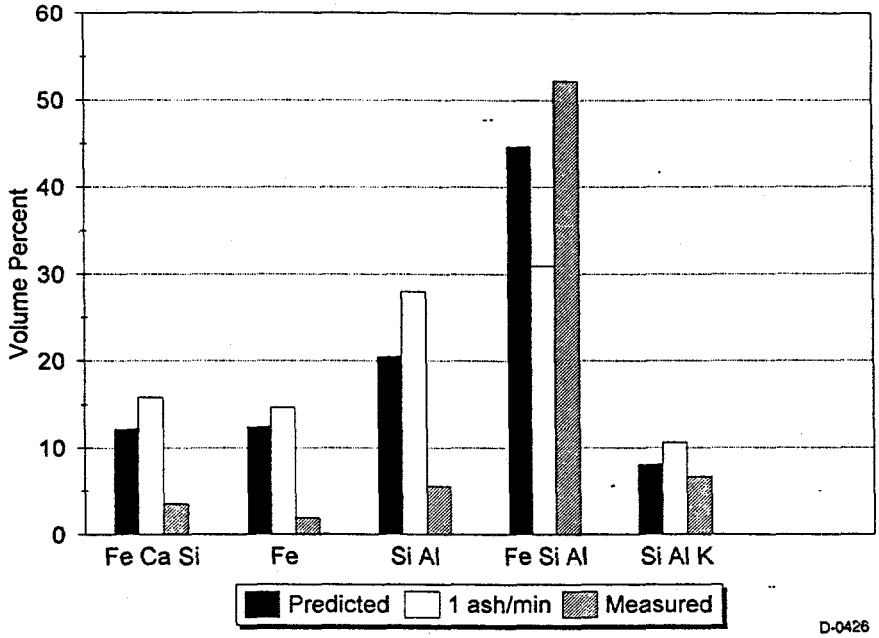

Figure 8-54. Comparison of measured and predicted ash composition - beneficiated Pittsburgh No. 8, SR=0.9.

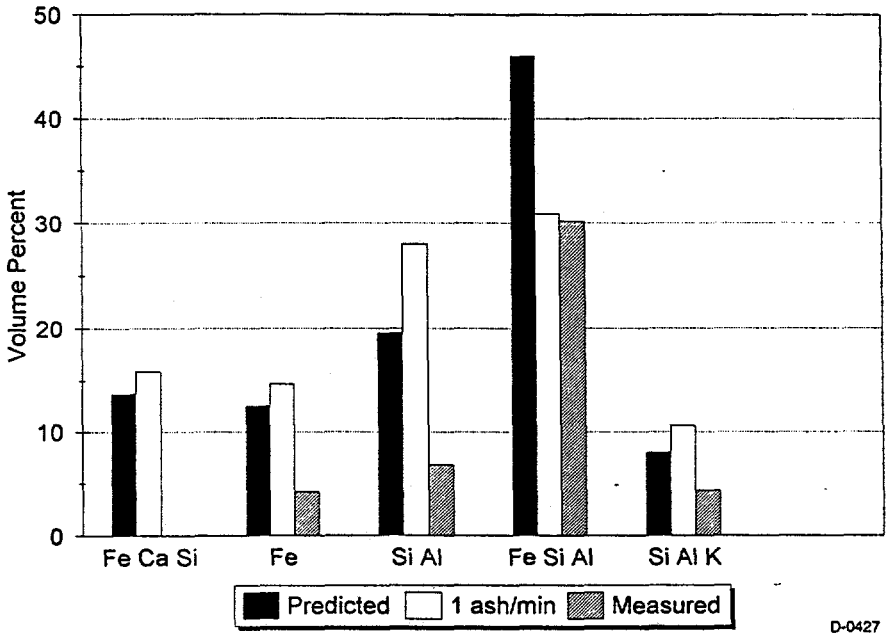

Figure 8-55. Comparison of measured and predicted ash composition - beneficiated Pittsburgh No. 8, SR=0.6.

Run-of-mine Pittsburgh No. 8:

The measured ash psd for this coal showed an interesting trend as a function of stoichiometric ratio (Figure 8-56). At the lowest stoichiometric ratio there was little evidence of mineral coalescence. At the intermediate stoichiometric ratio some coalescence occurred. However, at the highest stoichiometric ratio there was evidence of significant mineral fragmentation. The predicted ash psd for this coal (Figures 8-57 through 8-59) suggests that the model was in good agreement for those conditions where mineral fragmentation did not occur. However, as discussed above, the model does not account for mineral fragmentation, and therefore does not fit the data for the stoichiometric ratio equal to 1.2 case.

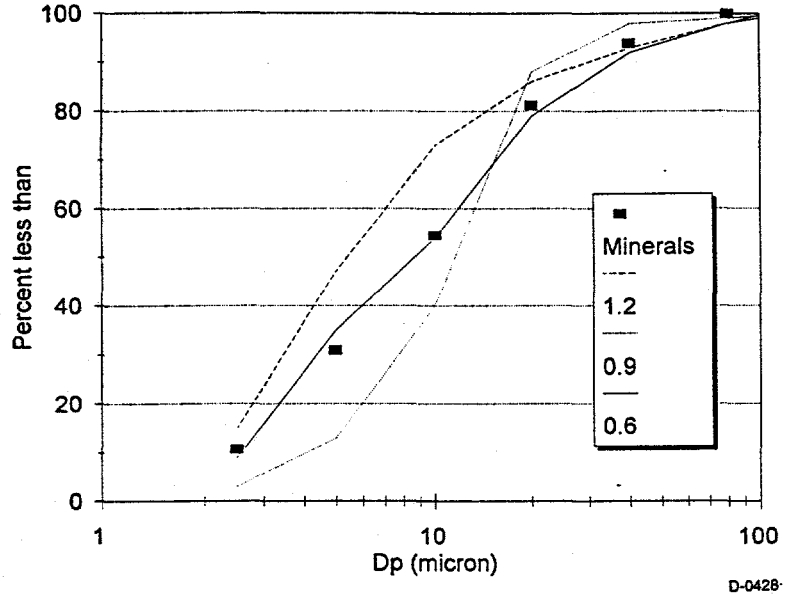

Figure 8-56. Measured ash psd (CCSEM) - run-of-mine Pittsburgh No. 8.

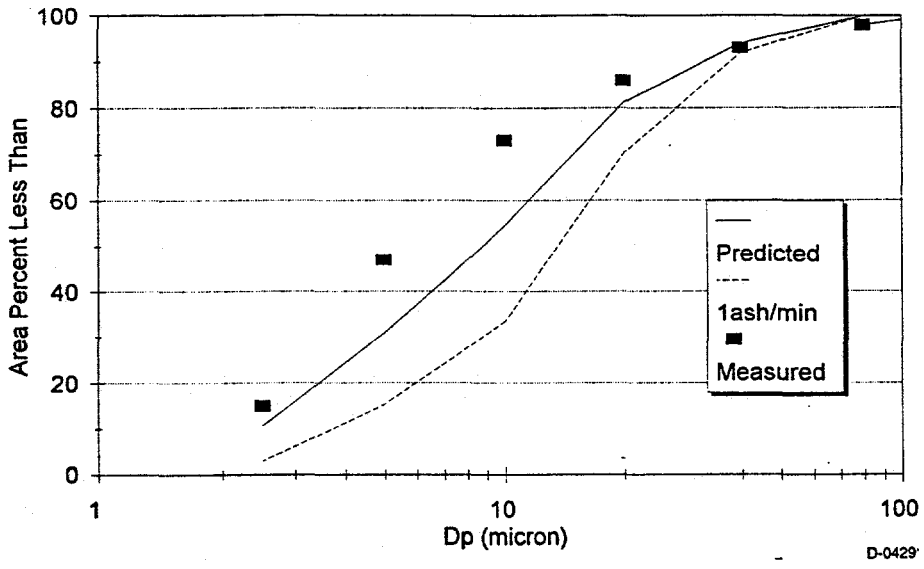

Figure 8-57. Comparison of measured and predicted ash psd - run-of-mine Pittsburgh No. 8, SR=1.2.

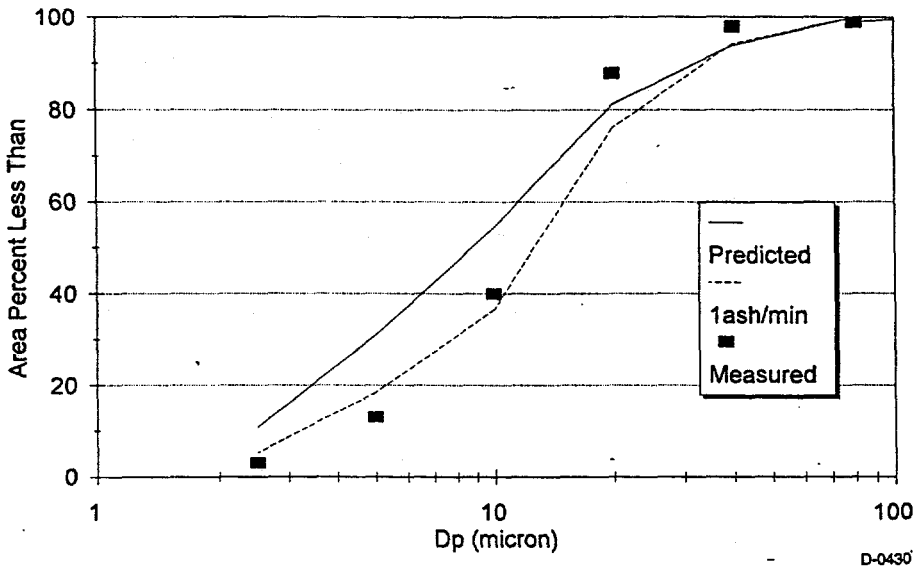

Figure 8-58. Comparison of measured and predicted ash psd - run-of-mine Pittsburgh No. 8, SR=0.9.

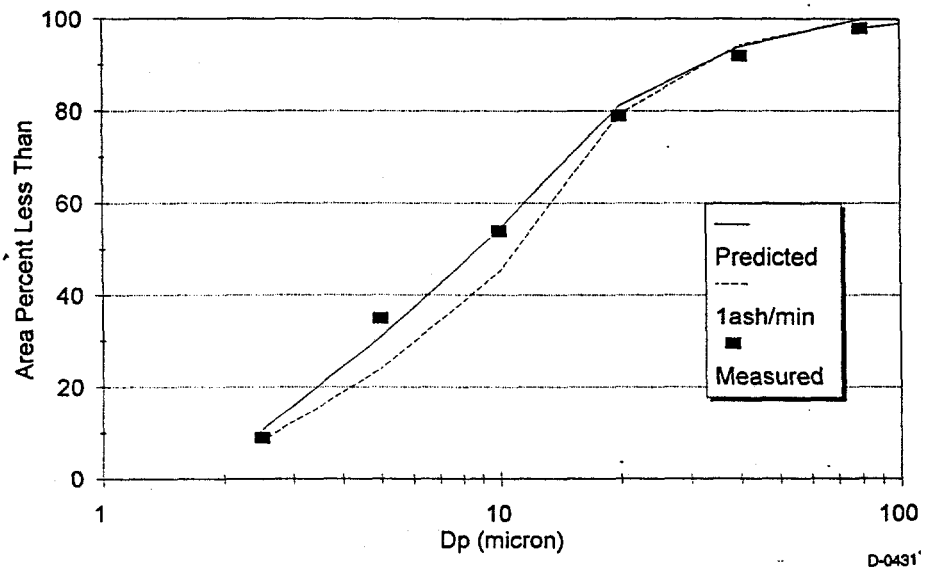

Figure 8-59. Comparison of measured and predicted ash psd - run-of-mine Pittsburgh No. 8, SR=0.6

The predicted and measured ash compositions for this coal can be seen in Figures 8-60 through 8-62. As can be seen from these figures the model is in good agreement for those conditions where mineral fragmentation is not important, but overpredicts coalescence for the high stoichiometric ratio experiments. In addition, the high Si Al category suggests that the original CCSEM analysis of this coal may have been slightly biased, as noted above.

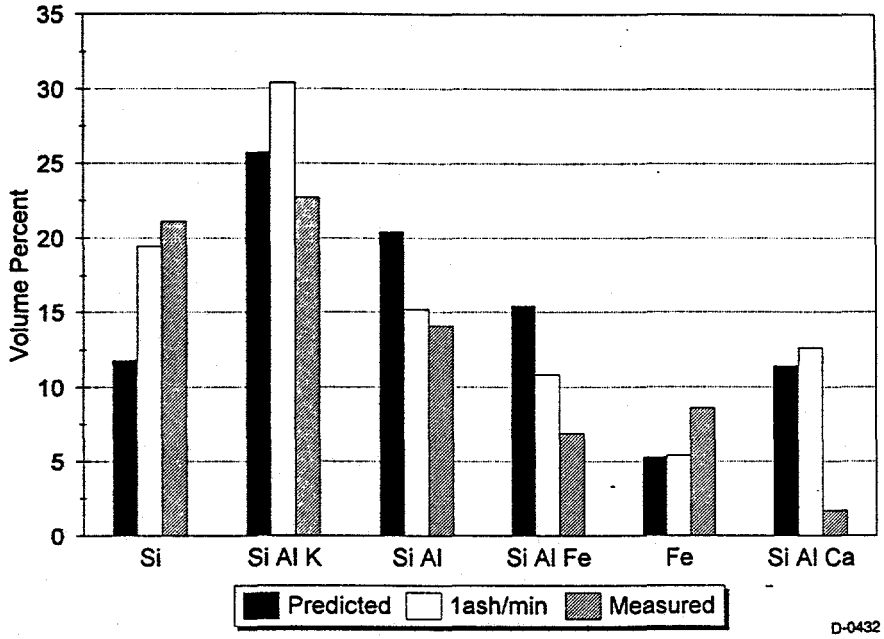

Figure 8-60. Comparison of measured and predicted ash composition - run-of-mine Pittsburgh No. 8, SR=1.2.

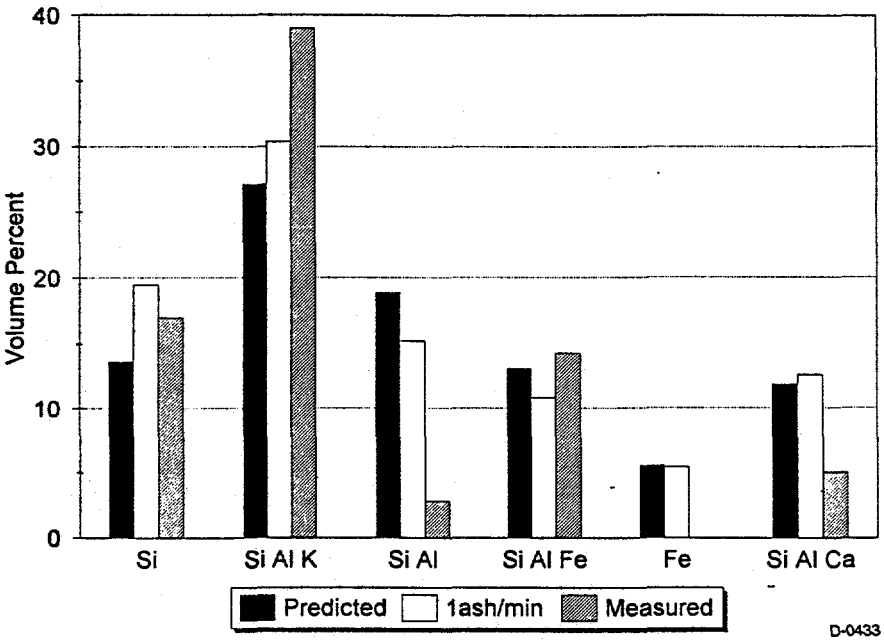

Figure 8-61. Comparison of measured and predicted ash composition - run-of-mine Pittsburgh No. 8, SR=0.9.

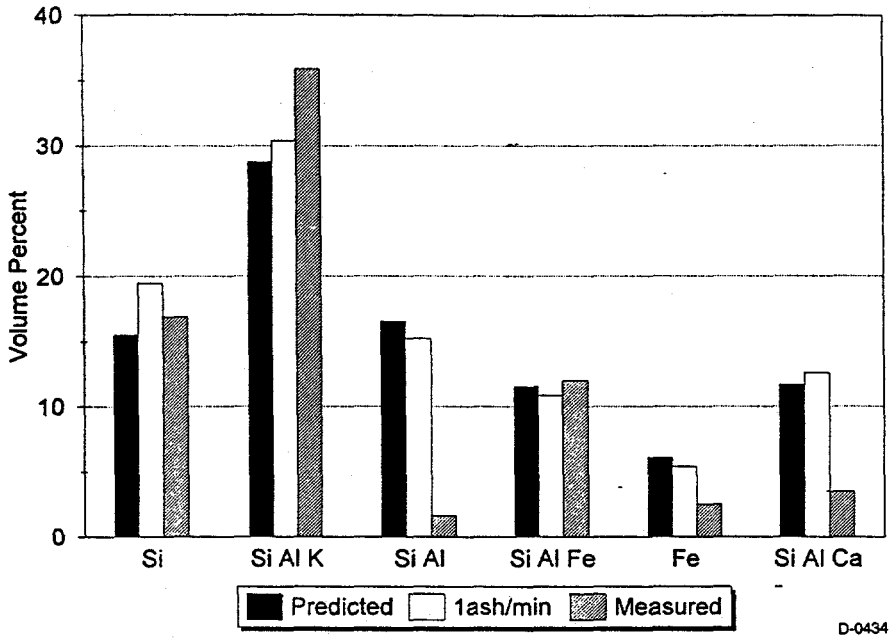

Figure 8-62. Comparison of measured and predicted ash composition - run-of-mine Pittsburgh No. 8, SR=0.6.

Black Thunder:

The final coal for which predictions were made under this program was the Black Thunder. The measured ash psd (Figure 8-63) suggests that very little coalescence occurred during burnout of this coal. The predicted ash psd (Figures 8-64 through 8-66) are in good agreement with the measurements, although the model slightly overpredicts coalescence in the stoichiometric ratio 1.2 experiments. This trend can also be seen in the ash composition predictions, Figures 8-67 through 8-69. The underprediction of the Ca category and overprediction of the Si Al Ca category suggests that the model is overpredicting mineral coalescence for this coal. Another possible explaination for the discrepancies between the model predictions and the measurements is the surface bias of the CCSEM measurements as discussed earlier in this section.

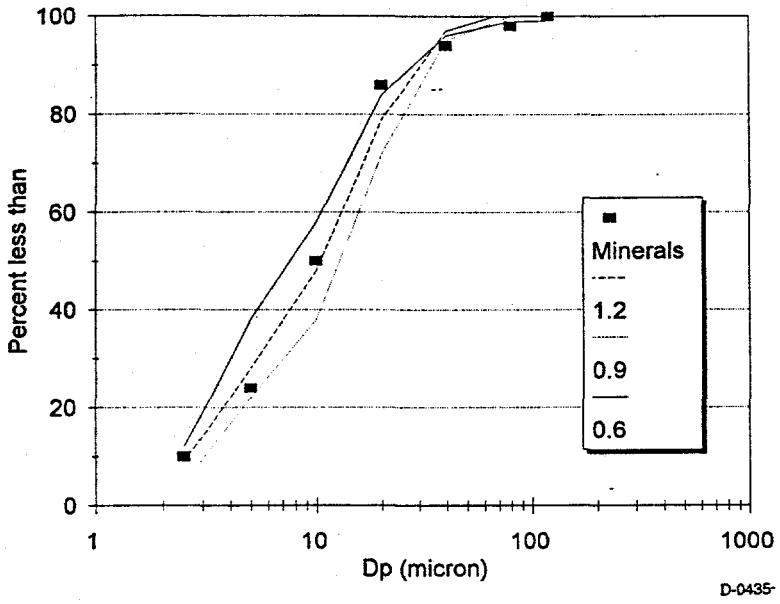

Figure 8-63. Measured ash psd (CCSEM) - Black Thunder.

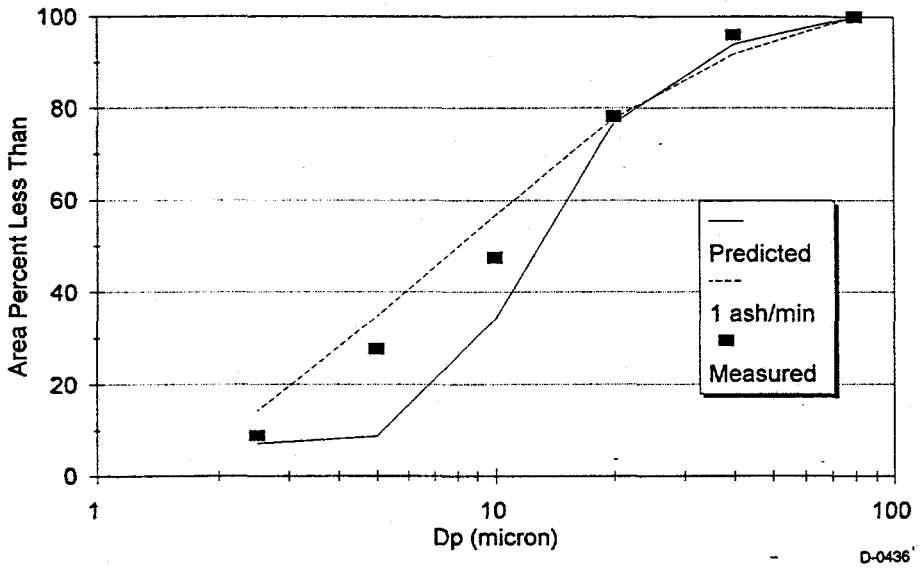

Figure 8-64. Comparison of measured and predicted ash psd - Black Thunder, SR=1.2.

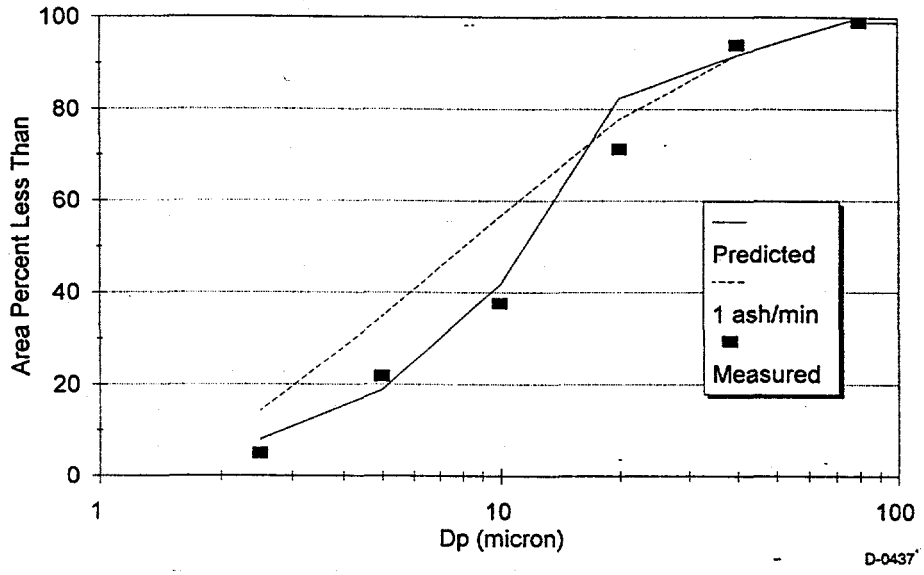

Figure 8-65. Comparison of measured and predicted ash psd - Black Thunder, SR=0.9.

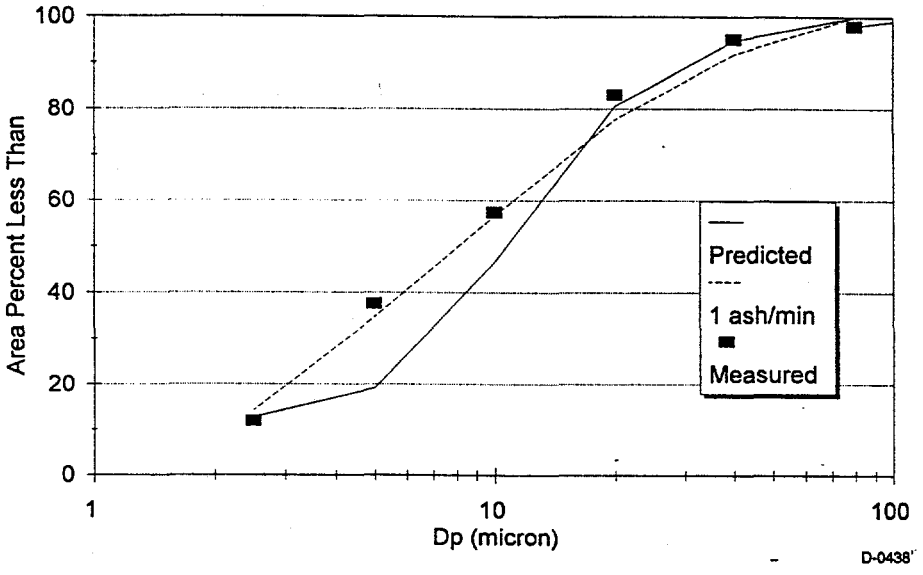

Figure 8-66. Comparison of measured and predicted ash psd - Black Thunder, SR=0.6.

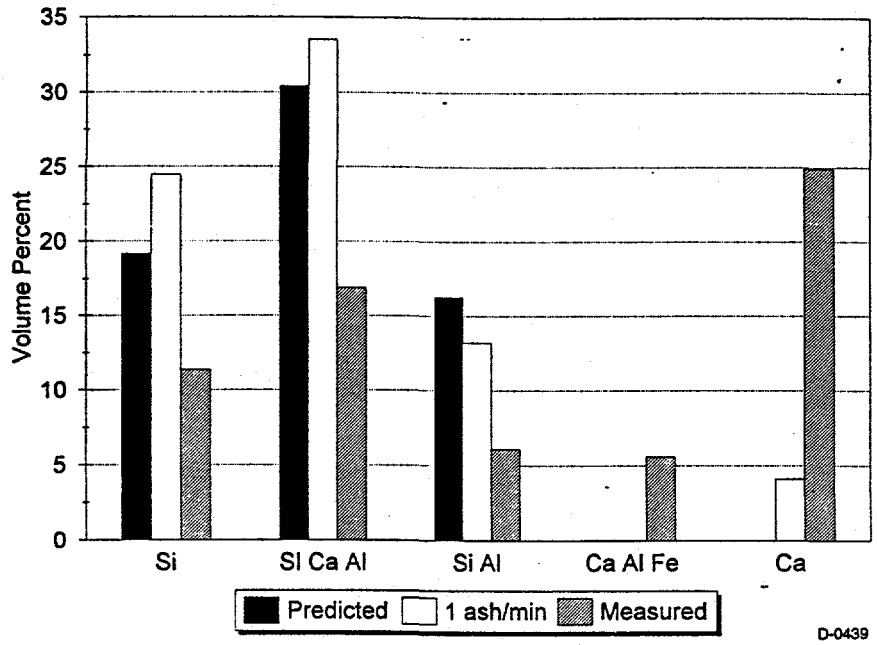

Figure 8-67. Comparison of measured and predicted ash composition - Black Thunder, SR=1.2.

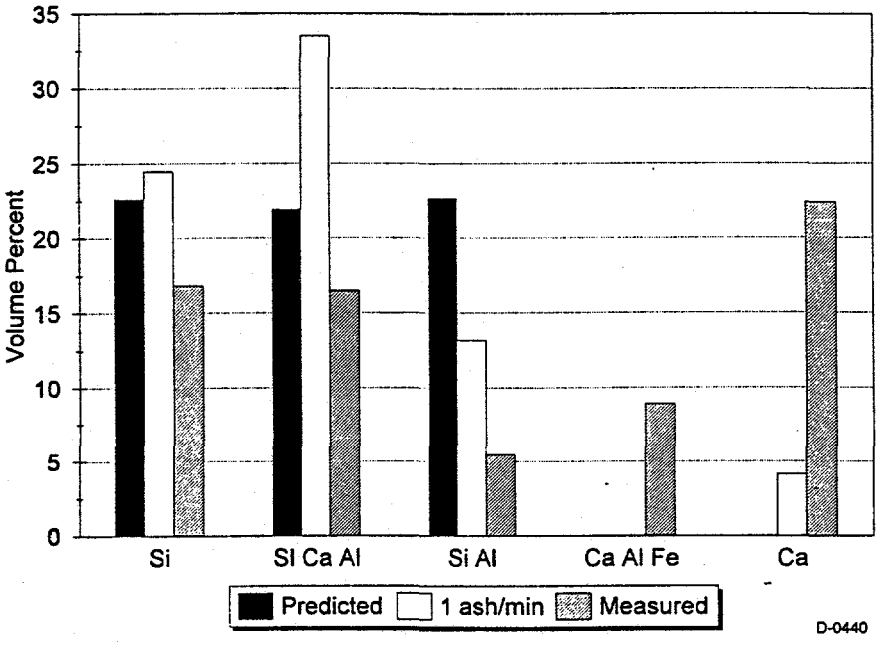

Figure 8-68. Comparison of measured and predicted ash composition - Black Thunder, SR=0.9.

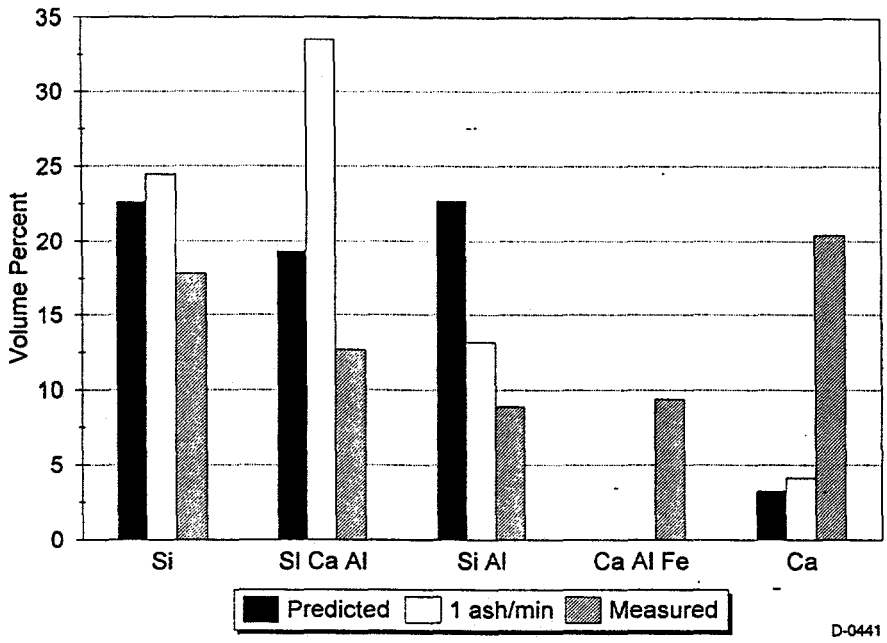

Figure 8-69. Comparison of measured and predicted ash composition - Black Thunder, SR=0.6.

8.5 References

Barta, L. E., Beér, J. M., Sarofim, A. F., Teare, J. D., and Toqan, M. A., Coal Fouling Tendency Model, *Proceedings Engineering Foundation Conference on the Impact of Ash Deposition on Coal-Fired Plants,* Solihull, UK, June, 1993.

Boni, A. et al., "Transformations of Inorganic Coal Constituents in Combustion Systems", Phase I Final Report, U.S. DoE Contract No. DE-AC22-86PC90751, 1991.

Bool, L.E., Peterson, T.W., Wendt, J.O.L, "The Partitioning of Iron During the Combustion of Pulverized Coal.", *Comb. and Flame*, Vol 99, pp.262-270, 1995.

Bool, L.E., Ph.D. Dissertation, University of Arizona, 1993.

Charon, O., Sarofim, A.F., and Beèr, J.M., *Prog. Energy Combust. Sci.* vol. 16, pp. 319, 1990.

Dryer, F.L., and Glassman, I.; "High Temperature Oxidation of CO and CH_4"; *Fourteenth Symposium (International) on Combustion*, The Combustion Institute, Pittsburgh, PA, 1973

Groves, S.J., Williamson, J., and Sanyal, A.; "Decomposition of Pyrite During Pulverized Coal Combustion", *Fuel*, 66, 1987.

Helble, J.J., et al.; "Transformations of Inorganic Coal Constituents in Combustion Systems"; Phase II Final Report, U.S. Department of Energy Contract No. DE-AC22-86PC90751, Pittsburgh Energy Technology Center, Pittsburgh, PA, 1992.

Hurt, R.H. and Hardesty, D.R., "The Rates and Mechanisms of Coal Char Combustion", Coal Combustion Science Quarterly Progress Report Oct-Dec 1991, Sandia Report SAND92-8211 UC-362, 1992.

Hurt, R.H., and Mitchell, R.E.; "Unified High-Temperature Char Combustion Kinetics for a Suite of Coals of Various Rank"; *The Twenty Fourth International Symposium on Combustion*; Sidney, Australia, June 5-10, 1992.

Hurt, R.H, and Mitchell, R.E.; "On the Combustion Kinetics of Heterogeneous Char Particle Populations";*The Twenty Fourth International Symposium on Combustion*; Sidney, Australia, June 5-10, 1992.

Westbrook, C.K., and Dryer, F.L.; "Simplified Reaction Mechanisms for the Oxidation of Hydrocarbon Fuels in Flames"; *Combust. Sci. Technol.*, 27, 1981.

Flagan, R.C. and Friedlander, S.K., Recent Developments in Aerosol Science, J. Davis ed., John Wiley and Sons, N.Y., p.25, 1978.

Freidlander, S.K., Smoke, Dust and Haze, John Wiley and Sons, NY, 1977.

Gallagher, N.B., Ph.D. Dissertation, University of Arizona, 1992.

Helble, J.J. et al., "Transformations of Inorganic Coal Constituents in Combustion Systems", Final Report submitted to the U.S. DoE/PETC, document DE/DC/90751-T15 (BE93013076). 1992.

Helble, J.J. et al., "Fundamental Study of Ash Formation and Deposition: Effect of Reducing Stoichiometry", Quarterly Report No. 2, U.S. DoE Contract No. DE-AC22-93PC92190, Pittsburgh Energy Technology Center, Pittsburgh, PA. 1993.

Hurley, J.P. and Shobert, H.H., "Ash Formation During Pulverized Subbituminous Coal Combustion. 1. Characterization of Coals, Inorganic Transformations during Early Stages of Burnout", *Energy & Fuels* **6**, 47-58 , 1992.

Joutensaari, J., Kauppinen, E.I., Jokiniemi, J.K., and Helble, J.J., "Studies on ash vaporization in power plant scale pulverized coal combustion," paper presented at the Engineering Foundation Conference on The Impact of Ash Deposition on Coal Fired Power Plants, Solihull, UK, 20-25 June, 1993.

Kang, S.G., "Fundamental Studies of Mineral Matter Transformation during Pulverized Coal Combustion: Residual Ash Formation," Ph.D. Thesis, M.I.T. Department of Chemical Engineering, Cambridge MA, 1991.

Kang, S. G., Kerstein, A. R., Helble, J. J., and Sarofim, A. F., *Aerosol Science and Technology*, Vol. 13, pp. 401-412, 1990.

Kang, S.G., Helble, J.J., Sarofim, A.F., and Béer, J.M., "Time Resolved Evolution of Fly Ash During Pulverized Coal Combustion," *Twenty-Second Symposium (Int'l) on Combustion*, The Combustion Institute, 231-238, 1988.

McElroy, M.W., Carr, R.C., Ensor, D.S., and Markowski, G.R., "Size Distribution of Fine Particles from Coal Combustion," *Science* **215**, 13-19, 1982.

Monroe, L. S., An Experimental and Modeling Study of Residual Fly Ash Formation in Combustion of a Bituminous Coal, Ph.D. Thesis, Massachusetts Institute of Technology, Cambridge, MA , 1989.

Quann, R.J.,Sc.D. Thesis, Massachusetts Institute of Technology, 1992.

Quann, R.J. and Sarofim, A.F., "Vaporization of refractory oxides during pulverized coal combustion," *Nineteenth Symposium (International) on Combustion*, The Combustion Institute, 1982.

Schmidt, E.W., Gieseke, J.A., and Allen, J.M., "Size Distribution of Fine Particulate Emissions from a Coal-Fired Power Plant," *Atm.Env.* **10**, 1065-1069, 1976.

Wilemski, G., Srinivasachar, S., and Sarofim, A. F., "Modeling of Mineral Matter Redistribution and Ash Formation in Pulverized Coal Combustion," *Proceedings of the Engineering Foundation Conference on Inorganic Transformations and Ash Deposition during Combustion*, Ed., S. A. Benson, A.S.M.E. Press, New York, pp. 545-564, 1992.

Zygarlicke, C.J., Ramanathan, M. and Erickson, T.A., "Fly Ash Particle-Size Distribution and Composition: Experimental and Phenomenological Approach," in *Inorganic Transformations and Ash Deposition During Combustion*, ed by S.A. Benson, p. 525, ASME, New York, 1992.

APPENDIX A

Comparison of Laboratory Results for Program Coals

The sample of Black Thunder coal examined in this program is a sub-sample of a larger reserve held at EERC; CCSEM analytical data for the larger EERC sample were also provided by EERC. Although not acquired on the specific sample of coal used in this program, the EERC data are of interest because 1) comparison with the University of Kentucky (UK) results provides an indication of the potential variability between labs and samples (although the individual effects of lab and sample cannot be separated), 2) the EERC CCSEM results can be used to interpret included/excluded mineralogical data for the Black Thunder coal (also provided by EERC). Another sub-sample of the Black Thunder coal was provided by EERC to Dr. John Harb of Brigham Young University (BYU) for examination in the program "Investigation of Mineral Transformations and Ash Deposition During Staged Combustion," DOE program DE-FG22-93PC93226; Dr.. Harb has characterized his particular sub-sample of Black Thunder by CCSEM at BYU. Mineral composition distributions for Black Thunder reported by EERC for the EERC sample, by UK for the PSIT sub-sample, and by BYU for the BYU sub-sample are compared in Table A-1. Aluminosilicates and quartz are the major mineral categories identified in all three samples. A calcium aluminum phosphate phase was also observed in all three samples. Examination of the reported quantities of each mineral phase suggests that the PSIT and BYU sub-samples were similar, with both having higher concentrations of quartz and kaolinite (aluminosilicate) than the EERC sample. It remains unclear whether these differences arise from actual differences in the sample, or rather from differences in analysis. Detailed comparison of compositional categories is complicated by the use of different mineral characterization schemes by UK and EERC. Differences in aluminosilicate characterization are the most pronounced. An example is the different methods of characterizing K-Al-Si containing minerals, as shown in Figure A-1. The categorization scheme used by BYU was not available for comparison. Given the differences in sample and in categorization scheme, the level of agreement among the three different CCSEM analyses suggest that kaolinite-type aluminosilicates and quartz are similarly dominant for all three Black Thunder samples.

Table A-1. Comparison of BYU-UND-UK Black Thunder Coal

	Weight % of Mineral Matter		
	UND, QR 3	UK, QR 3	BYU
Quartz	24.1	26.6	30
Iron Ox/Carb	4.6	0	6
Kaol/AlSi	29.1	38.2*	41
Montmorill	4.6	3.9	3
Pyrite	4.7	1.9	1
CaAl Phos	9.8	6.2	7
Other	16.0	23.2	18

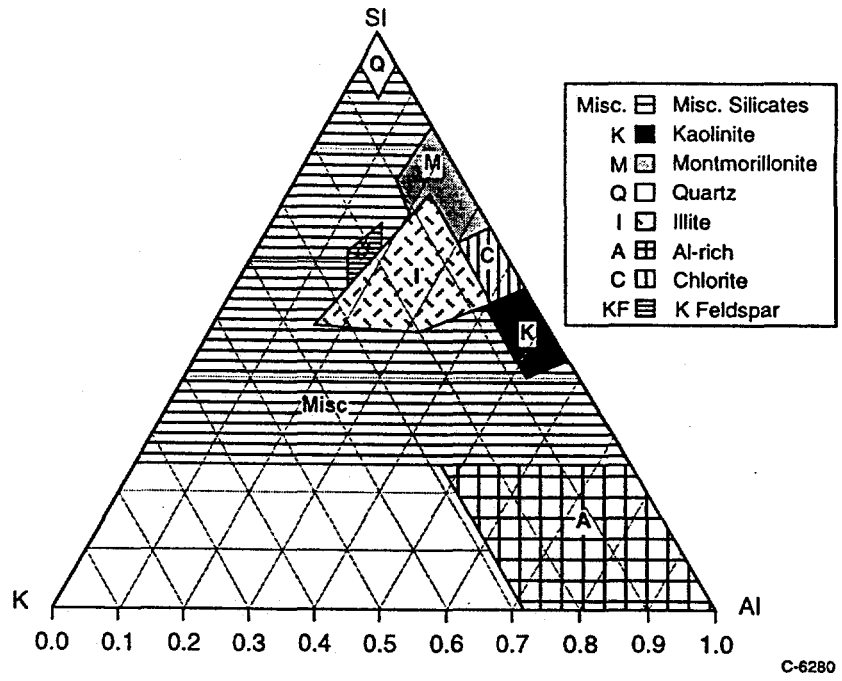

(a)

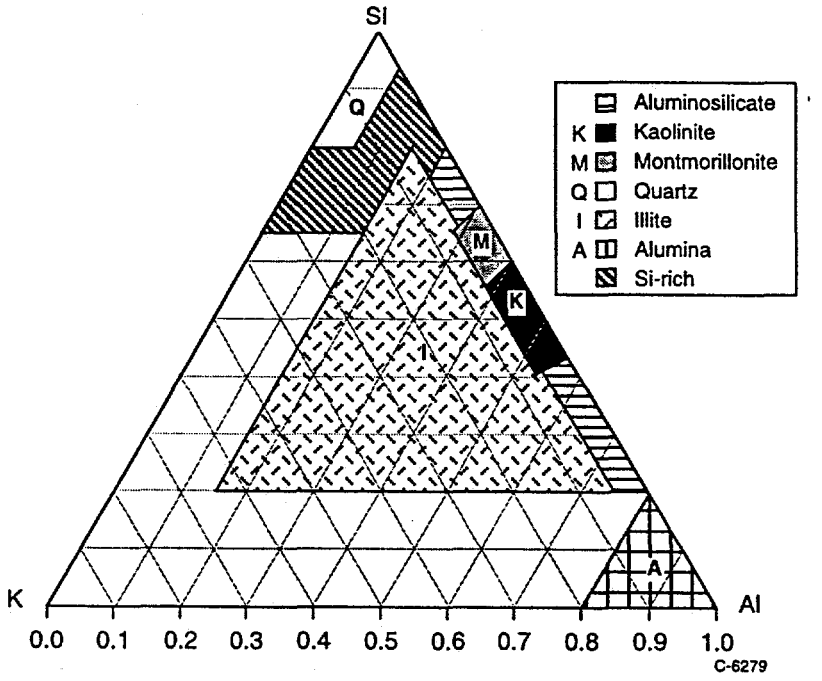

(b)

Figure A-1. Mineral category definitions for K-Al-Si minerals by CCSEM analysis. (a) UK classification scheme. (b) EERC classification scheme.

The overall mineral size distributions provided by CCSEM can be compared without regard to mineral categorization scheme. As seen in Figure A-2, a comparison of EERC and UK measured mineral size distributions, trends were similar although the distributions were not identical. Standard deviations of mineral weight fractions of 20% have been reported between laboratories analyzing the same sample (Casuccio et al., 1990); similar uncertainty is to be expected with mineral size distribution measurements. It is therefore impossible to determine whether the differences observed in Figures A-2 and A-3 are the results or sample variation or are simply inter-laboratory differences. The overall similarities of mineral size and composition distributions, however, suggest that the PSIT sub-sample is similar to the BYU sub-sample and to the sample being held at EERC. Chemical fractionation data and included/excluded CCSEM data provided by EERC for the larger sample are therefore relevant to understanding the combustion behavior of the PSIT sub-sample.

A portion of the PSIT sample was also sent to a commercial analytical laboratory, Microbeam Technologies Inc. (MTI) of Grand Forks, ND, for included/excluded mineral analysis. Standard CCSEM analysis was also conducted by MTI. The size distribution derived from the MTI included/excluded analysis was similar to that reported by UK. The standard CCSEM analysis reported by MTI, however, suggested a considerably smaller mineral size distribution. To resolve this discrepancy, MTI re-analyzed the sample using standard CCSEM analysis along with a ZAF correction of the composition data (for atomic number, absorption, and fluorescence). The results of these four size distribution analyses are shown in Figure A-4. The ZAF-corrected MTI size distribution data fell between the two earlier MTI analyses, and were close to the UK data. Comparing mineral composition distributions (Table A-2), the MTI included/excluded analysis was closest to the UK analysis.

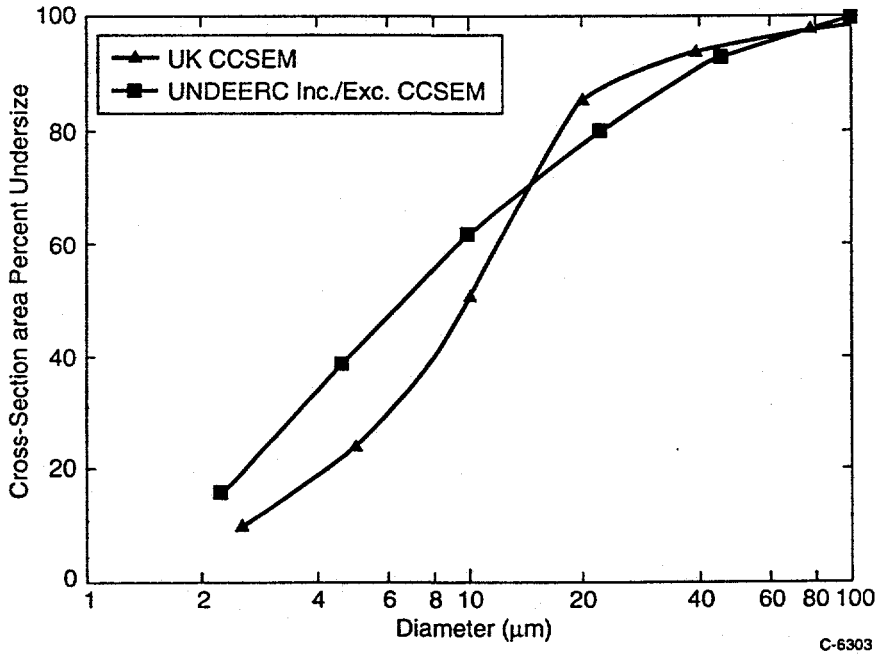

Figure A-2. Mineral size distributions for Black Thunder coal samples analyzed by UK (PSIT sample) and EERC (EERC sample).

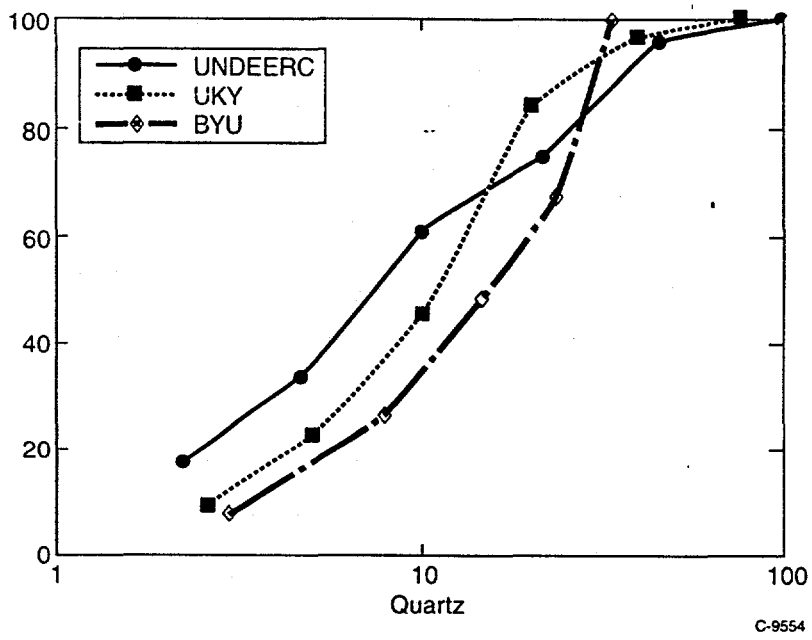

Figure A-3. Mineral size distributions for the mineral quartz in Black Thunder coal, analyzed by UK (PSIT sample), EERC (EERC sample), and BYU (BYU sample).

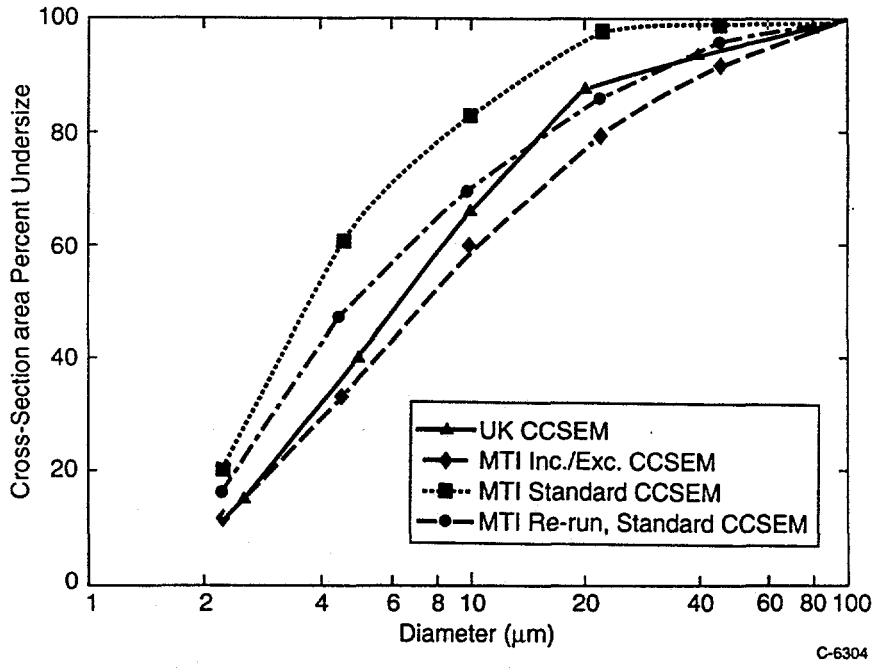

Figure A-4 CCSEM-measured mineral size distributions for the run-of-mine Pittsburgh No. 8 coal.

Table A-2. Comparison of Pittsburgh No. 8 CCSEM Mineral Data -- UK and MTI (results expressed in wt%)

Mineral	UK	MTI (Inc/exc Analysis)	MTI (Std Analysis)	MTI (Repeat)
Quartz	21.7	16.3	18.7	8.7
Kaolinite	6.4	12.0	11.0	7.8
Montmorillonite	0.2	3.9	4.8	4.2
K-Al silicate*	22.0	27.4	25.3	32.0
Pyrite	11.9	11.7	8.3	7.6
Misc. silicates	22.7	10.0	11.0	13.4
(Kaol + Mis. sil.)	29.1	22.0	22.0	21.2
*"Illite", with more restrictive chemical definition, in UK categorization.				

A small sub-sample taken from the PSIT washed Pittsburgh No. 8 was provided to Dr. Fraser Wigley of Imperial College. As part of a collaborative effort, Dr. Wigley provided CCSEM analysis of the PSIT Pittsburgh No. 8. A comparison of the UK and Wigley CCSEM-derived mineral size distributions are shown in Figure A-5. Good agreement between the two laboratories was noted. A complete set of data provided by Dr., Wigley for this coal is contained in Appendix B.

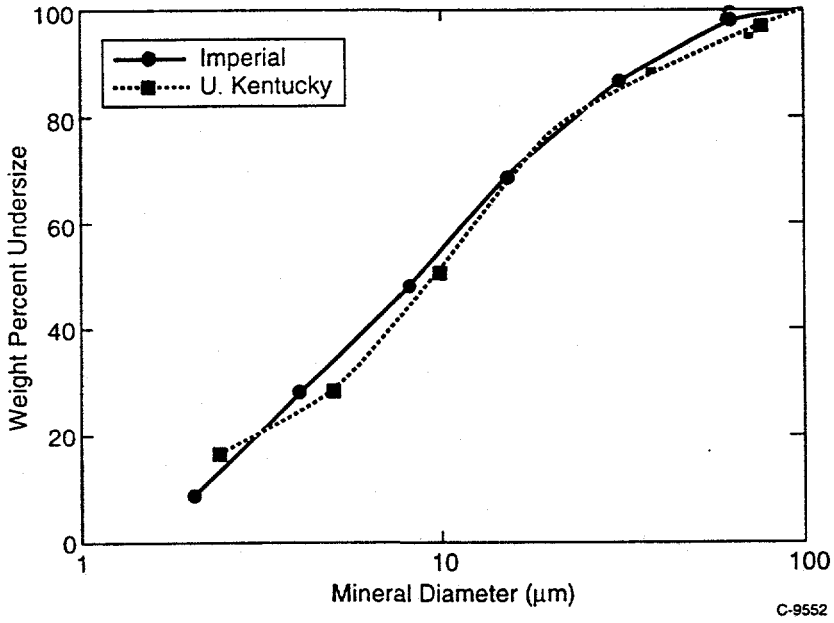

Figure A-5. CCSEM mineral size distributions for the PSIT washed Pittsburgh No. 8 bituminous coal measured by Imperial College and the University of Kentucky.

A sample of this Pittsburgh No. 8 coal was also provided to Dr. John Harb of BYU by Mr. Scott Smouse of DOE/PETC. Subsequent CCSEM analysis of the BYU sample was conducted at BYU. Results of this analysis are reported in Table A-3 (Harb, 1994). Data are reported only for those phases for which direct correspondence exists between UK and BYU mineral categories.

Table A-3. CCSEM analysis of BYU and PSIT samples of washed Pittsburgh #8, BYU sample analyzed at BYU; PSIT sample analyzed at UK (weight percentage of mineral matter)

Mineral	PSIT/UK Sample	BYU/BYU Sample
Quartz	9.1	7.8
Aluminosilicate (kaolinite)	23.2	24.8
K aluminosilicate (illite)	9.0	11.1
Pyrite	27.2	29.7
Calcite/CaO	2.8	5.8

A comparison of the size distributions for these two samples of Silverdale is provided in Figure A-6. The PSIT sample appears to have a smaller size distribution than the sample examined by Imperial College. It cannot be determined whether this is a sample difference or a laboratory difference. Given the close agreement of the two Pittsburgh No. 8 analysis discussed earlier (see Figure A-5), it is likely that the procedures used at Imperial College and UK yield similar data. It is therefore likely that the differences observed in Figure A-6 are actual sample differences.

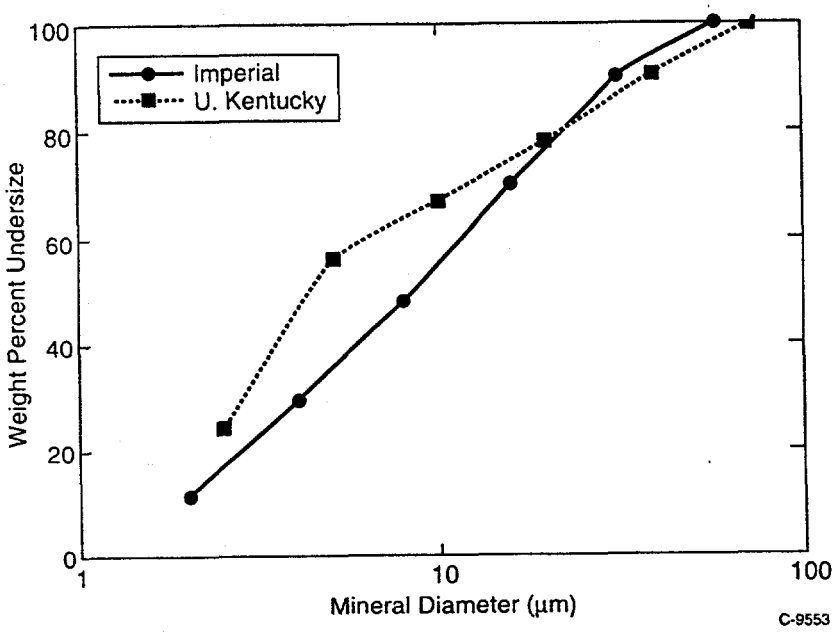

Figure A-6. CCSEM mineral size distributions for Silverdale bituminous coal as measured by Imperial College and the University of Kentucky. Each laboratory examined a different sample of coal.

3.7 References

Casuccio, G.S., Gruelich, F.A., Hamburg, G., Huggins, F.E., Nissen, D.A., and Vleeskens, J.M. (1990), Coal Mineral Analysis: A Check on Inter-Laboratory Agreement, *Scanning Microscopy* 4(2), 227-236.

Harb, J.N. (1994), "Investigation of Mineral Transformations and Ash Deposition During Staged Combustion," Quarterly Report for the period July 1, 1994 to September 30, 1994, submitted to the US DOE/PETC under contract number DE-FG22-93PC93226.

Average mineral properties for Pittsburgh pf

Average particle properties

Number	Wt %	Porosity	Shape	SiO2	Al2O3	Fe2O3	CaO	MgO	Na2O	K2O	TiO2	Mn3O4	P2O5	SO3
1268	100.00	0.04	2.14	46.73	20.70	11.34	3.43	1.39	1.20	2.92	1.93	0.54	0.40	9.42

Average mineral properties by chemical type

Type	*Number*	Wt %	Porosity	Shape	SiO2	Al2O3	Fe2O3	CaO	MgO	Na2O	K2O	TiO2	Mn3O4	P2O5	SO3
Alsil	*821*	59.61	0.05	2.40	55.56	31.73	3.40	0.40	1.02	0.60	3.97	0.98	0.32	0.41	1.60
Ca+Fe	*17*	4.86	0.00	1.45	0.90	0.60	25.99	52.75	12.98	0.06	0.04	0.14	2.46	0.12	3.97
Ca-alsil	*13*	0.48	0.00	2.26	20.00	9.86	2.96	29.63	0.31	0.42	0.95	0.87	0.30	3.81	30.90
Ca-rich	*10*	0.51	0.00	2.24	2.01	1.09	0.97	59.65	0.53	0.27	1.87	0.25	0.67	2.46	30.24
Fe-alsil	*74*	4.22	0.03	1.89	19.00	12.13	30.10	0.52	1.19	0.81	1.11	0.78	0.35	0.78	33.23
Fe-rich	*116*	13.20	0.01	1.60	1.18	0.64	49.36	0.26	0.32	0.88	0.16	0.15	0.28	0.19	46.59
non-CFAS	*44*	3.75	0.11	1.68	13.94	7.64	3.16	2.77	0.62	16.88	9.94	31.75	3.85	0.70	8.76
Si-rich	*173*	13.37	0.02	1.95	89.63	6.16	0.94	0.18	0.23	0.38	0.72	0.65	0.19	0.24	0.69

Average mineral properties by size

Size (µm)	*Number*	Wt %	Porosity	Shape	SiO2	Al2O3	Fe2O3	CaO	MgO	Na2O	K2O	TiO2	Mn3O4	P2O5	SO3
1 - 2	*360*	9.27	0.00	2.48	44.99	23.94	10.94	1.50	1.02	1.93	3.21	1.53	0.37	0.74	9.82
2 - 4	*214*	18.23	0.01	2.40	48.35	24.68	8.60	1.32	0.89	2.87	3.27	1.52	0.35	0.57	7.59
4 - 8	*157*	18.96	0.04	2.26	49.07	22.94	8.92	0.42	0.71	0.61	2.78	1.02	0.24	0.37	12.93
8 - 16	*433*	22.58	0.01	2.15	47.98	19.00	11.08	2.66	1.04	0.81	2.55	1.49	0.39	0.45	12.55
16 - 32	*91*	16.20	0.08	2.02	59.26	23.12	5.54	1.00	0.74	0.40	2.98	2.16	0.25	0.24	4.32
32 - 64	*12*	10.92	0.13	1.65	36.68	14.57	24.96	0.26	0.70	1.23	4.03	5.75	1.60	0.14	10.06
64 - 128	*1*	3.83	0.00	1.30	0.08	0.25	24.52	56.91	14.80	0.00	0.00	0.00	2.36	0.00	1.07

F. Wigley, Imperial College

Average mineral properties for Pittsburgh pf

Average mineral properties by chemical type and size

Type	Size (µm)	*Number*	Wt %	Porosity	Shape	SiO2	Al2O3	Fe2O3	CaO	MgO	Na2O	K2O	TiO2	Mn3O4	P2O5	SO3
Alsil	1 - 2	*246*	6.08	0.00	2.80	52.39	31.95	4.07	0.69	1.12	0.77	4.12	1.24	0.39	0.56	2.69
Alsil	2 - 4	*152*	12.71	0.02	2.58	53.22	33.02	3.82	0.42	1.04	0.55	4.07	0.75	0.30	0.46	2.35
Alsil	4 - 8	*103*	12.60	0.05	2.46	55.30	32.42	3.48	0.31	0.94	0.45	3.94	1.11	0.23	0.40	1.42
Alsil	8 - 16	*255*	12.43	0.02	2.41	56.33	31.17	3.27	0.42	1.08	0.59	4.03	1.13	0.29	0.46	1.23
Alsil	16 - 32	*59*	10.63	0.09	2.18	57.79	31.15	2.86	0.40	1.01	0.45	3.94	0.95	0.26	0.26	0.93
Alsil	32 - 64	*6*	5.16	0.19	1.79	59.27	29.22	2.82	0.16	0.94	1.24	3.57	0.60	0.73	0.30	1.15
Ca+Fe	1 - 2	*1*	0.03	0.00	1.37	4.74	3.29	25.39	23.45	0.05	0.38	0.32	0.00	0.75	0.14	41.48
Ca+Fe	2 - 4	*2*	0.32	0.00	2.01	2.56	1.71	45.70	30.07	0.39	0.07	0.16	0.95	2.97	0.64	14.77
Ca+Fe	4 - 8	*3*	0.08	0.00	2.05	8.81	5.45	20.25	31.91	3.09	0.00	0.53	1.75	3.63	0.60	23.98
Ca+Fe	8 - 16	*10*	0.59	0.00	2.05	3.98	1.41	25.58	42.48	10.10	0.42	0.15	0.39	2.69	0.52	12.28
Ca+Fe	64 - 128	*1*	3.83	0.00	1.30	0.08	0.25	24.52	56.91	14.80	0.00	0.00	0.00	2.36	0.00	1.07
Ca-alsil	1 - 2	*7*	0.16	0.00	1.82	16.59	10.84	2.02	25.07	0.31	0.44	1.45	0.83	0.41	0.55	41.49
Ca-alsil	2 - 4	*3*	0.16	0.00	3.41	16.97	12.45	1.54	27.73	0.47	0.57	0.70	0.23	0.04	8.94	30.37
Ca-alsil	8 - 16	*3*	0.16	0.00	1.54	26.65	6.17	5.38	36.33	0.15	0.26	0.68	1.56	0.44	1.94	20.43
Ca-rich	1 - 2	*2*	0.05	0.00	2.25	0.14	0.13	0.05	46.76	0.62	0.13	0.68	0.84	0.62	21.80	28.24
Ca-rich	2 - 4	*1*	0.04	0.00	2.75	3.49	2.43	0.39	34.85	0.33	0.53	0.66	0.07	1.81	0.78	54.65
Ca-rich	8 - 16	*6*	0.31	0.00	2.32	1.53	1.17	1.52	56.63	0.55	0.15	2.77	0.26	0.74	0.24	34.43
Ca-rich	16 - 32	*1*	0.11	0.00	1.76	3.72	0.74	0.00	85.07	0.50	0.61	0.23	0.00	0.00	0.50	8.62
Fe-alsil	1 - 2	*40*	1.08	0.00	1.98	22.90	16.42	29.80	0.48	1.52	1.05	1.64	1.62	0.37	0.94	23.27
Fe-alsil	2 - 4	*9*	0.93	0.00	2.05	18.33	12.78	35.31	0.98	1.88	1.05	1.18	1.20	0.35	0.87	26.07
Fe-alsil	4 - 8	*8*	1.00	0.11	1.66	13.91	10.18	29.05	0.19	0.42	0.71	0.78	0.02	0.43	0.51	43.81
Fe-alsil	8 - 16	*14*	0.75	0.00	1.96	19.34	11.21	25.85	0.61	1.45	0.70	1.06	0.48	0.17	0.88	38.26
Fe-alsil	16 - 32	*3*	0.46	0.07	1.75	21.66	6.60	29.43	0.24	0.31	0.16	0.58	0.06	0.41	0.64	39.91
Fe-rich	1 - 2	*24*	0.82	0.00	1.77	2.14	1.51	50.03	0.38	0.32	0.89	0.25	0.35	0.38	0.63	43.12
Fe-rich	2 - 4	*13*	1.31	0.00	1.74	1.18	0.81	43.73	0.28	0.26	0.64	0.36	0.28	0.21	0.32	51.92
Fe-rich	4 - 8	*14*	2.74	0.01	1.69	0.35	0.08	33.69	0.08	0.11	0.24	0.09	0.10	0.18	0.24	64.85
Fe-rich	8 - 16	*58*	3.97	0.01	1.59	1.43	0.70	42.04	0.18	0.17	0.60	0.21	0.19	0.39	0.21	53.88
Fe-rich	16 - 32	*4*	0.77	0.05	1.28	1.70	1.06	47.27	0.09	0.11	0.35	0.17	0.26	0.44	0.07	48.49
Fe-rich	32 - 64	*3*	3.57	0.01	1.52	1.21	0.63	71.88	0.50	0.71	1.87	0.05	0.02	0.22	0.00	22.90
non-CFAS	1 - 2	*13*	0.32	0.00	1.78	14.14	8.39	3.96	5.28	1.23	34.53	6.21	11.80	0.28	1.33	12.86
non-CFAS	2 - 4	*9*	0.83	0.02	1.59	11.65	5.88	1.22	1.62	0.36	51.43	5.76	18.54	0.38	0.77	2.40

F. Wigley, Imperial College

Average mineral properties by chemical type and size

Type	Size (μm)	*Number*	Wt %	Porosity	Shape	SiO2	Al2O3	Fe2O3	CaO	MgO	Na2O	K2O	TiO2	Mn3O4	P2O5	SO3
non-CFAS	4 - 8	*5*	0.12	0.00	2.35	20.55	15.32	1.11	4.48	0.54	23.07	2.54	24.35	1.24	0.56	6.25
non-CFAS	8 - 16	*11*	0.57	0.03	2.02	20.15	13.00	6.60	7.75	2.26	11.04	4.20	27.27	1.44	2.18	4.12
non-CFAS	16 - 32	*5*	0.67	0.06	2.09	28.34	17.57	8.48	3.56	0.40	0.58	4.15	34.02	0.13	0.41	2.37
non-CFAS	32 - 64	*1*	1.24	0.28	1.26	4.09	0.00	0.00	0.00	0.00	0.00	20.23	47.36	10.49	0.00	17.82
Si-rich	1 - 2	*27*	0.74	0.00	1.87	88.13	5.99	1.77	0.22	0.37	0.26	0.71	0.84	0.22	0.35	1.15
Si-rich	2 - 4	*25*	1.92	0.00	2.13	90.34	5.06	0.88	0.20	0.23	0.28	0.69	0.46	0.30	0.50	1.05
Si-rich	4 - 8	*24*	2.41	0.02	2.14	89.32	5.65	0.87	0.12	0.23	0.72	0.69	0.77	0.13	0.25	1.23
Si-rich	8 - 16	*76*	3.80	0.01	1.96	90.67	5.48	0.78	0.23	0.20	0.37	0.67	0.65	0.22	0.26	0.48
Si-rich	16 - 32	*19*	3.56	0.06	1.72	88.54	7.81	0.94	0.15	0.20	0.26	0.88	0.52	0.17	0.10	0.43
Si-rich	32 - 64	*2*	0.95	0.04	1.92	90.05	6.39	1.20	0.21	0.29	0.33	0.41	1.07	0.00	0.00	0.03

Particle properties:

Type - Assigned using the following scheme

non-CFAS - (CaO + Fe2O3 + Al2O3 + SiO2) < 80 wt%, otherwise

Si-rich - SiO2' > 80 wt%

Fe-rich - Fe2O3' > 80 wt%

Ca-rich - CaO' > 80 wt%

Alsil - (Al2O3' + SiO2') > 80 wt% and SiO2' < 80 wt%

Ca-alsil - (Al2O3' + SiO2') < 80 wt% and CaO' < 80 wt% and Fe2O3' < 20 wt% and CaO' > Fe2O3'

Fe-alsil - (Al2O3' + SiO2') < 80 wt% and Fe2O3' < 80 wt% and CaO' < 20 wt% and Fe2O3' > CaO'

Ca+Fe - CaO' > 20 wt% and Fe2O3' > 20 wt%

where CaO', Fe2O3', Al2O3' and SiO2' are normalised to (CaO' + Fe2O3' + Al2O3' + SiO2')=100%.

Size - The diameter of a circle with the same area as the analysed cross-section of the particle.

Number - Number of particles analysed.

Wt% - Mass percentage of particles analysed, using an estimated density.

Porosity - Area fraction of pores seen in cross-section (should be treated with caution).

Shape - Aspect ratio of particle cross-section (should be treated with caution).

Viscosity - Estimated using the scheme of Kalmanovitch and Frank (1988) (takes no account of the physical state of the phase, and should be treated with caution).

F. Wigley, Imperial College

Number of minerals by size and chemical type

Size (µm)	Fe-rich	Fe-alsil	Alsil	Ca-alsil	Ca-rich	Si-rich	Ca+Fe	non-CFAS
1 - 2	24	40	246	7	2	27	1	13
2 - 4	13	9	152	3	1	25	2	9
4 - 8	14	8	103			24	3	5
8 - 16	58	14	255	3	6	76	10	11
16 - 32	4	3	59		1	19		5
32 - 64	3		6			2		1
64 - 128							1	

Mass abundance (wt%) of minerals by size and chemical type

Size (µm)	Fe-rich	Fe-alsil	Alsil	Ca-alsil	Ca-rich	Si-rich	Ca+Fe	non-CFAS
1 - 2	0.82	1.08	6.08	0.16	0.05	0.74	0.03	0.32
2 - 4	1.31	0.93	12.71	0.16	0.04	1.92	0.32	0.83
4 - 8	2.74	1.00	12.60			2.41	0.08	0.12
8 - 16	3.97	0.75	12.43	0.16	0.31	3.80	0.59	0.57
16 - 32	0.77	0.46	10.63		0.11	3.56		0.67
32 - 64	3.57		5.16			0.95		1.24
64 - 128							3.83	

Average porosity of minerals by size and chemical type

Size (µm)	Fe-rich	Fe-alsil	Alsil	Ca-alsil	Ca-rich	Si-rich	Ca+Fe	non-CFAS
1 - 2	0.00	0.00	0.00	0.00	0.00	0.00	0.00	0.00
2 - 4	0.00	0.00	0.02	0.00	0.00	0.00	0.00	0.02
4 - 8	0.01	0.11	0.05			0.02	0.00	0.00
8 - 16	0.01	0.00	0.02	0.00	0.00	0.01	0.00	0.03
16 - 32	0.05	0.07	0.09		0.00	0.06		0.06
32 - 64	0.01		0.19			0.04		0.28
64 - 128							0.00	

Average shape of minerals by size and chemical type

Size (µm)	Fe-rich	Fe-alsil	Alsil	Ca-alsil	Ca-rich	Si-rich	Ca+Fe	non-CFAS
1 - 2	1.77	1.98	2.80	1.82	2.25	1.87	1.37	1.78
2 - 4	1.74	2.05	2.58	3.41	2.75	2.13	2.01	1.59
4 - 8	1.69	1.66	2.46			2.14	2.05	2.35
8 - 16	1.59	1.96	2.41	1.54	2.32	1.96	2.05	2.02
16 - 32	1.28	1.75	2.18		1.76	1.72		2.09
32 - 64	1.52		1.79			1.92		1.26
64 - 128							1.30	

F. Wigley, Imperial College

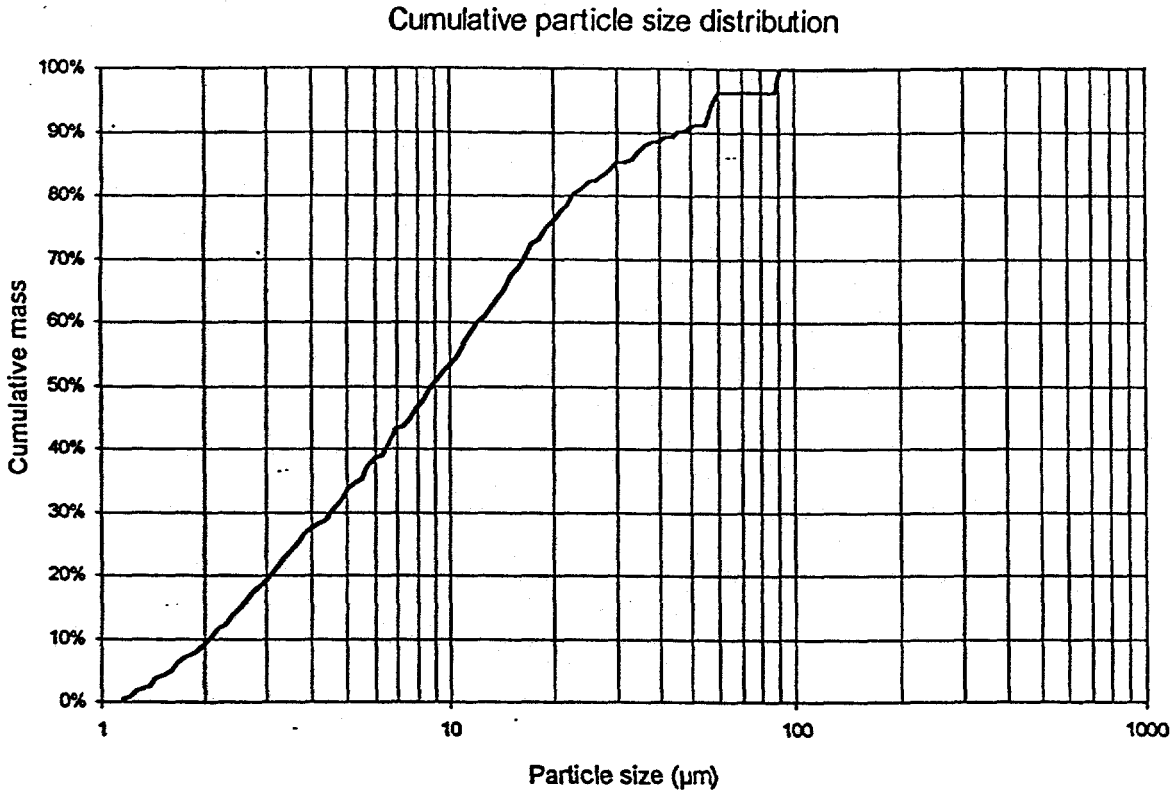

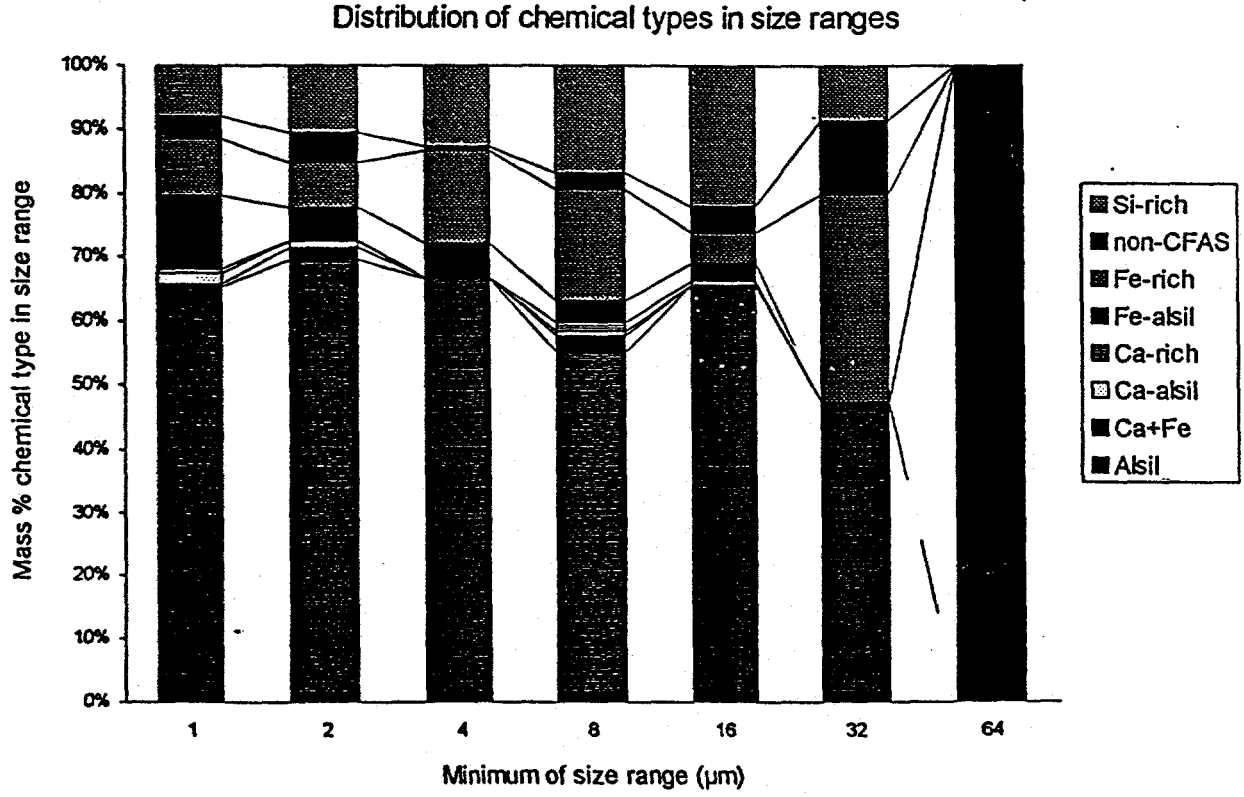

F. Wigley, Imperial College

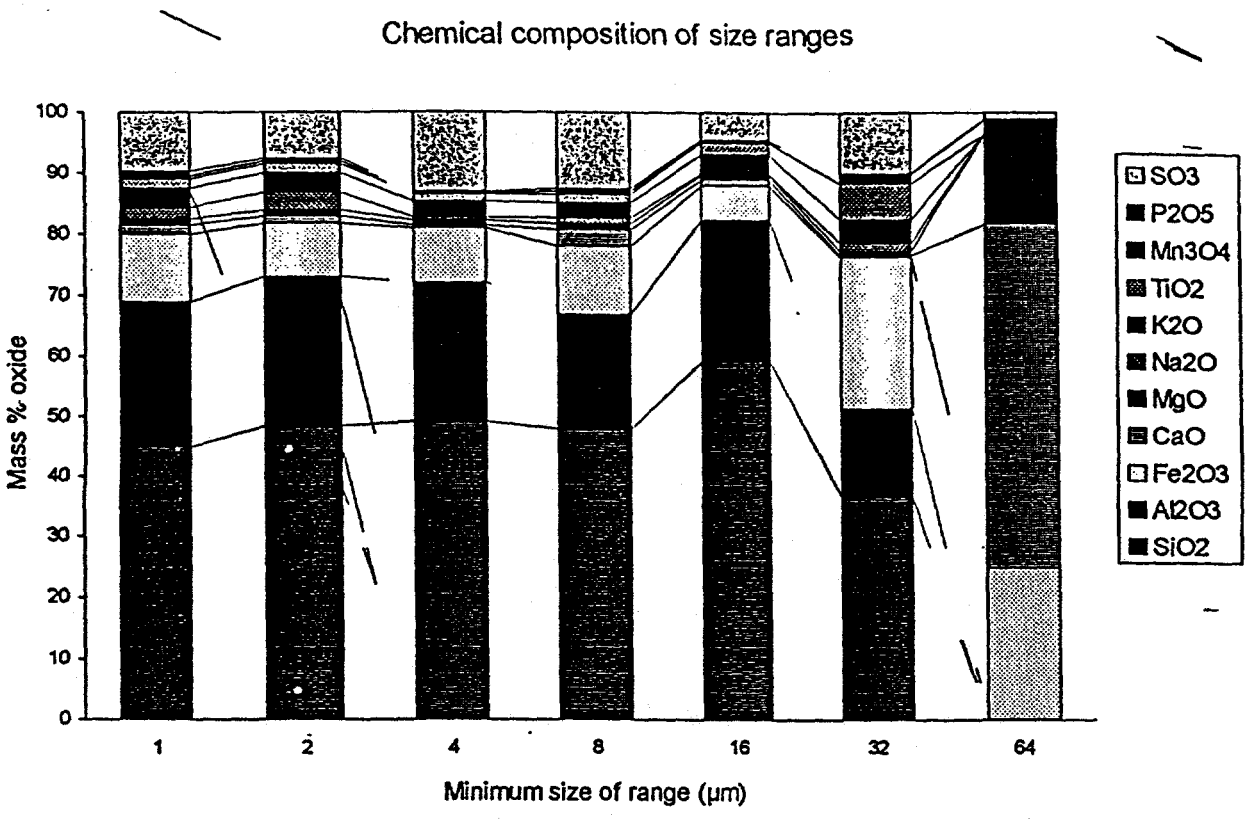

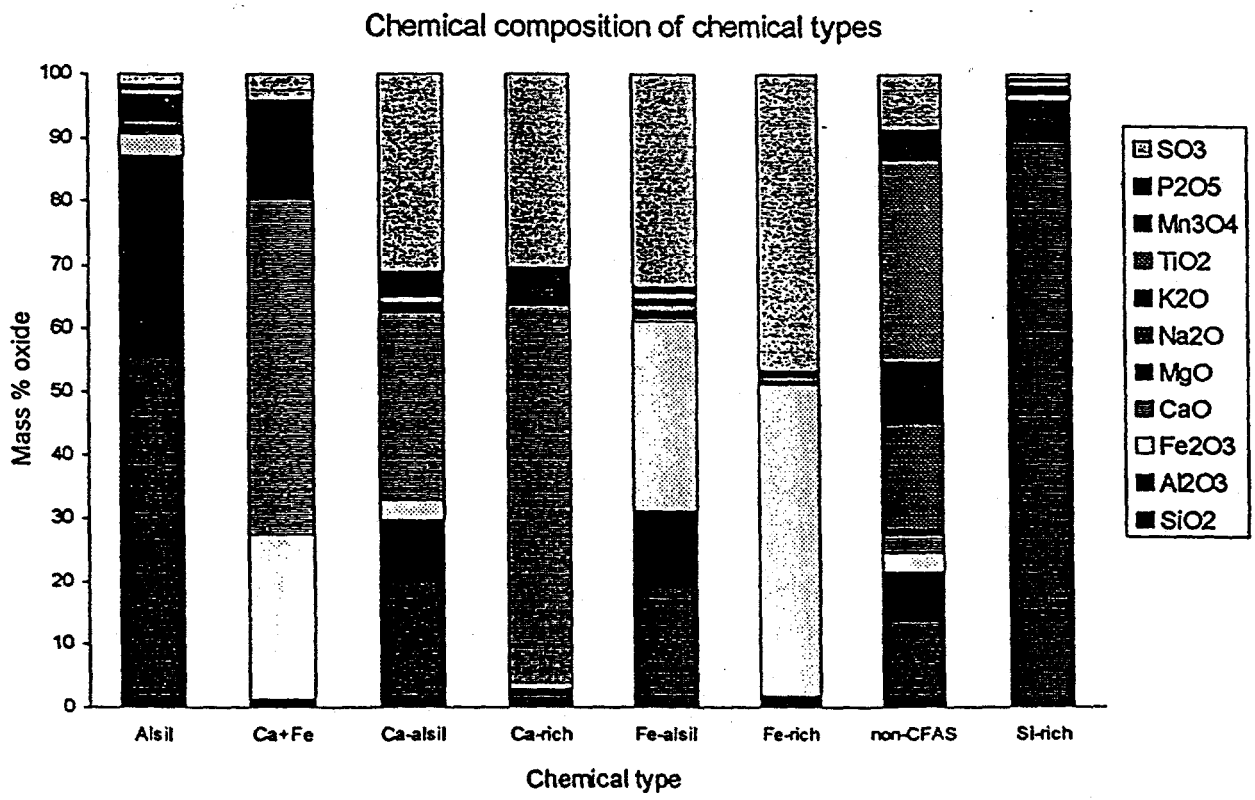

F. Wigley, Imperial College

Estimated cumulative viscosity distribution at 1250C

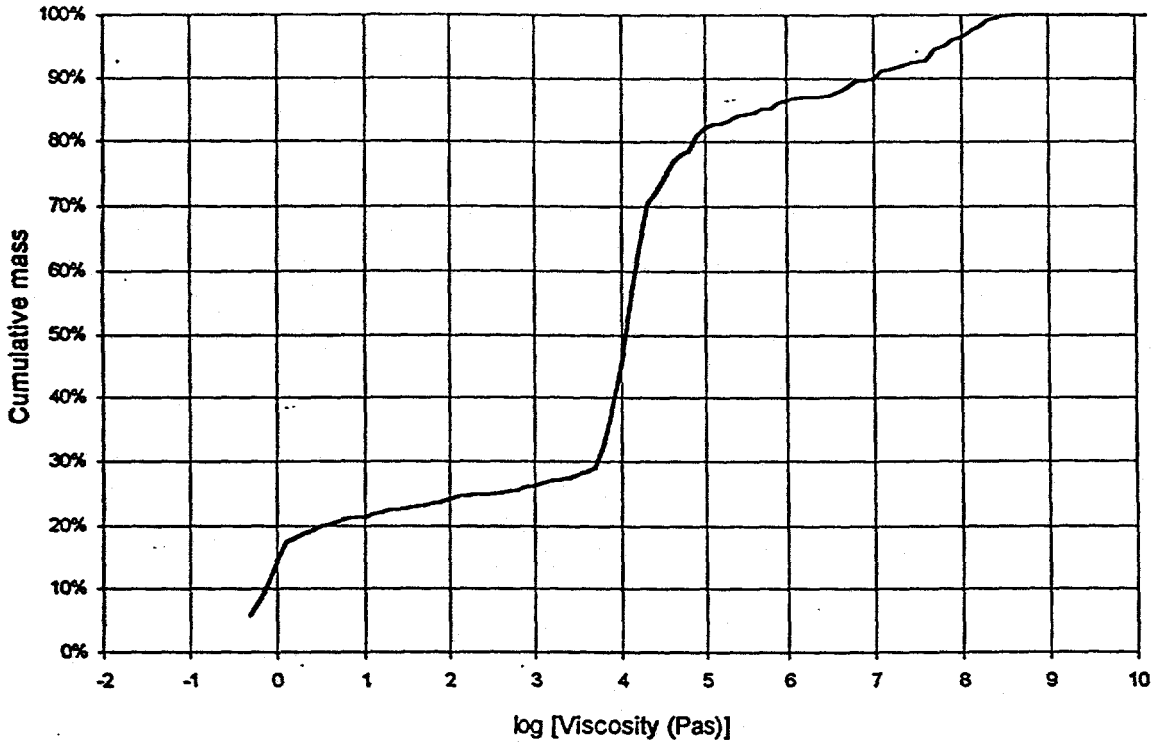

Estimated viscosity distribution at 1250C

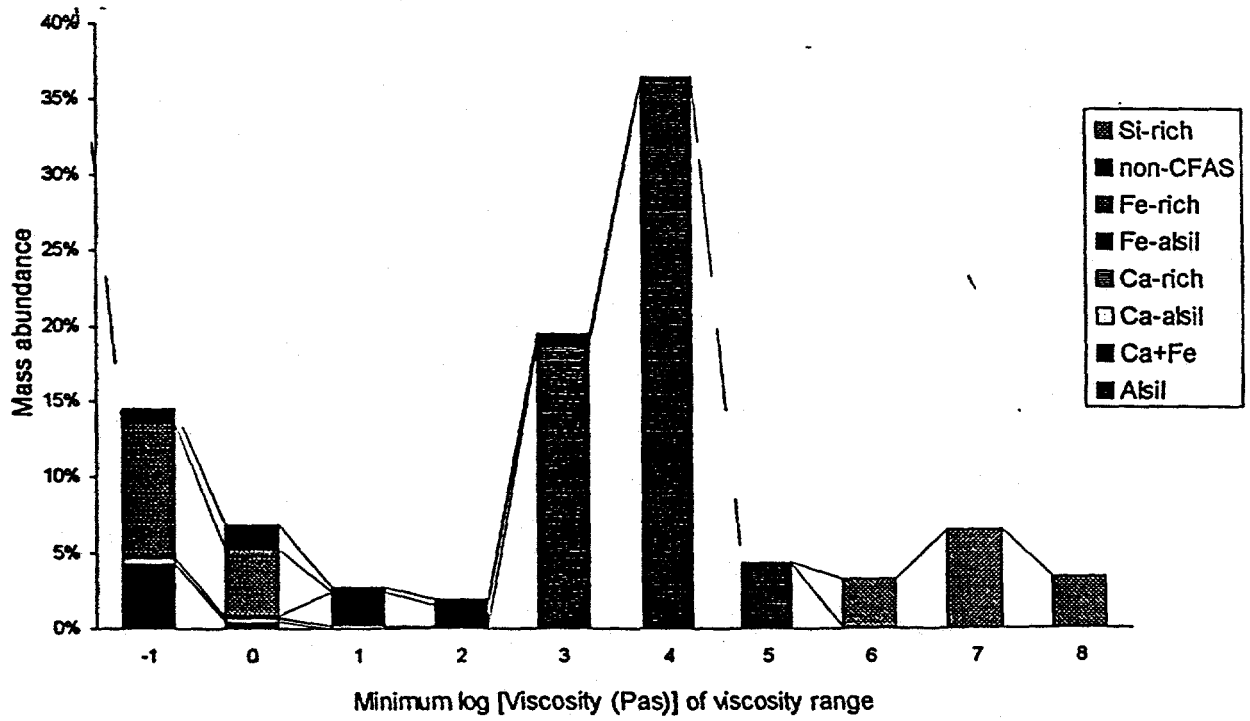

$Fe_2O_3 - Al_2O_3 - SiO_2$

for Si-rich, Alsil, Fe-alsil, Fe-rich and Ca+Fe chemical types

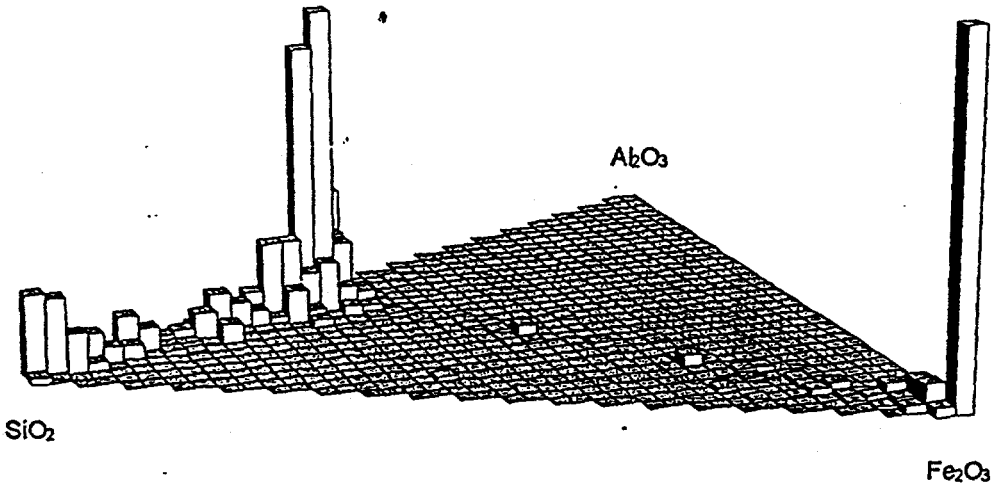

$CaO - Al_2O_3 - SiO_2$

for Si-rich, Alsil, Ca-alsil, Ca-rich and Ca+Fe chemical types

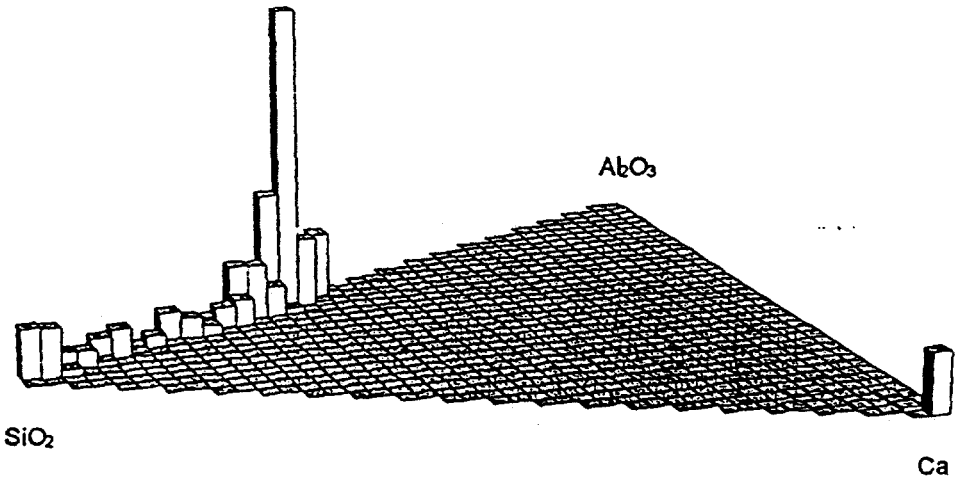

$CaO - Fe_2O_3 - (Al_2O_3 + SiO_2)$

for all chemical types except non-CFA

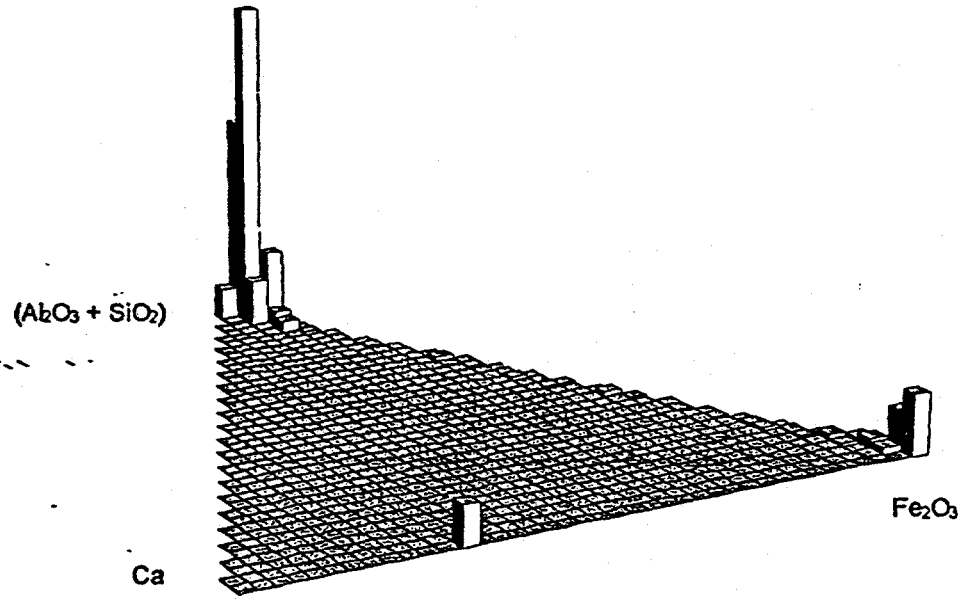

$10*K_2O - Al_2O_3 - SiO_2$

for Alsil and Si-rich chemical types

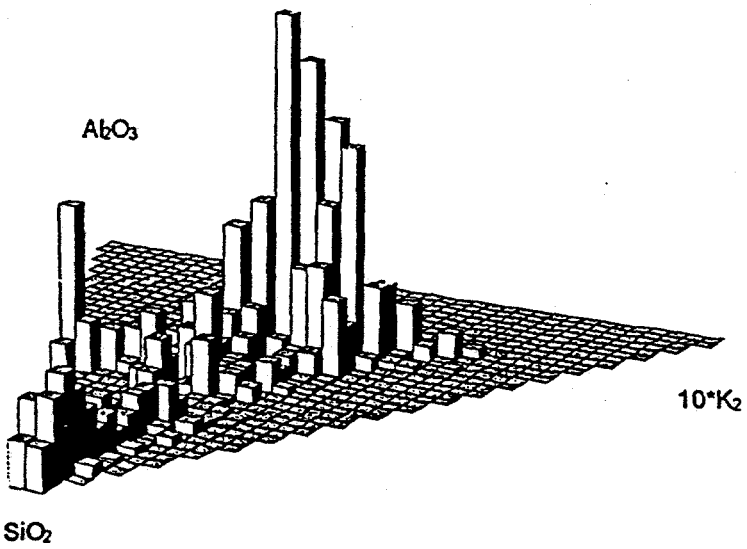

$Na_2O - K_2O - CaO$

where (Na_2O+K_2O+CaO) > 1wt%

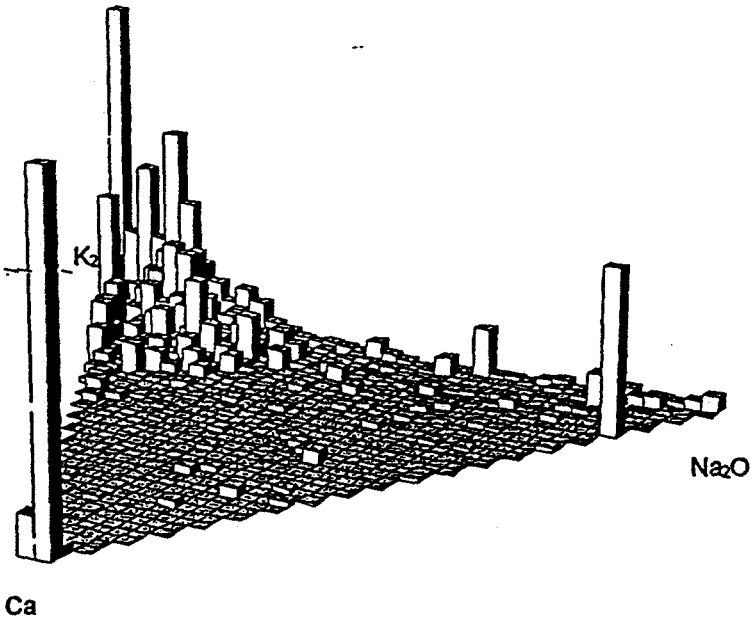

$MgO - Fe_2O_3 - CaO$

where ($MgO+Fe_2O_3+CaO$) > 20wt%

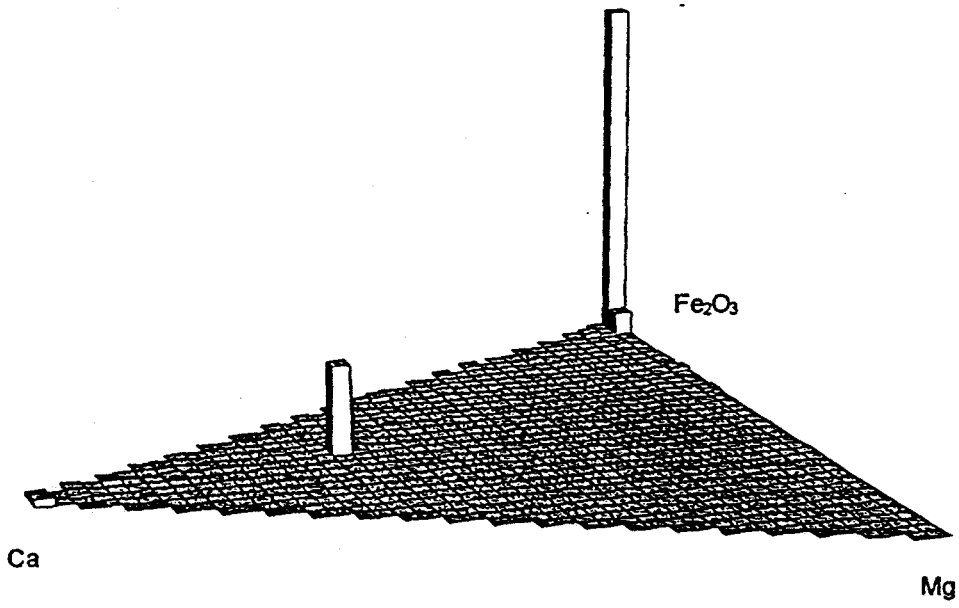

F. Wigley, Imperial College

Fe - S - O

for Fe-alsil, Fe-rich, Ca+Fe and non-CFAS chemical type

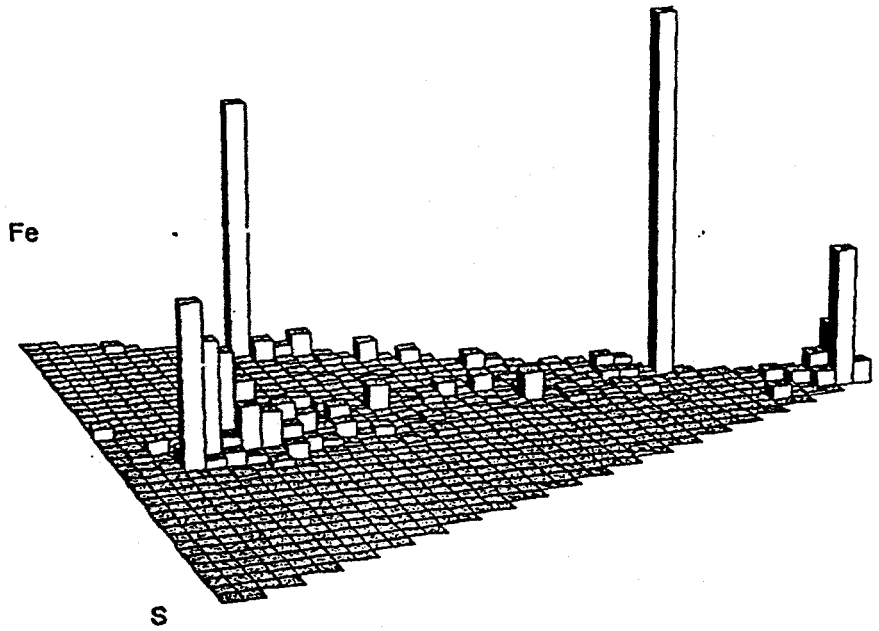

Ca - S - O

for Ca-alsil, Ca-rich, Ca+Fe and non-CFAS chemical type

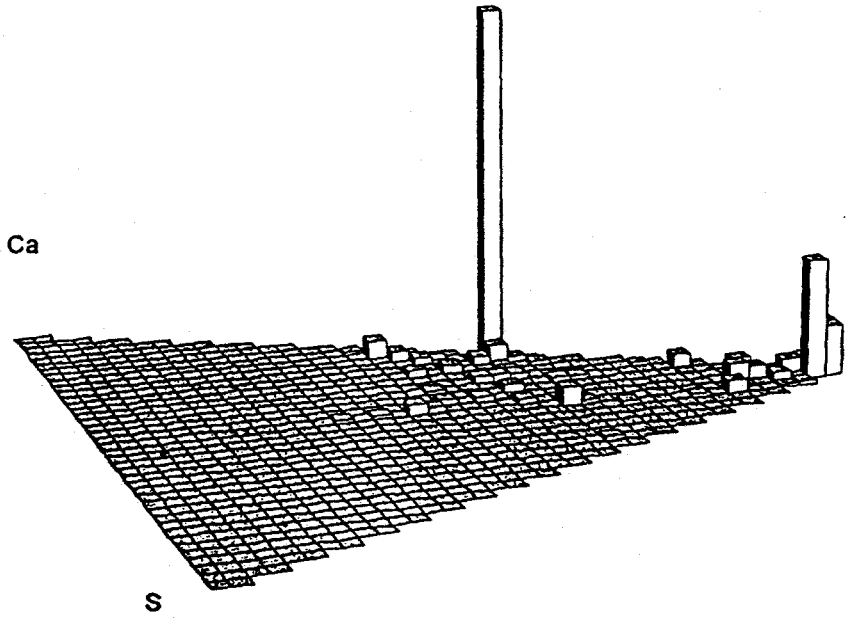

F. Wigley, Imperial College

Average mineral properties for Silverdale pf

Average particle properties

	Number	Wt %	Porosity	Shape	SiO2	Al2O3	Fe2O3	CaO	MgO	Na2O	K2O	TiO2	Mn3O4	P2O5	SO3
	1139	100.00	0.02	2.03	36.33	18.04	13.64	3.44	0.66	0.64	1.35	1.22	0.38	0.48	23.80

Average mineral properties by chemical type

Type	*Number*	Wt %	Porosity	Shape	SiO2	Al2O3	Fe2O3	CaO	MgO	Na2O	K2O	TiO2	Mn3O4	P2O5	SO3
Alsil	*590*	48.56	0.04	2.34	56.38	33.72	2.29	0.46	0.51	0.47	2.43	0.94	0.29	0.51	2.01
Ca+Fe	*4*	0.38	0.02	2.07	3.32	1.86	23.70	44.39	9.77	0.27	0.23	0.31	4.27	0.68	11.22
Ca-alsil	*11*	0.72	0.03	1.62	16.42	5.78	5.32	35.03	0.27	0.20	0.55	0.51	0.63	2.60	32.68
Ca-rich	*28*	3.05	0.01	2.21	1.65	0.82	1.01	59.37	0.26	0.24	0.18	0.22	0.44	1.49	34.31
Fe-alsil	*100*	8.08	0.02	1.84	14.73	10.01	29.60	0.75	0.56	0.44	0.58	0.40	0.66	0.52	41.74
Fe-rich	*277*	27.65	0.01	1.63	0.92	0.65	33.74	0.30	0.12	0.27	0.11	0.17	0.36	0.18	63.19
non-CFAS	*36*	3.71	0.05	1.76	9.06	2.62	15.23	22.28	7.40	7.40	0.81	17.17	1.01	1.29	15.73
Si-rich	*93*	7.85	0.01	1.89	89.04	6.45	1.05	0.17	0.22	0.25	0.74	0.53	0.19	0.39	0.98

Average mineral properties by size

Size (µm)	*Number*	Wt %	Porosity	Shape	SiO2	Al2O3	Fe2O3	CaO	MgO	Na2O	K2O	TiO2	Mn3O4	P2O5	SO3
1 - 2	*401*	11.77	0.00	2.28	35.25	19.28	14.00	1.16	0.48	0.64	1.42	1.51	0.38	0.70	25.17
2 - 4	*180*	17.53	0.00	2.32	43.01	22.87	9.34	2.70	0.69	1.28	1.52	1.26	0.36	0.67	16.30
4 - 8	*122*	18.19	0.03	1.87	37.63	16.77	15.24	4.27	1.18	0.57	1.37	2.63	0.43	0.39	19.51
8 - 16	*337*	21.73	0.01	2.06	29.68	14.60	15.83	4.35	0.65	0.59	1.24	0.89	0.47	0.55	31.14
16 - 32	*84*	20.12	0.04	1.87	36.69	19.19	14.02	4.08	0.51	0.43	1.38	0.59	0.40	0.34	22.38
32 - 64	*15*	10.65	0.06	1.83	37.15	15.74	12.38	2.66	0.28	0.21	1.16	0.32	0.13	0.25	29.71

F. Wigley, Imperial College

Average mineral properties for Silverdale pf

Average mineral properties by chemical type and size

Type	Size (µm)	*Number*	Wt %	Porosity	Shape	SiO2	Al2O3	Fe2O3	CaO	MgO	Na2O	K2O	TiO2	Mn3O4	P2O5	SO3
Alsil	1 - 2	*219*	5.98	0.00	2.78	53.13	34.43	2.75	0.59	0.55	0.58	2.39	1.21	0.39	0.69	3.29
Alsil	2 - 4	*118*	10.55	0.00	2.53	54.85	35.20	2.24	0.46	0.41	0.54	2.19	0.86	0.34	0.49	2.42
Alsil	4 - 8	*58*	8.36	0.04	2.20	55.96	33.23	2.83	0.24	0.61	0.41	2.58	0.73	0.23	0.38	2.80
Alsil	8 - 16	*144*	8.50	0.02	2.54	57.11	32.61	2.07	0.47	0.55	0.61	2.68	1.23	0.34	0.67	1.66
Alsil	16 - 32	*44*	10.58	0.07	2.07	58.94	32.68	2.05	0.48	0.46	0.37	2.36	0.93	0.23	0.39	1.10
Alsil	32 - 64	*7*	4.59	0.13	1.81	57.60	34.79	1.74	0.59	0.55	0.26	2.41	0.58	0.24	0.54	0.70
Ca+Fe	1 - 2	*1*	0.03	0.00	2.03	2.85	1.74	19.60	14.28	0.00	0.67	0.38	1.00	0.19	0.24	59.05
Ca+Fe	4 - 8	*1*	0.03	0.24	1.60	13.86	10.79	17.41	29.60	7.82	0.00	1.77	0.00	0.00	1.57	17.17
Ca+Fe	8 - 16	*1*	0.12	0.00	2.17	2.45	0.59	24.67	47.60	10.30	0.00	0.00	0.16	6.38	0.73	7.12
Ca+Fe	16 - 32	*1*	0.20	0.00	2.08	2.28	1.27	24.71	49.33	11.24	0.40	0.11	0.34	4.30	0.58	5.45
Ca-alsil	1 - 2	*1*	0.02	0.00	3.42	7.05	4.92	1.42	34.01	0.11	0.00	0.83	0.90	0.00	0.98	49.77
Ca-alsil	2 - 4	*3*	0.39	0.00	1.43	14.72	5.10	3.72	28.53	0.14	0.10	0.39	0.65	0.42	2.06	44.20
Ca-alsil	4 - 8	*3*	0.09	0.00	1.78	16.29	13.04	4.94	39.60	1.41	0.27	1.03	0.20	0.86	10.05	12.31
Ca-alsil	8 - 16	*4*	0.22	0.08	1.71	20.25	4.15	8.60	44.62	0.07	0.38	0.62	0.36	0.96	0.71	19.27
Ca-rich	1 - 2	*4*	0.10	0.00	2.35	1.28	1.75	2.38	50.88	0.00	0.69	0.12	0.54	0.37	6.08	35.90
Ca-rich	2 - 4	*3*	0.22	0.00	2.35	2.50	1.34	1.53	41.24	0.33	0.04	0.11	0.00	0.04	8.82	44.05
Ca-rich	4 - 8	*3*	0.48	0.00	1.84	1.06	0.77	2.59	58.03	0.58	0.00	0.22	0.47	0.59	0.08	35.61
Ca-rich	8 - 16	*13*	0.81	0.00	2.00	1.74	0.97	1.08	70.85	0.37	0.33	0.22	0.45	0.77	2.02	21.19
Ca-rich	16 - 32	*4*	0.75	0.02	1.37	2.63	1.16	0.53	74.50	0.20	0.00	0.11	0.05	0.51	0.36	19.95
Ca-rich	32 - 64	*1*	0.69	0.00	3.55	0.68	0.00	0.00	37.33	0.00	0.54	0.23	0.00	0.00	0.00	61.22
Fe-alsil	1 - 2	*38*	1.16	0.00	1.74	12.35	9.16	25.49	0.72	0.38	0.68	0.55	0.64	0.33	0.83	48.87
Fe-alsil	2 - 4	*7*	0.77	0.00	2.43	14.12	11.63	22.67	1.05	0.27	0.25	0.70	0.40	0.11	0.97	47.84
Fe-alsil	4 - 8	*11*	0.91	0.00	1.61	8.37	6.37	28.30	0.57	0.08	0.57	0.21	0.47	0.16	0.19	54.72
Fe-alsil	8 - 16	33	2.11	0.01	1.96	12.66	8.99	28.21	0.73	0.65	0.49	0.47	0.51	0.60	0.52	46.16
Fe-alsil	16 - 32	*11*	3.13	0.06	1.71	18.99	11.67	34.13	0.75	0.78	0.32	0.75	0.23	1.11	0.40	30.88
Fe-rich	1 - 2	*94*	3.34	0.00	1.69	1.31	0.85	34.63	0.33	0.10	0.51	0.18	0.56	0.41	0.20	60.91
Fe-rich	2 - 4	*24*	3.06	0.00	2.01	1.28	1.16	35.65	0.54	0.10	0.46	0.15	0.23	0.42	0.15	59.86
Fe-rich	4 - 8	*27*	4.42	0.00	1.57	1.24	0.82	42.03	0.89	0.12	0.26	0.14	0.14	0.98	0.31	53.08
Fe-rich	8 - 16	*106*	8.04	0.01	1.60	0.87	0.66	31.31	0.16	0.20	0.20	0.09	0.14	0.28	0.17	65.92
Fe-rich	16 - 32	*21*	4.81	0.00	1.36	0.57	0.35	30.68	0.08	0.04	0.20	0.03	0.07	0.13	0.18	67.67
Fe-rich	32 - 64	*5*	3.98	0.01	1.70	0.46	0.22	30.94	0.01	0.06	0.13	0.12	0.00	0.05	0.05	67.96

F. Wigley, Imperial College

Average mineral properties by chemical type and size

Type	Size (μm)	*Number*	Wt %	Porosity	Shape	SiO2	Al2O3	Fe2O3	CaO	MgO	Na2O	K2O	TiO2	Mn3O4	P2O5	SO3
non-CFAS	1 - 2	*12*	0.28	0.00	1.70	10.44	8.20	4.92	6.18	4.46	4.19	1.37	24.29	0.45	4.39	31.11
non-CFAS	2 - 4	*5*	0.78	0.04	1.68	4.10	1.31	11.46	24.65	8.35	18.86	1.43	13.90	1.08	1.62	13.23
non-CFAS	4 - 8	*8*	1.83	0.07	1.44	8.02	1.35	20.70	21.27	7.98	2.56	0.32	21.86	0.43	0.46	15.05
non-CFAS	8 - 16	*10*	0.68	0.00	1.84	15.39	5.78	12.34	21.30	7.06	6.45	1.37	7.92	2.96	2.12	17.31
non-CFAS	16 - 32	*1*	0.14	0.04	5.97	16.45	0.00	0.00	58.77	2.21	17.79	0.00	4.78	0.00	0.00	0.00
Si-rich	1 - 2	*32*	0.86	0.00	2.04	87.11	5.79	1.28	0.36	0.31	0.31	0.87	1.08	0.31	0.72	1.87
Si-rich	2 - 4	*20*	1.75	0.00	2.00	86.03	7.71	1.60	0.26	0.31	0.27	0.74	0.53	0.22	0.71	1.63
Si-rich	4 - 8	*11*	2.08	0.01	1.64	89.74	6.55	1.05	0.11	0.23	0.30	0.81	0.26	0.13	0.29	0.54
Si-rich	8 - 16	*26*	1.25	0.00	2.06	87.15	8.09	0.85	0.21	0.17	0.21	1.01	0.64	0.20	0.40	1.07
Si-rich	16 - 32	*2*	0.51	0.00	3.10	94.70	2.38	0.90	0.12	0.08	0.30	0.40	0.34	0.35	0.17	0.26
Si-rich	32 - 64	*2*	1.39	0.03	1.44	92.61	5.15	0.46	0.00	0.15	0.11	0.44	0.55	0.10	0.00	0.42

Particle properties:

Type - Assigned using the following scheme

non-CFAS - (CaO + Fe2O3 + Al2O3 + SiO2) < 80 wt%, otherwise
Si-rich - SiO2' > 80 wt%
Fe-rich - Fe2O3' > 80 wt%
Ca-rich - CaO' > 80 wt%
Alsil - (Al2O3' + SiO2') > 80 wt% and SiO2' < 80 wt%
Ca-alsil - (Al2O3' + SiO2') < 80 wt% and CaO' < 80 wt% and Fe2O3' < 20 wt% and CaO' > Fe2O3'
Fe-alsil - (Al2O3' + SiO2') < 80 wt% and Fe2O3' < 80 wt% and CaO' < 20 wt% and Fe2O3' > CaO'
Ca+Fe - CaO' > 20 wt% and Fe2O3' > 20 wt%

where CaO', Fe2O3', Al2O3' and SiO2' are normalised to (CaO' + Fe2O3' + Al2O3' + SiO2')=100%.

Size - The diameter of a circle with the same area as the analysed cross-section of the particle.
Number - Number of particles analysed.
Wt% - Mass percentage of particles analysed, using an estimated density.
Porosity - Area fraction of pores seen in cross-section (should be treated with caution).
Shape - Aspect ratio of particle cross-section (should be treated with caution).
Viscosity - Estimated using the scheme of Kalmanovitch and Frank (1988) (takes no account of the physical state of the phase, and should be treated with caution).

F. Wigley, Imperial College

Number of minerals by size and chemical type

Size (μm)	Fe-rich	Fe-alsil	Alsil	Ca-alsil	Ca-rich	Si-rich	Ca+Fe	non-CFAS
1 - 2	94	38	219	1	4	32	1	12
2 - 4	24	7	118	3	3	20		5
4 - 8	27	11	58	3	3	11	1	8
8 - 16	106	33	144	4	13	26	1	10
16 - 32	21	11	44		4	2	1	1
32 - 64	5		7		1	2		

Mass abundance (wt%) of minerals by size and chemical type

Size (μm)	Fe-rich	Fe-alsil	Alsil	Ca-alsil	Ca-rich	Si-rich	Ca+Fe	non-CFAS
1 - 2	3.34	1.16	5.98	0.02	0.10	0.86	0.03	0.28
2 - 4	3.06	0.77	10.55	0.39	0.22	1.75		0.78
4 - 8	4.42	0.91	8.36	0.09	0.48	2.08	0.03	1.83
8 - 16	8.04	2.11	8.50	0.22	0.81	1.25	0.12	0.68
16 - 32	4.81	3.13	10.58		0.75	0.51	0.20	0.14
32 - 64	3.98		4.59		0.69	1.39		

Average porosity of minerals by size and chemical type

Size (μm)	Fe-rich	Fe-alsil	Alsil	Ca-alsil	Ca-rich	Si-rich	Ca+Fe	non-CFAS
1 - 2	0.00	0.00	0.00	0.00	0.00	0.00	0.00	0.00
2 - 4	0.00	0.00	0.00	0.00	0.00	0.00		0.04
4 - 8	0.00	0.00	0.04	0.00	0.00	0.01	0.24	0.07
8 - 16	0.01	0.01	0.02	0.08	0.00	0.00	0.00	0.00
16 - 32	0.00	0.06	0.07		0.02	0.00	0.00	0.04
32 - 64	0.01		0.13		0.00	0.03		

Average shape of minerals by size and chemical type

Size (μm)	Fe-rich	Fe-alsil	Alsil	Ca-alsil	Ca-rich	Si-rich	Ca+Fe	non-CFAS
1 - 2	1.69	1.74	2.78	3.42	2.35	2.04	2.03	1.70
2 - 4	2.01	2.43	2.53	1.43	2.35	2.00		1.68
4 - 8	1.57	1.61	2.20	1.78	1.84	1.64	1.60	1.44
8 - 16	1.60	1.96	2.54	1.71	2.00	2.06	2.17	1.84
16 - 32	1.36	1.71	2.07		1.37	3.10	2.08	5.97
32 - 64	1.70		1.81		3.55	1.44		

F. Wigley, Imperial College

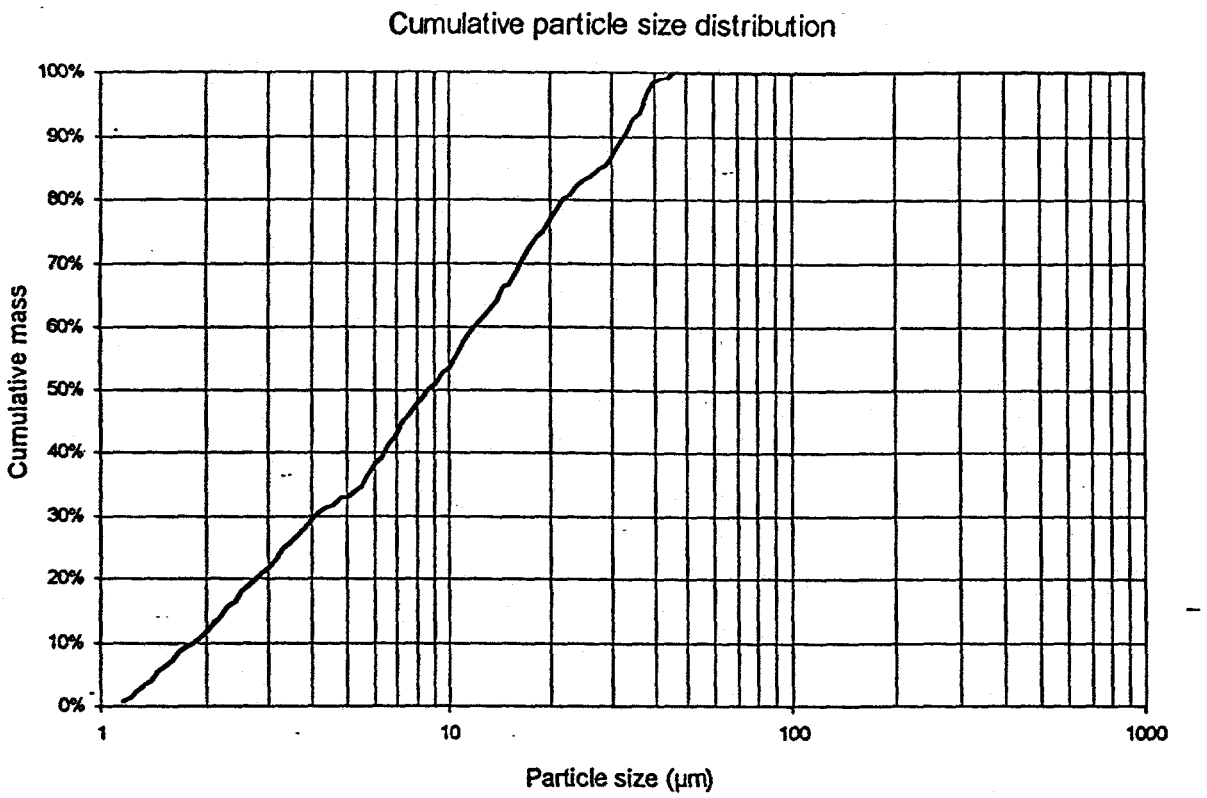

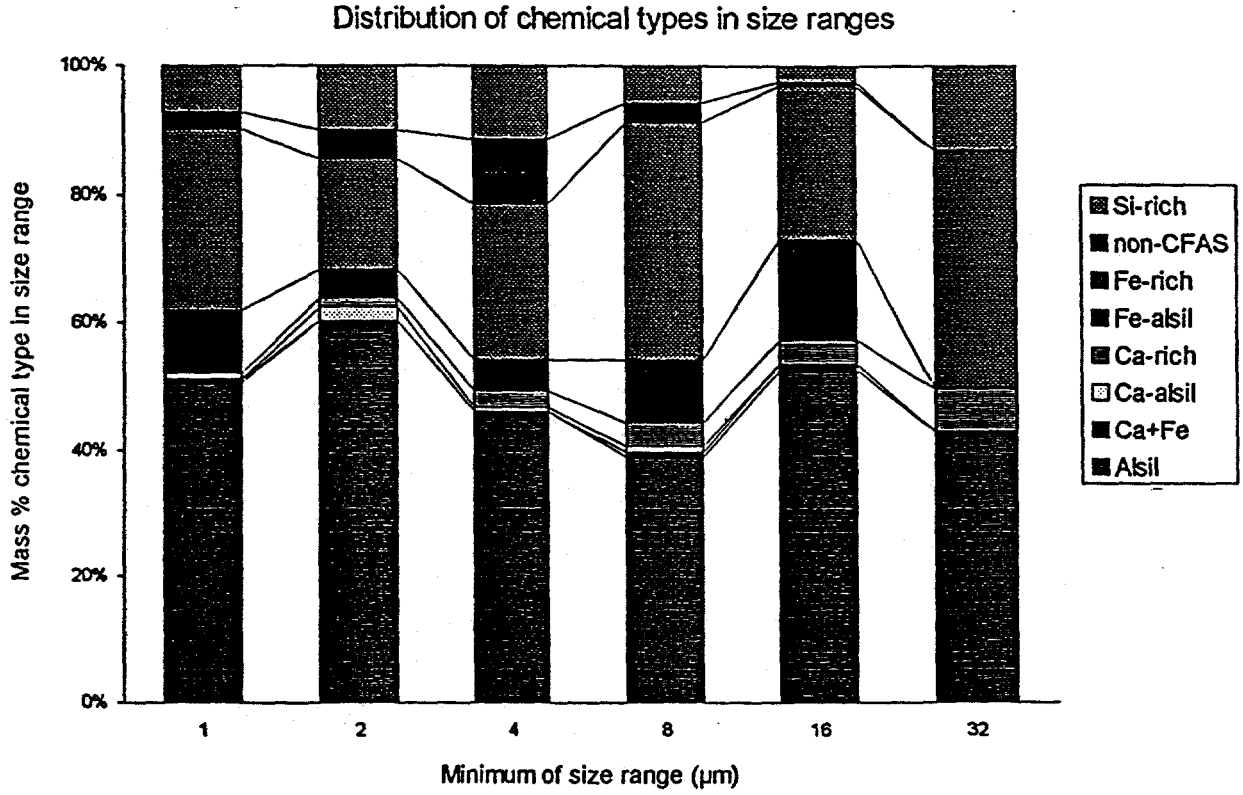

F. Wigley, Imperial College

Chemical composition of size ranges

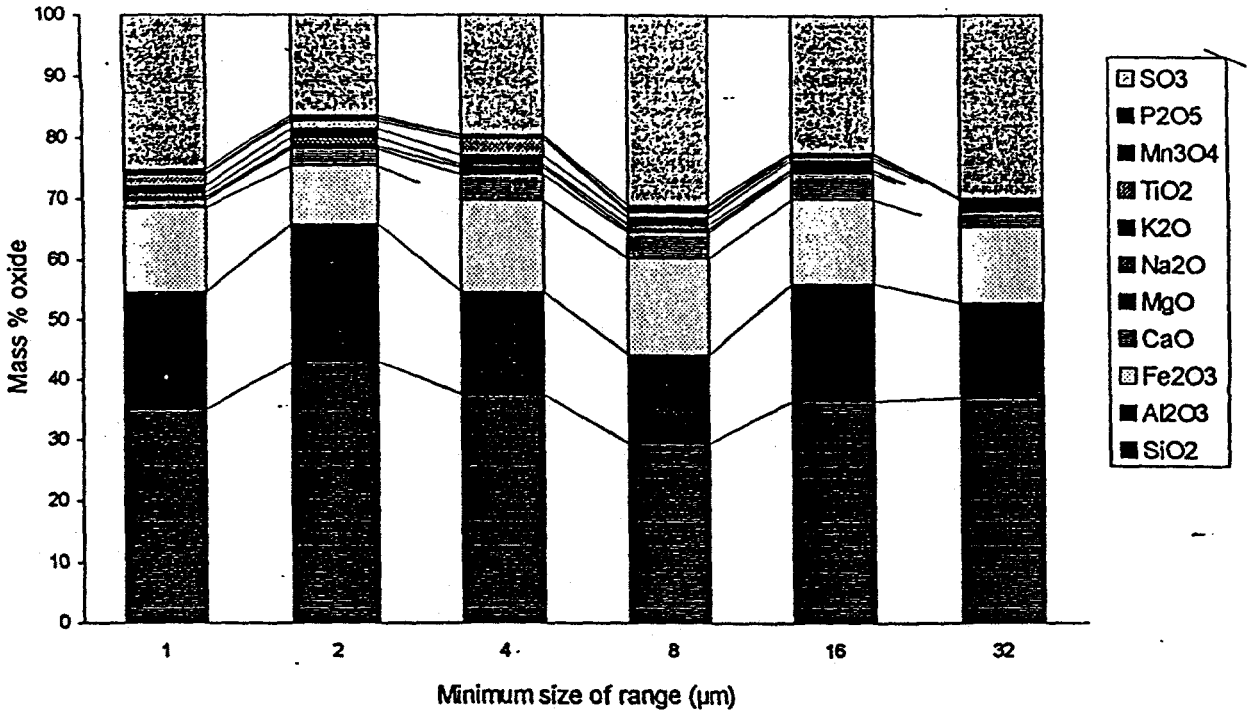

Chemical composition of chemical types

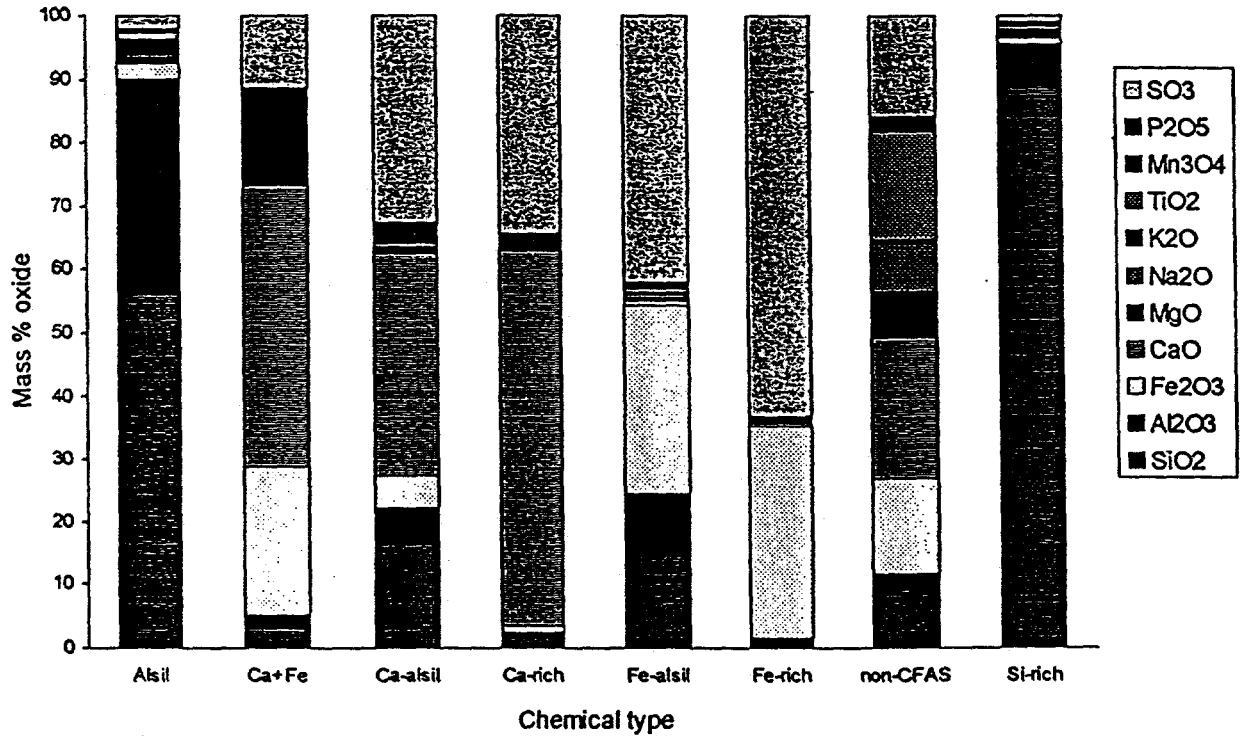

F. Wigley, Imperial College

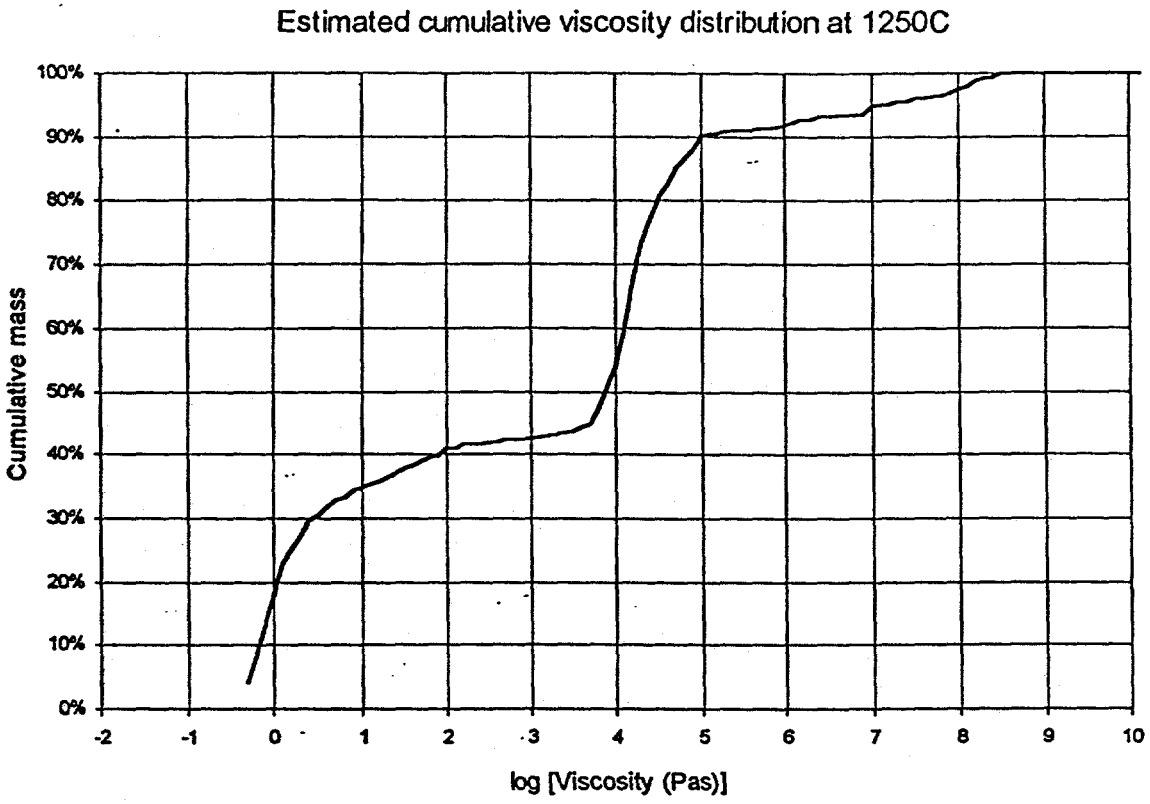

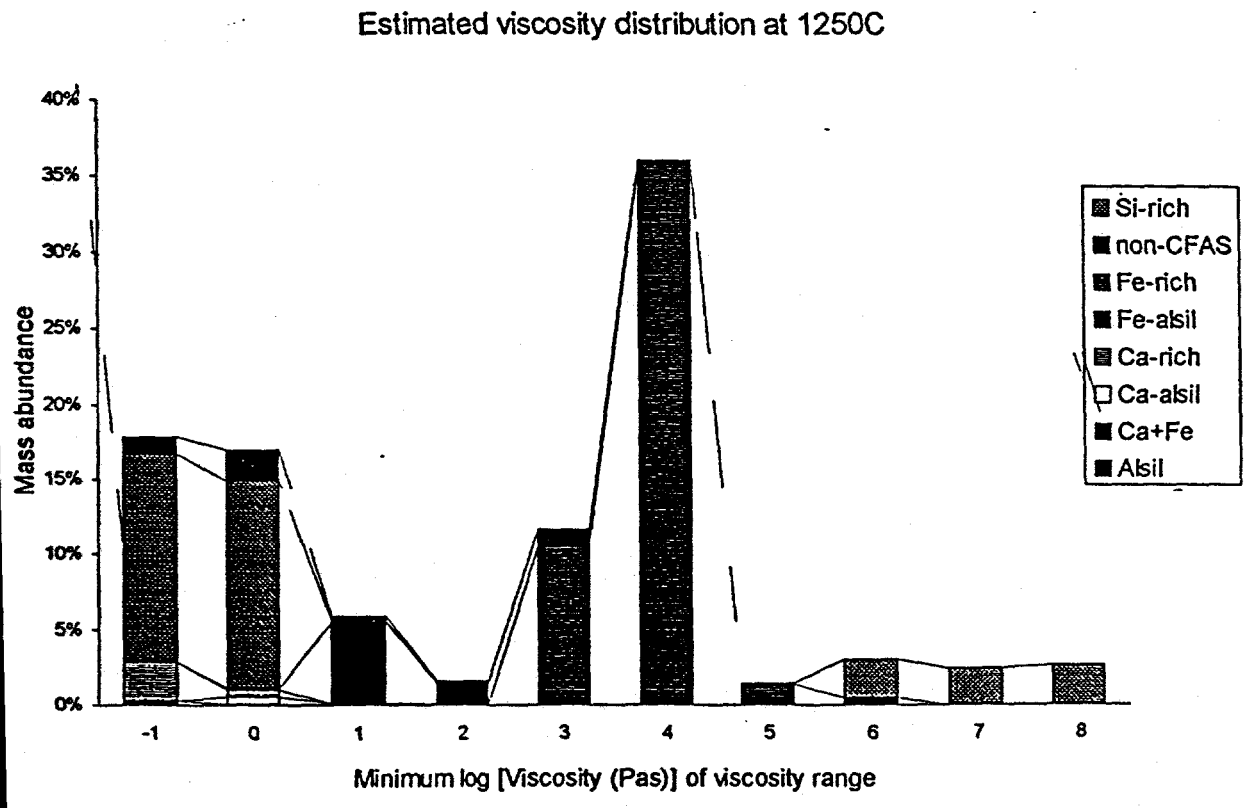

F. Wigley, Imperial College

Fe_2O_3 - Al_2O_3 - SiO_2

for Si-rich, Alsil, Fe-alsil, Fe-rich and Ca+Fe chemical types

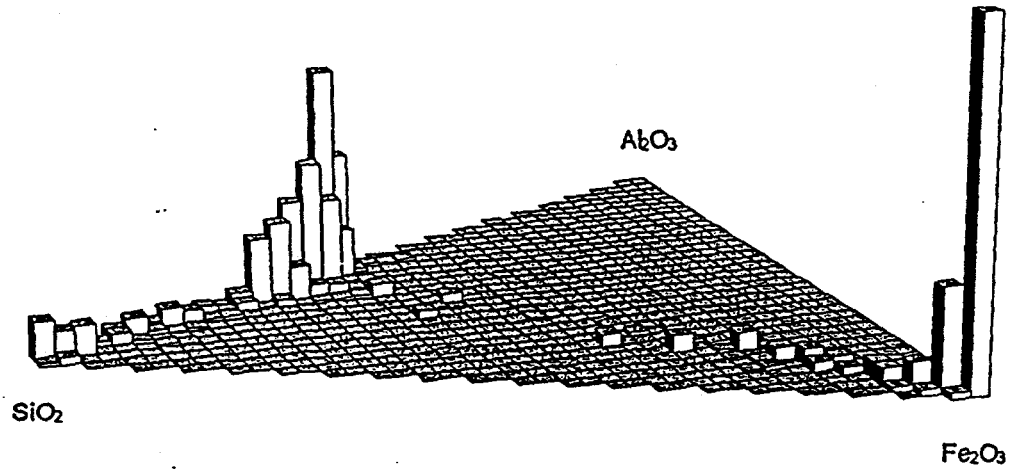

CaO - Al_2O_3 - SiO_2

for Si-rich, Alsil, Ca-alsil, Ca-rich and Ca+Fe chemical types

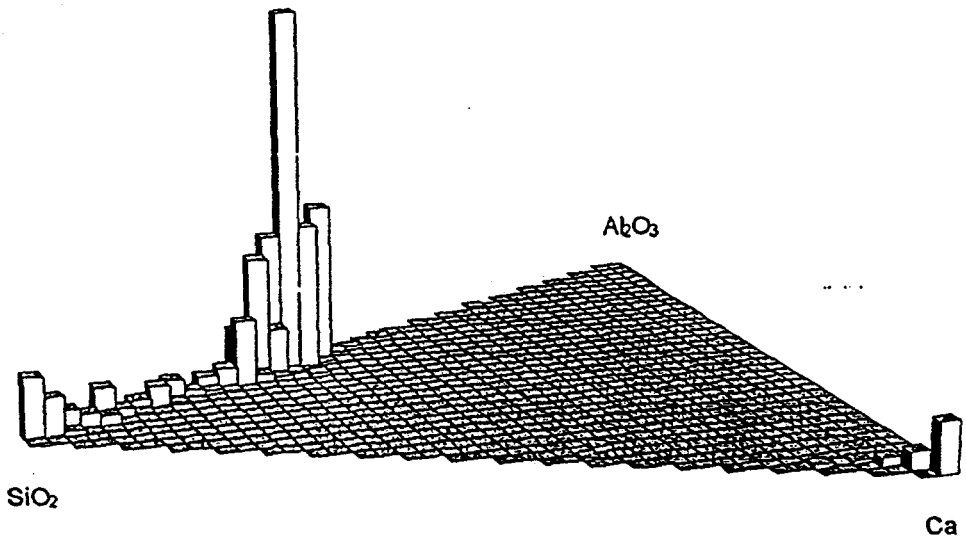

F. Wigley, Imperial College

$CaO - Fe_2O_3 - (Al_2O_3 + SiO_2)$

for all chemical types except non-CFA

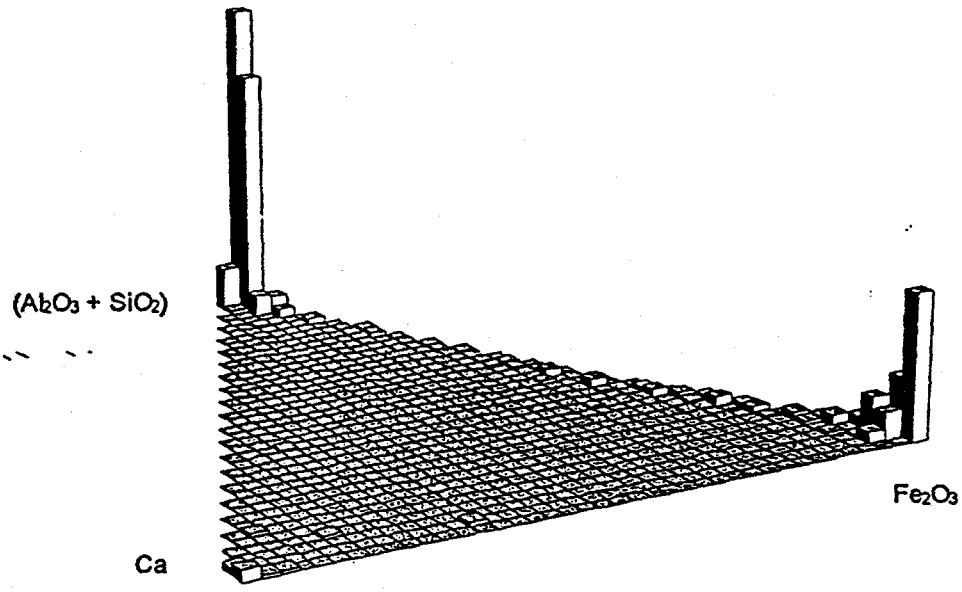

$10*K_2O - Al_2O_3 - SiO_2$

for Alsil and Si-rich chemical types

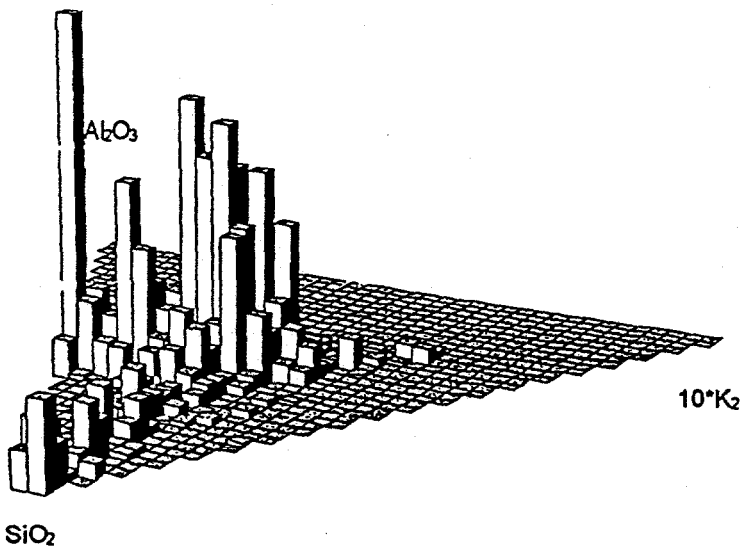

F. Wigley, Imperial College

$Na_2O - K_2O - CaO$

where $(Na_2O+K_2O+CaO) > 1wt\%$

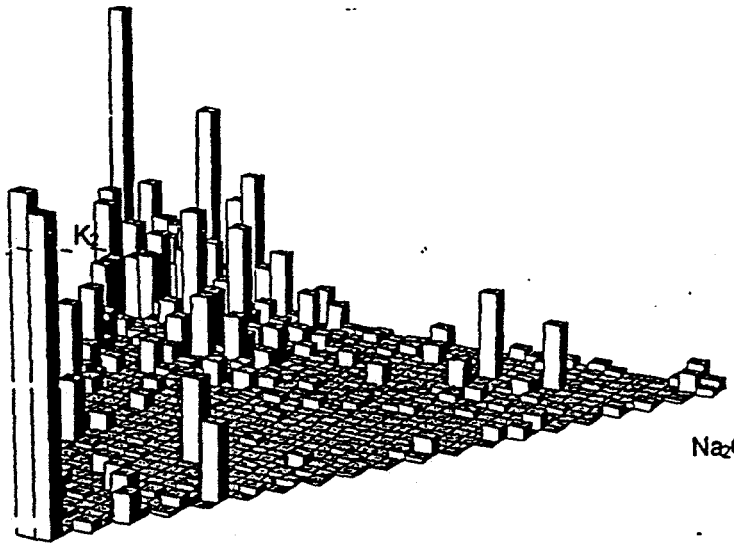

$MgO - Fe_2O_3 - CaO$

where $(MgO+Fe_2O_3+CaO) > 20wt\%$

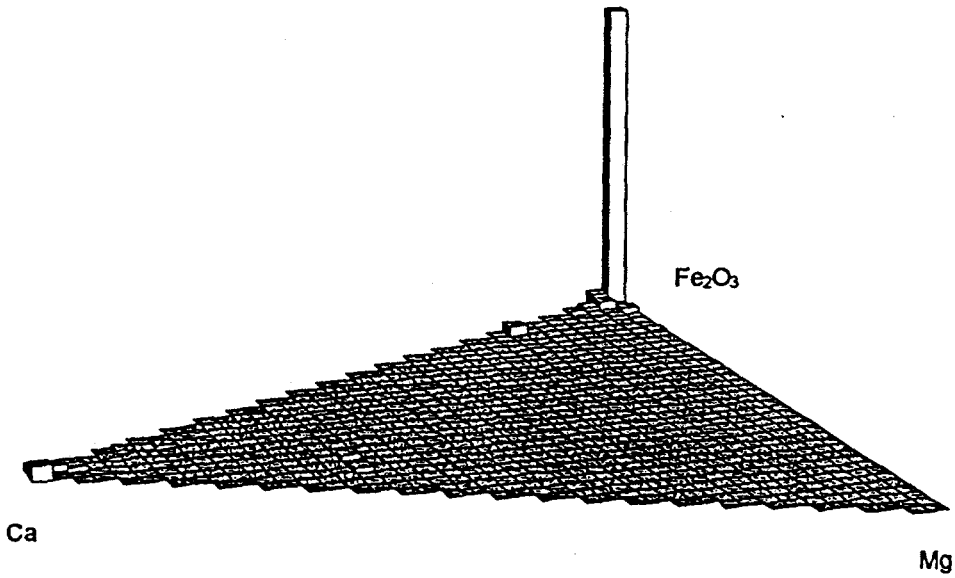

F. Wigley, Imperial College

Fe - S - O

for Fe-alsil, Fe-rich, Ca+Fe and non-CFAS chemical type

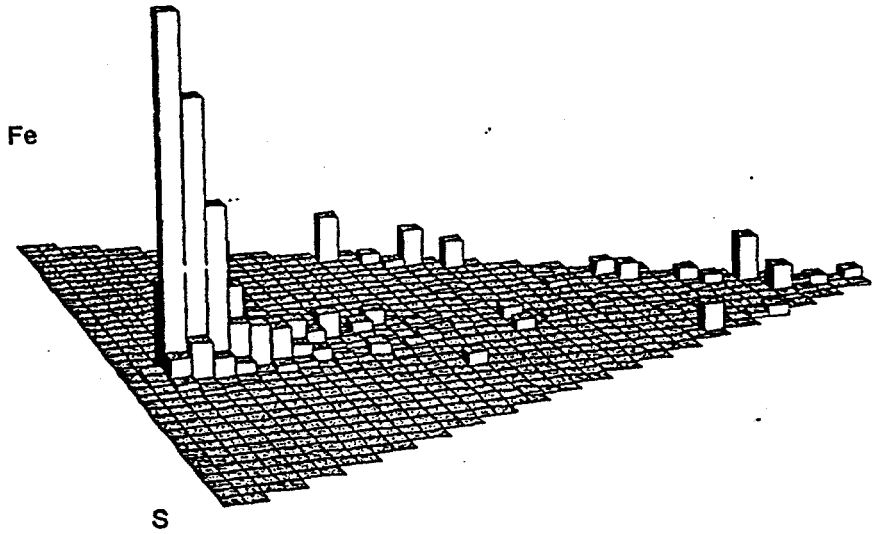

Ca - S - O

for Ca-alsil, Ca-rich, Ca+Fe and non-CFAS chemical type

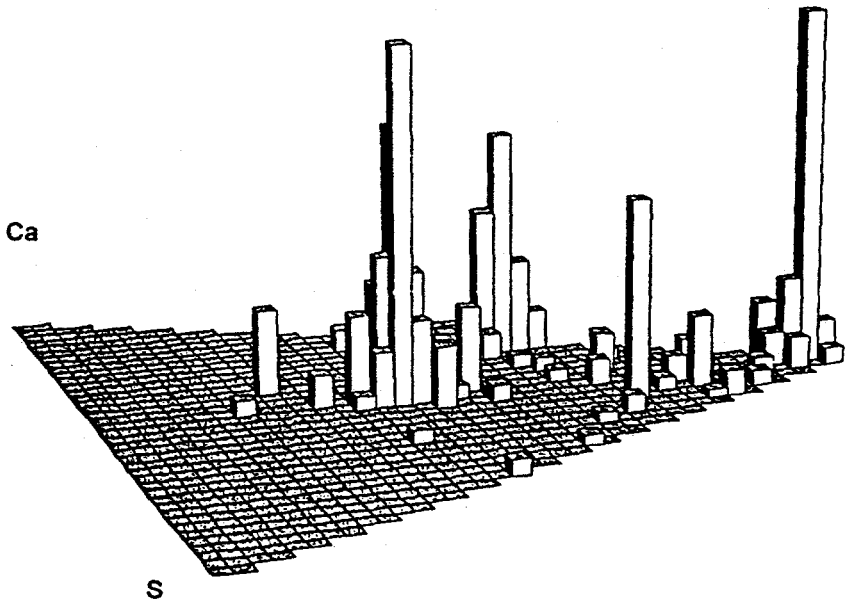

APPENDIX B

CCSEM Data for Washed Pittsburgh #8 and Silverdale Coals

Analysis and data provided by Dr. Fraser Wigley
Imperial College, London

Data Reports reproduced in their entirety

UMMARY OF CCSEM RESULTS: PROG VERSION 3BF 7/21/90
AMPLE DESCRIPTION ---> Black Thunder Coal-From EERC Blend Project
UBMITTER ---> Katrinak
CC # AND FUND # ---> 42586132
UN DATE AND TIME ---> 11 3 1993 15:28

ERCENT EPOXY USED	=	67.8
OTAL MINERAL AREA ANALYZED AT 800.0 MAG	=	1652.3
ORMALIZED AREA ANALYZED AT 800.0 MAG	=	194259.7
INERAL AREA ANALYZED 240.0 MAG	=	18159.4
ORMALIZED AREA ANALYZED 240.0 MAG	=	200047.1
OTAL MINERAL AREA ANALYZED AT 50.0 MAG	=	101628.7
UMBER OF FRAMES AT 800.0 MAG	=	99
UMBER OF FRAMES AT 240.0 MAG	=	99
UMBER OF FRAMES AT 50.0 MAG	=	47
OTAL MINERAL AREA ON A COAL BASIS	=	1.314 } ∴ coal is 2.6 wt % minerals
OTAL MINERAL WGHT % ON A COAL BASIS	=	2.606 }
OTAL NUMBER OF POINTS ANALYZED	=	960
UMBER OF POINTS UNDER THRESHOLD	=	9

EIGHT PERCENT ON A MINERAL BASIS

	1.0 TO 2.2	2.2 TO 4.6	4.6 TO 10.0	10.0 TO 22.0	22.0 TO 46.0	46.0 TO 100.0	TOTALS
UARTZ	4.3	3.7	6.8	3.5	5.0	.8	24.1
RON OXIDE	.4	.6	1.4	.9	1.3	.0	4.6
ERICLASE	.0	.0	.0	.0	.0	.0	.0
UTILE	.2	.0	.0	.8	.0	.0	1.0
LUMINA	.0	.0	.2	.0	.0	.0	.3
ALCITE	.0	.1	.1	.0	.2	.4	.9
OLOMITE	.0	.0	.0	.0	.0	.6	.7
NKERITE	.0	.0	.0	.0	.0	.0	.0
AOLINITE	3.9	8.4	6.2	4.8	3.8	1.9	29.1
ONTMORILLONITE	.4	2.0	.7	2.1	1.1	.8	7.1
AL-SILICATE	.2	.4	.1	.0	.0	.0	.7
E AL-SILICATE	.0	.3	.1	.0	.0	.0	.4
A AL-SILICATE	.1	.4	.1	.0	.1	.0	.8
A AL-SILICATE	.0	.0	.0	.0	.0	.0	.0
LUMINOSILICATE	.2	.9	.5	2.5	.1	.5	4.6
IXED AL-SILICA	.1	.1	.3	.0	.0	.0	.5
E SILICATE	.0	.0	.0	.0	.0	.0	.0
A SILICATE	.0	.0	.0	.0	.0	.0	.0
A ALUMINATE	.0	.0	.0	.0	.0	.0	.0
YRITE	.5	.0	.1	2.2	.6	1.4	4.7
YRRHOTITE	.1	.0	.0	.0	.0	.0	.1
XIDIZED PYRRHO	.1	.0	.0	.0	.2	.0	.2
YPSUM	.0	.2	.0	.0	.0	.0	.2
ARITE	.1	.2	.4	.0	.0	.0	.6
PATITE	.0	.0	.0	.0	.0	.0	.0
A AL-P	1.6	3.1	4.0	.9	.2	.0	9.8
CL	.0	.0	.0	.0	.0	.0	.0
YPSUM/BARITE	.1	.0	.0	.0	.0	.0	.1
YPSUM/AL-SILIC	.0	.0	.0	.0	.0	.0	.0
SI-RICH	.3	.7	.5	.0	.2	.4	2.1
CA-RICH	.0	.0	.0	.0	.1	.0	.1
CA-SI RICH	.0	.1	.0	.0	.0	.0	.1
UNKNOWN	3.0	1.0	1.2	.5	.8	.5	7.0
TOTALS	15.9	22.3	22.7	18.3	13.6	7.3	100.0

AREA PERCENT MINERAL BASIS

	1.0 TO 2.2	2.2 TO 4.6	4.6 TO 10.0	10.0 TO 22.0	22.0 TO 46.0	46.0 TO 100.0	TOTA
QUARTZ	4.5	3.9	7.2	3.7	5.3	.9	25
IRON OXIDE	.2	.3	.7	.5	.7	.0	2
PERICLASE	.0	.0	.0	.0	.0	.0	
RUTILE	.1	.0	.0	.4	.0	.0	
ALUMINA	.0	.0	.2	.0	.0	.0	
CALCITE	.1	.1	.1	.0	.2	.4	
DOLOMITE	.0	.0	.0	.0	.0	.6	
ANKERITE	.0	.0	.0	.0	.0	.0	
KAOLINITE	4.1	9.0	6.6	5.1	4.1	2.0	30
MONTMORILLONITE	.5	2.2	.8	2.4	1.2	.9	8
K AL-SILICATE	.2	.5	.2	.0	.0	.0	
FE AL-SILICATE	.0	.3	.1	.0	.0	.0	
CA AL-SILICATE	.1	.4	.1	.0	.1	.0	
NA AL-SILICATE	.0	.0	.0	.0	.0	.0	
ALUMINOSILICATE	.2	1.0	.5	2.6	.1	.5	4
MIXED AL-SILICA	.1	.1	.3	.0	.0	.0	
FE SILICATE	.0	.0	.0	.0	.0	.0	
CA SILICATE	.0	.0	.0	.0	.0	.0	
CA ALUMINATE	.0	.0	.0	.0	.0	.0	
PYRITE	.3	.0	.0	1.3	.3	.8	2
PYRRHOTITE	.1	.0	.0	.0	.0	.0	
OXIDIZED PYRRHO	.1	.0	.0	.0	.1	.0	
GYPSUM	.0	.2	.0	.0	.0	.0	
BARITE	.0	.1	.2	.0	.0	.0	
APATITE	.0	.0	.0	.0	.0	.0	
CA AL-P	1.6	3.1	4.0	1.0	.2	.0	9
KCL	.0	.0	.0	.0	.0	.0	
GYPSUM/BARITE	.0	.0	.0	.0	.0	.0	
GYPSUM/AL-SILIC	.1	.0	.0	.0	.0	.0	
SI-RICH	.4	.7	.5	.0	.2	.4	2
CA-RICH	.0	.0	.0	.0	.1	.0	
CA-SI RICH	.0	.1	.0	.0	.0	.0	
UNKNOWN	3.1	1.0	1.3	.5	.9	.5	7
TOTALS	16.0	23.2	22.9	17.5	13.5	7.0	100

STRIBUTION BY % OF EACH MINERAL PHASE

	1.0 TO 2.2	2.2 TO 4.6	4.6 TO 10.0	10.0 TO 22.0	22.0 TO 46.0	46.0 TO 100.0	TOTALS
JARTZ	17.7	15.3	28.1	14.5	20.9	3.5	100.0
RON OXIDE	9.5	13.4	29.5	19.9	27.8	.0	100.0
ERICLASE	.0	.0	.0	.0	.0	.0	.0
TTILE	20.8	.0	.0	79.2	.0	.0	100.0
LUMINA	15.8	.0	84.2	.0	.0	.0	100.0
LCITE	5.8	14.1	14.6	.0	19.8	45.7	100.0
LOMITE	5.4	.0	6.0	.0	.0	88.6	100.0
KERITE	.0	.0	.0	.0	.0	.0	.0
OLINITE	13.4	29.0	21.4	16.6	13.1	6.4	100.0
NTMORILLONITE	6.1	27.8	9.4	29.9	15.6	11.2	100.0
AL-SILICATE	20.8	59.1	20.1	.0	.0	.0	100.0
AL-SILICATE	5.9	74.5	19.6	.0	.0	.0	100.0
AL-SILICATE	15.5	51.5	16.7	.0	16.4	.0	100.0
AL-SILICATE	100.0	.0	.0	.0	.0	.0	100.0
LUMINOSILICATE	4.7	19.9	10.1	53.0	2.1	10.2	100.0
XED AL-SILICA	21.7	26.3	51.9	.0	.0	.0	100.0
SILICATE	.0	.0	.0	.0	.0	.0	.0
SILICATE	.0	.0	.0	.0	.0	.0	.0
ALUMINATE	.0	.0	.0	.0	.0	.0	.0
RITE	10.8	.0	1.7	47.0	11.8	28.8	100.0
RRHOTITE	100.0	.0	.0	.0	.0	.0	100.0
IDIZED PYRRHO	38.6	.0	.0	.0	61.4	.0	100.0
PSUM	8.8	75.9	15.3	.0	.0	.0	100.0
RITE	10.2	28.3	61.5	.0	.0	.0	100.0
PATITE	.0	.0	.0	.0	.0	.0	.0
AL-P	16.4	31.3	40.5	9.6	2.2	.0	100.0
L	.0	.0	.0	.0	.0	.0	.0
PSUM/BARITE	100.0	.0	.0	.0	.0	.0	100.0
PSUM/AL-SILIC	100.0	.0	.0	.0	.0	.0	100.0
-RICH	16.2	34.0	21.9	.0	7.5	20.4	100.0
-RICH	.0	.0	.0	.0	100.0	.0	100.0
-SI RICH	.0	100.0	.0	.0	.0	.0	100.0
KNOWN	42.7	14.3	17.2	7.2	11.7	6.9	100.0
TOTALS	16.0	23.2	22.9	17.5	13.5	7.0	100.0

NUMBER OF PARTICLES IN EACH SIZE RANGE

	1.0 TO 2.2	2.2 TO 4.6	4.6 TO 10.0	10.0 TO 22.0	22.0 TO 46.0	46.0 TO 100.0	TOTA
QUARTZ	111.0	26.0	94.0	11.0	36.0	1.0	279
IRON OXIDE	7.0	2.0	8.0	1.0	4.0	.0	22
PERICLASE	.0	.0	.0	.0	.0	.0	
RUTILE	3.0	.0	.0	1.0	.0	.0	4
ALUMINA	1.0	.0	1.0	.0	.0	.0	2
CALCITE	2.0	1.0	2.0	.0	2.0	1.0	8
DOLOMITE	1.0	.0	1.0	.0	.0	1.0	3
ANKERITE	.0	.0	.0	.0	.0	.0	
KAOLINITE	92.0	48.0	83.0	18.0	25.0	3.0	269
MONTMORILLONITE	11.0	13.0	11.0	7.0	8.0	1.0	51
K AL-SILICATE	3.0	2.0	3.0	.0	.0	.0	8
FE AL-SILICATE	1.0	1.0	1.0	.0	.0	.0	3
CA AL-SILICATE	4.0	3.0	1.0	.0	1.0	.0	9
NA AL-SILICATE	1.0	.0	.0	.0	.0	.0	1
ALUMINOSILICATE	5.0	4.0	5.0	7.0	1.0	1.0	23
MIXED AL-SILICA	2.0	1.0	2.0	.0	.0	.0	5
FE SILICATE	.0	.0	.0	.0	.0	.0	
CA SILICATE	.0	.0	.0	.0	.0	.0	
CA ALUMINATE	.0	.0	.0	.0	.0	.0	
PYRITE	9.0	.0	1.0	3.0	2.0	1.0	16
PYRRHOTITE	2.0	.0	.0	.0	.0	.0	2
OXIDIZED PYRRHO	2.0	.0	.0	.0	1.0	.0	3
GYPSUM	1.0	1.0	1.0	.0	.0	.0	3
BARITE	1.0	1.0	4.0	.0	.0	.0	6
APATITE	.0	.0	.0	.0	.0	.0	
CA AL-P	34.0	19.0	53.0	3.0	2.0	.0	111
KCL	.0	.0	.0	.0	.0	.0	
GYPSUM/BARITE	2.0	.0	.0	.0	.0	.0	2
GYPSUM/AL-SILIC	2.0	.0	.0	.0	.0	.0	2
SI-RICH	10.0	4.0	7.0	.0	1.0	1.0	23
CA-RICH	.0	.0	.0	.0	1.0	.0	1
CA-SI RICH	.0	1.0	.0	.0	.0	.0	1
UNKNOWN	72.0	7.0	16.0	2.0	5.0	1.0	103
TOTALS	379.0	134.0	294.0	53.0	89.0	11.0	960

DISTRIBUTION OF MINERAL PHASES - FREQUENCY PERCENT
TOTAL NUMBER OF POINTS = 960.0
% QUARTZ = 29.1

AMPLE DESCRIPTION ---> Black Thunder Coal-From EERC Blend Project
UBMITTER ---> Katrinak
CC # AND FUND # ---> 42586132
UN DATE AND TIME ---> 11 3 1993 15:28

UMMARY OF PARAMETERS

ERCENT EPOXY USED	=	67.8
OTAL MINERAL AREA ANALYZED AT 800.0 MAG	=	1652.3
ORMALIZED AREA ANALYZED AT 800.0 MAG	=	194259.7
INERAL AREA ANALYZED 240.0 MAG	=	18159.4
ORMALIZED AREA ANALYZED 240.0 MAG	=	200047.1
OTAL MINERAL AREA ANALYZED AT 50.0 MAG	=	101628.7
UMBER OF FRAMES AT 800.0 MAG	=	99
UMBER OF FRAMES AT 240.0 MAG	=	99
UMBER OF FRAMES AT 50.0 MAG	=	47
OTAL MINERAL WGHT % ON A COAL BASIS	=	2.606
OTAL NUMBER OF POINTS ANALYZED	=	960
UMBER OF POINTS UNDER THRESHOLD	=	9

EIGHT PERCENT ON A MINERAL BASIS

	1.0 TO 2.2	2.2 TO 4.6	4.6 TO 10.0	10.0 TO 22.0	22.0 TO 46.0	46.0 TO 100.0	TOTALS	% EXCLUDED	
UARTZ	4.3	3.7	6.8	3.5	5.0	.8	24.1	42.6	10.27
RON OXIDE	.4	.6	1.4	.9	1.3	.0	4.6	54.8	0.52
ERICLASE	.0	.0	.0	.0	.0	.0	.0	.0	
UTILE	.2	.0	.0	.8	.0	.0	1.0	17.2	.17
LUMINA	.0	.0	.2	.0	.0	.0	.3	15.8	.05
ALCITE	.0	.1	.1	.0	.2	.4	.9	90.2	.81
OLOMITE	.0	.0	.0	.0	.0	.6	.7	100.0	.70
NKERITE	.0	.0	.0	.0	.0	.0	.0	.0	12.46
AOLINITE	3.9	8.4	6.2	4.8	3.8	1.9	29.1	42.8	
ONTMORILLONITE	.4	2.0	.7	2.1	1.1	.8	7.1	63.3	4.40
AL-SILICATE	.2	.4	.1	.0	.0	.0	.7	27.1	0.10
E AL-SILICATE	.0	.3	.1	.0	.0	.0	.4	.0	
A AL-SILICATE	.1	.4	.1	.0	.1	.0	.8	22.9	0.18
A AL-SILICATE	.0	.0	.0	.0	.0	.0	.0	.0	
LUMINOSILICATE	.2	.9	.5	2.5	.1	.5	4.6	53.2	2.45
IXED AL-SILICA	.1	.1	.3	.0	.0	.0	.5	51.9	0.26
E SILICATE	.0	.0	.0	.0	.0	.0	.0	.0	
A SILICATE	.0	.0	.0	.0	.0	.0	.0	.0	
A ALUMINATE	.0	.0	.0	.0	.0	.0	.0	.0	
YRITE	.5	.0	.1	2.2	.6	1.4	4.7	77.9	3.66
YRRHOTITE	.1	.0	.0	.0	.0	.0	.1	46.3	0.05
XIDIZED PYRRHO	.1	.0	.0	.0	.2	.0	.2	15.3	0.03
YPSUM	.0	.2	.0	.0	.0	.0	.2	84.7	0.17
ARITE	.1	.2	.4	.0	.0	.0	.6	40.4	0.20
PATITE	.0	.0	.0	.0	.0	.0	.0	.0	
A AL-P	1.6	3.1	4.0	.9	.2	.0	9.8	19.3	1.89
CL	.0	.0	.0	.0	.0	.0	.0	.0	
YPSUM/BARITE	.1	.0	.0	.0	.0	.0	.1	46.4	0.05
YPSUM/AL-SILIC	.0	.0	.0	.0	.0	.0	.0	.0	
I-RICH	.3	.7	.5	.0	.2	.4	2.1	4.7	0.10
A-RICH	.0	.0	.0	.0	.1	.0	.1	100.0	0.10
A-SI RICH	.0	.1	.0	.0	.0	.0	.1	100.0	0.10
NKNOWN	3.0	1.0	1.2	.5	.8	.5	7.0	29.1	2.04
TOTALS	15.9	22.3	22.7	18.3	13.6	7.3	100.0		40.99

AMPLE DESCRIPTION ---> Black Thunder Coal-From EERC Blend Project

SUBMITTER ---> Katrinak
ICC # AND FUND # ---> 42586132
RUN DATE AND TIME ---> 11 3 1993 15:28

Percent excluded as a function of particle size and phase.

	1.0 TO 2.2	2.2 TO 4.6	4.6 TO 10.0	10.0 TO 22.0	22.0 TO 46.0	46.0 TO 100.0
QUARTZ	27.5	37.3	40.7	37.3	56.1	100.0
IRON OXIDE	31.2	30.3	86.7	.0	79.9	.0
PERICLASE	.0	.0	.0	.0	.0	.0
RUTILE	82.7	.0	.0	.0	.0	.0
ALUMINA	100.0	.0	.0	.0	.0	.0
CALCITE	100.0	100.0	100.0	.0	50.2	100.0
DOLOMITE	100.0	.0	100.0	.0	.0	100.0
ANKERITE	.0	.0	.0	.0	.0	.0
KAOLINITE	49.7	66.0	31.0	22.5	36.0	29.8
MONTMORILLONITE	.0	27.4	38.3	91.5	86.4	100.0
K AL-SILICATE	33.6	.0	100.0	.0	.0	.0
FE AL-SILICATE	.0	.0	.0	.0	.0	.0
CA AL-SILICATE	41.9	.0	.0	.0	100.0	.0
NA AL-SILICATE	.0	.0	.0	.0	.0	.0
ALUMINOSILICATE	29.9	87.6	62.5	29.6	100.0	100.0
MIXED AL-SILICA	.0	.0	100.0	.0	.0	.0
FE SILICATE	.0	.0	.0	.0	.0	.0
CA SILICATE	.0	.0	.0	.0	.0	.0
CA ALUMINATE	.0	.0	.0	.0	.0	.0
PYRITE	78.2	.0	.0	69.0	70.2	100.0
PYRRHOTITE	46.3	.0	.0	.0	.0	.0
OXIDIZED PYRRHO	39.5	.0	.0	.0	.0	.0
GYPSUM	100.0	100.0	.0	.0	.0	.0
BARITE	.0	.0	65.7	.0	.0	.0
APATITE	.0	.0	.0	.0	.0	.0
CA AL-P	17.8	38.8	10.5	.0	.0	.0
KCL	.0	.0	.0	.0	.0	.0
GYPSUM/BARITE	46.4	.0	.0	.0	.0	.0
GYPSUM/AL-SILIC	.0	.0	.0	.0	.0	.0
SI-RICH	.0	.0	21.4	.0	.0	.0
CA-RICH	.0	.0	.0	.0	100.0	.0
CA-SI RICH	.0	100.0	.0	.0	.0	.0
UNKNOWN	21.5	22.1	27.7	.0	43.5	100.0

SAMPLE DESCRIPTION ---> Black Thunder Coal-From EERC Blend Project
SUBMITTER ---> Katrinak
ICC # AND FUND # ---> 42586132

DATE AND TIME ---> 11 3 1993 15:28

rage phase composition.
rcent Relative X-ray Intensity)

	SI	AL	FE	TI	P	CA	MG	NA	K	S	BA	CL
RTZ	95.4	.1	.5	.5	.0	.8	.3	.2	.4	.6	.4	.6
N OXIDE	2.6	1.5	87.5	.8	.8	1.7	.8	.5	1.2	.9	.7	1.0
RICLASE	.0	.0	.0	.0	.0	.0	.0	.0	.0	.0	.0	.0
TILE	.3	.3	.3	49.6	.3	1.0	.5	.3	1.3	.8	44.9	.8
UMINA	.0	95.0	.5	1.5	.0	1.0	.0	.5	.5	.0	.5	.5
LCITE	1.1	.6	1.3	.6	.1	92.5	.3	.3	.3	1.5	.6	.9
LOMITE	4.3	.0	1.0	.7	.3	65.6	23.8	.3	1.3	1.3	.3	1.0
KERITE	.0	.0	.0	.0	.0	.0	.0	.0	.0	.0	.0	.0
OLINITE	48.3	45.0	.7	.8	.2	1.0	.1	.4	.8	1.0	.8	.9
NTMORILLONITE	57.9	31.1	1.4	1.0	.2	1.6	.3	.4	2.0	2.2	.7	1.1
AL-SILICATE	49.3	31.9	1.7	.4	.1	1.7	.0	1.0	10.6	.9	1.7	.6
AL-SILICATE	41.2	25.2	19.3	1.3	.0	4.3	1.0	2.3	.3	2.3	1.3	1.3
AL-SILICATE	46.2	35.1	1.2	1.2	.8	8.4	.7	.6	1.7	1.7	1.2	1.3
AL-SILICATE	72.3	18.8	.0	.0	.0	2.0	.0	5.9	.0	.0	.0	1.0
UMINOSILICATE	56.3	34.6	1.3	1.2	.7	1.2	.1	.5	1.0	.9	1.1	1.1
XED AL-SILICA	44.1	32.8	2.2	3.6	.4	3.4	1.4	1.0	3.4	3.0	2.4	2.6
SILICATE	.0	.0	.0	.0	.0	.0	.0	.0	.0	.0	.0	.0
SILICATE	.0	.0	.0	.0	.0	.0	.0	.0	.0	.0	.0	.0
ALUMINATE	.0	.0	.0	.0	.0	.0	.0	.0	.0	.0	.0	.0
RITE	.9	.6	22.8	.6	.3	.6	.4	.3	.3	73.0	.3	.1
RRHOTITE	2.0	1.5	36.4	1.5	1.0	1.5	.5	1.0	4.0	47.5	1.5	1.5
IDIZED PYRRHO	2.3	1.3	79.1	4.3	1.0	1.0	.7	1.3	.3	6.3	1.3	1.0
PSUM	.7	1.3	.7	1.3	.7	41.1	.7	.0	1.3	52.3	.0	.0
RITE	2.7	1.2	1.0	26.5	.3	2.5	.2	.3	1.0	34.5	29.8	.0
ATITE	.0	.0	.0	.0	.0	.0	.0	.0	.0	.0	.0	.0
AL-P	.1	40.3	1.9	2.7	21.1	25.3	.5	.7	1.4	.3	3.0	2.8
L	.0	.0	.0	.0	.0	.0	.0	.0	.0	.0	.0	.0
PSUM/BARITE	9.5	3.0	1.5	26.4	.0	7.5	.0	1.0	.0	30.3	20.9	.0
PSUM/AL-SILIC	37.0	37.0	2.5	.0	1.0	8.5	1.0	.0	2.5	6.5	3.0	1.0
-RICH	74.0	12.4	1.0	1.6	.3	1.8	.3	1.8	1.4	2.8	1.3	1.2
-RICH	9.0	3.0	2.0	1.0	1.0	77.0	3.0	.0	.0	1.0	.0	3.0
-SI RICH	30.0	.0	.0	.0	.0	61.0	3.0	.0	.0	6.0	.0	.0
KNOWN	18.2	19.0	7.9	4.1	15.7	13.9	1.7	1.0	3.8	6.6	3.7	4.4

APPENDIX C

UNDEERC/MTI Results for Black Thunder and Run-of-Mine Pittsburgh No. 8

SAMPLE DESCRIPTION ---> MTI 93-101 Pittsburgh #8 Parent Coal
SUBMITTER ---> Jones
ICC # AND FUND # ---> 48636179
RUN DATE AND TIME ---> 12 14 1993 11:58

SUMMARY OF PARAMETERS

PERCENT EPOXY USED	=	55.4
TOTAL MINERAL AREA ANALYZED AT 800.0 MAG	=	3674.9
NORMALIZED AREA ANALYZED AT 800.0 MAG	=	1516835.0
MINERAL AREA ANALYZED 240.0 MAG	=	53046.3
NORMALIZED AREA ANALYZED 240.0 MAG	=	2051502.0
TOTAL MINERAL AREA ANALYZED AT 50.0 MAG	=	853427.8
NUMBER OF FRAMES AT 800.0 MAG	=	27
NUMBER OF FRAMES AT 240.0 MAG	=	27
NUMBER OF FRAMES AT 50.0 MAG	=	45
TOTAL MINERAL WGHT % ON A COAL BASIS	=	16.355
TOTAL NUMBER OF POINTS ANALYZED	=	2780
NUMBER OF POINTS UNDER THRESHOLD	=	13

WEIGHT PERCENT ON A MINERAL BASIS

	1.0 TO 2.2	2.2 TO 4.6	4.6 TO 10.0	10.0 TO 22.0	22.0 TO 46.0	46.0 TO 100.0	TOTALS	% EXCLUDED	
QUARTZ	2.0	4.5	5.1	2.0	1.6	1.1	16.3	87.1	14.20
IRON OXIDE	.0	.0	.2	.0	.1	.2	.5	100.0	0.50
PERICLASE	.0	.0	.0	.0	.0	.0	.0	.0	
RUTILE	.1	.2	.1	.3	.0	.0	.6	72.7	0.44
ALUMINA	.0	.0	.0	.0	.0	.0	.0	.0	
CALCITE	.2	.3	.3	.5	.4	.6	2.3	98.1	2.26
DOLOMITE	.4	.5	.5	.8	.2	.6	2.9	98.7	2.86
ANKERITE	.0	.0	.0	.0	.0	.0	.0	.0	
KAOLINITE	1.6	2.9	3.1	2.8	1.3	.4	12.0	68.9	8.27
MONTMORILLONITE	.7	.8	1.1	.7	.5	.2	3.9	83.8	3.27
K AL-SILICATE	2.8	7.1	8.7	5.1	2.8	.9	27.4	83.7	22.93
FE AL-SILICATE	.2	.6	.7	.8	.2	.0	2.4	89.3	2.14
CA AL-SILICATE	.1	.0	.0	.2	.1	.0	.3	40.2	0.1
NA AL-SILICATE	.0	.0	.0	.0	.0	.0	.0	100.0	
ALUMINOSILICATE	.1	.2	.4	.6	.2	.1	1.6	93.0	1.4
MIXED AL-SILICA	.2	.1	.3	.3	.1	.0	1.1	79.7	0.8
FE SILICATE	.0	.0	.0	.0	.0	.0	.0	.0	
CA SILICATE	.1	.0	.0	.3	.1	.1	.6	96.2	0.5
CA ALUMINATE	.0	.0	.0	.0	.0	.0	.0	.0	
PYRITE	.6	2.4	2.3	1.5	2.8	2.1	11.7	76.5	8.95
PYRRHOTITE	.1	.0	.0	.0	.0	.0	.2	100.0	0.20
OXIDIZED PYRRHO	.0	.0	.0	.2	.2	.0	.5	100.0	0.5
GYPSUM	.1	.2	.3	.4	.5	.2	1.7	99.5	1.6
BARITE	.0	.0	.0	.0	.0	.0	.0	.0	
APATITE	.0	.0	.0	.0	.0	.0	.1	100.0	0.1
CA AL-P	.0	.0	.0	.0	.0	.0	.0	.0	
KCL	.0	.0	.0	.0	.0	.0	.0	.0	
GYPSUM/BARITE	.0	.0	.0	.0	.0	.0	.0	.0	
GYPSUM/AL-SILIC	.2	.1	.1	.1	.0	.0	.5	60.5	0.3
SI-RICH	.2	.4	.7	.7	.6	.2	2.9	87.2	2.5
CA-RICH	.2	.0	.1	.1	.1	.0	.5	96.4	0.4
CA-SI RICH	.0	.0	.0	.0	.0	.1	.1	100.0	0.1
UNKNOWN	1.6	1.9	2.1	2.2	1.1	1.0	9.9	84.9	8.4
TOTALS	11.6	22.1	26.0	19.5	12.9	7.8	100.0		83.7

SAMPLE DESCRIPTION ---> MTI 93-101 Pittsburgh #8 Parent Coa
SUBMITTER ---> Jones
ICC # AND FUND # ---> 48636179
RUN DATE AND TIME ---> 12 14 1993 11:58

Percent excluded as a function of particle size and phase.

	1.0 TO 2.2	2.2 TO 4.6	4.6 TO 10.0	10.0 TO 22.0	22.0 TO 46.0	46.0 TO 100.0
QUARTZ	77.0	89.6	87.3	78.4	94.3	100.0
IRON OXIDE	100.0	.0	100.0	.0	100.0	100.0
PERICLASE	.0	.0	.0	.0	.0	.0
RUTILE	100.0	.0	100.0	100.0	.0	.0
ALUMINA	.0	.0	.0	.0	.0	.0
CALCITE	86.8	100.0	95.5	100.0	100.0	100.0
DOLOMITE	97.4	100.0	94.4	100.0	100.0	100.0
ANKERITE	.0	.0	.0	.0	.0	.0
KAOLINITE	59.4	67.6	66.7	64.6	89.6	100.0
MONTMORILLONITE	85.8	87.6	61.6	100.0	95.8	100.0
K AL-SILICATE	78.8	85.3	81.3	83.8	86.2	100.0
FE AL-SILICATE	75.8	90.8	93.9	86.1	93.0	100.0
CA AL-SILICATE	100.0	.0	100.0	.0	82.7	.0
NA AL-SILICATE	.0	.0	.0	.0	100.0	.0
ALUMINOSILICATE	100.0	72.8	91.0	100.0	89.9	100.0
MIXED AL-SILICA	88.6	100.0	66.4	75.1	85.5	.0
FE SILICATE	.0	.0	.0	.0	.0	.0
CA SILICATE	57.9	.0	100.0	100.0	100.0	100.0
CA ALUMINATE	.0	.0	.0	.0	.0	.0
PYRITE	73.8	63.1	46.7	91.2	86.7	100.0
PYRRHOTITE	100.0	.0	.0	.0	100.0	.0
OXIDIZED PYRRHO	100.0	.0	100.0	100.0	100.0	.0
GYPSUM	100.0	100.0	100.0	100.0	98.3	100.0
BARITE	.0	.0	.0	.0	.0	.0
APATITE	100.0	.0	100.0	.0	100.0	.0
CA AL-P	.0	.0	.0	.0	.0	.0
KCL	.0	.0	.0	.0	.0	.0
GYPSUM/BARITE	.0	.0	.0	.0	.0	.0
GYPSUM/AL-SILIC	63.0	33.7	62.5	100.0	47.0	.0
SI-RICH	75.4	91.1	75.7	91.1	94.5	100.0
CA-RICH	88.1	100.0	100.0	100.0	100.0	100.0
CA-SI RICH	.0	.0	.0	.0	100.0	100.0
UNKNOWN	79.0	92.8	68.9	87.9	90.2	100.0

SAMPLE DESCRIPTION ---> MTI 93-101 Pittsburgh #8 Parent Coal
SUBMITTER ---> Jones
ICC # AND FUND # ---> 48636179
RUN DATE AND TIME ---> 12 14 1993 11:58

Average phase composition.
(Percent Relative X-ray Intensity)

	SI	AL	FE	TI	P	CA	MG	NA	K	S	BA	CL
QUARTZ	95.1	.5	.6	.5	.0	.5	.2	.2	.8	.6	.5	.4
IRON OXIDE	2.1	1.5	87.7	.8	.6	.1	.6	.6	2.1	2.0	1.4	.4
PERICLASE	.0	.0	.0	.0	.0	.0	.0	.0	.0	.0	.0	.0
RUTILE	3.5	2.0	.8	46.3	.8	.2	.2	.2	1.0	.2	44.1	.8
ALUMINA	.0	.0	.0	.0	.0	.0	.0	.0	.0	.0	.0	.0
CALCITE	1.6	1.3	.9	.6	.5	90.7	.9	.3	.6	1.1	.7	.8
DOLOMITE	3.6	.6	1.8	.8	.7	72.7	15.9	.0	.9	1.2	.8	1.0
ANKERITE	.0	.0	.0	.0	.0	.0	.0	.0	.0	.0	.0	.0
KAOLINITE	49.8	41.8	1.3	.9	.1	.7	.1	.3	2.1	1.3	.7	.8
MONTMORILLONITE	57.0	31.3	1.8	1.2	.1	1.0	.2	.3	3.5	1.8	.9	.8
K AL-SILICATE	52.6	29.8	2.0	1.0	.1	1.0	.3	.3	10.0	1.3	.9	.7
FE AL-SILICATE	45.1	26.9	15.9	1.2	.1	1.1	4.0	.1	2.8	1.4	.9	.4
CA AL-SILICATE	44.2	26.6	1.2	2.1	1.1	16.4	.5	.9	3.5	2.0	1.1	.4
NA AL-SILICATE	74.0	19.0	.0	.0	.0	.0	.0	7.0	.0	.0	.0	.0
ALUMINOSILICATE	65.2	25.0	1.4	.9	.1	.6	.2	.3	3.5	1.2	1.1	.6
MIXED AL-SILICA	51.1	26.4	6.2	1.7	.0	1.7	1.0	.3	7.5	2.0	1.4	.6
FE SILICATE	.0	.0	.0	.0	.0	.0	.0	.0	.0	.0	.0	.0
CA SILICATE	47.0	1.1	1.5	.4	.3	42.3	3.9	.4	.9	1.4	.5	.3
CA ALUMINATE	.0	.0	.0	.0	.0	.0	.0	.0	.0	.0	.0	.0
PYRITE	1.0	.8	22.2	.5	.3	.4	.2	.1	.4	73.6	.4	.0
PYRRHOTITE	2.6	1.8	40.1	1.3	.9	2.0	.9	1.0	5.0	44.4	.1	.0
OXIDIZED PYRRHO	1.4	1.0	74.0	2.3	.5	1.6	.3	.5	1.1	15.4	.8	1.1
GYPSUM	1.4	1.0	.9	.5	.6	43.8	.3	.3	.5	50.2	.6	.0
BARITE	.0	.0	.0	.0	.0	.0	.0	.0	.0	.0	.0	.0
APATITE	.0	3.3	1.8	.3	24.5	66.0	.8	.5	2.3	.0	.5	.3
CA AL-P	.0	.0	.0	.0	.0	.0	.0	.0	.0	.0	.0	.0
KCL	.0	.0	.0	.0	.0	.0	.0	.0	.0	.0	.0	.0
GYPSUM/BARITE	.0	.0	.0	.0	.0	.0	.0	.0	.0	.0	.0	.0
GYPSUM/AL-SILIC	35.2	17.8	2.7	1.6	.4	18.5	.6	.4	3.6	17.9	.7	.6
SI-RICH	73.1	13.8	1.9	.9	.1	1.0	.2	.8	4.9	1.3	1.0	.9
CA-RICH	11.6	2.7	2.8	.9	1.2	72.0	2.9	.5	1.9	2.3	.8	.5
CA-SI RICH	43.9	10.1	2.5	2.0	.0	37.4	.0	1.5	1.5	.5	.5	.0
UNKNOWN	44.9	13.8	6.9	2.8	1.2	11.7	1.5	1.7	5.2	6.7	2.7	1.0

AREA IN EACH SIZE RANGE

	1.0 TO 2.2	2.2 TO 4.6	4.6 TO 10.0	10.0 TO 22.0	22.0 TO 46.0	46.0 TO 100.0	TOTA
QUARTZ	230.8	508.9	6221.0	2423.9	76198.9	50571.5	13615
IRON OXIDE	1.4	.0	101.2	.0	1791.6	5839.6	773
PERICLASE	.0	.0	.0	.0	.0	.0	
RUTILE	4.1	9.6	47.8	179.3	.0	.0	24
ALUMINA	.0	.0	.0	.0	.0	.0	
CALCITE	24.9	27.7	384.9	540.6	18944.6	28043.6	4796
DOLOMITE	43.3	50.7	546.9	871.5	9000.2	26048.0	3656
ANKERITE	.0	.0	.0	.0	.0	.0	
KAOLINITE	183.6	331.4	3759.3	3393.0	59475.0	16965.8	8410
MONTMORILLONITE	80.0	101.9	1393.6	860.6	25167.0	7965.6	3556
K AL-SILICATE	324.6	820.9	10849.8	6327.9	134037.9	43882.3	19624
FE AL-SILICATE	19.9	60.8	752.5	882.8	8110.7	1938.8	1176
CA AL-SILICATE	6.0	.0	24.2	200.5	2557.1	.0	278
NA AL-SILICATE	.0	.0	.0	.0	729.7	.0	72
ALUMINOSILICATE	12.5	20.4	516.4	705.4	10688.8	2437.2	1438
MIXED AL-SILICA	28.0	15.5	373.3	375.1	4287.7	.0	507
FE SILICATE	.0	.0	.0	.0	.0	.0	
CA SILICATE	6.0	.0	26.2	348.7	5589.4	4466.5	1043
CA ALUMINATE	.0	.0	.0	.0	.0	.0	
PYRITE	39.2	143.8	1458.6	991.2	70411.9	52933.0	12597
PYRRHOTITE	8.6	.0	.0	.0	1232.3	.0	124
OXIDIZED PYRRHO	2.8	.0	18.4	141.9	4527.5	.0	469
GYPSUM	15.3	23.0	337.6	530.4	23749.6	12144.0	3679
BARITE	.0	.0	.0	.0	.0	.0	
APATITE	2.0	.0	44.9	.0	1919.9	.0	196
CA AL-P	.0	.0	.0	.0	.0	.0	
KCL	.0	.0	.0	.0	.0	.0	
GYPSUM/BARITE	.0	.0	.0	.0	.0	.0	
GYPSUM/AL-SILIC	19.6	12.7	149.1	83.6	1301.7	.0	156
SI-RICH	24.4	49.5	891.0	908.3	28110.9	7801.6	3778
CA-RICH	17.9	5.2	68.6	163.1	3307.8	2334.2	589
CA-SI RICH	.0	.0	.0	.0	1242.8	3335.1	457
UNKNOWN	183.6	214.6	2462.6	2690.3	49259.3	45078.8	9988
TOTALS	1278.2	2396.7	30428.2	22618.2	541642.2	311785.6	91014

DISTRIBUTION BY % OF EACH MINERAL PHASE

	1.0 TO 2.2	2.2 TO 4.6	4.6 TO 10.0	10.0 TO 22.0	22.0 TO 46.0	46.0 TO 100.0	TOTA
QUARTZ	12.4	27.4	31.4	12.2	9.9	6.6	100
IRON OXIDE	4.8	.0	32.3	.0	14.8	48.1	100
PERICLASE	.0	.0	.0	.0	.0	.0	
RUTILE	11.8	27.3	12.8	48.0	.0	.0	100
ALUMINA	.0	.0	.0	.0	.0	.0	
CALCITE	9.8	10.9	14.2	20.0	18.1	26.8	100
DOLOMITE	13.9	16.3	16.4	26.2	7.0	20.2	100
ANKERITE	.0	.0	.0	.0	.0	.0	
KAOLINITE	13.4	24.2	25.7	23.2	10.5	3.0	100
MONTMORILLONITE	16.9	21.5	27.6	17.0	12.9	4.1	100
K AL-SILICATE	10.2	25.8	31.9	18.6	10.2	3.3	100
FE AL-SILICATE	7.7	23.5	27.3	32.0	7.6	1.8	100
CA AL-SILICATE	18.0	.0	6.8	56.6	18.6	.0	100
NA AL-SILICATE	.0	.0	.0	.0	100.0	.0	100
ALUMINOSILICATE	7.0	11.4	27.0	36.9	14.4	3.3	100
MIXED AL-SILICA	22.6	12.5	28.2	28.4	8.4	.0	100
FE SILICATE	.0	.0	.0	.0	.0	.0	
CA SILICATE	9.1	.0	3.7	49.9	20.7	16.5	100
CA ALUMINATE	.0	.0	.0	.0	.0	.0	
PYRITE	5.5	20.2	19.2	13.1	24.0	18.0	100
PYRRHOTITE	74.2	.0	.0	.0	25.8	.0	100
OXIDIZED PYRRHO	9.6	.0	6.0	46.2	38.1	.0	100
GYPSUM	7.4	11.1	15.3	24.0	27.8	14.2	100
BARITE	.0	.0	.0	.0	.0	.0	
APATITE	18.0	.0	38.9	.0	43.0	.0	100
CA AL-P	.0	.0	.0	.0	.0	.0	
KCL	.0	.0	.0	.0	.0	.0	
GYPSUM/BARITE	.0	.0	.0	.0	.0	.0	
GYPSUM/AL-SILIC	34.2	22.2	24.4	13.7	5.5	.0	100
SI-RICH	7.4	15.0	25.3	25.8	20.7	5.7	100
CA-RICH	30.5	8.9	11.0	26.1	13.7	9.7	100
CA-SI RICH	.0	.0	.0	.0	27.1	72.9	100
UNKNOWN	16.5	19.3	20.8	22.7	10.8	9.8	100
TOTALS	11.9	22.4	26.6	19.8	12.2	7.1	100

NUMBER OF PARTICLES IN EACH SIZE RANGE

	1.0 TO 2.2	2.2 TO 4.6	4.6 TO 10.0	10.0 TO 22.0	22.0 TO 46.0	46.0 TO 100.0	TOT
QUARTZ	108.0	67.0	182.0	18.0	109.0	16.0	50
IRON OXIDE	1.0	.0	2.0	.0	4.0	1.0	
PERICLASE	.0	.0	.0	.0	.0	.0	
RUTILE	3.0	1.0	1.0	1.0	.0	.0	
ALUMINA	.0	.0	.0	.0	.0	.0	
CALCITE	13.0	4.0	17.0	3.0	25.0	7.0	6
DOLOMITE	22.0	7.0	17.0	5.0	10.0	8.0	6
ANKERITE	.0	.0	.0	.0	.0	.0	
KAOLINITE	81.0	41.0	112.0	21.0	74.0	5.0	33
MONTMORILLONITE	39.0	13.0	36.0	5.0	30.0	3.0	12
K AL-SILICATE	151.0	97.0	309.0	48.0	181.0	16.0	80
FE AL-SILICATE	10.0	6.0	20.0	6.0	13.0	1.0	5
CA AL-SILICATE	3.0	.0	1.0	1.0	3.0	.0	
NA AL-SILICATE	.0	.0	.0	.0	1.0	.0	
ALUMINOSILICATE	5.0	3.0	13.0	3.0	14.0	1.0	3
MIXED AL-SILICA	17.0	3.0	13.0	3.0	6.0	.0	4
FE SILICATE	.0	.0	.0	.0	.0	.0	
CA SILICATE	2.0	.0	1.0	1.0	6.0	1.0	1
CA ALUMINATE	.0	.0	.0	.0	.0	.0	
PYRITE	22.0	17.0	34.0	7.0	97.0	17.0	19
PYRRHOTITE	6.0	.0	.0	.0	2.0	.0	
OXIDIZED PYRRHO	1.0	.0	1.0	1.0	5.0	.0	
GYPSUM	7.0	2.0	9.0	4.0	30.0	4.0	5
BARITE	.0	.0	.0	.0	.0	.0	
APATITE	1.0	.0	1.0	.0	2.0	.0	
CA AL-P	.0	.0	.0	.0	.0	.0	
KCL	.0	.0	.0	.0	.0	.0	
GYPSUM/BARITE	.0	.0	.0	.0	.0	.0	
GYPSUM/AL-SILIC	9.0	3.0	4.0	1.0	2.0	.0	1
SI-RICH	12.0	6.0	24.0	8.0	41.0	3.0	9
CA-RICH	9.0	1.0	3.0	1.0	6.0	1.0	2
CA-SI RICH	.0	.0	.0	.0	1.0	1.0	
UNKNOWN	101.0	27.0	74.0	16.0	74.0	11.0	30
TOTALS	623.0	298.0	874.0	153.0	736.0	96.0	278